Claudio Smuclovisky
Editor

Coronary Artery CTA

A Case-Based Atlas

Second Edition

Springer

Coronary Artery CTA

Claudio Smuclovisky
Editor

Coronary Artery CTA

A Case-Based Atlas

Second Edition

Springer

Editor
Claudio Smuclovisky
Department of Radiology
Holy Cross Hospital
South Florida Medical Imaging
Cardiovascular Institute
Fort Lauderdale, FL
USA

ISBN 978-3-319-66986-1 ISBN 978-3-319-66988-5 (eBook)
https://doi.org/10.1007/978-3-319-66988-5

Library of Congress Control Number: 2017964482

Printed on acid-free paper

This Springer imprint is published by Springer Nature
The registered company is Springer International Publishing AG
The registered company address is: Gewerbestrasse 11, 6330 Cham, Switzerland

Preface

Since the publication of the first edition, there has been continued progression in the field of cardiac CT angiography (CCTA). The CT hardware and software currently has improved the image quality with less radiation and faster workflows. Hundreds of peer-reviewed publications solidly support the use of CCTA in many clinical situations.

The book has expanded in the second edition with many outstanding colleagues contributing additional new chapters:

Drs. Alain Vlassenbroek, Mani Vembar, and Michael Grass: Innovations in Cardiac CTA
Dr. Dianna Bardo: Pediatric CCTA
Drs. Christopher Brown and Charles White: CCTA Extracardiac Findings
Dr. Constantino Peña: CCTA in the Emergency Department
Drs. Lohendran Baskaran, Christopher Zarins, and James K. Min: CT Fractional Flow Reserve (CT-FFR)
Dr. Tariq Hameed: CT for TAVR Planning
Dr. Alex Llanos: A Cardiac Interventionist Perspective to CCTA
Dr. Daniel Weitz: CCTA for Electrophysiology (EP) Planning

The chapters on coronary anatomy, coronary artery disease, coronary intervention, and surgical revascularization have been revised and updated, and additional interesting cases for review have been added to help the reader.

As in the first edition, this book has been created to be an easy to review CCTA atlas with many "Pearls and Pitfalls" in order to help the reader expand their knowledge.

In summary, this second edition is expected to be an excellent reference guide for radiology and cardiology residents, fellows, and practitioners.

Fort Lauderdale, FL, USA — Claudio Smuclovisky, MD

Acknowledgements

I am deeply grateful to all the outstanding physicians and Ph.D's who have taken the time from their busy schedule to contribute chapters to the book and for sharing their expertise.

I would like to acknowledge and thank Dr. John J. Lee, an internal medicine resident from the University of Miami-Holy Cross Hospital in Fort Lauderdale, Florida, for his dedication to this project. In his free time, Dr. Lee spent countless hours revising, correcting, formatting new cases, and reviewing the literature regarding the chapters of coronary anatomy, CAD, PCI, and CABG. His tireless efforts expedited the entire project.

Dr. Lee also worked closely with Drs. Llanos and Weitz in the development of two new chapters. He also stayed in close contact (stalking) with the chapter contributors in order to coordinate the review and submission to our editors.

I would also like to thank the outstanding people at Springer, especially Ms. Janet Foltin and Ms. Jennifer Schneider, who made this book possible.

Claudio Smuclovisky, MD

Contents

About the Editor and Contributors

Editor

Claudio Smuclovisky, MD, FACC, FSCCT Department of Radiology, Holy Cross Hospital, South Florida Medical Imaging Cardiovascular Institute, Fort Lauderdale, FL, USA

Contributors

Rishi Anand, MD Electrophysiology Lab, Department of Cardiology, Holy Cross Hospital, Fort Lauderdale, FL, USA

Dianna M.E. Bardo, MD, FSCCT, FNASCI Department of Radiology, Phoenix Children's Hospital, Phoenix, AZ, USA

Lohendran Baskaran, MBBS, BSc Department of Radiology, Dalio Institute of Cardiovascular Imaging, New York-Presbyterian Hospital and Weill Cornell Medicine, New York, NY, USA

National Heart Centre, Singapore, Singapore

Christopher Brown, MD Department of Radiology, Hahnemann University Hospital, Drexel University School of Medicine, Philadelphia, PA, USA

Ricardo C. Cury, MD Department of Radiology, Miami Cardiac and Vascular Institute, Baptist Health of South Florida, Miami, FL, USA

Michael Grass, Ph.D Philips Research, Hamburg, Germany

Tariq A. Hameed, MD, FCPS Indiana University School of Medicine and Indiana University Health, Indianapolis, IN, USA

John J. Lee, MD Department of Medicine, University of Miami at Holy Cross Hospital, Fort Lauderdale, FL, USA

David Lehmkuhl, BS Herbert Wertheim College of Medicine, Florida International University, Miami, FL, USA

Alexander Llanos, MD Department of Cardiology, Holy Cross Hospital, Jim Morgan Heart and Vascular Research Institute, Fort Lauderdale, FL, USA

James K. Min, MD Department of Radiology, Dalio Institute of Cardiovascular Imaging, New York-Presbyterian Hospital and Weill Cornell Medicine, New York, NY, USA

Igor F. Palacios, MD Department of Medicine and Cardiology, Massachusetts General Hospital, Boston, MA, USA

Constantino S. Pena, MD Miami Cardiac and Vascular Institute, Baptist Hospital, Miami, FL, USA

Mani Vembar, MS Department of CT Clinical Science, Philips Healthcare, Cleveland, OH, USA

Alain Vlassenbroek, PhD Department of CT Clinical Science, Philips Healthcare, Brussels, Belgium

Daniel Weitz, MD Electrophysiology Lab, Department of Cardiology, Holy Cross Hospital, Fort Lauderdale, FL, USA

Charles S. White, MD Department of Diagnostic Radiology, University of Maryland, Baltimore, MD, USA

Christopher K. Zarins, MD HeartFlow, Inc., Redwood City, CA, USA

Introduction

1

Claudio Smuclovisky

"More powerful than the might of all the armies on Earth is an idea whose time has come." (On résiste à l'invasion des armées; on ne résiste pas à l'invasion des idées.)
Victor Hugo-1852

Cardiac CT angiography (CCTA) has become a broadly accepted diagnostic modality in cardiac imaging by both the medical community and payers. There is an abundance of published peer review articles in worldwide journals establishing the clinical value of CCTA in the evaluation of congenital and acquired cardiac diseases.

The manufacturers of CT hardware and software have made many significant improvements in simplifying patient workflow, acquisition, postprocessing, and interpretation of images. CCTAs can now be acquired in 1–4 heartbeats with very short breath holds. Single beat whole cardiac imaging is available as well as sub-millisiviert dose scans.

3-D workstations have become faster, more automated and easier to use for image review, coronary extraction and analysis. Once the CCTA is acquired the data can automatically be uploaded to a computer server for pre-processing and thin-client remote access from a network terminal.

Image quality continues to improve through innovations in both hardware and software.

Iterative reconstruction (IR) technology that can virtually eliminate noise on the images is now available and should be a strong consideration in the upgrade or purchase of a CT scanner. The major advantage of IR is that it improves both low and high contrast, resulting in images with less noise, artifact, and better spatial resolution.

It is remarkable that in less than a decade CCTA radiation dose has been dramatically reduced mainly by the combination of using lower Kv technique, axial-prospective acquisition and IR. Also, improved CT gantry (speed), x-ray tube, collimation and detector design/sensitivity. In our CT department, when compared to the various CTs performed, CCTAs went from being the highest radiation dose study to now among the lowest. It is now possible to acquire a CCTA with the equivalent radiation dose similar to a two-view chest radiograph. This second edition includes a new chapter on "Innovations in Cardiac Multi-Slice Computed Tomography" (Chap. 2).

CT myocardial perfusion and fractional flow reserve (FFR-ct) is not yet widely used but holds great promise in evaluating myocardial ischemia and to further help determine the need for revascularization.

A key to a successful CCTA program is to be able to integrate CCTA efficiently into the average busy CT schedule in a timely manner similar to any other CT angiogram and in which greater than 95% of the studies are of high diagnostic quality. With experience, the review and interpretation of a study should, in the majority of cases, take just a few brief minutes.

Although there is undeniable broad data supporting the use of CCTA in many clinical situations, no previous imaging technology has ever

C. Smuclovisky, MD, FACC, FSCCT
Department of Radiology, Holy Cross Hospital,
South Florida Medical Imaging Cardiovascular Institute,
Fort Lauderdale, FL, USA
e-mail: smuclovisky@gmail.com

C. Smuclovisky (ed.), *Coronary Artery CTA*, https://doi.org/10.1007/978-3-319-66988-5_1

been under such criticism and skepticism. Skeptics continue to argue that CCTA does not add clinical value, has excessive false positives, provides no myocardial physiology information, leads to additional testing, increases costs and delivers high radiation. Although the body of literature, particularly in the last 5 years, largely does not support most of the criticism, I feel compelled to answer these questions.

The high sensitivity and negative predictive value (95–99%) of CCTA does indeed add clinical value in ruling in or out coronary artery disease as the possible cause of chest pain, particularly in the emergency room setting [1]. The specificity and positive predictive value (60–80%), especially in calcified stenotic appearing coronary plaques, is currently the Achilles heel of CCTA. This is also true for invasive coronary angiography where studies (FAME Trial) [2] have shown that up to 20% of 70–90% high-grade stenotic plaques by quantitative coronary angiography (QCA) were not flow limiting by fractional flow reserve (FFR). It is well known that calcified plaques on CCTA cause blooming artifact that overestimate the degree of luminal stenosis, and there is no shame in reporting these plaques and/or coronary segments as "indeterminate" to cause high-grade stenosis. Intervention, both catheter based and surgery, focuses on revascularizing myocardial ischemic segments. Myocardial ischemia at a cellular level is known to be multifactorial with coronary stenosis being among one of several causes [3, 4].

CCTA can establish the presence of coronary artery disease and help in the risk stratification of the patient. The Courage Trial [5, 6] published in 2007 in patients with stable angina showed similar long-term results (cardiac events and death) in patients treated with optimal medical therapy (OMT) versus OMT + percutaneous coronary intervention (PCI).

In terms of CCTA not providing myocardial physiology information, FFR-ct [7] (HeartFlow, Inc.) is now FDA approved and holds great promise in the demonstration of ischemic myocardial segments on a CCTA. In Chap. 7, James Min and colleagues highlight the clinical value of FFR-ct. Myocardial perfusion is also now available and can be routinely performed [8].

Although further research is needed in patients with a low-intermediate likelihood of coronary artery disease, CCTA is a more accurate and efficient alternative noninvasive frontline diagnostic test than exercise ECG and SPECT. The increased downstream test utilization and subsequent revascularization following a coronary CTA strategy may allow for decreased myocardial infarction and mortality [9].

The argument of excessive radiation with CCTA can no longer be argued since studies can now be acquired with sub-millisiviert doses with the use of lower Kv techniques and iterative reconstruction. When compared with a Tc-99m myocardial perfusion scan with a dose of 15–25 mSv, the CCTA dose is in the range of 90% less radiation. I cannot recall reading much about the worries and concerns about the radiation from nuclear studies that are not infrequently performed yearly on patients.

On a personal note, it is interesting to reveal that my physician colleagues who have been the most vocal against the use of CCTA have been among the fastest to arrive at my office for a CCTA when "they" or close family members have any symptoms of chest pain or concern of having obstructive coronary artery disease. These even include doctors with nuclear cameras in their office! The reader can reach their own conclusions, but in my mind this is the most powerful testament of the value of CCTA.

Although many robust indications for CCTA are appropriate, such as screening patients that present to the emergency department with chest pain, it is important to remember that coronary artery atherosclerosis starts in the first or second decade of life. My main focus is cardiovascular disease prevention. An adult who presents with symptoms of coronary artery disease has undoubtedly had the disease for decades. A common first symptom of heart disease is sudden death, which occurs in one out of four patients. About half of the patients do not survive the first myocardial infarction (MI). The human tragedy and costs worldwide from cardiovascular diseases continues to rise and is staggering. There is no question that the best solution is "prevention" and I am convinced that cardiac CT can play a significant role.

Conventional clinical risk assessment (Framingham) is largely inaccurate and stratifies incorrectly a large group of patients particularly in the low to intermediate category, which is where a large percent of cardiac events occur. A less costly calcium score has been shown to be an effective test in risk stratification. We know that risk modification and pills work to reduce cardiovascular events. Thus, it is plain common sense to identify those patients at risk as early as possible in order to have a positive impact on morbidity and mortality outcomes.

Another important goal is to help cardiologists/interventionists and cardiovascular surgeons make better clinical and surgical decisions in the care of their patients. First, it has been published [10] in a large multicenter trial that up to 60% of patients with stable angina undergoing coronary angiography have either no disease or mild non-obstructing disease. With almost 100% negative predictive value of CCTA, the majority of the patients could have avoided an invasive procedure. CCTA can also help the interventionist focus his practice more on performing intervention than diagnostic work. If we look today at peripheral vascular intervention, most of the procedures involve intervention and not diagnostic angiography. CT or MRI angiography is performed prior to diagnose obstructions and aneurysms resulting in the intervention being preplanned. With the use of CCTA, cardiac interventionists now have the opportunity to do the same.

Second, the coronary angiogram (CA) is essentially a luminogram that does not show the true extent of CAD. I have seen many CCTA studies with advanced atherosclerotic disease in which the coronary angiogram is reported as having "clean coronaries." We have known for decades that nonstenotic "soft" plaques in the wall (positive wall remodeling) can rapidly grow, become stenotic, and in a relative short period of time rupture, causing an acute coronary event [11].

Third, when a CA is performed, the cardiologist may be essentially "guessing" the true extent of CAD. Also, there exists "blind spots" on the CA that may be very difficult to identify on standard projections, particularly short segment stenosis in the ostium of the left main, left anterior descending and right coronary arteries. CCTA can easily identify these stenotic areas and, if needed, provide the appropriate X-ray tube angle for CA visualization of the stenosis, thus avoiding additional acquisitions or runs.

Fourth, CCTA can demonstrate the location, length, and type of plaque (calcified, noncalcified, mixed) in the artery, which provides additional information for planning treatment.

Fifth, CCTA can demonstrate proximal critical coronary stenosis that may require catheter or surgical intervention as soon as possible. This is most noticeable in patients who present to the emergency department with chest pain and who were determined low to intermediate risk.

I have been teaching cardiac CT courses level 1, 2, and 3 for 10 years and about half of the participants are cardiologists. We show a wide variety of cases where CCTA correlates perfectly with CA and where it does not correlate: what I call "the good, the bad and the ugly." What I emphasize most is to look at the CCTA to determine how to use this test as a tool to make better clinical decisions.

It is important to emphasize that CCTA is *not* only a coronary CT but rather a cardiac CT. It is a mistake to only focus on the coronary anatomy. The field of view on the study includes the lungs, pleura, pericardium, myocardium, cardiac valves, pulmonary vessels, aorta, other mediastinal structures bones, chest wall, and infradiaphragmatic organs. What I tell students is that CCTA is a high-resolution accurate study as long as it is interpreted correctly. There may be many different findings on the CCTA that may explain the patient's symptoms: pulmonary embolism, cancer, cardiomyopathy, effusions both pleural and pericardial, aortic aneurysm/dissection, and too many others to list here. CAD is one of the many causes of chest pain.

In order to serve the best interests of patients, a cardiac CT specialist is required to be proficient in the proper interpretation of all the structures included in the field of view.

References

1. Hi L, Gatsonis C, Snyder B, et al. Ct angiography for safe discharge of patients with possible acute coronary syndromes. N Engl J Med. 2012;366:1393–403.

2. Tonino PA, Fearon WF, De Bruyne B, et al. Angiographic versus functional severity of coronary artery stenoses in the FAME study fractional flow reserve versus angiography in multivessel evaluation. J Am Coll Cardiol. 2010;55(25):2816–21.
3. Arbab-Zadeh A, Fuster V. The myth of the "vulnerable plaque": transitioning from a focus on individual lesions to atherosclerotic disease burden for coronary artery disease risk assessment. J Am Coll Cardiol. 2015;65(8):846–55.
4. Marzilli M, Merz CN, Boden WE, et al. Obstructive coronary atherosclerosis and ischemic heart disease: an elusive link! J Am Coll Cardiol. 2012;60(11):951–6.
5. Boden WE, O'rourke RA, Teo KK, et al. The evolving pattern of symptomatic coronary artery disease in the United States and Canada: baseline characteristics of the Clinical Outcomes Utilizing Revascularization and Aggressive Drug Evaluation (COURAGE) trial. Am J Cardiol. 2007;99(2):208–12.
6. Boden WE, O'Rourke RA, Teo KK, et al. COURAGE Trial Research Group Optimal medical therapy with or without PCI for stable coronary disease. N Engl J Med. 2007;356(15):1503–16.
7. Nørgaard BL, Leipsic J, Gaur S, Seneviratne S, et al. NXT Trial Study Group. Diagnostic performance of noninvasive fractional flow reserve derived from coronary computed tomography angiography in suspected coronary artery disease: the NXT trial (Analysis of Coronary Blood Flow Using CT Angiography: Next Steps). J Am Coll Cardiol. 2014;63(12):1145–55.
8. Kühl JT, George RT, Mehra VC, et al. Endocardial-epicardial distribution of myocardial perfusion reserve assessed by multidetector computed tomography in symptomatic patients without significant coronary artery disease: insights from the CORE320 multicentre study. Eur Heart J Cardiovasc Imaging. 2016;17(7):779–87.
9. Nielsen LH, Ortner N, et al. The diagnostic accuracy and outcomes after coronary computed tomography angiography vs. conventional functional testing in patients with stable angina pectoris: a systematic review and meta-analysis. Eur Heart J Cardiovasc Imaging. 2014;15(9):961–71.
10. Patel MR, Peterson ED, Dai D, Brennan JM, et al. Low diagnostic yield of elective coronary angiography. N Engl J Med. 2010;362(10):886–95.
11. Puri R, Nicholls SJ, Ellis SG, et al. High-risk coronary atheroma: the interplay between ischemia, plaque burden, and disease progression. J Am Coll Cardiol. 2014;63(12):1134–40.

Innovations in Cardiac CTA

2

Alain Vlassenbroek, Mani Vembar,
and Michael Grass

2.1 Introduction

Coronary artery disease (CAD) is one of the leading causes of death in the western world and more than half the people who die from a cardiac event have no previous symptoms. Hence, there is a clinical need for tools that enable an early and accurate diagnosis of CAD. Cardiac computed tomography (CT) angiography provides a comprehensive anatomic evaluation of the heart. Cardiac anatomy and function, coronary plaque, and coronary stenoses can be assessed in a single study that is acquired within a short breath hold over a few heart beats.

The 4-slice CT scanners started an unprecedented technological evolution in 1998 but it is only with the advent of the 64-slice CT systems in 2004 that the realm of noninvasive coronary imaging became an integrative part of the clinical routine. Although image quality and robustness had significantly improved compared to the early days, several challenges still remained, such as radiation dose and limited low contrast resolution, motion artifacts, and the evaluation of coronary segments with severe calcifications or coronary stents. Today, reduction of radiation exposure is still at the forefront of the developments. With the introduction of large coverage multi-slice CT scanners, prospectively ECG-triggered step-and-shoot acquisition has become a robust scanning mode, with effective doses ranging from 2.7 to 4.5 mSv [1]. Further significant dose reductions have been achieved recently with the introduction of advanced iterative reconstruction techniques enabling effective patient doses going below 1.0 mSv with improvements in spatial and contrast resolutions [2]. With an increased spatial resolution, the evaluation of calcified plaques and stents can be significantly improved due to the reduced blooming artifacts. An improved low contrast enables a better intra-plaque attenuation assessment and may help to better identify the plaques with the highest risk to rupture. In addition, new developments have recently taken place in the field of cardiac CT image reconstructions to improve the temporal resolution and the image quality. Motion compensated cardiac reconstruction incorporates the knowledge of the calculated motion vector field within the iterative reconstruction process to reduce the motion artifacts [3–5].

A. Vlassenbroek, PhD (✉)
Department of CT Clinical Science,
Philips Healthcare, 80 Rue des Deux Gares,
1070 Brussels, Belgium
e-mail: alain.vlassenbroek@philips.com

M. Vembar, MS
Department of CT Clinical Science, Philips Healthcare,
595 Miner Road, Cleveland, OH 44143, USA
e-mail: mani.vembar@philips.com

M. Grass, Ph.D
Philips Research, Röntgenstraße 24-26,
22335 Hamburg, Germany
e-mail: michael.grass@philips.com

C. Smuclovisky (ed.), *Coronary Artery CTA*, https://doi.org/10.1007/978-3-319-66988-5_2

With all these significant improvements in CT technology over the past 17 years, cardiac computed tomography angiography (cardiac CTA) has become the preferred noninvasive modality for the detection and rule-out of coronary artery disease (CAD), with various multicenter studies demonstrating robust diagnostic accuracy and negative predictive value (NPV) [6–8]. However, the hemodynamic significance of CAD is unknown [9]. New advanced computational developments including flow simulations and noninvasive fractional flow reserve (FFR-CT) assessment have recently been introduced and are currently evaluated in clinical studies. The promising results, combined with the new developments in first-pass and dynamic CT myocardial perfusion imaging indicate that multi-slice CT (MSCT) has a great potential to provide comprehensive information regarding the hemodynamic relevance of coronary artery stenosis. Finally, further improvements in myocardial perfusion, delayed enhancement imaging, and vulnerable plaque detection might be anticipated with the new spectral MSCT detectors enabling dual-energy imaging.

Experimental CT designs and applications which were proposed a few years ago are now part of the current clinical reality. So we can anticipate that the current innovations in cardiac CT could facilitate early, and comprehensive diagnosis of cardiovascular disease in the near future.

2.2 Cardiac CT: Requirements and CT Technology

Noninvasive cardiac imaging is an extremely demanding field and presents a number of clinical challenges. The most critical and challenging requirement for successful cardiac CT imaging is the minimization of motion artifacts because the coronary arteries undergo complex 3D motion during the cardiac cycle. These arteries are extremely small, with diameters ranging from 5 mm in the proximal sections to less than 1 mm distally. As a consequence, excellent spatial and temporal resolution requirements are prerequisites for CT scanners to assess the coronary arteries. In addition, they must have adequate and uniform contrast enhancement for proper visualization. As the scans are performed under a single breath-hold condition, the acquisition has to be completed in the shortest possible time to avoid any respiratory motion artifacts. Patients are exposed to radiation dose and hence dose-reduction techniques need to be employed. The large volume of image data generated also presents the user with visualization and workflow challenges. Lastly, the presence of plaques poses unique challenges. Calcified plaques often make it difficult to visualize the lumen whereas noncalcified plaques demand superior spatial and temporal resolution. Cardiac imaging is thus a demanding application for CT requiring multiparameter optimization.

In the early days, CT scanners were limited to scanning the patients in axial (or "step-and-shoot") mode with a one-dimensional detection system and with a patient translation occurring in sequential steps between the scans. A complete set of X-ray attenuation data was acquired during an X-ray tube rotation around the stationary patient, and these projections were used to reconstruct cross-sectional images of the patient anatomy. The patient table was then subsequently positioned to the next axial location and the data acquisition repeated. In this fan-beam CT configuration, axial slices of the object were sequentially acquired and reconstructed using a well-known mathematical technique (2D filtered back projection (2D-FBP)) [10] and subsequently assembled to build the volume. The introduction of spiral scanning in 1990 [11, 12] enabled continuous data acquisition with simultaneous patient translation at a constant speed. Spiral scanning provided volumetric acquisitions and enabled the reconstruction of overlapping slices leading to high-resolution imaging without the need to increase the patient dose. The time to cover a

volume of interest was minimized compared to the axial mode, reducing acquisition and examination times as well as image artifacts or misregistrations caused by the patient motion between the steps. Since then, CT scanners have been subject to tremendous technological innovations. The most important improvement was the stepwise replacement of the one-dimensional detection system, which consisted of one single row of detectors, to two-dimensional large area detectors with a detector array consisting of more than a single row of detectors. A dual-slice CT scanner with two rows of detectors (CT Twin, Elscint Haifa Israel) had already been on the market since 1992 when multi-slice CT (MSCT) scanners with four rows and 0.5 s gantry rotation times were introduced in 1998 by several manufacturers. The technological innovations brought by the 4-slice scanners subsequently paved the way for applications in cardiac imaging [13]. Simultaneous acquisition of electrocardiogram (ECG) data during spiral CT scanning enabled the development of acquisition and reconstruction techniques specific to cardiac imaging. Synchronizing the location of the peak of the QRS complex in the ECG with the projection data allowed the reconstruction and visualization of anatomy at various phases of the cardiac cycle, thus making functional imaging possible. Breath-hold times of 40 s needed to cover the cardiac anatomy, however, still posed a challenge, causing many patient groups to be excluded. To reduce the scan duration and mitigate these breath-hold limitations, the number of simultaneously acquired slices had to be increased. This meant the start of the "slice race" which became a phenomenon in the early 2000s and the use of wider detector arrays allowing for faster scanning and for a more effective use of the available X-ray flux due to the increased cone angle. The increase of the number of detector rows was not without consequence. With 2D area detectors and cone-beam geometry, a 3D volume had to be reconstructed from 2D projection data, which was referred to as "cone-beam reconstruction" [14]. It resulted in a paradigm shift from two-dimensional (2D-FBP) to volumetric reconstruction approaches (3D-FBP) which required a considerable increase in the computer power of the commercially installed scanners to reconstruct the clinical images in an acceptable time. The 3D reconstruction techniques were introduced in 2001 as the basic image reconstruction technique for the 16 detector row scanners [15–17], and further extended to cardiac reconstructions [18, 19]. One important benefit of the 3D reconstructions was their volumetric approach which provided overlapping slices leading to high-resolution imaging even in the axial step-and-shoot mode. This enabled an improved longitudinal resolution in the axial mode similar to the one achieved in spiral mode. One of the consequences of the cone-beam geometry is the need to overlap the consecutive shots in the axial step-and-shoot mode. This overlap is Field-of-View (FOV) dependent and achieved by using a table feed smaller than the X-ray beam collimation in the axial mode (overlap 20% at FOV = 25 cm). Consequently, a patient's radiation exposure could increase when the acquired FOV increases [20].

Higher temporal resolution was also considered necessary in the early 2000s and cardiac CT was the driving force for the new developments. One approach to improving temporal resolution in spiral cardiac CT scans is to combine data from consecutive cardiac cycles to be used in reconstruction thereby improving the temporal resolution [18, 19]. Improvements to temporal resolution can also be achieved with a reduction of the gantry rotation times. One major limitation which is associated with faster scanning is the required X-ray power which has to be increased inversely proportional to the decrease in rotation time to arrive at a constant mAs product and to keep the image quality at the required level. Another major limitation in speeding up the gantry rotation is due to the mechanical constraints associated with the increased centripetal acceleration $\omega^2 R$, which is proportional to the square of

the rotation frequency ω and to the radius of rotation R. The typical centripetal acceleration of a single-slice CT (SSCT) with a 1 s rotation was around 3 g (where g is the acceleration due to gravity). The current generation of MSCT acquires 256–340 slices simultaneously with an extremely fast gantry rotation of ($\geq$0.25 s) and the centripetal acceleration is around 40 g [21]. To give an order of magnitude, the effective weight of the X-ray tube (approx. 40 kg at rest) during the rotation is around 1.6 tons. Thus, mechanical design has to withstand this very fast rotation and the additional forces acting on the X-ray tube. In 2005, Siemens introduced the dual source CT (DSCT) design in order to improve the temporal resolution. DSCT combined two arrays of X-ray tube plus detectors that were arranged at a 90° angle. With this configuration, the temporal resolution was expected to be improved by a factor of 2 since only 90° of rotation was necessary to acquire the 180° of projections which were needed to reconstruct the images [22–24]. New generations of DSCT have been introduced on the market, and this dual tube design is still available today to perform cardiac imaging.

The modern MSCT scanners accommodate nearly a 1000-fold increase in speed over SSCT, enabling ultra-fast heart coverage with isotropic resolution, potentially making MSCT the modality of choice for noninvasive coronary artery imaging.

2.3 The Cardiac Motion and ECG Synchronization

2.3.1 The Cardiac Motion

The coronary arteries are subject to complex 3D motion during the cardiac cycle and the suppression of the associated motion artifacts remains the greatest challenge in imaging those vessels with MSCT. Early investigations in characterizing coronary artery motion used conventional angiography [25] where the motion of the bifurcation points between the main coronary arteries and their branches were used in modeling the left-ventricular wall motion and in demonstrating the variability of the "rest period" for different coronary arteries at various heart rates [26]. Investigations with electron beam CT showed that the left anterior descending artery (LAD) moves during each cardiac cycle at a rate of 22 mm/s on average, and that the velocity can be more than 3–4 times that value for portions of the right coronary artery (RCA) [27]. Furthermore, the total excursion of the artery during the cardiac cycle is a distance that can be multiples of its own diameter. More recent MSCT velocity measurements at various landmarks along the primary coronary arteries showed that this complex 3D motion depends not only on the specific coronary artery, but also on the location along the course of the vessel and patient heart rate [28, 29].

Motion artifacts caused by this complex 3D motion can be minimized in MSCT studies by limiting image acquisition or reconstruction to those parts of the cardiac cycle associated with the least motion.

Generally, the two phases of the cardiac cycle in which the motion of the coronary arteries is minimized are the "end-systolic rest period" during the isovolumic relaxation time (IVRT) of the myocardium and the "diastasis period" (or "mid/late-diastole") which takes place between the rapid ventricular filling and the atrial contraction. At slow heart rates (<65–70 bpm), the diastasis period is the most optimal imaging period. At faster heart rates (>70 bpm), the diastasis period shrinks, making the end-systolic period the one with the least coronary motion [30].

A consequence of this fast, large, and complex 3D motion is that a high temporal resolution at MSCT is not the only requirement to successfully image the cardiac vessels; imaging the heart during the rest period of the cardiac cycle is also a necessity and will lead to an improved visualization of the coronary arteries and of the entire cardiac anatomy in general. Thus, both image acquisition and reconstruction need to be synchronized with the ECG signal of the patient to determine when the quiescent phase occurs.

2.3.2 The Cardiac Physiological Phases and the Delay Algorithm

Different approaches have been used to determine specific cardiac phases from the ECG signal.

Those techniques use the peak of the QRS complex (The *R* wave) as a reference time point in the cardiac cycle. Typical ECG-based gating techniques use either a fixed absolute delay (i.e., delay offset) or a fixed percentage delay to identify when the heart is in a given state during the cardiac cycle. The fixed absolute delay refers to the point in time (in ms) either after the arrival of the current *R* wave or before the following *R* wave where the reconstruction is performed. The percentage delay refers to the percentage of the *R*-*R* interval where the image is reconstructed. However, it is well known that the relationship between the cardiac phase and the time from the *R* wave varies nonlinearly with the heart rate. Additionally, at a slow heart rate, systole occupies roughly 1/3 of the cycle and diastole 2/3. As heart rate increases, systole increases and diastole decreases to roughly 50% each of the heart cycle. Thus, the reconstruction phase (either as a fixed or percentage delay) that is optimal at one heart rate may contain motion artifacts at a different heart rate, even in the same patient. Consequently, using a fixed delay (absolute or percentage) is not sufficient to allow for these nonlinear variations as this approach is not adaptive enough to locate the same desired phase on a consistent basis. A dynamic model using certain compliance parameters to account for the nonproportional changes, while providing an estimate of the state of the heart irrespective of the variations of the heart rate for a given patient, was proposed as an alternative [31, 32]. This model assumes that for a reference heart rate, e.g., 72 bpm, the various phases of the heart cycle are known. At this reference, end diastole is identified at 0% of the R-R cycle, end-systole between 35 and 45% and mid-diastole between 70 and 80%. As the instantaneous heart rate varies from this reference, the model adjusts the delay such that the same physiological phase can be identified and reconstructed. The model uses a combination of percentage delay and delay offset components, while also incorporating various parameters like the instantaneous heart rate, compliance parameters, and trigger latency. The compliance parameters account for nonproportional change of the various phases of the cardiac cycle with the variation of heart rate and thus enable us to capture the effects of the heart rate change on the duration of systole and diastole. This dynamic delay algorithm enables to track a desired physiological cardiac phase for a particular individual. It is modeled to adapt to the nonuniform changes in the various phases of the cardiac cycle (systole vs. diastole) for a particular patient as the heart rate changes dynamically during an acquisition (i.e., intra-patient variations). However, this model does not address the inter-patient variations. The systolic duration, while less sensitive to the variations in the heart rate for a particular individual, cannot be assumed to be the same for all patients. Two ECG synchronization techniques are commonly employed in cardiac CT: prospectively ECG-triggered axial scans and retrospectively ECG-gated spiral scans.

Finding the cardiac phase during which the heart is quasi-stationary to obtain the outmost image quality is challenging due to interpatient variability. ECG information does not always represent the heart motion with adequate accuracy. A simple and efficient technique has been introduced which is able to deliver stable cardiac phases in an automatic and patient-specific way. From low-resolution four-dimensional data sets, the most stable phases are derived by calculating the object similarity between subsequent phases in the cardiac cycle. This information is used to perform optimized high-resolution reconstructions at phases of little motion [33, 34].

2.4 Prospective and Retrospective Cardiac Synchronizations

2.4.1 Prospective Synchronization: The Step-and-Shoot Acquisition

The prospective approach is essentially the same as that used in electron beam CT (EBCT) [35]. Axial scans are initiated via triggers derived prospectively from the ECG signal of the patient using a delay subsequent to the arrival of the R peak [32]. As described in Sect. 1.2.2, this delay is typically calculated to reflect the quiescent diastasis phase of the cardiac cycle and is measured on the base of the average duration of the previous cardiac cycles. A partial-angle scan is performed, with the patient couch stationary. Upon completion of data acquisition, the couch is indexed to the next position, and the scan is initiated again via the trigger from the next R wave of the ECG signal, and so on (see Fig. 2.1a). For image reconstruction, a minimum of half a rotation of the X-ray tube is necessary, plus the fan angle (the angle subtended in the transaxial plane by the divergent X-ray beam emanating from the focal spot of the tube), thus resulting in approximately 240° partial-angle scans. The temporal resolution of this mode of scanning is thus limited by the rotation time.

In the early days of cardiac CT, the 4-slice scanner had a limited temporal resolution due to the slow rotation time of 0.5 s. This temporal resolution was calculated to be $0.5 \times (240/360) = 333$ ms. A cardiac scan with full myocardial coverage was typically acquired in 20–25 s with a limited longitudinal resolution of 2.5–3 mm obtained with nonoverlapping slices reconstructed with a 2D-FBP algorithm. The detector coverage used for this examination was 4×0.25 cm = 1 cm and the cardiac examination required an average of 15 shots. The step-and-shoot technique, with this poor longitudinal resolution, was thus not suitable for coronary artery assessment and was limited to coronary artery calcium scoring. In modern MSCT scanners, however, the increased coverage of the detection systems (8–16 cm), the faster gantry rotations ($\geq$0.25 s) and the 3D-FBP have partly removed these limitations and the step-and-shoot mode has become the preferred mode of acquisition to assess the coronary arteries during diastasis for patients having a stable heart rate $\leq$ 65–70 bpm. Complete cardiac coverage can be obtained with 2 shots of a 256-slice scanner rotating in 0.27 s, providing submillimeter overlapping slices with a temporal resolution of 180 ms.

Fig. 2.1 Illustration of prospectively ECG-triggered axial scanning (**a**) and retrospectively ECG-gated spiral scanning (**b**). (**a**) Scans are triggered with a preprogrammed delay after the arrival of the R peak. The temporal resolution t_{res} is half the scan rotation time (plus the fan angle). In case of high heart rates (short t_{RR}) and as a result of the latency in advancing the table after an axial scan, scans can be acquired at every other cardiac cycle. We note the overlap between the successive slabs which is required to perform the 3D-cone beam reconstructions. (**b**) Continuous scanning with simultaneous table feed with a low pitch factor to ensure sufficient overlap in the continuously acquired projection data to facilitate image reconstructions at multiple cardiac phases at the same longitudinal location. The locations of the individual R peaks are stored with the projection data, allowing the user to retrospectively reconstruct stacks of overlapping images in any physiological phase within the cardiac cycle. Standard temporal resolution corresponding to half the scan rotation time is achieved, but can be improved by combining projection data from multiple cardiac cycles

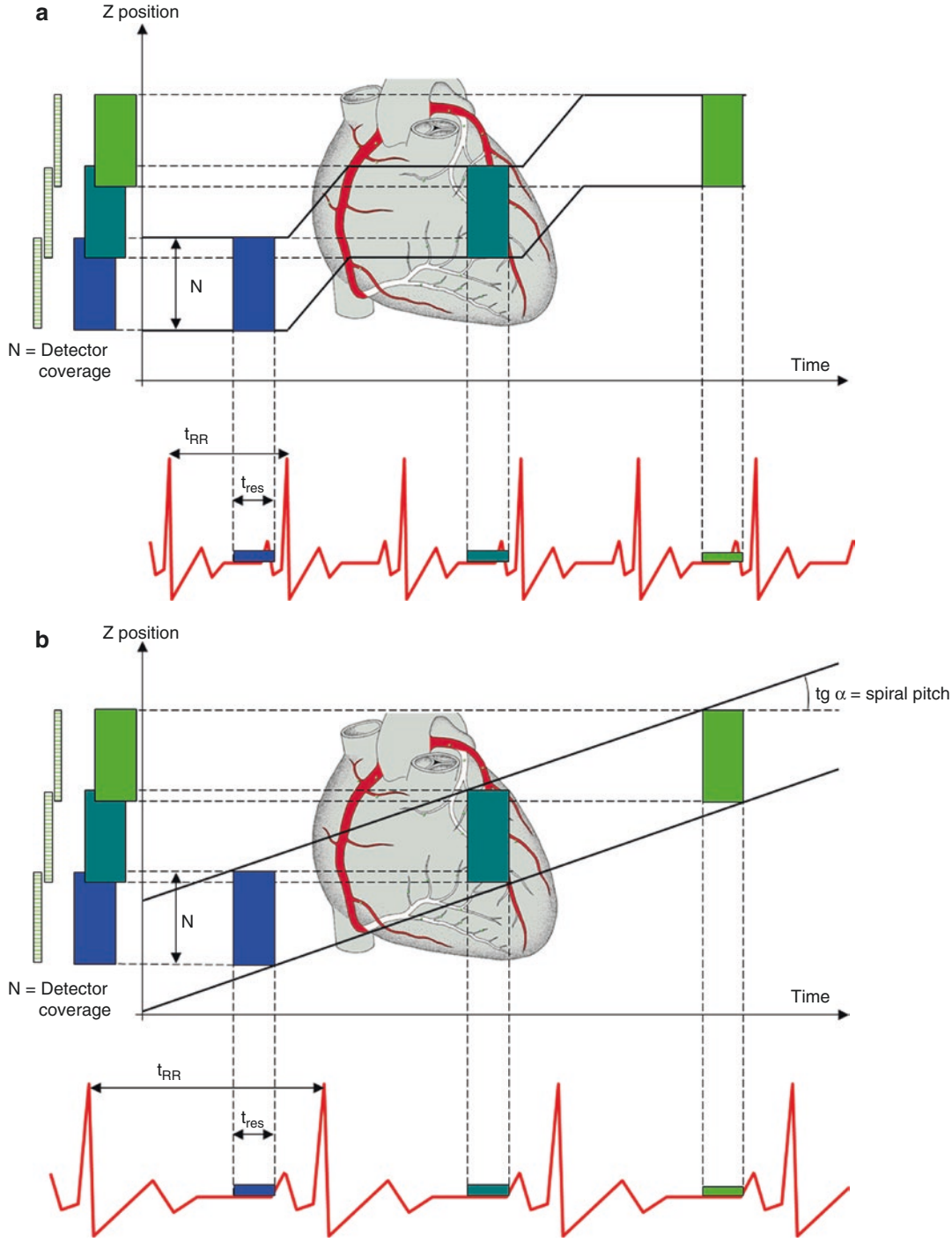
a
Z position
N
N = Detector coverage
Time
t_{RR}
t_{res}
b
Z position
tg α = spiral pitch
N
N = Detector coverage
Time
t_{RR}
t_{res}

"Phase tolerance" has been added as an acquisition option, allowing a larger scan time interval enabling the reconstruction of multiple cardiac phases centered around the targeted quiet phase with differences up to 5%. In other words, when the phase tolerance is turned ON, the step-and-shoot projection data centered in diastasis (75%) enables the reconstruction of any "mid-diastolic" phase between 70 and 80%. Of course, this increase in the duration of the X-ray irradiation is accompanied with a corresponding increase in radiation dose if the same tube current is used.

One of the limitations of prospective ECG gating is loss of image quality as a result of changes in heart rate or arrhythmia. Because each cycle of the study is an independent axial acquisition, demarcation lines are often visible between the individual steps and may be associated with step artifacts in the coronary arteries. The overlap between adjacent slabs, which is required by the 3D-FBP reconstructions, can be used to perform spatial interpolations in order to "mask" these demarcation lines and make some of the stair-step artifacts less conspicuous.

When an *R* wave arrives earlier than expected, the scan at that particular location may be acquired during a non-optimal cardiac phase resulting in blurring due to motion [36]. The likelihood of artifacts related to arrhythmia is proportional to the number of individual shots needed for the cardiac acquisition and is therefore inversely related to the detector coverage. Algorithms have been incorporated to overcome this limitation by recognizing ectopic beats in real time and to pause and wait until the next normal *R* wave is detected to continue the axial scans. In the setting of sustained arrhythmia, however, these techniques remain inferior to retrospective ECG gating.

2.4.2 Retrospective Gating: The Spiral Acquisition

For coronary CT angiography applications, spiral scanning equally provides excellent z-axis resolution with fast acquisition and volume coverage. The ECG signal is acquired simultaneously with the projection data. As the location of the *R* peak is known, the instantaneous heart rate during the scan is available. This enables the user to retrospectively reconstruct and visualize the anatomy in multiple physiological phases of the cardiac cycle, making functional imaging possible. For visualizing coronary arteries, submillimeter detector widths (ranging from 0.5 to 0.625 mm) coupled with low pitch factors (i.e., the ratio of the table feed per gantry rotation and the collimated slice width used) of 0.1–0.3 are commonly used. These low pitch factors ensure sufficient overlap in the continuously acquired projection data to facilitate image reconstructions at multiple cardiac phases at the same longitudinal location, while accounting for the variation of the instantaneous heart rate during the acquisition (see Fig. 2.1b). The continuous acquisition enables reconstruction of overlapping images with excellent longitudinal (z-axis) spatial resolution. In spiral scanning, improvement in temporal resolution is possible by combining data from consecutive cardiac cycles. This approach is useful especially at higher heart rates [37] where the diastasis is significantly reduced and the isovolumic relaxation time at the end of systole may have to be targeted for motion-free imaging. Dedicated cardiac adaptive multicycle (or multisegment) 3D cone-beam reconstruction techniques have been developed [38–40] that provide a significant improvement in the temporal resolution by combining data from as many as four cycles (see Fig. 2.2a, b). Figure 2.2c illustrates the influence of the pitch and the heart rate on the temporal resolution if a constant heart rate is assumed with the adaptive multicycle reconstruction. For each heart rate, an optimum pitch can be derived and vice versa to obtain the best compromise between the temporal resolution, the spatial resolution, and the scan duration and, hence, the given dose. If the heart rate is a harmonic or subharmonic of the rotation time, a decreased temporal resolution is obtained. The resolution

becomes worse than half the rotation time if the gating windows must be enlarged to assure that every voxel receives sufficient projection data for the 3D reconstruction. This is relevant for very low heart rates and high pitches.

With helical scans, the anatomy may be retrospectively reconstructed from different cardiac phases to compensate for changes in cardiac rhythm. The option of ECG editing is available to correct errors in ECG triggers due to the presence ectopic beats with arrhythmic patients.

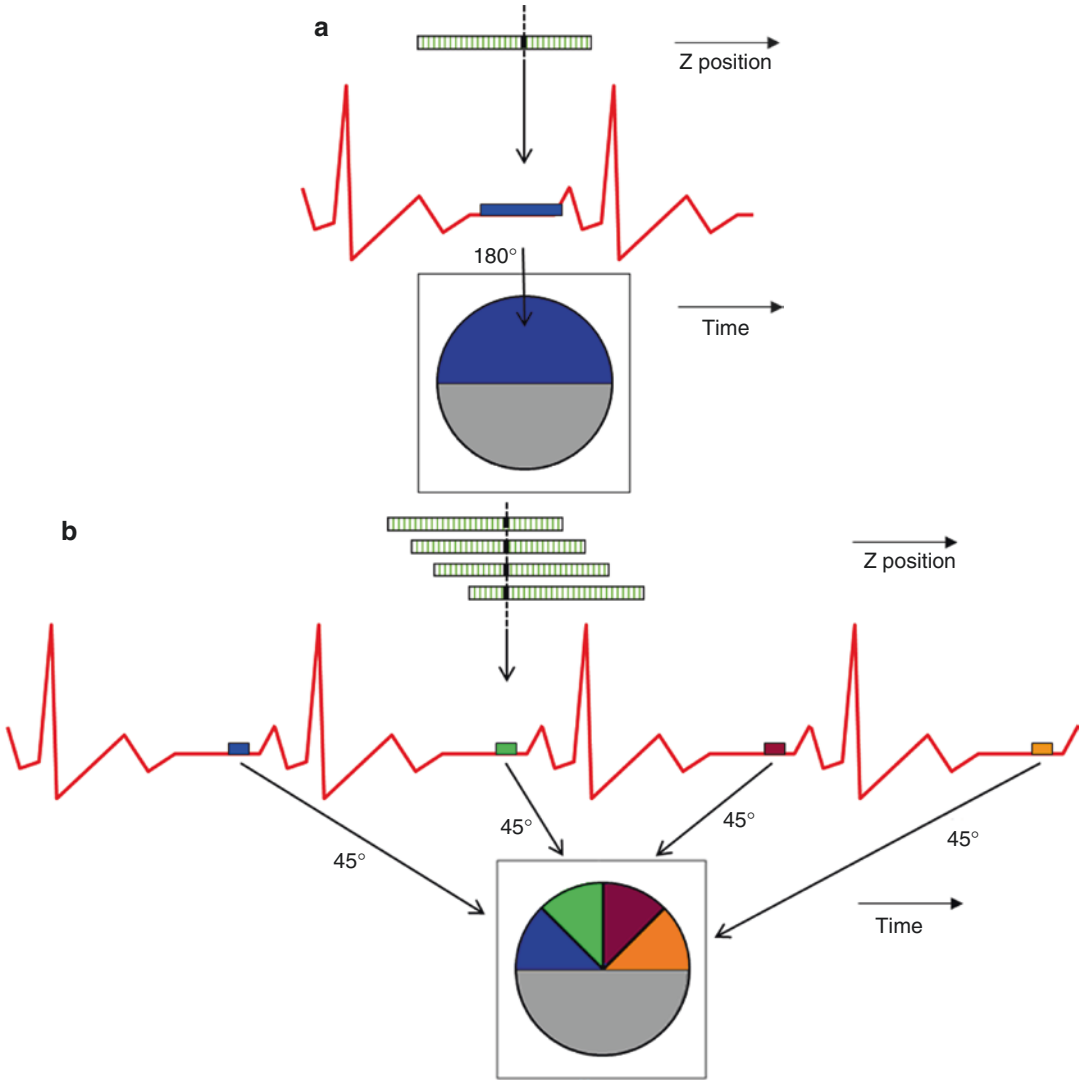

Fig. 2.2 The standard temporal resolution obtained in electrocardiogram-gated spiral scans is half the rotation time. (**a**) The circle represents the full data normally collected in one rotation of the X-ray source. Using 180°-based reconstruction approaches, the standard cardiac reconstructions obtained by information from one cardiac cycle will have a temporal resolution of 135 ms, assuming a 0.27-s rotation time. (**b**) This can be improved by combining projection data from consecutive cardiac cycles. For instance, it is possible to combine data from as many as four cycles, resulting in a temporal resolution of 34 ms, as shown here. (**c**) Illustrates the relation between the spiral pitch, heart rate, and the temporal resolution with a multicycle reconstruction. If the heart rate is equal to harmonics of the gantry rotation time, the temporal resolution is decreased. The resolution becomes worse than half the rotation time if the gating windows must be enlarged to assure that every voxel receives sufficient projection data for the 3D reconstruction. This is relevant for very low heart rates and high pitches. Note that a constant heart is assumed, without any variation

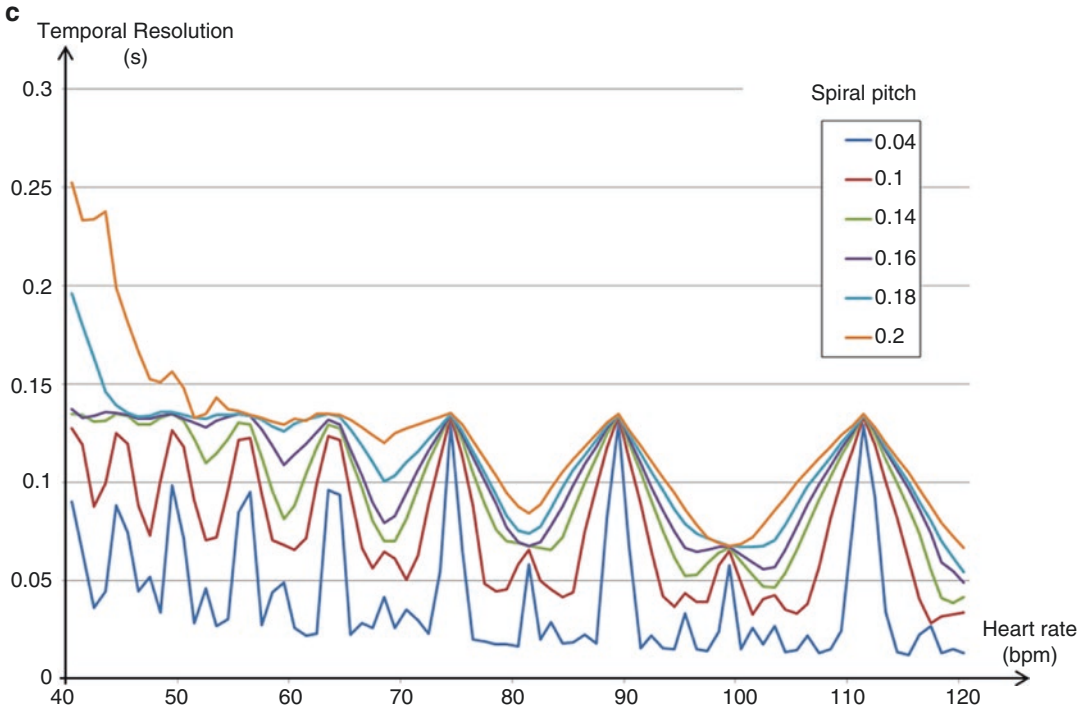

Fig. 2.2 (continued)

2.5 Radiation Exposure

2.5.1 ECG Dose Modulation

Imaging an organ over multiple physiological phases (e.g., over the cardiac cycle) can provide both anatomical and functional information (see Sect. 2.4.2). However, for many indications it is only necessary to image and expose a single phase. With the step-and-shoot cardiac techniques, the tube current is prospectively modulated to image only the desired phase in an axial scanning mode, thus enabling prospectively gated axial cardiac scanning during the "quiet" phase of the cardiac cycle. Step-and-shoot cardiac scans can result in a dose savings of up to 80% compared with a retrospectively gated helical technique [41], while maintaining optimum image quality. In other words, the roentgen tube is activated, and imaging is performed only during the short interval that is predicted to correspond to the quiet phase. In patients with a relatively regular cardiac rhythm, step-and-shoot can provide image quality and diagnostic performance equivalent to that of the retrospectively gated helical approach (see Fig. 2.3a). Coronary CTA with the step-and-shoot axial technique can image the entire coronary circulation with an average effective radiation dose from 2.7 to 4.5 mSv [1, 41].

With retrospective gating, the X-ray tube delivers radiation dose during the entire duration of the spiral scan, making it a very poor technique in terms of dose-efficiency. For this reason, ECG tube-current modulation was made available very early by all manufacturers as a dose-reduction mechanism for retrospectively gated helical coronary CTA. This technique enables to modulate the tube current during the acquisition: the tube current is kept at the nominal level (100%) during the targeted cardiac quiet phase of interest and is reduced to 20% during all other phases of the cardiac cycle, still providing sufficient image quality for the functional assessment. Using this approach, dose savings of up to 45% can be achieved without compromising the image quality in the cardiac quiet phase of interest, depending on the heart rate during

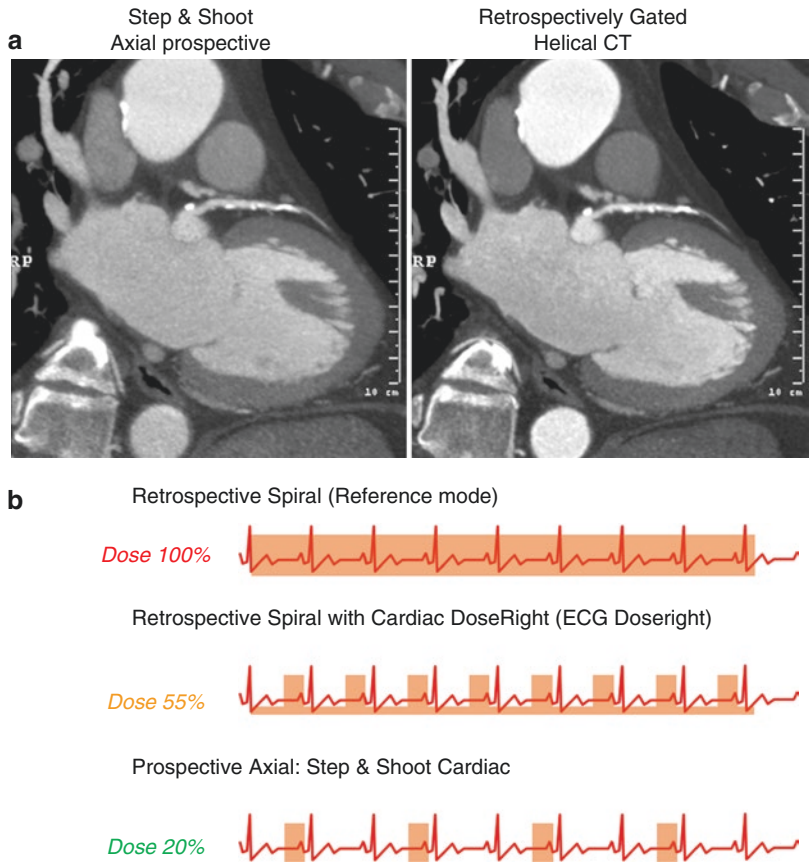

Fig. 2.3 (**a**) In patients with a relatively regular cardiac rhythm, step-and-shoot can provide image quality and diagnostic performance equivalent to that of the retrospectively gated helical approach. In this example, the full prospective axial acquisition delivered a patient dose of 2.8 mSv and the helical acquisition a dose of 11.9 mSv. (*Image courtesy of: Dr. John A. Osborne, MD, PhD, FACC, State of the Heart Cardiology, Grapevine, TX, USA*) (**b**) With retrospective gating during spiral scanning, the tube current can be kept at the nominal level (100%) during the targeted cardiac phase of interest (in this example, the diastolic phase) and can be reduced to 20% during all other phases of the cardiac cycle. Using this approach, dose savings of up to 45% can be achieved without compromising the image quality in the cardiac phase of interest, depending on the heart rate during the acquisition. With prospective gating, the tube current is prospectively modulated to image only the desired cardiac phase in an axial scanning mode. Step-and-shoot cardiac can result in a dose savings of up to 80% compared with a retrospectively gated reference helical technique

the acquisition (see Fig. 2.3b). Of course, tube-current modulation has to be prescribed prospectively which means that it suffers, to a certain extent, the same weakness as the step-and-shoot acquisition, in cases of heart rate variations or arrhythmia during the scan. In that case the peak tube current can be delivered during a wrong cardiac phase, providing noisy images during the quiet cardiac phase. Arrhythmia detection is usually available to cancel the ECG tube-current modulation for the remainder of the acquisition in case an irregular beat is detected.

2.5.2 Iterative Reconstructions

The most basic method to reduce radiation dose is to reduce the X-ray tube output. However, scans performed at lower tube currents and peak kilovoltage will have a lower signal-to-noise and projection data will appear noisy. Filtered back projection algorithms (2D-FBP and 3D-FBP) have been the industry standard for CT image reconstruction for decades [10]. While it is a very fast and fairly robust method, FBP is a suboptimal algorithm choice for poorly sampled data or for cases where noise overwhelms the projection

signal. Such situations may occur in low dose or tube-power-limited acquisitions. Noise in CT projection data is dominated by photon count statistics. As the dose is lowered, the variance in the photon count statistics increases disproportionately [42]. When these very high levels of noise are propagated through the reconstruction algorithm, the result is an image with significant artifacts and high quantum mottle noise. Over time, incremental enhancements were made to FBP to overcome some of its limitations. These improvements continued until recently, when a completely different approach to image reconstruction was explored through the clinical implementation of iterative reconstruction (IR) techniques. These algorithms differ from FBP methods in that the reconstruction becomes an optimization process that takes into account the data statistics, image statistics, and system models [43]. IR algorithms use initial estimates of the voxel attenuation to predict projection data. These estimates are then iteratively adjusted to minimize the difference between the predicted projection data and the measured projection data. The noisiest measurements are given low weight in the iterative process; therefore, they contribute very little to the final image. Hence, IR techniques treat noise properly at very low signal levels, and consequently reduce the noise and artifacts present in the resulting reconstructed image. This results in an overall improvement of image quality at any given dose. With IR techniques, the noise can be controlled for high spatial resolution reconstructions; hence providing high-quality, low contrast, and spatial resolution within the same image (see Fig. 2.4). While IR techniques have been used for many years in PET and SPECT imaging, the sampling density and the data set sizes in CT have historically caused IR techniques to perform extremely slowly when compared to FBP. However, recent innovations in hardware design and algorithm optimizations have permitted the clinical use of IR technique in CT. Recent clinical studies showed that additional dose reduction can be achieved with IR techniques in cardiac imaging [44].

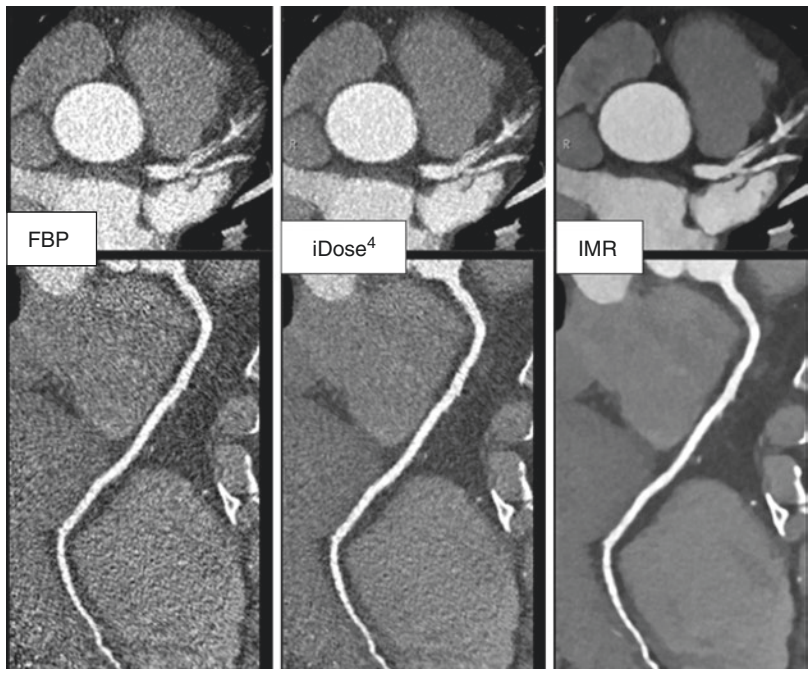

Fig. 2.4 This clinical study provides an example of the expected image quality improvement that may be achieved with two generations of iterative reconstructions (iDose^4 and IMR, Philips Healthcare, Cleveland, OH, USA). An ECG-gated coronary CT angiogram scanned with the step-and-shoot technique on a Philips iCT at 0.9 mSv (100 kVp, 110 mAs, 5.2 mGy, 67.1 mGy cm) and reconstruction with FBP (*left*), iDose^4 (*center*), and IMR (*right*). Study shows limited visualization of soft-plaque on FBP. With the latest generation of IR (IMR), there is a clear improvement in spatial resolution, low contrast, and noise characteristics (*Image courtesy of: Amakusa Medical Center, Japan*)

2.6 Image Post-processing

The amount of data produced by multidetector CT scanners as well as the time needed to review the resulting several thousand slices (e.g., 10 reconstructed cardiac phases with 400 slices each) have been continuously increasing, providing a workflow and diagnostic challenge to the clinician. Therefore, automatic image processing methods became a prerequisite to efficiently analyze the large amount of image data produced by cardiac CT during cardiac exams. Simple image-based segmentation methods like global thresholding, region growing, etc. usually fail to automatically segment an image because of noise, limited resolution, partial volume effect, or similar gray-value characteristics of different organs. With these methods, user interaction is needed to either initiate segmentation, control the progression of the algorithm, and/or to correct for segmentation errors [45, 46]. This may be time consuming and distracts the physician from his/her actual diagnosis. To overcome these limitations, sophisticated model-based methods for a reliable and automatic segmentation of the four cardiac chambers and major coronary arteries have been proposed. Shape-constrained deformable model for heart segmentation have been described in detail in [47]. These algorithms adapt an anatomical model of the heart chambers and main trunks of the coronary arteries to the MSCT image volume (see Fig. 2.5). They are coupled with automated vessel tracking algorithms, which provide curved multi-planar reformations of the individual coronary arteries, enabling automatic measurements, including that of coronary artery

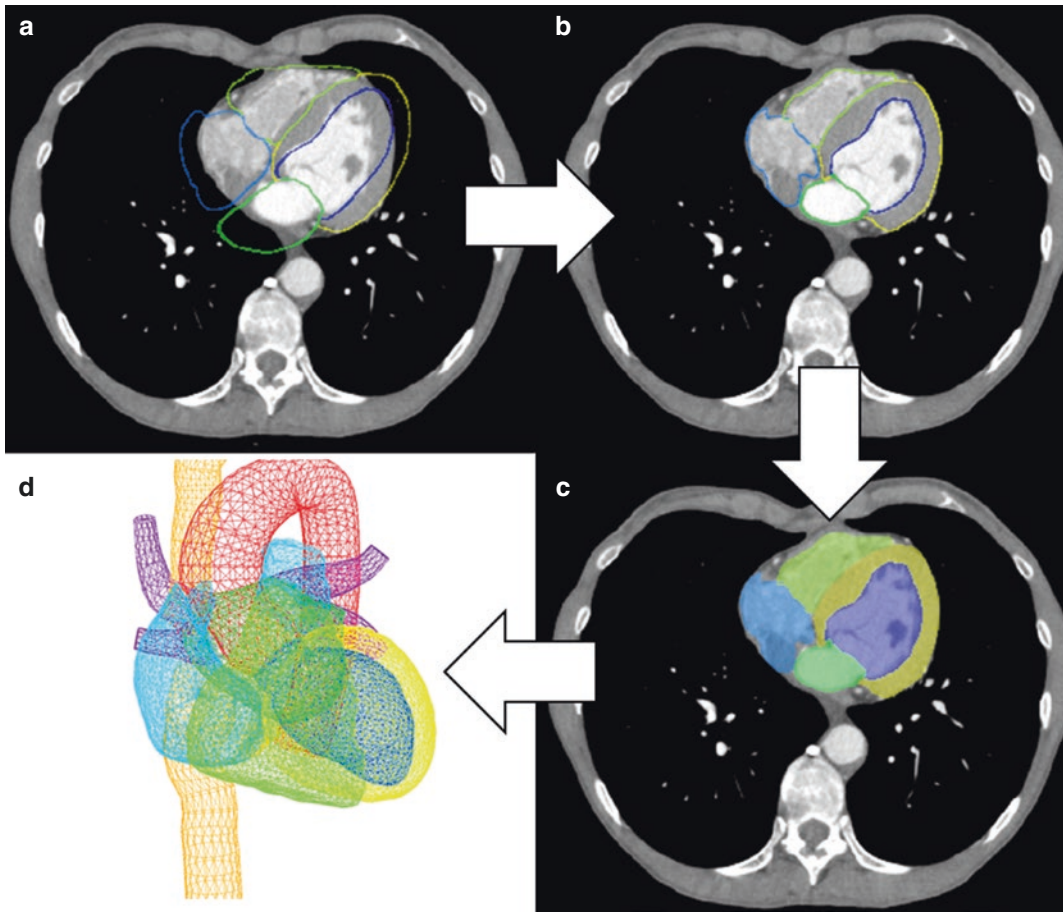

Fig. 2.5 After loading a trained cardiac model, boundaries of the heart are matched to the model, resulting in a segmentation of the various anatomic structures of the heart (a > d). A triangulated mesh model of the endocardial surfaces of the four cardiac chambers as well as the left-ventricular epicardium and short trunks of the major vasculature is obtained

area, diameters, and stenosis extent. An important application of the model-based methods is the successful automatic assessment of the global heart function in multiphasic retrospective cardiac studies [48]. The geometric heart models resulting from segmentation have been increasingly used to guide invasive therapeutic procedures. It has been proposed, for instance, to overlay heart models onto live fluoroscopy data to support ablation procedures for treating atrial fibrillation [49, 50] or stem cell injection for myocardial repair [51, 52]. For these applications, a heart model comprising only the four chambers and the main coronary arteries is often insufficient. It is, for instance, important to extract the left atrium and the proximal part of the pulmonary veins to support guidance of ablation procedures for atrial fibrillation treatment. For cardiac resynchronization therapy, a heart model including the coronary sinus is needed to facilitate implantation of the pacemaker lead.

2.7 Cardiac MSCT Future Directions

2.7.1 Myocardial Perfusion Using Cardiac CTA

Noninvasive myocardial perfusion imaging (MPI) using single-photon emission computed tomography (SPECT) has been the standard-of-care for the assessment of physiologic significance of coronary lesions, with studies showing good correlation of the infarcted and ischemic burden with long-term outcomes thereby aiding in the decision-making for medical therapy versus revascularization [53]. Magnetic resonance imaging (MRI) has also been used for the detection of myocardial regions that have a delayed wash-in of contrast which shows up as hypo-enhanced regions both under rest and pharmacological stress (indicating myocardial infarction) or only under stress (reversible defects or ischemia). In addition, MRI is also considered as the gold standard for the assessment of myocardial regions with a delayed wash-out of contrast, wherein imaging performed with a delay of 5–10 min after administration of contrast could show regions of hyper-enhancement indicating myocardial scar [54]. The presence of these delayed hyper-enhanced regions has been associated with adverse left-ventricular (LV) remodeling [55]. A combined analysis of early- and late-enhancement regions could provide additional information on the tissue viability and functional recovery after coronary revascularization [56].

The ability to provide anatomical and physiologic information could further expand the role of cardiac CT. Depending on the mode of scan performed, a comprehensive assessment of coronary arteries, myocardial perfusion defects, regional wall motion, and left-ventricular (LV) function can be obtained from a single scan. Such a comprehensive exam using CT comprises a stress scan, followed by a rest scan and in some cases a delayed scan [57–59].

A typical protocol is shown in Fig. 2.6. Patient preparation includes avoidance of caffeine for at least 12 h prior to the exam and medications such as nitroglycerine. Stress is typically induced pharmacologically (adenosine) by which blood flow is increased in the normal coronary segments and reduced in the diseased segments, causing the heart rate to elevate. The surview (scout) is used to plan the scans—typically from the carina to the diaphragm. Scans are initiated when the contrast reaches a threshold in the ascending or descending aorta (determined via a test bolus or automated bolus tracking). A volume of 50–70 cc of contrast is given at the rate of 5–6 cc/s designed to provide peak contrast enhancement in the coronary arteries.

Stress scans are typically performed using the conventional helical retrospective-gated techniques, with or without ECG-tube modulation (which could provide some radiation dose reduction). This enables multiple phases to be used for functional and perfusion assessment. The availability of multiple phases also helps to differentiate perfusion defects (which typically show up across all phases of the cardiac cycle) from artifacts (which may be seen in only one phase and may be mistaken for a perfusion defect). The selection of the tube voltage (kVp) and the current (mA) is based on the body habitus of the patient (based either on weight-based or body-mass-index [BMI]). The adenosine infusion is

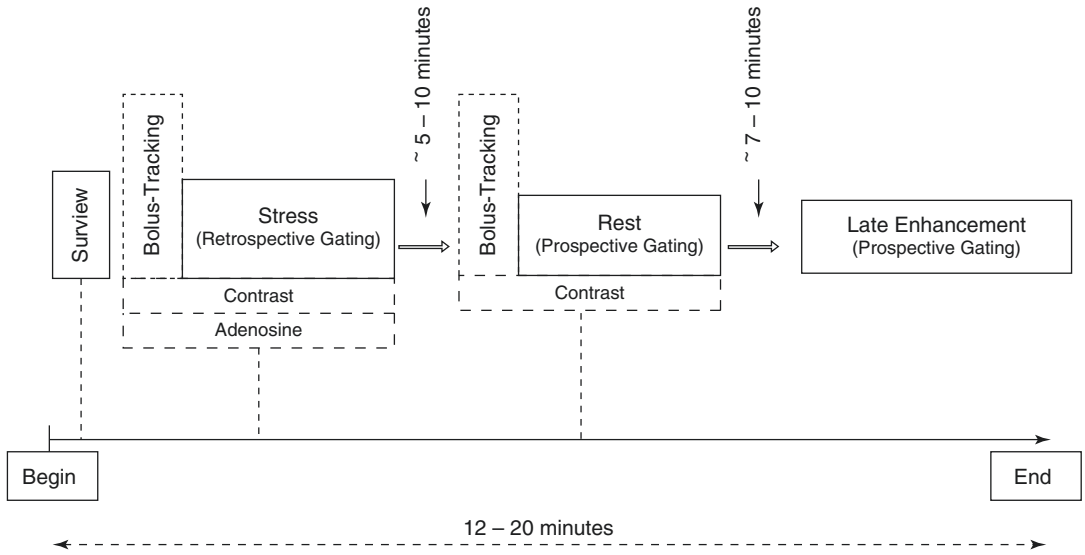

Fig. 2.6 A typical protocol for stress perfusion using CT

given at the rate of 140 μg/kg/min and stopped immediately at the conclusion of the scan.

Following the scan, the patient's vital symptoms are monitored while allowing the heart rate to return to the baseline in preparation for the rest scan. This typically takes 5–10 min. Once the heart rate is back to the baseline, beta-blockers are administered to lower and stabilize the heart rate and sublingual nitroglycerine given to dilate the arteries. For the rest scan, prospective-gated acquisition is commonly used to reduce radiation dose to the patient, with the targeted cardiac phase centered at 75% of the R-R cycle, corresponding to ventricular diastasis. For consistency, the value of kVp is kept the same as in the stress acquisition.

The third scan is a late-enhancement scan performed 7–10 min after the last contrast injection (in this case, after the rest scan). This is meant for the detection of hyper-enhanced regions (late enhancement) that could indicate myocardial necrosis [57, 58, 60]. As with the rest scan, prospective gating is used to reduce radiation dose, along with the use of a lower kVp (e.g., 100 kVp), and a thicker slice for reconstructions (e.g., 2 mm).

For the assessment of perfusion defects from all the three scans, images are usually visualized in a short-axis orientation. Images are viewed in thick slices (e.g., 5 mm) to reduce noise and improve contrast resolution. A narrow window and level setting is typically used (e.g., window of 150–200; level of 100). From the assessment of short axis images, it is possible to distinguish reversible defects (hypo-enhanced regions that show up only in stress scans) from the fixed defects (hypo-enhanced regions that are exhibited in both stress and rest scans). Figure 2.7a, b is an example of a short-axis image from a scan performed under stress exhibiting hypo-enhanced regions in the basal anteroseptal and basal inferolateral walls caused by lesions in the proximal LAD and LCX. The use of advanced iterative reconstructions, such as iterative model reconstruction (IMR) (Fig. 2.7b), could help reduce noise with improved low contrast detectability compared to filtered back projection (FBP) (Fig. 2.7a). Figure 2.8 is an example of a scan (of a different study) taken 7 min after the administration of contrast, showing late hyper-enhancement in the inferolateral wall indicating myocardial necrosis (infarct).

The sequence of the scans (stress followed by rest or vice versa) could be determined based on the risk factors. For patients with a low likelihood of disease, it may be preferable to administer beta-blockers, stabilize the heart

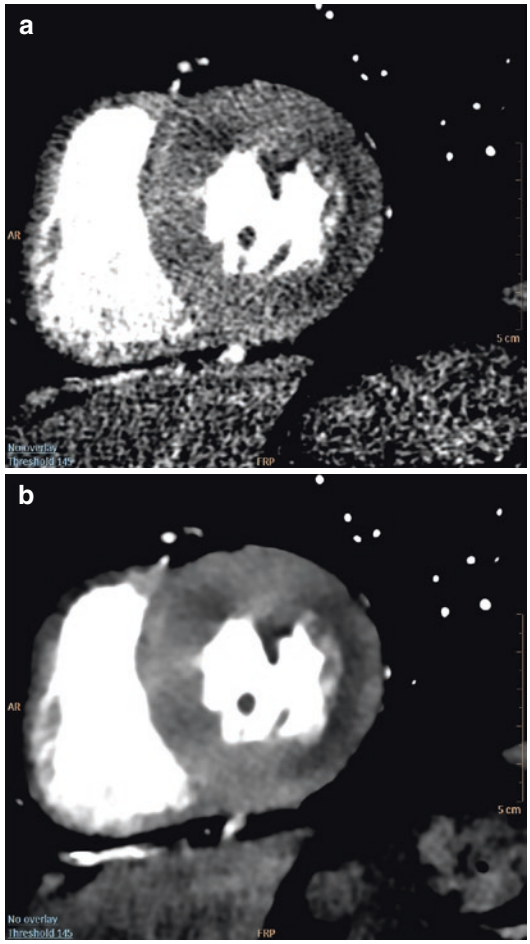

Fig. 2.7 (**a**, **b**) Is an example of a short-axis image from a scan performed under stress exhibiting hypo-enhanced subendocardial regions in the basal anteroseptal and basal inferolateral walls caused by lesions in the proximal LAD and LCX. The use of advanced iterative reconstructions, such as iterative model reconstruction (IMR) (**b**) could help reduce noise with increased low contrast detectability compared to filtered back projection (FBP) (**a**) (*Image courtesy of: Drs. G. Colin and B. Ghaye, Clinique universitaires Saint-Luc (UCL), Brussels, Belgium*)

rate, and perform a rest scan first. If no disease is found, a second scan can be avoided thereby resulting in radiation dose savings. On the other hand, since a stress scan may be more relevant in these exams especially in patients with intermediate likelihood of disease, performing this scan first may provide a more accurate assessment of the myocardium by avoiding any venous contamination from a prior injection used in a rest scan.

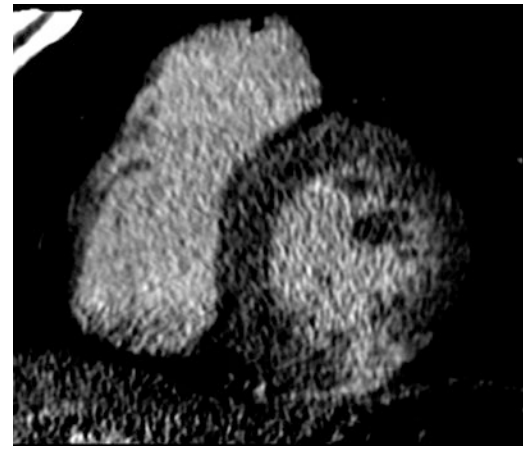

Fig. 2.8 A short-axis representation from a delayed scan performed 7 min after the injection of contrast, showing late hyper-enhancement of the mid inferolateral portion of the myocardium indicating myocardial damage (*Image courtesy of: Prof. L. Boussel, Hospices Civils de Lyon, Lyon, France*)

The perfusion assessment using cardiac CTA provides valuable adjunct information for the determination of hemodynamic significance of CAD, thus expanding the role of cardiac CTA. However, quantification (or semi-quantification) of the myocardial blood flow is still lacking since it requires a dynamic examination (again, typically performed under pharmacological stress) and the aforementioned scans are performed at a single time point. Various preclinical and clinical investigations have studied the feasibility of ECG-triggered dynamic myocardial perfusion (DMP) using CT targeting a physiologic cardiac phase for imaging over time. Dynamic scans with a narrow detector [61–63] require a back-and-forth table translation to cover the complete or a significant portion of the LV myocardium. Due to the lack of coverage, the superior and inferior sections of the myocardium are imaged at different time points which could require the user to employ a different arterial input function (AIF) for each "slab." Additionally, these scans are ECG-triggered and typically performed at higher heart rates (75–90 bpm), resulting in a lower temporal sampling at a given location which could impact quantification of perfusion measurements. Wide area detectors remove the need for table movement, allowing the user to program the sampling

interval accordingly (i.e., optimize the radiation dose) while at the same time providing imaging of a more homogenous distribution of contrast across the entire LV myocardium [64–68]. The quantification of perfusion is further improved with the use of elastic registration and temporal filtering to reduce anatomical motion and the presence of any noise spikes [67, 69]. Prior to the dynamic scans, the time corresponding to the peak contrast enhancement in the LV is first determined via a series of time lapse scans; alternatively, it can also be derived from a coronary CTA scan if such a scan is performed first as part of the overall cardiac exam. Once this is known, ECG-triggered dynamic scans can be initiated 5–6 s prior to the peak enhancement in order to establish a series of baseline measurements. By imaging over time and thus capturing the instance of the peak enhancement of the left ventricle, any reduction (or slow uptake) of blood flow in the regions of myocardium (ischemic regions) corresponding to the culprit coronary artery can be imaged and quantified. Figure 2.9 is a short-axis color-map representation from a DMP CT scan of a patient showing reduced peak enhancement in the inter-ventricular septum (blue regions) corresponding to a lesion in the mid-LAD.

One of the main drawbacks of the DMP-CT scans is the radiation dose. While reduction of tube energy and/or current is one obvious approach to address this, it can be complemented with the use of other innovative techniques. By adjusting the temporal sampling or with the use of appropriate levels of advanced reconstruction techniques (such as iterative approaches), further reductions in radiation dose reductions can be achieved, as demonstrated in early preclinical investigations [64, 70, 71].

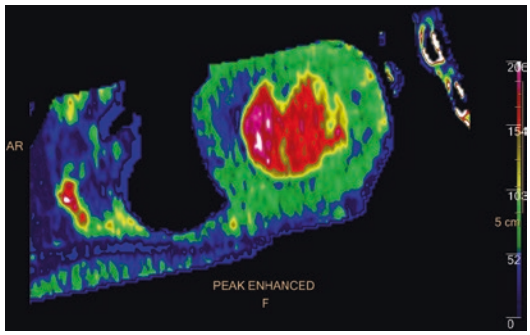

Fig. 2.9 A color-map representation of a short-axis image from a dynamic myocardial perfusion CT scan showing regions with low enhancement in the inter-ventricular septum (in *blue*) caused by a lesion in the mid-LAD (*Image courtesy of: Drs. Armin Huber, Daniela Muenzel and Bettina Gramer, Klinikum rechts der Isar der Technischen,Universität München, Munich, Germany*)

2.7.2 Fractional Flow Reserve Using CT (FFR-CT)

A newer alternative approach using cardiac CTA to determine the hemodynamic significance of a coronary lesion is gaining interest. Traditionally, the concept of fractional flow reserve (FFR), which represents the ratio of pressure distal to a lesion compared to the portion of the artery proximal to the lesion (i.e., "normal" section, or aorta) is the most commonly accepted approach for the assessment of lesion-specific ischemia—a value of ≤ 0.8 is considered hemodynamically significant. However, FFR is measured in the cath labs, as part of an invasive procedure. Recent work has focused on extending the role of cardiac CTA beyond anatomy for improved clinical decision-making.

Novel approaches (FFR-CT) are being developed that use the existing cardiac CTA data to simulate a drop in pressure in the presence of a coronary lesion [72–74]. These approaches are computationally intensive but have shown promise and good correlation with the gold standard (invasive FFR), making it possible to have a single non-invasive imaging test that can provide anatomical information along with physiology. This capability to include physiologic information to anatomy could make it possible to identify patients appropriate for coronary revascularization.

2.7.3 Motion Analysis and Compensation in Cardiac CT

The motion of the heart is one of the major challenges in cardiac CTA. Diagnostic accuracy is decreased when motion artifacts occur

in reconstructed tomographic images [75]. At the same time, knowledge about the cardiac motion pattern is an additional source of clinically useful information including, e.g., wall motion, ejection fraction, or valve motion [76, 77]. Novel approaches have been developed to address both challenges, functional motion analysis and motion artifact reduction, for improved anatomic analysis.

There are different approaches to detect and calculate motion in cardiac CT data sets. These include motion tracking and estimation from projection or image sequences [4, 78] or combined reconstruction of the image data and the motion vector field [79]. While the first approaches basically rely on image processing techniques like model-based segmentation (see Sect. 2.6) of image registration, the latter ones combine image reconstruction and optimization methods. All methods have in common that they finally aim to deliver a dense sampled 3D motion vector field [80] describing the temporal shape change of the anatomy for the time covered by the image or projection sequence. Figure 2.10 shows a surface representation of a heart segmented from a multi-phase cardiac CTA data set with a motion vector field at a single time point during the cardiac cycle displayed as arrows on the cardiac surfaces. The direction and length of the arrow represent the motion direction and strength. The data have been derived from a patient data set using model-based segmentation (see [81] for more details).

With this information available, functional information of the heart like the motion pattern of a coronary artery or the myocardium, temporal changes of the chamber volume, wall motion abnormalities, or even the motion of the cardiac valves can be derived. Using modern image processing techniques, the motion vector field can be analyzed qualitatively and quantitatively for selected cardiac structures.

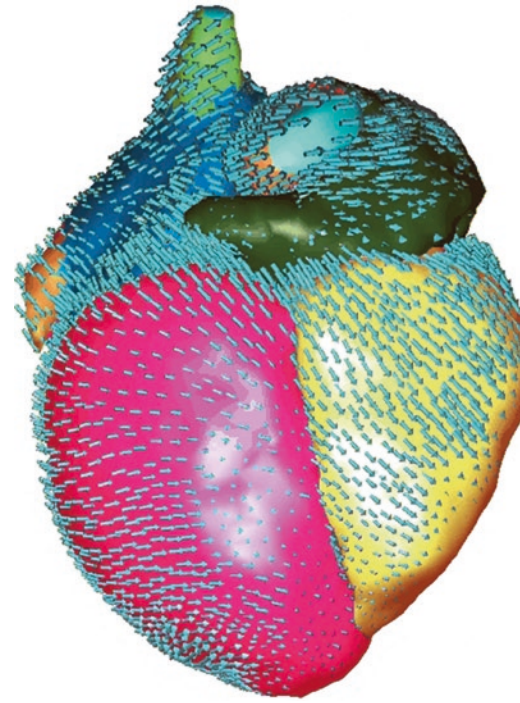

Fig. 2.10 A surface representation of a heart segmented from a multi-phase cardiac CTA data set with a motion vector field at a single time point during the cardiac cycle (displayed as arrows on the cardiac surfaces). The direction and length of the arrow represent the motion direction and strength

In addition, the calculated dense motion vector fields can be used subsequently in a motion compensated cardiac reconstruction method. Here, the filtered back projection [81–83] or iterative reconstruction [3, 4] scheme incorporate the motion vector field and thus deliver images with improved temporal resolution and image quality. The increase in image quality and definition of the cardiac anatomy will improve image-based diagnosis (see Fig. 2.11), while at the same time supplementing more sophisticated approaches involving advanced image analysis like myocardial perfusion and FFR described earlier.

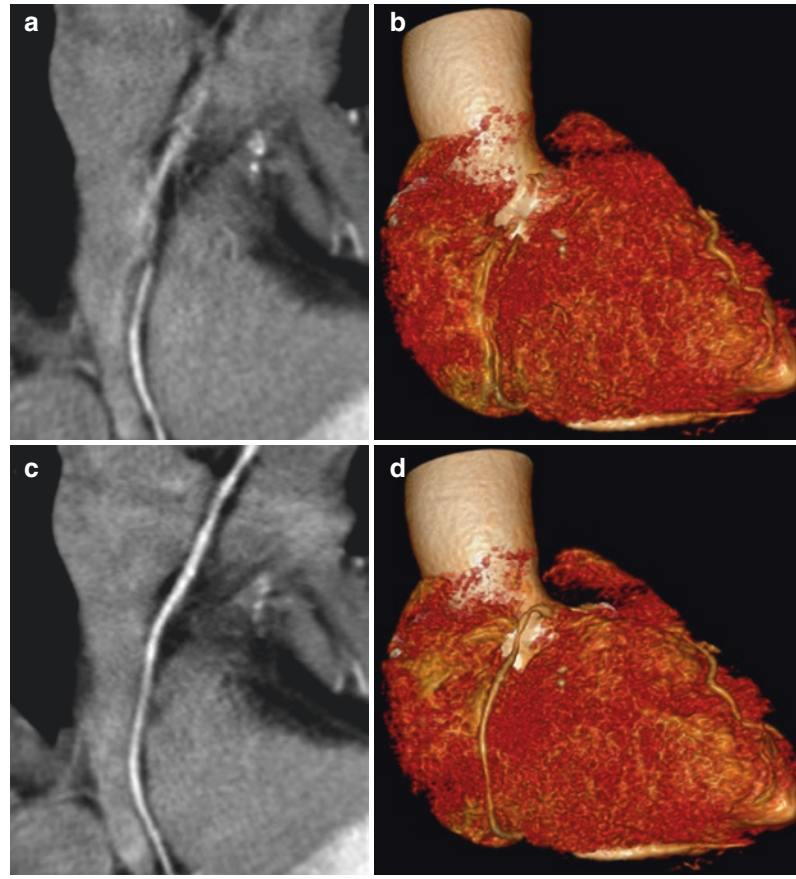

Fig. 2.11 Retrospectively gated helical cardiac reconstruction without (**a**, **b**) and with (**c**, **d**) motion compensation using the same amount of projection data during the filtered back projection reconstruction. Curved MPR (left column; L/W: 200/500 HU) of the right coronary artery and volume rendering (right column) of a patient data set with a mean heart rate of 82 bpm. The reduced motion artefact level can be clearly observed

2.7.4 Cardiac Spectral MSCT

Recent developments in scanner and detector technology and modern clinical requirements, like quantitative computed tomography and the need for tissue classification, have revived interest in spectral computed tomography. The current clinical spectral CT scanners enable the discrimination between different materials based on the differential X-ray attenuation properties in two "energy bands" of the spectrum instead of averaging the entire polychromatic beam like conventional CT does. In other words, the spectral dependencies of the net X-ray attenuation can be imaged and analyzed as a material characteristic and can be used to discriminate materials. With Dual Energy CT (DECT), this additional information can be obtained using several data acquisition methods: (1) Single X-ray source, Dual kVp Spin (Philips), (2) Single X-ray source, Dual kVp Switch (General Electric), (3) Dual X-ray source (Siemens), and (4) Single X-ray source, Dual-Layer Detector (Philips) [84, 85].

In a single source, dual-layer detector scanner configuration, one X-ray tube is used to expose a detector consisting of two layers of scintillators (Fig. 2.12). The two layers are directly on top of one another. A single CT scan is performed at a high kVp (e.g., 120 or 140 kVp). The first layer encountered by the X-ray photons absorbs most

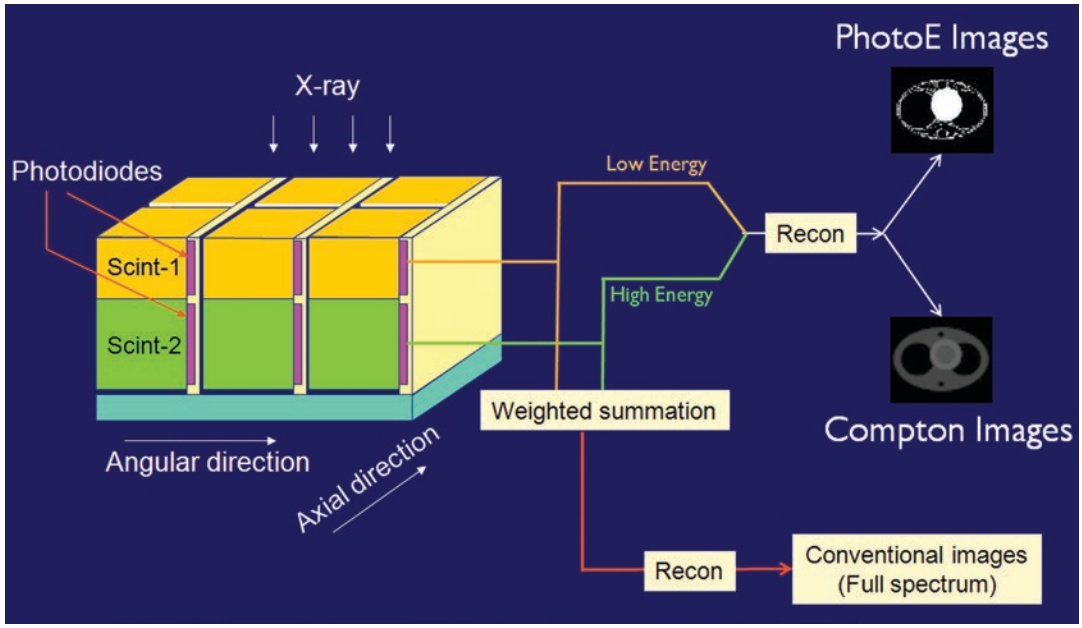

Fig. 2.12 A schematic illustration of the dual-layer detection system (only a few detector elements are shown). The photodiodes are parallel to the X-ray direction, attached to the sides of the two types of scintillator elements

of the low-energy spectrum, while the bottom detector layer absorbs the remaining higher energy photons. In contrast to other approaches of dual-energy CT, there is no need to redundantly expose materials with both low and high-energy X-rays. Furthermore, since the spectral energy separation is intrinsic to the detection system, rather than sequentially generated at the X-ray source, this approach eliminates the time lag of sequential techniques, making it ideal for imaging moving organs, as in the case of cardiovascular imaging. In other words, the dual-layer technique is fully registered both spatially and temporally. It has no spatial shift or dead time such as in dual kVp or dual tube techniques and this allows for projection space-based decomposition, and thus the opportunity for accurate beam hardening correction without the need for spatial or temporal interpolations (Fig. 2.13) [86, 87]. The low- and high-energy spectral attenuations can also be easily combined and used to reconstruct a conventional CT image reflecting the "full spectrum" attenuation without the need to compensate for warping and shifting due to the time lags. The use of a single source also obviates the cross scatter limitation of dual source techniques [88]. Furthermore, this approach allows full 50 cm Field-of-View (FOV) imaging so it can be used for both fast and large FOV MSCT cardiac spectral imaging, without any compromise.

The first investigations of dual energy methods for CT were made by Alvarez and Macovski in 1976 [89]. They demonstrated that, using a conventional X-ray source having a broad energy spectrum, one can separate the X-ray attenuation coefficients into the contributions from the photoelectric effect and Compton scatter. In other words, Alvarez and Macovski demonstrated that the X-ray attenuation coefficients of common materials can be expressed with sufficient accuracy as a linear combination of the photoelectric and Compton attenuation coefficients. As a consequence, the X-ray attenuation coefficients of any material can be expressed as a linear combination of the attenuation of two basis materials, where both materials differ in their photoelectric and Compton characteristics. If bone and water are chosen as the basis material for example, the information from the low and high attenuation data can be used to calculate the bone coefficients of the X-ray attenuation. These coefficients can

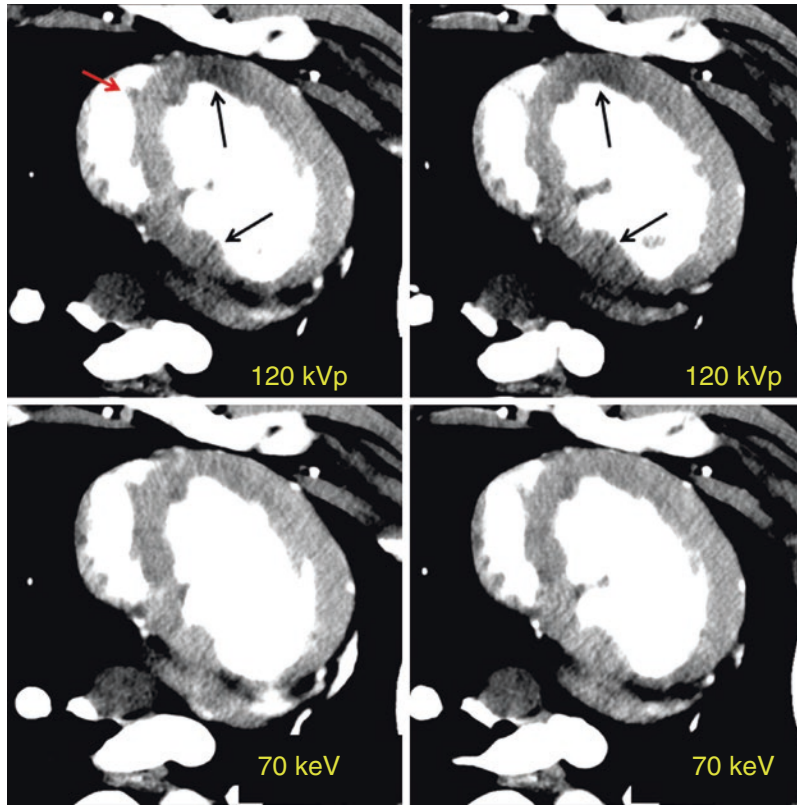

Fig. 2.13 Two different axial cardiac slices of a pig heart, corresponding to the conventional 120 kVp and the 70 keV monoE, respectively, under the condition FFR = 1. In this case, one should expect a relatively uniform enhancement on the nonischemic myocardium. However, due to BH artifacts, clear hypo-enhancements are noticed in the anterior and inferior walls in the conventional images as indicated by the black arrows. These artifacts can be misdiagnosed as perfusion defects. Hyper-enhancement in the septal wall (*red arrow*) is also the result of BH effects. On the other hand, these BH-induced hyper- and hypo-attenuations are significantly reduced on the 70 keV images resulting in a relatively more uniform enhancement of the entire myocardium (*Image courtesy of: Drs. Rachid Fahmi & David Wilson, Case Western Reserve University, Cleveland OH, USA and Dr. Hiram Bezerra, Harrington Heart & Vascular Center, University Hospitals Case Medical Center, Cleveland, OH, USA*)

then be used to create a bone image, which allows the assessment of bony structures and calcifications. Alternatively, the water coefficients can be calculated to generate a soft tissue image where the bony structures are suppressed and which improves the visualization of structures previously hidden by bony anatomy. Other pairs of basis material with clinical relevance are iodine and calcium or iodine and water. In cardiovascular imaging, the iodine images obtained from an iodine-calcium decomposition can be of primary importance because they can help to better assess the iodinated lumen of the coronary arteries which could be otherwise hidden by the presence of large calcified plaques. The water images obtained from an iodine-water decomposition is one in which all of the iodine is removed. This virtual non-contrast image (VNC) synthesizes a pre-contrast scan.

The photoelectric coefficient depends strongly on the effective atomic number Z (photoelectric effect proportional to Z^3) and thus provides an indication of the composition of the object. The Compton scatter coefficient depends on the electron density, which is proportional to the mass density for most materials. So the use of the information obtained by the decomposition of the X-ray attenuation coefficients of any material

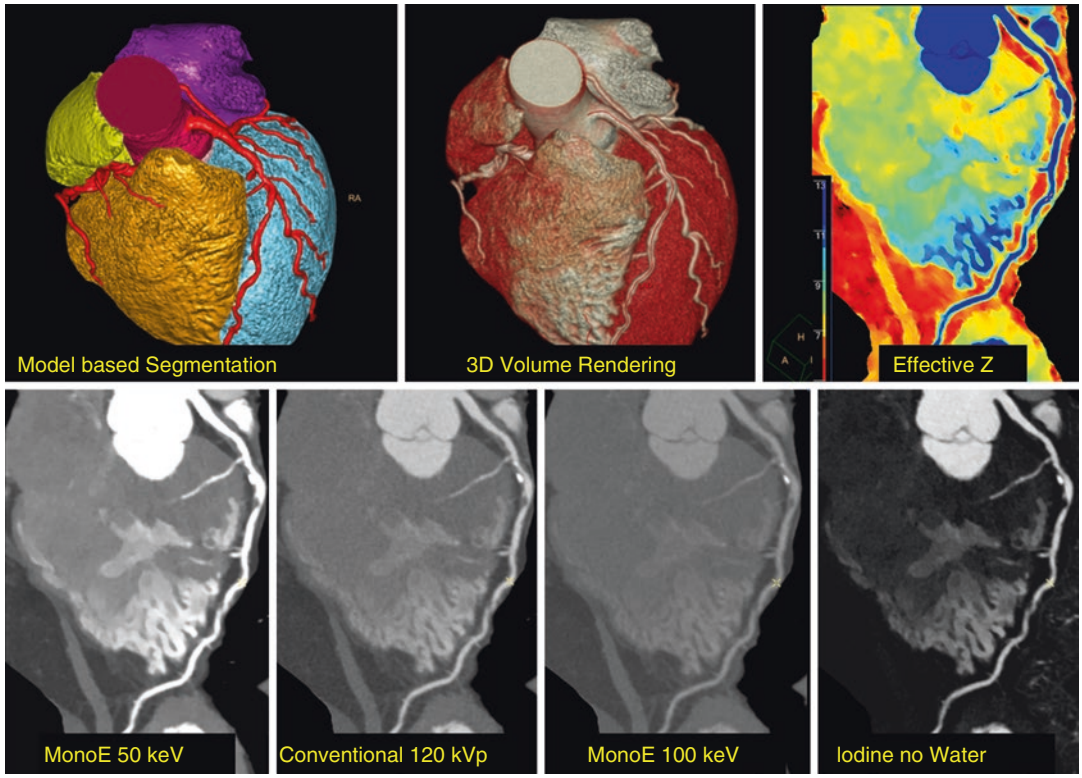

Fig. 2.14 Dual Energy measurements enable the generation of material-specific images like the effective Z images or the iodine images obtained after iodine-water decomposition. In addition, virtual monochromatic images at different energies can be synthesized and used for routine diagnosis similar to conventional images (obtained at 120 kVp in this example). Low keV (50 keV shown here) can be used to enhance the photoelectric absorption of high effective Z materials like iodine. High keV (100 keV) can be used to maximize the Compton scatter and hence minimize all types of artifacts (calcium blooming, etc.) (*Image courtesy of: Dr. Kazuhiro Katahira, Kumamoto Chuo Hospital, Kumamoto, Japan*)

into its photoelectric and Compton attenuation coefficients can be highly significant for medical purposes. For example, a lesion of increased attenuation coefficient can be due to either increased density or increased effective atomic number due to calcification. A dual-energy measurement can distinguish between these phenomena, and a color mapping of the effective atomic number Z provides a visual assessment of this additional information as is demonstrated in Fig. 2.14 [90]. In dual-energy CT, besides the material-specific information and images, one may also synthesize monochromatic images at different energies [91], which can be used for routine diagnosis similar to conventional images. With a single scan at usual 120 kVp (or 140 kVp for obese patients), a dual-layer spectral CT acquisition allows the reconstruction of virtual monochromatic images from 40 keV up to 200 keV. Since the photoelectric effect is dominant at lower keV and is relatively high for high Z materials, low keV imaging can be used to enhance the absorption of high Z material like iodine ($Z = 53$). This can be of particular interest to enhance the iodine uptake for patients with renal dysfunction where the total injected volume of iodinated contrast medium is very limited (Fig. 2.14). Compton scattering on the other hand is dominant at higher keVs and does not exhibit a strong relationship with Z. High keV imaging will then be of particular interest to minimize the absorption of high Z materials and minimize all types of associated artifacts (metal artifacts, calcium, or stent blooming).

References

1. Sun Z. Coronary CT angiography with prospective ECG-triggering: an effective alternative to invasive coronary angiography. Cardiovasc Diagn Ther. 2012;2(1):28–37. https://doi.org/10.3978/j.issn.2223-3652.2012.02.04.
2. Mehta D, Thomson R, Morton T, Dhanantwari A, Shefer E. Iterative model reconstruction: simultaneously lowered computed tomography radiation dose and improved image quality. Med Phys Int. 2013;1:147–55.
3. Isola A, Ziegler A, Köhler T, Niessen W, Grass M. Motion-compensated iterative cone-beam CT image reconstruction with adapted blobs as basis functions. Phys Med Biol. 2008;53:6777–97.
4. Isola A, Grass M, Niessen W. Fully automatic nonrigid registration-based local motion estimation for motion-corrected iterative cardiac CT reconstruction. Med Phys. 2010;37(3):1093–109.
5. Isola A, Ziegler A, Schäfer D, Köhler T, Niessen W, Grass M. Motion compensated iterative reconstruction of a region of interest in cardiac cone-beam CT. Comput Med Imaging Graph. 2010;34:149–59.
6. Garcia MJ, Lessick J, Hoffmann MH. Accuracy of 16-row multidetector computed tomography for the assessment of coronary artery stenosis. JAMA. 2006;296:403–11.
7. Budoff MJ, Dowe D, Jollis JG, Gitter M, Sutherland J, Halamert E, et al. Diagnostic performance of 64-multidetector row coronary computed tomographic angiography for evaluation of coronary artery stenosis in individuals without known coronary artery disease: results from the prospective multicenter ACCURACY (Assessment by Coronary Computed Tomographic Angiography of Individuals Undergoing Invasive Coronary Angiography) trial. J Am Coll Cardiol. 2008;52(21):1724–32.
8. Miller JM, Rochitte CE, Dewey M, Arbab-Zadeh A, Niinuma H, Gottlieb I, et al. Diagnostic performance of coronary angiography by 64-row CT. N Engl J Med. 2008;359(22):2324–36.
9. Meijboom WB, Van Mieghem CA, van Pelt N, Weustink A, Pugliese F, Mollet NR, et al. Comprehensive assessment of coronary artery stenoses: computed tomography coronary angiography versus conventional coronary angiography and correlation with fractional flow reserve in patients with stable angina. J Am Coll Cardiol. 2008;52(8):636–43.
10. Kak A, Slaney M. Principles of computerized tomographic imaging. New York: IEEE; 1988.
11. Kalender WA, Seissler W, Klotz E, Vock P. Spiral volumetric CT with single breath-hold technique, continuous transport and continuous scanner rotation. Radiology. 1990;176:181–3.
12. Crawford CR, King KF. Computed tomography scanning with simultaneous patient translation. Med Phys. 1990;17:967–82.
13. Ohnesorge B, Flohr T, Becker C, Kopp AF, Schoepf UJ, Baum U, et al. Cardiac imaging by means of electrocardiographically gated multi-section spiral CT: initial experience. Radiology. 2001;217:564–71.
14. Feldkamp L, Davis L, Kress J. Practical cone-beam algorithm. J Opt Soc Am A. 1984;1(6):612–9.
15. Grass M, Köhler T, Proksa R. 3D cone-beam CT reconstruction for circular trajectories. Phys Med Biol. 2000;45:329–47.
16. Proksa R, Koehler T, Grass M, Timmer J. The n-PI method for helical cone beam CT. IEEE Trans Med Imaging. 2001;19:848–63.
17. Koehler T, Bontus C, Brown K, Heuscher D, Grass M, Shechter G, et al. Evaluation of helical cone beam CT reconstruction algorithms. IEEE Nucl Sci Symp Conf Rec. 2002;2:1217–20.
18. Grass M, Manzke R, Nielsen T, Koken P, Proksa R, Natanzon M, et al. Helical cardiac cone beam reconstruction using retrospective ECG gating. Phys Med Biol. 2003;48:3069–84.
19. Shechter G, Naveh G, Altman A, Proksa R, Grass M. Cardiac image reconstruction on a 16-slice CT scanner using a retrospectively ECG-gated, multicycle 3D back projection algorithm. Proc SPIE Med Imaging. 2003;5032:1820–8.
20. Muenzel D, Noël PB, Dorn F, Dobritz M, Rummeny EJ, Huber A. Coronary CT angiography in step-and-shoot technique with 256-slice CT: impact of the field of view on image quality, craniocaudal coverage, and radiation exposure. Eur J Radiol. 2012;81(7):1562–8.
21. Vlassenbroek A. The use of isotropic imaging and computed tomography reconstructions. In: Coche EE, Ghaye B, de Mey J, Duyck P, editors. Comparative interpretation of CT and standard radiography of the chest, Medical radiology. Berlin/Heidelberg: Springer; 2011a. https://doi.org/10.1007/978-3-540-79942-9_3.
22. Flohr TG, McCollough CH, Bruder H, Petersilka M, Gruber K, Süss C, et al. First performance evaluation of a dual-source CT (DSCT) system. Eur Radiol. 2006;16:256–68.
23. Achenbach S, Ropers D, Kuettner A, Flohr T, Ohnesorge B, Bruder H, et al. Contrast-enhanced coronary artery visualization by dual-source computed tomography—initial experience. Eur J Radiol. 2006;57:331–5.
24. McCollough CH, Schmidt B, Yu L, Primak A, Ulzheimer S, Bruder H, et al. Measurement of temporal resolution in dual source CT. Med Phys. 2008;35(2).
25. Potel MJ, Rubin JM, MacKay SA, Aisen AM, Al-Sadir J, Sayre RE. Methods for evaluating cardiac wall motion in three dimensions using bifurcation points of the coronary arterial tree. Investig Radiol. 1983;18:47–57.
26. Wang Y, Vidan E, Bergman GW. Cardiac motion of coronary arteries: variability in the rest period and implications for coronary MR angiography. Radiology. 1999;213:751–8.
27. Achenbach S, Ropers D, Holle J, Muschiol G, Daniel WG, Moshage W. In-plane coronary arterial motion velocity: measurement with electron-beam CT. Radiology. 2000;216:457–63.
28. Vembar M, Garcia MJ, Heuscher DJ, Haberl R, Matthews D, Boehme GE, et al. A dynamic approach

to identifying desired physiological phases for cardiac imaging using multislice spiral CT. Med Phys. 2003;30:1683–93.
29. Vembar M, Walker MJ, Johnson PC. Cardiac imaging using multislice computed tomography scanners: technical considerations. Coron Artery Dis. 2006;17:115–23.
30. Gurudevan SV. Postprocessing and reconstruction techniques for the coronary arteries. In: Cardiac CT imaging: diagnosis of cardiovascular disease. London: Springer; 2010. https://doi.org/10.1007/978-1-84882-650-2.
31. Chandra S, Heuscher DJ, Vembar M, Shreter U, Garcia M. Algorithm for acquiring/reconstructing any phase of the heart cycle in multi-slice cardiac CT. First Annual Cardiac CT Conference; 2000 Sept; Heidelberg.
32. Heuscher DJ, Chandra S. Multi-phase cardiac imager. United States Patent 6,510,337. 2003.
33. Manzke R, Köhler T, Nielsen T, Hawkes D, Grass M. Automatic phase determination for retrospectively gated cardiac CT. Med Phys. 2004a;31(12):3345–62.
34. Hoffmann MH, Lessick J, Manzke R, Schmid FT, Gershin E, Boll DT, et al. Automatic determination of minimal cardiac motion phases for computed tomography imaging: initial experience. Eur Radiol. 2006;16:365–73.
35. Stanford W, Rumberger J. Ultrafast computed tomography in cardiac imaging: principles and practice. New York: Futura; 1992.
36. Halpern EJ. Technique, protocols, instrumentation, and radiation dose. In: Clinical cardiac CT, anatomy and function. 2nd ed. Stuttgart, Germany: Thieme Medical Publishers; 2011.
37. Dewey M, Laule M, Krug L, Schnapauff D, Rogalla P, Rutsch W, et al. Multisegment and halfscan reconstruction of 16-slice computed tomography for detection of coronary artery stenosis. Investig Radiol. 2004;39:223–9.
38. Manzke R, Grass M, Nielsen T, Shechter G, Hawkes D. Adaptive temporal resolution optimization in helical cardiac cone beam CT reconstruction. Med Phys. 2003;30:3072–80.
39. Hoffmann MH, Heshui S, Manzke R, Schmid FT, De Vries L, Grass M, et al. Noninvasive coronary angiography with 16-detector row CT: effect of heart rate. Radiology. 2005;234:86–97.
40. van Stevendaal U, Koken P, Begemann PG, Koester R, Adam G, Grass M. ECG gated continuous circular cone-beam multi-cycle reconstruction for in-stent coronary artery imaging: a phantom study. Proc SPIE. 2006;6142:61420L. https://doi.org/10.1117/12.652011.
41. Klass O, Jeltsch M, Feuerlein S, Brunner H, Nagel H-D, Walker MJ, et al. Prospectively gated axial CT coronary angiography: preliminary experiences with a novel low-dose technique. Eur Radiol. 2009;19(4):829–36. https://doi.org/10.1007/s00330-008-1222-4. Epub 2008 Nov 15.
42. Whiting BR, Massoumzadeh P, Earl OA, O'Sullivan JA, Snyder DL, Williamson JF. Properties of preprocessed sinogram data in X-ray computed tomography. Med Phys. 2006;33(9):3290–303.
43. Brown K, Zabic S, Koehler T. Acceleration of ML iterative algorithms for CT by the use of fast start images. Proc. SPIE. 2012;8313:831339. https://doi.org/10.1117/12.911412.
44. Oda S, Weismann G, Vembar M, Weigold WG. Iterative model reconstruction: improved image quality of low-tube-voltage prospective ECG-gated coronary CT angiographyimages at 256-slice CT. Eur J Radiol. 2014. https://doi.org/10.1016/j.ejrad.2014.04.027.
45. Higgins WE, Chung N, Ritman EL. Extraction of left-ventricular chamber from 3-D CT images of the heart. IEEE Trans. Med. Imaging. 1990;9(4):384–94.
46. Redwood AB, Camp JJ, Robb RA. Semiautomatic segmentation of the heart from CT images based on intensity and morphological features. Proc SPIE Med Imaging. 2005;5747:1713–9.
47. Ecabert O, Peters J, Schramm H, Lorenz C, von Berg J, Walker M, et al. Automatic model-based segmentation of the heart in CT images. IEEE Trans Med Imaging. 2008;27(9):1189–201.
48. Ecabert O, Peters J, Walker M, Ivanc T, Lorenz C, von Berg J, et al. Segmentation of the heart and great vessels in CT images using a model-based adaptation framework. Med Image Anal. 2011;15:863–76.
49. Rhode KS, Sermesant M, Brogan D, Hegde S, Hipwell J, Lambiase P, et al. A system for real-time XMR guided cardiovascular intervention. IEEE Trans Med Imaging. 2005;24:1428–40.
50. Knecht S, Skali H, O'Neill MD, Wright M, Matsuo S, Chaudhry GM, et al. Computed tomography-fluoroscopy overlay evaluation during catheter ablation of left atrial arrhythmia. Europace. 2008;10:931–8.
51. Gutiérrez LF, de Silva R, Ozturk C, Sonmez M, Stine AM, Raval AN, et al. Technology preview: X-ray fused with magnetic resonance during invasive cardiovascular procedures. Catheter Cardiovasc Interv. 2007;70:773–82.
52. Lehmann H, Kneser R, Neizel M, Peters J, Ecabert O, Kühl H, et al. Integrating viability information into a cardiac model for interventional guidance. In: Functional imaging and modeling of the heart, FIMH 2009. LNCS, vol. 5528. Berlin/Heidelberg: Springer; 2009. p. 312–20.
53. Hachamovitch R, Berman DS, Shaw LJ, Kiat H, Cohen I, Cabico JA, et al. Incremental prognostic value of myocardial perfusion single photon emission computed tomography for the prediction of cardiac death: differential stratification for risk of cardiac death and myocardial infarction. Circulation. 1998;97(6):535–43.
54. Gerber BL, Belge B, Legros GJ, Lim P, Poncelet A, Pasquet A, et al. Characterization of acute and chronic myocardial infarcts by multidetector computed tomography: comparison with contrast-enhanced magnetic resonance. Circulation. 2006;113(6):823–33.
55. Gerber BL, Rochitte CE, Melin JA, McVeigh ER, Bluemke DA, Wu KC, et al. Microvascular obstruction and left ventricular remodeling early after acute myocardial infarction. Circulation. 2000;101:2734–41.

56. Gerber BL, Garot J, Bluemke DA, Wu KC, Lima JA. Accuracy of contrast-enhanced magnetic resonance imaging in predicting improvement of regional myocardial function in patients after acute myocardial infarction. Circulation. 2002;106:1083–9.
57. Blankstein R, Okada DR, Rocha-Filho JA, Rybicki FJ, Brady TJ, Cury RC. Cardiac myocardial perfusion imaging using dual-source computed tomography. Int J Cardiovasc Imaging. 2009. https://doi.org/10.1007/s10554-009-9438-1.
58. Blankstein R, Shturman LD, Rogers IS, Rocha-Filho JA, Okada DR, Sarwar A, et al. Adenosine-induced stress myocardial perfusion imaging using dual-source cardiac computed tomography. J Am Coll Cardiol. 2009;54(12):1072–84. https://doi.org/10.1016/j.jacc.2009.06.014.
59. George RT, Arbab-Zadeh A, Miller JM, Kitagawa K, Chang HJ, Bluemke DA, et al. Adenosine stress 64- and 256-row detector computed tomography angiography and perfusion imaging. A pilot study evaluating the transmural extent of perfusion abnormalities to predict atherosclerosis causing myocardial ischemia. Circ Cardiovasc Imaging. 2009;2:174–82. https://doi.org/10.1161/circimaging.108.813766.
60. Lessick J, Dragu R, Mutlak D, Rispler S, Beyar R, Litmanovich D, et al. Is functional improvement after myocardial infarction predicted with myocardial enhancement patterns at multidetector CT? Radiology. 2007;244(3):736–44. https://doi.org/10.1148/radiol.2443061397. Epub 2007 Aug 9.
61. Mahnken AH, Klotz E, Pietsch H, Schmidt B, Allmendinger T, Haberland U, et al. Quantitative whole heart stress perfusion CT imaging as noninvasive assessment of hemodynamics in coronary artery stenosis: preliminary animal experience. Investig Radiol. 2010;45(6):298–305. https://doi.org/10.1097/RLI.0b013e3181dfa3cf.
62. Bamberg F, Klotz E, Flohr T, Becker A, Becker CR, Schmidt B, et al. Dynamic myocardial stress perfusion imaging using fast dual-source CT with alternating table positions: initial experience. Eur Radiol. 2010;20(5):1168–73. https://doi.org/10.1007/s00330-010-1715-9. Epub 2010 Mar 24.
63. Bamberg F, Becker A, Schwarz F, Marcus RP, Greif M, von Ziegler F, et al. Detection of hemodynamically significant coronary artery stenosis: incremental diagnostic value of dynamic CT-based myocardial perfusion imaging. Radiology. 2011;260(3):689–98. https://doi.org/10.1148/radiol.11110638.
64. Gramer BM, Muenzel D, Leber V, von Thaden AK, Feussner H, Schneider A, et al. Impact of iterative reconstruction on CNR and SNR in dynamic myocardial perfusion imaging in an animal model. Eur Radiol. 2012;22(12):2654–61. https://doi.org/10.1007/s00330-012-2525-z. Epub 2012 Jul 3.
65. Kurata A, Kawaguchi N, Kido T, Inoue K, Suzuki J, Ogimoto A, et al. Qualitative and quantitative assessment of adenosine triphosphate stress whole-heart dynamic myocardial perfusion imaging using 256-slice computed tomography. PLoS One. 2013;8(12):e83950. https://doi.org/10.1371/journal.pone.0083950. eCollection 2013.
66. Huber AM, Leber V, Gramer BM, Muenzel D, Leber A, Rieber J, et al. Myocardium: dynamic versus single-shot CT perfusion imaging. Radiology. 2013;269(2):378–86. https://doi.org/10.1148/radiol.13121441. Epub 2013 Jun 20.
67. Muenzel D, Kabus S, Gramer B, Leber V, Vembar M, Schmitt H, et al. Dynamic CT perfusion imaging of the myocardium: a technical note on improvement of image quality. PLoS One. 2013;8(10):e75263. https://doi.org/10.1371/journal.pone.0075263. eCollection 2013.
68. Muenzel D, Noël PB, Gramer BM, Leber V, Schneider A, Leber A, et al. Dynamic CT perfusion imaging of the myocardium using a wide-detector scanner: a semi-quantitative analysis in an animal model. Clin Imaging. 2014;38(5):675–80. https://doi.org/10.1016/j.clinimag.2014.05.011. Epub 2014 Jun 2.
69. Isola AA, Schmitt H, van Stevendaal U, Begemann PG, Coulon P, Boussel L, et al. Image registration and analysis for quantitative myocardial perfusion: application to dynamic circular cardiac CT. Phys Med Biol. 2011;56(18):5925–47. https://doi.org/10.1088/0031-9155/56/18/010. Epub 2011 Aug 22.
70. Eck B, Fahmi R, Wen G, Fuqua C, Vembar M, Dhanantwari A, et al. Low dose dynamic myocardial CT perfusion using advanced iterative reconstruction. Proc. SPIE. 2014;9417:94170Z. https://doi.org/10.1117/12.2081418.
71. Fahmi R, Eck BL, Vembar M, Bezerra HG, Wilson DL. Dose reduction assessment in dynamic CT myocardial perfusion imaging in a porcine balloon-induced-ischemia model. Proc. SPIE. 2014;9033:903305. https://doi.org/10.1117/12.2043748.
72. Koo BK, Erglis A, Doh JH, Daniels DV, Jegere S, Kim HS, et al. Diagnosis of ischemia-causing coronary stenoses by noninvasive fractional flow reserve computed from coronary computed tomographic angiograms. Results from the prospective multicenter DISCOVER-FLOW (Diagnosis of Ischemia-Causing Stenoses Obtained Via Noninvasive Fractional Flow Reserve) study. J Am Coll Cardiol. 2011;58(19):1989–97. https://doi.org/10.1016/j.jacc.2011.06.066.
73. Min JK, Leipsic J, Pencina MJ, Berman DS, Koo BK, van Mieghem C, et al. Diagnostic accuracy of fractional flow reserve from anatomic CT angiography. JAMA. 2012;308(12):1237–45.
74. Nørgaard BL, Leipsic J, Gaur S, Seneviratne S, Ko BS, Ito H, et al. NXT Trial Study Group. Diagnostic performance of noninvasive fractional flow reserve derived from coronary computed tomography angiography in suspected coronary artery disease: the NXT trial (Analysis of Coronary Blood Flow Using CT Angiography: Next Steps). J Am Coll Cardiol. 2014;63(12):1145–55. https://doi.org/10.1016/j.jacc.2013.11.043. Epub 2014 Jan 30.
75. Manzke R, Grass M, Hawkes D. Artifact analysis and reconstruction improvement in helical cardiac cone beam CT. IEEE Trans. Med. Imaging. 2004b;23(9):1150–64.

76. von Berg J, Barschdorf H, Blaffert T, Kabus S, Lorenz C. Surface based cardiac and respiratory motion extraction for pulmonary structures from multi-phase CT. Proc SPIE Med Imaging Conf. 2007;6511:65110Y-1–65110Y-11.
77. Peters J, Ecabert O, Schmitt H, Grass M, Weese J. Local cardiac wall motion estimation from retrospectively gated CT images. In: Ayache N, Delingette H, Sermesant M, editors. FIMH 2009, LNCS 5528; 2009; pp. 191–200.
78. Hansis E, Schomberg H, Erhard K, Dössel O, Grass M. Four-dimensional cardiac reconstruction from rotational x-ray sequences: first results for 4D coronary angiography. In: Samei E, Hsieh J, editors. Medical imaging 2009: physics of medical imaging, 72580B; 2009.
79. Rohkohl C, Lauritsch G, Biller L, Prümmer M, Boese J, Hornegger J. Interventional 4D motion estimation and reconstruction of cardiac vasculature without motion periodicity assumption. Med Image Anal. 2010;14:687–94.
80. Forthmann P, van Stevendaal U, Grass M, Köhler T. Vector field interpolation for cardiac motion compensated reconstruction. Proceeding of the IEEE NSS-MIC Conference; 2008.
81. van Stevendaal U, von Berg J, Lorenz M, Grass M. A motion-compensated scheme for helical cone-beam reconstruction in cardiac CT angiography. Med Phys. 2008;35(7):3239–51.
82. Schäfer D, Borgert J, Rasche V, Grass M. Motion-compensated and gated cone beam filtered back-projection for 3-D rotational X-ray angiography. IEEE Trans Med Imaging. 2006;25(7):898–906.
83. Schirra C, Bontus C, van Stevendaal U, Dössel O, Grass M. Improvement of cardiac CT reconstruction using local motion vector fields. Comput Med Imaging Graph. 2009;33:122–30.
84. Fornaro J, Leschka S, Hibbeln D, Butler A, Anderson N, Pache G, et al. Dual- and multi-energy CT: approach to functional imaging. Insights Imaging. 2011;2:149–59.
85. Vlassenbroek A, Dual Layer CT. Dual energy CT in clinical practice, Medical radiology. Berlin/Heidelberg: Springer; 2011b. https://doi.org/10.1007/978-3-642-01740-7.
86. Maass N, Baer M and Kachelriess M. Image-based dual energy CT using optimized precorrection functions: a practical new approach of material decomposition in image domain. Med Phys. 2009;36(8).
87. Fahmi R, Eck BL, Fares A, Levi J, Wu H, Vembar M, et al. Dynamic myocardial perfusion in a porcine balloon-induced ischemia model using a prototype spectral detector CT. Proc. SPIE. 2015;9417:94170Y-8.
88. Engel KJ, Herrmann C, Zeitler G. X-ray scattering in single and dual-source CT. Med Phys. 2008;35(1):318–32.
89. Alvarez RE, Macovski A. Energy-selective reconstructions in X-ray computerized tomography. Phys Med Biol. 1976;21(5):733–44.
90. Goodsitt MM, Christodoulou EG, Larson SC. Accuracies of the synthesized monochromatic CT numbers and effective atomic numbers obtained with a rapid kVp switching dual energy CT scanner. Med Phys. 2011;38:2222–32.
91. Yu L, Leng S, McCollough CH. Dual energy CT-based monochromatic imaging. AJR Am J Roentgenol. 2012;199(5 Suppl):S9–S15.

Coronary Anatomy

3

Claudio Smuclovisky

The left main coronary artery (LM) originates from the left coronary sinus of Valsalva and gives origin to the left anterior descending coronary artery (LAD) and left circumflex coronary artery (LCX). The LAD courses in the anterior epicardial ventricular septum and gives origin to various diagonals and septal perforators. The LAD is divided into proximal, mid, and distal segments. The first septal perforator generally divides the proximal and mid-segments of the LAD. The diagonals are varied in number and caliber and are labeled from proximal to distal, D1, D2, D3, and so forth. The LCX runs in the left atrial–ventricular sulcus and gives origin to obtuse marginal branches (OM). The OMs are labeled from proximal to distal, OM1, OM2, OM3, and so forth. Ostium refers to the segment of origin of the artery (Fig. 3.1a–z).

The right coronary artery (RCA) originates from the right coronary sinus and is divided in proximal, mid, and distal segments. The proximal segment of the RCA is from the ostium to the origin of the first acute marginal artery. In the majority of patients, the conus artery originates from the ostium of the RCA or separately from the right coronary sinus and is generally the first visualized branch. The conus artery has a cranial and anterior course. The sinoatrial (SA) artery is generally the second branch to be visualized and originates from the proximal RCA and has a posterior course in to the left atrium. The RCA gives origin to acute marginal (AM) branches, which vary in size and number and are labeled from proximal to distal, AM1, AM2, AM3, and so forth.

C. Smuclovisky, MD, FACC, FSCCT
Department of Radiology, Holy Cross Hospital, South Florida Medical Imaging Cardiovascular Institute, Fort Lauderdale, FL, USA
e-mail: smuclovisky@gmail.com

C. Smuclovisky (ed.), *Coronary Artery CTA*, https://doi.org/10.1007/978-3-319-66988-5_3

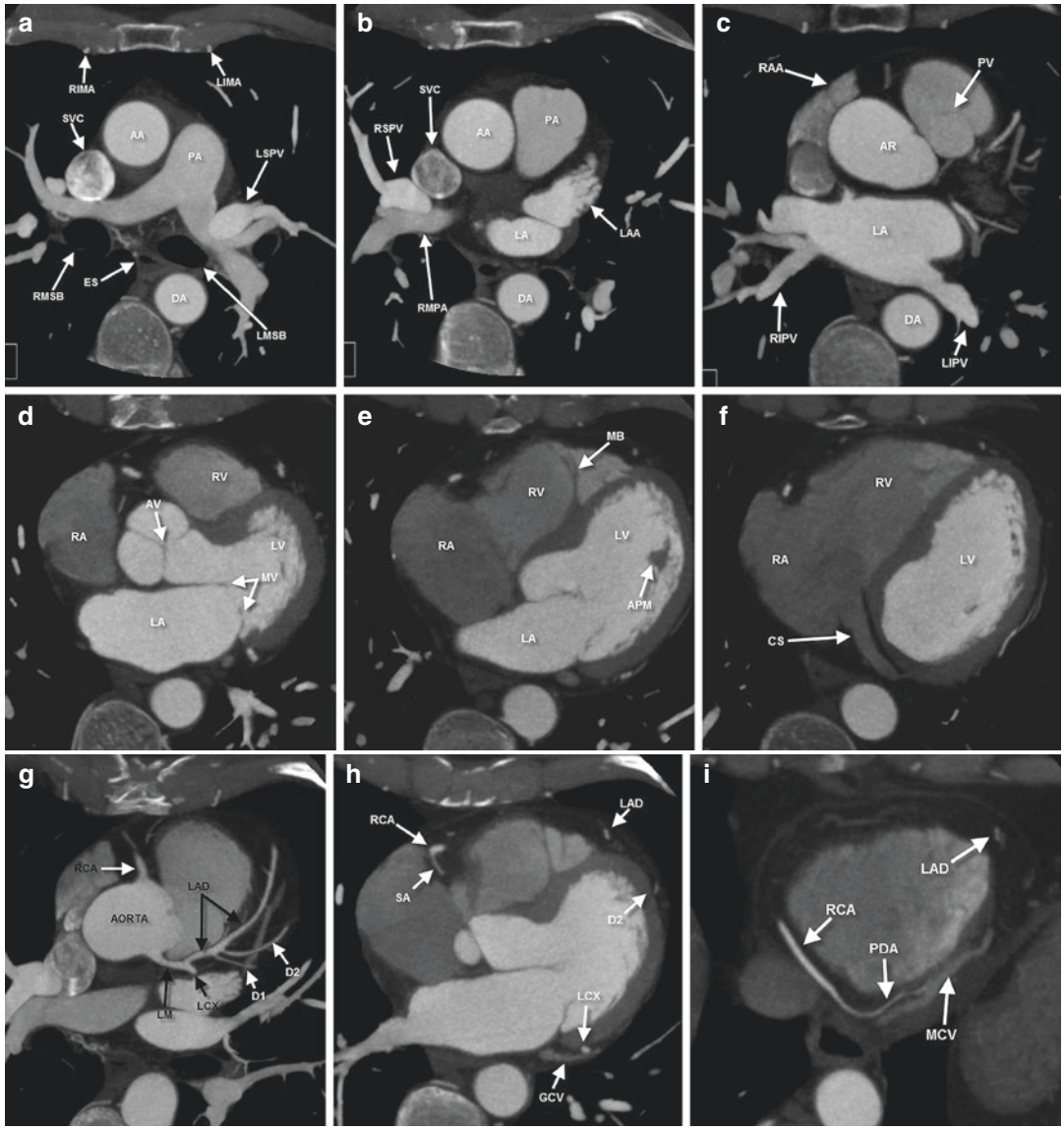

Fig. 3.1 (**a**–**f**) Anatomy. (**g**–**i**) Axial. (**j**–**n**) Coronal. (**o**–**t**) Sagittal. (**u**–**y**) VR. (**z**) 2D composite. *A* anterior; *AA* ascending aorta; *APM* anterior papillary muscle; *AR* aortic root; *AV* aortic valve; *CA* conus artery; *CS* coronary sinus; *D1* diagonal 1; *D2* diagonal 2; *DA* descending aorta; *ES* esophagus; *GCV* great cardiac vein; *I* inferior; *IVC* inferior vena cava; *LA* left atrium; *LAA* left atrial appendage; *LAD* left anterior coronary artery; *LCX* left circumflex coronary artery; *LIMA* left internal mammary artery; *LIPV* left inferior pulmonary vein; *LM* left main coronary artery; *LMSB* left main stem bronchus; *LSPV* left superior pulmonary vein; *LV* left ventricle; *MB* moderator band; *MCV* middle cardiac vein; *MV* mitral valve; *OM1* obtuse marginal 1; *P* posterior; *PA* pulmonary artery; *PAB* pulmonary artery branch; *PDA* posterior descending artery; *PM* papillary muscles; *PV* pulmonic valve (axial C and coronal D); pulmonary vein (sagittal D); *PVB* pulmonary vein branch; *RA* right atrium; *RAA* right atrial appendage; *RCA* right coronary artery; *RIMA* right internal mammary artery; *RIPV* right inferior pulmonary vein; *RMPA* right main pulmonary artery; *RPV* right pulmonary veins; *RPA* right pulmonary artery; *RMSB* right main stem bronchus; *RSPV* right superior pulmonary vein; *RV* right ventricle; *RVOT* right ventricular outflow tract; *S* superior; *SA* sinoatrial artery; *SVC* superior vena cava; *STE* sternum

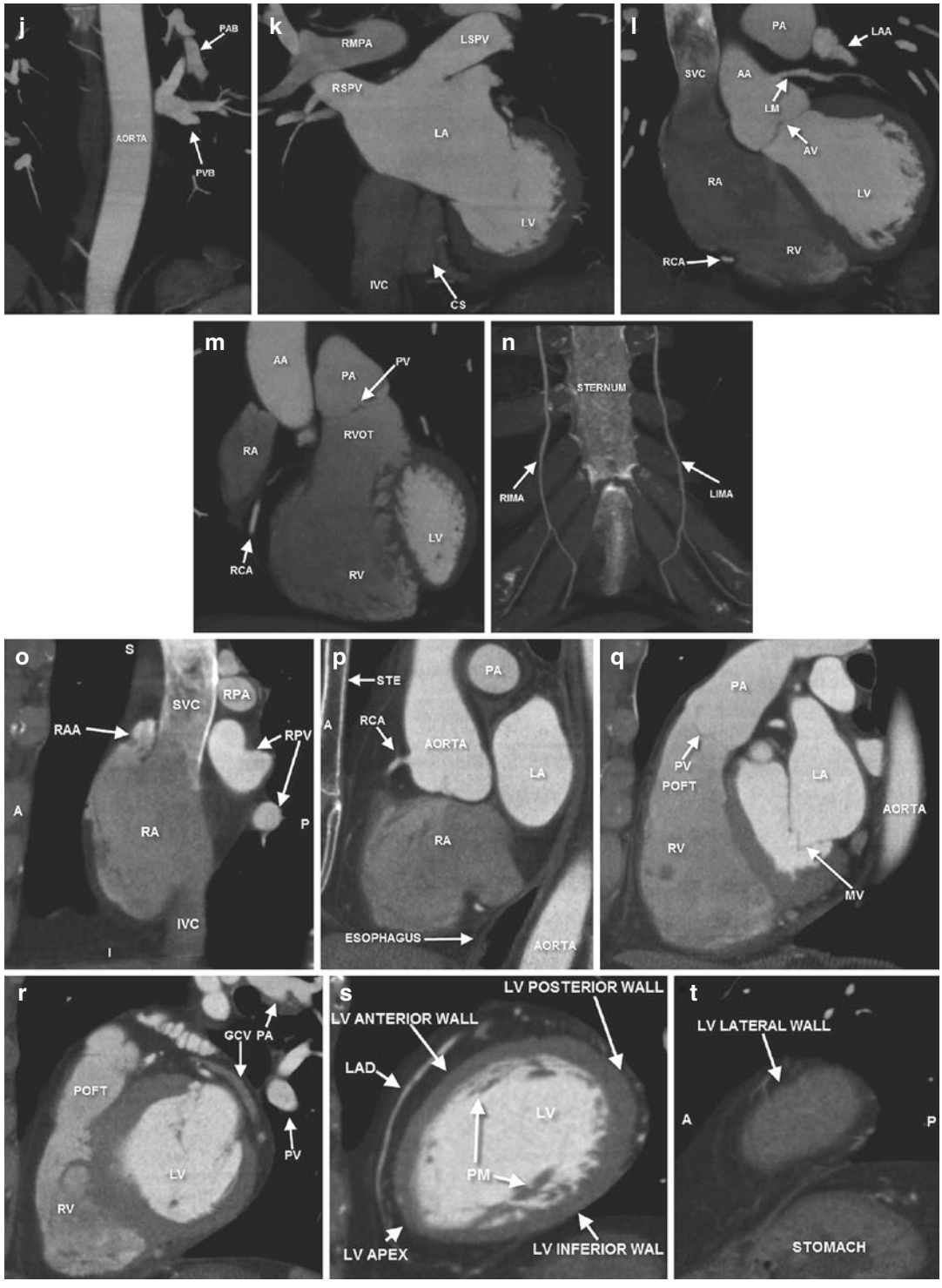

Fig. 3.1 (continued)

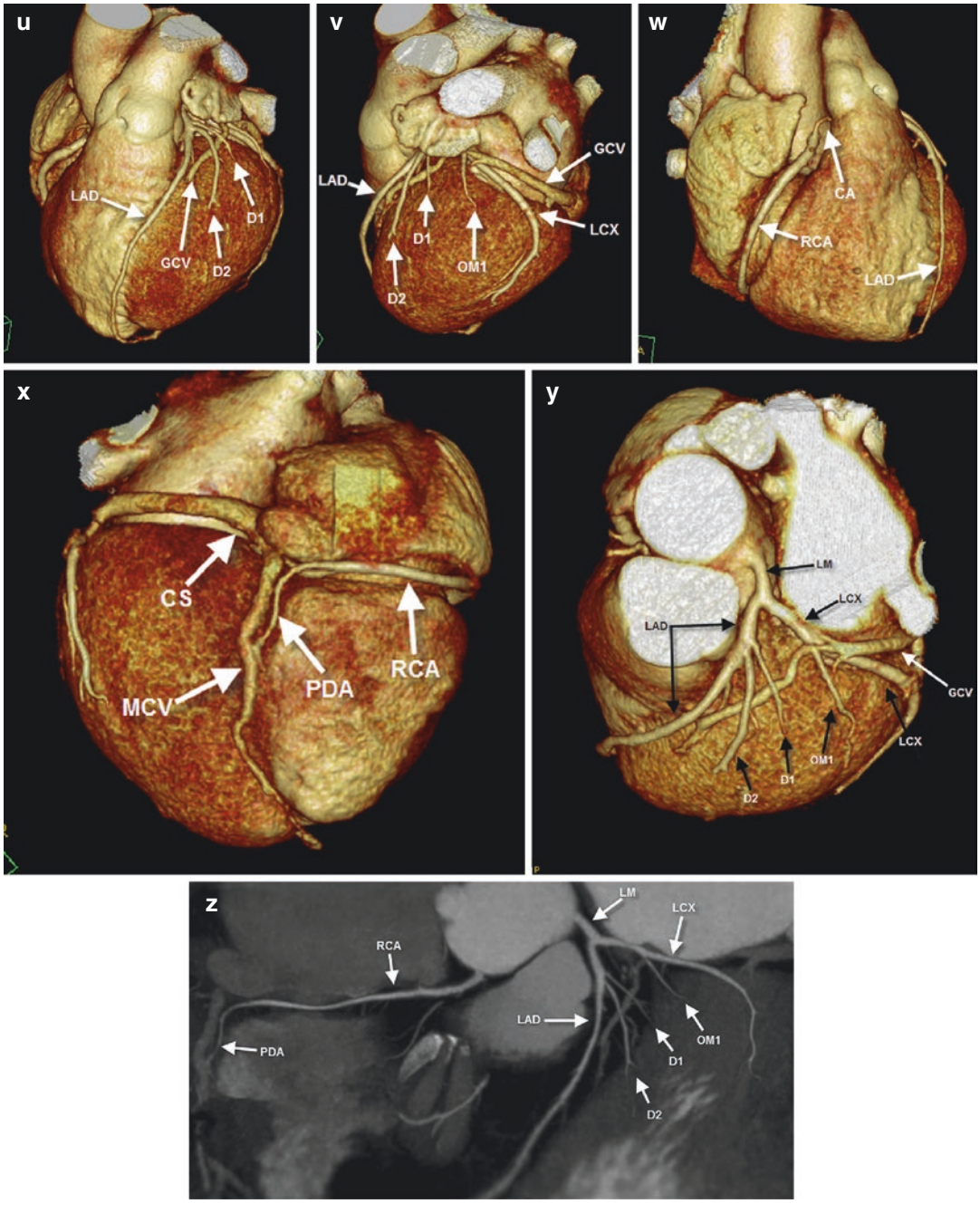

Fig. 3.1 (continued)

Dominance refers to whether the posterior descending artery (PDA) originates from the RCA (right dominant), LCX (left dominant), or both (co-dominant; Fig. 3.2). Approximately 80% of humans are right dominant. In right dominance, the distal RCA at the level of the crux of the heart typically bifurcates into the PDA and a posterolateral branch. The PDA courses in the posterior ventricular septum giving origin to the SA nodal artery and posterior ventricular branch. In left dominance, the PDA originates from the distal LCX. In co-dominance, there are right and left PDAs originating from the RCA and LCX.

The coronary venous system is variable. Generally, the great cardiac vein (GCV) and the middle cardiac (MCV) vein are present. The GCV runs parallel to the LAD and then courses superiorly, crossing the LCX and posteriorly draining into the coronary sinus. The MCV runs inferiorly at midline parallel to the PDA and drains into the coronary venous sinus.

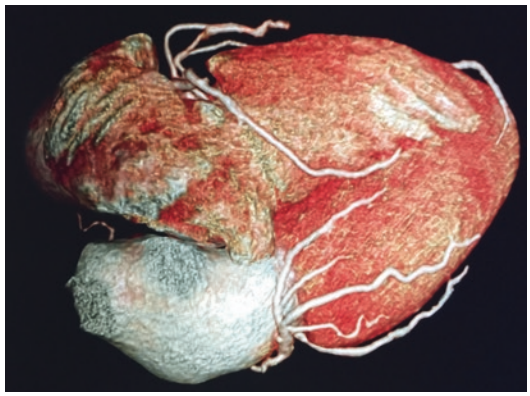

Fig. 3.2 Volume rendered showing co-dominance

The coronary anatomy has great variability. The arteries vary in size, length, course, and branches. It is important to understand the individual anatomy of a patient in order to avoid mistakenly report disease or occlusion of an artery. Close observation must be made as to how the myocardium is receiving its blood supply in normal and diseased arteries. This will be of great importance in the subsequent chapters that illustrate normal coronary variants, congenital coronary anomalies, coronary artery disease (CAD), and collateral pathways.

If the IV contrast bolus is timed correctly in the arterial phase, you will note that the veins are less dense and generally larger than the adjacent coronary arteries. The veins should not be mistaken for diseased or occluded arteries. When in doubt, follow the vessel to its origin (artery) or drainage (vein).

3.1 Case 3.1

3.1.1 History

A 47-year-old asymptomatic male presented with strong family history of coronary disease.

3.1.2 Findings

The study demonstrated a right dominant coronary anatomy and without disease (Fig. 3.3a–i).

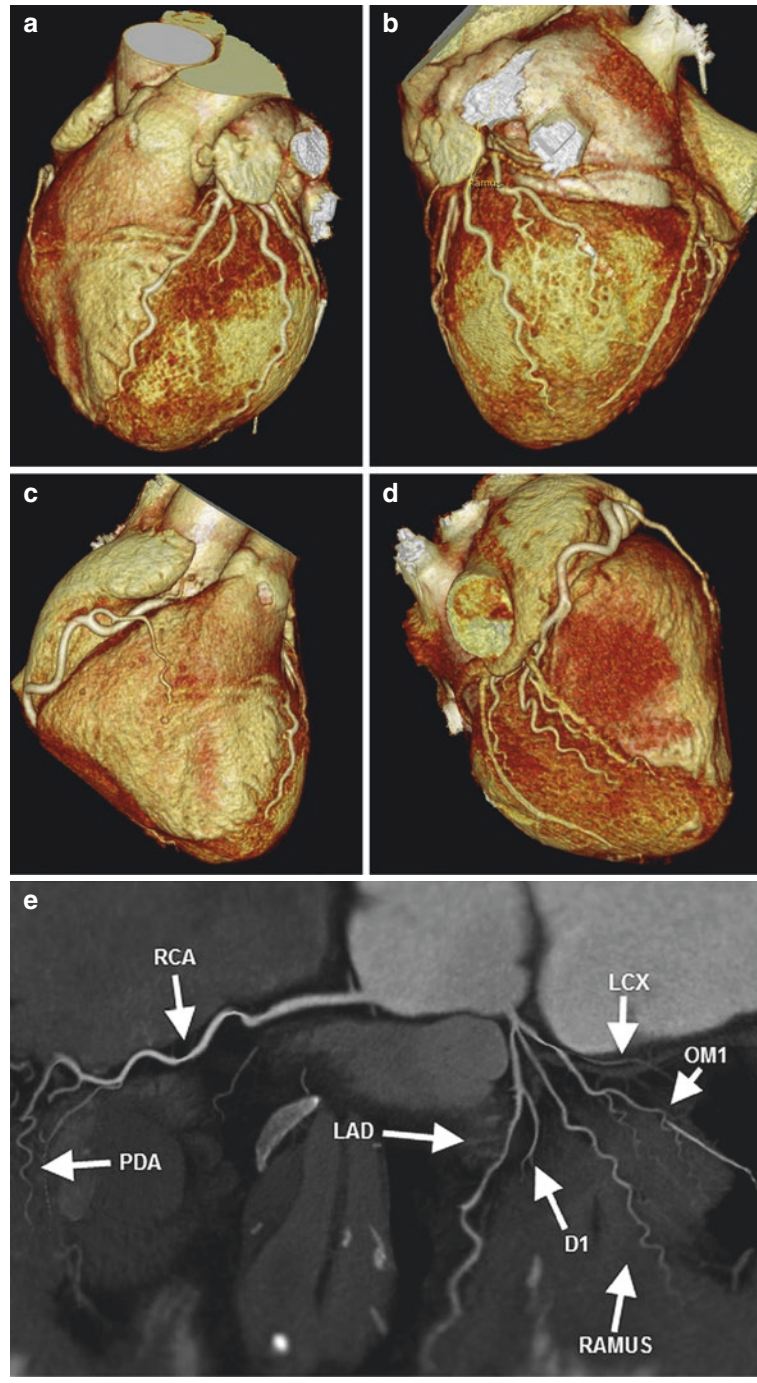

Fig. 3.3 (**a**–**d**) VR: Normal PGA CCTA. (**e**) 2D composite. PGA normal coronary arteries. (**f**–**i**) cMPR of the coronary arteries. With appropriate patient selection and acquisition, the quality of the PGA images is excellent. Also, the spatial resolution is the same as a retrospective acquisition

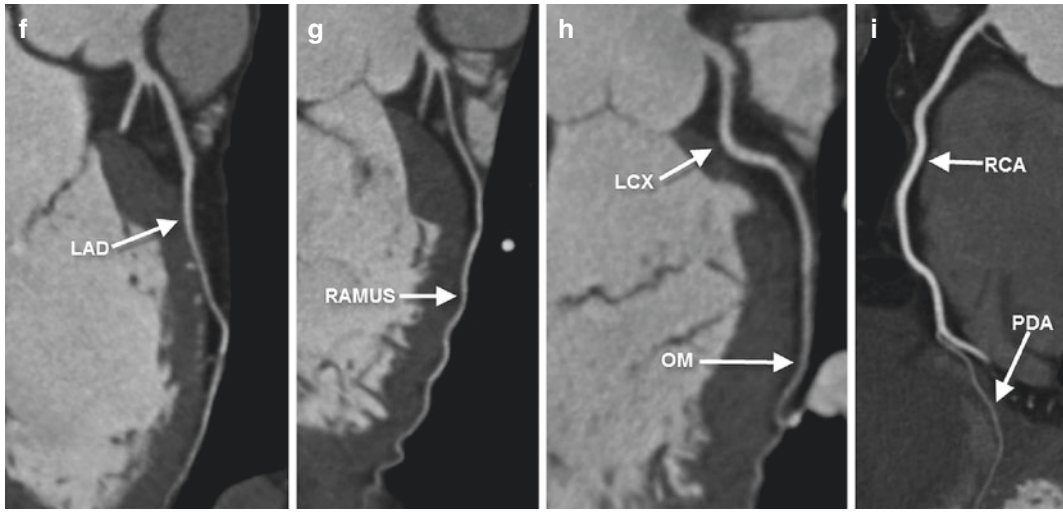

Fig. 3.3 (continued)

3.1.3 Diagnosis

Normal coronary CTA was acquired with prospective gated axial technique (PGA), also known as step and shoot.

3.1.4 Discussion

Radiation exposure is of significant concern, particularly in younger patients. The cardiac CTAs in all modern scanners can be acquired using a single cycle prospective technique known as prospective gated axial (PGA) which are also referred to as "axial acquisition" or "Step and Shoot" (Fig. 3.4). PGA consists of a single cycle acquisition targeted optimally to the mid-diastolic phase of the cardiac cycle where there is the least coronary excursion in order to avoid motion artifact. With PGA, only about 20% of the cardiac cycle is exposed to radiation thus reducing the dose by 80% (≅ 3.0 mSv). By using lower Kv techniques (80–100 Kv), the radiation dose can be further reduced by 90% or more (1 mSv or <) when compared to retrospective acquisition.

The tube exposure is centered on the 75% of the cardiac cycle (EKG R-R interval); however, minimal motion artifact can still degrade the quality of the images. In order to avoid suboptimal images, a slightly wider exposure of 5% on both sides of the 75% phase is commonly performed and is referred to as "padding." Thus, the reconstructed phases of the CCTA will consist of three phases: 70, 75, and 80%.

With retrospective acquisition, multiple cardiac cycles are required with radiation exposure during the entire cycle (approximately 8–30 mSv). The study is acquired gated with CT helical technique. Methods have been developed to reduce radiation exposure by decreasing the X-ray tube output in the non-diastolic phase of the cycle. This is also known as dose modulation, which can achieve, depending on the heart rate, a reduction of the radiation reported in the range of 20–40%.

Currently, we use PGA in all patients, including stents and CABG that do not have a significant arrhythmia like atrial fibrillation. These, we acquire with helical retrospective technique.

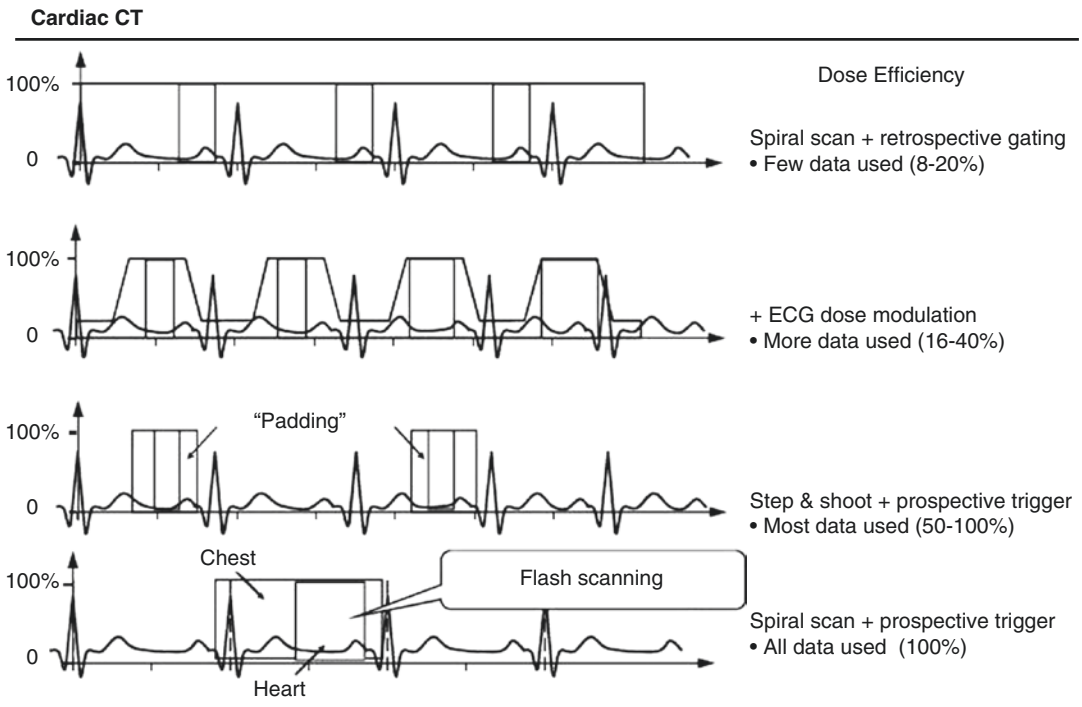

Fig. 3.4 Different cardiac CT acquisition techniques with varying dose efficiencies

In order to acquire a diagnostic study, a low stable heart rate is required below 65 bpm in order to have an adequate diastolic phase of the heart cycle. The use of oral and or IV beta blockers and the vasodilator nitroglycerin, spray or sublingual, is recommended. In our laboratory, the success rate of PGA has been greater than 95%.

3.1.5 Pearls and Pitfalls

The right coronary artery tends to have the most excursion thus is the most frequent to cause motion artifact on the CT. We currently perform the PGA with an IV dose of 60 mL of high-density low-osmolar contrast (370 mg/mL). Following the acquisition, the reconstructed images are immediately assessed to determine whether these are of diagnostic quality. If the study is not considered diagnostic, a second acquisition is quickly performed, unless contra-indicated; with a second IV injection of contrast. The combined total iodine dose generally does not exceed 50 g. This protocol avoids the patient having to be rescheduled. With PGA, limited diastolic phases are acquired; consequently, cardiac wall motion cannot be assessed.

3.2 Case 3.2

3.2.1 History

A 47-year-old male presented with dyslipidemia and a strong family history of CAD.

3.2.2 Findings

The RCA and LCX are short arteries of small caliber. The posterior descending artery was not identified. The LAD and ramus intermedius (RI) arteries are long and have large caliber (Fig. 3.5a, b).

3.2.3 Diagnosis

The diagnosis is normal variant of left coronary dominant anatomy.

3.2.4 Discussion

It is important to differentiate normal variant coronary anatomy from acquired and congenital abnormalities. The LAD and RI in this case provide flow to the inferior and posterior wall of the left ventricle, compensating for the lack of a posterior descending artery originating from the RCA or LCX.

3.2.5 Pearls and Pitfalls

The differentiation between an acquired obstruction of the PDA with compensatory hypertrophy of the LAD and RI versus a normal variant can be ascertained by the identification of a very small RCA and LCX.

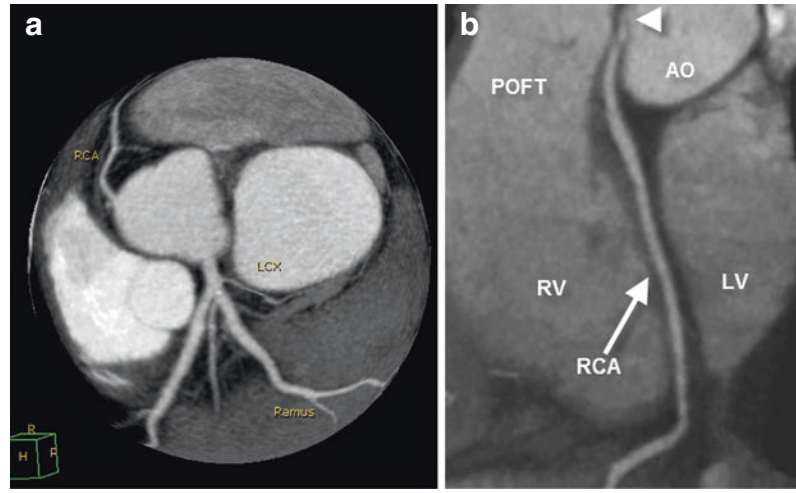

Fig. 3.5 (**a**) Globe sphere. LAD and ramus arteries. Small right coronary artery and left circumflex. (**b**) Axial. Absent posterior descending artery. Middle cardiac vein (*arrow*, MCV)

3.3 Case 3.3

3.3.1 History

A 59-year-old female presented with atypical chest pain and a normal cardiac perfusion scan result.

3.3.2 Findings

There is absence of the right coronary artery. Mild disease is seen in the mid-LAD. Coronary circulation is left dominant, with the left circumflex extending into the right atrial–ventricular sulcus (Fig. 3.6a–c).

3.3.3 Diagnosis

The diagnosis is congenital absence of the right coronary artery, with a super-dominant left circumflex.

3.3.4 Discussion

Knowledge of the cardiac physiology, normal, variant anatomy, and anomalies of coronary circulation is an increasingly vital component in managing congenital and acquired heart disease. In this case, the absence of the right coronary artery is well compensated by the LAD and a long large-caliber left circumflex coronary artery (LCX).

3.3.5 Pearls and Pitfalls

The lack of visualization of the RCA originating from the right sinus of Valsalva, with a dominant left circumflex coronary artery, usually indicates an anatomic variant rather than an occluded RCA.

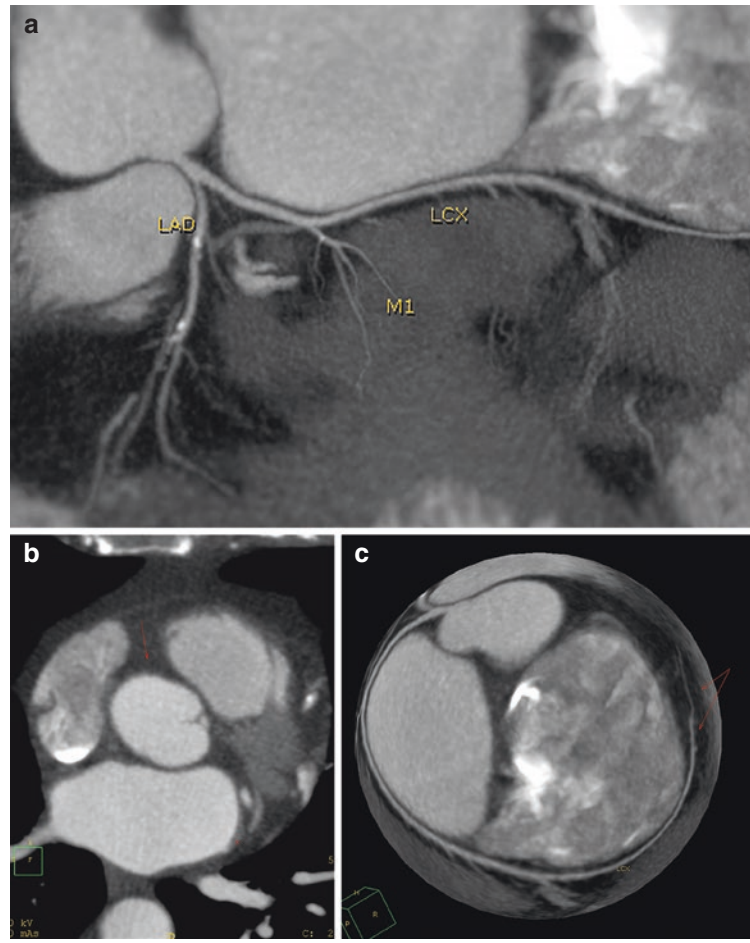

Fig. 3.6 (**a**) 2D map. Left anterior coronary artery and left circumflex coronary artery. (**b**) Axial. Absent right coronary artery (*arrow*). (**c**) Globe sphere: Left circumflex coronary artery extension into the right atrial–ventricular sulcus

3.4 Case 3.4

3.4.1 History

A 59-year-old male presented to the emergency department with chest heaviness and epigastric pain for several days.

3.4.2 Findings

There is absence of the left main artery (Fig. 3.7a, b). Mild non-obstructing multi-vessel coronary artery disease.

3.4.3 Diagnosis

Congenital absence of the left main coronary artery.

3.4.4 Discussion

Not infrequently, absence of the left main coronary artery is identified with separate origins of left anterior descending artery and left circumflex artery from the left sinus of Valsalva.

3.4.5 Pearls and Pitfalls

Congenital absence of the left main coronary artery should be reported as a normal variant and not as a congenital anomaly. Personally, I would rather have this anatomy than left main with the eggs in one basket.

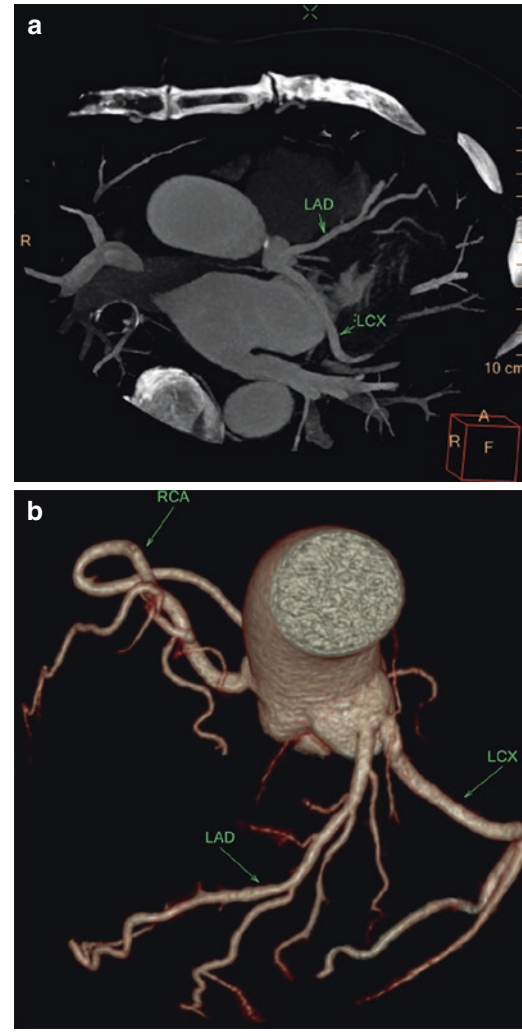

Fig. 3.7 (**a**) Axial MIP. (**b**) Volume rendered coronary tree. LAD and LCX originating from the left sinus of Valsalva and RCA originating from the right sinus of Valsalva

3.5 Case 3.5

3.5.1 History

A 57-year-old female with no past medical history presented to the emergency department complaining of chest pain.

3.5.2 Findings

There is no left circumflex coronary artery (LCX) (Fig. 3.8a–c). No coronary artery disease (CAD). Coronary circulation is right dominant.

3.5.3 Diagnosis

Congenital absence of the left circumflex coronary artery.

3.5.4 Discussion

It is uncommon to encounter a congenital absent LCX, which needs to be differentiated from an occluded artery. In right coronary dominance, the LCX is typically of small or moderate caliber.

3.5.5 Pearls and Pitfalls

There was no visualized LCX ostium to indicate a stump from a thrombus. Flush coronary ostial occlusion is uncommon without a stump. The fact that the other coronary branches are large and have no CAD is conclusive that this is a normal variant.

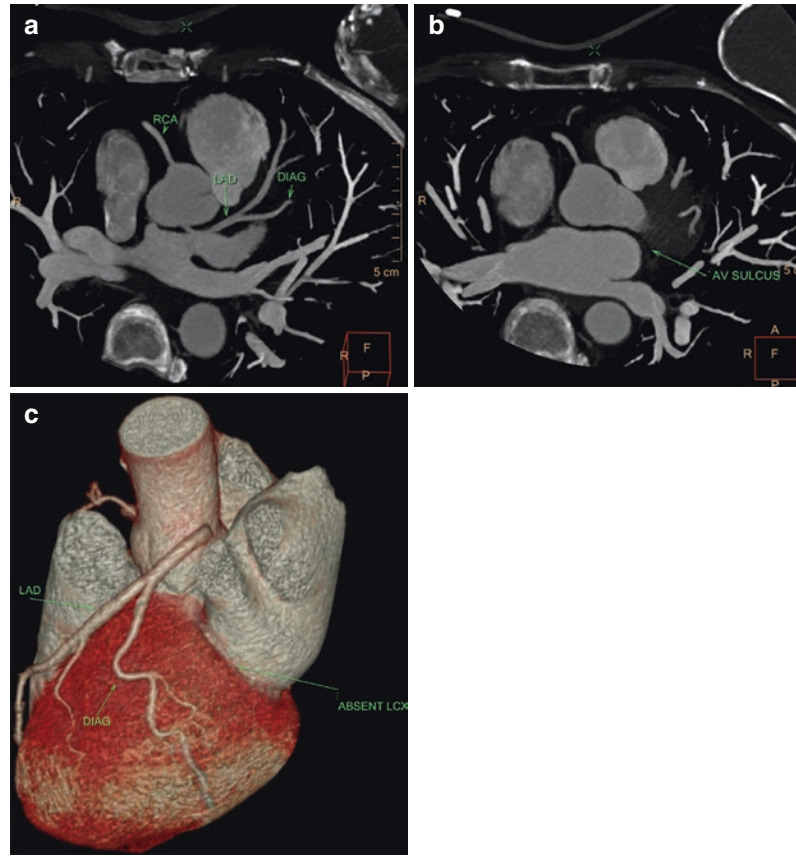

Fig. 3.8 (**a**, **b**) Axial MIP. Absence of LCX over the left atrioventricular sulcus. (**c**) Volume rendered

3.6 Case 3.6

3.6.1 History

A 60-year-old female outpatient with atypical chest pain. No previous cardiac history.

3.6.2 Findings

There is supra-annular anterior origin of the right coronary artery (RCA) (Fig. 3.9a–c). There is a small diverticulum arising from the right inferior wall of the left atrium (Fig. 3.9d). No atherosclerotic coronary artery disease.

3.6.3 Diagnosis

Supra-annular origin of the RCA.

3.6.4 Discussion

Although, some may argue that this is a congenital anomalous origin of the coronary, the RCA has no interarterial course, narrowed ostium, acute angulation, or intramural segment.

Diverticulum arising from the left atrium are common and are usually small. They mostly arise from the superior anterior wall of the left atrium and are of no clinical significance.

3.6.5 Pearls and Pitfalls

The findings are of no clinical significance.

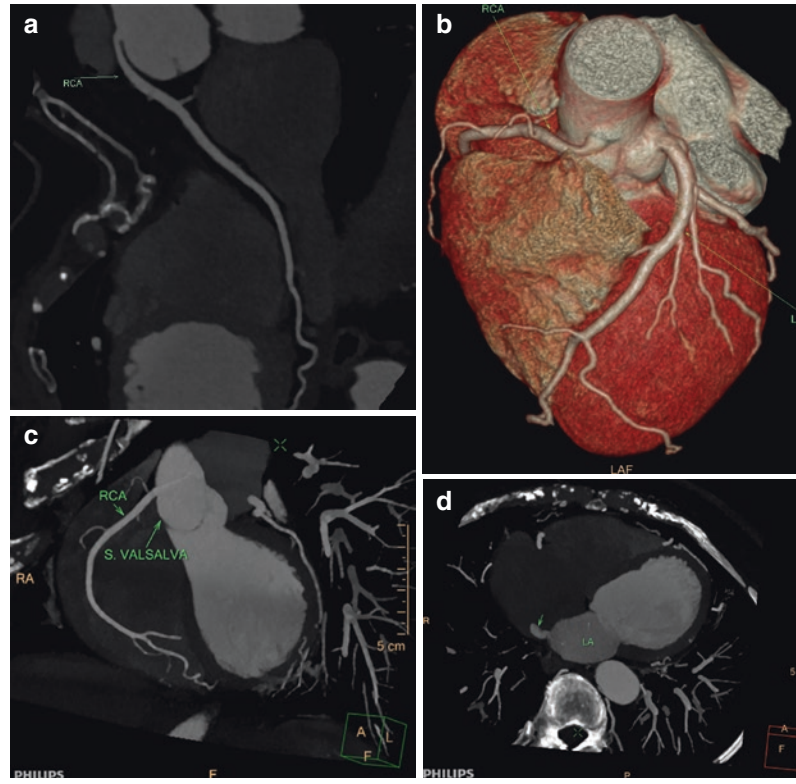

Fig. 3.9 (**a**) cMPR. Supra-annular anterior origin of the RCA. (**b**) VR. (**c**) Coronal. (**d**) Axial. Small diverticulum (*Arrow)* arising from the left atrium

3.7 Case 3.7

3.7.1 History

A 39-year-old male presented to ED with atypical chest pain. No previous cardiac history.

3.7.2 Findings

CCTA was read as a complete obstruction of the mid-LAD with decreased perfusion to the anterior wall and the cardiac apex (Fig. 3.10a–c). Cardiac catherization showed an anatomic variation of the left anterior descending coronary artery (LAD) without any significant obstructive disease (Fig. 3.10d).

3.7.3 Diagnosis

Anatomical variation of the left anterior descending artery.

3.7.4 Discussion

This anatomical variation of LAD was read as a complete obstruction by a less experience reader. Short LAD is a normal variant of coronary anatomy.

The LAD is a short artery that extends into the myocardial septum. The first diagonal branch is long and large caliber and extends to the LV apex in the anterior wall, essentially perfusing the territory of the expected LAD.

3.7.5 Pearls and Pitfalls

It is important to keep in mind the possibility of an anatomical variation of the coronary arteries and appropriately distinguish it from a cardiac disease process.

It is important to distinguish an acute thrombus in the LAD from a chronic total occlusion with a hypertrophied branch serving as a collateral.

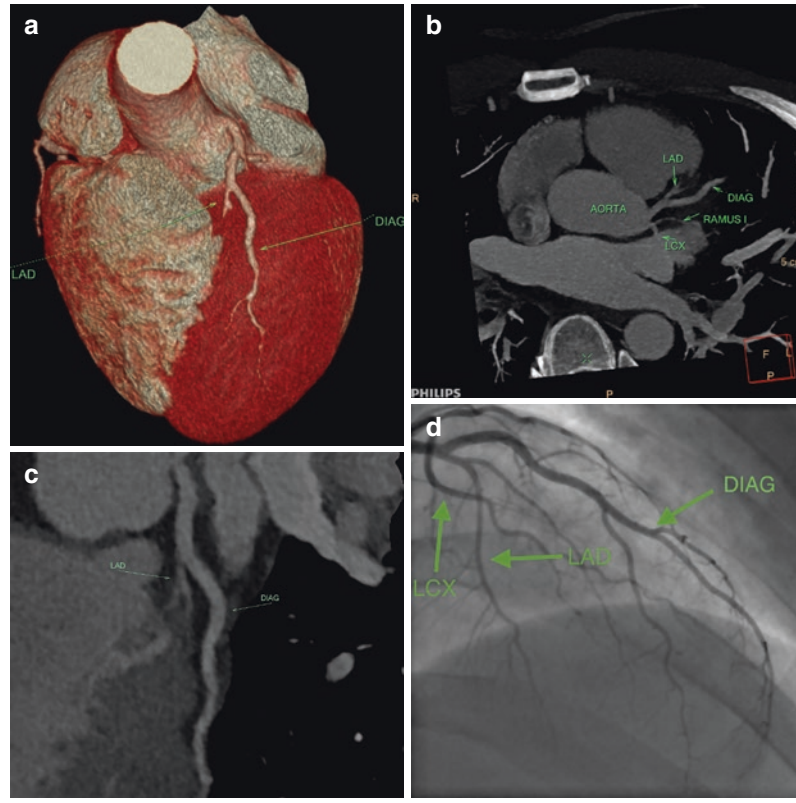

Fig. 3.10 (**a**) Volume rendered. (**b**) olique MIP. (**c**) cMPR. (**d**) Coronary angiogram to confirm short but patent LAD

In this case, there was no thrombus identified in the LAD or atherosclerotic disease, which substantiates a normal anatomical variant.

Suggested Reading

Bastarrika Alemañ G, Alonso Burgos A, Azcárate Agüero PM, et al. Normal anatomy, anatomical variants, and anomalies of the origin and course of the coronary arteries on multislice CT. Radiologia. 2008;50(3):197–206.

Genc B, Solak A, Sahin N, Gur S, Kalaycioglu S, Ozturk V. Assessment of the coronary venous system by using cardiac CT. Diagn Interv Radiol. 2013;19(4):286–93.

Germans T, Nijveldt R, van Rossum AC. A more detailed view calls for more detailed definition: description of cardiac morphology with high-resolution CT and MRI. AJR Am J Roentgenol. 2008;190(2):W169.

Kini S, Bis KG, Weaver L. Normal and variant coronary arterial and venous anatomy on high-resolution CT angiography. AJR Am J Roentgenol. 2007;188(6):1665–74.

Lacomis JM, Goitein O, Deible C, et al. Dynamic multidimensional imaging of the human left atrial appendage. Europace. 2007;9(12):1134–40.

Manghat NE, Rachapalli V, Van Lingen R, et al. Imaging the heart valves using ECG-gated 64-detector row cardiac CT. Br J Radiol. 2008;81(964):275–90.

Mao SS, Ahmadi N, Shah B, et al. Normal thoracic aorta diameter on cardiac computed tomography in healthy asymptomatic adults: impact of age and gender. Acad Radiol. 2008;15(7):827–34.

Medrano-Gracia P, Ormiston J, Webster M, Beier S, Ellis C, Wang C, Young AA, Cowan BR. Construction of a coronary artery atlast from CT angiography. Med Image Comput Comput Assist Interv. 2014;17(Pt 2):513–20.

Poh AC, Juraszek AL, Ersoy H, et al. Endocardial irregularities of the left atrial roof as seen on coronary CT angiography. Int J Cardiovasc Imaging. 2008;24(7):729–34.

Sirineni GK, Stillman AE. Understanding the heart: CT and MRI for coronary heart disease. J Thorac Imaging. 2007;22(1):107–13.

Stolzmann P, Scheffel H, Leschka S, et al. Reference values for quantitative left ventricular and left atrial measurements in cardiac computed tomography. Eur Radiol. 2008;18(8):1625–34.

Thilo C, Schoepf UJ, Gordon L, et al. Integrated assessment of coronary anatomy and myocardial perfusion using a retractable SPECT camera combined with 64-slice CT: initial experience. Eur Radiol. 2008. [Epub ahead of print].

Van de Veire NR, Schuijf JD, De Sutter J, et al. Noninvasive visualization of the cardiac venous system in coronary artery disease patients using 64-slice computed tomography. J Am Coll Cardiol. 2006;48(9):1832–8.

Van Werkhoven JM, Schuijf JD, Jukema JW, et al. Multislice computed tomography coronary angiography: anatomic vs functional assessment in clinical practice. Minerva Cardioangiol. 2008;56(2):215–26.

Wang C, Smedby O. Coronary artery segmentation and skeletonization based on competing fuzzy connectedness tree. Med Image Comput Comput Assist Interv. 2007;10(Pt 1):311–8.

Pediatric Cardiac CTA

4

Dianna M.E. Bardo

4.1 Introduction

The use of cardiac computed tomographic angiography (cardiac CTA) as a diagnostic modality has increased because CT scanner technology has improved. Modern CT scanners have an increased number of detector rows allowing more tissue to be scanned rapidly which reduces motion artifact and need for sedation in children. Iterative image reconstruction techniques reduce image noise, enabling proactive reduction of radiation dose and improved ECG-gating techniques are particularly important for accurate detection of the high heart rates found in children. New multi-energy spectral CT technology may become important in cardiac imaging through enhancing our ability to differentiate tissue composition and enable detection of myocardial perfusion defects. To effectively utilize the tools and technology available on the CT scanner, one must be committed to understanding the physics of CT image acquisition and the use of protocol parameters and image processing techniques designed for imaging with a radiation dose as low as reasonably achievable (ALARA) in children and young adults with acquired and congenital heart disease (CHD).

D.M.E. Bardo, MD, FSCCT, FNASCI
Department of Radiology, Phoenix Children's Hospital, Phoenix, AZ, USA
e-mail: dbardo@phoenixchildrens.com

Patients with CHD have a heart defect which has been present from birth and is most often discovered in the first year of life. In developed countries, steady progress in repairing or palliating congenital heart defects since the mid-twentieth century has led to there being more adults living with CHD than there are children living with CHD.

When examining cross-sectional images in patients with CHD, it is important to begin with standardized or routine search pattern of intra- and extra-cardiac connections. Look for the anatomic differences in the shape of the ventricles, shape of atrial appendages, hepatic, pulmonary and venae cavae connections, and aortic and pulmonary valve and artery connections, and position of the chambers in relation to one another (Table 4.1).

Position of the RV and LV and the cardiac apex in the thorax is determined through a process of looping of the cardiac tube which occurs in the embryological period. Normally, the cardiac tube loops to the right or D-loop which positions the RV anterior and to the right of the LV and the cardiac apex to the left. An abnormal leftward or L-loop of the cardiac tube the right ventricle is positioned to the left of the LV and the cardiac apex may be is rotated into the right thorax. Position of the heart relates to visceroatrial situs or the relative position of the cardiac atria and the abdominal viscera. Normal situs exists when abdominal, cardiothoracic, and bronchopulmonary anatomy is normally arranged in the

C. Smuclovisky (ed.), *Coronary Artery CTA*, https://doi.org/10.1007/978-3-319-66988-5_4

Table 4.1 Normal intra- and extra-cardiac connections and structural features

Structure	Connections	Identifying structural features
Left ventricle (LV)	Inflow: from left atrium (LA) through mitral valve (MV) Outflow: through aortic valve (AV) to ascending aorta (AAo)	Papillary muscles—anterior and posterior muscles in the LV—chordae tendinae extend from tip of each papillary muscle to leaflets of the mitral valve
Right ventricle (RV)	Inflow: from right atrium (RA) through tricuspid valve (TV) Outflow: through pulmonic valve (PVn) to main pulmonary artery (MPA)	Moderator band—near RV apex a muscular band courses from the base of the anterior papillary muscle in the RV toward the intraventricular septum—trabeculation are more prominent than in then LV
Left atrium (LA)	Inflow: from pulmonary veins (PVn) Outflow: to LA	Left atria appendage—a narrow muscular "pouch" extending from the left atrium
Right atrium (RA)	Inflow: from superior vena cava (SVC), inferior vena cava (IVC), and hepatic veins (HV) Outflow: to RA	Right atrial appendage—a broad based cone-shaped extension of the right atrium
Aortic valve (AV) and ascending aorta (AAo)	Inflow: from LV Outflow: to coronary arteries and aortic arch	AV—trileaflet valve with right, left, and noncoronary cusps within the sinuses of Valsalva—lies posterior and to the right of the pulmonary valve (PV) AAo—tubular segment above the sinuses of Valsalva proximal to the aortic arch
Pulmonary valve (PV) and main pulmonary artery (MPA)	Inflow: from RV Outflow: to right and left branch pulmonary arteries (RPA) and (LPA)	PV—trileaflet valve with right, left, and anterior cusps—lies anterior and to the left of the AV MPA—tubular artery above the PV, bifurcates to right and left pulmonary artery branches
Pulmonary veins (PVn)	Inflow: from pulmonary capillary bed Outflow: to LA	PVns—right and left superior and inferior veins and occasionally a right middle pulmonary vein join the LA—left-sided veins often form a common confluence prior to meeting the LA
Superior vena cava (SVC)	Inflow: from jugular, subclavian, and other veins of the head and upper extremities Outflow: to RA	SVC—the major venous drainage pathway of the upper body—typically R sided—a persistent L SVC if present drains to the coronary sinus—there may or may not be a bridging brachiocephalic vein when both R SVC and L SVC are present
Inferior vena cava (IVC)	Inflow: from femoral, renal, and other veins of the lower body Outflow: to RA	IVC—the major venous drainage pathway of the lower extremities and lower body—typically R sided and courses through the liver and along with the RA—may be interrupted in some forms of CHD—if interrupted, the azygous vein continues drainage to the SVC
Hepatic veins (HV)	Inflow: from mesenteric veins to portal veins Outflow: to RA	HV—drain liver parenchyma to the RA—venous drainage from the liver contains a factor which prohibits the formation of arterial venous malformations (AVMs)in the lungs—when hepatic factor is present (as in normal systemic/pulmonary blood flow) pulmonary AVMs do not form)
Mitral valve (MV)	Separates the LA and LV	MV—bileaflet valve separates the LA and the LV—in transposition the MV remains associated with the LV
Tricuspid valve (TV)	Separates the RA and RV	TV—trileaflet valve separates the RA and the RV—in transposition the TV remains associated with the RV

usual manner may be found in patients with CHD, but it is more often that CHD is seen in patients in whom the visceral and atrial anatomy is inverted or ambiguous (Table 4.2).

Noting connections between the key structural components of the heart and the cardiothoracic vasculature and visceroatrial situs, other key anatomic relationships, the relative position or relationship of the aortic and pulmonary valves, and the origins and proximal course of the coronary arteries, allows thorough assessment of mild and complex forms of CHD (Tables 4.3 and 4.4).

With this basic knowledge and an organized anatomic search pattern approach to identify anatomy in cross-sectional images of CHD patients, the collection of the following 25 cases or group of cases reinforce principles which may be applied in daily practice. Each case or group of cases also provides detailed findings of the most common forms of simple and complex CHD.

Table 4.2 Basics of visceroatrial situs

	Situs solitus	Situs inversus	Situs ambiguous
Visceralatrial anatomy	Normal	Reverse of normal	Heterotaxy
Right atrium (RA) Liver	On the right	On the left	Two distinct forms of heterotaxy or situs ambiguous are recognized as most common: *Right isomerism (asplenia)* • bilateral trilobed lungs • bilateral right-sided bronchi • large symmetric liver • absence of the spleen • total anomaly of the pulmonary venous return *Left isomerism (polysplenia)* • bilateral bilobed lungs • interruption of the IVC (with lower body venous flow returning to the heart via azygous vein continuation to the SVC) • multiple spleens • pulmonary veins drain to the right and the left atria Heterotaxy exists as combinations of one or more of the above features—when reporting or discussing a case describe findings independently and use the term heterotaxy.
Left atrium (LA) Stomach Spleen	On the left	On the right	
Trilobed lung Early origin of the upper lobe bronchus from the right main bronchus	Right-sided trilobed lung Right main bronchus with early origin of the upper lobe bronchus	Left-sided trilobed lung Left main bronchus with early origin of the upper lobe bronchus	
Bilobed lung Distal origin of the upper lobe bronchus from the left main bronchus	Left-sided bilobed lung Distal origin of the left upper lobe bronchus	Right-sided bilobed lung Distal origin of the right upper lobe bronchus	
Eparterial bronchial position	Right pulmonary artery (RPA) lies in front of the right bronchus	Left pulmonary artery (LPA) lies in front of the left bronchus	
Hyparterial bronchial position	RPA crosses above the main bronchus	LPA crosses above the main bronchus	

Table 4.3 Features of the aortic valve and pulmonary valve

Structure	Normal position	Leaflet nomenclature	Abnormal position
Aortic valve (AV)	Lies posterior and to the right of the PV	Trileaflet valve with right, left, and noncoronary cusps within the sinuses of Valsalva—The noncoronary cusp always lies adjacent to the intra-atrial septum—even if there is a coronary artery arising from that cusp	**D-TGA**—AV lies anterior and to the right of the PV **L-TGA**—AV lies anterior and to the left of the PV **DORV**—AV lies side-by-side and R of the PV
Pulmonary valve (PV)	Lies anterior and to the left of the AV	Trileaflet valve with right, left, and anterior cusps—lies anterior and to the left of the AV	In TGA, the coronary artery origins are described as from the **R-facing, L-facing, and non-facing sinuses** of the AV—depending on whether they are adjacent to or not adjacent to the PV

Table 4.4 Coronary arteries in CHD

Structure	Coronary artery origin, branches, and course	Key anatomy
Left coronary artery (LM)	**LM** arises from the left sinus of the AV, courses under the LAA—bifurcates to the left anterior descending (LAD) and left circumflex (LCx) coronary arteries **LAD** remains epicardial and courses along the intraventricular septum with diagonal and septal branches **LCx** courses in the left atrioventricular groove with obtuse marginal (OM) branches	The artery which supplies the PDA is referred to as the dominant coronary artery; most often the RCA The LM and RCA should arise at a nearly 90° orientation from the sinus of Valsalva An anomalous coronary artery origin can arise from another sinus, the AAo, or the MPA Anomalous coronary arteries may course in the wall of the AAo, between the AAo and the MPA, behind the AAo and anterior to the atria, over the right ventricle outflow tract, or through the myocardium at the base of the heart
Right coronary artery (RCA)	**RCA** arises from the right sinus of the AV, remains epicardial as it courses in the right atrioventricular groove with acute marginal (AM), conus, posterior descending (PDA), and often a posterolateral (PL) branches **PDA** is a terminal branch which most often arises from the RCA (80%) and courses in the posterior intraventricular groove	

4.2 Azygous Continuation of an Interrupted IVC

Embryological development of the venous drainage of the gut, abdominal viscera, and lower extremities progresses through several stages, beginning in the fifth week of gestation as parallel anterior and posterior cardinal and subcardinal veins which extend the length of the embryo, less than 10 mm in length. Supracardinal veins join the cardinal and subcardinal veins and transverse anastomoses are formed. Communication with the heart is achieved through formation of the intrahepatic segment of the inferior vena cava (IVC) as the right subcardinal vein joins the hepatocardiac canal. The right superior cardinal vein becomes the superior vena cava (SVC). The left superior cardinal vein usually regresses; when it persists drainage continues to the coronary sinus [1].

The dorsally positioned azygous venous system is formed from the cranial portion of the supracardinal veins, becoming the azygous vein on the right and the hemiazygous vein on the left. In the normal situation each of these veins is small caliber, but when the intrahepatic segment of the IVC fails to develop, the azygous vein caliber is enlarged as a larger volume of venous return to the heart must flow through the azygous vein, to the SVC, to the right atrium.

As development of the heart, its arterial and venous connections as well as abdominal visceral formation develop simultaneously during these early embryological weeks, it is not uncommon to have associated other cardiac, pulmonary, and abdominal organ anomalies.

Heterotaxy, a term used to generically describe the presence of cardiothoracic and abdominal situs abnormalities, is often found when the intrahepatic segment of the IVC is interrupted. Not uncommonly, left-sided structures are dominant or there is bilateral left-sidedness (left isomerism), manifested as polysplenia or multiple splenic structures which may be located in either or both upper abdominal quadrants or throughout the peritoneal cavity. Other frequently associated abnormalities include complete or partial abdominal situs inversus with horizontal position of the liver, absence of the gallbladder, and malrotation of the bowel. Anomalies of cardiovascular connections, anomalous pulmonary venous drainage, atrial (ASD) and ventricular (VSD) septal defects or malalignment, bilateral SVCs, and cardiac malposition dominate the cardiothoracic anomalies. Bilateral left-sided lungs (2 lobes each) with hyparterial bronchi and bilateral left-sided atria are often present [2, 3].

4.2.1 Clinical Presentation

Patients with interruption of the intrahepatic IVC and azygous continuation may be discovered in utero with an abnormal structural exam, present as a newborn due to structural congenital heart disease, or may remain asymptomatic and therefore undiscovered prior to imaging performed for other indications.

4.2.2 Case 4.1

See Fig. 4.1.

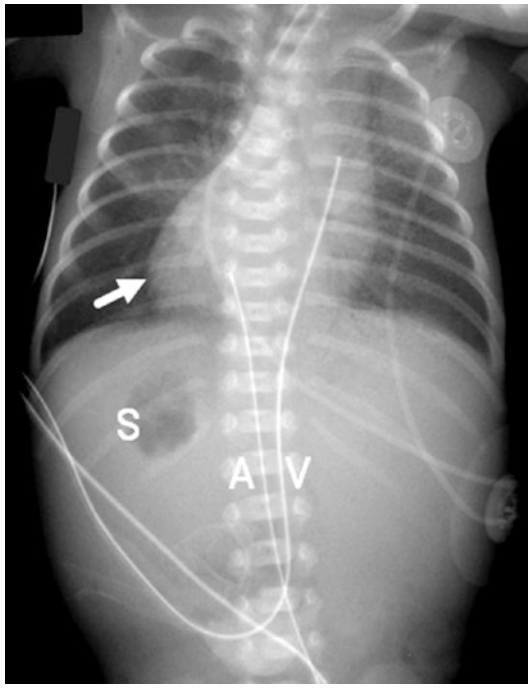

Fig. 4.1 On the first day of life, this newborn who was known to have situs inversus had an umbilical venous catheter (UVC) (*V*) and umbilical arterial catheter (UAC) (*A*) placed prior to a chest and abdomen radiograph. The cardiac apex (*arrow*) and gastric air bubble (*S*) are on the right and the liver shadow is on the left. The tip of the UVC is more cephalad than expected, within the lumen of the left-sided hemiazygous vein in this patient found to have situs inversus and an interrupted IVC and hemiazygous continuation to the hemiazygous arch which drained to the SVC. In this situation, situs inversus, the L SVC drains to the morphologic right atrium and a persistent R SVC (if present) would drain to the coronary sinus. This patient does not have a persistent R SVC

4.2.3 Case 4.2

See Figs. 4.2, 4.3, and 4.4.

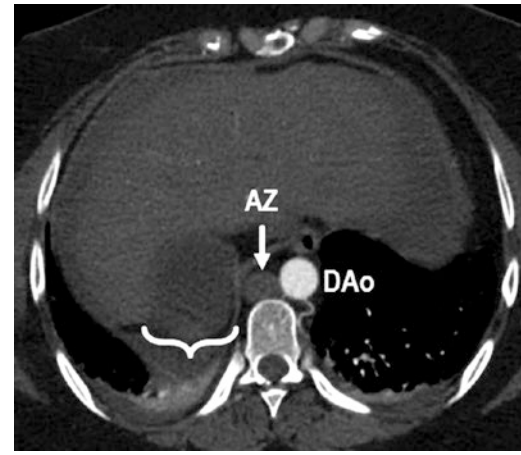

Fig. 4.2 An arterial phase contrast enhanced axial image of the upper abdomen shows the large caliber azygous vein (AZ) and absence of the intrahepatic segment of the IVC. In the right upper quadrant, a low attenuation structure is a spleen (*bracket*); numerous other splenic nodules were located in the right upper quadrant on caudal images. The descending aorta (DAo) is on the left of midline

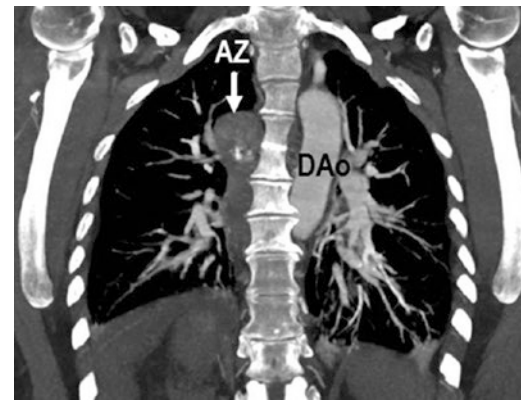

Fig. 4.3 A coronal view of the chest from the contrast enhanced CT shows the extension of the enlarged azygous vein (*AZ*) nearly to the level of the aortic arch. The azygous vein and descending aorta (DAo) caliber are similar and pulmonary vasculature is enlarged

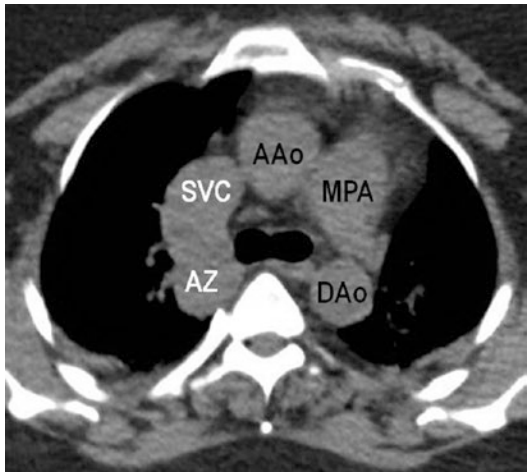

Fig. 4.4 The patient had a previous CT exam, performed without IV contrast. An axial image at the level of the carina is all that is needed to know that the intrahepatic IVC is interrupted. The azygous vein (AZ) and the azygous arch which connects the vein to the superior vena cava (SVC) are enlarged, similar in caliber to the ascending (AAo) and descending (DAo) aorta. The superior surface of the main pulmonary artery (MPA) is also seen

4.2.4 Case 4.3

This adult patient has been healthy all her life. She presents to the emergency room with abdominal pain. See Fig. 4.5.

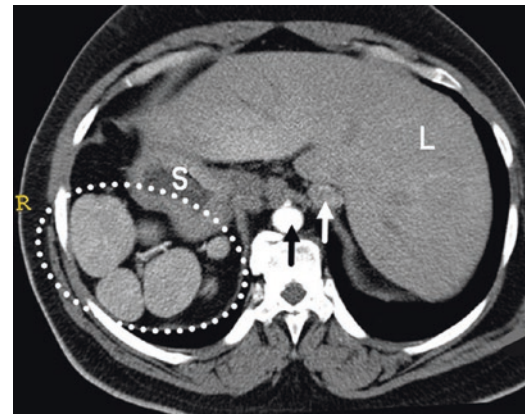

Fig. 4.5 An axial contrast enhances CT image of the upper abdomen shows that several splenic structures (*dotted ellipse*) are in the right upper quadrant along with the stomach (S). The liver (L) is in the right upper quadrant and the intrahepatic segment of the IVC (*white arrow*) is present and the azygous vein is not enlarged. The abdominal aorta (*black arrow*) is at the midline. Remember that polysplenia may be found without interruption of the IVC

4.3 Persistent Left Superior Vena Cava

Persistent left superior vena cava (PLSVC) is the most common congenital venous anomaly in the thorax. Most individuals with PLSVC are asymptomatic throughout their entire life; the reported incidence of BSVC in the general population is less than 0.5%. In patients with congenital heart disease, PLSVC is known to occur much more frequently, in up to 12%.

PLSVC may occur with or without the presence of a right SVC, i.e., bilateral SVC (BSVC). When bilateral, the SVCs may be similar or dissimilar in caliber and the brachiocephalic (innominate) vein may or may not be patent; as a bridging vein between the SVCs, but is absent in most (65%).

Systemic venous drainage via a PLSVC most often occurs via the coronary sinus to the right atrium (80–92%). If the coronary sinus is unroofed, deoxygenated blood from the PLSVC drains to the right and left atria. A PLSVC may drain entirely to the left atrium through a direct connection to the roof of the atrium.

Of course, a PLSVC is also found in situs inversus and when the right SVC is absent. In this situation venous drainage of the upper body is to the anatomic right atrium which also lies on the left.

4.3.1 Clinical Presentation

An asymptomatic adolescent underwent chest CT for an unrelated indication.

4.3.2 Case 4.4

4.3.2.1 Patient 1

See Fig. 4.6.

4.3.3 Clinical Presentation

Two newborn patients with congenital heart disease underwent CTA to define intracardiac and great vessel anatomy; the underlying CHD lesions will not be discussed. In the course of diagnosis, in each patient PLSVC was discovered.

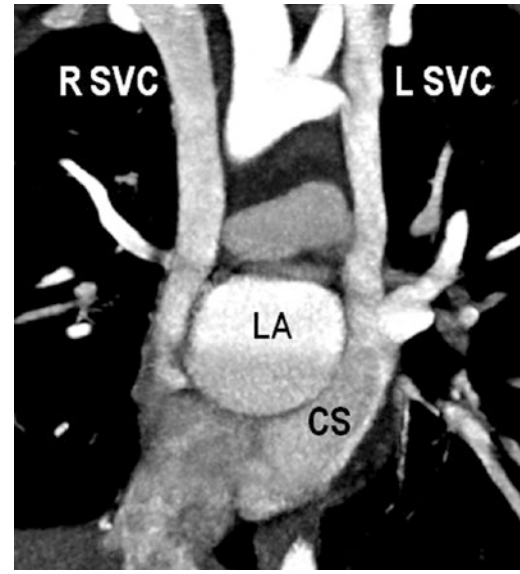

Fig. 4.6 A coronal oblique view of the thorax shows both a right (R SVC) and left (L SVC) superior vena cava. The L SVC drains to the coronary sinus (CS). There was not a patent bridging vein

4.3.4 Case 4.5

4.3.4.1 Patient 2

See Figs. 4.7, 4.8, and 4.9.

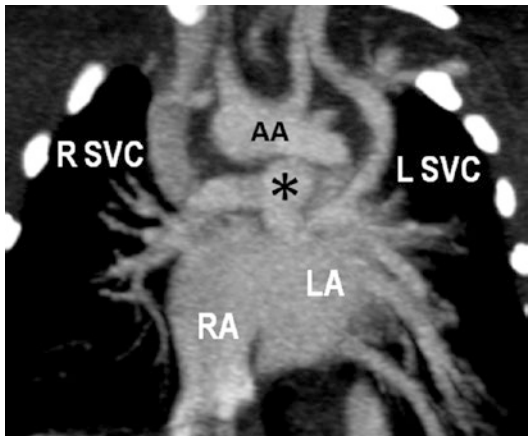

Fig. 4.7 A large defect in the intra-atrial septum results in what is effectively a single atrial chamber. A right (R SVC) and left (L SVC) drain to the superior aspect of the right (RA) and left (LA) side of the atria, respectively. The main pulmonary artery (*Asterisk*) and aortic arch (AA) are seen in the midline

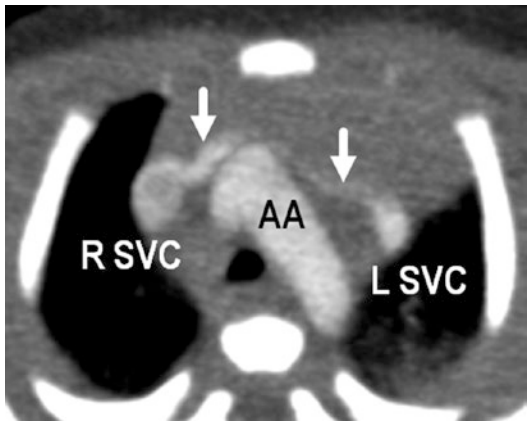

Fig. 4.8 An axial image at the level of the aortic arch (AA) shows the right SVC (R SVC), the smaller caliber left SVC (S SVC), and the very small caliber bridging vein (*arrows*)

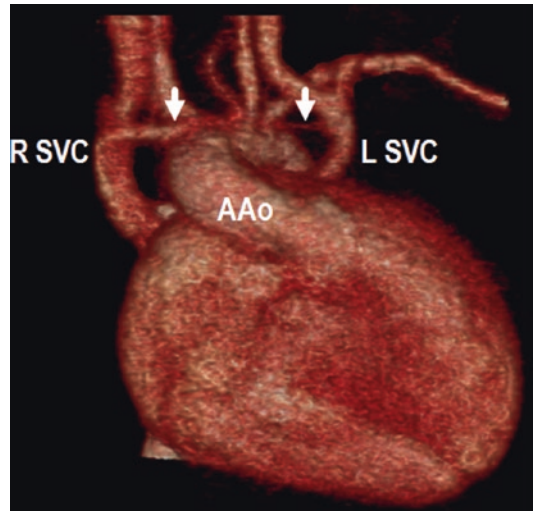

Fig. 4.9 The right (R SVC) and left (L SVC) superior venae cavae are seen in a 3D surface rendered reconstruction. The wispy, small caliber bridging brachiocephalic vein (*arrows*) is anterior to the ascending aorta (AAo) at the level of the aortic arch

4.3.4.2 Patient 3

See Figs. 4.10, 4.11, and 4.12.

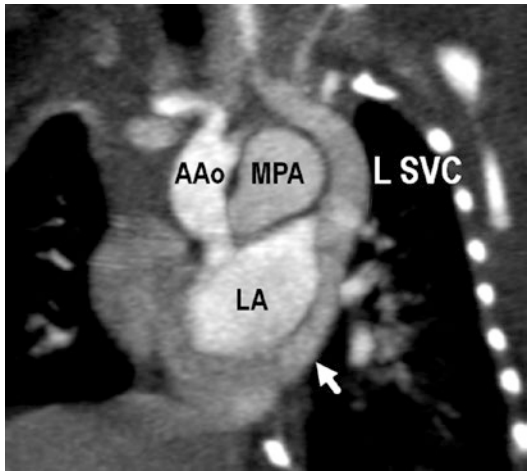

Fig. 4.10 A less common form of PLSVC is seen, with persistence of the left SVC (L SVC) and absence of the right SVC in this patient with normal situs. The L SVC drains to the coronary sinus (*arrow*); the roof of the coronary sinus is intact (proved by the difference in density of contrast in the left atrium (LA) and the coronary sinus). The ascending aorta (AAo) and main pulmonary artery (MPA) have a normal relationship

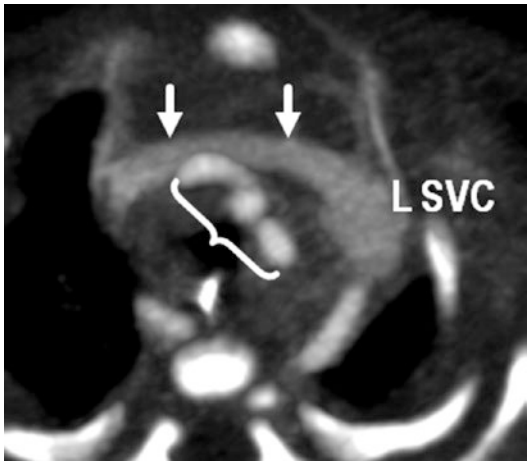

Fig. 4.11 The brachiocephalic vein (*arrows*) courses from right to left, anterior to the brachiocephalic arteries (*bracket*), to the left superior vena cava (L SVC). The right SVC is absent

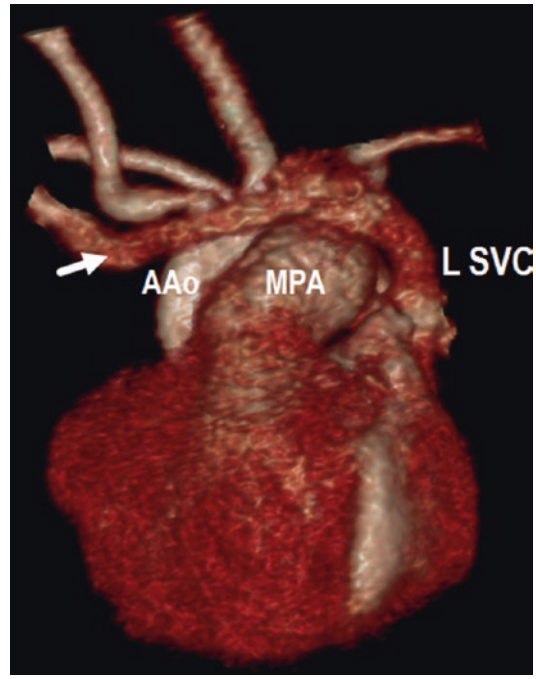

Fig. 4.12 A 3D surface rendered reconstruction shows the position of the brachiocephalic vein (*arrow*) which courses anterior to the ascending aorta (AAo) and main pulmonary artery (MPA) and drains to the left SVC (L SVC)

4.4 Coarctation of the Aorta

Coarctation of the aorta refers to focal stenosis of the aorta. The most common location of coarctation is at the aortic isthmus (also referred to as the aortic infundibulum), at the insertion of the ductus arteriosus.

The ductus arteriosus is an in utero structure which allows blood flow from the right side of the heart to the descending aorta. Histologically, the ductus arteriosus is composed of loosely arranged muscular fibers and connective tissue matrix surrounded by an adventitial layer of fibrous connective tissue which is contiguous with the adventitia of the aorta and pulmonary artery. The regularly spaced internal elastic lamellae seen in the wall of the muscular wall of the aorta or pulmonary artery are absent in the ductus arteriosus [4]. Ductal intima is composed of a thick irregular cell layer with mucoid material. It was found several years ago that the intima of the ductus arteriosus which has not closed normally contains a subendothelial internal elastic lamina [5, 6]. The tissues of the aorta and ductus arteriosus behave differently after birth when changes in oxygen tension occur in the blood, resulting in closure of the ductus arteriosus within a few days after birth [5, 7].

In the 1979 paper by Ho and Anderson, histological findings showed evidence of extension of ductal media tissue into the isthmus and proximal descending aorta (DAo), resulting in varied degrees of coarctation. The differences in the response of each tissue type are thereby responsible for coarctation; ductal tissue, infiltrated, or misplaced into the aorta responding normally, constricts resulting in narrowing of the aorta. Occasionally, ductal tissue is suspected to be present in the origin and proximal left subclavian artery as stenosis of this vessel may be found in coarctation patients.

Concurrent with coarctation of the aorta, tubular hypoplasia of the aortic arch, and bicuspid aortic valve are not uncommon. These associations raise concern that a generalized aortopathy is present in patients so affected.

The classification of coarctation into pre-ductal and post-ductal lesions has long been known to be ineffectual. Terminology has changed, for the past few decades the term juxtaductal is used to describe the typical location and etiology of aortic coarctation; for all practical purposes simply using the word coarctation is adequate. Further, descriptions of a "shelf" of aortic and ductal intimal tissue which have been described are also probably not accurate and the partial or completely circumferential narrowing of the aorta is due to extension of ductal tissue into the media of the aorta.

4.4.1 Clinical Presentation

4.4.1.1 Fetus

The diagnosis of coarctation in the fetus is difficult, perhaps due to challenges in obtaining acoustic window and the small size of cardiac structures. Prenatal diagnosis may be suspected if there is right/left asymmetry of the heart.

4.4.1.2 Infants

It is most common that coarctation of the aorta is diagnosed in utero or in the newborn period. In utero, a routine fetal anatomic examination includes visualization of the aortic arch and direction of blood flow in the ductus arteriosus which should be patent.

A murmur that persists beyond the time of expected closure of the ductus arteriosus suggests a shunt lesion or perhaps coarctation. Echocardiography is indicated as the first examination.

The caliber of the aortic arch, brachiocephalic artery branching, and the presence of ductal patency, coarctation, atrial or ventricular septal defect, or lack thereof should be documented.

4.4.1.3 Older Children and Adults

Diagnosis of coarctation of the aorta may escape clinical awareness either because it is clinically inconsequential or due to a lack of concern on the part of the primary physician, even if a murmur or other signs are present. Bilateral upper and lower extremity pulse and blood pressure may not be routinely performed as part of a physical exam unless the diagnosis is first suspected.

Depending upon the severity of the coarctation development of compensatory collateral blood flow around the coarctation will be well developed, with large caliber intercostal, internal mammary, axillary, and vertebral collateral arteries which supply the descending aorta.

4.4.2 Case 4.6

A 1-day-old newborn male has a prenatal diagnosis of hypoplasia of the aortic arch and coarctation of the aorta. He is treated with intravenous prostaglandin to maintain patency of the ductus arteriosus in order to maintain blood flow to the descending aorta. In order to better define the severity of arch hypoplasia and coarctation as well as branching pattern of the brachiocephalic arteries from the arch prior to surgical intervention, cardiac CTA was requested. See Figs. 4.13 and 4.14.

In reporting the findings, it is helpful to the surgeon to measure the diameter of each segment of the aorta and the length of the hypoplastic segments.

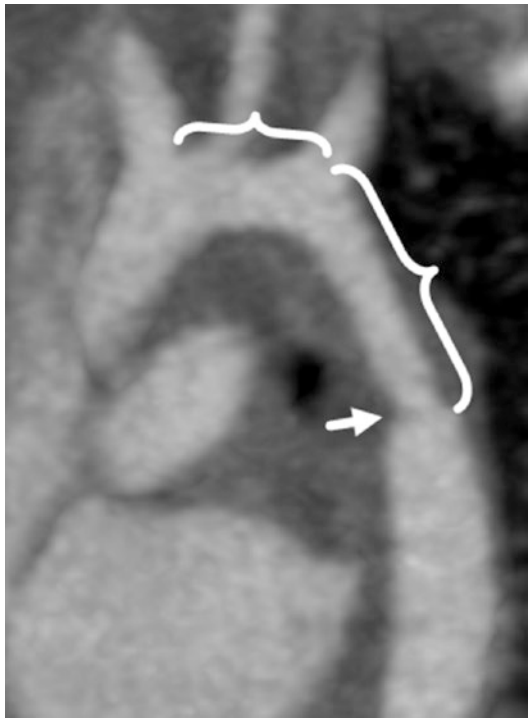

Fig. 4.13 A sagittal oblique "candy cane" view of the aortic arch shows hypoplasia of the transverse (*short bracket*) and distal (*long bracket*) segments of the arch and elongation of the distal segment as well as discrete narrowing or coarctation (*arrow*)

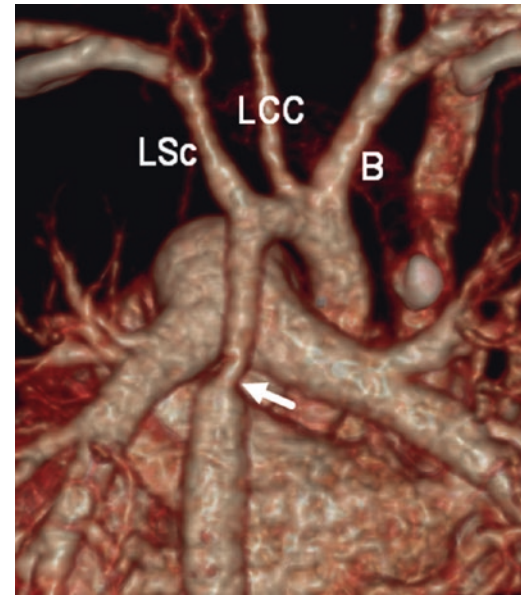

Fig. 4.14 A 3D surface rendered view of the aorta shown from a posterior perspective reveals the hypoplastic aortic arch and normal branching pattern of the brachiocephalic arteries; innominant or brachiocephalic artery (B), left common carotid artery (LCC), and left subclavian artery (LSc). The elongated segment of the distal aortic arch and discrete coarctation (*arrow*) are also shown

4.4.3 Case 4.7

A 15-year-old boy reported intermittent left arm pain at his school physical examination. His pediatrician heard a low pitched murmur throughout systole and the first part of diastole and found relatively lower blood pressure in the left upper extremity compared to the right upper extremity and decreased femoral pulses. Subsequently, an echocardiogram showed acceleration of blood flow velocity in the proximal descending aorta and discrete coarctation of aorta. Cardiac CTA was requested in order to better reveal the degree of coarctation and extent of collateral arteries. See Figs. 4.15, 4.16, and 4.17.

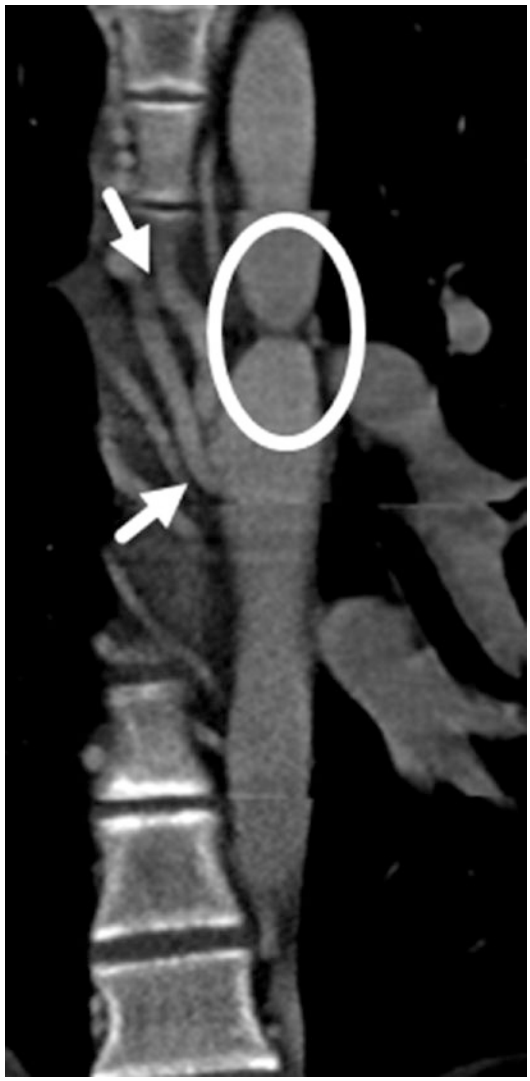

Fig. 4.15 A coronal reformatted maximum intensity projection (MIP) image of the thoracic descending aorta reveals large caliber intercostal arterial collaterals (*arrows*) draining to the aorta distal to the discrete coarctation (oval)

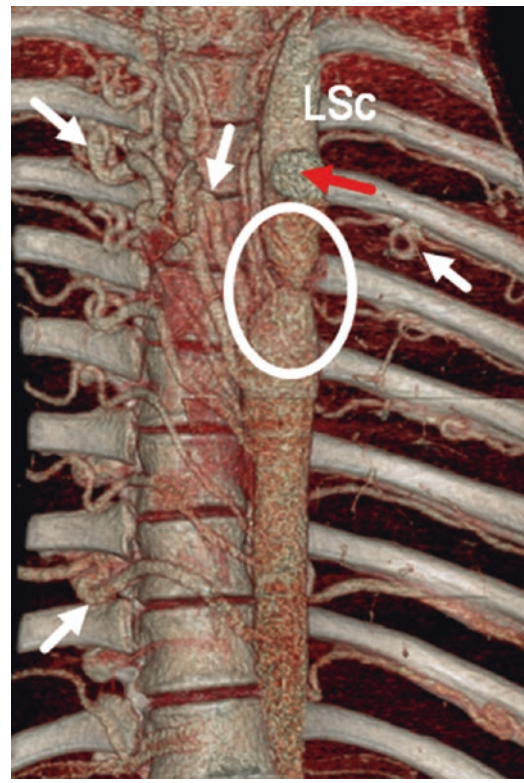

Fig. 4.16 The DAo and intercostal arterial collaterals (*arrows*) and the discrete coarctation (*oval*) are again seen in this 3D surface rendered cardiac CTA reconstruction. The left subclavian artery (LSc), proximal to the coarctation is large caliber; the aortic arch has been cut away (*red arrow*)

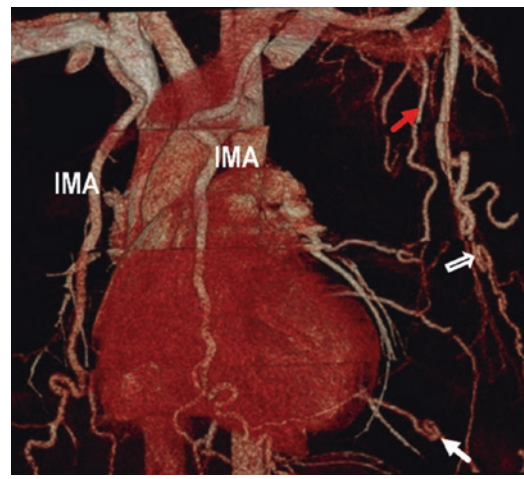

Fig. 4.17 This 3D surface rendered image of the heart and collateral arteries shows large caliber right and left internal mammary (IMA), axillary (*red arrow*), lateral thoracic (*open arrow*), and intercostal (*white arrow*) arteries

4.5 Interrupted Aortic Arch

Discontinuity of the lumen of the aortic arch, or interruption of the aortic arch (IAA), is a rare congenital vascular anomaly (<1.5%), which can occur in any arch segment. Interruption just distal to the left subclavian artery (type A) occurs in nearly 1/3 of cases, when between the left common carotid artery and the left subclavian artery (type B) interruption is more common, found in more than 2/3 of patients, and the rarest variety of arch interruption which is seen in only 3–5% occurs between the brachiocephalic and the left common carotid arteries (type C).

The embryologic basis of the segments of the aorta, pulmonary arteries, and major branch brachiocephalic arteries lies in the development and regression of a series of paired vessels which form within the pharyngeal pouches around the pharynx. Each pharyngeal pouch contains endodermal tissue, including a vascular component termed a pharyngeal or aortic arch and neural crest cells which influence development and migrate to the heart. Six pairs of aortic arches connect the dorsal aortae to the aortic sac.

As development proceeds the first, second, and fifth paired arches involute almost entirely; with only small remnants persisting as the first pair forms maxillary and partial external carotid artery segments. The second paired arches persist as the stapedial arteries of the middle ear; the fifth pair completely regresses during the fetal period in about 50%, and forms only transient rudimentary vessels in the other 50%. The third, fourth, and sixth pharyngeal arches give rise to segments of the aorta and major branching arteries. The third pharyngeal arches become the common and internal carotid arteries. The right and left fourth arches develop independently. The left fourth pharyngeal arch, along with the dorsal aorta and the aortic sac, forms the arch of the aorta; the right fourth arch, along with the seventh intersegmental artery, contributes to the formation of the right subclavian artery. The right and left sixth pharyngeal arch arteries also develop uniquely; the distal right sixth arch degenerates completely and the proximal persists as the proximal right pulmonary artery. The left sixth arch creates left pulmonary artery and the ductus arteriosus.

The site of each type of aortic arch interruption may be based in this embryology. IAA type A may be the result of abnormal regression of the left fourth aortic arch just beyond the left subclavian artery origin, at the site of its connection with the dorsal aorta. IAA type B occurs when a segment of the left fourth aortic arch regresses abnormally between the origins of the common carotid arteries. Type C IAA occurs when the left ventral third and fourth aortic arches regress, resulting in a proximal interruption, while the common carotid arteries form from tissue which would typically regress if the aortic arch had formed normally.

IAA is often associated with other cardiovascular abnormalities, most often patent ductus arteriosus which maintains perfusion to the descending aorta in utero. Only rarely is IAA an isolated cardiovascular malformation.

4.5.1 Pearls (•) and Pitfalls (#)

• Clinical suspicion of IAA may not occur until the ductus arteriosus begins to close.

Severe coarctation of the aorta may present in a similar manner or have complications similar to those seen in patients with IAA.

4.5.2 Clinical Presentation

A newborn with suspected aortic arch hypoplasia and coarctation of the aorta on prenatal US underwent postnatal echo which raised suspicion of interruption of the aortic arch; cardiac CTA was requested for further definition of the aortic arch.

4.5.3 Case 4.8 Presentation

See Figs. 4.18, 4.19, 4.20, and 4.21.

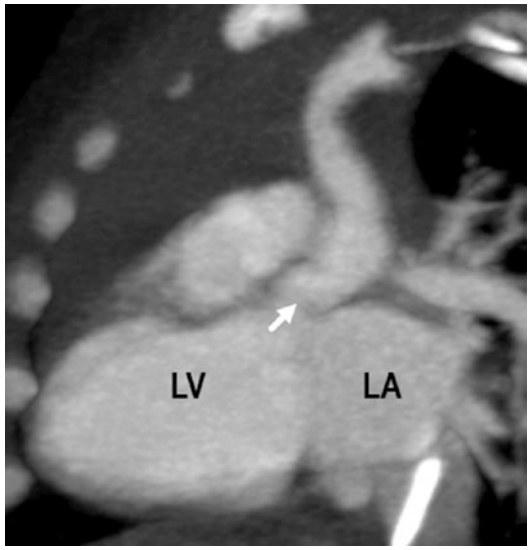

Fig. 4.18 An in-and-out view of the left side of the heart shows the left atrium (LA), left ventricle (LV), the left ventricular outflow tract, and the aortic valve (*arrow*). The ascending aorta is normal caliber but the aortic arch is interrupted

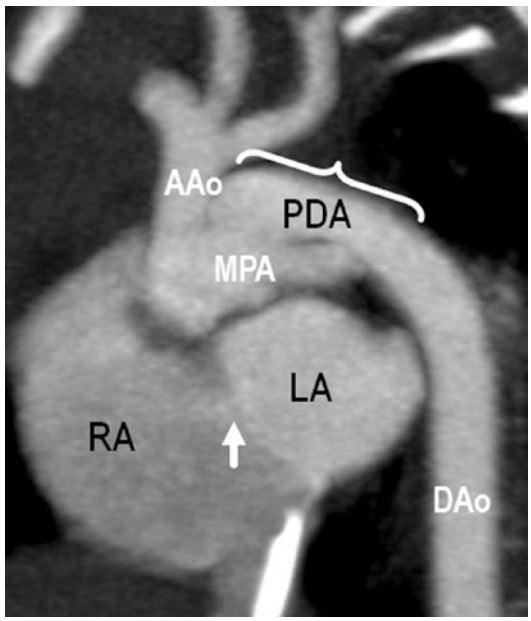

Fig. 4.19 A sagittal oblique view which includes the ascending (AAo) and descending (DAo) aorta shows the type A interruption of the aortic arch (*bracket*), just distal to the left subclavian artery origin. The patent ductus arteriosus (PDA) connects the main pulmonary artery (MPA) to the DAo. A small volume of contrast spills from the left (LA) to the right atrium (RA), through the patent foramen ovale (*arrow*)

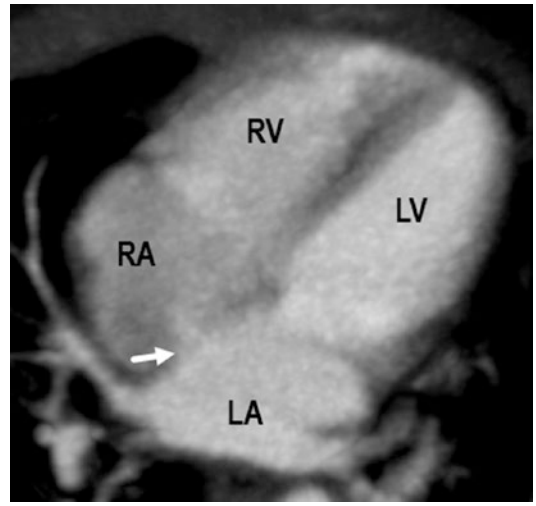

Fig. 4.20 A four-chamber view of the heart confirms the defect in the interatrial septum (*arrow*)

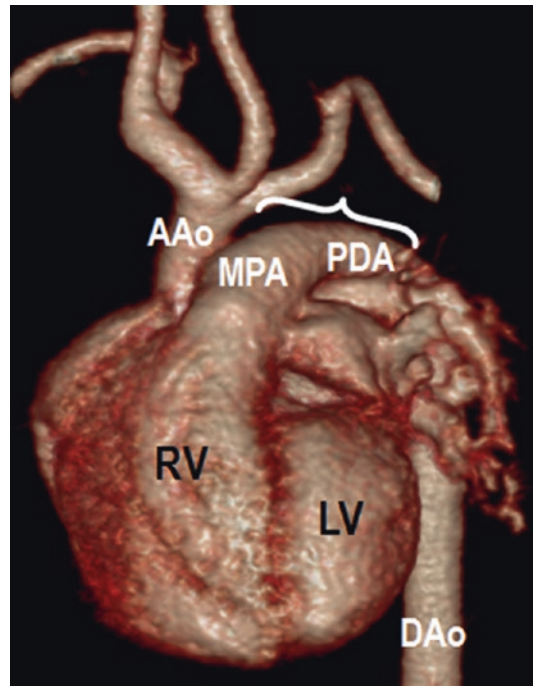

Fig. 4.21 The findings of a type A interruption are easily seen on a 3D surface rendered CTA image. The ascending aorta (AAo) is normal caliber and the three brachiocephalic arteries branch from the proximal aortic arch. The aortic arch is interrupted distal to the left subclavian artery (*bracket*). The main pulmonary artery (MPA) exits the right ventricle (RV) and continues as the patent ductus arteriosus (PDA) to supply blood flow to the descending aorta (DAo)

4.5.4 Clinical Presentation

A newborn with diagnosis of right ventricle hypertrophy and a dysplastic pulmonic valve on prenatal echocardiogram has an additional diagnosis of suspected interruption of the aortic arch on a postnatal echo. Cardiac CTA was requested to further characterize the aortic arch and anatomy of the brachiocephalic artery origins.

4.5.5 Case 4.9 Presentation

See Figs 4.22, 4.23, 4.24, and 4.25.

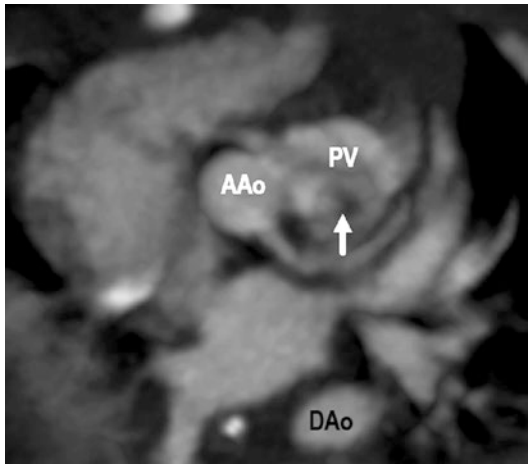

Fig. 4.22 An axial oblique view of the heart shows the proximal ascending aorta (AAo) and the pulmonic valve (PV); thickened soft tissue (*arrow*) of the dysplastic pulmonic valve leaflets is prominent

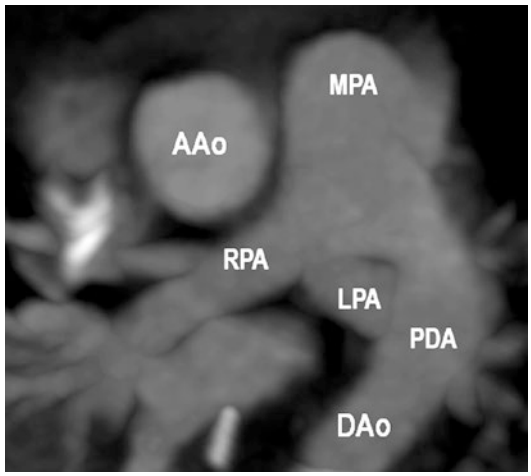

Fig. 4.23 An axial oblique view of the superior mediastinal structures shows the ascending (AAo) and descending (DAo) aorta and the main (MPA), right (RPA) and left (LPA) pulmonary arteries as well as the patent ductus arteriosus (PDA) which supplies blood flow to the DAo distal to the aortic arch interruption

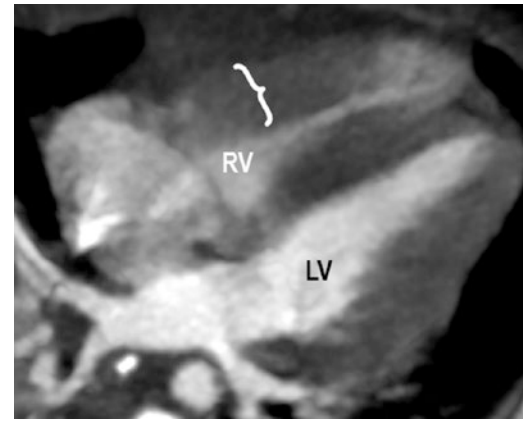

Fig. 4.24 The four-chamber view confirms right ventricle (RV) hypertrophy (*white bracket*), secondary to stenosis of the dysplastic and stenotic pulmonic valve. The left ventricle (LV) is normal volume

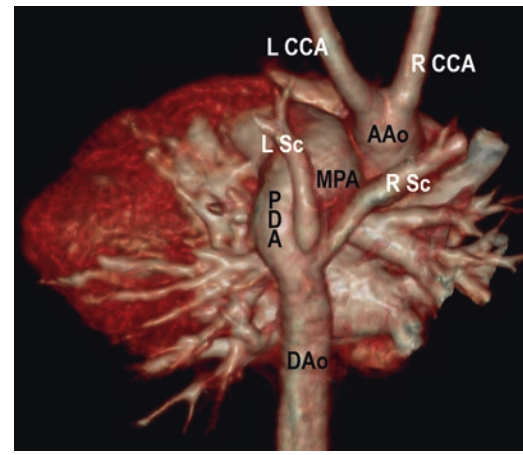

Fig. 4.25 A 3D surface rendered view of the heart shows the ascending (AAo) and descending (DAo) aorta, and absence of a connection between the two segments. The type B interruption in the aortic arch is between the left common carotid (L CCA) and the left subclavian (L Sc) arteries. The patent ductus arteriosus (PDA) provides blood flow to the descending aorta (DAo) from the main pulmonary artery (MPA) to the DAo. The origin of the right subclavian artery (R Sc) is aberrant, from the distal aortic arch

4.6 Truncus Arteriosus

In the early stages of cardiac embryology, bilateral heart tubes fold to form the atria and ventricle chambers of the heart. At the cephalad margin of the heart tubes is the primitive conus which has vertical and horizontal portions and becomes ventricular outflow tract including the tissue which divides the outflow. Shortly thereafter, the truncus arteriosus forms above the outflow tracts then twists and divides to form the aorta and main pulmonary artery and fuses with the primitive conus. The ventriculoarterial (aortic and pulmonic) valves form in the plane at which and the conus and truncus arteriosus meet.

Formation and division of the truncus arteriosus is based on the precision and timing as well as signals from neural crest tissue. Although rare (1–3 in 10,000) errors occur, the development of the truncus arteriosus may not divide completely to a separate aorta and main pulmonary artery but persists as a single or common truncal vessel arising above the primitive conus; this malformation or failed septation is named after the embryologic structure, the truncus arteriosus (TA). The branch pulmonary arteries arise from the common truncus either as a common trunk which divides to the right and left (type 1) or from separate origins, usually from the posterolateral surface of the common truncus (type 2). While other variations, namely pulmonary arteries from the ductus arteriosus, descending aorta, or the ventral surface of the common truncal vessel have been reported and more elaborate classification schemes have been published, TA type 1 and TA type 2 are the commonest, most clinically relevant forms.

The ventriculoarterial valves also typically malformed when the TA is maldeveloped, existing as a single truncal valve, most often with morphology of the aortic valve and trileaflet, though a bicuspid valve, or a quadricuspid valve which incorporates pulmonic valve tissue may be seen. The coronary artery origins may also be abnormal.

Associated congenital heart defects include ventricular septal defect (VSD), transposition of the great arteries (TGA), double outlet right ventricle (DORV), and conduction abnormalities.

4.6.1 Pearls (•) and Pitfalls (#)

• The truncal valve is most often morphologically similar to the aortic valve.

• Truncus arteriosus represents failure of septation of the primitive structure rather than an abnormal communication between the aorta and main pulmonary artery.

A focal abnormal communication between otherwise normally formed aorta and pulmonary artery is called an aorticopulmonary (AP) window.

4.6.2 Clinical Presentation

A newborn was suspected to have a diagnosis of tetralogy of Fallot on prenatal echocardiogram due to small caliber branch pulmonary arteries. Postnatal echo revealed findings of truncus arteriosus and a dysplastic truncal valve. As branch pulmonary artery anatomy remained in question, cardiac CTA was requested.

4.6.3 Case 4.10 Presentation

See Figs. 4.26, 4.27, 4.28, and 4.29.

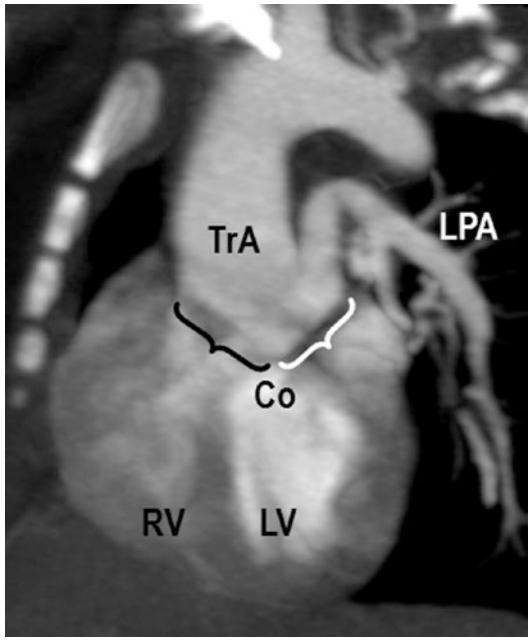

Fig. 4.26 A sagittal oblique view of the base of the heart shows the common truncal vessel (TrA) and conal tissue (Co) under the common truncal valve which appears to have components of both the aortic (*black bracket*) and pulmonic (*white bracket*) valves. The left pulmonary artery (LPA), but not the right pulmonary artery, is seen

4.6.4 Clinical Presentation

A newborn with a known diagnosis of truncus arteriosus on prenatal echocardiography underwent cardiac CTA so branch pulmonary artery anatomy could be evaluated.

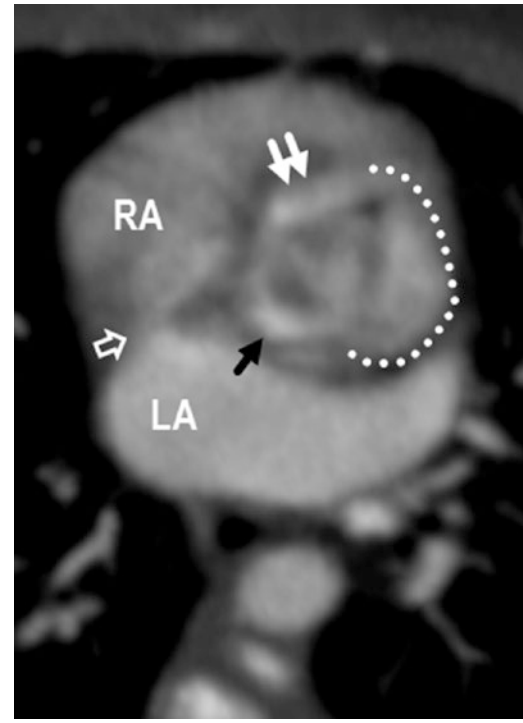

Fig. 4.27 The truncal valve is seen in this axial oblique maximum intensity projection (MIP) image. The right (RA) and left (LA) and position of the interatrial septum (*open arrow*) are seen. The truncal valve with predominantly aortic morphology has a noncoronary artery cusp (*black arrow*) nearly aligned with the interatrial septum, right coronary cusp (*double arrow*) and a larger, dysmorphic cusp (*dotted line*) which is likely composed of left coronary cusp and pulmonic valve tissue

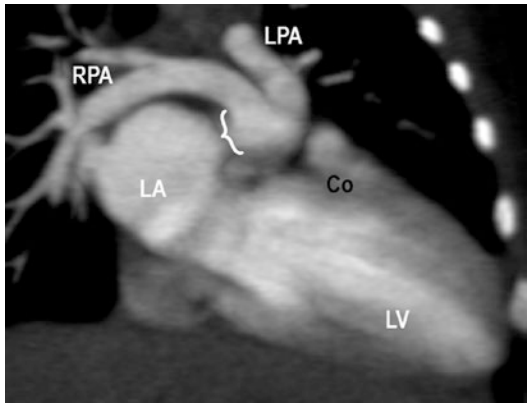

Fig. 4.28 A two-chamber view of the left side of the heart shows the left ventricle (LV) and atrium (LA) and the posterior aspect of the truncus arteriosus which reveals the pulmonic component of the TA which has a common origin several millimeters above the truncal valve (*white bracket*). The right (RPA) and left (LPA) branch pulmonary arteries bifurcate several millimeters above the common pulmonary origin. Myocardial tissue (Co) which divides and forms the ventricular outflow below the common truncal valve originates from the primitive conus

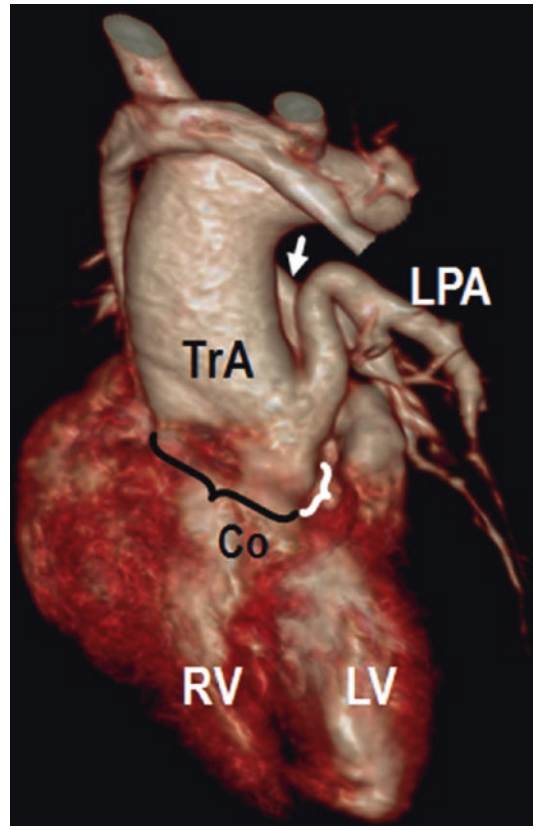

Fig. 4.29 The complex plane of the common truncal valve composed of aortic (*black bracket*) and pulmonic (*white bracket*) tissue divides tissue from the primitive conus (Co) and the truncus (TrA). The left pulmonary artery (LPA) obscures view of the right pulmonary artery (*arrow*)

4.6.5 Case 4.11 Presentation

See Figs. 4.30, 4.31, 4.32, and 4.33.

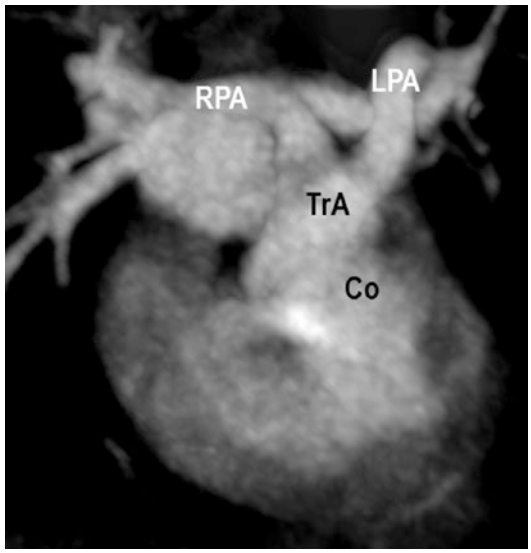

Fig. 4.30 An axial oblique view of the heart shows the separate origins of the right (RPA) and the left (LPA) pulmonary arteries from the common truncal vessel (TrA) and the outflow tract, the lumen of the primitive conus (CO)

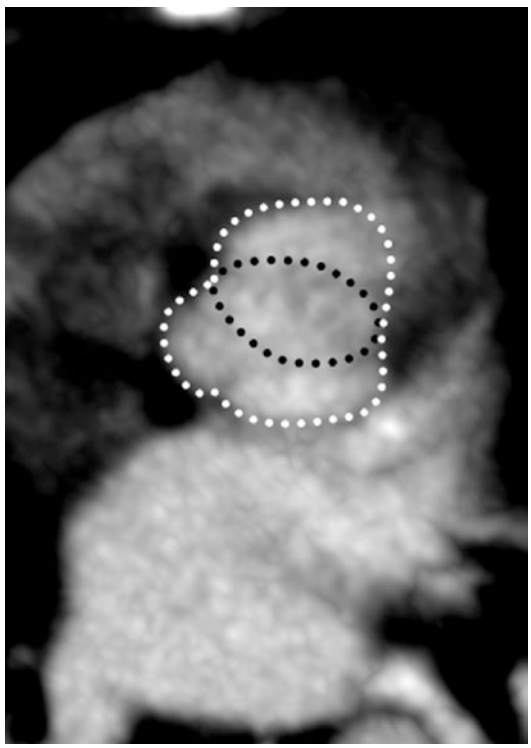

Fig. 4.31 An axial oblique view of the heart shows bicuspid morphology of the truncal valve. The anterior leaflet is larger and two smaller posterior leaflets are fused (*white dotted outline*). The fish mouth shape of the valve orifice (*black dotted outline*) is typical of a bicuspid aortic valve

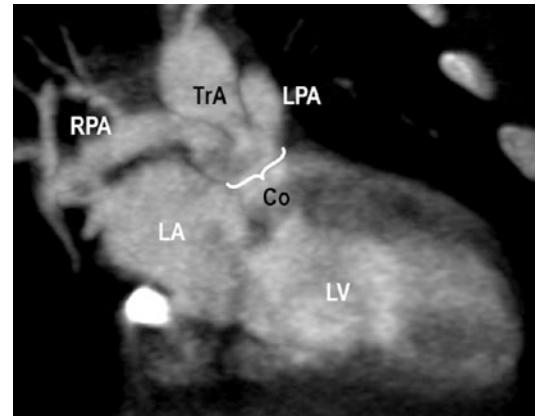

Fig. 4.32 An in and out maximum intensity projection (MIP) image of the left side of the heart shows the left atrium (LA), left ventricle (LV), and the outflow tract which is composed of tissue derived from the primitive conus (CO). Separate origins of the right (RPA) and left (LPA) pulmonary arteries arise just above the truncal valve (*bracket*)

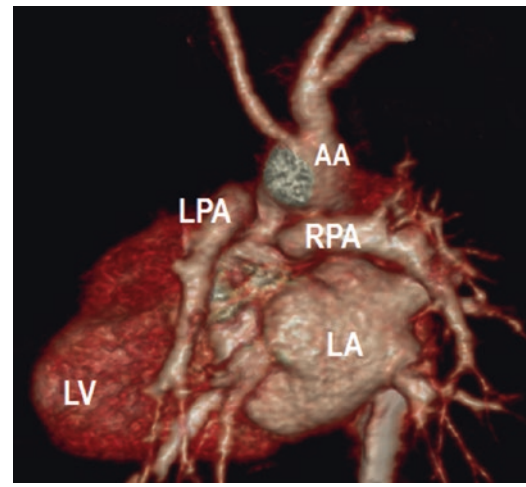

Fig. 4.33 The descending aorta has been cut away in this 3D surfaced rendered view of the posterior surface of the heart. From the posterolateral surface of the common truncal vessel the right (RPA) and left (LPA) branch pulmonary artery origins are separate. The aortic arch (AA), left atrium (LA), and left ventricle (LV) are normal

4.7 Vascular Rings

Embryological development of the heart and its vessels begins around 20 days and proceeds through the eighth week of gestation. The development of the great vessels, the aorta and pulmonary arteries, and the head and neck vessels, or brachiocephalic arteries proceeds through organized stages of involution, coalescence, and septation which typically result in a left-sided aortic arch with three brachiocephalic arteries branching from the arch and a main pulmonary artery which branches to the right and left [8, 9].

During development, the distal outflow portion of the primitive embryonic heart tube separates, forming six paired arches termed aortic or pharyngeal arches. The first, second, and fifth paired arches involute almost entirely; remnants of the first pair forms maxillary and external carotid artery segments, the second pair persists only as the stapedial arteries of the middle ears, and the fifth pair completely degenerates during the fetal period in about 50%, and forms only transient rudimentary vessels in the other 50% of humans. The third, fourth, and sixth arches give rise to parts of the aorta and brachiocephalic arteries. Segments of the third arches form the common and internal carotid arteries. The right and left fourth arches develop independently. On the right, the fourth arch and the seventh intersegmental artery contribute to the formation of the right subclavian artery. The left fourth pharyngeal arch artery, along with the dorsal aorta and the aortic sac forms the arch of the aorta. The right and left sixth aortic arches also develop uniquely. The distal right sixth arch degenerates completely but the proximal segment persists as the proximal right pulmonary artery. The left sixth arch becomes left pulmonary artery and the ductus arteriosus [9].

When all of these stages of vascular development and regression proceed in a normal fashion, the usual left aortic arch is the usual result. There are however variations in this developmental pattern which may occur in isolation or in conjunction with complex congenital heart disease. A right arch with mirror image branching is found when these steps proceed in the opposite right to left relationships and when not associated with another congenital heart defect is an isolated and benign condition [10].

Symptomatic aortic arch anomalies can occur in isolation or in combination with complex congenital heart disease. When an arch anomaly is present, it is vital to examine the course and caliber of the trachea, the position of the carina and branching pattern of the trachea to the main bronchi, and the course of the esophagus. The normal situation is that the aortic arch is to the left of the trachea, therefore a left aortic arch. A right aortic arch lies to the right of the trachea. When both the right and left sixth arches persist, a double aortic arch is present. The typical arrangement of arch anatomy results in a larger caliber right arch which lies more cephalad in relation to the left arch. Brachiocephalic artery branching is a common carotid artery and subclavian artery from each arch and the descending aorta (DAo) can lie to the left, right, or midline [11].

A vascular ring composed of the two aortic arches is created by the double aortic arch; the ring encircles the trachea and esophagus. The vascular ring may also be present when a right aortic arch is accompanied by an aberrant origin and course of the left subclavian artery and either a patent ductus arteriosus (PDA) or an atretic ductus arteriosus or the ductal ligament [12]. When a left aortic arch is accompanied by an aberrant right subclavian artery, even when a PDA or ductal ligament is present, a vascular ring is not.

Other variations in aortic arch embryological development may result in a true vascular ring, left aortic arch with an aberrant origin of the right subclavian artery and a right-sided ligamentum arteriosum, or a left or right circumflex aortic arch, characterized by the retroesophageal position of the distal aortic arch and contralateral position of the DAo. Not uncommonly a diverticulum at the aorta insertion site of the ductus arteriosus may be present, as described by Kommerell [13]. Though not a true vascular ring, the presence of the diverticulum may cause symptoms of dysphagia which are similar to those experienced by patients with a ring.

4.7.1 Case 4.12

A newborn presents with wheezing and feeding difficulty on day of life 2. Following a chest radiograph which was indeterminate for aortic arch position and an echocardiogram which was limited due to excessive crying, a low dose CTA of the chest was performed to investigate detailed anatomy of the aortic arch and the tracheobronchial tree.

See Figs. 4.34, 4.35, 4.36, and 4.37.

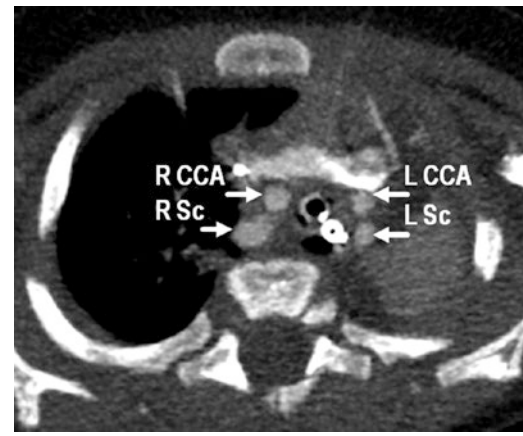

Fig. 4.34 An axial MIP image just above the level of the aortic arches shows the typical arrangement of the brachiocephalic vessels in a patient with double aortic arches; a common carotid artery (CCA) and subclavian artery (Sc) arise from both the right and left arches

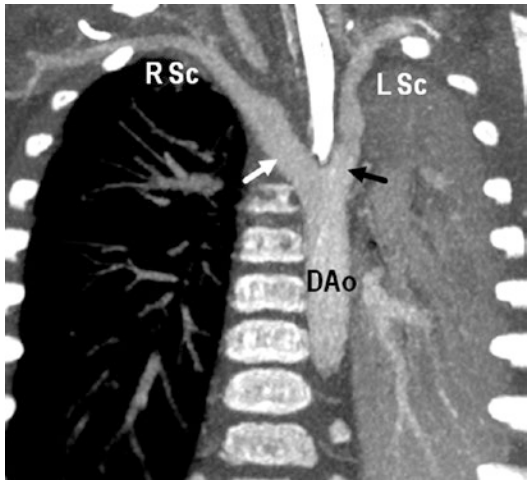

Fig. 4.36 In a coronal reformation, the distal right (*white arrow*) and left (*black arrow*) aortic arches and the right (R Sc) and the left (L Sc) subclavian arteries are noted. The descending aorta (DAo) is to the left of the spine

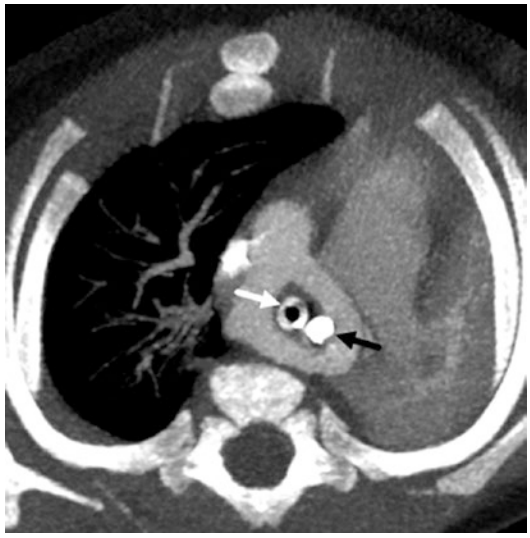

Fig. 4.35 An axial oblique MIP image shows both aortic arches as they form a vascular ring; the arches encircle a nasogastric tube (*black arrow*) and endotracheal tube (*white arrow*) which define the position of the esophagus and trachea

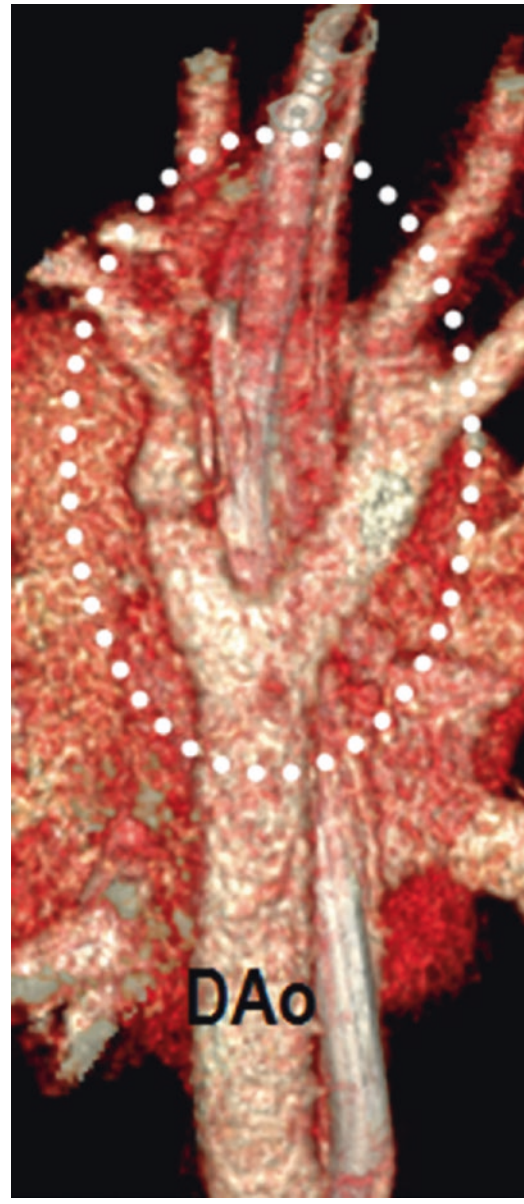

Fig. 4.37 A 3D surface rendered reconstruction shows the double aortic arch and vascular ring anatomy from a posterior view (*dotted ellipse*)

4.7.2 Case 4.13

An 18-month-old infant has swallowing difficulty with solids. Her pediatrician ordered a swallow study which showed a posterior extrinsic impression on the upper esophagus (not shown). A low dose cardiac CTA of the aorta was subsequently performed.

See Figs. 4.38, 4.39, 4.40, and 4.41.

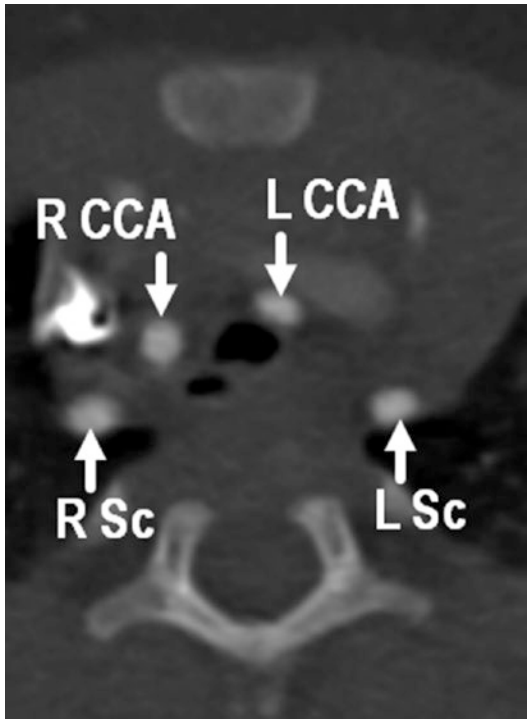

Fig. 4.38 An axial MIP view above the aortic arch shows the position of the right (R CCA) and left (L CCA) carotid and the right (R Sc) and left (L Sc) subclavian arteries and the air filled esophagus and trachea lying between the sets of arteries

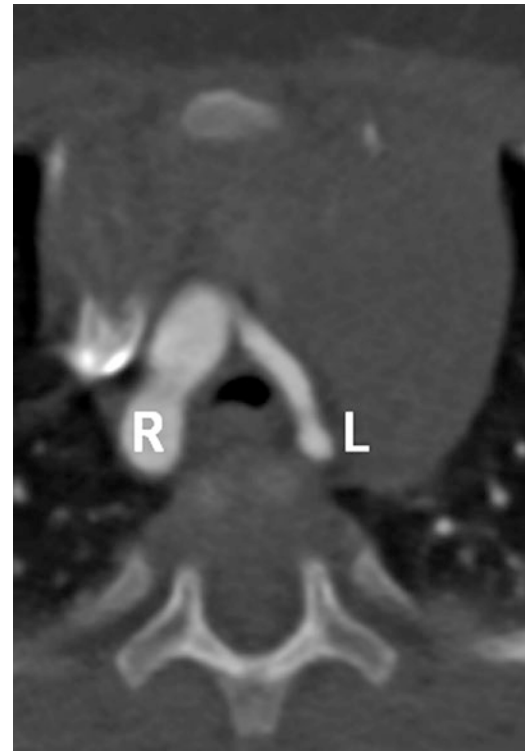

Fig. 4.39 An axial MIP image reveals the asymmetric caliber of the right (R) and left (L) aortic arches

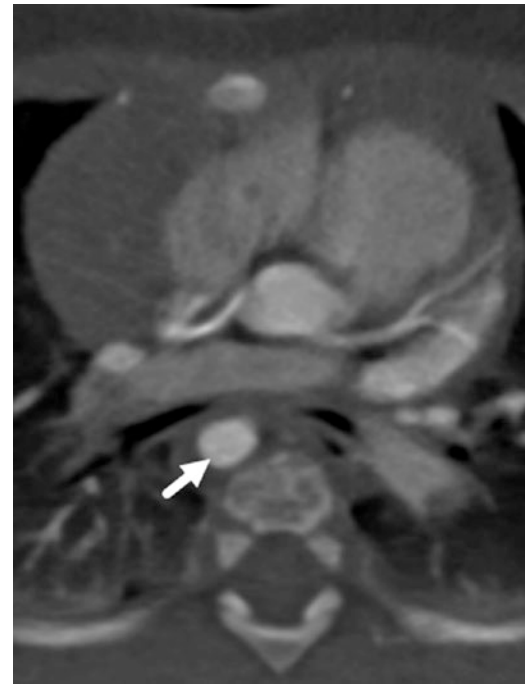

Fig. 4.40 At the level of the sinuses of Valsalva, the coronary artery origins are clearly seen. The DAo is on the right

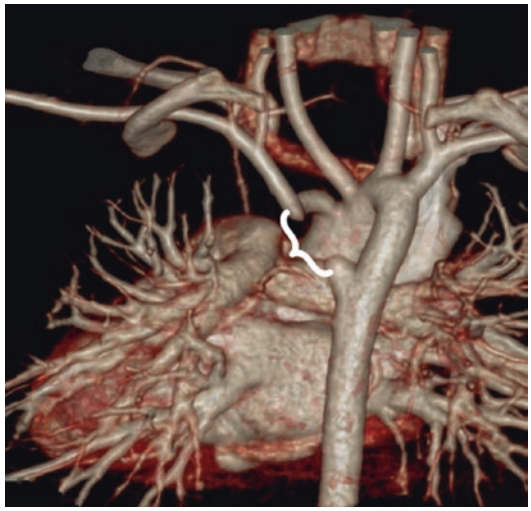

Fig. 4.41 A 3D surface rendered view of the aortic arches from the posterior projection shows there is apparent discontinuity in the distal left arch (*bracket*). As this segment does not fill with contrast material, it appears as if the vessel is discontinuous. In reality, there is an atretic segment of the left arch which remains as a "ligament," completing the vascular ring

4.7.3 Case 4.14

A third newborn presented with anomalous pulmonary venous connection for which a cardiac CTA was requested. See Fig. 4.42.

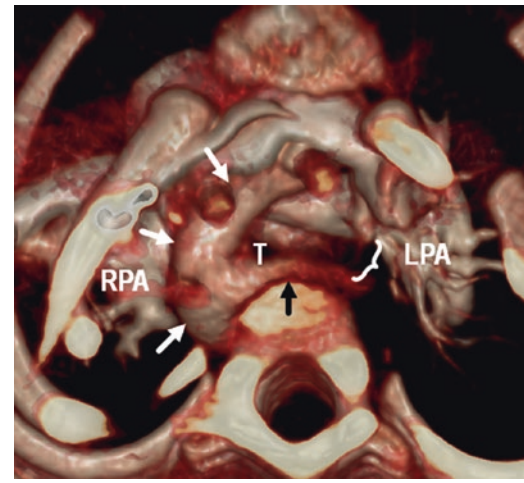

Fig. 4.42 In addition to anomalous pulmonary venous drainage (not shown), this patient also has a right aortic arch (*white arrows*) and an aberrant origin and course of the right subclavian artery (*black arrow*). With this anatomy a vascular ring is completed with a ductal ligamentum arteriosum which extends between the left pulmonary artery (LPA) and the subclavian artery (*bracket*). The right pulmonary artery (RPA) is also seen

4.8 Transposition of the Great Arteries (TGA)

Transposition of the great arteries (TGA), a rare form of congenital heart disease (3%), occurs in a variety of arrangements, depending upon the direction of ventricular looping, presence or absence of intraventricular septal defects, and displacement of the intraventricular septum. These variations include TGA with ventricular septal defect (VSD), which is most common, TGA with intact ventricular septum, and TGA with VSD and left ventricular outflow tract obstruction (LVOT).

Early in embryogenesis, a crescent of cardiogenic tissue forms a tube which folds (loops) upon itself and divides into the atria, left ventricle, bulbus cordis (right ventricle) and truncus arteriosus (which divides into the great arteries, the ascending aorta and main pulmonary artery). Normally the cardiogenic crescent folds to the right (dextro, D) – forming a D-loop – which positions the bulbus cordis to the right of the left ventricle. When the cardiogenic crescent folds leftward (levo, L) – forming an L-loop – the right ventricle is positioned to the left. D-looping is found in normal hearts and in D-TGA while L-looping is seen in L-TGA. In either condition the heart may be normally positioned in the left side of the chest or may be rotated or malpositioned into the right side of the thorax. Whether there is D-looping or L-looping of the heart tube the atrioventricular valve accompanies its ventricle; i.e., the tricuspid valve remains connected to the morphologic right ventricle and the mitral valve associated with the morphologic left ventricle.

As ventricular looping occurs the right and left ventricles are separated by a layer of myocardium, the intraventricular septum. The intraventricular septum is contiguous with the conal septum, tissue composed from the portion of the bulbus cordis that separates the right and left ventricular outflow tracts. These details of cardiac embryology help in understanding how formation of the intraventricular septum and ventricular looping are linked and perhaps why septal defects and septal displacement occur in TGA.

In TGA the origins of the coronary arteries as they arise from the aortic sinuses of valsalva have an abnormal position relative to the pulmonary artery and are therefore named differently. The aortic sinuses that lie adjacent to or "face" the pulmonary artery are referred to as the right-facing and left-facing sinus. The third sinus, the one that lies anterior and lateral and does not about the pulmonary artery, is labeled the non-facing sinus. It is important to note the position of the coronary arteries in your report of the cardiac CTA exam as this important finding which may change how and arterial switch procedure is performed.

4.8.1 Levo-Transposition of the Great Vessels (L-TGA)

L-TGA is a rare congenital heart malformation (<1%) which results in malposition or inversion of the position of the ventricular chambers of the heart. Ventricular inversion (RV in the LV position and LV in the RV position) results in both atrioventricular and ventriculoarterial discordance, which is often referred to as physiologically or "congenitally" corrected transposition. Patients are not cyanotic unless there is an additional intracardiac defect. L-TGA patients without cyanosis may live in a seemingly normal manner even into adulthood before becoming symptomatic.

The morphologic left atrium lies on the left, receives oxygenated blood through pulmonary veins and drains it through the tricuspid valve, to the morphologic right ventricle which lies to the left, and pumps blood through the aortic valve to the systemic circulation (left–right–left). The morphologic right atrium lies on the right, receives deoxygenated systemic venous blood from the superior and inferior vena cavae and the coronary sinus and drains it through the mitral valve into the morphologic left ventricle which lies on the right, and pumps it

through the pulmonic valve to the lungs (right–left–right). The position and relationship of the aortic and pulmonic valves is abnormal when L-looping of the ventricles occurs, with the aortic valve lying anterior and to the left of the pulmonic valve resulting in a discordant relationship between the ventricles and great arteries. The atria and ventricle relationship is also discordant.

Oxygenated and deoxygenated blood flow is separated in patients with L-TGA as in a normal heart, so it is possible for patients with "corrected" or L-TGA survive, sometimes well into adulthood, without knowledge of their congenital heart disease. Though the arrangement of cardiac chamber inflow, outflow, and arterial vascular supply is normal, the right ventricle is the systemic pumping chamber, delivering blood to the high resistance systemic arterial bed, a situation for which the right ventricle is not built, at least not for the long term. Initially the RV responds to this inappropriate stress with hypertrophy, but over time becomes dilated and eventually, the RV fails and will no longer be capable of pumping against systemic arterial pressures. The LV pumps blood to the lower resistance pulmonary arterial bed, and over the long term, the normally muscular myocardium becomes deconditioned. The plumbing is as important to understand as the anatomy because the potential for successful surgical palliation/repair of L-TGA decreases if the diagnosis is delayed or goes unrecognized for months or even years, as both ventricles fail in their own manner. A deconditioned LV cannot often in be successfully retrained to be a systemic chamber.

4.8.2 Clinical Presentation

A newborn with history of L-TGA on fetal echocardiography underwent cardiac CTA after pulmonary venous anatomy was not completely defined on an early postnatal echocardiogram and oxygen saturation was persistently decreased.

4.8.3 Case Presentation

See Figs. 4.43, 4.44, and 4.45.

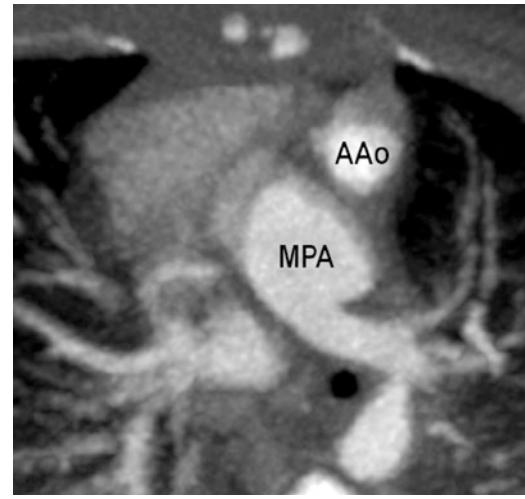

Fig. 4.43 An axial oblique image oriented to the proximal ascending aorta (AAo) and main pulmonary artery (MPA) is shown to confirm relative position of the aortic and pulmonic valves. The aortic valve lies anterior and to the left of the pulmonic valve

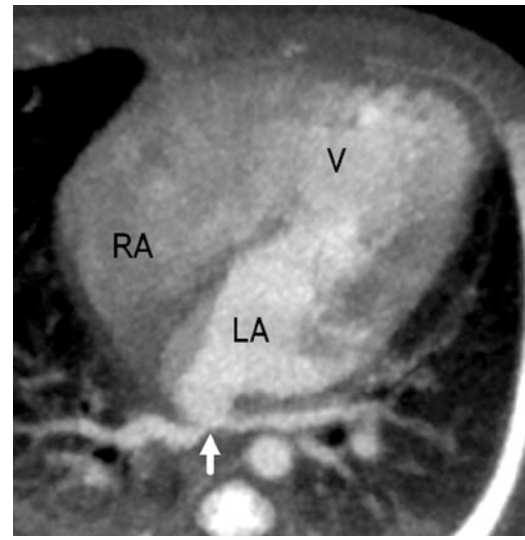

Fig. 4.44 The right (RA) and left (LA) atria are in normal position. The appearance of the ventricles (V) is abnormal; the intraventricular septum is absent, resulting in single ventricle physiology; the moderator band is not shown in this image but is in the posterior, morphologic right ventricle. The pulmonary veins drain to a narrow confluence (*arrow*) into the left atrium. Thought not anomalous, to an inappropriate chamber, there may be a degree of obstruction to pulmonary vein drainage with this configuration

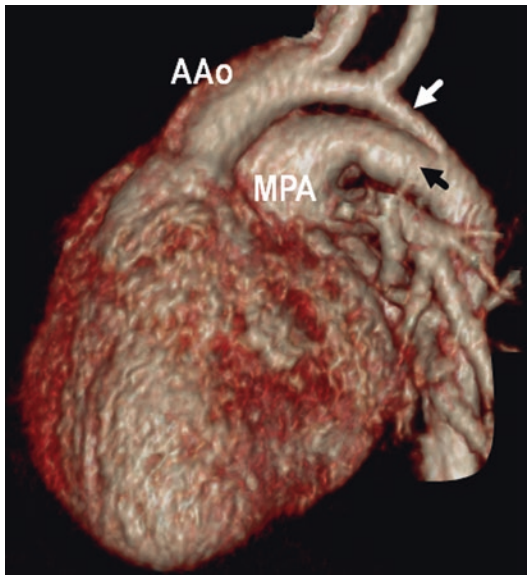

Fig. 4.45 A 3D surface rendered image of the heart shows the abnormal anterior position of the aortic valve and therefore the ascending aorta (AAo) to the pulmonic valve in relation to the main pulmonary artery (MPA). The AAo and MPA course is parallel to one another, rather than crossing as seen in a normal heart. In addition to L-TGA this patient also has a hypoplasia of the aortic arch (*white arrow*) and a large caliber patent ductus arteriosus (PDA) (*black arrow*)

4.8.4 Dextro-Transposition of the Great Vessels (D-TGA)

D-TGA, also a rare congenital heart malformation but more common than L-TGA, results in malposition of the great vessels as they arise from the heart. The aortic valve lies anterior and to the right of the pulmonic valve and has an abnormal relationship with the cardiac ventricles, or ventriculoarterial discordance. The aorta arises from the RV and the pulmonary artery arises from the LV. The right and left atria have a normal anatomic relationship with the right and left ventricles, atrioventricular concordance. Patients are typically cyanotic, a problem which is most severe if there is not a ventricular septal defect (VSD) because the blood flow circuits are parallel and do not mix.

The morphologic left atrium lies on the left, receives oxygenated blood through pulmonary veins and drains it through the mitral valve, to the morphologic left ventricle which lies on the left, and pumps blood through the pulmonic valve to the lungs (left–left–right). The morphologic right atrium lies on the right, receives deoxygenated systemic venous blood from the superior and inferior vena cavae and the coronary sinus and drains it through the tricuspid valve to the morphologic right ventricle which lies on the right, and pumps it through the aortic valve to the aortic valve to the systemic circulation (right–right–left). The position and relationship of the aortic and pulmonic valves is abnormal when D-looping of the ventricles occurs, with the aortic valve lying anterior and to the left of the pulmonic valve and a discordant relationship between the ventricles and great arteries. The atrial and ventricle relationship is also discordant.

Oxygenated and deoxygenated blood flow circuits are separate and parallel in patients with D-TGA, rather than in series, resulting in oxygenated blood continually drained by and then supplied to the lungs and deoxygenated blood continually drained from and then supplied to the systemic circulation. It is obvious that this situation is not sustainable as oxygenated blood never reaches the system circulation, the brain, other organ systems, and ultimately life is not sustainable. In newborns an atrial septal defect (ASD), ventricular septal defect (VSD), or other shunt is required to allow flow of oxygenated blood to the systemic circulation. If not present, intervention to create this shunt is required in order to maintain life until to allow flow of oxygenated blood to the systemic circulation. If not present, intervention to create this shunt is required in order to maintain life until definitive surgical palliation can be performed.

4.8.5 Pearls (•) and Pitfalls (ü)

• Use an axial oblique image plane to accurately identify the position of the aortic and pulmonic valves.

• Normally the aortic valve is posterior and slightly to the right of the pulmonic valve. In D-TGA the aortic valve is anterior and to the right; in L-TGA the aortic valve is anterior and to the left.

ü Be certain to identify associated cardiac abnormalities; ASD, VSD, and DORV are commonly found in patients with TGA.

ü Patients with L-TGA may survive into adulthood; their congenital heart disease may be first discovered on chest CT performed for other reasons.

4.8.6 Clinical Presentation

A newborn with a prenatal diagnosis of D-TGA is not cyanotic. Postnatal echocardiogram shows a large secundum atrial septal defect (ASD) and multiple muscular ventricular septal defects (VSD). The coronary artery origins were not well visualized on echo images. As an arterial switch procedure which includes reimplantation of coronary arteries was planned, cardiac CTA was requested to delineate coronary artery origins.

4.8.7 Case Presentation

See Figs. 4.46, 4.47, 4.48, and 4.49.

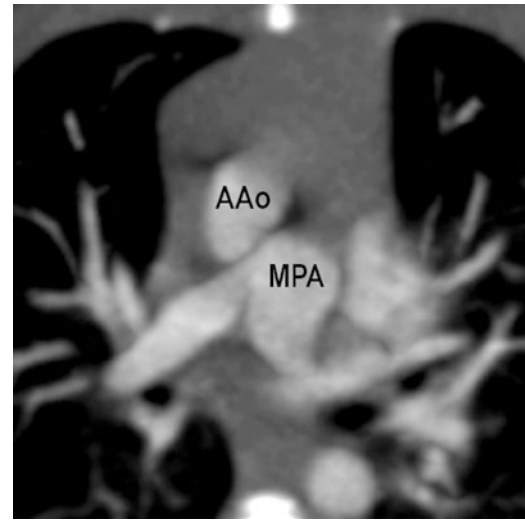

Fig. 4.46 An axial oblique image oriented to the proximal ascending aorta (AAo) and main pulmonary artery (MPA) indicating the relative position of the aortic and pulmonic valves. The aortic valve lies anterior and to the right of the pulmonic valve

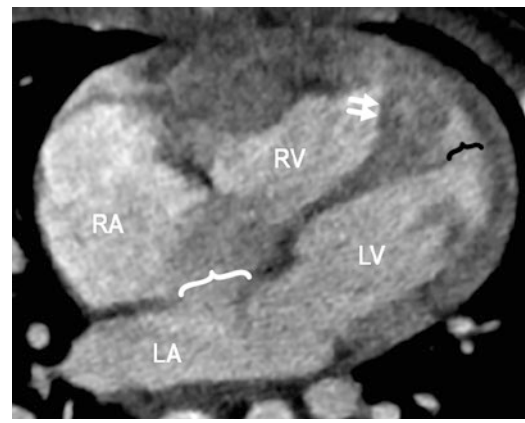

Fig. 4.47 A four-chamber view of the heart shows normal right atrial (RA) to right ventricle (RV) and left atrial (LA) to left ventricle (LV) relationships, atrioventricular concordance. The moderator band (*double arrow*), a morphologic feature of the RV, is in the anterior ventricle, indicating D-looping. An apical muscular ventricular septal defect (VSD) (*black bracket*) and a secundum atrial septal defect (ASD) (*white bracket*) are seen

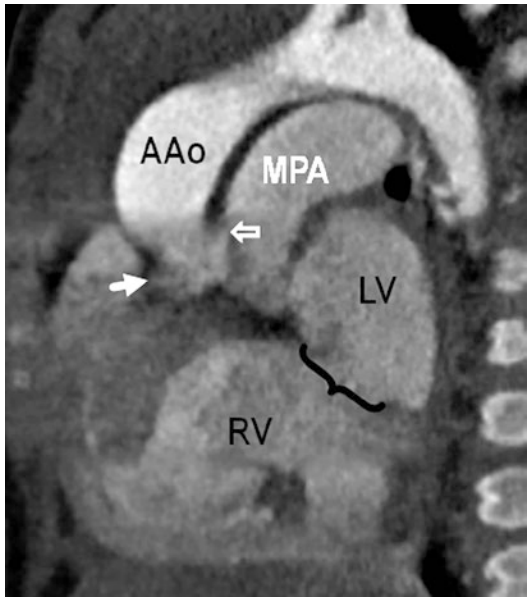

Fig. 4.48 The ascending aorta (AAo) and main pulmonary artery (MPA) lie parallel in a sagittal oblique view rather than crossing as in a normal heart. A mid-chamber muscular VSD (*black bracket*) near the base of the heart is between the LV and RV. The origin of the left coronary artery (*arrow*) arises from the left non-facing cusp of the aorta. The origin of the right coronary artery arises from the facing sinus, adjacent to the MPA (*open arrow*)

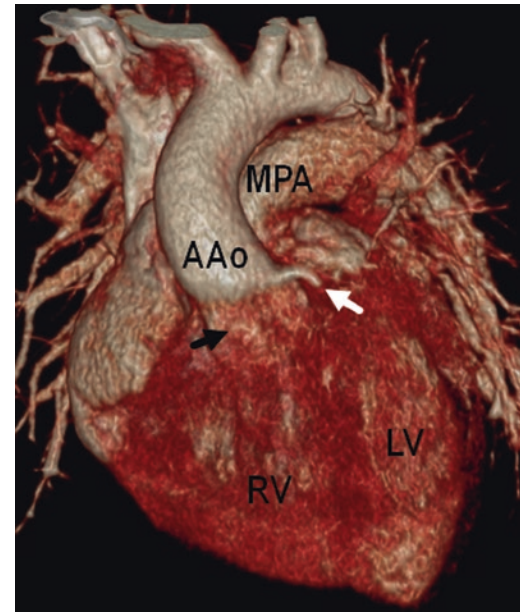

Fig. 4.49 A 3D surface rendered CTA image shows the anterior position of the ascending aorta (AAo) and the origin of the left coronary artery (*arrow*), arising from the non-facing cusp of the aorta. The origin of the right coronary artery from the right facing sinus of the aorta is not seen in this image. The right non-facing sinus is indicated (*black arrow*)

4.9 Tetralogy of Fallot (TOF)

In congenital heart disease, it is common to find more than one cardiac defect in a patient. Though described by others previously a group of four cardiac defects often found together, known as the tetralogy of Fallot (TOF) was described by Dr. Étienne Fallot in 1888 [14]. The four cardiac defects often found together and are easily understood in a cause and effect relationship. Stenosis of the right ventricular outflow tract (RVOT), pulmonary artery, and/or pulmonic valve occurs due to superior and leftward displacement of the outlet septum in the ventricular outflow tract which occurs at the time of formation and septation of the conus and the truncus arteriosus. Given abnormal division of the conus and truncus arteriosus resulting in small caliber structures on the right side of the heart, while left-sided structures are larger caliber than normal.

Stenosis or complete obstruction of right ventricle (RV) outflow may range from mild to severe narrowing of the pulmonary artery or atresia of the pulmonic valve and results in high pressure in and secondary hypertrophy of the RV, another of the lesions in the tetralogy. A ventricular septal defect (VSD), a third lesion of the tetralogy allows decompression of high pressure in the RV. Asymmetric division of the conus and larger size of the aortic valve and ascending aorta allows these structures to override the VSD and receive blood flow from both ventricles is the fourth component of TOF.

The mixture of blood from both ventricles is ejected to the aorta and systemic circulation along with a relative decrease in blood reaching the lungs to be oxygenated results in low oxygen saturation and cyanosis in most patients with TOF. TOF is the commonest form of cyanotic congenital heart disease (3 in 10.000 births). Spells of acute hypoxia in patients with TOF, termed "tet spells" are due to rapid onset of worsened cyanosis and syncope.

TOF with pulmonary atresia is a severe variant which results in the formation of collateral pulmonary arterial supply, often in the form of major aorticopulmonary collateral arteries (MAPCAs) from the descending thoracic aorta or in pulmonary arteries arising from the ductus arteriosus. As in other forms of congenital heart disease, additional cardiac lesions may accompany the tetralogy: right aortic arch (25%), anomalous coronary artery origin or course (10%), and bicuspid pulmonic valve (>50).

4.9.1 Pearls (•) and Pitfalls (√)

• Right ventricle infundibular, pulmonic valve, main pulmonary artery, branch pulmonary artery, and/or peripheral pulmonary artery stenosis may be present.

• The length of regional stenosis of the RV infundibulum or pulmonary arteries should be included in your report.

√ In patients with pulmonary atresia, branch pulmonary arteries may arise from the ductus arteriosus or as MAPCAs from descending aorta.

4.9.2 Clinical Presentation

4.9.3 Case 4.15

After a prenatal echocardiogram which revealed diffuse narrowing of the pulmonary arteries, a diagnosis of TOF was suspected. Postnatal echo confirmed pulmonary artery narrowing, relative enlargement of the diameter of the ascending aorta as well as a large ventricular septal defect (VSD). Cardiac CTA was requested for assessment of the aortic arch and branch pulmonary arteries (Figs. 4.50, 4.51, 4.52, and 4.53).

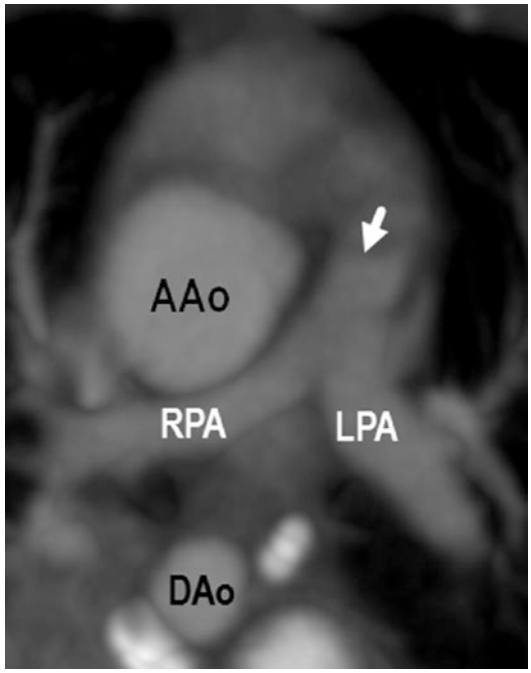

Fig. 4.50 An axial oblique view of the main pulmonary artery, right (RPA) and left (LPA) branch pulmonary arteries shows narrowing of the pulmonic valve (*arrow*) as well as the large caliber ascending aorta (AAo). The descending aorta (DAo) lies to the right

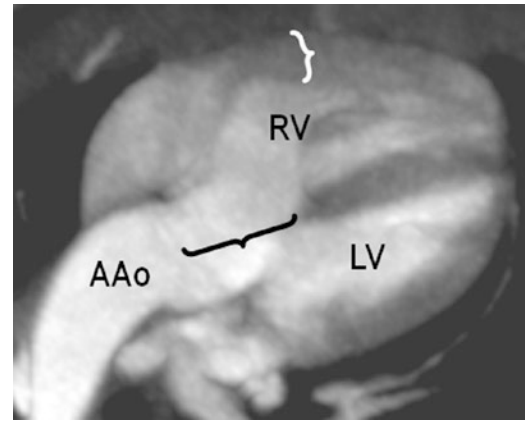

Fig. 4.51 An axial oblique view of the left ventricular outflow tract shows a large ventricular septal defect (*black bracket*) and position of the aortic valve plane and ascending aorta (AAo) overriding the VSD. The free wall of the right ventricle (RV) is thickened (*white bracket*) due to hypertrophy and the RV appears larger volume than the left ventricle (LV)

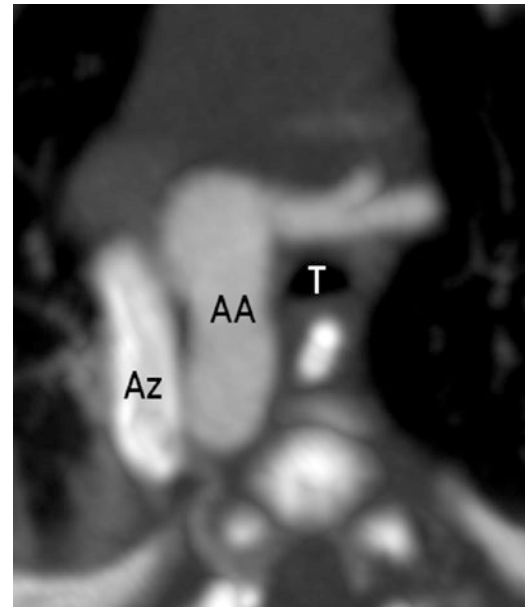

Fig. 4.52 An axial view at the level of a right sided aortic arch (AA) shows the arch is to the right of the trachea (T). The azygous arch (Az) is also seen

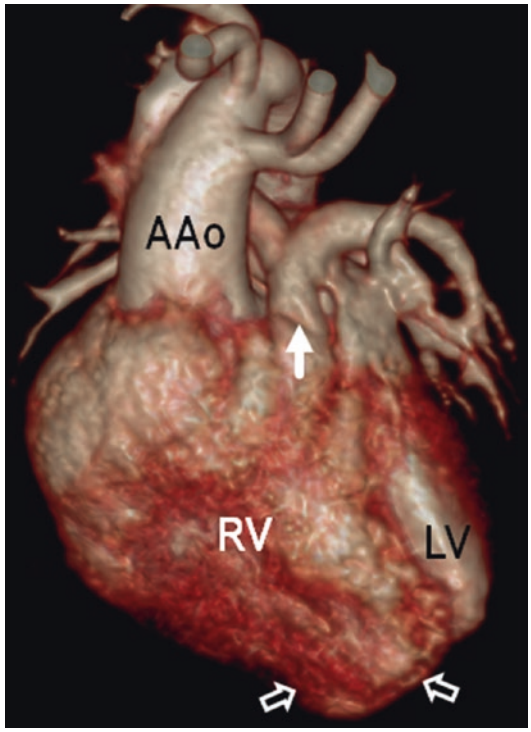

Fig. 4.53 A 3D surface rendered view of the heart shows the small caliber of the infundibulum (*arrow*) of the right ventricle (RV) and the enlarged apex of the RV (*open arrows*) which is due to RV hypertrophy. The left ventricle (LV) apex is less prominent than the RV apex. The ascending aorta (AAo) is much larger caliber than the RV outflow and main pulmonary artery

4.9.4 Case 4.16

A newborn with prenatal diagnosis of TOF underwent chest radiograph and echocardiogram shortly after birth. The chest radiograph indicated the main pulmonary artery was small, a finding which was confirmed on echo. Cardiac CTA was requested to accurately evaluate the size of the pulmonary arteries. See Figs. 4.54, 4.55, 4.56, and 4.57.

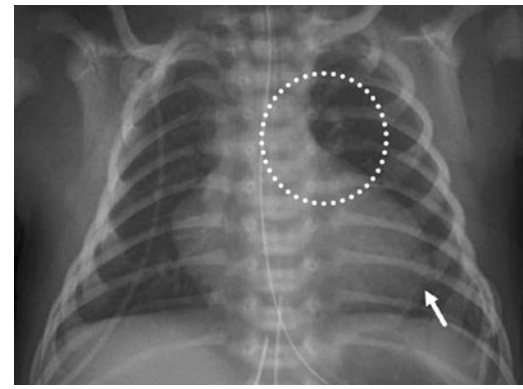

Fig. 4.54 A chest radiograph shows absence of the pulmonary artery shadow along the left heart border (*dotted circle*), due to small size of the main and left pulmonary arteries in this patient, resulting in a marked concavity of the superior left border of the cardiomediastinal silhouette. The apex of the heart is "lifted up" away from the diaphragm, a finding which is due to right ventricle hypertrophy

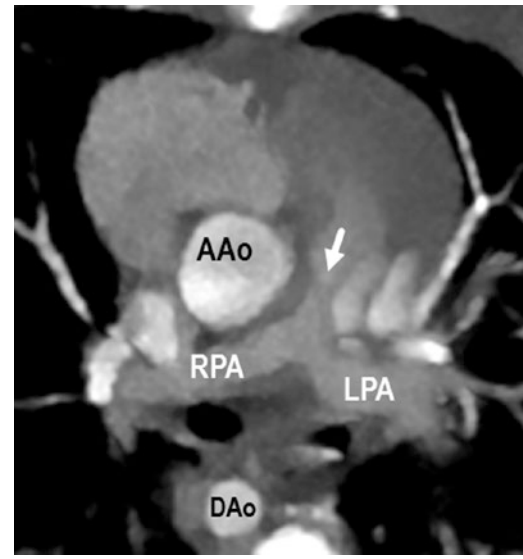

Fig. 4.55 An axial oblique view of the main and branch right (RPA) and left (LPA) pulmonary arteries shows their small caliber. Also note stenosis of the right ventricle infundibulum (*arrow*). The ascending (AAo) and descending (DAo) are on the right in this TOF patient with a right aortic arch

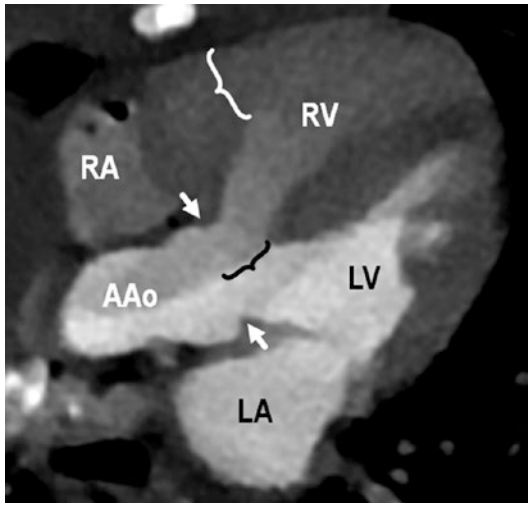

Fig. 4.56 The four-chamber view of the heart shows three components of TOF; the free wall of the right ventricle (RV) is thickened (*white bracket*) due to hypertrophy, a ventricular septal defect (VSD) (*black bracket*) is present and the aortic valve annulus (*white arrow*) overrides the VSD. Other cardiac chambers the left ventricle (LV) and the right (RA) and left (LA) atria are normal. Note the combination of densely contrast opacified and non opacified blood in the RV and LV and that a similar contrast mixture has been ejected into the AAo

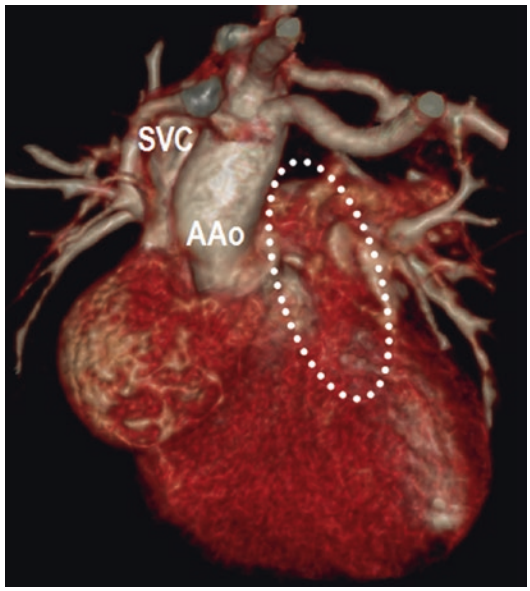

Fig. 4.57 A 3D surface rendered image shows narrowing of the right ventricular infundibulum (*dotted ellipse*). The ascending aorta (AAo) is on the right, immediately adjacent to the superior vena cava (SVC)

4.9.5 Case 4.17

A postnatal echocardiogram was performed to investigate the cause of hypoxia in this newborn. The right ventricle was enlarged and the right pulmonary artery was small caliber; the left pulmonary artery was not seen but the ductus arteriosus was patent. Cardiac CTA was requested in order to investigate anatomy of the left pulmonary artery. See Fig. 4.58, 4.59, and 4.60.

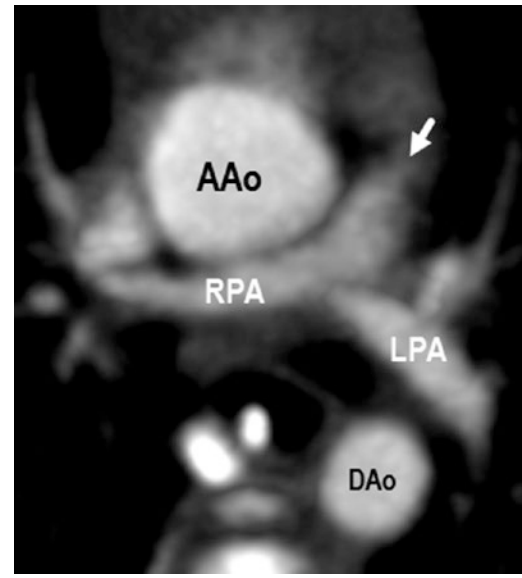

Fig. 4.58 An axial view through the superior mediastinum shows the small caliber main (*arrow*) and right (RPA) pulmonary arteries. The vessels are much smaller caliber than the ascending aorta (AAo); the descending aorta (DAo) is on the left. The left pulmonary artery (LPA) is also small caliber. The density of contrast in the lumen of the LPA is similar to the contrast in the aortic lumen which is brighter than the contrast in the RPA. The main pulmonary artery ends as the RPA and is not connected to the LPA

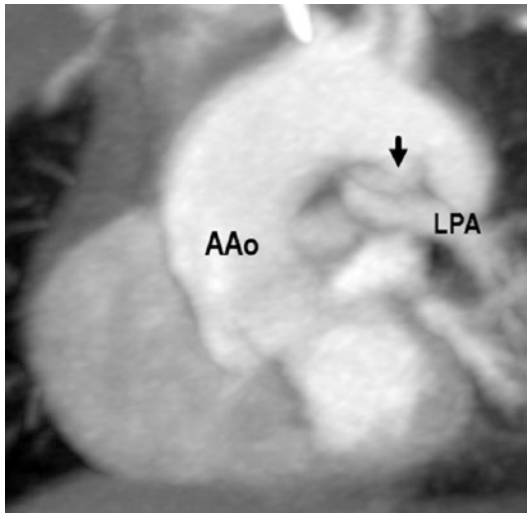

Fig. 4.59 An axial oblique view of the ascending aorta (AAo) and the aortic arch shows the origin of the patent ductus arteriosus (PDA) (*arrow*) and the tortuous course of the vessel which continues as the LPA. This explains the difference in the density of contrast material in the LPA in Fig. 4.59 as the LPA blood supply is from the aorta, via the PDA

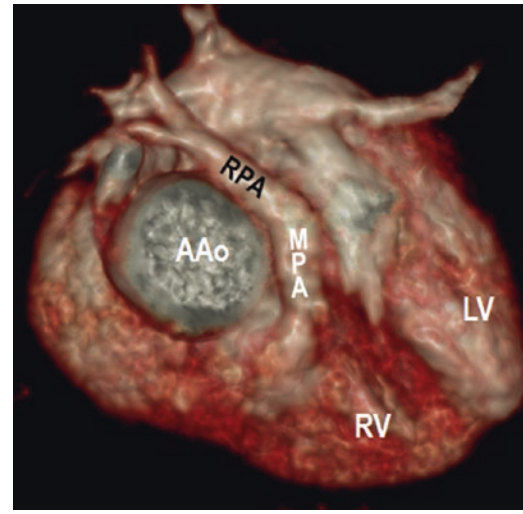

Fig. 4.60 A 3D surface rendered image of the heart shows the diffusely narrowed main (MPA) and right (RPA) pulmonary arteries. The aortic arch and descending aorta have been cut away to reveal absence of the LPA origin from the MPA

4.9.5.1 Transposition of the Great Arteries

In transposition of the great arteries (TGA), the connection between the atrioventricular valves and the ventricles of the heart is reversed, i.e., the aortic valve arises from the right ventricle (RV) and the pulmonic valve arises from the left ventricle (LV). In TGA, the relationship between or relative position of the aortic valve to the pulmonic valve is abnormal, ranging from an anterior and rightward position to an anterior and leftward position of the aortic valve. This abnormal arrangement assures that the aortic valve arises from the anteriorly positioned right ventricle in dextro or D-TGA or from the posteriorly positioned right ventricle in levo or L-TGA. When a VSD is present, the pulmonic valve (in D-TGA) or aortic valve (in L-TGA) may override it to varying degrees; when >50% of the valve is committed to the morphologic RV, the diagnosis of DORV is made in addition to TGA.

4.9.5.2 Double Outlet Right Ventricle

The term double outlet right ventricle (DORV) does not define just a single entity or malformation of the heart but is found in hearts with normally related great arteries and in hearts with transposed great arteries and occurs in situs solitus and situs anomalies. DORV is a cardiac malformation in which both the atrioventricular valves arise partially or completely from the right ventricle (RV). Displacement or malalignment of the infundibular septum at the base of the heart in DORV results in a ventricular septal defect (VSD) allowing one of the ventriculoarterial valves to override the VSD to varying degree; if more than 50% of that valve is committed to the RV rather than the LV, the term DORV applies. The VSD may be subaortic (underlying the aortic valve), subpulmonic (underlying the pulmonic valve), doubly committed (underlying the aortic and pulmonic valves equally), or non-committed (remote from the aortic and pulmonic valves).

The spectrum of cardiac malformation in which DORV is most commonly seen includes Tetralogy of Fallot (TOF), Taussig-Bing malformation, and in transposition of the great arteries. In each the position of the aortic and pulmonic valves are important to note. When the aortic and pulmonic valve positions are abnormal such as in Taussig-Bing malformation and transposition of the great arteries (TGA) the aortic-mitral relationship, which is normally in continuity, may also be abnormal.

4.9.5.3 Taussig-Bing Malformation

The Taussig-Bing malformation in which the aortic valve is to the right and side by side with the pulmonic valve may be a specialized form of DORV or a variation of TGA, but this is controversial. A subpulmonic VSD is present and the infundibulum underlies both AV valves and the pulmonic valve.

4.9.6 Clinical Presentation

A newborn, whose mother did not have prenatal care beyond a sonogram at approximately week 20 of gestation, became cyanotic shortly after birth.

4.9.7 Case 4.18

Echo showed stenosis of the pulmonic valve and the main pulmonary artery (MPA), hypertrophy of the right ventricle (RV), a large VSD and that the aortic valve was positioned to overlie the VSD, findings of tetralogy of Fallot (TOF). As the aortic arch was not well seen and coronary artery origins were not identified, cardiac CTA was requested. See Figs. 4.61, 4.62, 4.63, and 4.64.

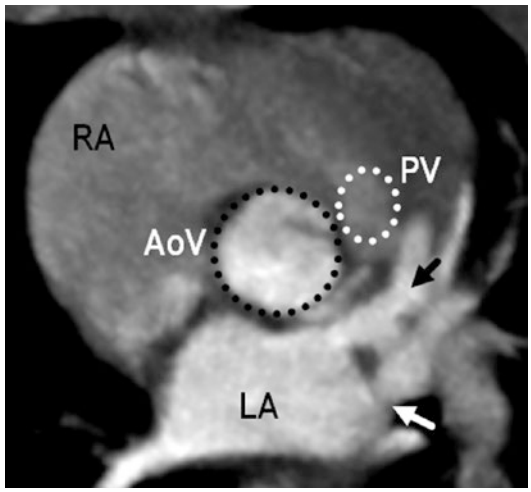

Fig. 4.61 An axial oblique image shows the normal position of the aortic valve (AoV) in relation to the pulmonic valve (PV), slightly posterior and to the right. The right atrium (RA), left atrium (LA), and position of the mitral valve (MV) annulus (*white arrow*) are seen. The AoV and MV annuli are in direct continuity as they would be in a normal heart. The left atrial appendage (LAA) (*black arrow*) overlies and partially obscures the mitral annulus

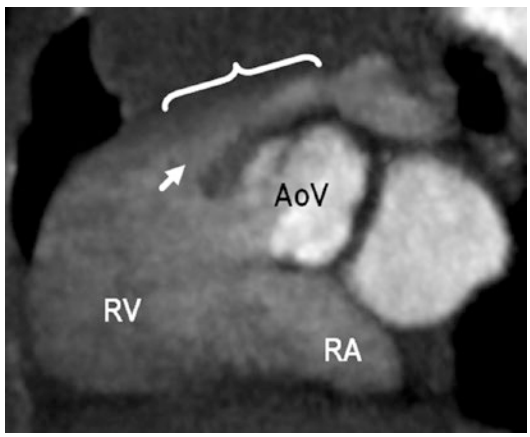

Fig. 4.62 The right ventricular outflow tract (RVOT) (*bracket*) is diffusely narrow and the muscular wall is thickened [RV hypertrophy]. The size of the aortic valve (AoV) is much larger than the RVOT. The pulmonary outflow (*arrow*) and the AoV both arise from the right ventricle (RV)

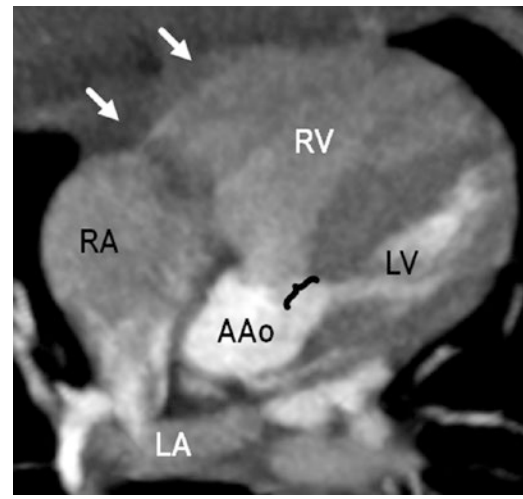

Fig. 4.63 In a four-chamber view of the heart, more than 50% of the aortic valve and the ascending aorta (AAo) arise from the right ventricle (RV) and overlies a membranous ventricular septal defect (VSD) (*bracket*). The free wall of the RV is hypertrophied (*arrows*)

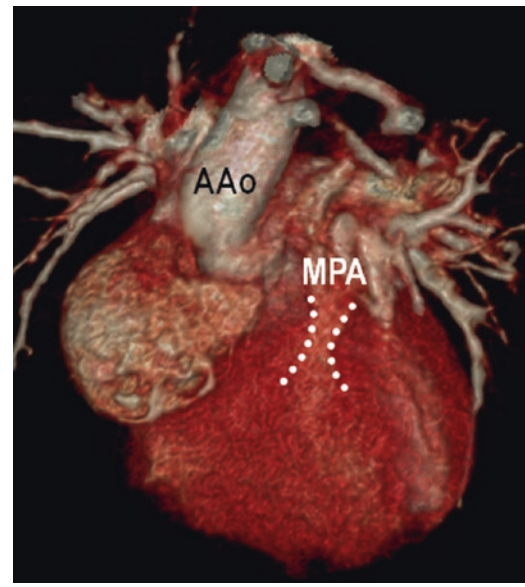

Fig. 4.64 A 3D surface rendered reconstruction shows the small caliber of the RVOT (*dotted lines*) and main pulmonary artery (MPA) and the much larger caliber ascending aorta (AAo) and their normal anatomic relationship

4.9.8 Clinical Presentation

Following birth, a newborn with known D-TGA experienced hypoxia, with O2 saturation at 85%.

4.9.9 Case 4.19

This newborn infant is known to have D-TGA as the aortic valve and ascending aorta (AAo) were noted to arise from the anterior, morphologic right ventricle (RV) and the pulmonic valve and main pulmonary artery (MPA) arise from the posterior morphologic left ventricle above a large ventricular septal defect (VSD).

A postnatal echo confirms the prenatal findings and raised concern for hypoplasia of the aortic arch. CTA of the heart and great vessels was requested.

A short axis image at the base of the heart (the atrioventricular valve plane) shows the anterior position of the aortic valve position (white arrow) in relation to the pulmonic valve position (black arrow) (Fig. 4.66). The pulmonic valve and the main pulmonary artery (MPA) are straddle a ventricular septal defect (VSD) (bracket), but are more committed to the RV than the LV.

The anterior position of the aortic valve (black arrow) and posterior position of the mitral valve (white arrow) indicate that their annuli are not in continuity as seen in a normal heart.

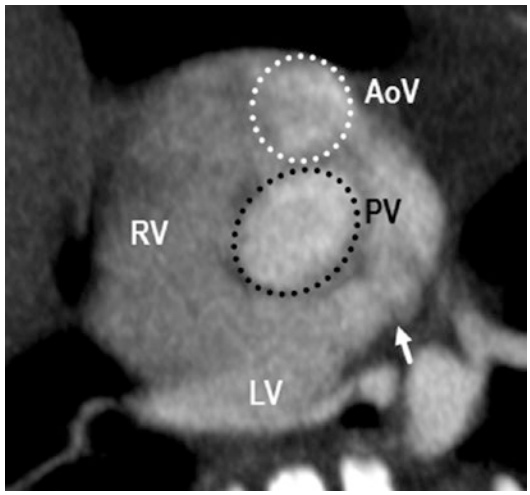

Fig. 4.65 An axial oblique image shows the anterior position of the aortic valve (AoV) in relation to the pulmonic valve (PV)

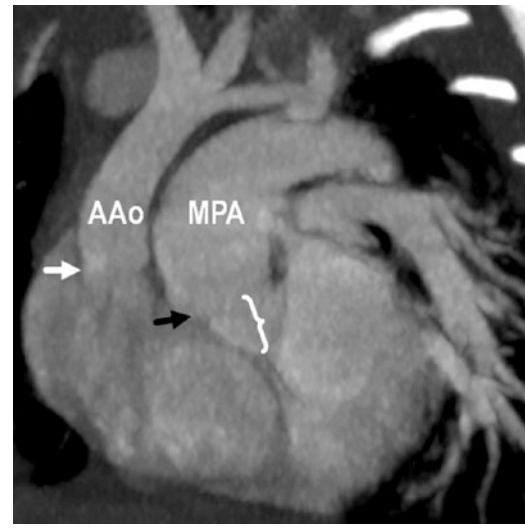

Fig. 4.66 A short axis image at the base of the heart (the atrioventricular valve plane) shows the anterior position of the aortic valve position (*white arrow*) in relation to the pulmonic valve position (*black arrow*) and the parallel course of the ascending aorta (AAo) and the main pulmonary artery (MPA). The pulmonic valve and the MPA straddle a ventricular septal defect (VSD) (*bracket*), but are more committed to the RV than the LV

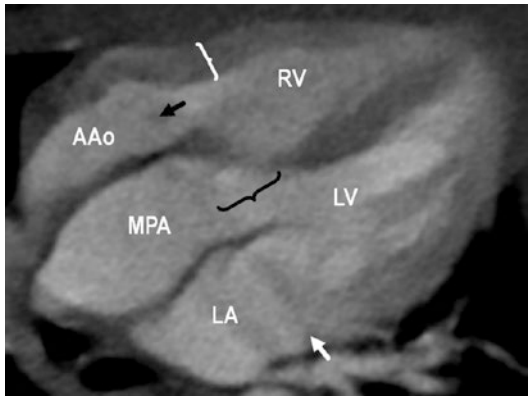

Fig. 4.67 In an attempt to show a four-chamber view of this heart the right atrial chamber is obscured by the ascending aorta (AAo) and main pulmonary artery (MPA). The left atrium (LA), left ventricle (LV), and right ventricle (RV) are seen. The pulmonary valve straddles the VSD (*black bracket*) but is more committed to the RV than the LV. The RV free wall and outflow tract are thickened (*white bracket*)

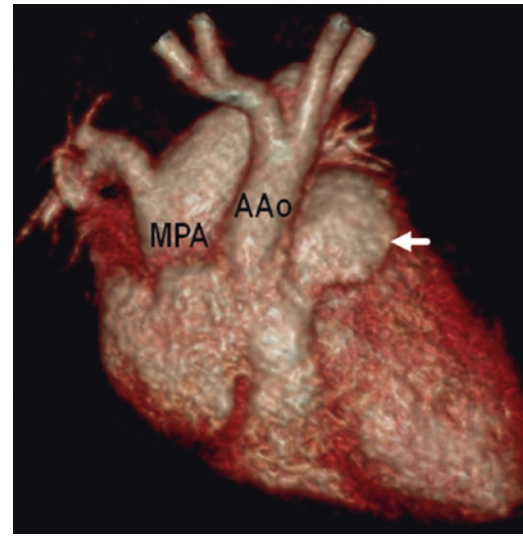

Fig. 4.68 A 3D surface rendered image of the heart again shows the anterior position of the ascending aorta (AAo). Also note the great arteries are parallel, another indication of transposition. The left atria appendage (LAA) (*arrow*) overlies the base of the left ventricle to the left of the AAo

4.10 Pulmonary Sling

The phenomena of pulmonary sling occur when the left pulmonary artery (LPA) origin is anomalous, arising from the proximal right pulmonary artery (RPA) rather than from the main pulmonary artery (MPA) and courses between the trachea and esophagus. Depending upon the location of the sling, there may be airway narrowing associated with anomalous branching of the trachea. An anterior impression on the esophagus is also present and, in some patients, may be a cause of dysphasia.

Two types of pulmonary sling are recognized:

Type 1—This is the less common and less complex form of LPA sling and is associated with tracheobronchomalacia. The position of the sling is typically at the level of the aortic arch, approximately T4–T5. As the LPA courses posterior to the trachea, it may cause extrinsic narrowing.

Type 2—More common and more complex form of LPA sling and is often seen with long segment tracheal stenosis due to the presence of complete tracheal cartilaginous rings. The tracheal and bronchial anomalies are more extensive; the position of the LPA sling is caudal, at the level of T6–T7 and may involve the bronchus as well as the distal trachea. There are more often other cardiovascular and pulmonary abnormalities including right tracheal bronchus, right lung hypoplasia, persistent left superior vena cava, and patent ductus arteriosus.

CTA is essential in imaging patients with LPA sling as definition of the contrast filled blood pool and air filled tracheobronchial tree are ideally imaged.

4.10.1 Misplaced Left Pulmonary Artery Origin

The anomalous origin of the LPA, resulting in the formation of a sling is believed to occur when development of the left sixth aortic arch fails and the left-sided lung buds establish a connection with branches of the right sixth aortic arch. The vascular supply of the left lung therefore comes from the RPA and the vessel passes between the trachea and the esophagus.

It is possible that the connection between the right sixth aortic arch and the left lung buds is made anterior to the trachea. In this case, the origin of the LPA is anomalous, but a sling is not present.

4.10.2 Complete Tracheal Rings

The cartilaginous rings of the trachea are normally incomplete, with an interruption in the ring along the dorsal surface of the trachea. This results in the normal U-shaped contour of the anterior trachea and the flattened dorsal surface.

When the tracheal cartilaginous rings are not interrupted, but completely encircle the lumen of the trachea, the affected segment is narrowed and typically has a circular shape. While growth of the trachea and of complete rings does occur the affected segment remains small.

4.10.3 Clinical Presentation

A 3-month-old infant with life-long stridor and a murmur underwent echocardiogram. A secundum atrial septal defect (ASD) was found, the cause of the murmur. The origin of the LPA was from the RPA. CTA was requested to confirm anatomy of LPA sling and to define tracheobronchial anatomy.

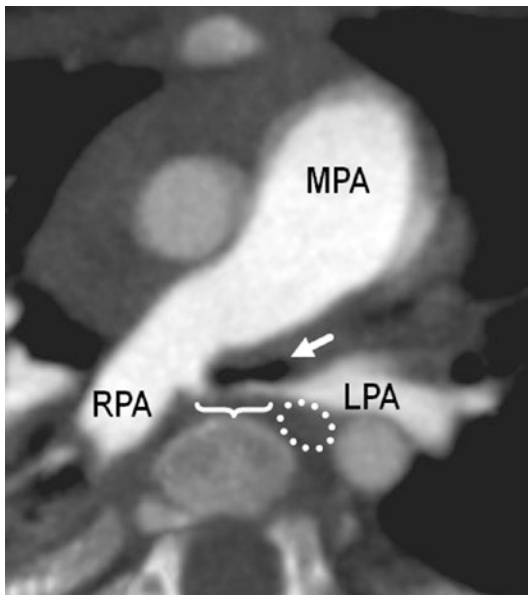

Fig. 4.69 The main (MPA) and right (RPA) pulmonary arteries are normal caliber. The left pulmonary artery (LPA) arises from the RPA and is severely narrowed (*bracket*) as it courses between the carina and the esophagus (*dotted ellipse*). In this patient, the spine may also contribute to narrowing of the proximal LPA

4.10.4 Case 4.20

See Fig. 4.69, 4.70, and 4.71.

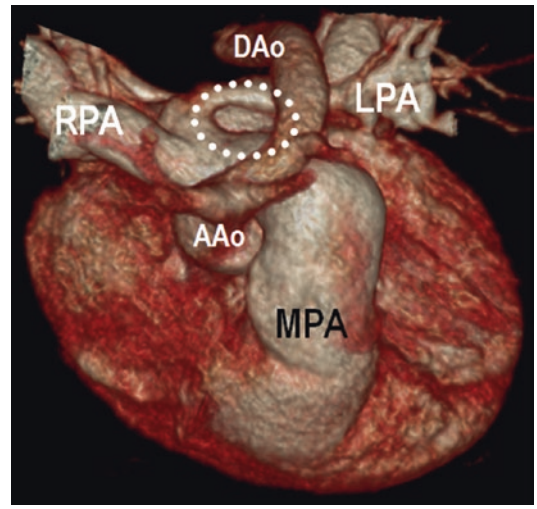

Fig. 4.70 A 3D surface rendered reconstruction of the heart and pulmonary arteries show the origin of the LPA from the RPA. Though not seen in this reconstruction, the trachea passes through the space anterior to the proximal LPA to the right of the aortic arch (*dotted ellipse*)

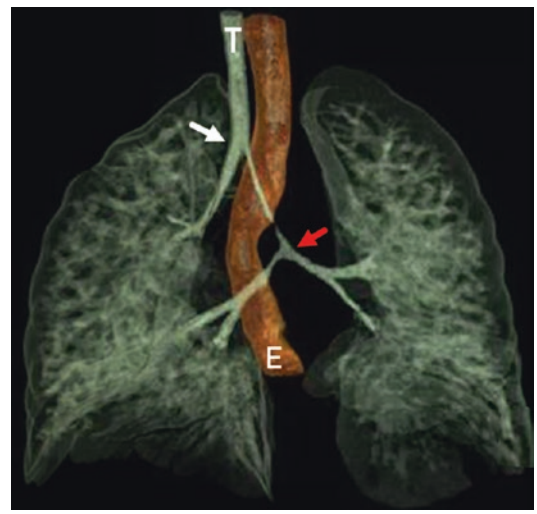

Fig. 4.71 A 3D reconstruction of the tracheobronchial tree and lung tissue is shown. The trachea (T) bifurcates at the level of the aortic arch (*white arrow*). The right bronchus is normal caliber but supplies only the right upper lobe. The left bronchus is diffusely small caliber and a second bifurcation (*red arrow*) divides to bronchi for the left upper and lower lobes and the right middle and lower lobes. The esophagus (E) is also seen

4.10.5 Case 4.21

Another infant presented with a murmur on a well-baby checkup. Echocardiography showed an unusual relationship in the pulmonary artery origins, raising a question of LPA sling. CTA was requested to investigate the anatomy.

The origin of the left pulmonary artery (LPA) arises from the superior surface of the right pulmonary artery (RPA) and courses leftward, forming an acute angle (*dotted arrow*), perhaps leading to the murmur heard on physical exam. The ascending aorta (AAo) and aortic arch have been cut away to show the branch pulmonary arteries.

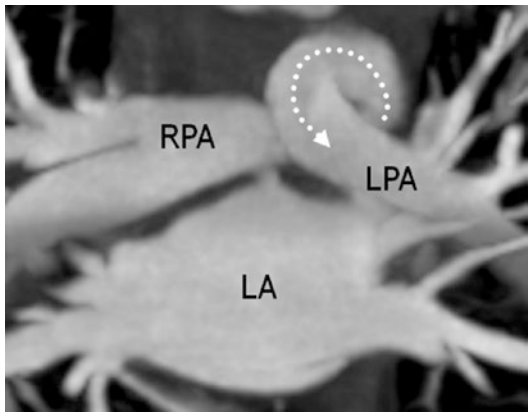

Fig. 4.72 A coronal oblique MIP image of the branch pulmonary arteries shows the anomalous origin of the LPA from the RPA and a circuitous course of the proximal LPA as it courses from right to left. Axial images showed the LPA traveling anterior to the trachea; therefore, a sling was not present

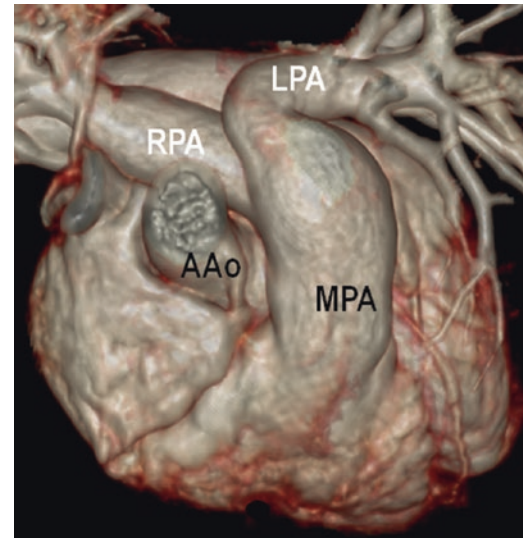

Fig. 4.73 A 3D surface rendered image of the heart shows the origin of the left pulmonary artery (LPA) arises from the superior surface of the right pulmonary artery (RPA) and courses leftward, forming an acute angle, the likely source of the murmur heard on physical exam. The ascending aorta (AAo) and aortic arch have been cut away to show the branch pulmonary arteries

4.11 Atrioventricular Septal Defect

When defects of the interatrial and interventricular septa occur together and affect formation of the atrioventricular valves, the malformation fits into the category of atrioventricular septal defects (AVSD). The term "endocardial cushion defect" is also used to describe an atrioventricular septal defect. The malformation involves defects of the primum segment of the interatrial septum which abuts the atrial side of the atrioventricular (AV) valve plane and the membranous segment of the interventricular septum which touches the ventricular side of the AV valve plane. The muscular interventricular septum may also be involved to varying degrees. The annulus of each of the AV valves, the mitral valve and tricuspid valve, which normally lie perpendicular to the intraatrial and interventricular septum and in nearly the same plane may be abnormal.

In the human embryo, a crescent of cardiogenic tissue forms a tube which folds (loops) upon itself and divides into the atria, left ventricle, and bulbus cordis (right ventricle). Before septation of the right and left ventricles a ridge of tissue, the bulboventricular fold, distinguishes the bulbus cordis from the left ventricle. The interventricular septum is formed from three independent tissue sources, muscular, inlet and outlet components. The muscular portion of the septum forms from an anterior segment of the bulboventricular fold, derived from the bulbous cordis, and grows posteriorly to fuse with the muscular ventricular segment which is derived solely from ventricular tissue. Just above the basal edge of the fused anterior (outlet) and posterior (inlet) muscular interventricular septum is a space, the interventricular foramen, which closes as the developing endocardial cushions (inlet) and conal truncal ridges (outlet) form the membranous septum and fuse to muscular septal tissue.

The endocardial cushions are contiguous across the atrioventricular valve plane; inlet portion of the interventricular membranous segment from the inferior endocardial cushions and the superior endocardial cushions extend across the ostium primum to join the primum segment of the interatrial septum. The secundum segment invaginates from the atrial wall, extending to overlap with the primum segment. This overlapping portion remains open in utero as the foramen ovale and in most hearts fuses to close after birth.

The atrioventricular valve plane and the anterolateral mitral and septal tricuspid valve leaflets are partially derived from tissue of the endocardial cushions. A defect in valvular tissue or annulus of either or both AV valves is variable and may be symmetric (balanced) or asymmetric (unbalanced). When balanced the common atrioventricular valve may have the appearance of a dysmorphic valve which opens to both the right and left ventricles. Alternatively, an unbalanced common atrioventricular valve may drain primarily to the right ventricle (right dominant) or to the left ventricle (left dominant).

Approximately 50% of infants born with Down syndrome have congenital heart disease, many of them will have and atrioventricular septal defect (45%).

4.11.1 Pearls (•) and Pitfalls (√)

• Examine cardiac CT images in short axis (SA), horizontal (4 chamber), and vertical (2 chamber) long axes in order to accurately characterize defects of the interatrial and interventricular septae.

√ The short axis view of the atrioventricular valve plane may be helpful in characterizing malformation of the mitral and tricuspid valves; however, echocardiography is typically much better for delineating valve structure.

4.11.2 Clinical Presentation

A full-term newborn with facial features of Down syndrome, but without suspected congenital heart disease, was born. Shortly after birth, the baby developed respiratory distress. Physical exam revealed a definite murmur; a chest radiograph and echocardiogram were performed.

4.11.3 Case Presentation

See Figs. 4.74, 4.75, 4.76, and 4.77.

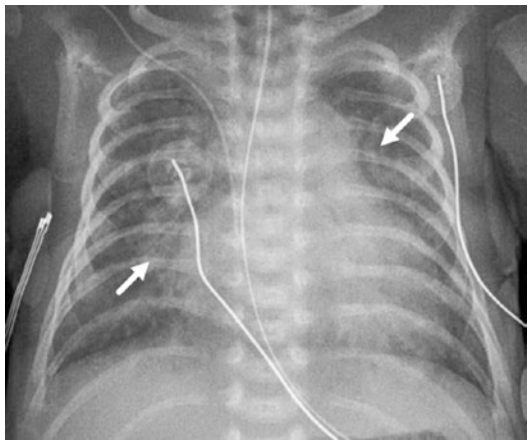

Fig. 4.74 The chest radiograph showed moderate cardiomegaly and increased pulmonary vascular markings (*arrows*). Echocardiography revealed small size of the left ventricle compared to the right and a primum and secundum atrial septal defects (ASD). The aortic arch was not well visualized and the ductus arteriosus was patent. Coarctation of the aorta was suspected. Cardiac CTA was requested to evaluate the aortic arch and to measure relative volumes of the ventricles

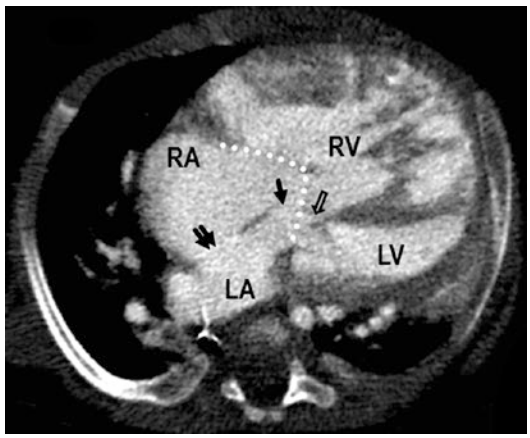

Fig. 4.75 A four-chamber view of the heart shows dilation and hypertrabeculation of the right ventricle (RV) and small volume of the left ventricle (LV). The membranous segment of the interventricular septum, just below the atrioventricular valve plane, shows a small defect (*open arrow*). Primum (*single arrow*) and secundum (*double arrow*) interatrial and membranous (*open arrow*) interventricular septal defects are noted. The atrioventricular valve plane (*dotted line*) shows the valves open predominantly to the RV in this patient with an unbalanced AVSD

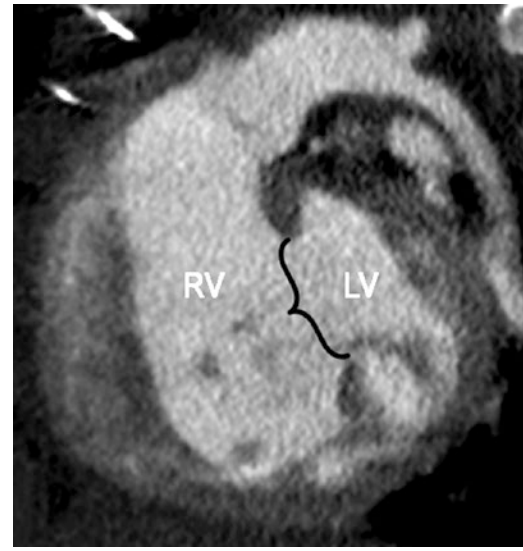

Fig. 4.76 The membranous interventricular septal defect (*black bracket*) is much larger in the short axis plane near the base of the heart. than was suspected in the 4 chamber view. Asymmetry of the right (RV) and left (LV) ventricles is also apparent in this view

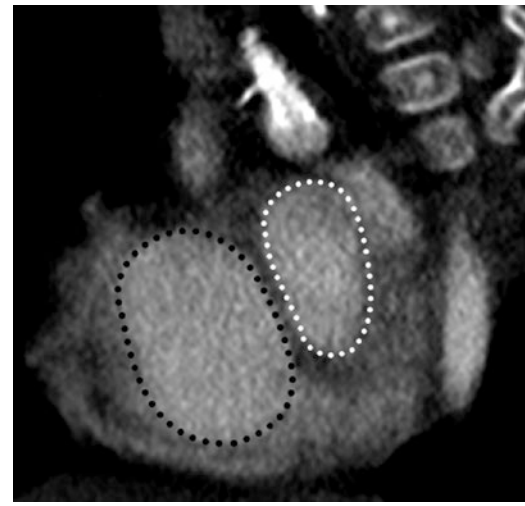

Fig. 4.77 At the level of the atrioventricular valve plane, the mitral annulus (*white dotted ellipse*) and the tricuspid annulus (*black dotted ellipse*) shows asymmetry, indicating the patient has an unbalanced atrioventricular septal defect which has right dominant valve components and ventricle

4.11.4 Clinical Presentation

A newborn infant with Down syndrome had a prenatal diagnosis of atrioventricular septal defect. She underwent cardiac CTA because of suspected aortic arch hypoplasia.

4.11.5 Case 4.22 Presentation

See Figs. 4.78, 4.79, 4.80, and 4.81.

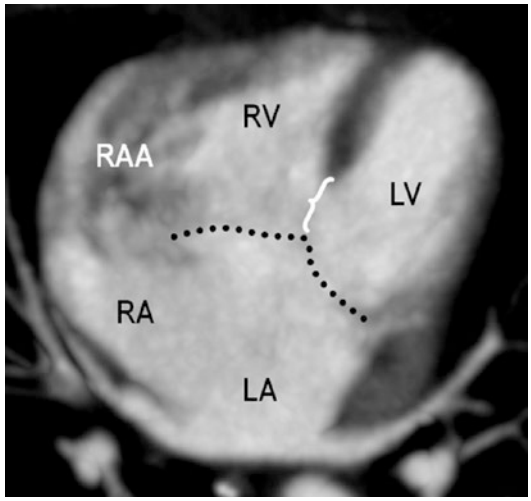

Fig. 4.78 A four-chamber view of the heart shows that the right (RV) and left (LV) ventricles are similar in size and that the plane of the atrioventricular valves (*dotted line*) opens symmetrically to both the right (RV) and left (LV) ventricles. A defect in the membranous portion of the interventricular septum (*bracket*) is accompanied by near complete absence of the interatrial septum. The right (RA) and left (LA) appear normal size, but the right atrial appendage (RAA) is dilated

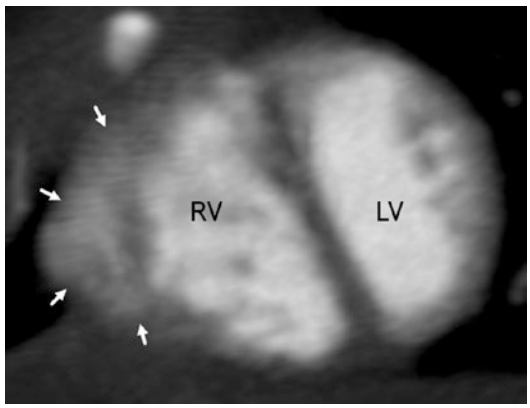

Fig. 4.79 In a short axis plane, the symmetry of the right (RV) and left (LV) ventricles is apparent as is the dilated right atrial appendage (*arrows*) which overlies the RV free wall

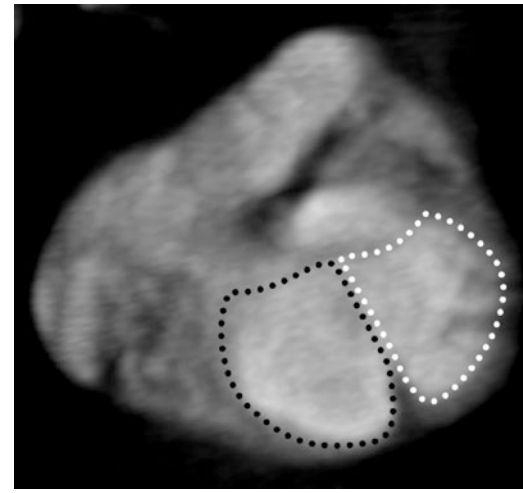

Fig. 4.80 At the level of the atrioventricular valve plane, the mitral annulus (*white dotted ellipse*) and the tricuspid annulus (*black dotted ellipse*) show symmetry, indicating the patient has a balanced atrioventricular septal defect, or co-dominant valve components and ventricles

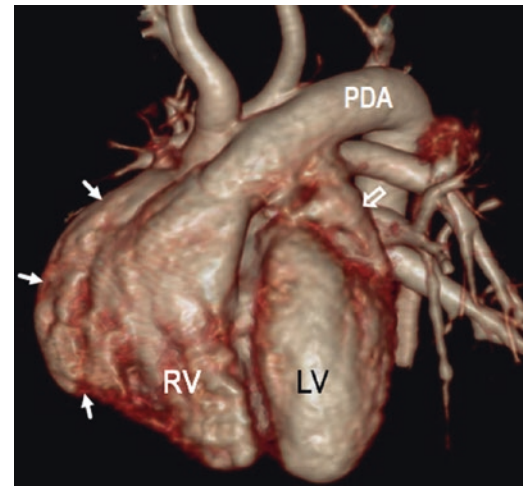

Fig. 4.81 A 3D surface rendered image shows the right (RV) and left (LV) ventricles are similar in size, and the large size of the right atrial appendage (*arrows*), and the left atrial appendage (*open arrow*). The ductus arteriosus (PDA) is patent and large caliber

4.12 Partial and Total Anomalous Pulmonary Venous Connection

Anomalous pulmonary venous connection occurs in many different types or combinations and results in drainage of oxygenated pulmonary venous blood to the right side of the interatrial septum, to systemic veins, or to a blind ending confluence behind the left atrium, without a direct connection to the heart. Anomalous veins may drain to structures above the heart (supracardiac), to a cardiac chamber (intracardiac), or below the heart (infracardiac).

The embryological development of the pulmonary veins begins as the cardinal veins, but regresses as a common pulmonary vein projects from the primitive left atrium toward the pulmonary parenchyma and eventually connects with the parenchymal venous system via four pulmonary veins to the left atrium.

4.12.1 Total Anomalous Pulmonary Venous Connections

Complete failure of the formation of the common pulmonary vein from the left *atrium* therefore results in total anomalous pulmonary venous connection (TAPVC). The extent of failed pulmonary vein development varies from persistence of primitive connections to the right rather than the left atrium (intracardiac), to infracardiac connections to the inferior vena cava or to the portal or hepatic veins, or most commonly, to supracardiac connections, the superior vena cava or the brachiocephalic veins. In supracardiac and infracardiac forms of TAPVC, a pulmonary vein confluence forms behind the left atrium. A vertically oriented vein which drains to the brachiocephalic vein and superior vena cava (SVC) in supracardiac TAPVC courses anterior or posterior to the left pulmonary artery; when posterior to the artery and anterior to the left bronchus pulmonary venous blood flow may be obstructed. When a confluence of pulmonary veins behind the left atrium drains inferiorly through the diaphragmatic hiatus, it is most often to the portal vein and less commonly to the hepatic veins or inferior vena cava (IVC). This connection too may become obstructed (90%), typically as the draining vein traverses the diaphragmatic hiatus. A combination of intra, supra, or infracardiac or mixed TAPVC may also be found.

Occasionally, an insufficient pathway for drainage or a complete lack of pulmonary parenchymal venous drainage occurs and results in rapid onset of postnatal pulmonary venous congestion which is incompatible with life. Cardiac CTA is especially important in imaging these clinically severely ill infants as the high spatial resolution capabilities of the modality lend toward defining the very small caliber venous structures.

4.12.2 Partial Anomalous Pulmonary Venous Connection

When only some of the pulmonary venous buds develop normal connections to the common pulmonary vein and left atrium but other connections are not made normally partial anomalous pulmonary venous connection (PAPVC) is the result.

The most commonly detected form of PAPVC is drainage of some or all of the right pulmonary veins to the superior vena cava (SVC). This anomaly typically is associated with a defect at the superior aspect of the sinus venosus. Though this type of defect is commonly referred to as a sinus venosus atrial septal defect (ASD) the terminology is inaccurate as the sinus venosus is not a component of the interatrial septum. PAPVC of all or part of the left lung is also possible superiorly via a vertical vein, intracardiac through the coronary sinus or to the right side of an intraatrial septum. Scimitar syndrome which includes right-sided PAPVC to the IVC also includes hypoplasia of the right lung and pulmonary artery, dextroposition of the heart, and occasionally components of sequestration in the right lower lobe with abnormal aortopulmonary collateral arteries.

Patients with TAPVC and PAPVC very often have accompanying intracardiac anomalies. An increased volume of blood flow to the right side of the heart occurs through the anomalous pulmonary veins in TAPVC and PAPVC. Intracardiac shunts, atrial septal (ASD) or ventricular septal (VSD) defects are commonly present and are important contributors to volume overloading of the right side of the heart. Severe and complex forms of congenital heart disease (CHD), hypoplastic left heart syndrome (HLHS), transposition of the great arteries (TGA), and tetralogy of Fallot (TOF) may also include anomalies of pulmonary venous connections.

4.12.3 Clinical Presentation

An infant with a loud murmur at a well-baby checkup underwent echocardiography which showed a muscular VSD and suspected abnormal right upper lobe pulmonary venous drainage. CTA of the heart was requested to investigate pulmonary vein anatomy.

4.12.4 Case 4.23

See Figs. 4.82, 4.83, 4.84, and 4.85.

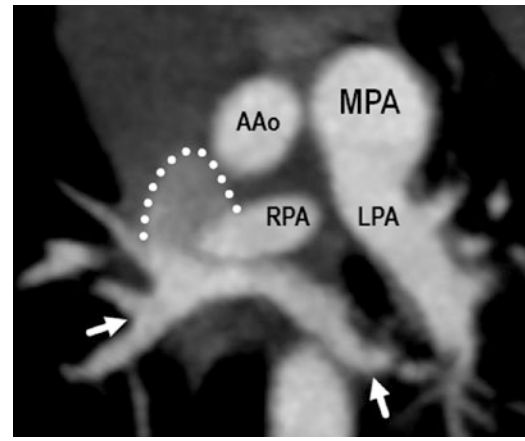

Fig. 4.82 An axial image of the superior mediastinum shows right- and left-sided pulmonary veins (*arrows*) draining to the superior vena cava (*dotted outline*) at the level of the pulmonary arteries (RPA and LPA). Differences in density of contrast enhancement indicate the mixing of the systemic and pulmonary venous drainage

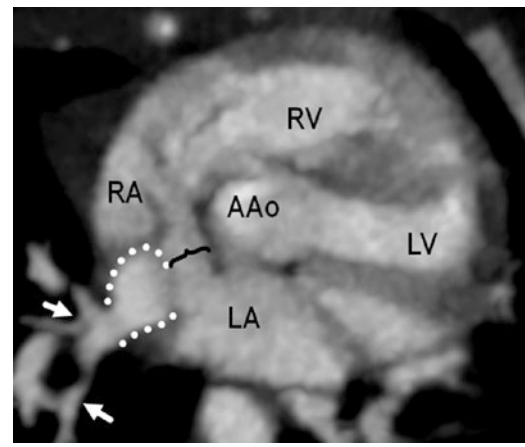

Fig. 4.83 An axial image of the heart, at the level of the superior margin of the atria, shows the sinus venosus defect (*bracket*) which commonly accompanies PAPVC to the SVC. Right pulmonary veins (*arrows*) drain to the SVC (*dotted outline*) and to the region of the sinus venosus defect, allowing shunting of a mixture of systemic and pulmonary venous blood to the atria. Note thickening of the wall of the right ventricle (RV) may be an indication of overload of the right side of the heart

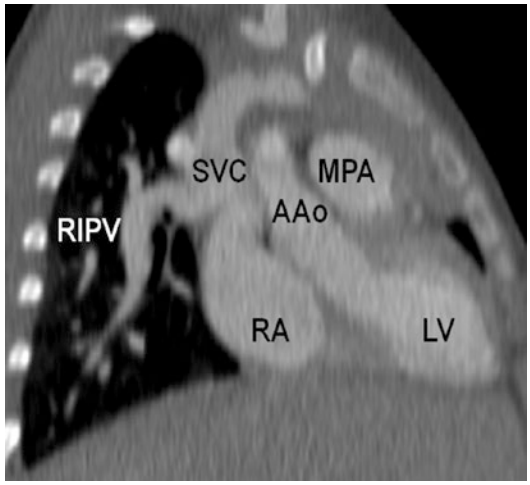

Fig. 4.84 A coronal oblique view of the heart shows the typical appearance of anomalous drainage of the right inferior pulmonary vein (RIPV) to the SVC, toward the right atrium (RA). It is helpful for the surgeon if you provide a measurement between the anomalous pulmonary vein and the RA/SVC junction in your report

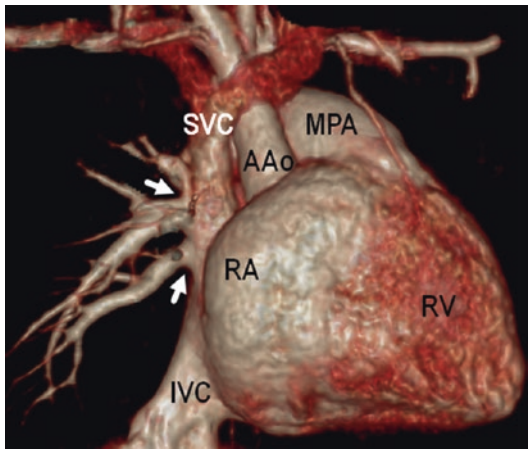

Fig. 4.85 In a 3D surface rendered reconstruction of cardiac CTA data, the position of several anonymously draining right pulmonary veins to the SVC are clearly depicted. The right side of the heart, particularly the right atrium (RA), is enlarged due to increased blood flow

4.12.5 Clinical Presentation

This patient presented in utero when a superior mediastinal vascular structure appeared abnormal. Postnatal echocardiography confirmed the finding and showed supracardiac anomalous pulmonary venous drainage. A cardiac CTA was requested.

4.12.6 Case 4.24

See Figs. 4.86, and 4.87.

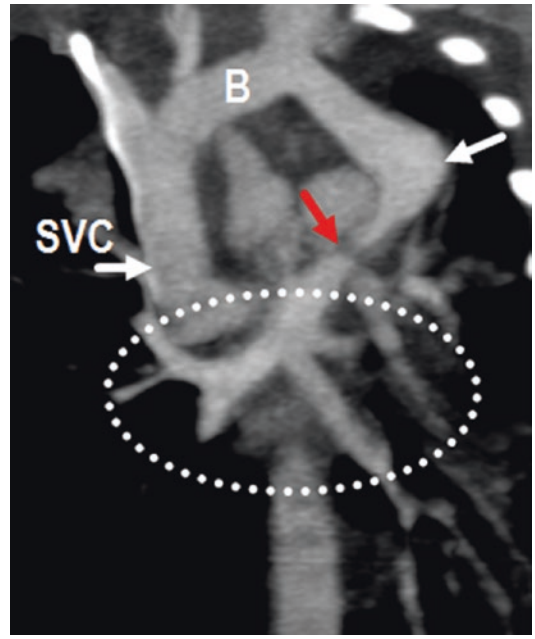

Fig. 4.86 A coronal MIP image of the anomalously draining pulmonary veins (*dotted ellipse*) shows supracardiac drainage toward the brachiocephalic vein (B) and the SVC. There is a focal dilatation (*white arrow*) just distal to a focal stenosis (*red arrow*) in the vertical vein

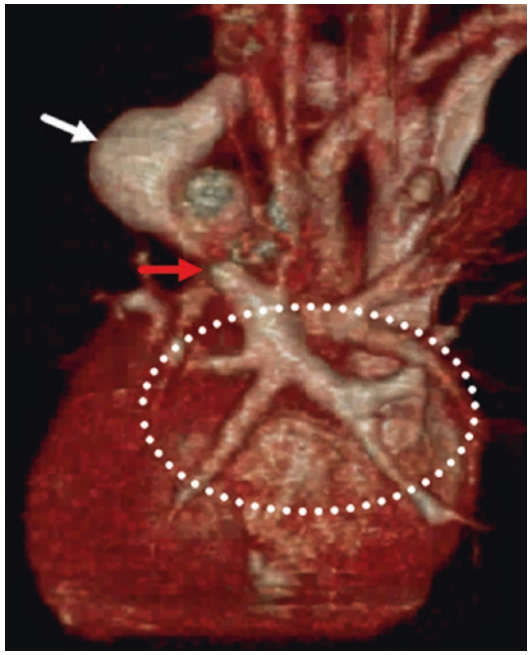

Fig. 4.87 A 3D reconstruction shows the four-pulmonary veins connecting to a confluence behind the left atrium (*dotted ellipse*). The stenosis (*red arrow*) and distal dilated segment (*white arrow*) of the vertical vein are seen

4.12.7 Clinical Presentation

An infant with a murmur on new baby exam underwent echocardiogram which showed an ASD, anomalous drainage of the pulmonary veins on the right and a patent ductus arteriosus (PDA).

4.12.8 Case 4.25

See Figs. 4.88, 4.89, 4.90, and 4.91.

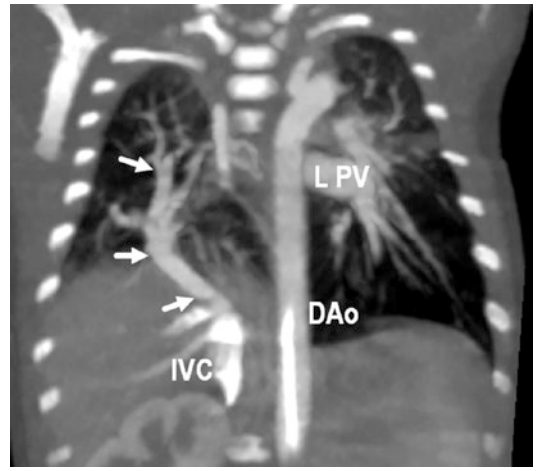

Fig. 4.88 A coronal MIP view of the chest and upper abdomen shows anomalous right pulmonary venous drainage below the diaphragm to the IVC (*arrows*) and small size of the right hemithorax and lung; diagnostic of Scimitar syndrome

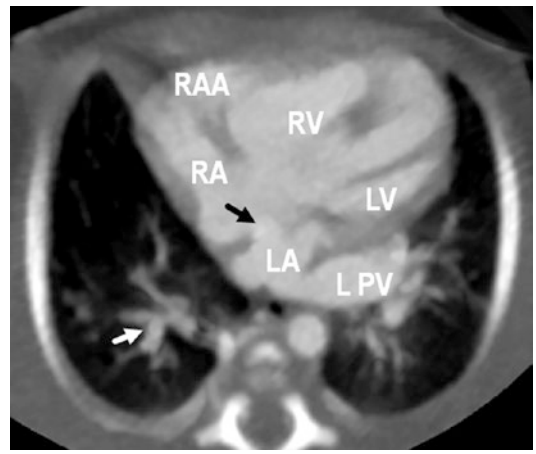

Fig. 4.89 A four-chamber view of the heart shows the anonymously draining right pulmonary vein (*white arrow*) and a secundum ASD (*black arrow*). A left pulmonary vein (L PV) confluence is dilated, and the right atrium (RA), right atrial appendage (RAA), and right ventricle (RV) are dilated by the high volume of blood flowing to the right side of the heart

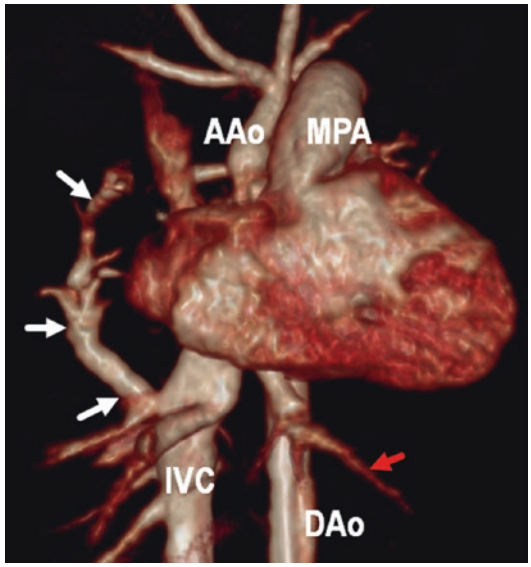

Fig. 4.90 A 3D reconstruction confirms the Scimitar vein draining the right lung (*arrows*) to the IVC. The left hepatic veins (*red arrow*) drain toward the IVC and right atrium

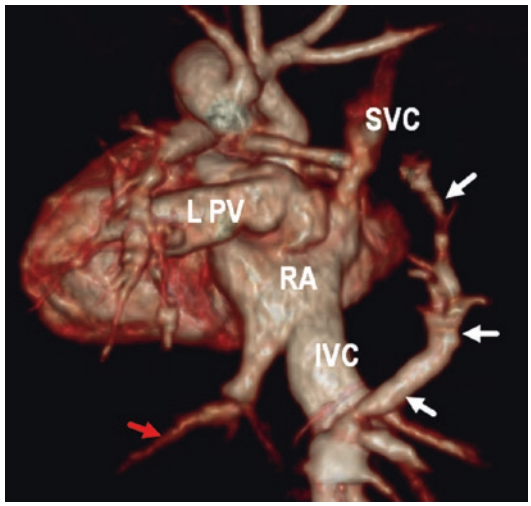

Fig. 4.91 A 3D reconstruction view from posterior again shows the scimitar vein (*arrows*) to the IVC and the left hepatic veins (*red arrow*) draining separately to the right atrium (RA). The dilated left pulmonary veins enter a left atrium which is superior to the RA

4.12.9 Clinical Presentation

A newborn with prenatal echocardiogram which revealed anomalous pulmonary venous drainage and a large ASD underwent cardiac CTA to confirm anatomy and define the extent of the anomalous venous drainage.

4.12.10 Case 4.26

See Figs. 4.92, 4.93, 4.94, and 4.95.

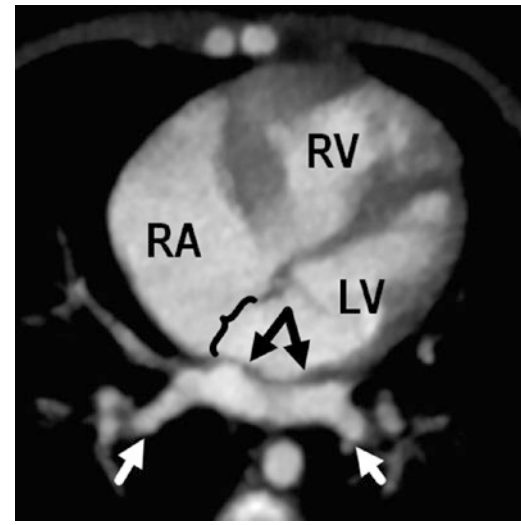

Fig. 4.92 An axial oblique, four-chamber view of the heart shows the right and left inferior pulmonary veins (*white arrows*) form a confluence behind the left atrium but do not communicate with the chamber (*black angled arrows*). The right atrium (RA) and right ventricle (RV) are markedly dilated compared to the left-sided chambers; a large secundum atrial septal defect (ASD) (*bracket*) is also present

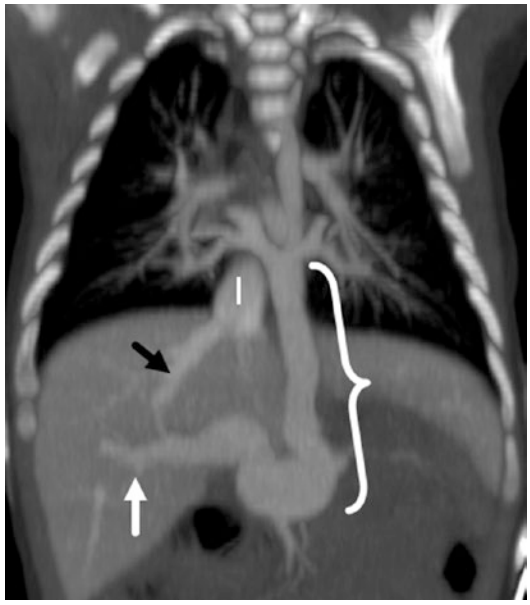

Fig. 4.93 A coronal oblique view of the pulmonary venous drainage shows a large caliber draining vein (*bracket*) extending below the diaphragm to the portal venous system (*white arrow*). Hepatic veins (*black arrow*) and the inferior vena cava (I) are partially in view

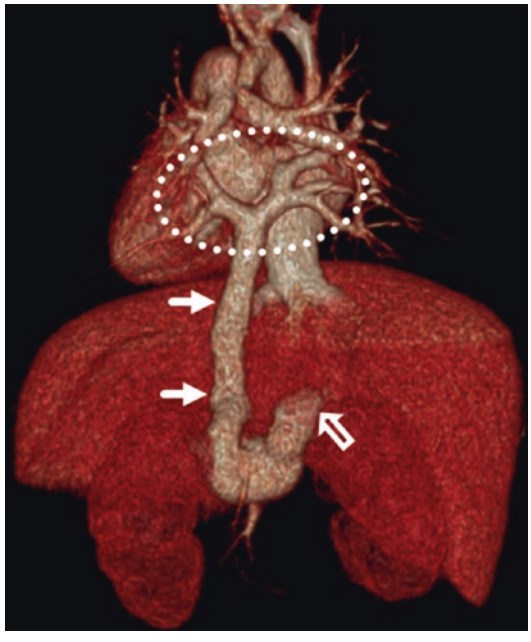

Fig. 4.94 A 3D coronal surface rendered view of the pulmonary venous anatomy shows anatomy from posterior. The branch pulmonary veins form a small confluence behind left atrium (*dotted ellipse*) and the large caliber draining vein (*arrows*) as it extends below the diaphragm to the portal venous system (*open arrow*)

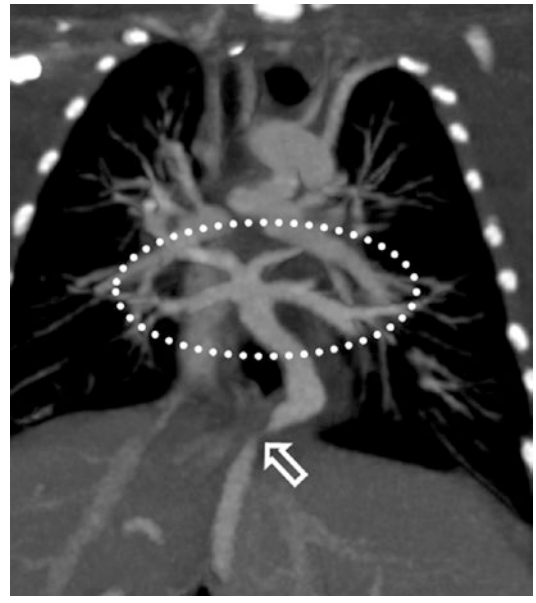

Fig. 4.95 A coronal oblique view of the thorax in another patient with infracardiac TAPVC shows a similar confluence of anonymously draining pulmonary veins behind the left atrium (*dotted ellipse*) and a single vein draining below the diaphragm. At the diaphragmatic hiatus, the vein is stenotic (*open arrow*)

4.12.11 Case 4.27

A newborn without suspected congenital heart disease had poor Apgar Scores and rapidly worsening cyanosis. Echocardiography showed pulmonary venous drainage was abnormal and patent ductus arteriosus (PDA). Cardiac CTA was requested to investigate pulmonary vein anatomy.

See Figs. 4.96, 4.97, and 4.98.

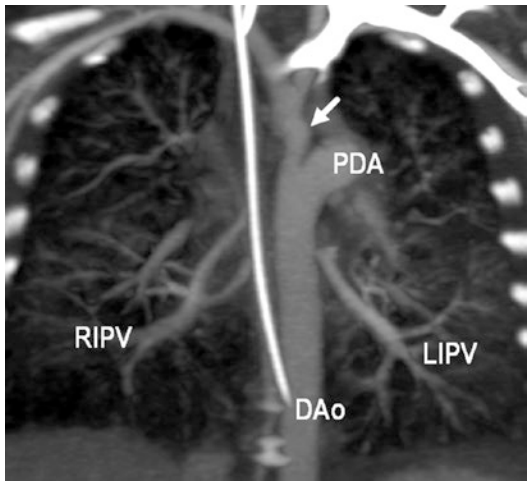

Fig. 4.96 Very tiny caliber right (RIPV) and left (LIPV) anomalous pulmonary veins are seen and the density of pulmonary parenchyma is increased due to venous congestion. A large caliber patent ductus arteriosus (PDA) projects between the distal aortic arch (*arrow*) and the descending aorta (DAo); its connection with the pulmonary artery is out of the image plane

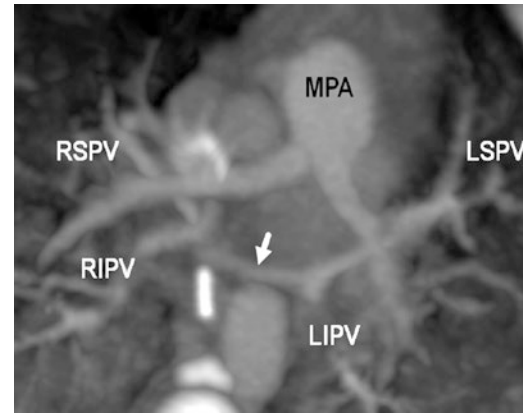

Fig. 4.97 In an oblique imaging plane, the right and left superior (RSPV and LSPV) and the right and left inferior (RIPV and LIPV) pulmonary veins drain toward a tiny caliber confluence (*arrow*) located behind the left atrium

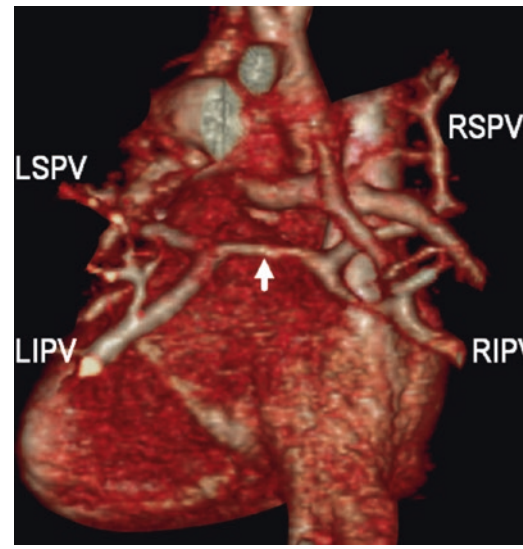

Fig. 4.98 The right and left superior (RSPV and LSPV) and the right and left inferior (RIPV and LIPV) pulmonary veins are seen on this 3D reconstruction. The veins drain toward a tiny caliber confluence located behind the left atrium (*arrow*)

4.13 Hypoplastic Left Heart Syndrome and Shone's Complex

The malformations of cardiac development affecting the left side of the heart are defined by a collection of malformations or hypoplasia or absence of a structure or groups of structures. Two of the most common forms of left heart malformation seen in neonates are hypoplastic left heart syndrome and Shone's syndrome.

4.13.1 Shone's Complex

Shone's complex (aka Shone's Anomaly and Shone's Syndrome), described by the physician for whom it is named, is a collection of left heart errors in formation that tend to occur together. The complete form of Shone's complex involves multiple levels of left heart obstructive lesions which include a supravalvar mitral ring, abnormal chordae tendineae insertion into one papillary muscle resulting in mitral valve stenosis and parachute configuration of the mitral valve, subaortic stenosis, and coarctation of the aorta [15].

Partial forms or the Shone's complex in which components are present in variable expression are also recognized and since its description in 1963 the definition has been variably expanded to include other mitral and aortic valve lesions and supravalar aortic stenosis.

Even with improving surgical techniques and treatment of children with Shone's complex the prognosis remains poor. The lesions which appear to be most difficult to treat are the supravalvar mitral ring within the left atrium and repair of mitral valve stenosis which is related to malposition and in many cases thickening of the chordae tendineae [16, 17]. Therefore, it is imperative to as fully as possible to describe the degree of supravalvar mitral annular narrowing in multiple dimensions, the size and position of papillary muscles in the left ventricle, and if possible to describe the morphology of the mitral valve leaflets and chordae tendineae. Though echocardiography is the ideal imaging modality for investigating cardiac valve morphology and function CT and often cardiac MR play a valuable role in defining cardiac structures.

4.13.2 Clinical Presentation

Infants with Shone's complex may be identified using prenatal sonography as coarctation of the aorta is often readily diagnosed before birth. In addition, limitations of mitral inflow to the left ventricle (LV) has the consequence of poor growth of the LV such that it is smaller than the right ventricle (RV), a finding which alerts one to probable congenital heart disease and close antenatal and postnatal follow-up imaging.

There are reports of the rare occurrence of patients with partial expression of the Shone's complex presenting as an adult [18].

4.13.3 Hypoplastic Left Heart Syndrome

In hypoplastic left heart syndrome (HLHS), all left-sided heart structures, the left atrium (LA), mitral valve (MV), left ventricle (LV), aortic valve (AV), and the ascending aorta (AAo) are small. The embryological events or miscues which result in this complex form of CHD remain uncertain as do developmental cause and effect relationships. It has been theorized that maldevelopment of the MV apparatus which results in severe MV stenosis or aplasia leads to small size of the LV and so on, such that the AV and AAo do not grow normally due to lack of inflow or blood flow into or through the structures [19].

The right heart structures, caliber of the aortic arch and descending aorta (DAo) are normal size because of blood flow to these structures from systemic sources and through the ductus arteriosus. Depending on the presence and size of a patent foramen ovale (PFO) in utero, and atrial (ASD) and/or ventricular (VSD) septal defect the size of the LA and LV are variable, ranging between moderately to severely hypoplastic. In utero, blood flows through defects in the atrial and ventricular septae and through the PDA, maintaining oxygenated perfusion of the brain, gut, and viscera; retrograde blood flow in the AAo via the PDA allows perfusion of the coronary arteries as antegrade flow through the AV is absent or severely limited. It is imperative that the ductus arteriosus remain patent following birth so perfusion of all these vital structures is maintained. If restrictive the ASD is enlarged, often using interventional techniques.

4.13.4 Case 4.28

See Figs. 4.99, 4.100, 4.101, and 4.102.

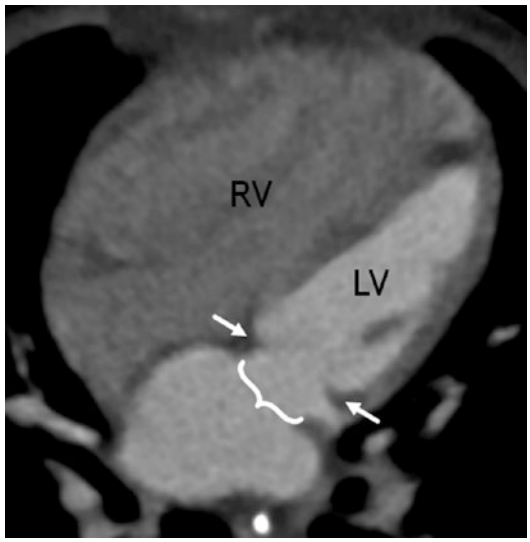

Fig. 4.99 A newborn with a prenatal diagnosis of congenital heart disease is suspected of having Shone's complex due to small size of the left ventricle (LV) compared to the right ventricle (RV). On cardiac CT a 4 chamber view of the heart reveals the small size of the left ventricle (LV) compared to the right ventricle (RV). In the left atrium a thickened fibrous ring narrows the left atrium (*bracket*) just above the mitral valve annulus. The annulus of the mitral valve lies several millimeters below this thickened tissue (*arrows*)

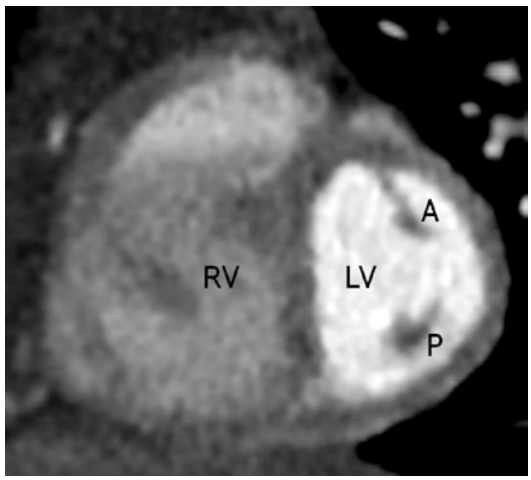

Fig. 4.100 A CT image in the short axis plane at the mid chamber level confirms the abnormal small LV chamber size compared to the RV. The anterior (A) and posterior (P) papillary muscles which should be similar in size are asymmetric, with small size of the anterior muscle. Echo showed that most of the chordae tendineae insert on the larger posterior papillary muscle and the mitral valve leaflet motion was abnormal

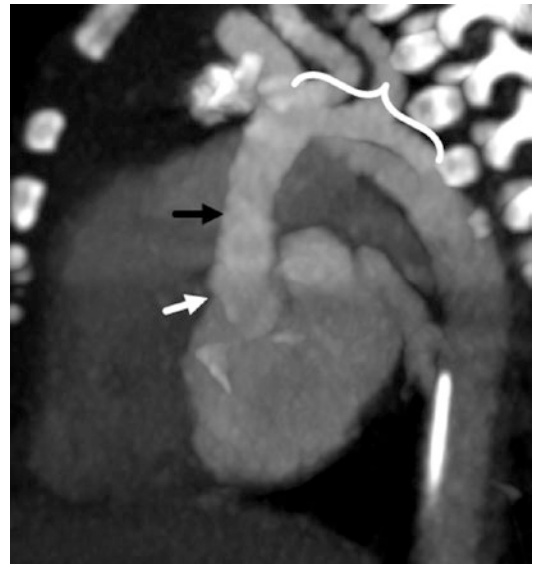

Fig. 4.101 A "candy cane" view of the aorta shows the level of the aortic valve (*white arrow*), caliber of the ascending aorta (*black arrow*) and hypoplasia of the aortic arch (*bracket*)

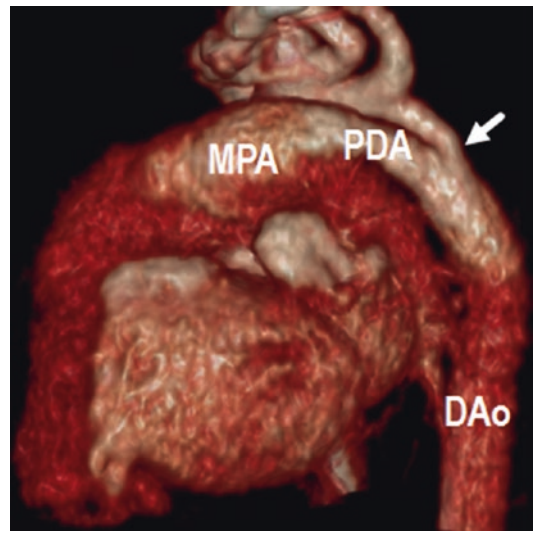

Fig. 4.102 A 3D surface rendered image of the heart and aorta reveals focal coarctation of the aorta (*arrow*). The main pulmonary artery (MPA) obscures the ascending aorta and the patent ductus arteriosus (PDA) is larger caliber than the hypoplastic aortic arch

4.13.5 Case 4.29

A newborn male is known to have a prenatal diagnosis of HLHS given findings on prenatal sonogram. Following birth, echo images confirm all relevant findings and as aortic arch hypoplasia was now suspected, cardiac CTA was requested.

See Figs. 4.103, 4.104, 4.105, and 4.106.

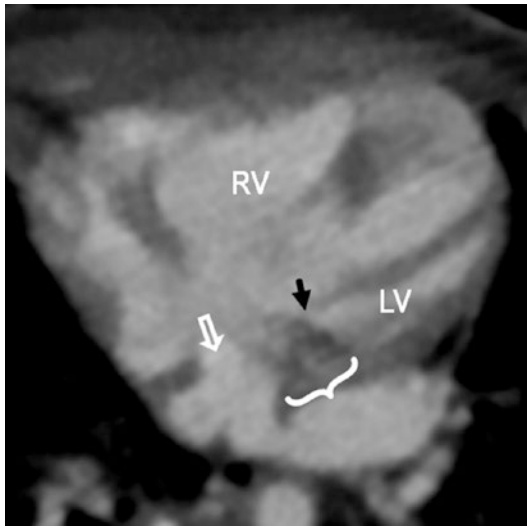

Fig. 4.103 A four-chamber view of the heart shows dysplastic tissue related to mitral valve aplasia (*bracket*) and a very small left ventricle (LV). A small ventricular septal defect (*black arrow*), likely restrictive, has contributed to poor LV growth as blood flow into the LV has been restricted through this potential shunt. The RV appears relatively large, but volume estimation by CT is normal for birth weight. An atrial septal defect (*open arrow*) is also present

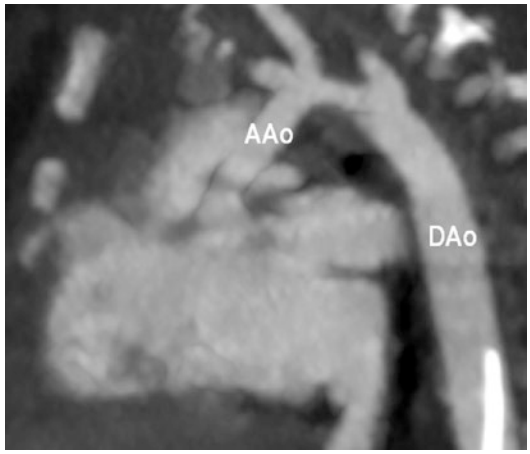

Fig. 4.104 A sagittal oblique "candy cane" view of the aorta reveals the small caliber of the ascending aorta (AAo) and confirms the small caliber of the aortic arch. The descending aorta (DAo) is normal caliber. Aortic arch hypoplasia is not an uncommon finding in HLHS as it is only large enough to support retrograde flow from the PDA into brachiocephalic arteries and the coronary arteries via the hypoplastic ascending aorta

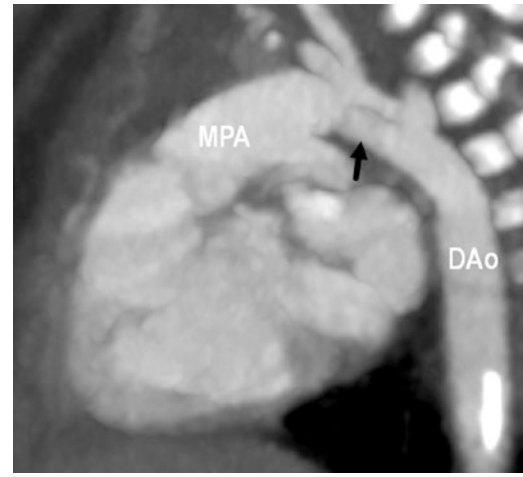

Fig. 4.105 By rotating the candy cane view slightly, the main pulmonary artery (MPA), the patent ductus arteriosus (*arrow*) [commonly referred to as the ductal arch], and the descending aorta (DAo)

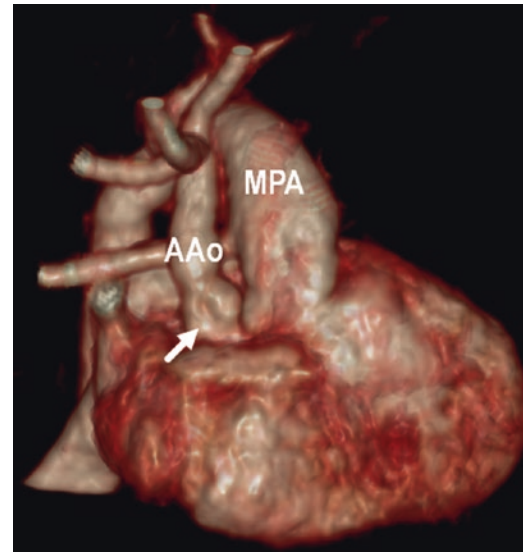

Fig. 4.106 A 3D surface rendered view of the heart allows one to easily visualize the degree of ascending aorta (AAo) hypoplasia and the small size of the aortic valve (*white arrow*), compared to the main pulmonary artery (MPA)

4.14 Anomalous Coronary Artery Origins

The origins of two coronary arteries from the sinuses of Valsalva of the ascending aorta is nearly always constant, with the left main coronary artery (LM) arising from the left sinus and the right coronary artery (RCA) from the right sinus of Valsalva.

Occasionally, the origins of the coronary artery arise from an unexpected location, the LM from the right sinus or RCA from the left sinus, either artery from the noncoronary cusp, above the sinuses from the tubular segment of the ascending aorta, or from a pulmonary artery. When its origin is anomalous, the proximal course of the coronary artery is also abnormal, in the wall of the ascending aorta, anteriorly between the ascending aorta and main pulmonary artery, posteriorly behind the ascending aorta and the noncoronary cusp, over the right ventricular outflow tract (RVOT), or through the myocardium of the intraventricular septum.

It is possible to live an asymptomatic, normal life with an anomalous coronary artery origin; it is occasionally found in an asymptomatic adult or in an autopsy of a person who expired due to another cause. When symptomatic, chest pain, arrhythmia, and even sudden cardiac death may occur in patients with an anomalous coronary artery, presumably due to compromised myocardial perfusion.

Anomalous origin of a coronary artery may be and isolated finding or may be seen concurrent with other complex congenital heart disease. The incidence of anomalous origin of a coronary artery is reported to be 0.17% in children using echocardiography [20]. There is however a broad variance in reported incidence of coronary artery anomalies depending upon the imaging modality utilized to make the diagnosis, with 1.07% of anomalous coronary arteries arising from the opposite sinus of Valsalva, found at coronary angiography [21]. The incidence of origin and course of anomalous coronary arteries also varies; a left coronary arising from the right sinus appears to be most often found in symptomatic patients and at necroscopy [22].

In children without complex congenital heart disease, the presence of an anomalous coronary artery is generally not investigated and therefore not recognized, if asymptomatic. Though it is routine to identify coronary artery origins using echocardiography in patients with congenital heart disease, it is often difficult or impossible to visualize the small caliber arteries in infants and an acoustic window maybe suboptimal in older children. Cardiac CTA is the recommended examination to make or confirm the diagnosis of an anomalous coronary artery origin.

Treatment of and the need to treat coronary artery anomalies are controversial. The points of controversy include the belief that a coronary artery which courses between the AAo and the MPA may or may not be symptomatic; it may be that only a course in the wall of the AAo (intramural) becomes symptomatic and therefore requires treatment. It is generally regarded as benign and therefore not requiring intervention if the course of an anomalous coronary is intermural rather than intramural, posterior to the AAo, or overlying the RVOT [21]. Timing of warranted intervention is also controversial in that some believe it is necessary to intervene as soon as possible upon discovery of the anomaly and others advocating for delayed intervention in asymptomatic young children. Those who argue for delayed intervention cite that the caliber of the coronary arteries are small, which increases the difficulty and therefore risk of surgical reimplantation and that a young child is unlikely to be symptomatic. It appears that more children with anomalous coronary artery arising from the opposite sinus of Valsalva become symptomatic and therefore require surgery or other intervention to avoid sudden cardiac death as they enter the second decade of life, corresponding to increased physical activity such as participation in competitive sports [23].

4.14.1 Case 4.30

A 12-year-old male complains of chest pain during baseball practice. His pediatrician refers him to a pediatric cardiologist and an echocardiogram shows absence of the normal left coronary artery origin and its anomalous origin from the right sinus of Valsalva. The proximal left coronary appears narrow. Due to the suspected coronary artery, anomaly CTA of the coronary arteries is requested (Figs. 4.107, 4.108, 4.109, and 4.110).

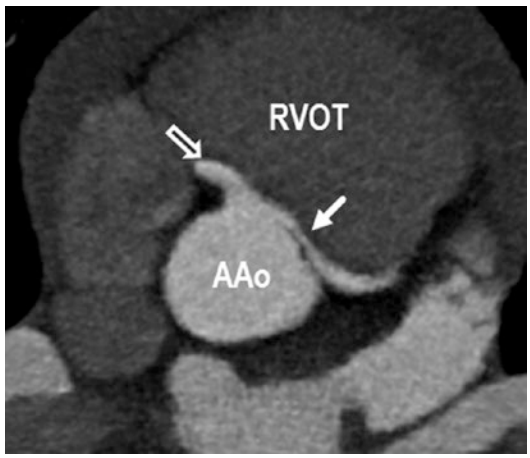

Fig. 4.107 An axial oblique MIP image of the AAo at the level of the sinuses of Valsalva shows a single coronary artery origin from the anterior, right sinus, and the proximal left (*arrow*) and right (*open arrow*) coronary arteries. The proximal left main coronary artery arises at an extremely acute angle relative to the AAo and the proximal segment is severely narrowed as it courses between the RVOT and AAo

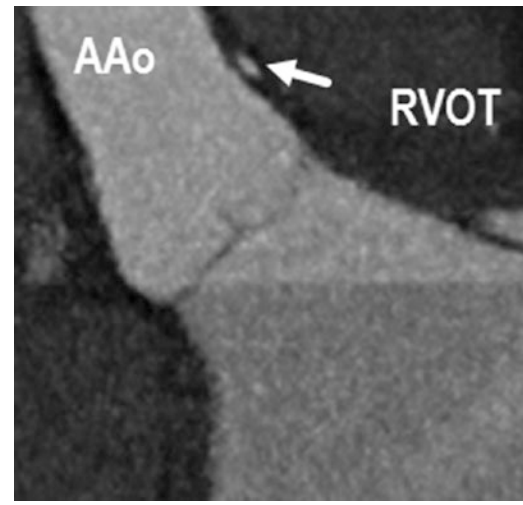

Fig. 4.108 The left main coronary artery (*arrow*) is narrow as it courses over the AAo and has an elliptical shape which is an indication that the vessel is intramural, within the wall of the AAo rather than merely coursing over the aorta. This course is considered malignant and is more often symptomatic and the cause of sudden cardiac death

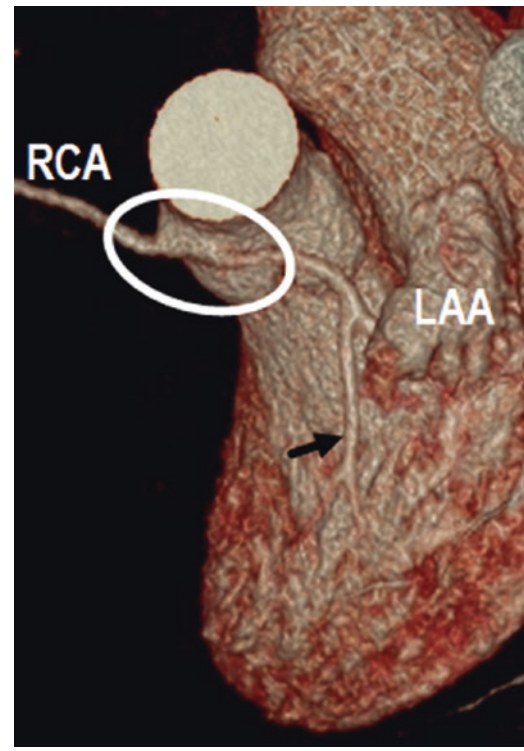

Fig. 4.109 The common origin of the right and left coronary arteries from the right sinus (*ellipse*) is shown in a 3D surface rendered image. The left coronary artery branches to the left circumflex which courses under the left atria appendage (LAA) and the left anterior descending (LAD). The LAD is a short vessel (*black arrow*); does not reach the LV apex as is usually expected

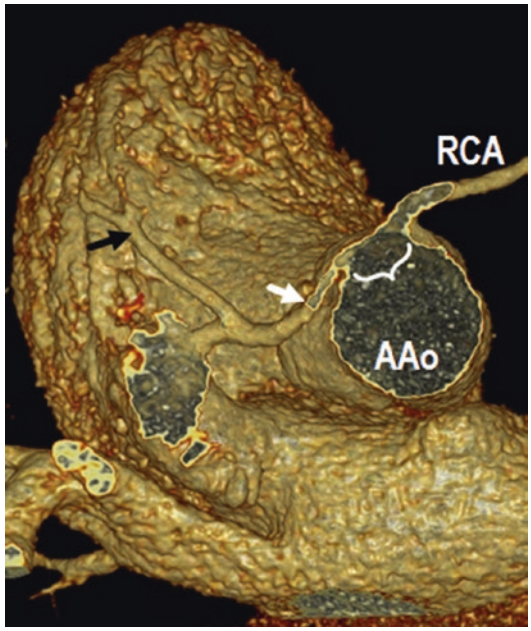

Fig. 4.110 In this "hollow" 3D view of the common coronary artery origin (*bracket*), the acute angulation and proximal stenosis of the left coronary artery is seen (*white arrow*). The short LAD (*black arrow*) is again seen

4.14.2 Case 4.31

A 9-year-old girl experienced a syncopal event while running. An echocardiogram performed in the emergency room showed normal cardiac function and left coronary artery origin. The origin of the right coronary artery was not seen. Two weeks later after a second syncopal event, her pediatrician ordered a coronary artery CTA after consultation with a pediatric cardiologist (Figs. 4.111, 4.112, and 4.113).

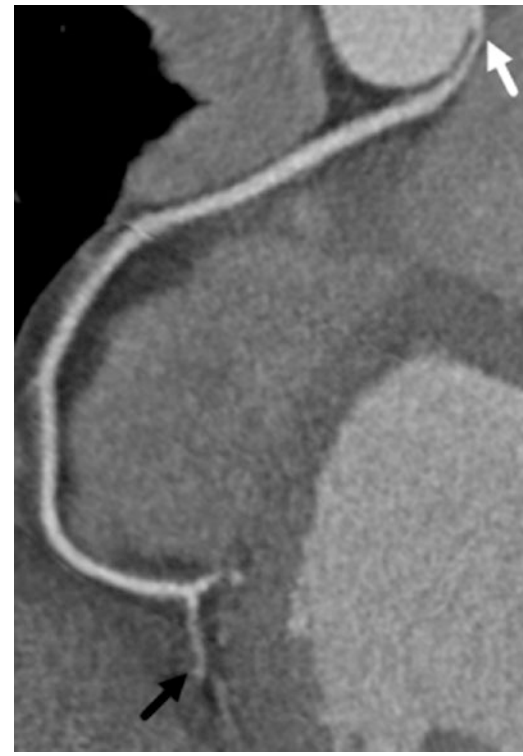

Fig. 4.111 A low dose coronary artery CTA was performed. A curved multiplanar reconstruction of the right coronary artery (RCA) shows its entire course. The artery arises from the left sinus of Valsalva (*white arrow*) and shows a markedly narrow proximal segment which courses at an acute angle in relation to the ascending aorta. The RCA courses to the crux of the heart ends branching to a very small posterior descending artery (PDA) (*black arrow*) and a short posterolateral branch

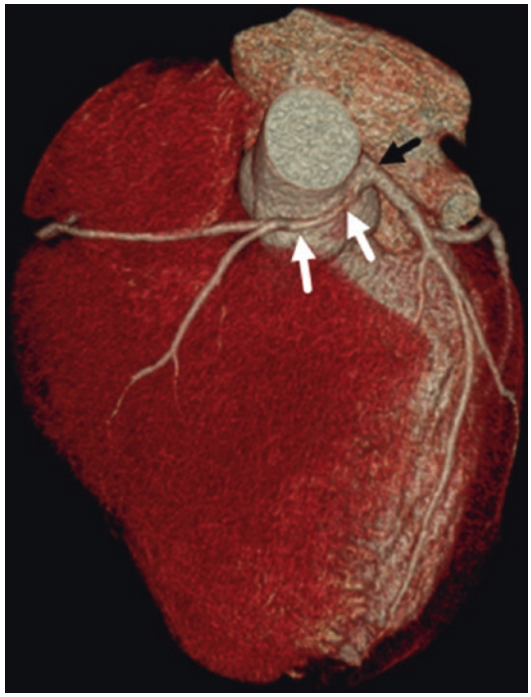

Fig. 4.112 In a 3D surface rendering, the anomalous RCA origin is seen arising from a common origin with the left (*black arrow*). The proximal intramural segment is narrow as it courses over the AAo (*white arrow*)

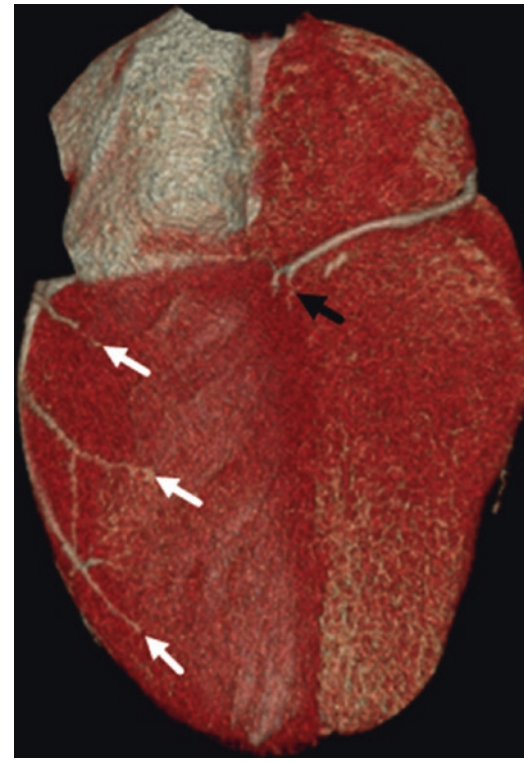

Fig. 4.113 Looking at the inferior surface of the heart in a 3D surface rendering the distal branches of the epicardial coronary arteries show the very short PDA segment (*black arrow*) and prominent obtuse marginal vessels extending to supply the inferior wall of the LV (*white arrows*)

4.15 Kawasaki Disease

Kawasaki disease is an idiopathic systemic vasculitis which affects young children almost exclusively. The classic presentation includes fever, lip and tongue swelling (strawberry tongue), injected conjunctiva, polymorphous rash, desquamation of extremities, and cervical lymphadenopathy.

Kawasaki disease is recognized as a cause of acquired heart disease in children. The most serious complication of Kawasaki disease is development of coronary artery aneurysms which are diagnosed in up to 25% of patients who do not receive treatment and in approximately 15% of those treated for Kawasaki disease. Subsequent coronary artery occlusion and myocardial infarction are known to occur in the acute phase of the disease as well as in the remote time frame. Though coronary artery aneurysms typically do not progress coronary artery diameter does not return to normal. Therefore, long-term clinical and imaging follow-up is required to monitor coronary artery aneurysm diameter, development of coronary artery stenosis and development of coronary artery aneurysm calcification.

4.15.1 Pearls (•) and Pitfalls (#)

• Coronary artery CTA and MRI are more sensitive than echocardiography for diagnosis and follow-up imaging of coronary artery aneurysms, especially in older children and adults, in whom acoustic windows may be limited.

Coronary artery imaging with MRI will not reveal extent of coronary artery aneurysm calcification.

4.15.2 Clinical Presentation

A 4-year-old girl presented with fever and tongue swelling. Her condition deteriorated and echo showed very poor cardiac function. Coronary artery CTA was requested to assess coronary artery patency and potential aneurysm formation.

4.15.3 Case 4.32 Presentation

See Figs. 4.114, 4.115, 4.116, and 4.117.

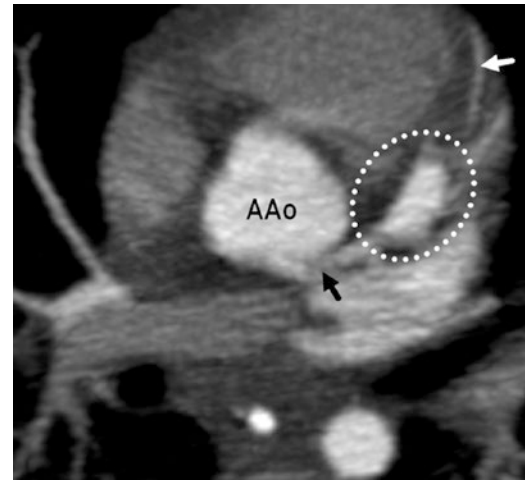

Fig. 4.114 An axial oblique image of the ascending aorta (AAo) at the level of the sinuses of Valsalva shows the origin of the left coronary artery (*black arrow*) and aneurysm of the proximal left anterior descending coronary artery (LAD) (*dotted ellipse*) and the normal caliber LAD distal to the aneurysm

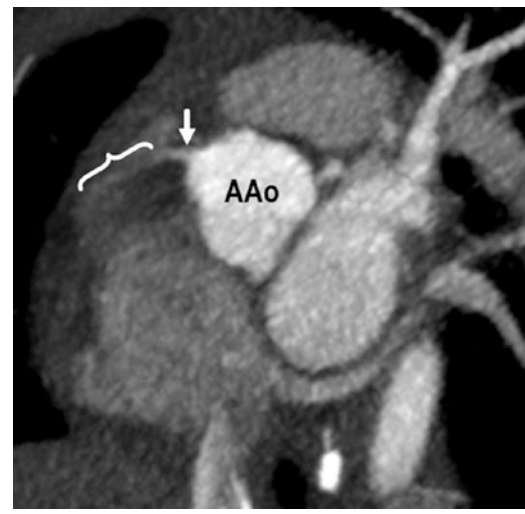

Fig. 4.115 In a coronal oblique plane, the ascending aorta (AAo) is shown at the base of the heart. The origin of the right coronary artery (*white arrow*) is very small caliber and the proximal segment of the vessel (*bracket*) is not filled with contrast material, indicating occlusion of the vessel

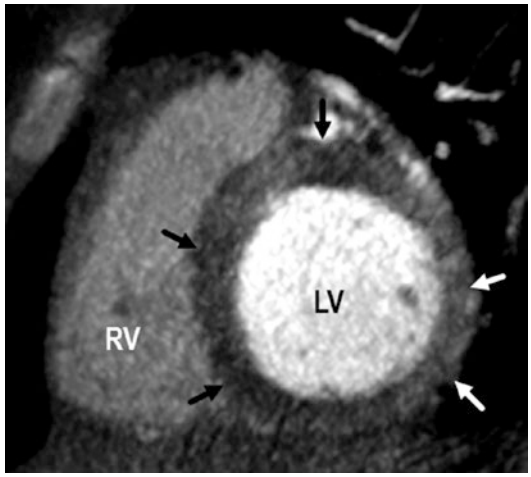

Fig. 4.116 In a basal short axis view of the heart, the myocardium of the left ventricle (LV) shows heterogeneous attenuation. The lateral wall (*white arrows*) is normal. The anterior and septal walls (*black arrows*) are lower attenuation than the lateral wall due to poor perfusion and infarction

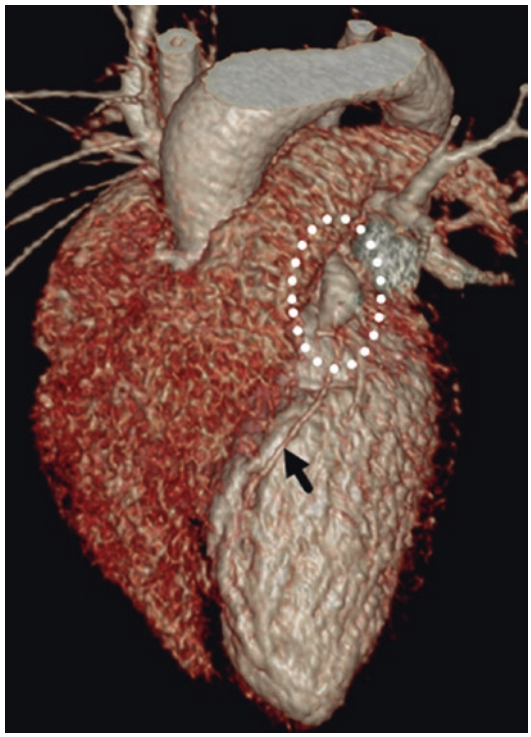

Fig. 4.117 A 3D surface rendered view of the heart shows the aneurysm of the proximal left anterior descending artery (LAD) (*dotted ellipse*) and the normal caliber LAD distal to the aneurysm

References

1. Minniti S, Visentini S, Procacci C. Congenital anomalies of the venae cavae: embryological origin, imaging features and report of three new variants. Eur Radiol. 2002;12:2040–55.
2. Moller JH, Nakib A, Anderson RC, Edwards JE. Congenital cardiac disease associated with polysplenia. Circulation. 1967;36:789–99.
3. Applegate KE, Goske MJ, Pierce G, Murphy D. Situs revisited: imaging of the heterotaxy syndrome. Radiographics. 1999;19:837–52.
4. Tynan MJ, Becker AE, Macartney FJ, Jimenez MQ, Shinebourne EA, Anderson RH. Nomenclature and classification of congenital heart disease. Br Heart J. 1979;41:544–53.
5. Gittenberger-De Groot AC, Van Ertbruggen I, Moulaert AJ, Harinck E. The ductus arteriosus in the preterm infant: histologic and clinical observations. J Pediatr. 1980;96:88–93.
6. Chuaqui BJ, Piwonka GC, Farro A. Oer den Wandbau des persistierenden Ductus Arteriosus. Virchows Arch (Pathol Anat). 1977;372:315.
7. Schneider DJ, Moore JW. Patent ductus arteriosus. Circulation. 2006;114:1873–82.
8. Moore KL, Persaud TVN. The developing human: clinically oriented embryology. 8th ed. Philadelphia, PA: Saunders.
9. Davies M, Guest PJ. Developmental abnormalities of the great vessels of the thorax and their embryological basis. Br J Radiol. 2003;76:491–502.
10. Miranda JO, Callaghan N, Miller O, Simpson J, Sharland G. Right aortic arch diagnosed antenatally: associations and outcome in 98 fetuses. Heart. https://doi.org/10.1136/heartjnl-2013-304860.
11. Dillman JR, Yarram SG, D'Amico AR, Hernandez RJ. Interrupted aortic arch: spectrum of MRI findings. AJR. 2008;190:1467–74.
12. Dillman JR, Attili AK, Agarwal PP, Dorfman AL, Hernandez RJ, Strouse PJ. Common and uncommon vascular rings and slings: a multi-modality review. Pediatr Radiol. 2011;41:1440–54.
13. Kommerell B. Verlagerung des Ösophagus durch eine abnorm verlaufende Arteria subclavia dextra (Arteria lusoria). Fortschr Geb Roentgenstrahlen. 1936;54:590–5.
14. Fallot ELA. Contribution a l'anatomie pathologique de la maladie bleu (cyanose cardiaque). Mars Med. 1888;25:77–93.
15. Shone JD, Sellers RD, Anderson RC, Adams P, Lillehei CW, Edwards JE. The developmental complex of "parachute mitral valve", supravalvular ring of left atrium, subaortic stenosis and coarctation of aorta. Am J Cardiol. 1963;11:714–25. https://doi.org/10.1016/0002-9149(63)90098-5.
16. Brauner RA, Laks H, Drinkwater DC, Scholl F, McCaffery S. Multiple left heart obstructions (Shone's anomaly) with mitral valve involvement: long-term

surgical outcome. Ann Thorac Surg. 1997;64:721–9. https://doi.org/10.1016/s0003-4975(97)00632-2.
17. Brown JW, Ruzmetov M, Vijay P, et al. Operative results and outcomes in children with Shone's anomaly. Ann Thorac Surg. 2005;79:1358–65.
18. Narvencar KPS, Jaques e Costa AK, Patil VP. Shone's complex. JAPI. 2009;57:415–6.
19. Bardo DME, Frankel DG, Applegate KE, Murphy DJ, Saneto RP. Hypoplastic left heart syndrome. Radiographics. 2001;21:705–17.
20. Gumbiene L, Karaluis R. Congenital coronary artery anomalieS in patients with tetralogy of Fallot. Medicina. 2002;38(suppl 1):191–3.
21. Angelini P, Villason S, Chan AV, Diez JG. Normal and anomalous coronary arteries in humans. In: Angelini P, editor. Coronary artery anomalies: a comprehensive approach. Philadelphia: Lippincott Williams & Wilkins; 1999. p. 27–150.
22. Eckart RE, Scoville SL, Campbell CL, Shry EA, Stajduhar KC, Potter RN, Pearse LA, Virmani R. Sudden death in young adults: a 25-year review of autopsies in military recruits. Ann Intern Med. 2004;141:829–34.
23. Mery CM, Lawrence SM, Krishnamurthy R, et al. Anomalous aortic origin of a coronary artery: toward a standardized approach. Semin Thorac Cardiovasc Surg. 2014;26(2):110–22.

Further Reading

Bailliard F, Anderson RH. Tetralology of fallot. Orphanet J Rare Dis. 2009;4:2.

Berdon WE. Rings, slings, and other things: Vascular compression of the infant trachea updated from the midcentury to the millennium—the legacy of Robert E. Gross, MD, and Edward B. D. Neuhauser, MD. Radiology. 2000;216:624–32.

Chu WCW, Mok GF, Lam WWM, Yam MC, Sung RYT. Assessment of coronary artery aneurysms in paediatric patients with Kawasaki disease by multidetector row CT angiography: feasibility and comparison with 2D echocardiography. Pediatr Radiol. 2006;36(11):1148–53.

Collett RW, Edwards JE. Persistent truncus arteriosus: a classification according to anatomic types. Surg Clin North Am. 1949;29:1245.

de la Cruz MV, Gimenez-Ribotta M, Saravalli O, Cayre R. The contribution of the inferior endocardial cushion of the atrioventricular canal to cardiac septation and to the development of the atrioventricular valves: study in the chick embryo. Am J Anat. 1983;166:63–72.

Double outlet right ventricle. Texas Heart Institute. http://www.texasheart.org/HIC/Topics/Cond/dorv.cfm. Accessed 31 Oct 2014.

Down syndrome and congenital heart disease. http://pediatricheartspecialists.com/blog/down-syndrome-and-congenital-heart-disease. Accessed 13 Dec 2014.

Goyal SK, Punnam SR, Verma G, Ruberg FL. Persistent left superior vena cava: a case report and review of literature. Cardiovasc Ultrasound. 2008;6:50.

Han BK, Lesser JR. CT imaging in congenital heart disease: an approach to imaging and interpreting complex lesions after surgical intervention for tetralogy of Fallot, transposition of the great arteries, and single ventricle heart disease. J Cardiovasc Comput Tomogr. 2013;7(6):338–53.

Hovels-Gurich H. Pulmonary venous return anomaly. 2003. http://www.orpha.net/data/patho/GBuk-PVRA.pdf.

Jaggers JJ, Cameron DE, Ungerleider RM. Congenital Heart Surgery Nomenclature and Database Project: transposition of the great arteries. Ann Thorac Surg. 2000;69(3):205–35. https://doi.org/10.1016/S0003-4975(99)01282-5.

Koren G, Lavi S, Rose V, Rowe R. Kawasaki disease: review of risk factors for coronary aneurysms. J Pediatr. 1986;108(3):388–92.

Lapierre C, Déry J, Guérin R, Viremouneix L, Dubois J, Garel L. Segmental approach to imaging of congenital heart disease. RadioGraphics. 2010;30:397–411. https://doi.org/10.1148/rg.302095112.

Newman B, Cho Y. Left pulmonary artery sling—anatomy and imaging. Semin Ultrasound CT MR. 2010;31(2):158–70.

Robida A, Venkatraman B. Anomalous left pulmonary artery without pulmonary artery sling. Heart. 1998;79:521–2.

Rojas CA, Jaimes C, Abbara S. Ventricular septal defects embryology and imaging findings. Thorac Imaging. 2013;28(2):W28–34.

Siegel MJ. Cardiac CTA: congenital heart disease. Pediatr Radiol. 2008;38(Suppl 2):S200–4. https://doi.org/10.1007/s00247-008-0765-5.

Suda KM, Iemura M, Nishiono H, et al. Long-term prognosis of patients with Kawasaki disease complicated by giant coronary aneurysms. Circulation. 2011;123(17):1836–42.

Tan JL, Davlouros PA, McCarthy KP, Gatzoulis MA, Ho SY. Intrinsic histological abnormalities of aortic root and ascending aorta in tetralogy of Fallot. Circulation. 2005;112:961–8.

Transposition of the Great Arteries. http://pedclerk.bsd.uchicago.edu/sites/pedclerk.uchicago.edu/files/uploads/Transposition%20of%20the%20Great%20Arteries.pdf. Accessed 23 Nov 2014

Uehara R, Belay ED. Epidemiology of Kawasaki disease in Asia, Europe, and the Unites States. J Epidemiol. 2012;22(2):79–85.

Van Praagh R, Van Praagh S. The anatomy of common aorticopulmonary trunk (truncus arteriosus communis) and its embryologic implications. Am J Cardiol. 1965;16(3):406–25.

Vyas HV, Greenberg SB, Krishnamurthy RMR. imaging and CT evaluation of congenital pulmonary vein abnormalities in neonates and infants. Radiographics. 2012;32:87–98.

Wenink ACG. Embryology of the ventricular septum separate origin of its components. Virchows Arch [Pathol Anat]. 1981;390:71–9.

Yoo SJ, Thabit O, Lee W, Goo HW. Double outlet right ventricle in your hands. International Medical Image Bank for Congenital Heart Diseases. www.imib-chd.com.

Cardiac CTA of Congenital Coronary and Other Anomalies

5

Claudio Smuclovisky

5.1 Case 5.1

5.1.1 History

A 48-year-old female presented with a history of an abnormal myocardial perfusion stress test result in the anterior wall.

5.1.2 Findings

Congenital anomalous origin of the left circumflex coronary artery is seen arising from the right sinus of Valsalva. The left circumflex coronary artery courses posteriorly between the aortic annulus and the left atrium and continues into the left atrial–ventricular sulcus (Fig. 5.1).

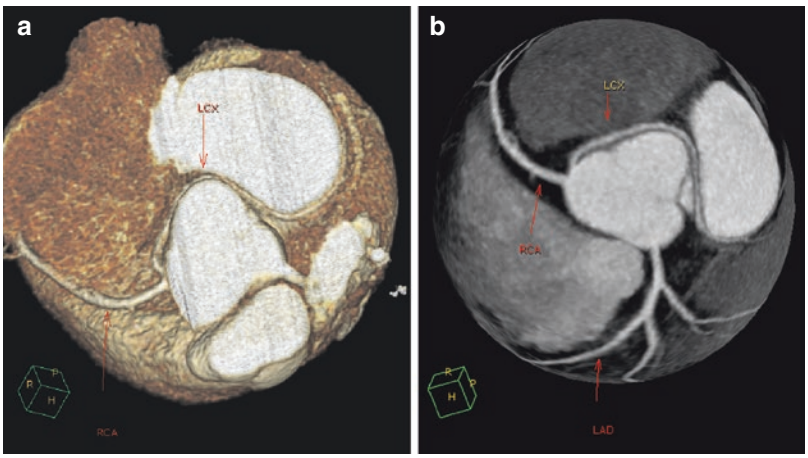

Fig. 5.1 (**a**) Volume rendered. *LCX* left circumflex coronary artery, *RCA* right coronary artery. (**b**) Globe 3D map. The left circumflex coronary artery arises from the right sinus of Valsalva. *LAD* left anterior descending artery, *CRX* left circumflex artery, *RCA* right coronary artery

C. Smuclovisky, MD, FACC, FSCCT
Department of Radiology, Holy Cross Hospital, South Florida Medical Imaging Cardiovascular Institute, Fort Lauderdale, FL, USA
e-mail: smuclovisky@gmail.com

C. Smuclovisky (ed.), *Coronary Artery CTA*, https://doi.org/10.1007/978-3-319-66988-5_5

5.1.3 Diagnosis

Congenital anomalous origin of the left circumflex coronary artery from the right sinus of Valsalva.

5.1.4 Discussion

Coronary artery anomalies are observed in 0.3–1.3% of patients undergoing diagnostic coronary angiography. It has been reported in approximately 1% of routine autopsy examinations and in 4–15% of young people who experience sudden death. Since the left circumflex coronary artery has a posterior course, along the root of the aorta and left atrium, it is considered a benign anomaly.

5.1.5 Pearls and Pitfalls

This case represents the most frequent congenital coronary anomaly.

5.2 Case 5.2

5.2.1 History

A 45-year-old male presented with atypical chest pain and normal nuclear perfusion stress test.

5.2.2 Findings

Congenital anomalous high origin of the right coronary artery (RCA) is seen from the left sinus of Valsalva (Fig. 5.2a–d). The artery has a narrow ostium with acute angulation. The RCA is dominant and has an interaterial course between the aorta and the pulmonary artery.

5.2.3 Diagnosis

The diagnosis is congenital anomalous origin of the right coronary artery from the left sinus of Valsalva, with an interarterial course.

5.2.4 Discussion

As discussed in Case 5.5, this type of anomaly is significant and considered potentially lethal. Treatment of congenital coronary anomalies of origin and course in adults is controversial, particularly without a previously documented cardiac event or ischemia on a nuclear stress test. The patient decided against surgical correction and was placed on beta blockers.

5.2.5 Pearls and Pitfalls

Surgical repair would not be considered if the RCA was nondominant.

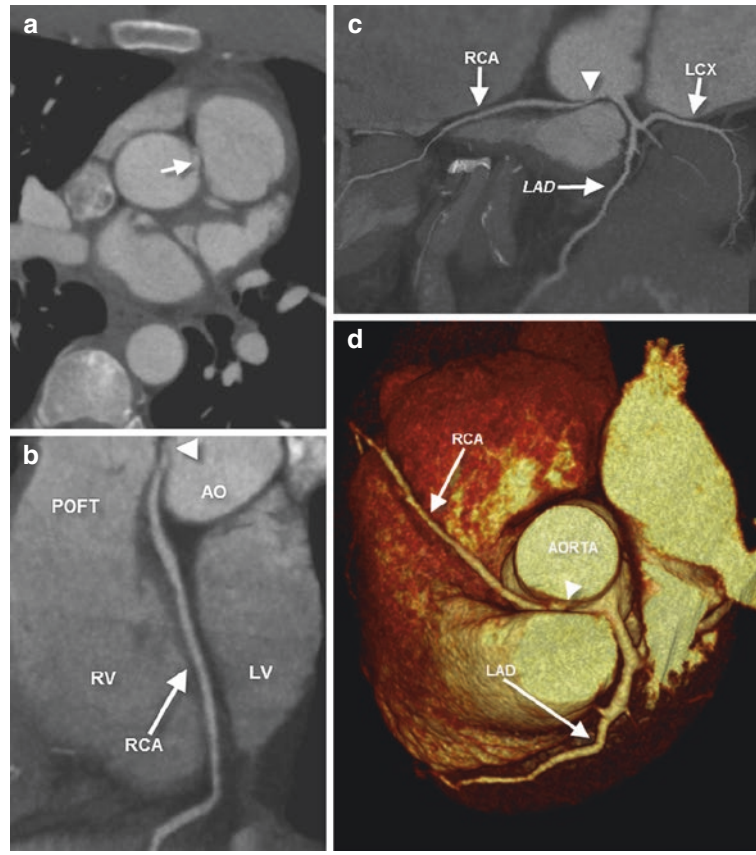

Fig. 5.2 (**a**) Axial: High origin of the RCA from the left sinus of Valsalva (*arrow*). Congenitally narrowed ostium with acute angulation. (**b**) cMPR: Interarterial course of the RCA and ostium (*arrowhead*). *AO* aorta, *POFT* pulmonary outflow tract, *RV* right ventricle, *LV* left ventricle. (**c**, **d**) 2D composite and volume rendered cranial view: Ostium of the RCA (*arrowhead*)

5.3 Case 5.3

5.3.1 History

A 57-year-old male was worked up for CAD and with a history of congenital anomalous origin of the LAD identified on a recent coronary angiogram.

5.3.2 Findings

The left anterior descending coronary artery (LAD) arises in a common trunk with the RCA from the right sinus of Valsalva (Fig. 5.3a, b). The LAD courses anteriorly in the plane of the pulmonary outflow tract and right ventricle.

5.3.3 Diagnosis

Congenital anomalous origin of the LAD from the right sinus of Valsalva with an anterior (precardiac) course and clinically considered benign was seen. The CTA was acquired with prospective gated axial technique (PGA).

5.3.4 Discussion

The anomalous LAD from the right sinus of Valsalva may take a septal, anterior (precardiac), posterior, or interarterial course. Of these, the interarterial course of the LAD (between the pulmonary artery and aorta) is the most frequently associated with sudden death.

5.3.5 Pearls and Pitfalls

Cardiac CTA is currently the best noninvasive study for the evaluation of congenital coronary anomalies. One can easily evaluate the anomalous origin, course, and termination of the artery. To the contrary, this can be very challenging with coronary angiography and may necessitate placement of a second catheter in the pulmonary artery. PGA is an excellent low-radiation technique for the evaluation of these patients.

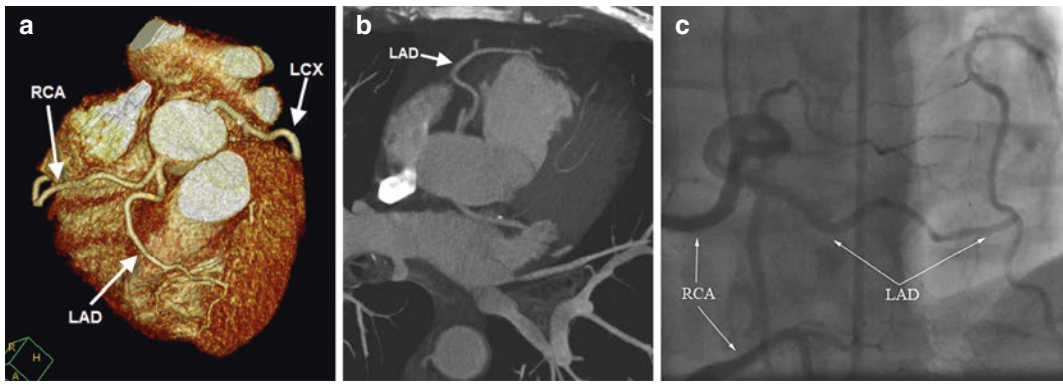

Fig. 5.3 (**a**, **b**) VR. Axial MIP: LAD originating from the right sinus of Valsalva with an anterior (precardiac) course. (**c**) Right coronary angiogram performed prior to the CTA

5.4 Case 5.4

5.4.1 History

A 43-year-old male presents with atypical chest pain. The patient had a previous coronary angiogram, but it was not possible to determine the course of the left main coronary artery.

5.4.2 Findings

Congenital anomalous origin of the left main coronary artery from the right sinus of Valsalva is seen. The left main coronary artery courses posteriorly along the aortic annulus and left atrium (Fig. 5.4).

5.4.3 Diagnosis

The diagnosis is congenital anomalous origin of the left main coronary artery from the right sinus of Valsalva with a posterior course.

5.4.4 Discussion

The left main coronary artery has a posterior course, which is considered a benign anomaly.

5.4.5 Pearls and Pitfalls

The cardiac CTA has been established as an excellent noninvasive test to identify and classify congenital coronary anomalies, which commonly are difficult to evaluate with coronary angiography.

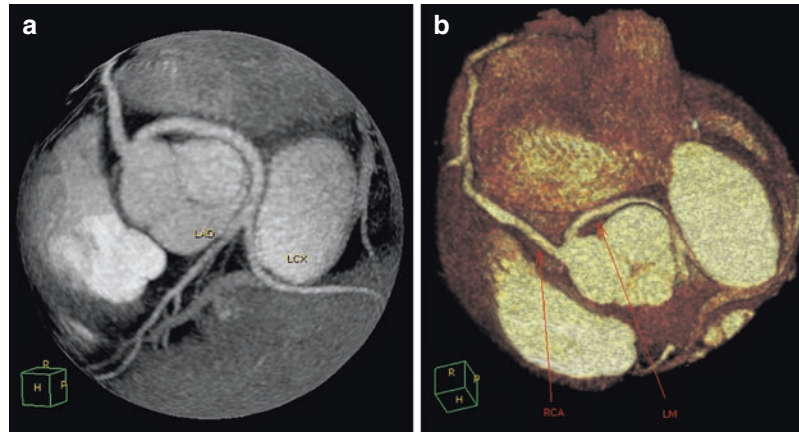

Fig. 5.4 (**a**) Globe 3D map. The left main coronary artery originates from the right sinus of Valsalva. *LAD* left anterior descending artery, *CRX* left circumflex artery. (**b**) Volume rendering. *LM* left main artery, *RCA* right coronary artery

5.5 Case 5.5

5.5.1 History

A 17-year-old boy collapsed during a football game, arriving at the hospital in cardiogenic shock. A coronary angiogram was performed, with failure to cannulate the left main coronary artery. A cardiac CTA was requested for further evaluation.

5.5.2 Findings

An anomalous origin of the left main coronary artery (Fig. 5.5a–d) from the right coronary sinus of Valsalva was seen. The left main had an abnormal ostium, an acute angulation, and an interarterial course. An additional aggravating factor was that the coronary circulation was left dominant. The left ventricular ejection fraction was estimated at 15%, which was consistent with a stunned myocardium.

5.5.3 Diagnosis

The diagnosis is interarterial course of a congenital anomalous origin of the left main coronary artery arising from the right sinus of Valsalva.

5.5.4 Discussion

This type of congenital coronary anomaly is the most frequently reported to be associated with sudden death. Coronary anomalies are classified according to their origin, course, and termination.

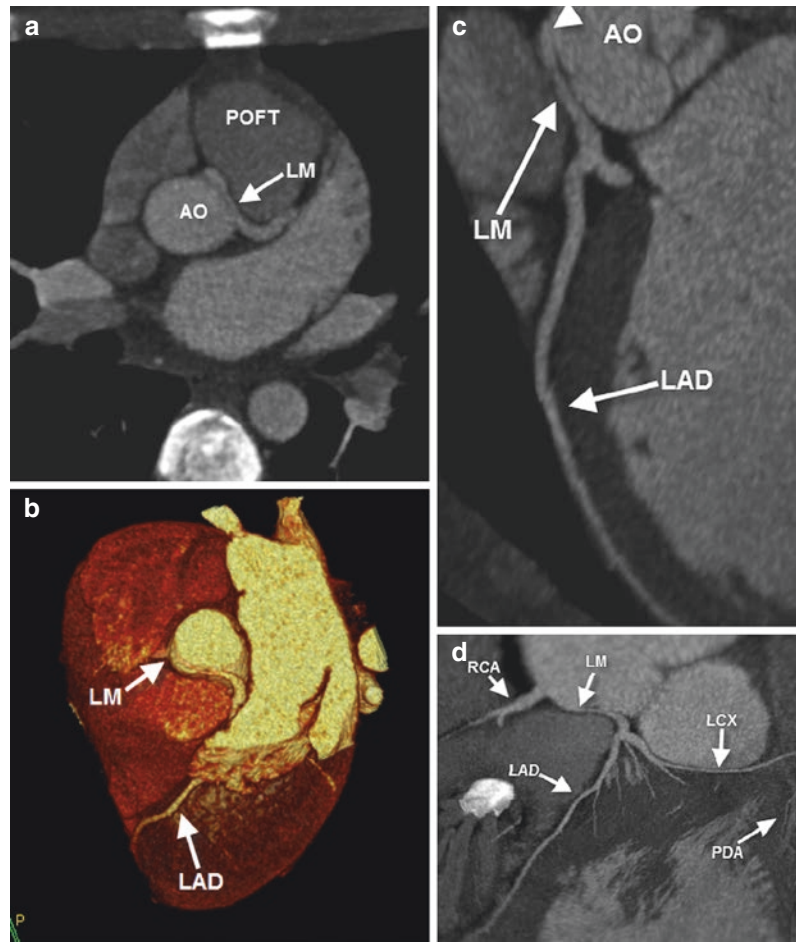

Fig. 5.5 (**a**, **b**) Axial and volume rendering (VR): Left main arising from the right sinus of Valsalva with an interarterial course. *AO* aorta, *POFT* pulmonary outflow tract. (**c**) cMPR: left main—abnormal ostium (*arrowhead*) and interarterial course. (**d**) 2D composite: Anomalous left main coronary artery from the right sinus of Valsalva. Left dominant coronary anatomy: *LM* left main, *LAD* left anterior descending, *LCX* left circumflex, *PDA* posterior descending artery, *RCA* right coronary artery

Depending on anomaly, they are considered either benign or potentially lethal, as in this case. The combination of an interarterial course, abnormal ostium (often referred to as *fish mouth* appearance), and acute angulation is potentially lethal. The increase in pulmonary arterial pressure during workload causes torque on the left main coronary artery, resulting in severely diminished arterial flow. The patient survived the acute event and subsequently underwent successful coronary reimplantation surgery.

5.5.5 Pearls and Pitfalls

Cardiac CTA (CCTA) has been demonstrated to be a reliable, accurate noninvasive test in the assessment of congenital coronary anomalies and is the preferred diagnostic test. Its use in newborns and infants is limited due to an accelerated heart rate and the concern about radiation.

5.6 Case 5.6

5.6.1 History

A 46-year-old male presented with progressive shortness of breath.

5.6.2 Findings

There is congenital anomalous origin of the left main coronary artery from the pulmonary artery (Fig. 5.6a). The coronary arteries are hypertrophied, with extensive epicardial and intramyocardial collaterals (Fig. 5.6b). Mild cardiomegaly is seen.

5.6.3 Diagnosis

The diagnosis is anomalous origin of the left main coronary artery from the pulmonary artery (ALCAPA) and also known as Bland–White–Garland syndrome.

5.6.4 Discussion

ALCAPA is one of the most serious congenital coronary artery anomalies. Approximately 90% of untreated infants die in the first year of life and only a few patients survive to adulthood. Cardiac CT can easily confirm the diagnosis of ALCAPA and demonstrates collateral circulation between the RCA and LCA and a coronary *steal* into the pulmonary artery. There is a chronic ischemic cardiomyopathy. Note that the RCA is markedly hypertrophied and is providing retrograde flow into the territory of the left main coronary artery.

5.6.5 Pearls and Pitfalls

Due to the incidence of high morbidity/mortality, it is important to properly identify and classify this congenital coronary anomaly.

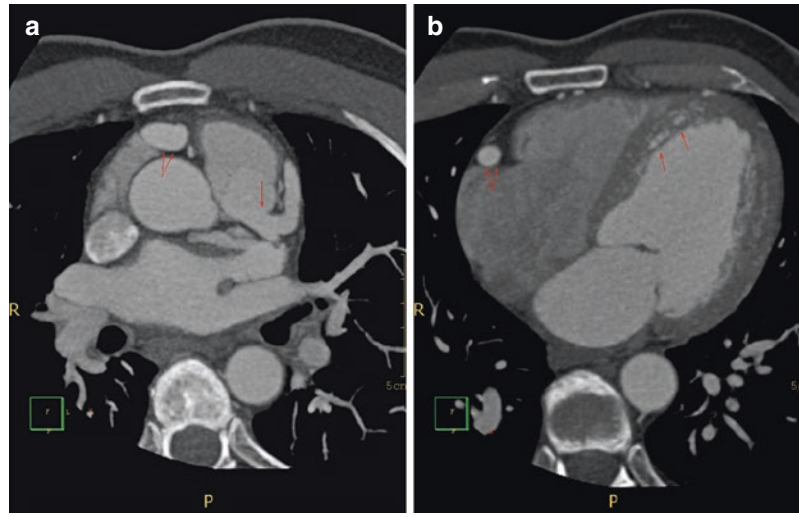

Fig. 5.6 (**a**) Axial maximum intensity projection. The left main coronary artery originates from the pulmonary artery (*arrows*). There is marked hypertrophy of the right coronary artery (*double arrows*). (**b**) Axial slice through the heart demonstrates markedly enlarged septal perforators (*arrows*) and right coronary artery (*double arrows*) (Courtesy of Dr. William Bugni, Tampa, FL.)

5.7 Case 5.7

5.7.1 History

A 71-year-old male presented with shortness of breath.

5.7.2 Findings

Congenital anomalous origin of the right coronary artery from the pulmonary artery is seen (Fig. 5.7a). The coronary arteries are hypertrophied, with extensive epicardial and intramyocardial collaterals (Fig. 5.7b).

5.7.3 Diagnosis

The diagnosis is potentially lethal congenital anomalous origin of the right coronary artery arising from the pulmonary artery.

5.7.4 Discussion

A chronic ischemic cardiomyopathy exists in this patient. Note that the density in the RCA is higher than that in the adjacent pulmonary artery, which is from shunting and retrograde flow from the coronary collaterals. The septal perforators are hypertrophied as demonstrated in Fig. 5.7b.

5.7.5 Pearls and Pitfalls

The presence of a congenital coronary anomaly should be considered in the presence of enlarged coronary arteries without atheromatous disease. It is remarkable that this patient has been clinically stable during his lifetime with this anomaly.

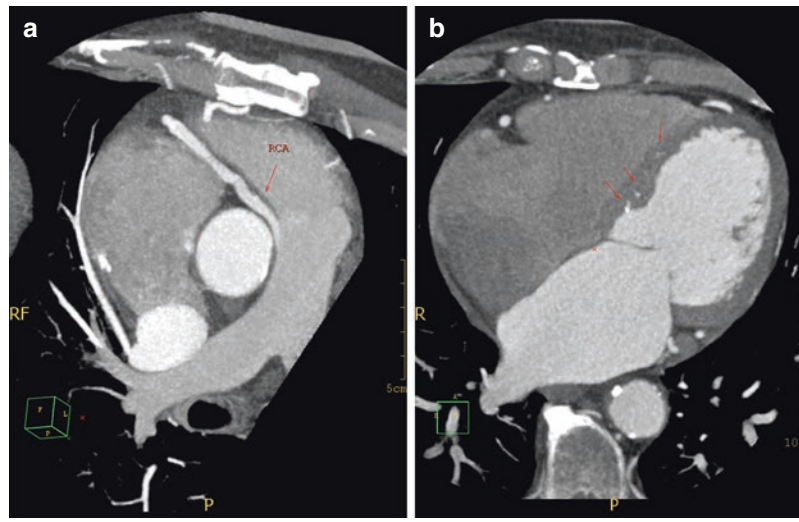

Fig. 5.7 (**a**) Axial oblique maximum intensity projection. The right coronary artery originates from the pulmonary artery (*arrow*). (**b**) Axial slice through the heart demonstrates enlarged septal perforators (*arrows*)

5.8 Case 5.8

5.8.1 History

An 84-year-old female presented with intermittent shortness of breath and a history of an abnormal stress test result.

5.8.2 Findings

There is congenital anomalous origin of the left main coronary artery from the posterior noncoronary sinus (Fig. 5.8a–d). There is multi-vessel nonobstructive disease.

5.8.3 Diagnosis

The diagnosis is anomalous origin of the left main coronary artery from the noncoronary sinus of Valsalva.

5.8.4 Discussion

Anomalous origin of the left main coronary artery from the posterior noncoronary sinus of Valsalva is extremely rare and has been previously noted in only a few reports. Most of these cases were diagnosed incidentally in asymptomatic patients. Due to the extreme rarity of this anomaly, the natural history and risk of adverse events related to this anomaly are unknown.

It was considered a benign anomaly in this case, based on the patient's advanced age and no history of a prior cardiac event. Additional low-risk indicators are the origin of the left main is posterior; the ostium has a normal diameter; and the vessel does not possess an acute angulation.

5.8.5 Pearls and Pitfalls

In order to diagnose and determine clinical relevance of a congenital coronary anomaly, it is important to carefully observe the origin, course, dominance, and morphology of the vessels.

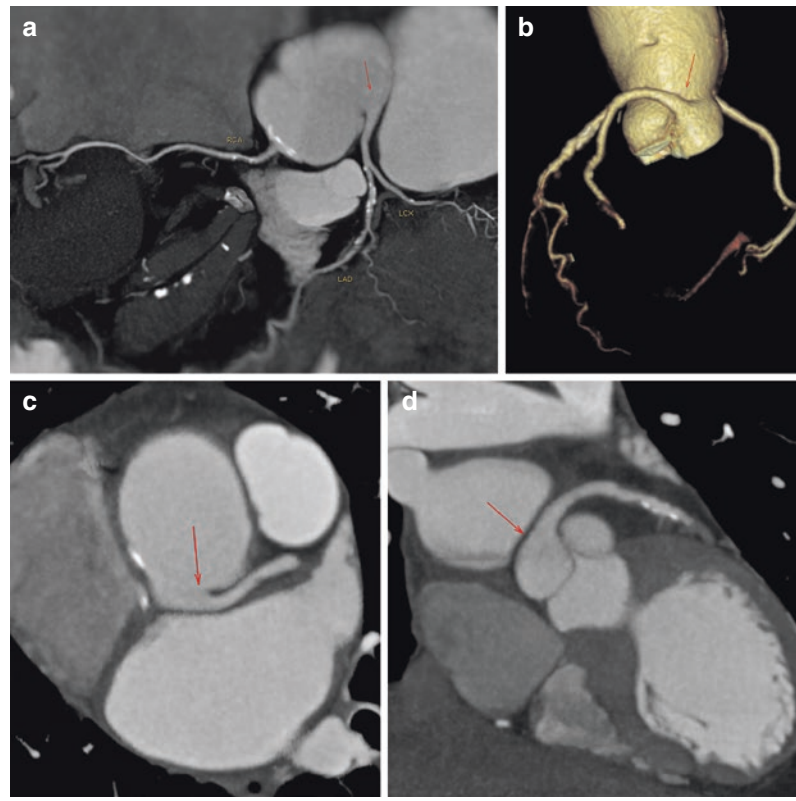

Fig. 5.8 (**a**) 2D map. Anomalous origin of the left main from the posterior noncoronary sinus of Valsalva (*arrow*). (**b**) 3D volume rendered vessel tree. Left main ostium (*arrow*). (**c**, **d**) Axial and coronal oblique views of the ostium of the left main (*arrow*)

5.9 Case 5.9

5.9.1 History

A 38-year-old male presented with shortness of breath.

5.9.2 Findings

There is an arterial venous malformation, with a fistula between the LAD and the great cardiac vein. There is dilatation of the left main coronary artery and proximal LAD and massive dilatation of the great cardiac vein (Fig. 5.9).

5.9.3 Diagnosis

The diagnosis was coronary AV malformation.

5.9.4 Discussion

The incidence of this anomaly is approximately 0.002% of all patients with congenital heart disease. Patients may present with symptoms of congestive heart failure, myocardial ischemia, and sudden death.

5.9.5 Pearls and Pitfalls

A dilated vessel in the heart is the major clue of the presence of an AV fistula. Secondary signs are dilated cardiac chambers, same contrast density of the arteries and veins, small caliber thoracic aorta, and dilated pulmonary artery trunk.

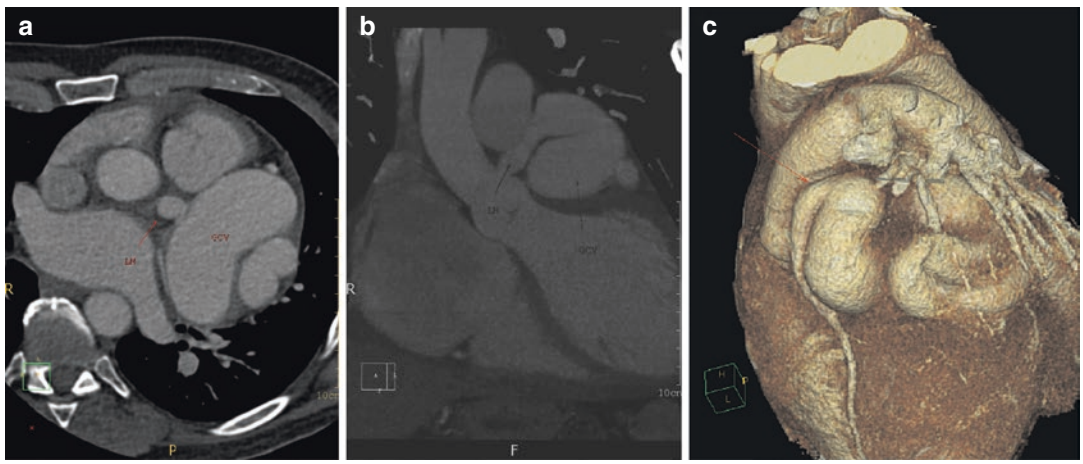

Fig. 5.9 (**a**) Axial. The left main coronary artery and great cardiac vein are dilated. *LM* left main coronary artery, *GCV* great cardiac vein. (**b**) Coronal. Dilated LM, left main coronary artery. (**c**) Volume rendered. AV fistula (*arrow*)

5.10 Case 5.10

5.10.1 History

A 57-year-old asymptomatic male presented with dyslipidemia.

5.10.2 Findings

There is mild disease with calcified plaque in the left main coronary artery. The mid-LAD has an intramyocardial course (Fig. 5.10a–c).

5.10.3 Diagnosis

The diagnosis is intramyocardial course of the mid-segment of the left anterior descending coronary artery (myocardial bridge), with mild CAD.

5.10.4 Discussion

The main coronary arteries are located in the epicardial surface of the heart. Occasionally, a coronary artery may have an intramyocardial course. Myocardial bridging is a clinically uncommon congenital anomaly characterized by tunneling of the coronary artery within the myocardial tissue, usually seen surrounding the left anterior descending artery. Myocardial bridging is associated with altered intracoronary hemodynamics during systole and diastole, determined by the severity and the location of the bridging within the coronary artery. Patients with myocardial bridging may present with angina in the absence of other coronary risk factors.

5.10.5 Pearls and Pitfalls

It is important not to confuse an intramyocardial course with an obstructed and/or occluded artery. Typically, the intramyocardial segment has a smaller caliber than the proximal segment. With obstructive coronary artery disease in which surgical revascularization is warranted, a long myocardial bridge may preclude grafting of the LAD.

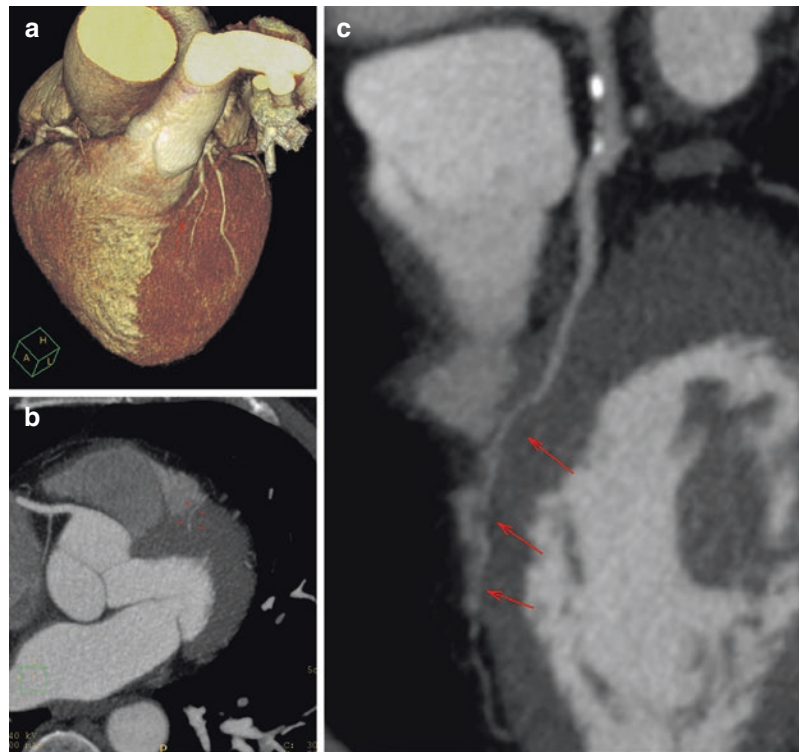

Fig. 5.10 (**a**) 3D. Myocardial bridge left anterior coronary artery (*arrow*). (**b**) Axial. Intramyocardial course of the left anterior coronary artery (*arrows*). (**c**) cMPR: Intramyocardial course of the left anterior coronary artery (*arrows*)

5.11 Case 5.11

5.11.1 History

A 45-year-old asymptomatic female presented for a follow-up study.

5.11.2 Findings

Aneurysmal dilatation of the right sinus of Valsalva is seen (Fig. 5.11).

5.11.3 Diagnosis

Sinus of Valsalva aneurysm is the diagnosis.

5.11.4 Discussion

Aneurysm of a sinus of Valsalva is a rare congenital cardiac defect that can rupture, causing heart failure or other catastrophic cardiac events. The incidence is approximately 0.1–3.5% of all congenital cardiac anomalies. If the aneurysm remains unruptured, it occasionally causes obstruction of coronary flow, resulting from compression of normal structures. Under the strain of aortic pressure, the sinus gradually weakens and dilates, causing the formation of an aneurysm. Lack of supporting tissue (e.g., ventricular septal defect) may contribute to instability and progressive distortion of the aortic sinus, often with associated aortic insufficiency.

5.11.5 Pearls and Pitfalls

Aneurysms of the sinus of Valsalva most often involve the right sinus (67–85%), followed by the noncoronary sinus, while an aneurysm of the left sinus is less common. The CTA is an excellent noninvasive study for the diagnosis and follow-up of these patients.

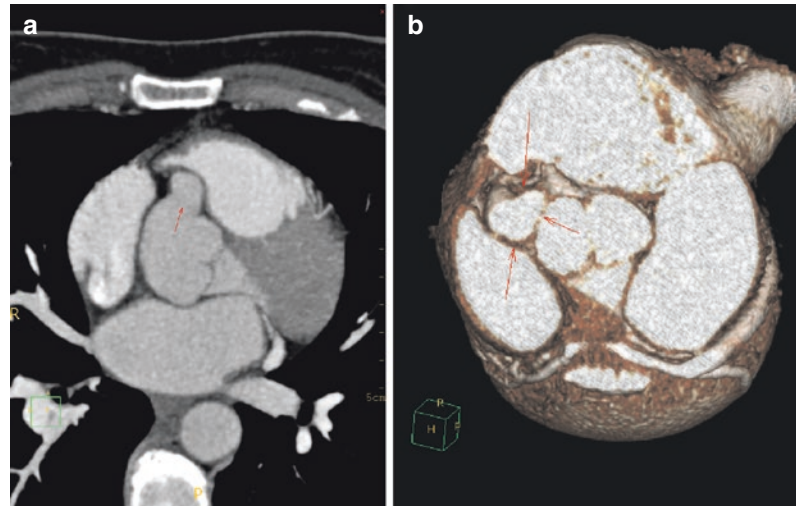

Fig. 5.11 (**a**) Axial. Right sinus of Valsalva aneurysm (*arrow*). (**b**) Volume rendering. Right sinus of Valsalva aneurysm (*arrows*)

5.12 Case 5.12

5.12.1 History

A 77-year-old male presented with a history of atypical chest pain.

5.12.2 Findings

There is a small focal defect in the fossa ovale, with adjacent redundancy of the atrial septum (Fig. 5.12a, b).

5.12.3 Diagnosis

The diagnosis is patent foramen ovale (PFO).

5.12.4 Discussion

Most patients with isolated PFO are asymptomatic. Patients may have a history of stroke or transient ischemic event of unknown etiology. PFO is an anatomic interatrial communication with potential for right-to-left shunt. PFO is a flap like opening between the atrial septa primum and secundum at the location of the fossa ovalis that persists after age 1. In utero, the foramen ovale serves as a physiologic conduit for right-to-left shunting. Once the pulmonary circulation is established after birth, left atrial pressure increases, allowing functional closure of the foramen ovale. This is followed by anatomical closure of the septum primum and septum secundum by age 1.

PFOs are detected in 10–15% of the population by contrast transthoracic echocardiography. Autopsy studies show a 27% prevalence of probe-patent foramen ovale. The vast majority of patients with a PFO experience no symptoms throughout life. Morbidity, although rare, is predominantly due to paradoxical embolism. Cerebrovascular ischemic events can be attributed to paradoxical embolism through a patent foramen ovale. This usually occurs in patients without other risk factors, although deep venous thrombosis and hypercoagulable states may significantly increase this risk. Migraine headaches, especially with aura, have been found to be associated with the presence of a PFO. Up to 50% of patients with migraine headaches can be found to have a PFO, compared with a 15–30% prevalence in the normal population. The reason for this correlation has not been established. PFOs may also be associated with an atrial septal aneurysm and other cardiac congenital anomalies.

5.12.5 Pearls and Pitfalls

A small defect in the fossa ovalis, with a redundant atrial septum, may indicate the presence of a PFO.

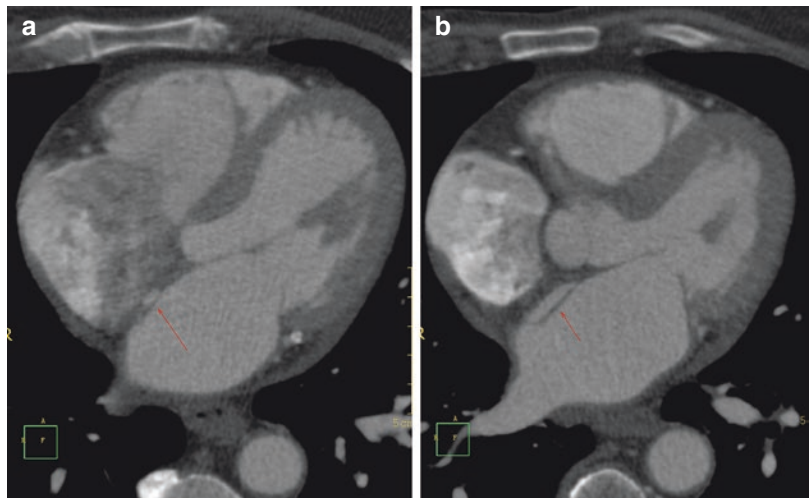

Fig. 5.12 (**a**) Axial. Patent foramen ovale (*arrow*). (**b**) Axial. Redundant atrial septum (*arrow*)

5.13 Case 5.13

5.13.1 History

A 54-year-old female presented with history of progressive shortness of breath.

5.13.2 Findings

There is an ostium secundum type atrial septal defect (ASD) (Fig. 5.13a). There is right chamber enlargement and cardiomegaly. There is left-to-right shunt with equalization of the contrast density between the right and left chambers. There is dilatation of the pulmonary arterial trunk (Fig. 5.13b).

5.13.3 Diagnosis

The diagnosis is secundum ASD.

5.13.4 Discussion

The ASD was successfully repaired percutaneously with a closure device (Fig. 5.13a). There are four basic types of ASDs: The most common is the ostium secundum defect and is the least serious. The defect occurs in the area of the fossa ovalis as a result of excessive fenestration or resorption of the septum primum, underdevelopment of the septum secundum, or a combination of both. A variant of ostium

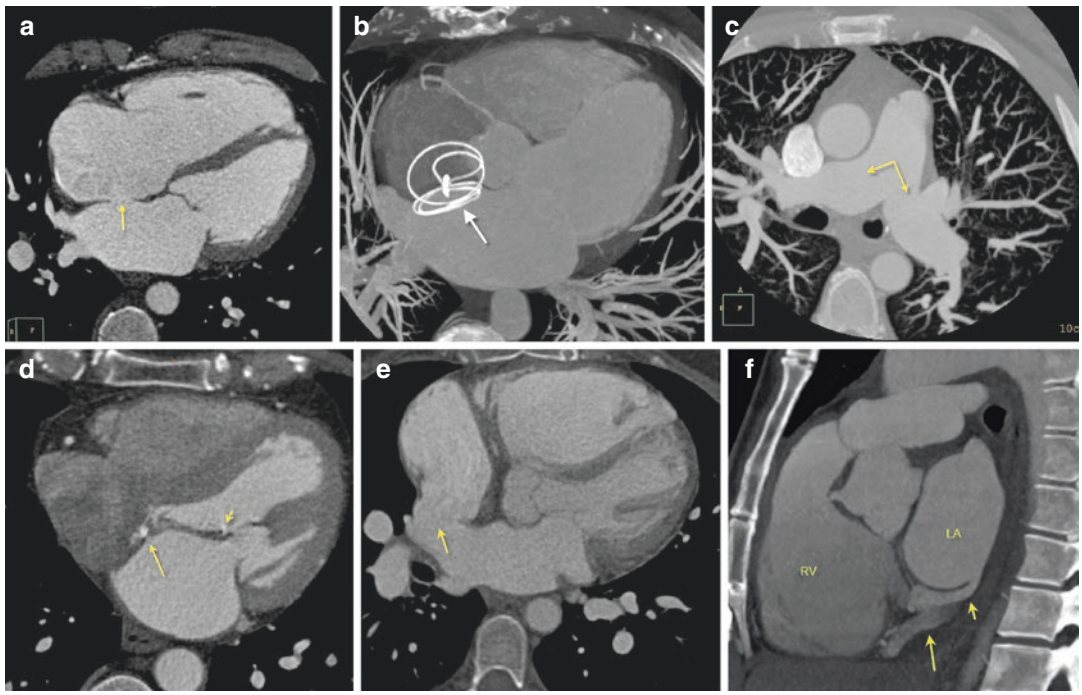

Fig. 5.13 (**a**) Axial. Ostium secundum atrial septal defect (ASD) (*arrow*). (**b**) Axial thick maximum intensity projection: ASD closure with a 35-mm Helix Septal Occluder (*arrow*). (**c**) Axial. Dilated pulmonary arteries (*double arrows*). (**d**) Axial. In a different patient, previous surgical repair of an ostium primum ASD with placement of a Dacron patch (*long arrow*). Also, status post repair of a cleft in the anterior leaflet of the mitral valve (*short arrow*). (**e**) Axial. Sinus venosus ASD (*arrow*) in a different patient. (**f**) Sagittal. In a different patient, coronary sinus defect (*long arrow*) with anomalous vein (*short arrow*) communicating with the left atrium. Right ventricle (RV) and left atrium (LA)

secundum defect is the association with an aneurysm of the atrial septum.

The second type of ASD is the ostium primum defect (Fig. 5.13c). This type of ASD results from failure of closure of the endocardial cushion and is associated with a cleft in the anterior leaflet of the mitral valve.

The third type of ASD is a sinus venosus defect (Fig. 5.13d). This is located in the posterior aspect of the septum near the superior vena cava and is associated with right partial anomalous pulmonary venous return.

The fourth and least common type is a coronary sinus septal defect (Fig. 5.13d). This results from an unroofed coronary sinus or coronary sinus septal defect. A segment of the roof of the coronary sinus is absent, with blood shunted from the left atrium into the coronary sinus and subsequently into the right atrium. It may also be associated with a persistent left superior vena cava.

5.13.5 Pearls and Pitfalls

ASDs may not be readily apparent on the CTA and require careful inspection of the images. Secondary clues alerting to the presence of a shunt are equalization of the contrast density between the right and left chambers, right chamber enlargement, and dilatation of the pulmonary arteries.

5.14 Case 5.14

5.14.1 History

A 64-year-old male presented with a history of CAD and recent abnormal stress test result.

5.14.2 Findings

There is a small defect in the muscular septum that communicates with the right and left ventricles. There is mild dilatation of the main pulmonary arteries (Fig. 5.14a–c).

5.14.3 Diagnosis

The diagnosis is muscular septum restrictive ventricular septal defect (VSD).

5.14.4 Discussion

The small VSD was previously undiagnosed and found incidentally on the cardiac CT. VSDs represent approximately one fifth of all congenital cardiac anomalies. It is usually diagnosed during childhood. A VSD refers to a defect in the interventricular septum that is composed of muscular

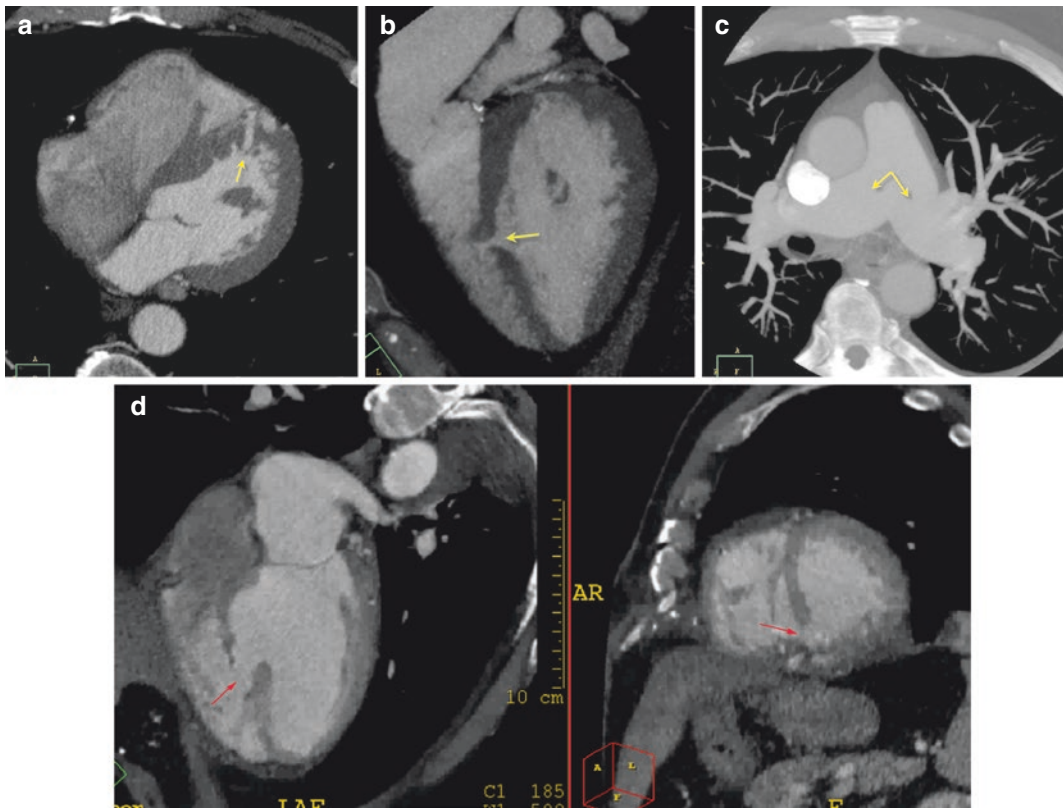

Fig. 5.14 (**a**, **b**) Axial coronal maximum intensity projection (MIP). Restrictive muscular septum ventricular septal defect (VSD) (*arrow*). (**c**) Axial MIP. Mildly dilated pulmonary arteries (*double arrows*). (**d**) Septal rupture from an MI (*arrows*) (Courtesy of Dr. Robert Quaife, University of Colorado, Denver.)

and membranous segments. Defects are most commonly classified according to occurring in or adjacent to one or more septal components. The most common defect occurs in the region of the membranous septum and is referred to as a *paramembranous* or *perimembranous defect* because it is larger than the membranous septum itself and has a muscular defect in the segment of its perimeter.

The second type is entirely within the muscular rim, as in this case. These muscular defects can be defined as inlet, trabecular, central, apical, marginal or Swiss cheese, or outlet and may vary greatly in size, shape, and number. The third type of VSD occurs when the outlet septum is deficient and commonly is referred to as a supracrystal, subpulmonic, outlet, infundibular, or conoseptal.

The hemodynamic significance of a VSD depends primarily on its size and the status of the pulmonary vascular bed rather than the location of the defect. When a small communication is present (usually <0.5 cm^2), the VSD is referred to as restrictive, and the right ventricular pressure is normal. A small VSD with high resistance to flow permits only a small left-to-right shunt. Larger VSDs, particularly of the nonrestrictive type (usually >1.0 cm^2), are hemodynamically significant and may cause dyspnea, congestive heart failure, arrhythmias, or sudden death or progress to Eisenmenger's syndrome.

An acquired VSD (Fig. 5.14d) may result from myocardial rupture from an acute myocardial infarct, blunt and penetrating trauma, primary cardiac infection, primary and secondary tumors, infiltrative diseases of the heart, and aortic dissection. These have extremely high mortality.

5.14.5 Pearls and Pitfalls

Larger and hemodynamically significant VSDs are usually diagnosed in infancy. Clinically silent VSDs that are incidentally found in adults are visualized as small communicating defects. These can be suspected on the axial images in a localized segment of LV non-compaction. Coronal sagittal and oblique views may be needed to confirm the communication. Other findings include equalization of the contrast density in the right and left ventricles, cardiac chamber enlargement, and enlargement of the pulmonary arteries.

5.15 Case 5.15

5.15.1 History

A 77-year-old male with a previous CABG was evaluated for an abnormal nuclear perfusion stress test result.

5.15.2 Findings

The IV contrast was injected into the left arm. There is a dilated vascular structure adjacent to the left atrium, lipomatous hypertrophy of the atrial septum, and heavily diseased anomalous origin of the left circumflex coronary artery from the right coronary sinus (Fig. 5.15a). There is a dilated coronary sinus (Fig. 5.15b).

5.15.3 Diagnosis

The diagnosis is persistent left superior vena cava.

5.15.4 Discussion

Persistent left superior vena cava is also called *double superior vena cava.* It is caused by the failure of regression of the left anterior cardinal vein and of the left horn of the venous sinus between the 24th and 56th days of pregnancy. It is the most common cause of a dilated coronary sinus.

Persistent left superior vena cava occurs in 0.1–0.5% of the general population, with 8% draining into the left atrium. Unroofed coronary sinus ASD is seen in 75% of patients with an LSVC that drains into the left atrium and is usually associated with other forms of congenital heart disease and heterotaxy syndromes.

5.15.5 Pearls and Pitfalls

Left superior vena cava should be suspected in the presence of a dilated coronary sinus.

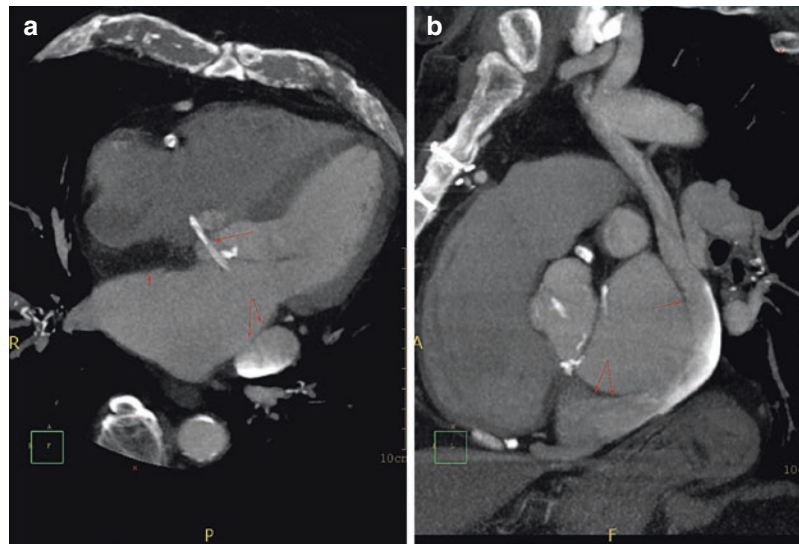

Fig. 5.15 (**a**) Axial maximum intensity projection. Left superior vena cava (*double arrows*), anomalous left circumflex artery (*single long arrow*), lipomatous hypertrophy of the atrial septum (*short arrow*). (**b**) Sagittal maximum intensity projection. Left superior vena cava (*single arrow*). Dilated coronary sinus (*double arrows*)

5.16 Case 5.16

5.16.1 History

A 43-year-old male presented to outpatient clinic with atypical chest pain. Normal EKG.

5.16.2 Findings

There is a single large coronary trunk arising from the right sinus of Valsalva (Fig. 5.16a–d).

5.16.3 Diagnosis

Congenital single coronary trunk.

5.16.4 Discussion

The case demonstrates a rare congenital coronary anomaly, where a single arterial trunk is present, perfusing the entire myocardium.

5.16.5 Pearls and Pitfalls

Since the patient has "all his eggs in one basket," it is important to minimize the risk of developing coronary artery disease by careful risk stratification and preventive measures.

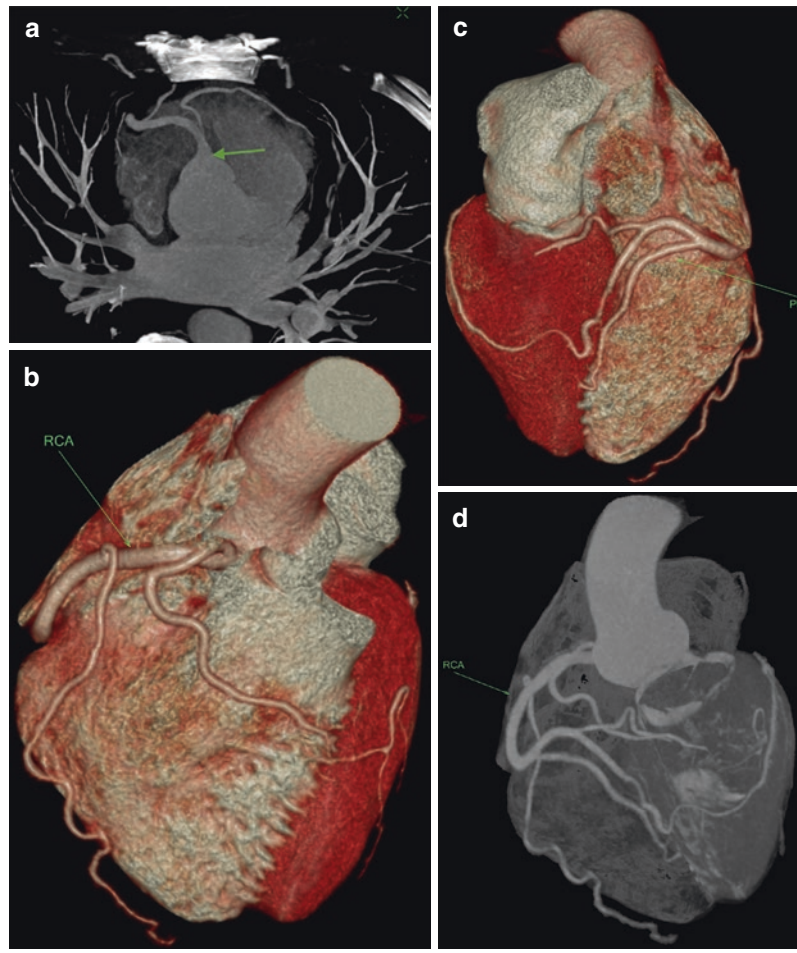

Fig. 5.16 (**a**) Oblique MIP. Single right trunk (*arrow*). (**b**) Volume Rendered (VR)-anterior view. (**c**) VR-posterior view. Posterior descending artery coming off of the right coronary artery. (**d**) Coronary tree

5.17 Case 5.17

5.17.1 History

A 31-year-old male presented to emergency department with SOB with previous outside diagnosis of dextrocardia.

5.17.2 Findings

The anatomic right and left ventricles are switched in position with anatomical atrioventricular discordance. There is a small perimembranous ventricular septal defect (Fig. 5.17a–d).

5.17.3 Diagnosis

Congenital corrected transposition of great vessels (TGA) with a ventricular septal defect.

5.17.4 Discussion

Congenital corrected transposition is a rare congenital heart defect, where aortopulmonary septum fails to rotate 180° with atrioventricular discordance, during embryogenesis. Effectively, venous blood flows through the right atrium to the left ventricle (via mitral valve) and eventually to the lungs via pulmonary veins. Oxygenated blood

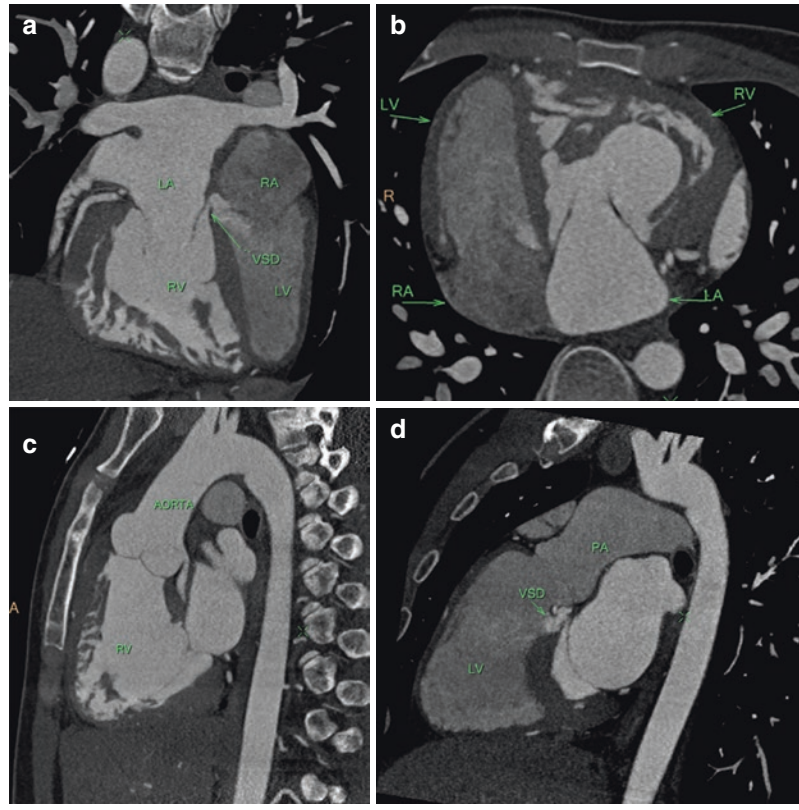

Fig. 5.17 (**a**) Coronal. The right atrium draining to the left ventricle. The left atrium draining to the right ventricle, which supplies the systemic circulation. VSD noted (*arrow*). (**b**) Axial. (**c**, **d**) Sagittal. The right ventricle pumping blood into the aorta for the systemic circulation. VSD noted (*arrow*)

is returned via pulmonary arteries back to the left atrium and out to systemic circulation via the right ventricle and the aorta. Unlike congenital transposition of great arteries, which require a shunt for survival, this condition manifests in childhood or in early adulthood. Symptoms mimic heart failure and are usually due to right ventricular decompensation because the right ventricle supports the systemic circulation. Moreover, this condition is associated with AV heart block and tachyarrhythmia. Symptomatology will vary depending on other associated anomalies like tricuspid valve abnormalities, pulmonic stenosis, and/or ventricular septal defects.

5.17.5 Pearls and Pitfalls

Finding complex coronary anomalies in adults is becoming more common since there are thousands of patients that have had corrective surgery during the first decade of life. Thorough knowledge of the expected congenital and post-surgical findings is essential for an accurate diagnosis and appropriate patient management.

5.18 Case 5.18

5.18.1 History

A 65-year-old female status post mitral valve replacement and tricuspid valve repair in the previous week. Patient developed persistent congestive heart failure with pleural effusions. An astute cardiologist heard a roaring precordial murmur on physical examination and requested CCTA to rule out a post-surgical fistula complication.

5.18.2 Findings

Figure 5.18a demonstrates the cardiac surgery, a pacemaker wire and a large pleural effusion. Figure 5.18b demonstrates a patent ductus arteriosus (PDA). Figure 5.18c confirms PDA on invasive angiography. Figure 5.18d demonstrates successful placement of a closure device. The IV contrast opacification was suboptimal due to the patient's hemodynamic status.

5.18.3 Diagnosis

Patent ductus arteriosus in an adult.

5.18.4 Discussion

A patent ductus arteriosus is a process, where the ductus arteriosus fail to close after birth. The ductus

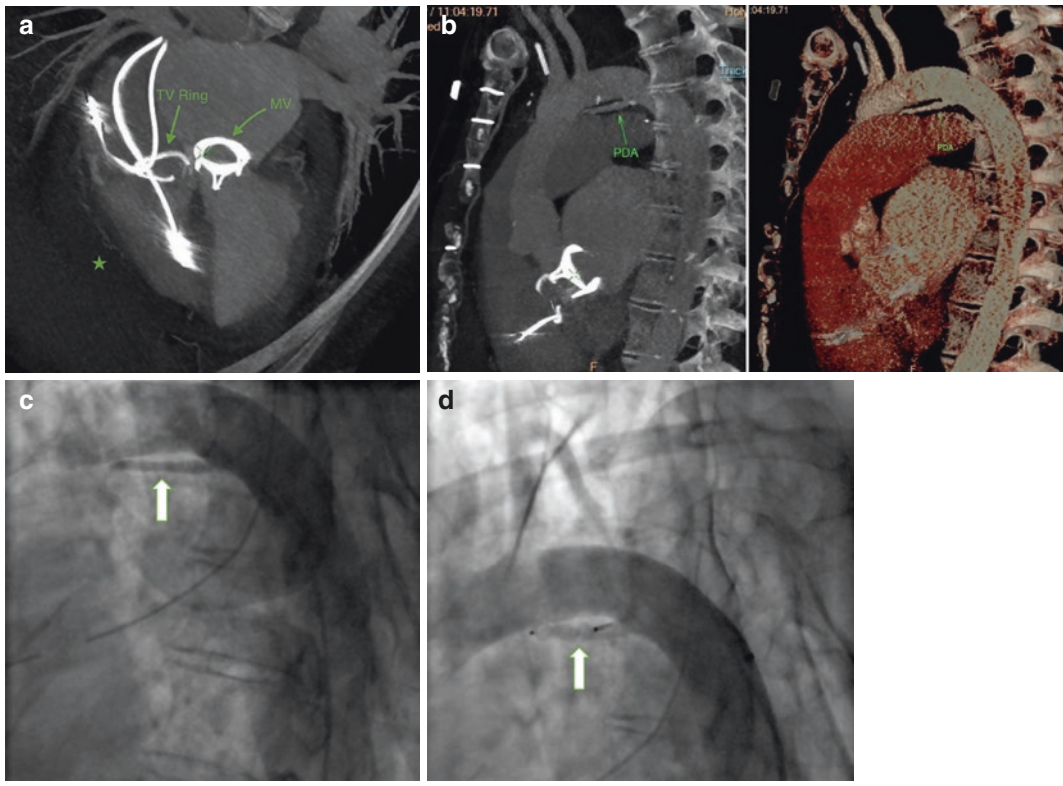

Fig. 5.18 (**a**) Oblique coronal. Large pleural effusion noted (*star*). Mechanical mitral valve and tricuspid valvular ring (labeled MV and TV Ring, respectively) (**b**) MIP and VR. Patent Ductus Arteriosus (PDA) (**c**, **d**) Coronary angiogram. Figure (**c**) showing PDA and figure (**d**) showing closed PDA, post intervention

arteriosus creates a shunt from the pulmonary artery to the aorta, effectively shunting fetal blood around the lungs. After delivery, physiological circulation pressure change constricts this blood vessel and the ductus arteriosus eventually obliterates. If left uncorrected, especially in adults, this condition can lead to pulmonary vascular disease. In adults with a patent ductus arteriosus, a percutaneous intervention is recommended.

This case is remarkable that even though she had two previous cardiac surgeries, PDA was never diagnosed, which aggravated her postoperative course. Following the percutaneous closure of the PDA, the patient was promptly diuresed with resolution of symptoms and was discharged after 3 days.

5.18.5 Pearls and Pitfalls

In complex clinical situations, it is advisable to expand the field of view on the CT scan in order to obtain a complete assessment of thoracic structures.

5.19 Case 5.19

5.19.1 History

A 65-year-old male with atypical chest pain referred as an outpatient.

5.19.2 Findings

The CCTA demonstrated obstructing multi-vessel coronary disease, but also a patent foramen ovale with a small atrial left to right shunt (Fig. 5.19a–c).

5.19.3 Diagnosis

Patent foramen ovale.

5.19.4 Discussion

There are two types of holes in the atrial septum. One is an atrial septal defect (ASD) and the other is a patent foramen ovale (PFO), which occurs in the fossa of ovalis. The PFO is necessary in fetal life and closes during the first breath at birth in about 75% of the time [1, 2]. If there is a persistent PFO, there is a flap like opening between the septum primum and secundum at the location of the fossa ovalis that persist after age of 1 year. Most patients with isolated PFO are asymptomatic. When symptoms do occur, patient may present with the following:

- Stroke or transient ischemic event of undefined etiology
- Migraine like symptoms

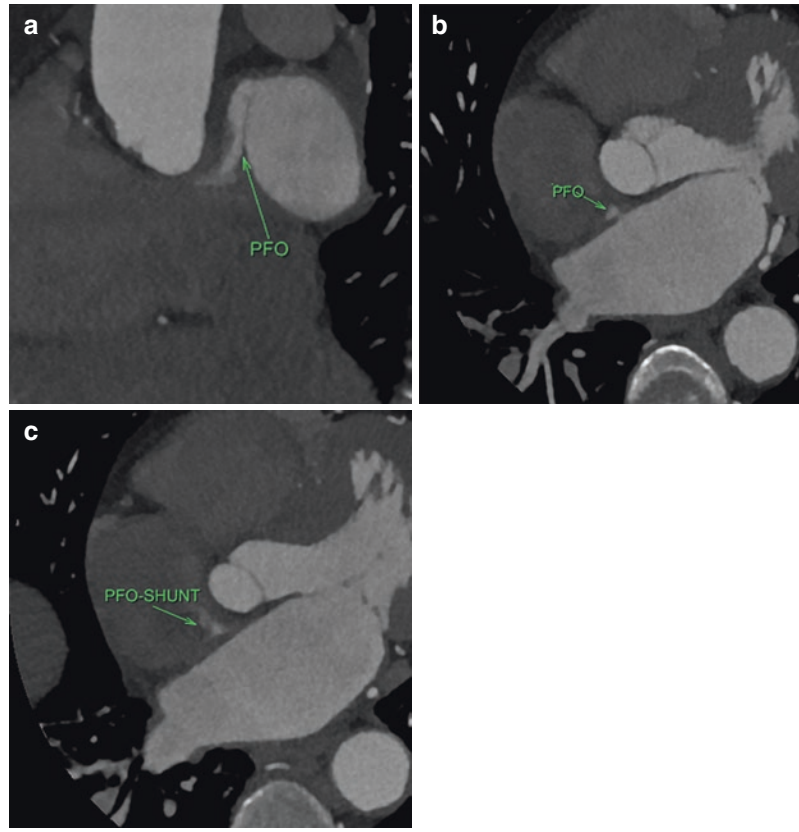

Fig. 5.19 (**a**) Oblique coronal view. PFO (*arrow*) (**b**, **c**) Axial view. PFO (*arrow*)

- Neurological decompression sickness, seen in small percent of scuba divers
- Other clinical presentations are much less common

5.19.5 Pearls and Pitfalls

The diagnosis of PFO on the CCTA can be made when there is a visualization of lack of fusion of the atrial septum primum and secundum with a small left to right shunt with predominantly caudal direction. The appearance is different than a secundum ASD which lacks the atrial flap and the direction of the shunt is straight across the hole in the fossa ovalis.

References

1. Mojadidi MK, Christia P, Salamon J, Liebelt J, Zaman T, et al. Patent foramen ovale: unanswered questions. Eur J Intern Med. 2015;26(10):743–51. https://doi.org/10.1016/j.ejim.2015.09.017. Epub 2015 Oct 17.
2. Hagen PT, Scholz DG, Edwards WD. Incidence and size of patent foramen ovale during the first 10 decades of life: an autopsy study of 965 normal hearts. Mayo Clin Proc. 1984;59(1):17–20.

Suggested Reading

Bayne EJ, Cronin L. Sinus of Valsalva aneurysm, http://www.emedicine.com/ped/topic2106.htm.

Bhatti S, Hakeem A, Ahmad U, et al. Persistent left superior vena cava (PLSVC) with anomalous left hepatic vein drainage into the right atrium: role of imaging and clinical relevance. Vasc Med. 2007;12(4):319–24.

Cademartiri F, La Grutta L, Malagò R, et al. Prevalence of anatomical variants and coronary anomalies in 543 consecutive patients studied with 64-slice CT coronary angiography. Eur Radiol. 2008;18(4):781–91. Epub 2008 Feb 2.

Cademartiri F, Malagò R, La Grutta L, et al. Coronary variants and anomalies: methodology of visualisation with 64-slice CT and prevalence in 202 consecutive patients. Radiol Med. 2007;112(8):1117–31.

Carr MR. Atrial septal defect, general concepts. http://www.emedicine.com/ped/topic171.htm.

Carr MR, Thapar M, King BR. Atrial septal defect, general concepts. http://www.emedicine.com/ped/topic171.htm.

Castorina S, Mignosa C, Degno S, et al. Demonstration of an anomalous connection between the left coronary artery and the pulmonary artery using a multislice CT 64. Clin Anat. 2008;21(4):319–24.

Crean A. Cardiovascular MR and CT in congenital heart disease. Heart 2007;93(12):1637–1647 (Review).

Dodd JD, Ferencik M, Liberthson RR, et al. Congenital anomalies of coronary artery origin in adults: 64-MDCT appearance. AJR Am J Roentgenol. 2007;188(2):W138–46. (Review).

El-Menyar AA, Das KM, Al-Suwaidi J. Anomalous origin of the three coronary arteries from the right aortic sinus Valsalva: role of MDCT coronary angiography. Int J Cardiovasc Imaging. 2006;22(5):723–9.

Gufler H, Voigtlander T, Nowak B, et al. Left circumflex coronary artery fistula to the superior vena cava: assessment of the exact anatomy by multidetector CT. Clin Res Cardiol. 2008;97(4):272–6.

Hegde AN, Desai SB. Two cases of anomalous origins of left coronary artery with a course between the aortic root and the free standing subpulmonary infundibulum on CT coronary angiography. Interact Cardiovasc Thorac Surg. 2005;4(4):297–8.

Hussain F, Sculte PA. Multimodality imaging of an inter-arterial anomalous left main. Int J Cardiol. 2008;127(3):e134–5.

Kacmaz F, Ozbulbul NI, Alyan O, et al. Imaging of coronary artery anomalies: the role of multidetector computed tomography. Coron Artery Dis. 2008;19(3):203–9.

Kadiyala M, Beasley HS, Dua A. A rare case of anomalous left anterior descending artery with a large interarterial communication: an invasive and CT angiographic study. J Invasive Cardiol. 2007;19(3):E69–72.

Karaca M, Kirilmaz A, Oncel G, et al. Contrast-enhanced 64-slice computed tomography in detection and evaluation of anomalous coronary arteries. Tohoku J Exp Med. 2007;213(3):249–59.

Khositseth A, Siripornpitak S, Pornkul R, et al. Case report: Giant coronary aneurysm caused by Kawasaki disease: follow-up with echocardiography and multidetector CT angiography. Br J Radiol. 2008;81(964):e106–9.

Kim SY, Seo JB, Do KH, et al. Coronary artery anomalies: classification and ECG-gated multi-detector row CT findings with angiographic correlation. Radiographics. 2006;26(2):317–33; discussion 333–334 (Review).

Kim YJ, Hur J, Choe KO, et al. Interatrial shunt detected in coronary computed tomography angiography: differential features of a patent foramen ovale and an atrial septal defect. J Comput Assist Tomogr. 2008;32(5):663–7.

Ko SM, Choi JS, Nam CW, et al. Incidence and clinical significance of myocardial bridging with ECG-gated 16-row MDCT coronary angiography. Int J Cardiovasc Imaging. 2008;24(4):445–52.

Kristensen T, Kofoed KF, Helqvist S, et al. Anomalous origin of the left coronary artery from the pulmonary artery (ALCAPA) presenting with ventricular fibrillation in an adult: a case report. J Cardiothorac Surg. 2008;3:33.

Kuo KH, Tiu CM. Coronary CT angiography with reformatting demonstrates a sinus of Valsalva aneurysm. Pediatr Radiol. 2008;38(11):1262.

Lerner CB, Frush DP, Boll DT. Evaluation of a coronary-cameral fistula: benefits of coronary dual-source MDCT angiography in children. Pediatr Radiol. 2008;38(8):874–8.

Leschka S, Koepfli P, Husmann L, et al. Myocardial bridging: depiction rate and morphology at CT coronary angiography—comparison with conventional coronary angiography. Radiology. 2008;246(3):754–62.

Liu CY, Juan CW, Pai YL, et al. Congenital left circumflex coronary artery atresia detected by 64-slice computed tomography: a case report. Kaohsiung J Med Sci. 2007;23(6):313–7.

Love BA, Portman MA. Atrial septal defect, patent foramen ovale. http://www.emedicine.com/ped/topic2494.htm.

Ou P, Iserin F, Vouhe P, et al. Anomalous origin of the left coronary artery from the right aortic sinus: surgery based on diagnosis by 64-slice CT. Eur J Cardiothorac Surg. 2006;29(4):610.

Qamar UR, Khan MU, Umair S, et al. CT angiography images of an anomalous right coronary artery. Int J Cardiol. 2009;132:49–50.

Richard A, Godart F, Brevière GM, et al. Abnormal origin of the left coronary artery from the pulmonary artery: a retrospective study of 36 cases. Arch Mal Coeur Vaiss. 2007;100(5):433–8.

Romaguera R, Paya R, Ridocci F, et al. Ventricular septal defect as casual finding in non-invasive CT-angiography. Eur Heart J. 2008;29(11):1438.

Rommel M, Griffin R, Harrison EE. Coronary anomalies: cardiac CT evaluation of the symptomatic adult athlete. Curr Sports Med Rep. 2007;6(2):85–92. (Review).

Saremi F, Channual S, Raney A, et al. Imaging of patent foramen ovale with 64-section multidetector CT. Radiology. 2008;249(2):483–92. Epub 2008 Sep 9.

Shiga Y, Tsuchiya Y, Yahiro E, et al. Left main coronary trunk connecting into right atrium with an aneurysmal coronary artery fistula. Int J Cardiol. 2008;123(2):e28–30.

Singh Nijjar P, Parameswaran A, Amanullah AM. Evaluation of anomalous aortic origins of the coronaries by 64-slice cardiac computed tomography. Rev Cardiovasc Med. 2007;8(3):175–81.

Srinivasan KG, Gaikwad A, Kannan BR, et al. Congenital coronary artery anomalies: diagnosis with 64 slice multidetector row computed tomography coronary angiography: a single-centre study. J Med Imaging Radiat Oncol. 2008;52(2):148–54.

Utsunomiya D, Nakao K, Yamashita Y. Single coronary artery with spasm. Radiat Med. 2008;26(5):309–12.

Utsunomiya D, Nishiharu T, Urata J, et al. Coronary arterial malformation depicted at multi-slice CT angiography. Int J Cardiovasc Imaging. 2006;22(3–4):547–51.

Waite S, Ng T, Afari A, et al. CT diagnosis of isolated anomalous origin of the RCA arising from the main pulmonary artery. J Thorac Imaging. 2008;23(2):145–7.

Weinstein S, Michler RE. Atrial septal defect, unroofed coronary sinus: surgical perspective. http://www.emedicine.com/ped/topic2815.htm.

Welker M, Salanitri J, Deshpande VS, et al. Coronary artery anomalies diagnosed by magnetic resonance angiography. Australas Radiol. 2006;50(2):114–21. (Review).

Williamson EE, Kirsch J, Araoz PA, et al. ECG-gated cardiac CT angiography using 64-MDCT for detection of patent foramen ovale. AJR Am J Roentgenol. 2008;190(4):929–33.

Zeina AR, Blinder J, Sharif D, et al. Congenital coronary artery anomalies in adults: non-invasive assessment with multidetector CT. Br J Radiol. 2009;82:254–61.

Zeina AR, Odeh M, Blinder J, et al. Myocardial bridge: evaluation on MDCT. AJR Am J Roentgenol. 2007;188(4):1069–73.

Zhang LJ, Lu GM, Guo H, et al. Myocardial bridging on dual-source CT: comparison with conventional coronary angiography. Zhonghua Yi Xue Za Zhi. 2008;88(12):826–9. Chinese.

Cardiac CTA of Coronary Artery Disease

6

Claudio Smuclovisky

6.1 Case 6.1

6.1.1 History

A 54-year-old male presented with a history of hyperlipidemia.

6.1.2 Findings

Positive remodeling in the proximal LAD is seen, with a large non-calcified plaque that has fat density (lipid-rich core). There is preservation of the diameter of the arterial lumen (Fig. 6.1a, b).

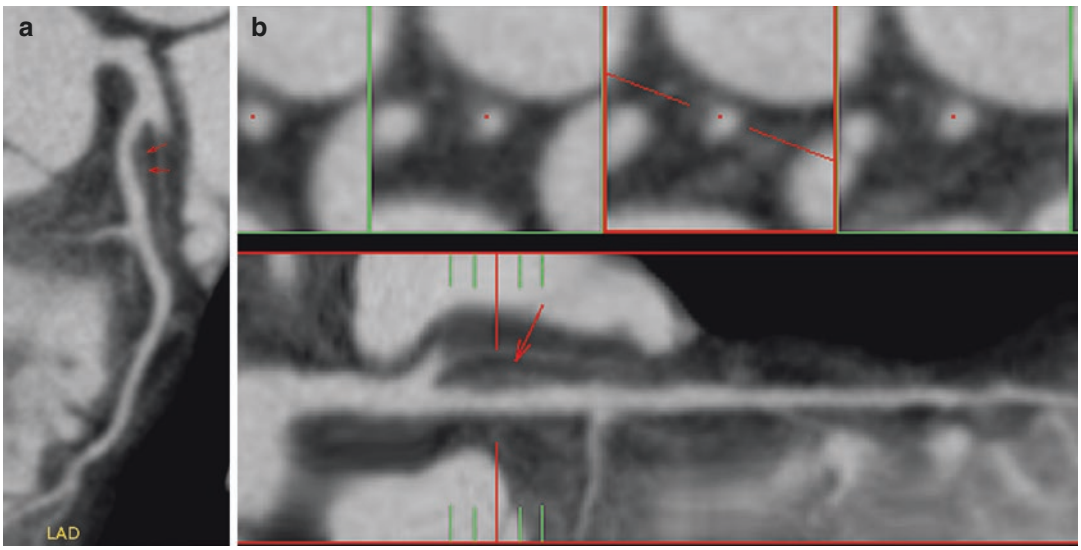

Fig. 6.1 (**a**) Curved MPR: Left anterior coronary artery (LAD) non-calcified plaque (*arrow*). (**b**) Stretched curved MPR: LAD non-calcified plaque (*arrows*)

C. Smuclovisky, MD, FACC, FSCCT
Department of Radiology, Holy Cross Hospital, South Florida Medical Imaging Cardiovascular Institute, Fort Lauderdale, FL, USA
e-mail: smuclovisky@gmail.com

C. Smuclovisky (ed.), *Coronary Artery CTA*, https://doi.org/10.1007/978-3-319-66988-5_6

6.1.3 Diagnosis

The diagnosis is non-calcified plaque in the proximal LAD, with preserved arterial lumen.

6.1.4 Discussion

Positive remodeling is an outward compensatory remodeling (the Glagov phenomenon) in which the arterial wall bulges outward and the lumen remains uncompromised. As plaques progress, it usually do not cause angina because it does not become hemodynamically significant for a long time. In fact, the plaque does not begin to encroach on the lumen until it occupies 40% of the cross-sectional area. The diameter of the stenosis must be 50% or greater to cause flow limitation on cardiac CT and quantitative coronary angiography. Such positively remodeled lesions form the bulk of the vulnerable plaques. Although they can grow for years, they are more prone to result in plaque rupture and acute coronary syndrome, rather than stable angina, as documented by intravascular ultrasound studies. The importance of early disease detection is to manage the patient with improved risk stratification and secondary medical preventive therapy.

6.1.5 Pearls and Pitfalls

The coronary arteries should be inspected with thin slices (usually 0.9 mm or less), curved MPR, and vessel analysis, in order to detect early disease and other subtle abnormalities. The use of maximum intensity projection (MIP) and 3D volume rendering may mask the disease. On visual examination of coronary angiography, high-grade stenosis is considered with a luminal diameter stenosis of greater than 50% in the left main coronary artery and greater than 70% stenosis in the rest of the coronary tree. There may be significant discrepancy between the CTA and non-quantitative coronary angiogram.

6.2 Case 6.2

6.2.1 History

A 72-year-old asymptomatic female physician presented with a family history of CAD. The study was obtained for risk assessment.

6.2.2 Findings

The initial CTA (Fig. 6.2a, b) demonstrated a complex plaque in the proximal RCA, causing luminal stenosis estimated at 30%. A 1-year follow-up study demonstrates retraction of the plaque, which has increased in calcification and

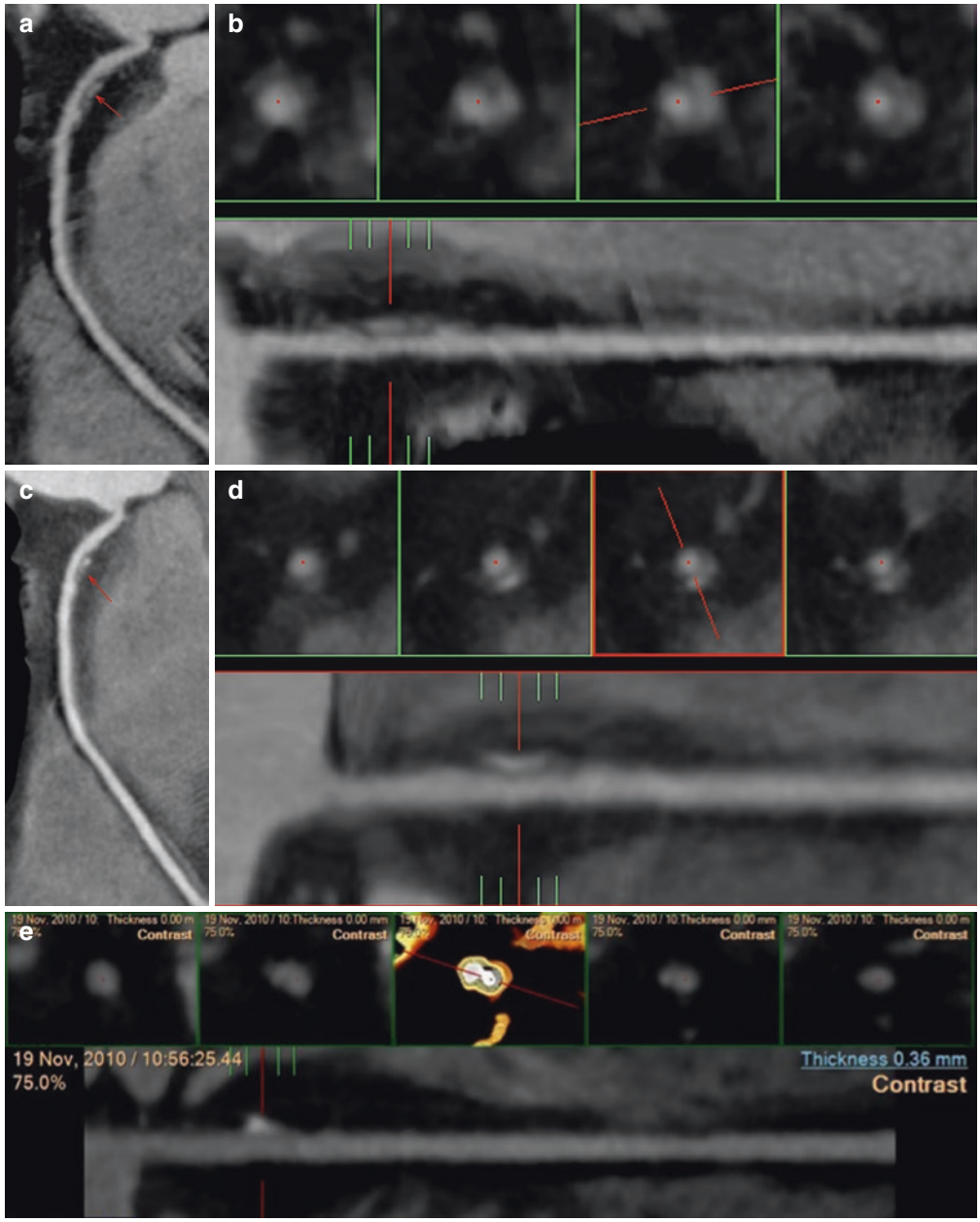

Fig. 6.2 (**a**) cMPR: Right coronary artery (RCA) large complex plaque (*arrow*). (**b**) Stretched cMPR: RCA complex plaque. (**c**) At 12-month follow-up, CMPR: RCA (*arrow*). (**d**) At 12-month follow-up, stretched cMPR: Proximal RCA plaque demonstrates retraction and increased calcification in the plaque. (**e**) At 5-year follow-up, stretched cMPR showing complete calcification and retraction of the plaque

with less than 10% luminal stenosis (Fig. 6.2c, d). A 5-year follow-up study demonstrates retraction and total calcification of the plaque causing negligible luminal obstruction (Fig. 6.2e).

6.2.3 Diagnosis

The diagnosis is large complex plaque in the proximal RCA demonstrating significant improvement on a 12-month and 5-year follow-up study following medical therapy.

6.2.4 Discussion

The initial study demonstrates a large complex plaque in the proximal RCA that is not causing high-grade obstruction. However, because of the large size and complex characteristics of the plaque, there is risk of plaque rupture.

The patient was placed on 10 mg of atorvastatin calcium (Lipitor; note: a higher dose had been recommended) and 81 mg of aspirin daily. The 12-month follow-up study demonstrates remarkable changes in the plaque, which appears retracted, with less encroachment on the lumen, and has increased in calcification. There has been a good response to medical therapy.

Studies have demonstrated that plaque vulnerability is greatest in the intermediate stage of progression (Glagov), where there is positive remodeling in the wall and a relative preservation of the lumen. Cardiac CT has the potential for monitoring the success or failure of modifying CAD risk factors particularly in patient with hyperlipidemia, family history of CAD, diabetes, hypertension, and smoking.

6.2.5 Pearls and Pitfalls

In order to minimize radiation exposure to patients, dose-reduction techniques, such as prospective axial acquisition (step and shoot), should be the protocol of choice.

6.3 Case 6.3

6.3.1 History

A 54-year-old female presented with atypical chest pain.

6.3.2 Findings

There is a non-calcified plaque in the proximal LAD causing positive remodeling, with relative preservation of the artery lumen. Note the minimal scalloping of the arterial lumen (Fig. 6.3a, b).

6.3.3 Diagnosis

The diagnosis is non-calcified plaque in the proximal LAD, with positive remodeling of the artery wall.

6.3.4 Discussion

The word *atherosclerosis* is of Greek origin and literally means focal accumulation of lipid (i.e., *athere* [gruel]) and thickening of arterial intima (i.e., *sclerosis* [hardening]). Coronary artery atherosclerosis or CAD refers to the atherosclerotic changes within the walls of the coronary arteries, which cause impairment or obstruction of normal blood flow with resultant myocardial ischemia. CAD is a progressive inflammatory disease process that generally begins in the second decade of life and manifests clinically in mid-to-late adulthood. The distribution of lipid and connective tissue in the atherosclerotic lesions determines whether they are stable or at risk of rupture, thrombosis, and clinical sequelae.

Histopathology of Atherosclerotic Lesions

- Stary I lesion: The endothelium also expresses surface adhesion molecules E selectin and P selectin, attracting more polymorphonuclear cells and monocytes in the subendothelial space.
- Stary II lesion: Macrophages begin to take up large amounts of LDL (fatty streak).
- Stary III lesion: As the process continues, macrophages eventually become foam cells.
- Stary IV lesion: Lipid exudes into the extracellular space and begins to coalesce to form the lipid core.
- Stary V lesion: Smooth muscle cells and fibroblasts move in, forming fibroatheromas with soft inner lipid cores and outer fibrous caps.

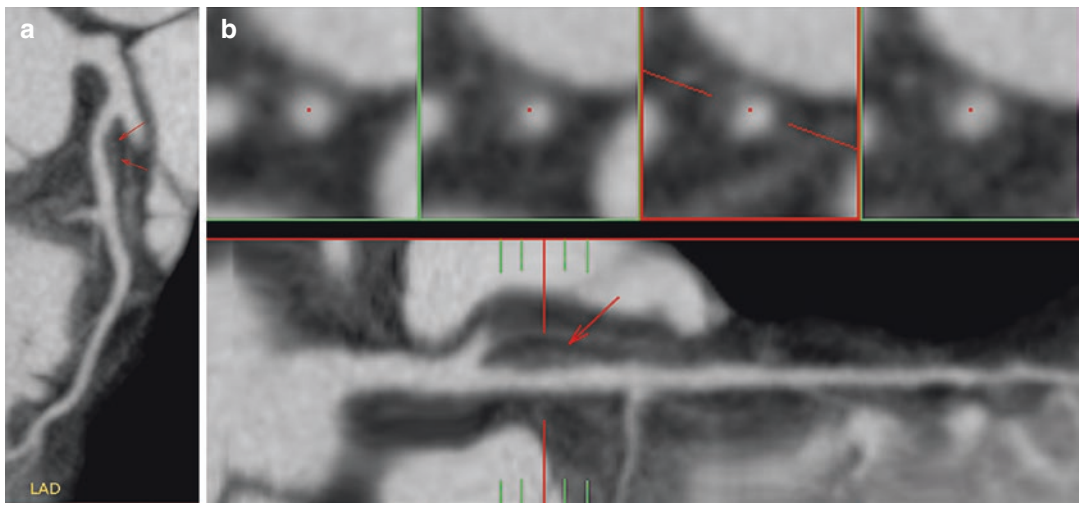

Fig. 6.3 (**a**) cMPR: Left anterior coronary artery (LAD) non-calcified plaque causing positive remodeling of the arterial wall (*arrows*). (**b**) Stretched cMPR: LAD non-calcified plaque (*arrow*)

- Stary VI lesion: Rupture of the fibrous cap with resultant thrombosis causes acute coronary syndrome.
- Stary VII and VIII lesions: As lesions stabilize, they become fibrocalcific (Stary VII lesion) and, ultimately, fibrotic with extensive collagen content (Stary VIII lesion).

CTA has been established for the detection of atheromatous plaque in the coronary arteries. Plaques are divided into soft tissue, fibrocalcific, and calcified. Based on Hounsfield units (HU), it has been described that plaques may be further characterized as follows:

- Thrombus: 20 HU
- Lipids: 50 HU
- Fibrous: 100 HU
- Calcium: >300 HU

The HU numbers have been found to be unreliable to differentiate non-calcified plaque due to voxel averaging. Also, based on the CT findings, the potential of rupture of a non-calcified plaque has not yet been established.

6.3.5 Pearls and Pitfalls

Due to the histologic diversity of plaques and voxel volume averaging, it may not be possible to differentiate between a lipid-rich core and fibrous plaque. When there is negative remodeling in the presence of a non-calcified plaque, it is reasonable to assume that the plaque is fibrous. Thin curved reformatted multiplanar reconstructed slices (cMPR) are our preferred technique used for the evaluation of atheromatous disease. We have found that 3D volume rendered and MIP techniques may obscure plaques.

6.4 Case 6.4

6.4.1 History

A 46-year-old male physician presented with new onset of atypical chest pain.

6.4.2 Findings

A non-calcified plaque is seen in the mid-LAD coronary artery, causing negative remodeling and high-grade (greater than 70%) luminal stenosis (Fig. 6.4a–c). Additionally, there is non-obstructive calcified plaque in the mid-LAD.

6.4.3 Diagnosis

Non-calcified plaque in the mid-LAD, with negative remodeling causing high-grade stenosis.

6.4.4 Discussion

Fewer plaques exhibit almost no compensatory vascular dilation, and the atheroma steadily grows inward, causing gradual luminal narrowing. Many of the plaques with initial positive remodeling eventually progress to the negative remodeling stage, causing narrowing of the vascular lumen. These plaques can lead to the development of stable angina. These are also vulnerable to plaque rupture and thrombosis. The patient underwent an angiogram with stenting of the lesion (Fig. 6.4d, e).

6.4.5 Pearls and Pitfalls

Non-calcified plaques, causing high-grade stenosis, are commonly subtle and traverse only a short segment. In order not to miss the abnormality, it is important to use thin slice cMPR technique on a 3D workstation.

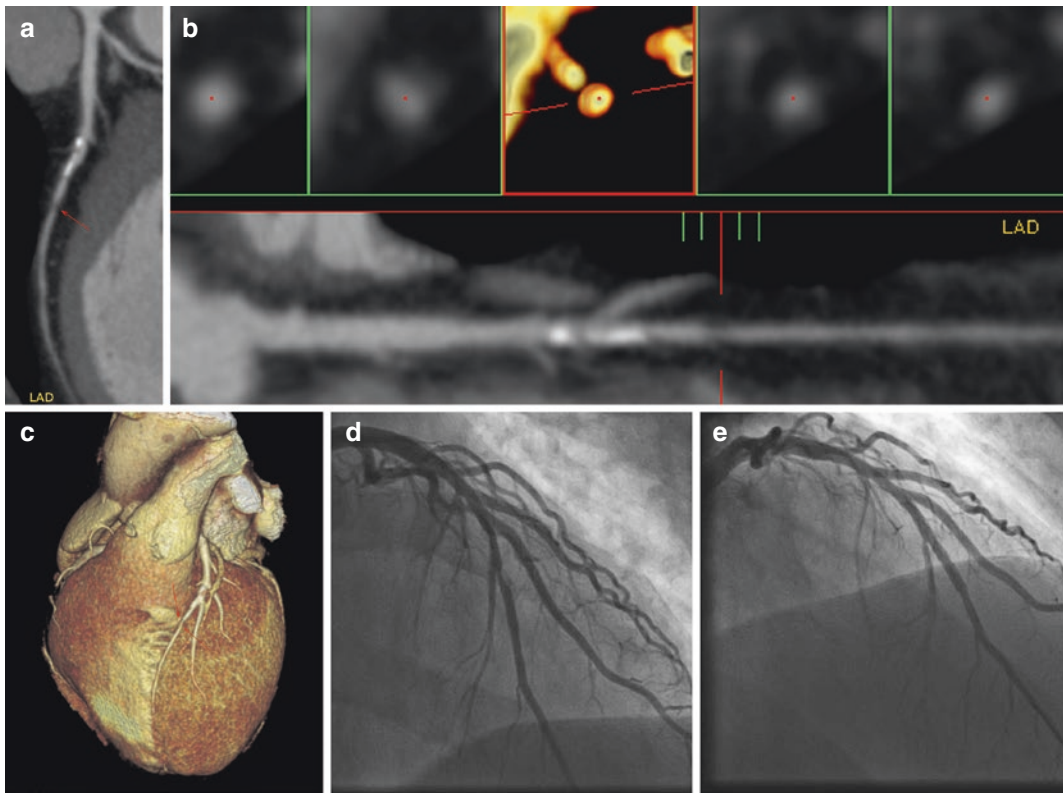

Fig. 6.4 (**a**) cMPR: Mid-left anterior coronary artery (LAD) non-calcified plaque causing negative remodeling and high-grade obstruction (*arrows*). (**b**) Stretched cMPR: Mid-LAD non-calcified plaque. (**c**) 3D volume rendered: Mid-LAD (*arrows*). (**d**) Coronary angiogram: LAD. (**e**) Coronary angiogram: Post-stenting

6.5 Case 6.5

6.5.1 History

An 80-year-old male presented with a history of increasing shortness of breath and no prior cardiac history.

6.5.2 Findings

A non-calcified plaque is seen in the mid-left circumflex, with positive and negative remodeling and high-grade obstruction of the lumen (Fig. 6.5a–c). Additionally, there is a complex plaque in the mid-LAD, adjacent to the ostium

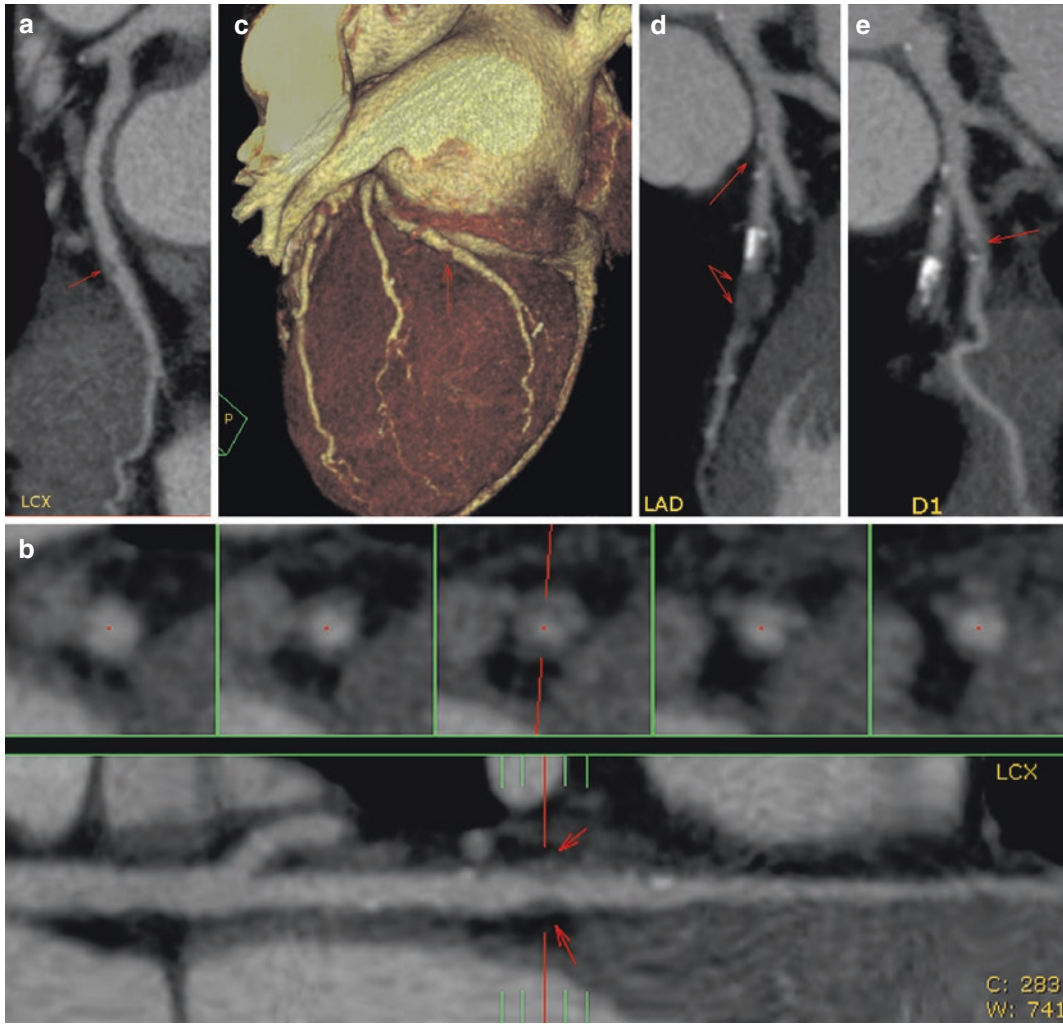

Fig. 6.5 (**a**) cMPR: Mid-left circumflex coronary artery (LCX) non-calcified plaque causing both positive and negative remodeling and high-grade obstruction (*arrows*). (**b**) Stretched cMPR: Mid-LCX non-calcified plaque (*arrows*). (**c**) 3D volume rendered: Mid-LCX (*arrow*). (**d**) cMPR: LAD. High-grade obstruction adjacent to the ostium of D1 (*single arrow*). Thrombus in the mid-LAD, with total occlusion of the artery (*double arrows*), and retrograde flow in the distal LAD. (**e**) cMPR: D1. High-grade obstruction in the proximal segment of the artery (*arrow*)

of D1, causing high-grade obstruction. Distal to D2, there is calcified plaque in the LAD and a thrombus of undetermined age, with total occlusion of the artery and retrograde flow into the distal LAD (Fig. 6.5d). The first diagonal branch is a long vessel of large caliber and has a mixed plaque in the proximal segment that is also causing high-grade obstruction (Fig. 6.5e). There was no evidence of a prior myocardial infarct.

6.5.3 Diagnosis

Non-calcified plaque in the mid-LCX, with positive and negative remodeling, causing high-grade obstruction in the lumen. There is thrombus in the mid-LAD, which is totally occluded, with retrograde flow from collaterals into the distal LAD. There is also high-grade obstruction in the proximal first diagonal artery.

6.5.4 Discussion

The case depicts the typical findings of progression of disease in the wall of the artery (LCX), with both positive and negative remodeling causing high-grade luminal stenosis.

6.5.5 Pearls and Pitfalls

Atherosclerosis is a systemic and inflammatory disease. It is common to encounter multiple plaques at different stages of disease progression.

6.6 Case 6.6

6.6.1 History

An 80-year-old male presented with a 2-week history of chest pain.

6.6.2 Findings

There is a complex plaque in the mid-RCA causing high-grade stenosis (Fig. 6.6a). The atheroma is causing expansion of the intima, with a *donut sign* appearance on the axial slice (Fig. 6.6b). There is a mixed plaque in the proximal RCA that is non-obstructive. The patient underwent stenting of the RCA and subsequent intensive medical therapy. A 14-month follow-up CTA demonstrates a patent stent in the mid-RCA, with decrease remodeling in the adjacent wall and also diminished soft tissue component in the proximal plaque (Fig. 6.6d).

6.6.3 Diagnosis

Complex plaque in the mid-RCA, causing high-grade stenosis.

6.6.4 Discussion

A lesion causing mild stenosis may rupture suddenly and cause bleeding into the wall of the vessel (plaque hemorrhage), causing high-grade obstruction and/or occlusion of the vessel because of thrombosis. Injury to the endothelial lining of arteries, active uptake by the vascular wall of atherogenic lipoprotein particles, inflammatory and oxidative reactions, thrombosis, calcification, and hemorrhage all contribute to arteriosclerosis and scarring of an artery wall.

6.6.5 Pearls and Pitfalls

We have observed in a number of patients the CCTA donut sign. It is typical of a complex atheroma, causing high-grade stenosis that is consistent with intramural hemorrhage (acute/subacute). Since this type of lesion is considered unstable, it is important to differentiate it from negative remodeling of an atheroma.

Fig. 6.6 (**a**) cMPR: Right coronary artery (RCA), complex plaque in the mid-RCA, causing high-grade obstruction (*arrows*). There is a mixed plaque in the proximal RCA that is not flow limiting. (**b**) Axial RCA. Complex plaque, with expansion of the intima: donut sign (*arrow*). (**c**) Axial RCA. Proximal to the lesion, the lumen has normal diameter (*arrow*). (**d**) cMPR: RCA. 14-month follow-up post-stenting of the mid-RCA (*arrow*)

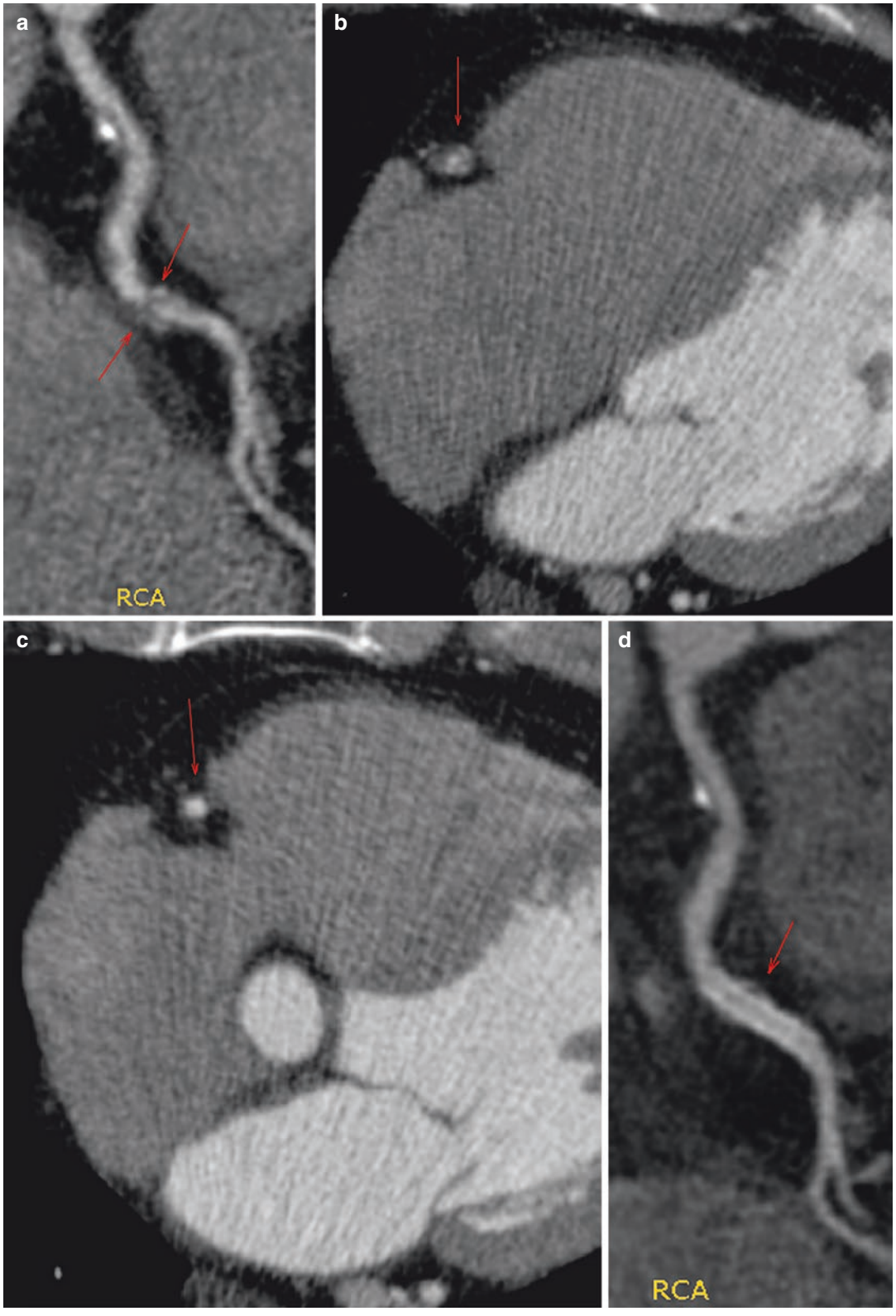
a
RCA
b
c
d
RCA

6.7 Case 6.7

6.7.1 History

A 56-year-old male physician presented with a family history of CAD and new onset of chest discomfort during exercise.

6.7.2 Findings

There are scattered mixed plaques throughout the LAD. There is a non-calcified plaque in the proximal LAD causing high-grade critical stenosis (Fig. 6.7a–c).

6.7.3 Diagnosis

Non-calcified plaque in the proximal LAD, causing high-grade critical stenosis.

6.7.4 Discussion

The combination of findings, proximal LAD large non-calcified plaque (potentially vulnerable) causing a critical stenosis, should be communicated immediately to the referring physician. The patient was sent directly to the hospital from the outpatient center and underwent a subsequent angiogram and successful stenting of the lesion (Fig. 6.7d, e). The patient responded well and is currently asymptomatic (and very grateful).

6.7.5 Pearls and Pitfalls

In evaluating cardiac CT, and in the presence of high-grade stenosis, one should attempt to differentiate stable from potentially unstable disease, which could lead to a coronary event. As the utilization of cardiac CTA becomes more commonplace (such as in the emergency room setting), the medical and legal implications become apparent.

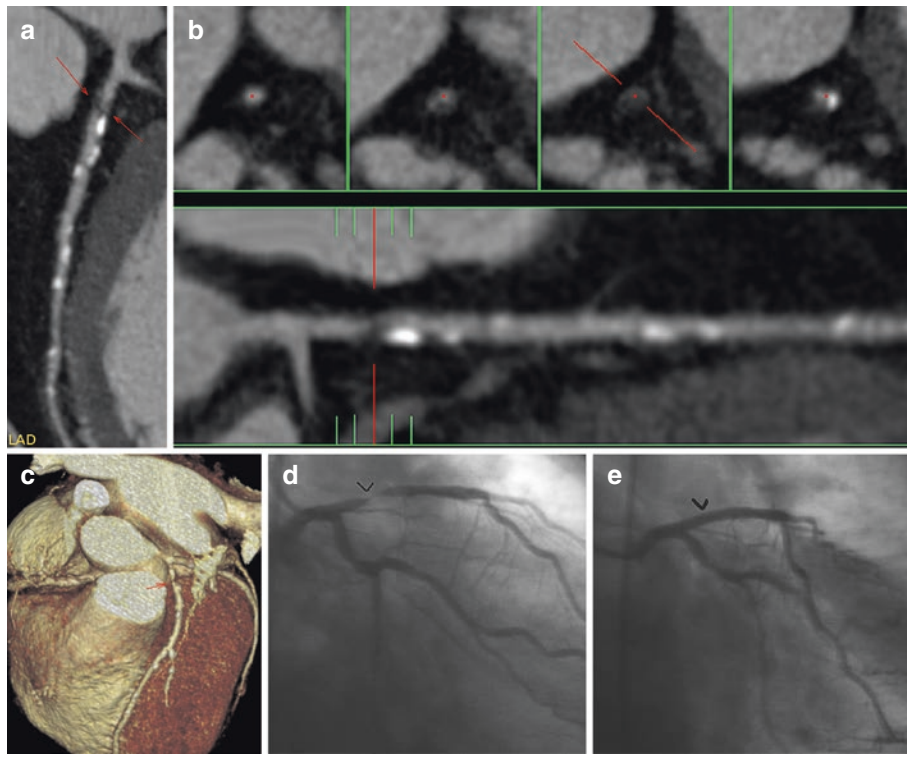

Fig. 6.7 (**a**) cMPR: LAD. Soft tissue plaque in the proximal LAD, causing high-grade critical stenosis (*arrow*). (**b**) cMPR-stretched LAD. Same findings as 2.7A. (**c**) 3D volume rendered. Proximal left anterior coronary artery (LAD) (*arrow*). (**d**) Coronary angiogram: 99% (string sign) proximal LAD stenosis (*arrowhead*). (**e**) Coronary angiogram: PCI with drug-eluting stent placement in the proximal LAD with excellent results (*arrowhead*)

6.8 Case 6.8

6.8.1 History

A 72-year-old asymptomatic male presented with inferior wall ischemia on a nuclear perfusion scan.

6.8.2 Findings

There is penetration of contrast into the wall of the proximal RCA. Two additional distal areas of high-grade stenosis are noted in the RCA (Fig. 6.8a, b).

6.8.3 Diagnosis

The diagnosis is ruptured plaque in the proximal RCA.

6.8.4 Discussion

The case illustrates a fissure in the intimae of the proximal RCA, with penetration of contrast into the wall, the classic appearance of a ruptured plaque. The lesion was considered unstable, implying the potential to lead to thrombus

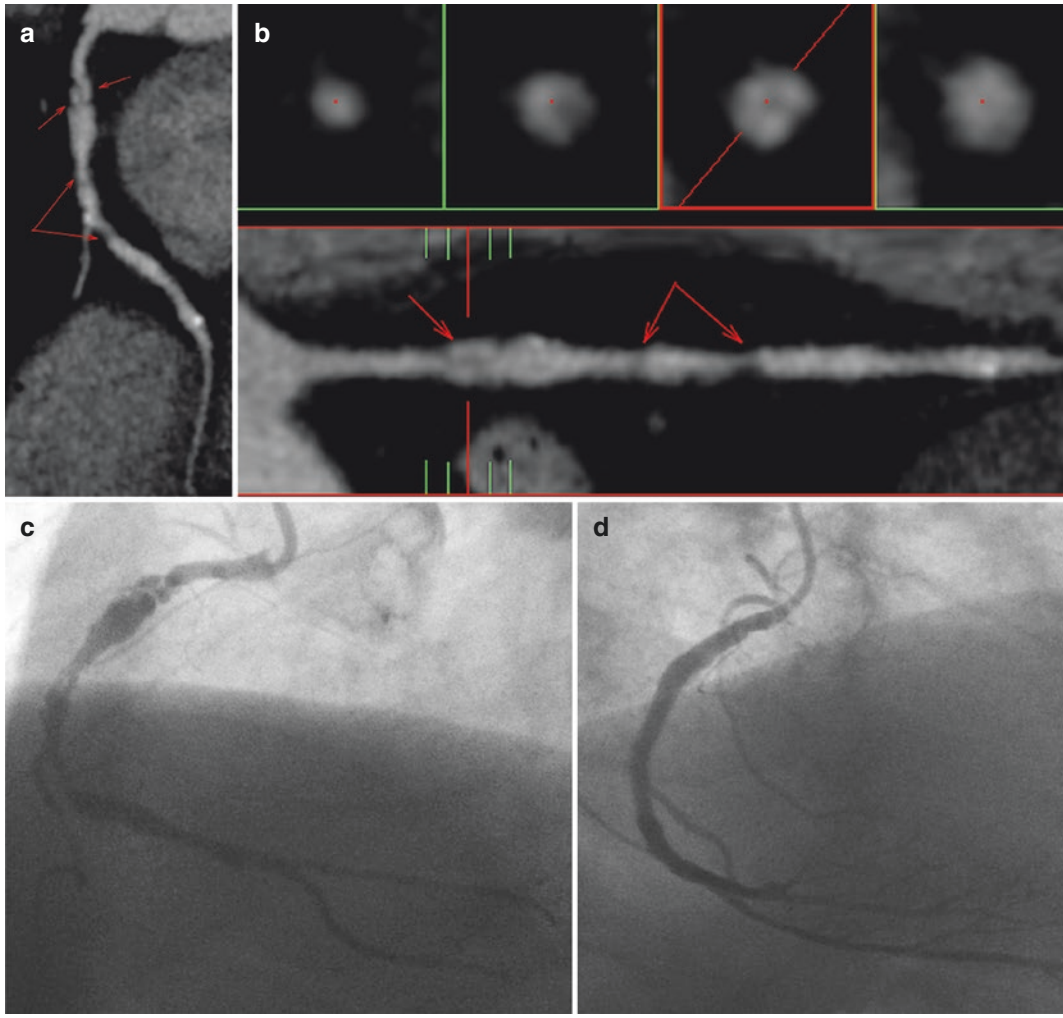

Fig. 6.8 (**a** and **b**) cMPR: Right coronary artery (RCA). Ruptured plaque with a fissure in the proximal RCA. There is penetration of contrast into the wall (*proximal arrows*). There are two distal areas of high-grade obstruction (*double arrows*). (**c**) Coronary angiogram. (**d**) Post-stenting coronary angiogram

formation and potentially an acute coronary syndrome. The patient underwent coronary angiography the following day, with successful ballooning and placement of sequential drug-eluting stents in the proximal to mid-RCA (Fig. 6.8c, d).

Most plaque ruptures occur because of disruption of the fibrous cap, which allows contact between the highly thrombogenic lipid core and the blood. These modestly obstructive plaques, which have a greater burden of soft lipid core and thinner fibrous caps with chemoactive cellular infiltration particularly adjacent to the shoulder region, are called vulnerable plaques. The amount of collagen in the fibrous cap depends on the balance between synthesis and destruction of intercellular matrix and inflammatory cell activation.

6.8.5 Pearls and Pitfalls

Careful observation of atheromas with thin curved reformatted reconstruction and cross-sectional imaging is recommended in order not to miss a ruptured plaque. Proper windowing and analysis of Hounsfield density is additionally necessary to differentiate a complex plaque from a fissure. Three-dimensional volume rendered and thick MIP images may obscure the abnormality. Since the lesion is unstable, immediate therapy (medical/intervention) is warranted to prevent an acute coronary syndrome.

6.9 Case 6.9

6.9.1 History

A 57-year-old physician complained of mild chest discomfort during extreme exercise.

6.9.2 Findings

There is advanced mixed plaque in the left main coronary artery, causing high-grade stenosis. There was also disease in the proximal LAD and LCX (Fig. 6.9a–d).

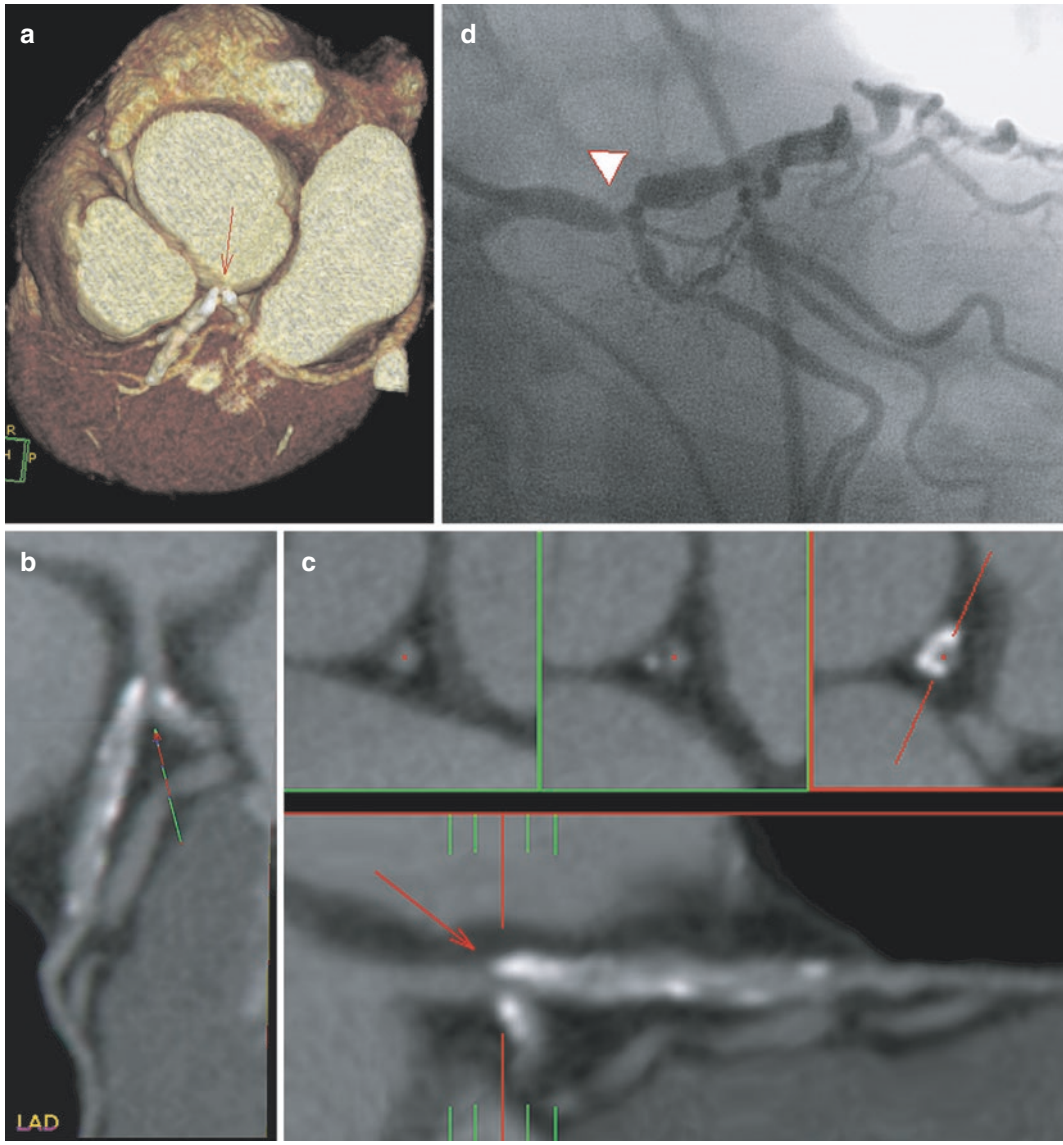

Fig. 6.9 (**a**) A. 3D volume rendered: Left main stenosis (*arrow*). (**b** and **c**) cMPR LM–LAD (*arrow*). (**d**) Coronary angiogram: LM stenosis confirmed on angiography (*arrowhead*)

6.9.3 Diagnosis

The diagnosis is high-grade stenosis in the left main coronary artery.

6.9.4 Discussion

Left main coronary artery disease is defined as >50% left main diameter narrowing, often characterized by symptoms of unstable angina sometimes with hemodynamic compromise, diffuse ST depression in inferior and precordial leads on ECG, and poor prognosis due to sudden death and massive infarction. CABG is the first-line therapy, while stenting is commonplace in many countries as an alternative to surgery. The patient had a diagnostic angiogram confirming the high-grade left main coronary stenosis and underwent double bypass surgery.

6.9.5 Pearls and Pitfalls

The left main coronary artery has variable origin, length, and diameter. Comparison with the diameter of the proximal LAD and circumflex may prove helpful in assessing the degree of stenosis in the left main.

6.10 Case 6.10

6.10.1 History

A 43-year-old male presented with a history of eosinophilia and cardiac angina.

6.10.2 Findings

There is diffuse coronary artery ectasia, with multiple aneurysms and LAD, left circumflex, and RCA chronic total occlusions. There is also a left coronary sinus aneurysm (Fig. 6.10a–e).

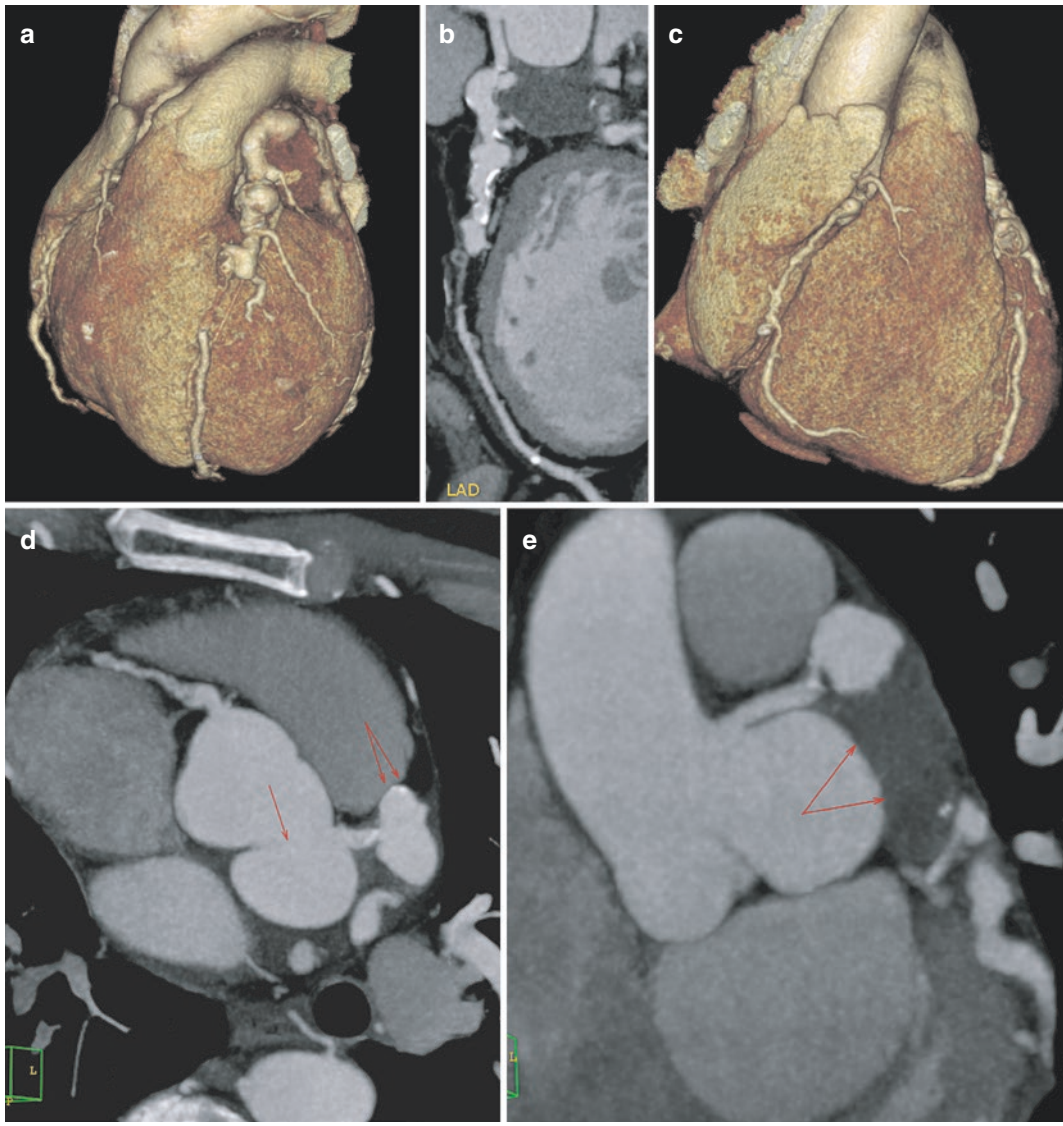

Fig. 6.10 (**a** and **b**) Aneurysmal dilatation of the left anterior coronary artery (LAD) with mid-segment chronic total occlusion and retrograde flow in the distal segment. (**c**) 3D volume rendered: Proximal RCA aneurysm and mid-segment chronic total occlusion. (**d**) Axial. Left coronary sinus aneurysm (*single arrow*). Proximal LAD aneurysm (*double arrow*). (**e**) Coronal. Thrombosed aneurysm of the proximal left circumflex coronary artery (*double arrow*). (Courtesy of Dr. Martin H. K. Hoffmann, Ulm, Germany)

6.10.3 Diagnosis

The diagnosis is Churg–Strauss syndrome.

6.10.4 Discussion

Churg–Strauss syndrome is a systemic vasculitis. The disease was first described in 1951 by Dr. Jacob Churg and Dr. Lotte Strauss as a syndrome consisting of "asthma, eosinophilia, fever, and accompanying vasculitis of various organ systems." Churg–Strauss syndrome shares many of the clinical and pathologic features of polyarteritis nodosa. Churg and Strauss discovered that the presence of granulomas as well as the abundance of eosinophils distinguished this disease from polyarteritis nodosa. Another name for Churg–Strauss syndrome is *allergic granulomatosis*.

The mechanism behind the changes that produce coronary artery disease in vasculitis involves immunologically mediated inflammation with intimal thickening from the accumulation of fibrous tissue and proliferation of smooth muscle cells. There is also pathologic evidence that stimulated eosinophils are directly toxic to myocardial cells and arterial wall components. Aneurysmal dilatation is associated with destruction of the media. The most notable vasculitis to affect the coronary arteries is Kawasaki's disease. Kawasaki's disease, however, occurs predominantly in children, presenting with fever lasting several days. It is commonly associated with *strawberry* tongue, palmar erythema, rash, or cervical lymphadenopathy.

Churg–Strauss syndrome usually responds to prednisone. Initially, high doses of oral prednisone are used in an attempt to get the disease into remission as quickly as possibly (e.g., using oral prednisone 40–60 mg/day). After the first month or so, this high dose of prednisone is gradually tapered down over the ensuing months. Other immunosuppressive drugs, such as azathioprine, mycophenolate mofetil (CellCept), methotrexate, or cyclophosphamide may be used in addition to prednisone. High doses of intravenous steroids (usually methylprednisolone) may be useful for those patients with severe disease or for those who are unresponsive to the combination of oral prednisone used with other immunosuppressive medications.

6.10.5 Pearls and Pitfalls

Vasculitis should be suspected, particularly in younger patients, with abnormally dilated coronary arteries and aneurysms.

6.11 Case 6.11

6.11.1 History

A 76-year-old asymptomatic male presented with a history of inferior wall ischemia on a nuclear perfusion scan.

6.11.2 Findings

There is high-grade stenosis in the proximal segment of the RCA and chronic total occlusion in the mid-segment of the RCA, with retrograde filling of the distal segment. There is non-obstructive disease in the proximal left circumflex, with critical subtotal occlusion in the ostium of the first obtuse marginal artery (Fig. 6.11a–e).

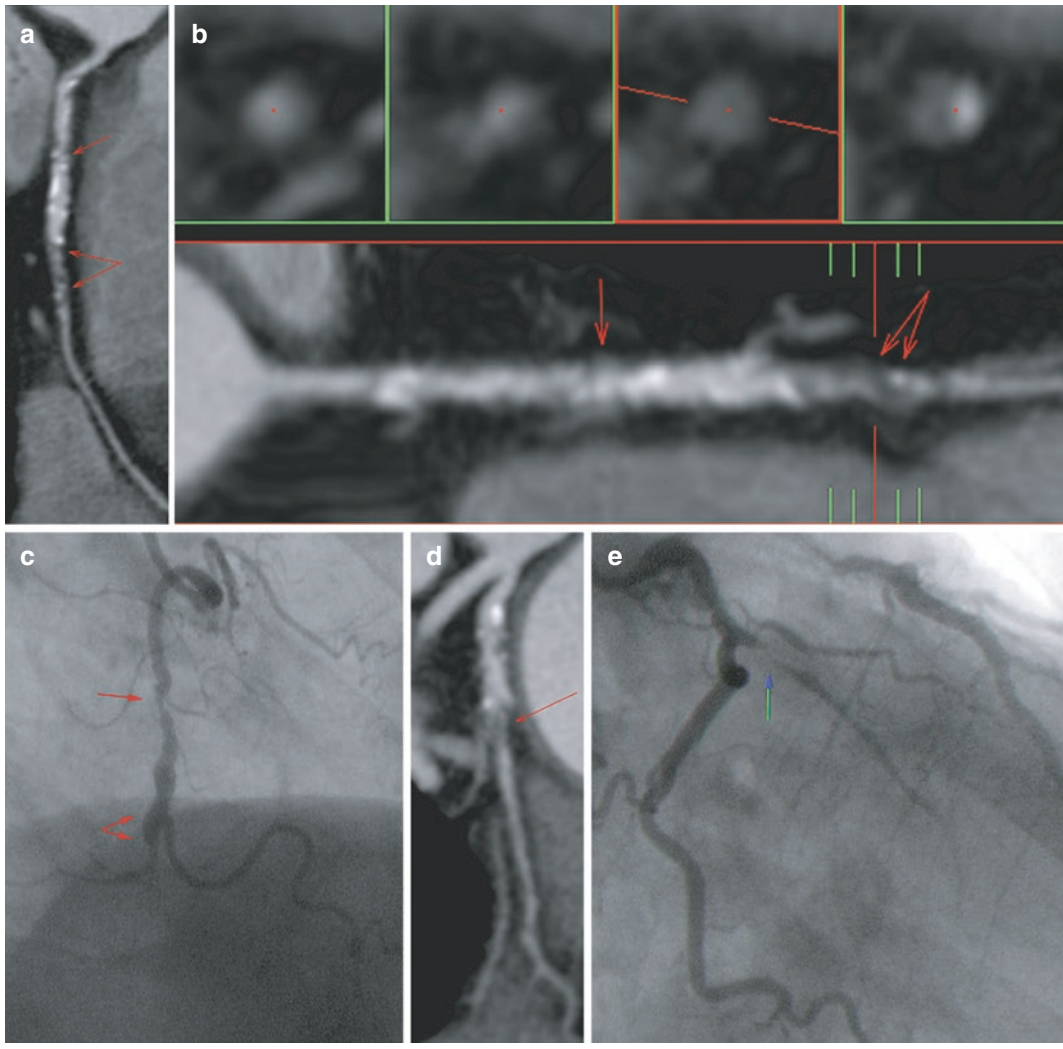

Fig. 6.11 (**a** and **b**) Curved and stretched MPR RCA: Proximal segment high-grade stenosis (*single arrow*). Mid-segment chronic total occlusion (*double arrows*). (**c**) Angiogram RCA. (**d**) cMPR LCX: Ostial subtotal occlusion of OM1. (**e**) Angiogram: LCX–OM1 (*arrow*)

6.11.3 Diagnosis

RCA mid-segment chronic total occlusion and critical subtotal occlusion of the first obtuse marginal artery (OM1).

6.11.4 Discussion

The mid-RCA has a low-density transition zone that is diagnostic of a totally occluded artery. It is common to see contrast opacification of the distal segment from retrograde filling from collaterals. The thrombus in the occluded segment of the artery commonly has low density and may contain calcified atheromas. Although the age of the thrombus in a patient without an acute coronary syndrome usually cannot be ascertained, these are commonly referred to as chronic total occlusion (CTO). It may be challenging with CT to differentiate a subtotal from a total occlusion. In the subtotal occlusion, the transition zone is typically shorter, and a small channel of contrast density is identified.

6.11.5 Pearls and Pitfalls

Due to the timing of the acquisition of a CCTA, it cannot be determined whether the arterial flow is antegrade or retrograde.

6.12 Case 6.12

6.12.1 History

A 77-year-old asymptomatic female with a strong family history of CAD presented for presurgical orthopedic clearance. The patient had a prior negative myocardial perfusion scintigram result.

6.12.2 Findings

There is advanced diffuse disease in the proximal LAD. There is short-segment chronic total occlusion in the mid-LAD. There is diminished contrast density in the distal LAD from retrograde collateral flow (Fig. 6.12a–d).

6.12.3 Diagnosis

Mid-LAD chronic total occlusion.

6.12.4 Discussion

The mid-LAD has a short low-density transition zone with a lack of contrast density, indicating a totally occluded artery. The distal LAD appears to have diminished caliber and is being opacified by retrograde flow from collaterals. The findings were confirmed on an angiogram. The patient had subsequent bypass surgery to the distal LAD.

6.12.5 Pearls and Pitfalls

The distal segment of an occluded artery commonly appears of small caliber due to the retrograde flow from collaterals and under-filling of the vessel. Therefore, it cannot be assumed that the caliber of the artery is too small for bypass surgery.

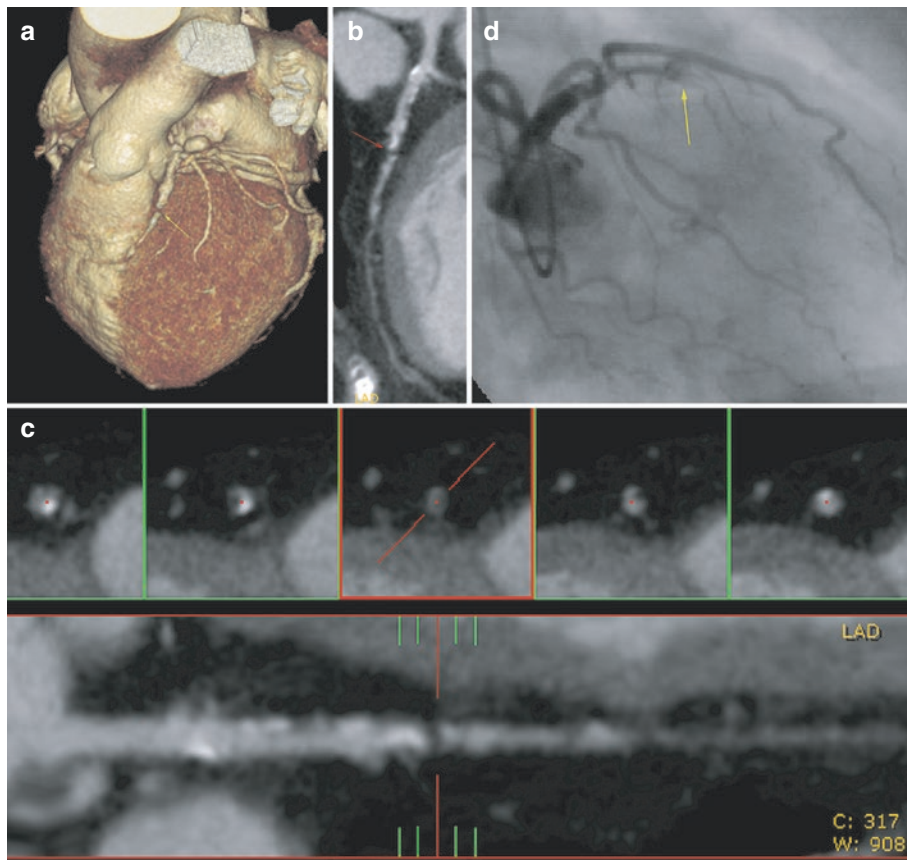

Fig. 6.12 (**a**–**c**) 3D volume rendered, curved, and stretched MPR: Mid-left anterior coronary artery (LAD) chronic total occlusion (*arrow*). (**d**) Angiogram: Confirms the occluded LAD (*arrow*)

6.13 Case 6.13

6.13.1 History

A 45-year-old male presented with exertional chest pain and reported a normal exercise myocardial perfusion scan result.

6.13.2 Findings

There is advanced diffuse non-calcified and calcified plaque extending from the distal left main to the mid-LAD. There is long-segment tubular-type high-grade stenosis in the proximal and mid-LAD (Fig. 6.13a, b, and e). There is also

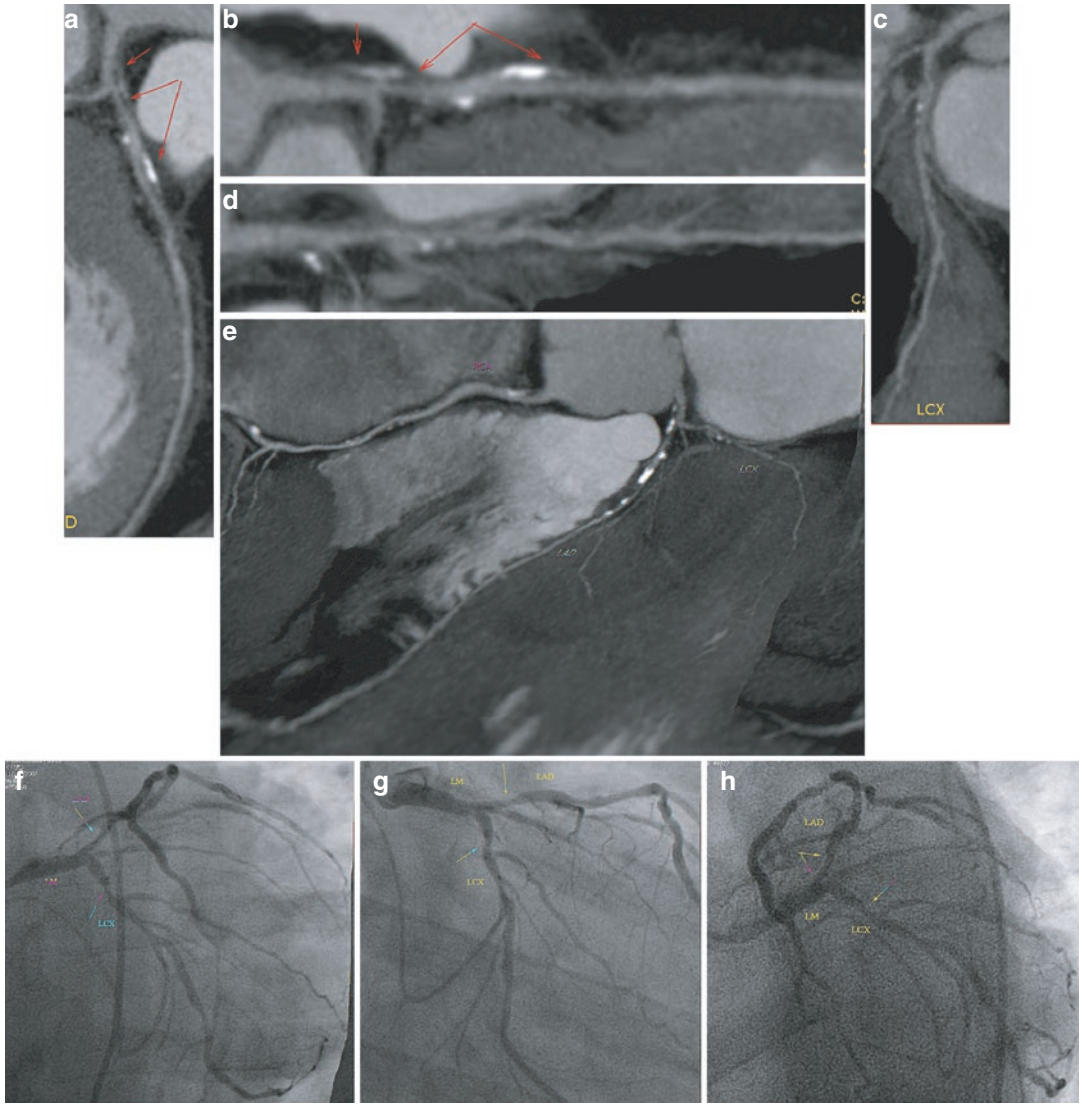

Fig. 6.13 (**a** and **b**) cMPR LM–LAD. (**c** and **d**) cMPR LCX: Diffuse disease with proximal high-grade stenosis. (**e**) 2D map: Advanced multi-vessel disease. (**f–h**) Coronary angiogram

high-grade stenosis by mostly non-calcified plaque in the proximal left circumflex (Fig. 6.13c, d, and e). The RCA has moderate diffuse non-obstructive disease (Fig. 6.13e).

6.13.3 Diagnosis

Advanced multi-vessel coronary artery disease, with long-segment tubular high-grade stenosis in the proximal to mid-LAD and short-segment high-grade stenosis in the proximal left circumflex.

6.13.4 Discussion

The CTA demonstrates well the extent of disease, which can be helpful in planning coronary intervention and/or surgical management. It is well documented in the literature, with intravascular ultrasound (IVUS) correlation, that conventional coronary angiography commonly underestimates the amount and extent of disease in the artery wall. The angiogram in this case demonstrates significantly less disease than identified on the CTA (Fig. 6.13f–h). Percutaneous coronary intervention was not performed in this case due to the extent of disease in the left main and LAD, which is also well demonstrated on the CTA. Also based on the CTA, the angiographer did not deem it necessary to perform additional IVUS, or flow wire measurement. The patient had subsequent bypass surgery to the LAD and left circumflex.

6.13.5 Pearls and Pitfalls

The CCTA provides valuable information to the angiographer prior to the diagnostic or interventional procedure, thus, contributing to the decision-making process and management of the case. It may also potentially shorten the time of the procedure, save additional costs (e.g., IVUS), radiation to patient and operator and added risk to the patient.

6.14 Case 6.14

6.14.1 History

A 62-year-old male presented with atypical chest pain and reported a normal exercise myocardial perfusion scan result.

6.14.2 Findings

There is advanced diffuse non-calcified and calcified plaque involving the left main, and proximal to mid-LAD, with high-grade stenosis. There is also high-grade stenosis in the proximal to mid-ramus intermedius branch (Fig. 6.14a–c and e). The other major coronary arteries had scattered non-obstructive disease.

6.14.3 Diagnosis

The diagnosis is high-grade stenosis in the left main coronary artery, left anterior descending, and ramus intermedius artery.

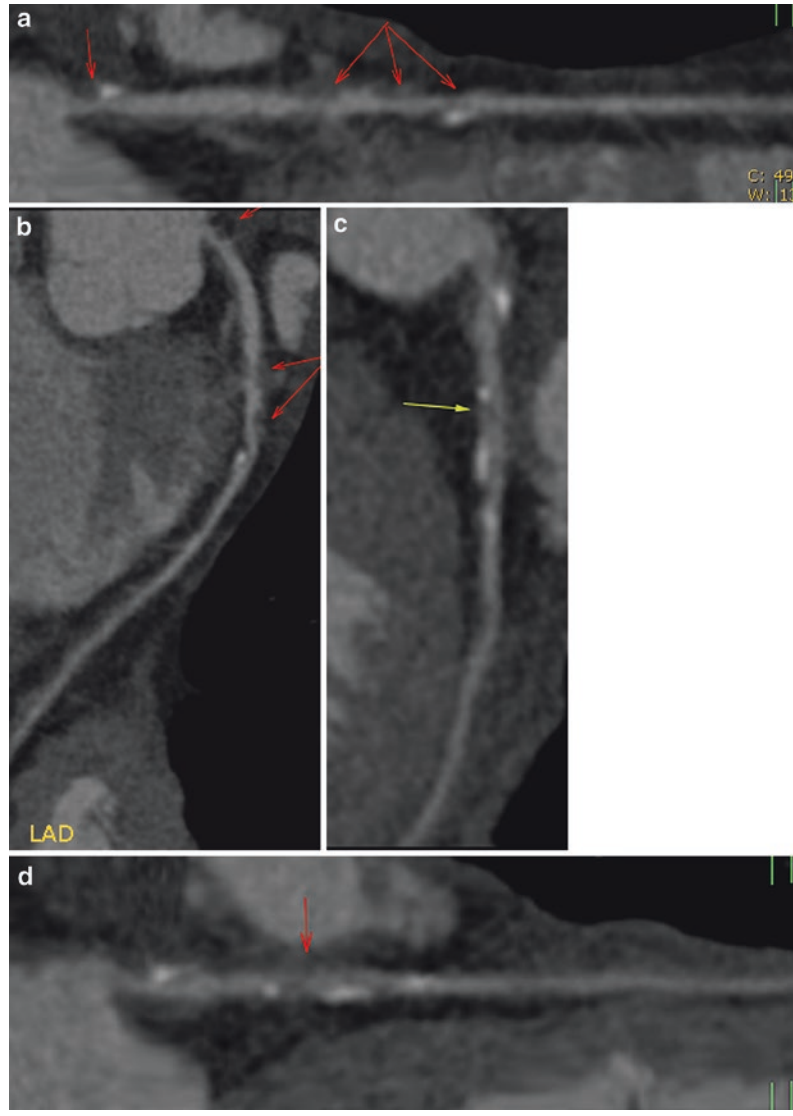

Fig. 6.14 (**a** and **b**) cMPR LM–LAD: High-grade stenosis (*arrows*). (**c** and **d**) cMPR ramus intermedius artery: High-grade stenosis (*arrows*). (**e**) 2D map: Advanced multi-vessel disease. (**f**–**h**) Diagnostic angiogram

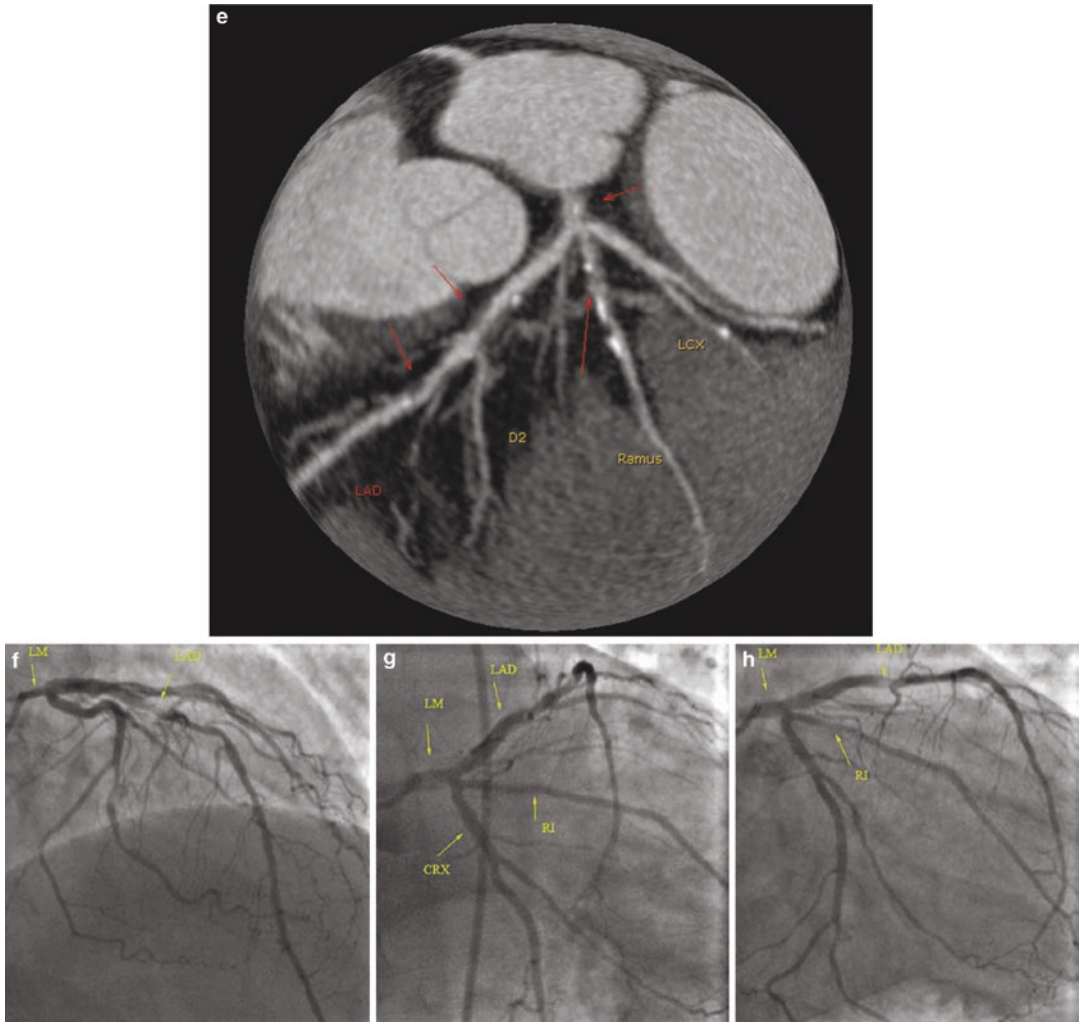

Fig. 6.14 (continued)

6.14.4 Discussion

The patient became severely hypotensive during the diagnostic angiogram. A balloon pump catheter was placed in the aorta, and the patient was moved to the intensive care unit to await surgical revascularization.

High-grade left main disease is a major cause of morbidity and mortality. It is helpful for the angiographer to previously be aware of the presence of significant left main coronary artery disease, since the tip of the angiography catheter may occlude the lumen of the artery or unroof a plaque, which may cause significant adverse or catastrophic cardiac complications. Awareness of the high complication rate in such patients has changed the diagnostic procedure: cannulation of the left main coronary artery and is performed with more caution, and fewer angiographic views are obtained.

6.14.5 Pearls and Pitfalls

Greater than 50% luminal stenosis in the left main is considered flow limiting.

6.15 Case 6.15

6.15.1 History

A 56-year-old male presented with ventricular ectopy.

6.15.2 Findings

There is high-grade, tubular type, stenosis in the mid-LAD immediately distal to the ostium of the second diagonal (Fig. 6.15a–e). There is also mild non-stenotic fibrocalcific plaque at the ostium of the LAD.

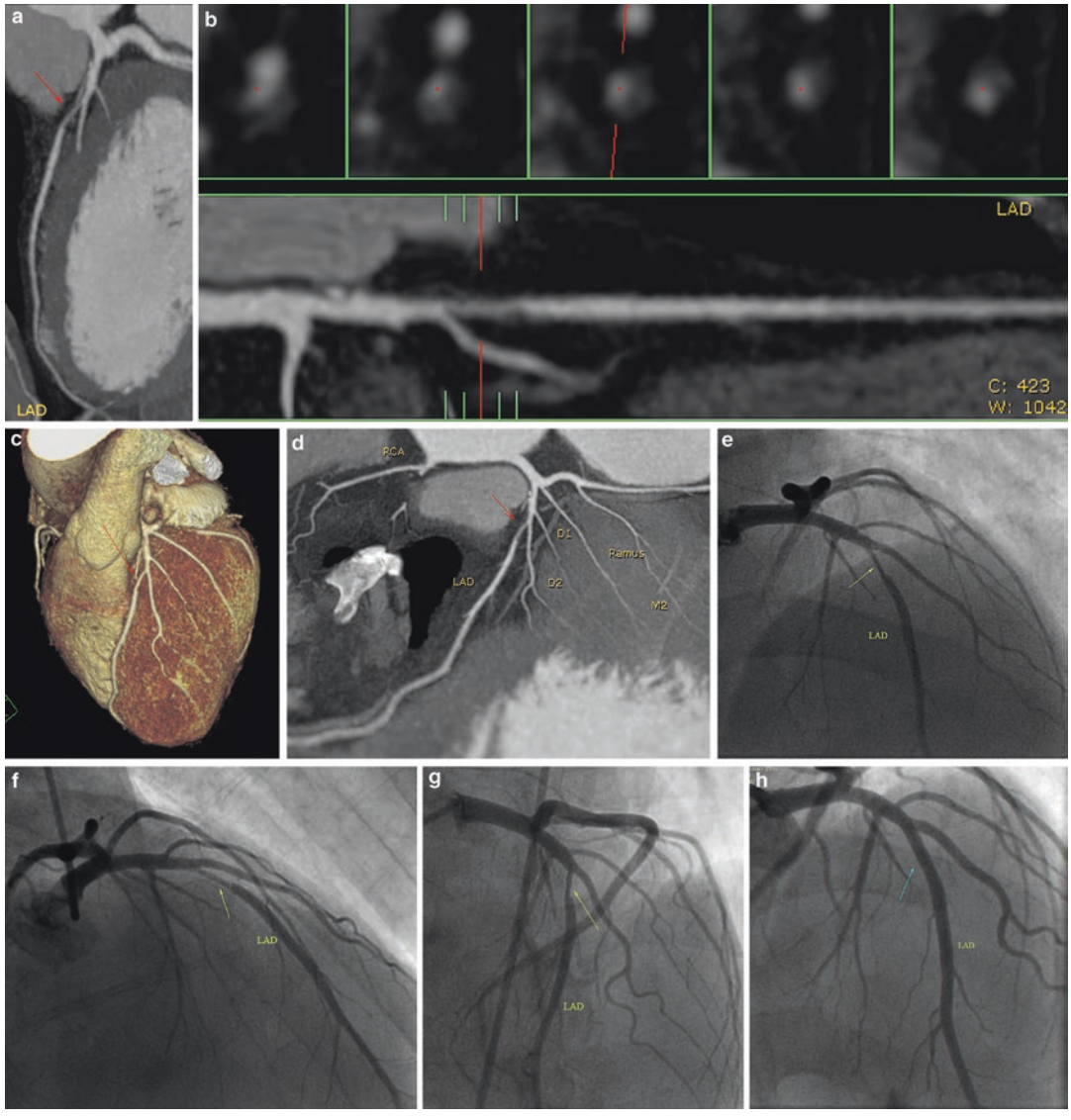

Fig. 6.15 (**a** and **b**) cMPR LM–LAD: High-grade stenosis (*arrow*). (**c** and **d**) 3D and 2D MAP: left anterior coronary artery (LAD) (*arrow*). (**e**–**g**) Angiogram (*arrow*). (**h**) Angiogram post-LAD stenting (*arrow*)

6.15.3 Diagnosis

The diagnosis is high-grade (70–80%) tubular stenosis in the mid-LAD.

6.15.4 Discussion

High-grade obstructing atheromatous plaques are commonly eccentric. This case demonstrates a variation, where there is circumferential narrowing of the lumen in the mid-LAD. Note that there is diminished contrast density in the stenotic segment that is estimated at 70–80% and confirmed on angiography (Fig. 6.15e–h).

6.15.5 Pearls and Pitfalls

With tubular stenosis, there is no change in luminal diameter with rotation of the curved multiplanar reconstructed images.

6.16 Case 6.16

6.16.1 History

A 53-year-old asymptomatic male presented with inferior wall ischemia on a routine nuclear perfusion exercise stress test.

6.16.2 Findings

There is chronic total occlusion in the mid-LAD. The mid-RCA has a predominantly non-calcified plaque causing high-grade stenosis that is proximal to a hypertrophied acute marginal artery. There is mild non-obstructive disease in the proximal left circumflex (Fig. 6.16a–d).

6.16.3 Diagnosis

Chronic total occlusion of the mid-LAD that is receiving retrograde collateral flow from the RCA. There is high-grade stenosis in the mid-RCA.

6.16.4 Discussion

When there is an occlusion of a major coronary artery, as in this case, three usual clinical scenarios may occur:

- An acute MI with sudden death, which occurs in approximately 50% of new acute coronary syndromes.
- A large MI, which may carry significant morbidity and disability.
- Nothing may occur, as in this case, and the patient may remain asymptomatic.

If the luminal stenosis is chronic, and enough time lapses for the development of collaterals, if and when the affected artery finally totally occludes, the collaterals may avert a myocardial infarct. This patient did not have a myocardial infarct. The distal LAD receives collateral retrograde flow from an acute marginal artery that is hypertrophied but was compromised proximal to its ostium by a high-grade obstructing, mostly non-calcified and potentially vulnerable plaque (Fig. 6.16a–d). The patient's life was considered to be at significant risk since the RCA is dominant and is supplying two major vascular territories.

The patient subsequently underwent coronary angiography with intervention of the mid-RCA lesion, with deployment of a drug-eluting stent. The patient did well and remained asymptomatic. A repeat nuclear perfusion scan 11 months later demonstrated inferior wall ischemia, for which a repeat cardiac CT was ordered. The new CTA demonstrated progression of disease, with a new high-grade stenotic complex plaque in the distal RCA (Fig. 6.16e–g). A repeat coronary angiogram was performed with stenting of the lesion (Fig. 6.16h–k).

It is important to note that ischemia at the myocardial cellular level is complex and not only dependent on large vessel coronary obstruction. Other factors include vasospasm, platelet and coagulation dysfunction, endothelial dysfunction, microvascular dysfunction, and inflammation.

6.16.5 Pearls and Pitfalls

Not only is it important to determine whether an atheroma is or is not flow limiting, but it is equally important to understand the overall coronary artery anatomy, as this case illustrates, the critical importance a lesion may have when other coronary territories are compromised. It can be hypothesized that if the plaque in the mid-RCA had ruptured, it likely would have caused a catastrophic event.

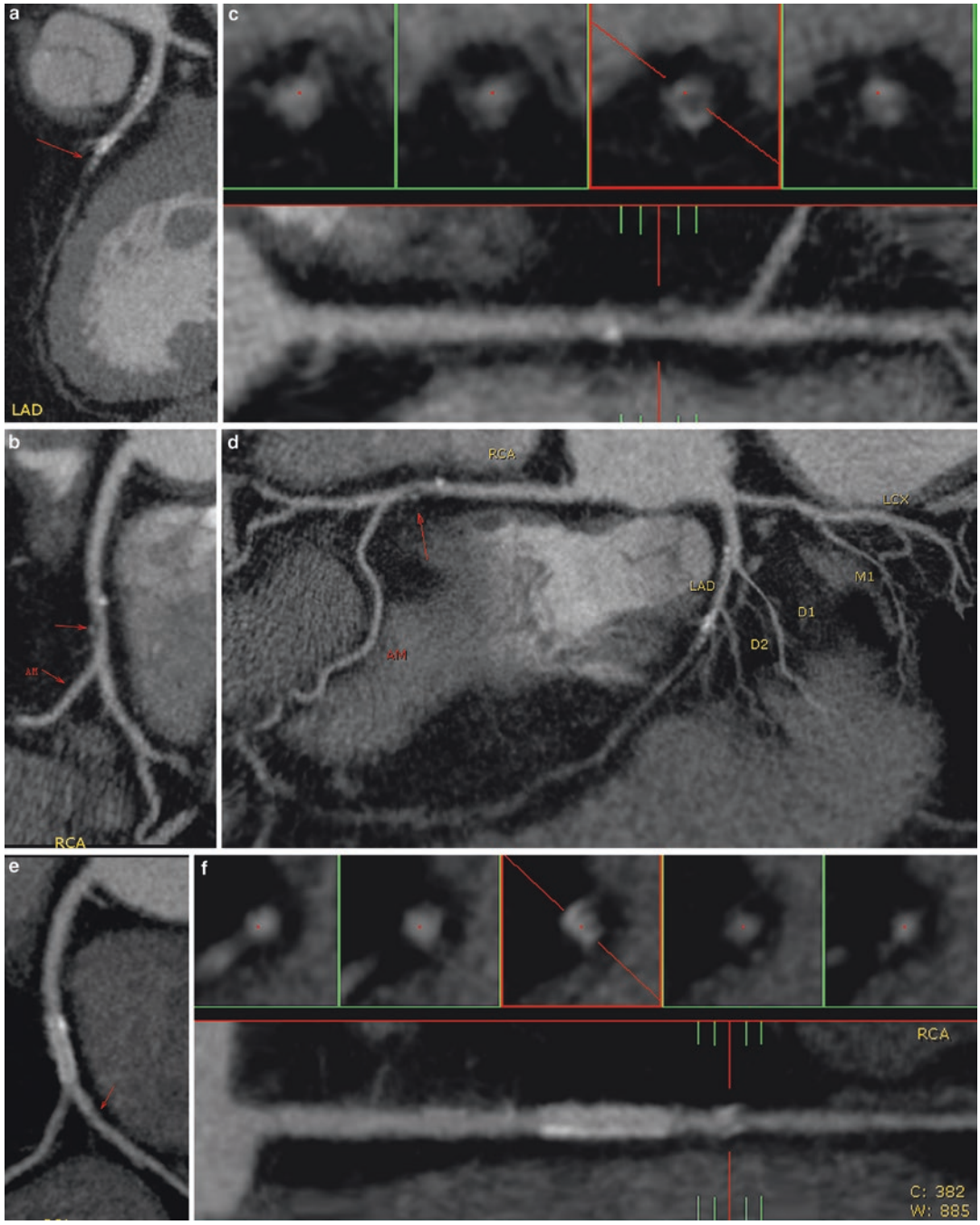

Fig. 6.16 (**a**) cMPR LM–LAD: Mid-left anterior coronary artery (LAD) chronic total occlusion (*arrow*). (**b**–**d**) RCA cMPR, stretched, and 2D MAP: Mid-RCA high-grade stenosis (*arrow*). (**e**–**g**) RCA cMPR, stretched, and 2D MAP: Repeat CTA at 11 months: patent stent in the mid-RCA. New high-grade stenosis in the distal RCA (*arrow*). Coronary angiogram. (**h**) RCA: distal RCA high-grade stenosis (*arrow*), stent (*double arrow*). (**i**) LAD chronic total occlusion (*arrow*). (**j**) Retrograde collateral flow into the distal LAD (*arrow*) from a hypertrophied acute marginal from the RCA. (**k**) Post-stenting of the RCA (*arrow*)

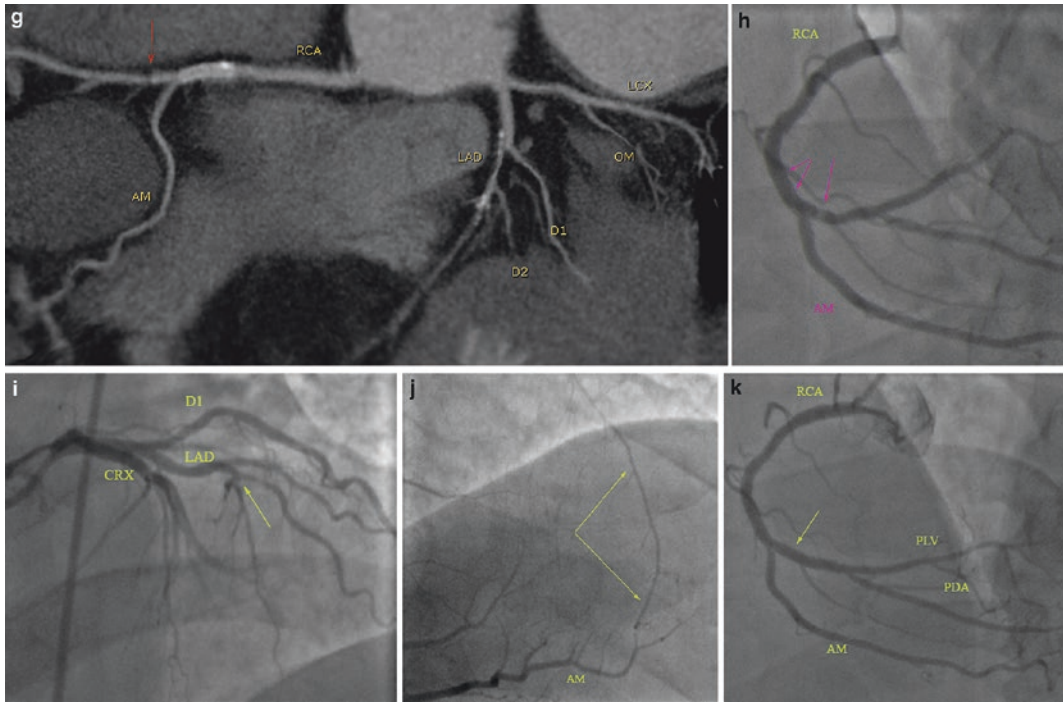

Fig. 6.16 (continued)

6.17 Case 6.17

6.17.1 History

A 50-year-old male presented with a history of a prior MI approximately 1 year ago and abnormal myocardial perfusion scan in the inferior wall.

6.17.2 Findings

There is a double lumen in the proximal LAD (Fig. 6.17a, b). The RCA has a proximal segment intimal flap. The distal segment of the RCA has high-grade stenosis with a chronic hematoma in the wall (Fig. 6.17c, d). There is subendocardial

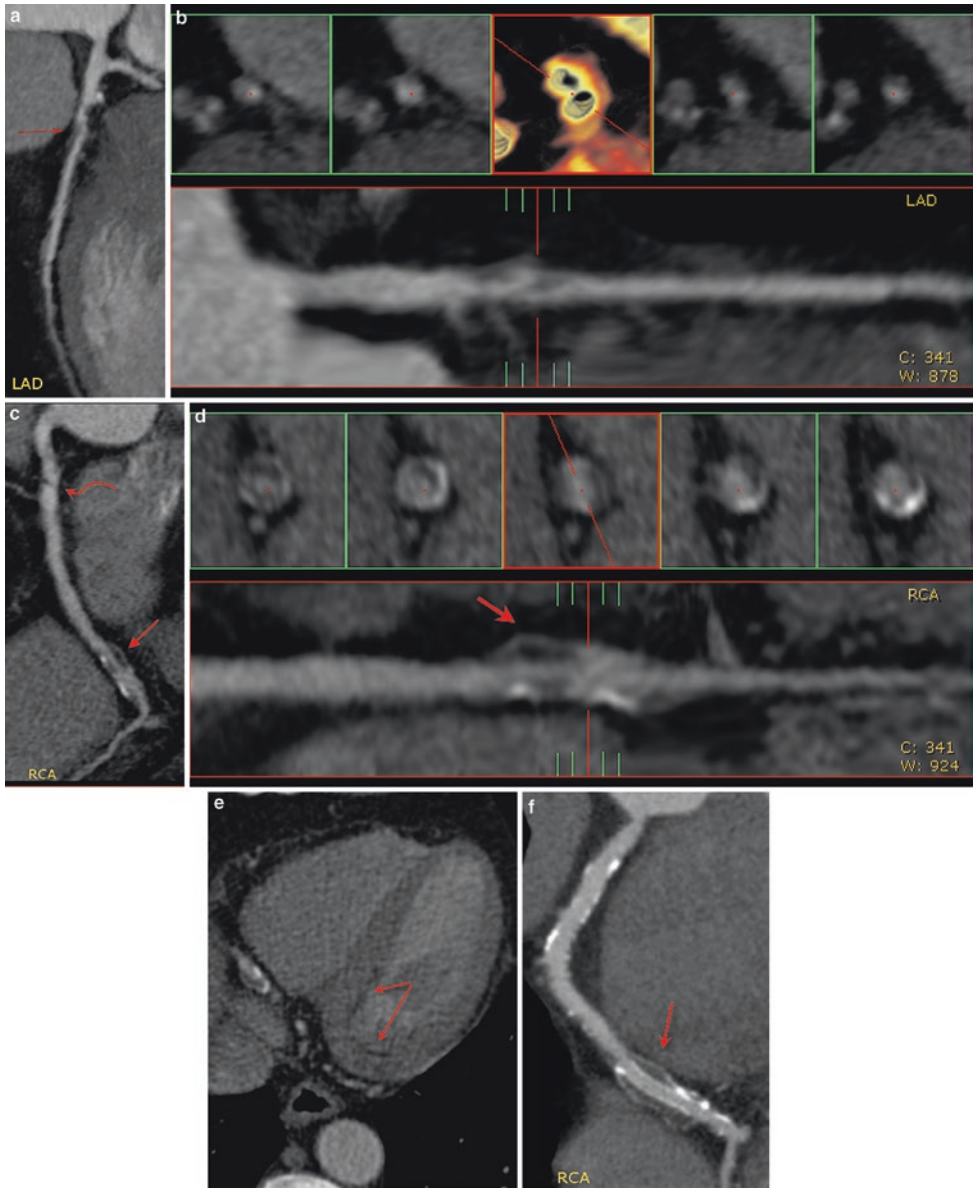

Fig. 6.17 (**a** and **b**) cMPR and stretched LM–LAD: Proximal left anterior coronary artery (LAD) dissection with a double lumen on the cross section (**b**) (*arrow*). (**c** and **d**) RCA cMPR, stretched: Proximal segment dissection (*curved arrow*). Distal segment post-balloon angioplasty wall hematoma and high-grade restenosis (*arrow*). (**e**) Axial, posterior LV wall low-density scarring from a chronic subendocardial MI (*arrows*). (**f**) Comparison case from a different patient: Postangioplasty and stenting of the distal RCA. Chronic artery wall hematoma (*arrow*)

low density in the posterior wall of the left ventricle (Fig. 6.17e).

6.17.3 Diagnosis

Chronic dissection in the proximal LAD. There is a localized dissection in the proximal RCA. There are post-balloon angioplasty (PTCA) changes in the distal RCA, with high-grade restenosis. Chronic inferior wall subendocardial MI.

6.17.4 Discussion

The patient was admitted approximately 1 year before to a local university teaching hospital with an acute coronary syndrome. The patient underwent coronary angiography, with ballooning of the distal RCA. A stent was not deployed. The CCTA demonstrated findings typical of overexpansion of a balloon with a chronic hematoma in the artery wall and restenosis. For comparison, Fig. 6.17f represents a different patient who underwent PCI of the distal RCA, with deployment of a stent and with a similar chronic hematoma in the adjacent wall of the artery.

About 30–50% of patients with successful balloon angioplasty (no stent) may develop recurrent narrowing (restenosis) at the site of the balloon inflation, usually within 6 months following intervention. Restenosis occurs with a significantly higher frequency in patients with diabetes and other comorbidities. The dissections in the LAD and in the proximal RCA were likely a complication from the procedure and not spontaneous.

Percutaneous coronary intervention, which depends on mechanical dilatation of the artery or ablation of atherosclerotic plaque, is requisitely associated with plaque fracture, intimal splitting, and localized medial dissection; these tears may extend into the media for varying distances and may even extend through the adventitia resulting in frank perforation.

The National Heart, Lung and Blood Institute classification system for intimal tears, developed by the Coronary Angioplasty Registry, was put forth in the pre-stent era for the classification of dissection types after balloon angioplasty. Dissections in this scheme are graded based on their angiographic appearances as types A through F.

Type A dissections represent minor radiolucent areas within the coronary lumen during contrast injection with little or no persistence of contrast after the contrast has cleared. Type B dissections are parallel tracts or a double lumen separated by a radiolucent area during contrast injection, with minimal or no persistence after contrast clearance. Type C dissections appear as contrast outside the coronary lumen *(extraluminal cap)* with persistence of contrast after contrast has cleared from the lumen. Type D dissections represent spiral *(barber shop pole)* luminal filling defects, frequently with excessive contrast staining of the dissected false lumen. Type E dissections appear as new, persistent filling defects within the coronary lumen. Type F dissections represent those that lead to total occlusion of the coronary lumen without distal antegrade flow. In rare cases, a coronary artery dissection may propagate retrograde and involve the ascending aorta.

Although infrequent, coronary artery dissection can occur spontaneously and may involve single or multiple coronary arteries. The incidence of spontaneous coronary dissection occurs at rates of 0.1–0.28% of all angiographic studies.

6.17.5 Pearls and Pitfalls

A spontaneous ruptured plaque, with an intramural hematoma, may have a similar appearance on CT as a result of balloon angioplasty. However, a ruptured plaque is usually short segment as opposed to the long segment of disease demonstrated in this case. In a coronary artery dissection, visualizing the cross-sectional image with color can be helpful to demonstrate the double lumen.

6.18 Case 6.18

6.18.1 History

An 81-year-old male presented with a history of exertional chest pain.

6.18.2 Findings

There is a long complex non-calcified and calcified plaque extending from the distal left main into the proximal LAD, causing high-grade stenosis. There is also a mixed plaque in the mid-LAD that appears flow limiting (Fig. 6.18a, b). The RCA is a large-caliber

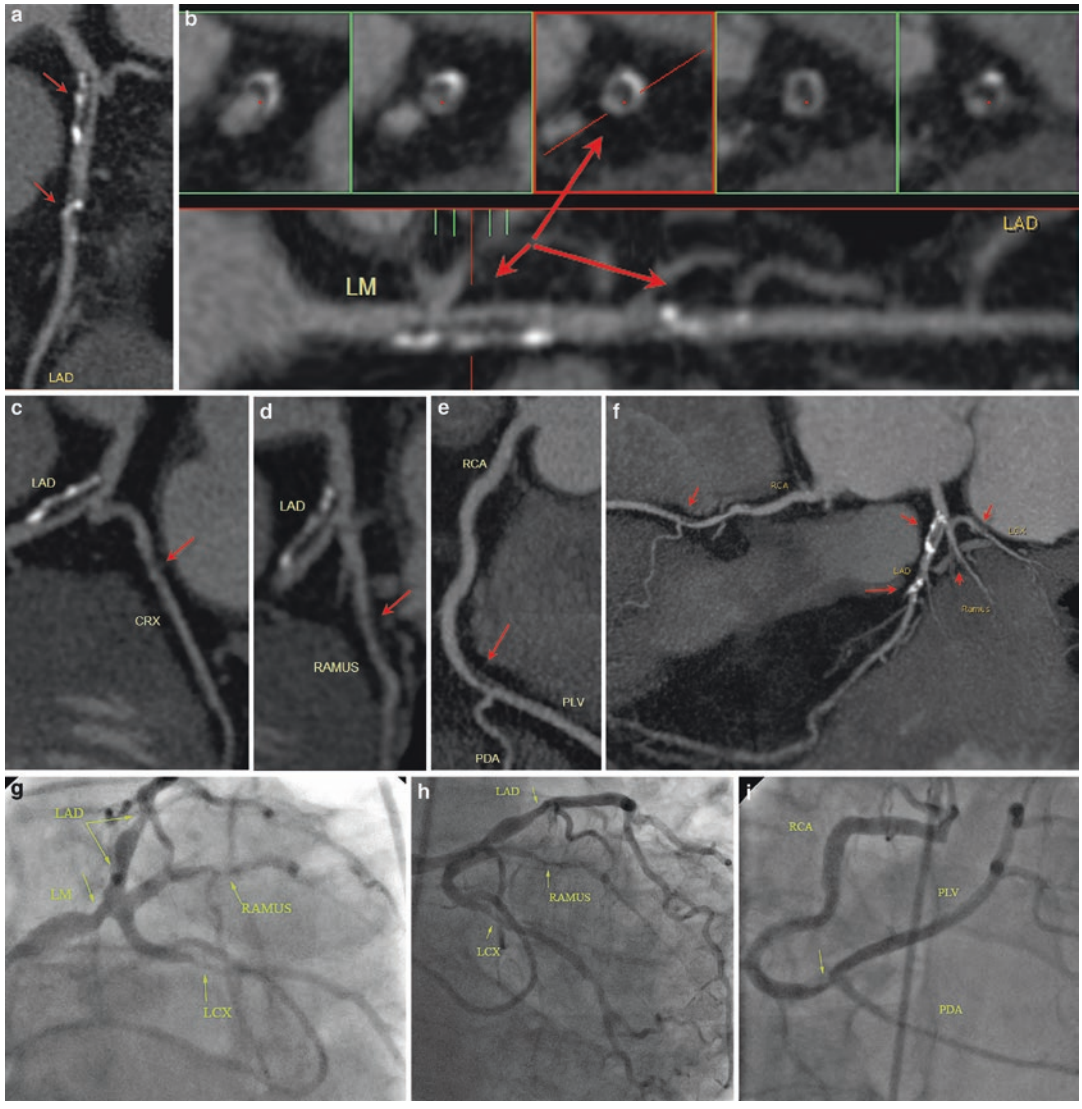

Fig. 6.18 (**a** and **b**) cMPR and stretched LM–LAD: Distal left main coronary artery and left anterior coronary artery (LAD) stenosis (*arrows*). (**c**) LCX cMPR: non-calcified plaque in the proximal segment causing high-grade obstruction. (**d**) Ramus: non-calcified in the proximal segment causing high-grade obstruction. (**e**) CA cMPR: Distal segment borderline high-grade stenosis (*arrow*). (**f**) 2D MAP: multi-vessel high-grade stenosis (*arrows*). (**g–i**) Coronary angiography correlation

dominant artery and has a non-calcified plaque in the distal segment that appears borderline flow limiting (Fig. 6.18c). Also, there is non-calcified plaque causing high-grade stenosis in the proximal left circumflex and also in the ramus intermedius artery (Fig. 6.18d, e).

6.18.3 Diagnosis

Multi-vessel coronary artery disease with high-grade stenosis.

6.18.4 Discussion

The patient underwent coronary angiography, and it was believed that there was no high-grade stenosis in the left main, LAD, and left circumflex coronary arteries. Subsequent stenting of the distal RCA and ramus intermedius arteries was performed.

The case illustrates the potential benefit of a cardiac CT prior to coronary angiography. However, good communication between the CT interpreter and the angiographer is needed to integrate the CT findings and other diagnostic studies. The CT can also serve as a roadmap for the angiographer to focus on significant findings and planning of the intervention. It would have been indicated in this case to have performed a fractional flow reserve (FFR) in the left main coronary artery, LAD, and left circumflex. And if performed at the time, it seems likely that surgical revascularization would have been recommended.

It is documented in the literature that conventional coronary angiography (luminogram) commonly underestimates coronary artery stenosis. Furthermore, it has been demonstrated with pathology correlation that when a vessel is visually estimated to have 70% stenosis on the angiogram, there is 90% stenosis on the pathology specimen.

6.18.5 Pearls and Pitfalls

When the findings on CCTA and coronary angiogram do not correlate, particularly in a symptomatic patient, further studies with FFR may be indicated to clarify the discordant interpretations. Patient expired within a year from a massive MI.

6.19 Case 6.19

6.19.1 History

A 66-year-old asymptomatic male presented with a history of questionable abnormal myocardial perfusion scan in the LV apex.

6.19.2 Findings

There is high-grade critical stenosis in the mid-RCA by a non-calcified plaque (Fig. 6.19a, b). The rest of the coronary arteries had no significant disease. Coronary anatomy is right dominant.

6.19.3 Diagnosis

High-grade critical stenosis in the mid-RCA.

6.19.4 Discussion

A coronary angiogram was subsequently performed, confirming the findings on the CT and with successful stenting of the RCA (Fig. 6.19c, d).

6.19.5 Pearls and Pitfalls

The patient did not undergo a previous calcium score but would have been reported as 0. This finding is not surprising since one of the limitations of the calcium score scan is the inability to detect non-calcified plaques. In a study that evaluated 668 consecutive symptomatic patients undergoing CT coronary angiography, 7% of patients with a calcium score of 0 had obstructive coronary disease [1].

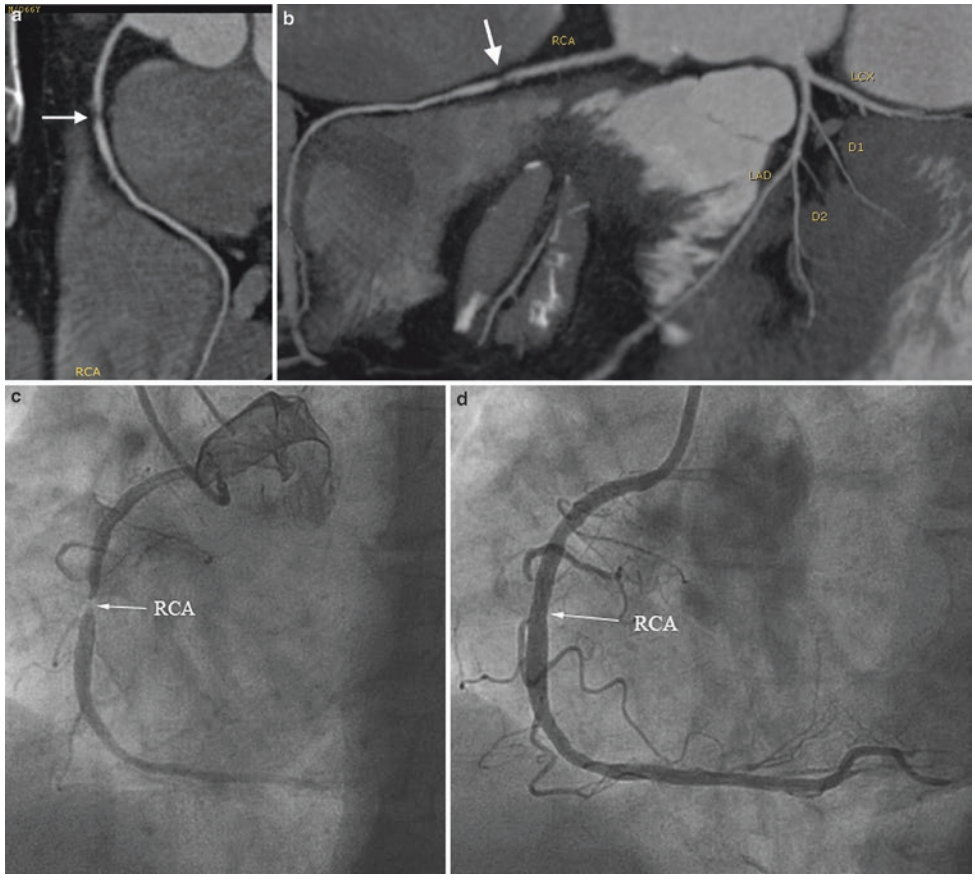

Fig. 6.19 (**a** and **b**) Prospective gated axial cMPR, 2D composite: High-grade critical obstruction in the mid-RCA by a non-calcified plaque (*arrow*). (**c** and **d**) Coronary angiogram before and after stenting

6.20 Case 6.20

6.20.1 History

A 54-year-old female marathon runner presented with new onset exertional chest discomfort. No risk factors. Negative ECG and biomarkers. Initially sent home from the ED and subsequently referred for an outpatient CCTA.

6.20.2 Findings

There is a critical ostial LAD obstruction with non-calcified plaque in the proximal LAD causing a high-grade obstruction (Fig. 6.20a, b).

6.20.3 Diagnosis

Non-calcified plaque causing a critical obstruction in the proximal LAD.

6.20.4 Discussion

This case highlights the importance of performing a cardiac CT in an emergency department setting, in patients that are in low- to intermediate-risk categories. That particular ED, since then, is currently performing CCTA.

Despite the presence of a life-threatening disease, the patient was discharged from the ED, demonstrating a failure that can occur with the

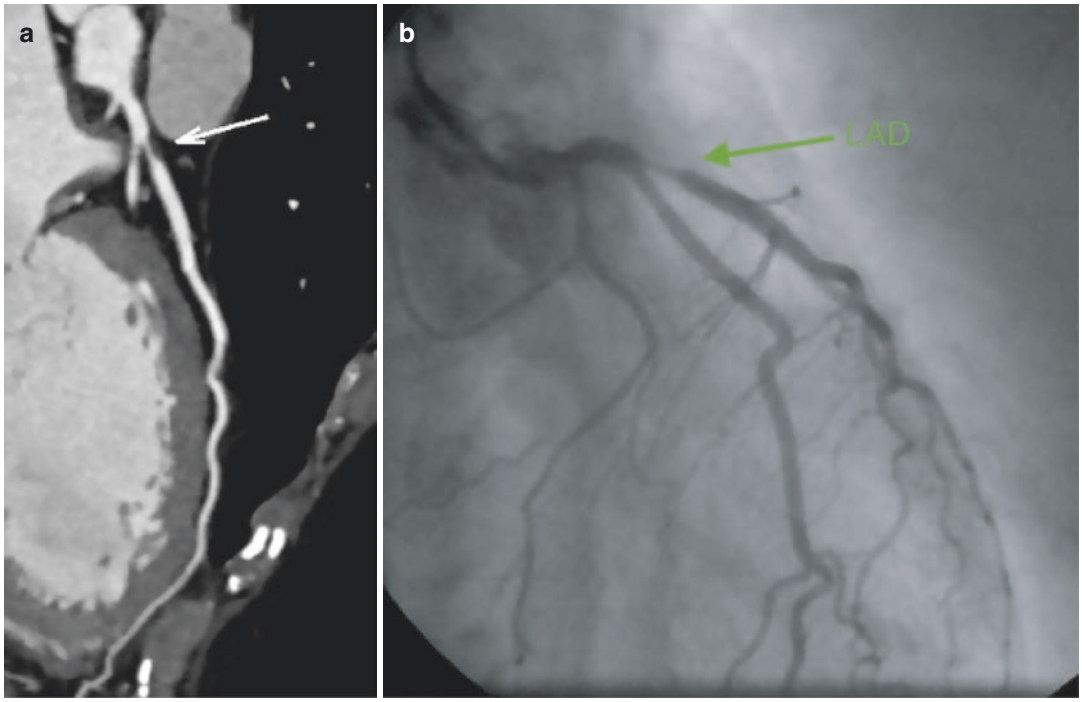

Fig. 6.20 (**a**) cMPR: Critical left anterior descending artery obstruction (*arrow*). (**b**) Coronary angiogram

usual standard of care with serial EKGs and troponins. She did not undergo a nuclear stress test, which may have yielded a normal study, since the patient is a marathon runner and likely not able to achieve an optimal exercise tolerance (stress irrelevant).

Luckily, the patient's friend who is a doctor referred her to our private office the following day for the CCTA. The patient was referred back to the hospital for an invasive coronary angiogram, with subsequent cardiac surgical revascularization.

6.20.5 Pearls and Pitfalls

Without the CCTA, the patient was at a high risk for an acute myocardial infarct, which could have resulted in death. It is estimated that in one out of four patients, the first symptom of coronary artery disease is sudden death. Additionally, approximately half of patients that sustain a first MI result in death from a fatal arrhythmia.

It is worthy to note that a calcium score would have been zero and likely have led to erroneous risk stratification. It has been reported that up to 15% of patients with cardiac symptoms have a very low or zero calcium score.

On a side note, this case was very helpful in convincing the medical staff at the hospital of the necessity to add CCTA to the chest pain center in the ED, which was subsequently and successfully established.

6.21 Case 6.21

6.21.1 History

A 53-year-old male presented with exertional chest pain. No previous cardiac history.

6.21.2 Findings

There is a multi-vessel coronary artery disease with a ruptured plaque in the mid-LAD causing critical obstruction (Fig. 6.21a, b). There is also a low-density lipid-rich appearing mixed plaque at the ostium of the LAD.

6.21.3 Diagnosis

Critical obstruction in the proximal LAD from a ruptured plaque.

6.21.4 Discussion

It is now better understood that atheromatous plaque accumulation growth and ruptures are multi-phasic, not a linear process. Plaques that are non-obstructing are known to grow and become obstructive in a relatively short period of time, as little as few months [2].

6.21.5 Pearls and Pitfalls

Plaques that are predominantly non-calcified are much easier to accurately quantify the degree of obstruction.

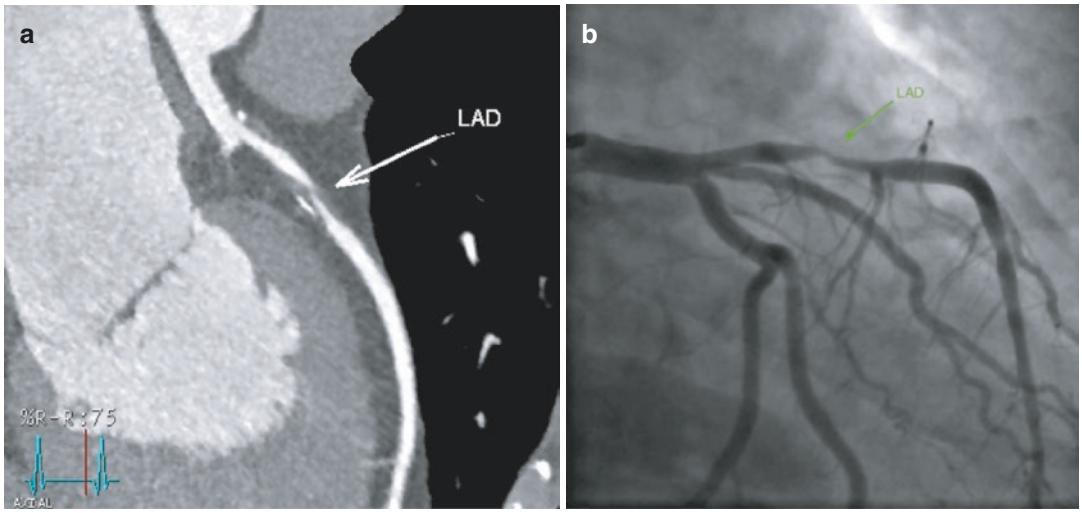

Fig. 6.21 (**a**) cMPR. (**b**) Coronary angiogram

6.22 Case 6.22

6.22.1 History

A 51-year-old male with past medical history of hypertension, presented with atypical chest pain for 1 month. An EKG and a recent myocardial perfusion scan were interpreted as normal.

6.22.2 Findings

High-grade obstruction at the ostium of the LAD and chronic total occlusion (CTO) in the mid-LAD (Fig. 6.22a–c). There is a high-grade obstruction in the mid-RCA (Fig. 6.22d, e).

6.22.3 Diagnosis

CTO of the LAD and high obstruction in the mid-RCA with epicardial collaterals.

6.22.4 Discussion

Since the patient had a CTO of the LAD without a myocardial infarct, there was a retrograde flow from the RCA collateralizing the distal LAD. The high-grade obstruction in the RCA was likely the cause of chest pain due to decreased perfusion to a large territory of the myocardium, which placed patient at a very high risk for a fatal cardiac event.

6.22.5 Pearls and Pitfalls

CTOs can easily be identified in major coronary branches on the CCTA by observing a transition of contrast density (transition zone) of high to low between the non-occluded and occluded coronary segments.

It is helpful to report the length of the occlusion and the type of the plaque in the coronary segment, in order to assess whether catheter-based revascularization may be attempted.

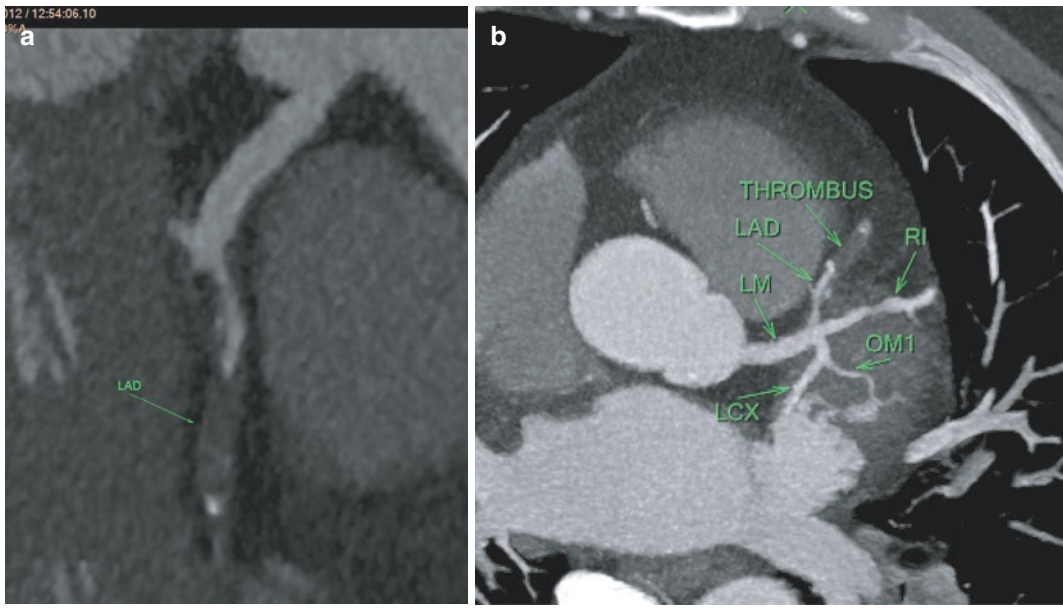

Fig. 6.22 (**a**) cMPR (**b**) Axial. (**c**) Coronary angiogram—Left (**d**) cMPR (**e**) Coronary angiogram—Right

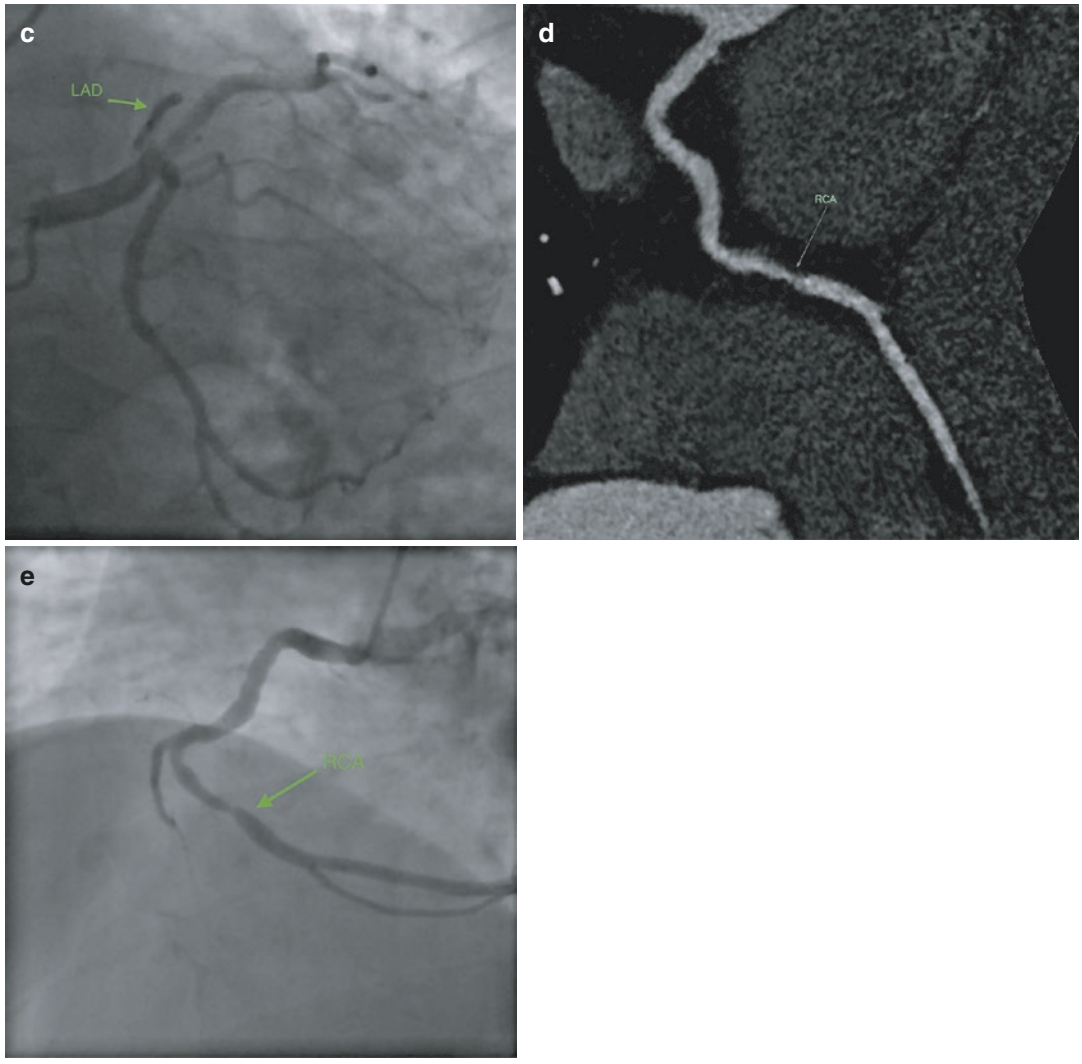

Fig. 6.22 (continued)

6.23 Case 6.23

6.23.1 History

A 60-year-old male presented to the hospital with stable chest pain.

6.23.2 Findings

Presence of a significant multi-vessel coronary artery disease. There is a critical obstruction in the mid-RCA (Fig. 6.23a, b) as well as a very short high-grade obstruction at the ostium of the LAD confirmed with invasive coronary angiography (Fig. 6.23c–e).

6.23.3 Diagnosis

High-grade short-segment obstruction at the ostium of the LAD and multiple obstructions in the RCA.

6.23.4 Discussion

This case demonstrates multiple significant coronary obstructions. The short-segment obstruction in the LAD can be easily missed with the CCTA if one does not pay careful attention. The obstruction in the RCA was much easier to identify.

6.23.5 Pearls and Pitfalls

Short-segment ostial major coronary branch obstructions are much easier to identify with the CCTA than with invasive coronary angiography. It is important to alert the angiographer of these findings in order to not miss a critical finding. In this case, the angiographer had a very difficult time identifying the ostial LAD obstruction and had to resort to FFR for confirmation, which changed the management from catheter to surgical intervention.

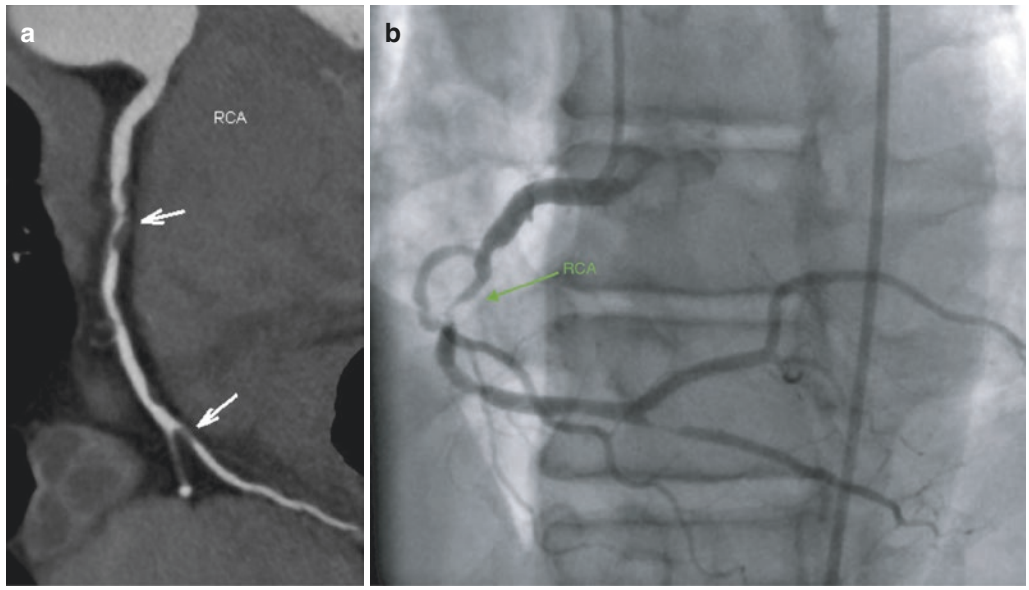

Fig. 6.23 (**a**) cMPR. Obstructions seen in RCA (*arrow*) (**b**) Coronary angiogram (**c**) cMPR; the ostial obstruction of the left main coronary artery (*arrow*) (**d** and **e**) Coronary angiography

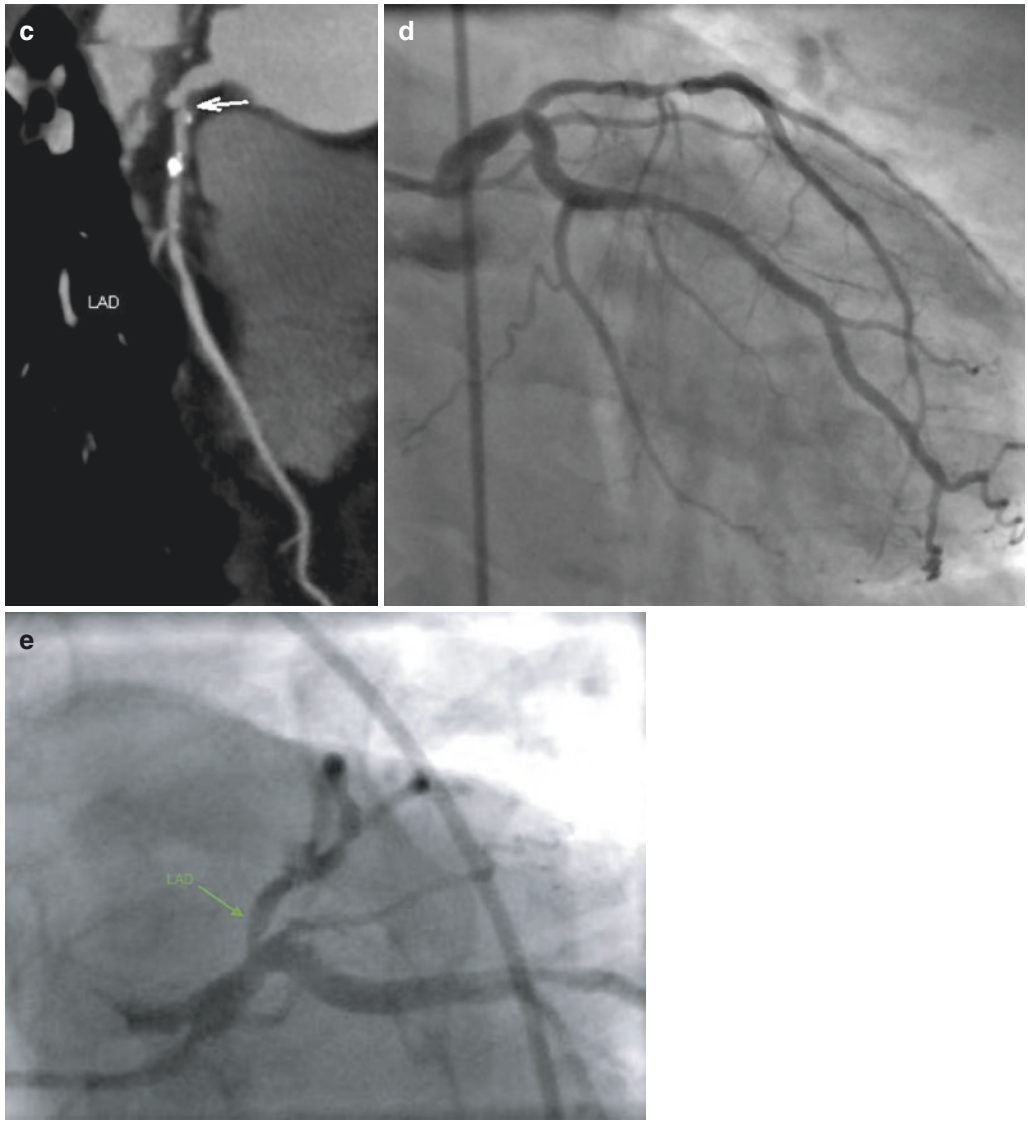

Fig. 6.23 (continued)

6.24 Case 6.24

6.24.1 History

A 60-year-old male with acute severe epigastric pain. History of hyperlipidemia and no previous cardiac disease. Nonspecific ECG changes and negative serial troponins. Initially, the atypical chest pain was attributed to severe gastritis.

6.24.2 Findings

Numerous mixed plaques seen in the proximal LAD with an acute thrombus in the mid-LAD causing a total occlusion (Fig. 6.24a–d).

6.24.3 Diagnosis

Acute thrombus in the mid-LAD.

6.24.4 Discussion

The patient was thought to have acute severe gastritis with atypical chest symptoms. Luckily, the CCTA was ordered, which demonstrated a thrombus with a complete occlusion in the LAD (Fig. 6.24a–c). Note the contrast low-density transition change in the occluded segment. The patient was transported directly from the CT suite to the catheterization lab for an emergency angiogram, which confirmed the findings on the CCTA. The area of the obstruction in the mid-LAD was successfully stented with excellent results (Fig. 6.24e).

6.24.5 Pearls and Pitfalls

This case highlights the importance of communicating critical findings in order to help improve patient outcomes. This patient had immediate intervention after the CCTA without having sustained a myocardial infarction. The patient is the father of an employee of the hospital. To say the least, they were extremely grateful for the service provided.

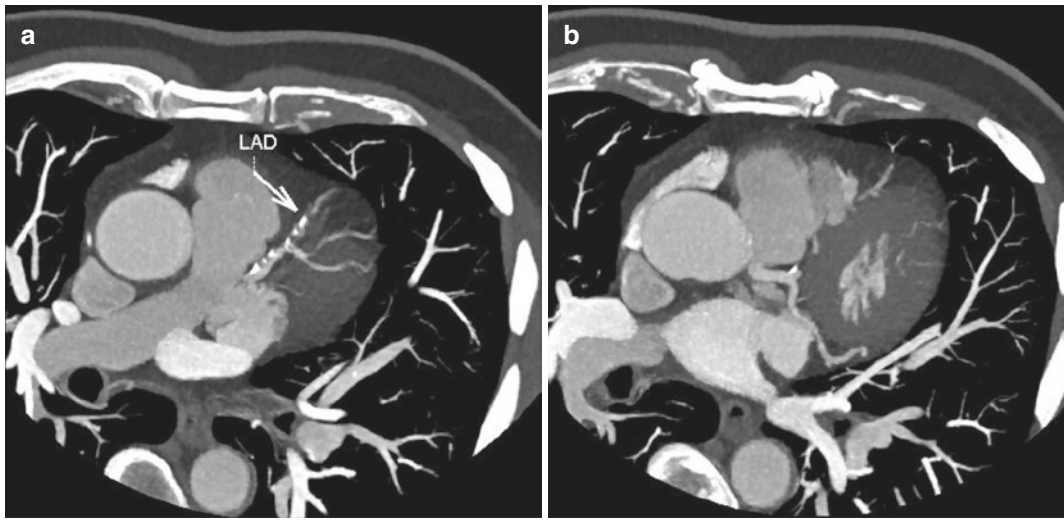

Fig. 6.24 (**a**–**c**) Serial Axial MIP (**d**) Coronary angiogram: pre-intervention (**e**) Coronary angiogram: post-PCI

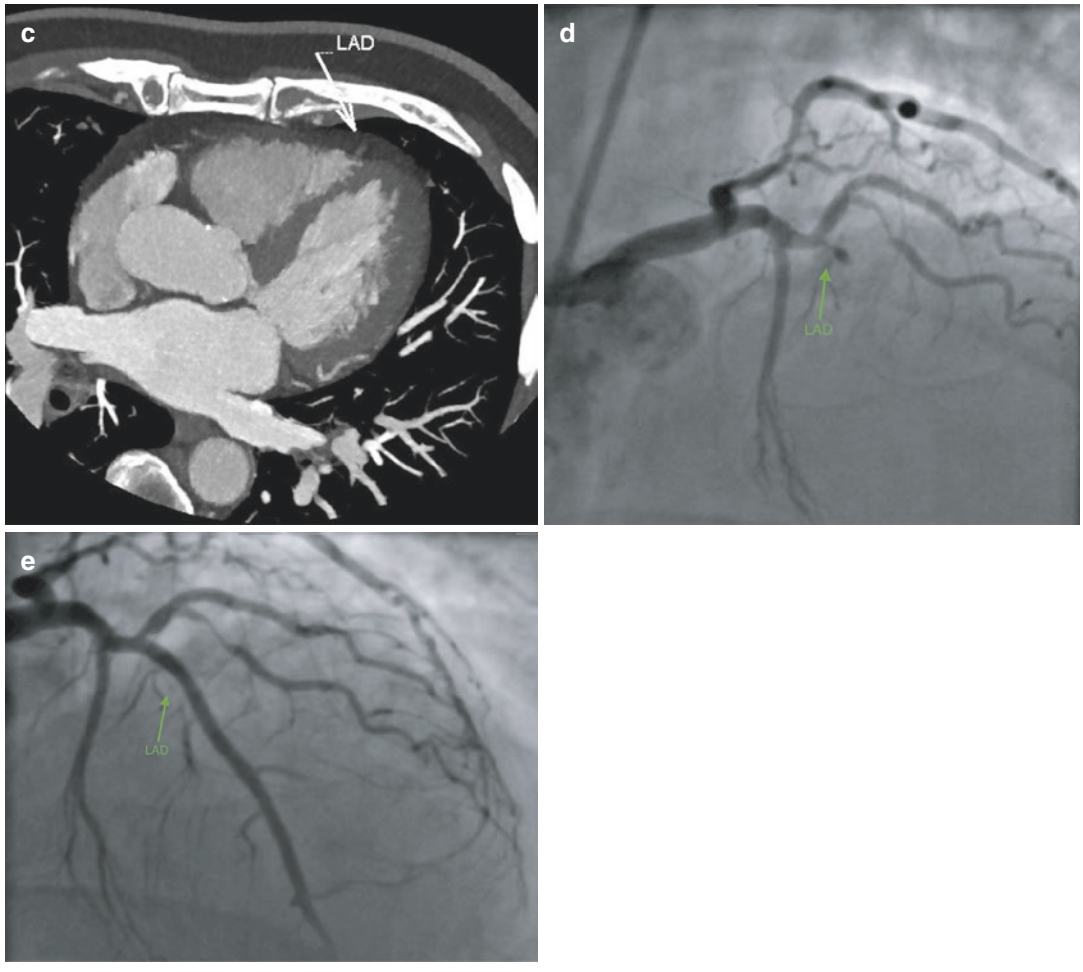

Fig. 6.24 (continued)

6.25 Case 6.25

6.25.1 History

A 62-year-old female presented with chest pain. Normal EKG and stress test.

6.25.2 Findings

A critical short-segment ostial lesion at the left circumflex artery with a separate ostium from the LAD (Fig. 6.25a–c). No critical lesions in the LAD. Coronary circulation is left dominant.

6.25.3 Diagnosis

A critical obstruction at the ostial LCX.

6.25.4 Discussion

This is potentially a life-threatening lesion, in this patient with a left dominant system. It is important for the angiographer to know these findings prior to the angiogram in order to avoid occluding the LCX with the catheter tip. Again, ostial short-segment stenosis can be easily missed on angiography and may require, as in this case, magnification views to better assess intervention (Fig. 6.25c).

6.25.5 Pearls and Pitfalls

Short-segment critical lesions in the coronary arteries can be easily missed on CCTA without appropriate reconstruction and segmentation of the coronary tree.

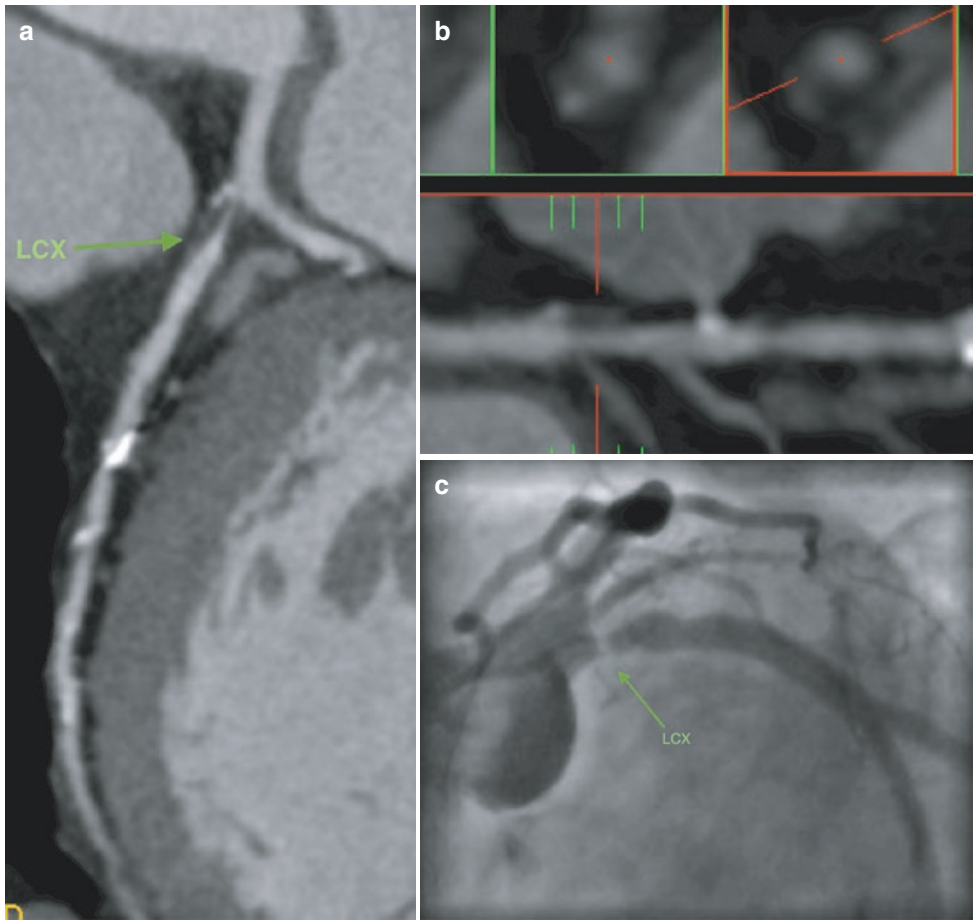

Fig. 6.25 (**a**) cMPR (**b**) Stretched cMPR (**c**) Coronary angiogram

6.26 Case 6.26

6.26.1 History

A 61-year-old male with a mild area of ischemia on exercise echocardiogram.

6.26.2 Findings

There is a significant coronary artery disease. There are ischemic appearing changes in the anteroseptal wall with hypokinesis (Fig. 6.26a). There is an appearance of chronic total occlusion of the mid-LAD (Fig. 6.26b–e).

6.26.3 Diagnosis

Chronic total occlusion of the LAD with ischemic changes seen on anteroseptal wall.

6.26.4 Discussion

Poorly collateralized segments of total coronary occlusions can demonstrate hypoperfusion of the effected myocardial segment and are seen as areas of low density on the CCTA.

6.26.5 Pearls and Pitfalls

Ischemia in the myocardium can be inferred from the CCTA in areas of low density with preserved thickness of the myocardium.

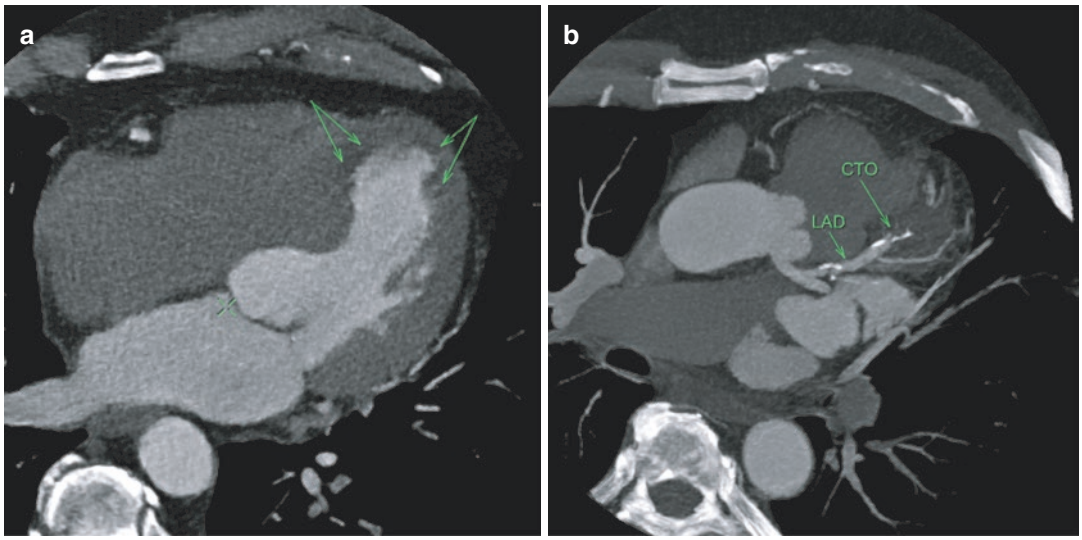

Fig. 6.26 (**a**) Axial MIP. Areas of ischemia indicated by *arrows*. (**b**) Axial MIP demonstrating a chronic total occlusion of the mid LAD. (**c**) cMPR. (**d**-**e**) Coronary angiogram

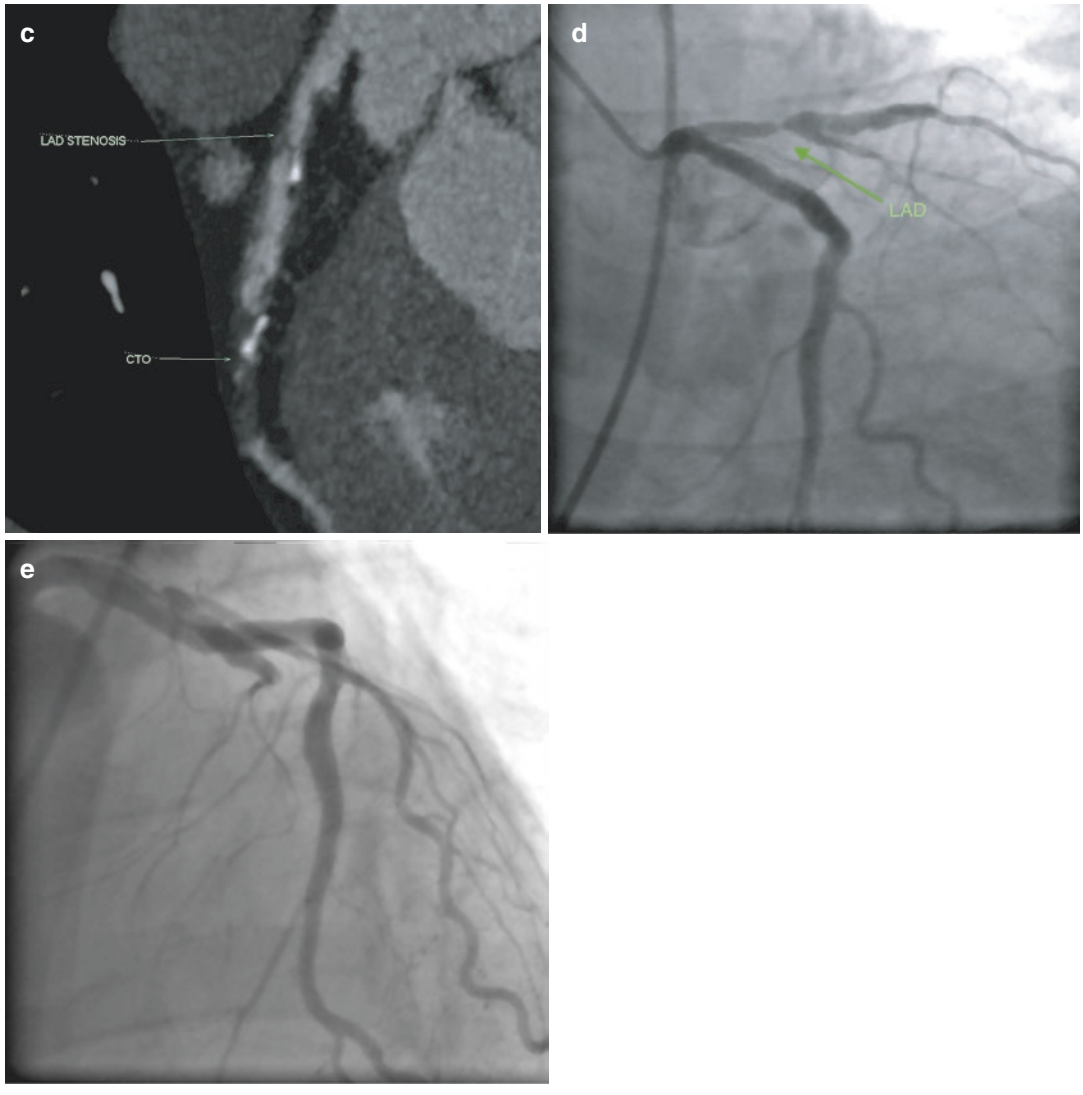

Fig. 6.26 (continued)

6.27 Case 6.27

6.27.1 History

A 63 year-old male with a 20-year history of a myocardial infarction treated medically. The patient did not have a coronary angiography.

The patient is an avid tennis player and underwent an echocardiogram showing questionable mass in the left atrium. A cardiac CTA was ordered for the evaluation of a cardiac mass.

6.27.2 Findings

There is a persistent left superior vena cava with dilatation of the coronary venous sinus (Fig. 6.27a, b).

There is a critical obstruction in the proximal LAD, which has a small atherosclerotic aneurysm (Fig. 6.27c). There is a high-grade obstruction in the proximal RCA with appearance of a chronic ruptured plaque and/or recanalized thrombus (Fig. 6.27d). There is a diffuse multivessel disease.

6.27.3 Diagnosis

Persistent left superior vena cava. Absence of a right superior vena cava.

Severe obstructing multi-vessel coronary artery disease.

6.27.4 Discussion

The patient was lucky to have a CCTA, which was done to evaluate for a left atrial mass seen on an echocardiography, which turned out to correspond to a dilated coronary venous sinus. There was no mass in the left atrium.

There was a life-threatening multi-vessel coronary artery disease with poor collateral formation (Fig. 6.27f, g). It is incredible that the patient was able to play competitive tennis for 4–5 days a week without cardiac symptoms. The patient underwent a surgical revascularization with double internal mammary grafts and within 6 weeks, he was back playing tennis.

6.27.5 Pearls and Pitfalls

Congenital vascular anomalies are not infrequently confused with a cardiac mass on echocardiography. CCTA can easily identify and definitively diagnose this type of vascular anomaly.

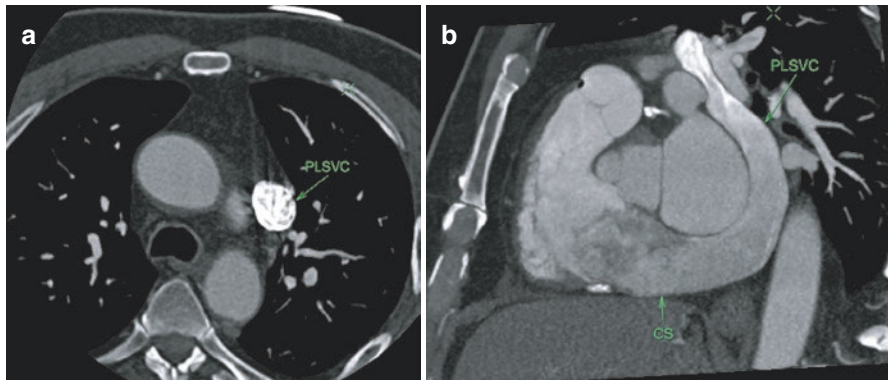

Fig. 6.27 (**a**) Axial MIP showing persistent left SVC (**b**) Sagittal MIP (**c**) cMPR-LM (**d**) cMPR-RCA (**e**) stretched cMPR (**f**) Left coronary angiogram (**g**) Right coronary angiogram

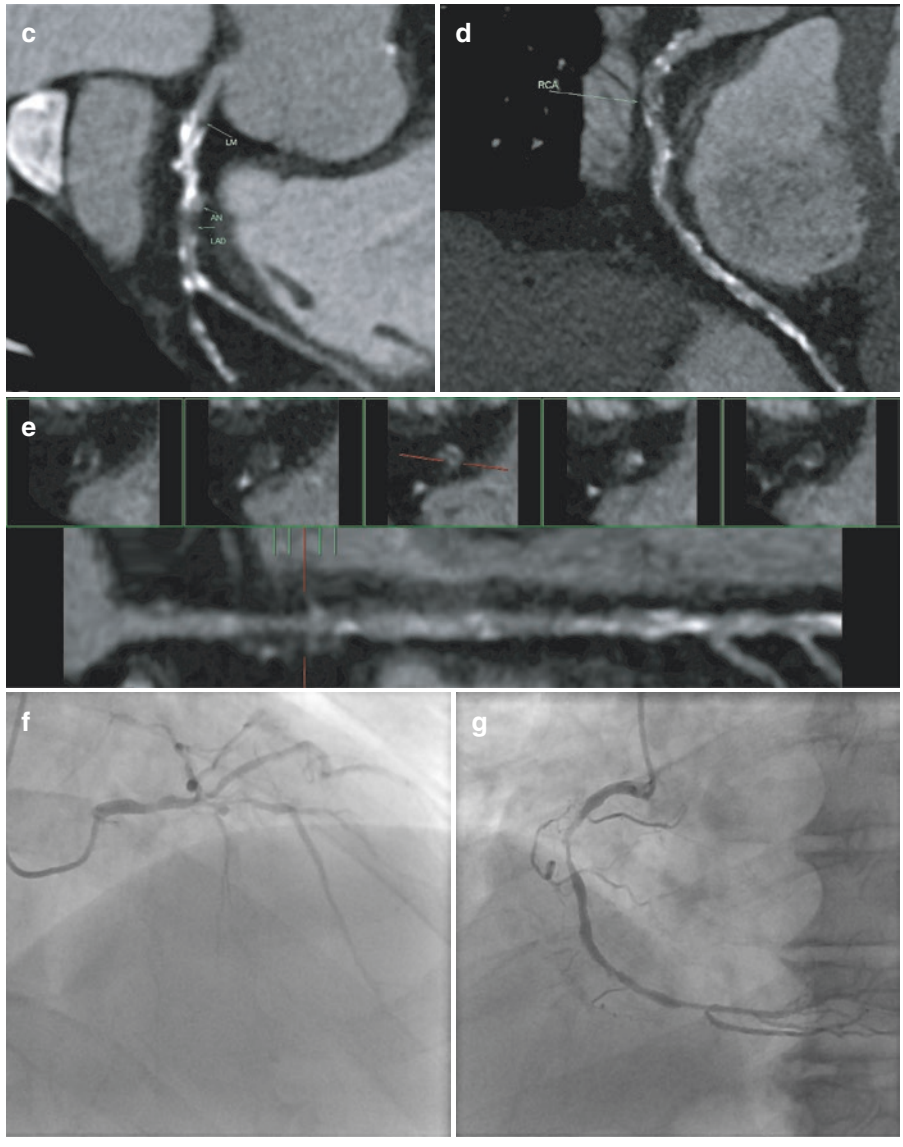

Fig. 6.27 (continued)

6.28 Case 6.28

6.28.1 History

A 49-year-old male with a past medical history of hyperlipidemia, hypertension, and diabetes, presented to the hospital with atypical chest pain.

6.28.2 Findings

There is an advanced diffuse multi-vessel coronary artery disease without a flow limiting stenosis (Fig. 6.28a–d). Coronary circulation is right dominant. There is an ovoid low-density nodule in the right cardiophrenic angle fat pad consistent with a pericardial cyst, which is of no clinical significance (Fig. 6.28e).

6.28.3 Diagnosis

Metabolic syndrome with advanced diffuse coronary artery disease.

6.28.4 Discussion

It is uncommon to see diffuse advanced coronary artery disease in this age group, which should raise the question of an underlying severe metabolic disorder.

Metabolic syndrome consists of five chronic conditions: central obesity, hypertension, diabetes, hyperlipidemia, and hypertriglyceridemia, all of which this patient had. Patients with metabolic syndrome are at high risk of developing cardiovascular disease.

6.28.5 Pearls and Pitfalls

Patients with metabolic syndrome with stable angina require aggressive optimal medical therapy in order to avoid a future cardiovascular event.

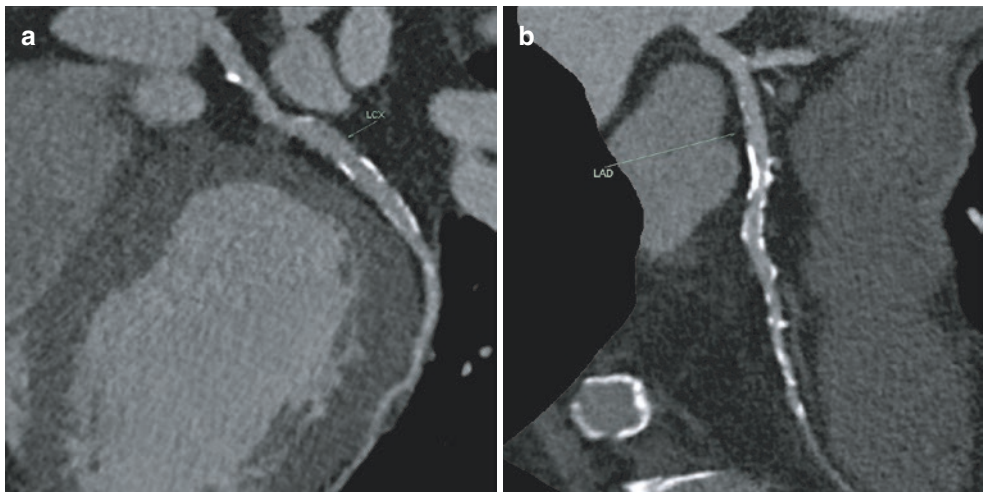

Fig. 6.28 (**a**) cMPR-LCX (**b**) cMPR-LAD (**c**) cMPR-RCA (**d**) Coronary tree (**e**) Axial MIP demonstrating pericardial cyst

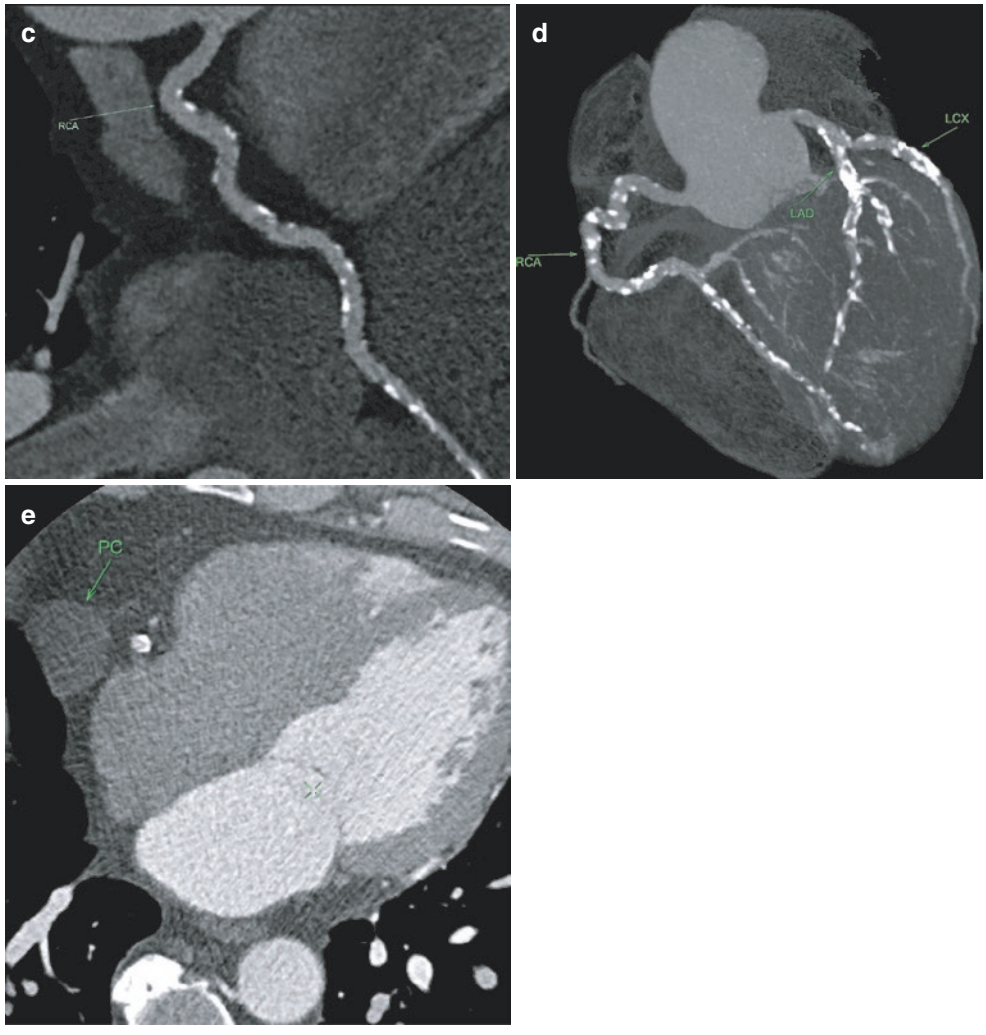

Fig. 6.28 (continued)

6.29 Case 6.29

6.29.1 History

A 52-year-old male admitted to the hospital with an acute cerebrovascular accident (CVA). No prior cardiovascular history. Standard testing was performed, demonstrated a troponin of 0.04. A CCTA was ordered.

6.29.2 Findings

There is a significant coronary artery disease. There is a CTO of the mid-LAD (Fig. 6.29a, b). Another CTO is seen in the RCA with recanalization of the proximal to mid-RCA (Fig. 6.29c, d). There is a CTO in mid-LCX as well (Fig. 6.29e). Incidentally noted is extensive bilateral pulmonary embolism (PE) (Fig. 6.29f).

6.29.3 Diagnosis

Lipoproteinemia causing PE, CVA, and MI.

6.29.4 Discussion

The combination of acute CVA, PE, multiple coronary thrombosis should raise suspicions for systemic causes of coagulopathy or other metabolic dysfunction. This patient was found to have a lipoprotein A level of 500 nmol/L (normal is less than 75 nmol/L). Patient underwent a plasmapheresis and successful cardiac surgical revascularization. He was eventually discharged home in stable condition.

6.29.5 Pearls and Pitfalls

The severity of coronary artery disease findings with additional new onset of PE and CVA should alert an underlying systemic disease beyond the usual atherosclerotic disease seen in this age group.

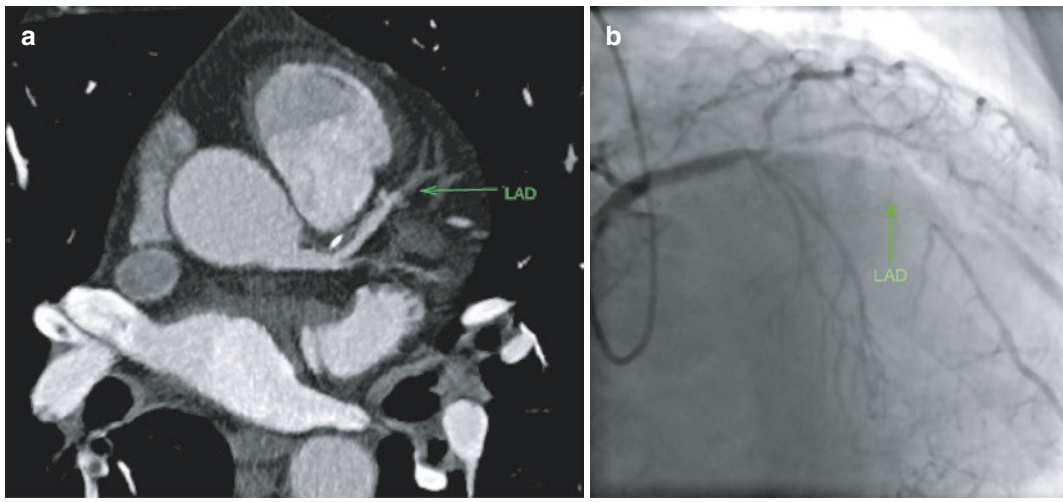

Fig. 6.29 (**a**) Axial MIP demonstrating occluded LAD (**b**) Left coronary angiogram (**c**) cMPR (**d**) Right coronary angiogram (**e**) Axial MIP showing occluded LCX (**f**) Axial MIP showing bilateral pulmonary embolism

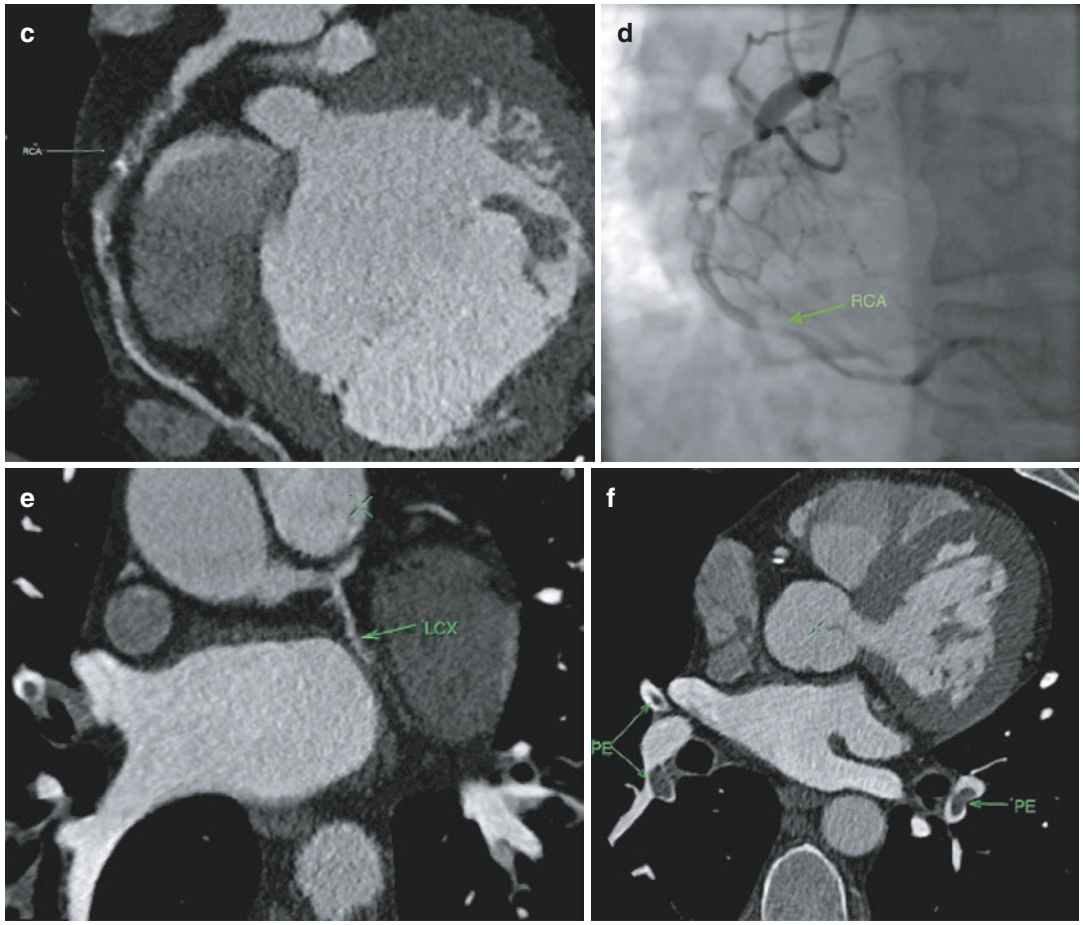

Fig. 6.29 (continued)

6.30 Case 6.30

6.30.1 History

A 49-year-old male with a history of hypertension presented to the hospital with atypical chest pain.

6.30.2 Findings

Right dominant coronary circulation. There is a critical obstruction in the proximal LAD (Fig. 6.30a, b). No plaques in the RCA (Fig. 6.30c, d) and no plaques in the LCX (Fig. 6.30e).

6.30.3 Diagnosis

Critical obstruction in the proximal segment of the LAD.

6.30.4 Discussion

Atherosclerotic events are usually thought to be linearly correlated to plaque burden; meaning the greater the plaque burden, the greater the chance of a coronary event. However, as this case delineates, it can take only one plaque to cause a major cardiac event.

6.30.5 Pearls and Pitfalls

It only takes one plaque rupture in a major proximal coronary branch to ruin your day.

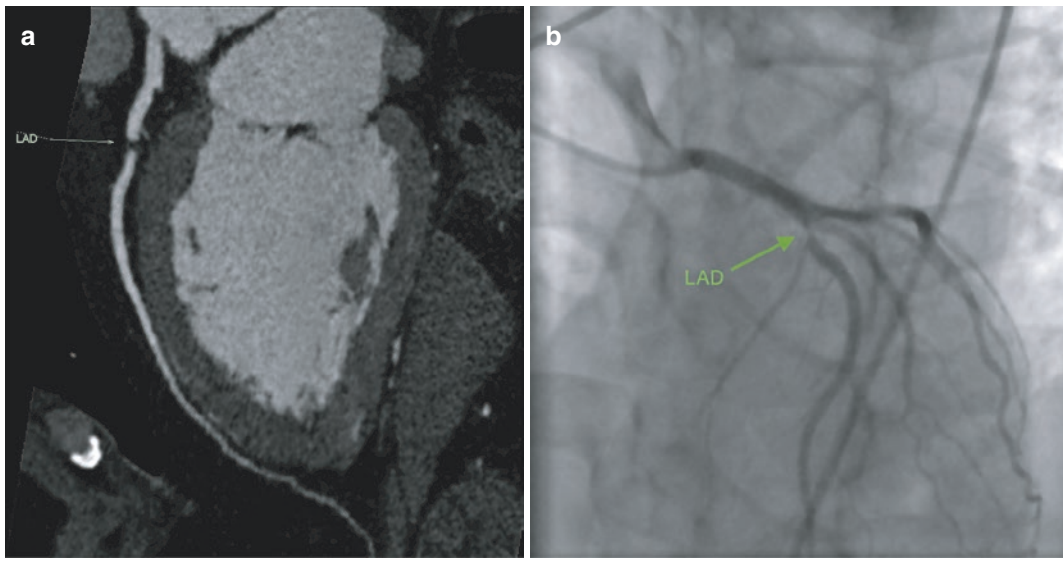

Fig. 6.30 (**a**) cMPR: LAD (**b**) Left coronary angiogram (**c**) cMPR: RCA (**d**) Right coronary angiogram (**e**) cMPR: LCX

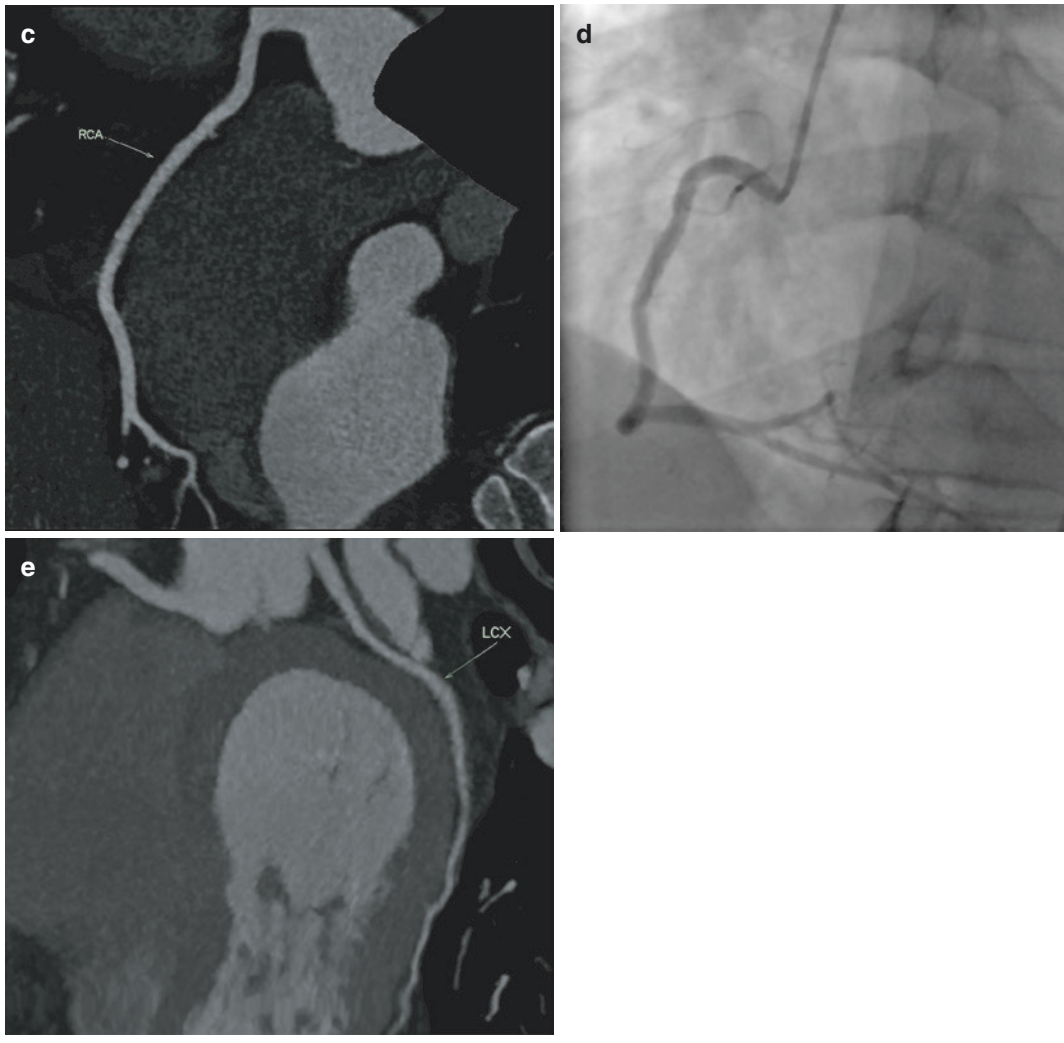

Fig. 6.30 (continued)

6.31 Case 6.31

6.31.1 History

A 54-year-old presented to the hospital with chest pain.

6.31.2 Findings

Right dominant coronary circulation. There is a thrombus in the ostium of the ramus intermedius (RI) artery (Fig. 6.31a–d).

6.31.3 Diagnosis

Acute thrombus in the ramus intermedius artery.

6.31.4 Discussion

The RI is typically a small branch, but sometimes as in this case, it can be a large branch and cause significant ischemia to a large segment of the myocardium.

6.31.5 Pearls and Pitfalls

Significant obstructive CAD can be subtle and the reader needs to pay careful attention to the proximal branches. The critical finding was initially missed by another reviewer.

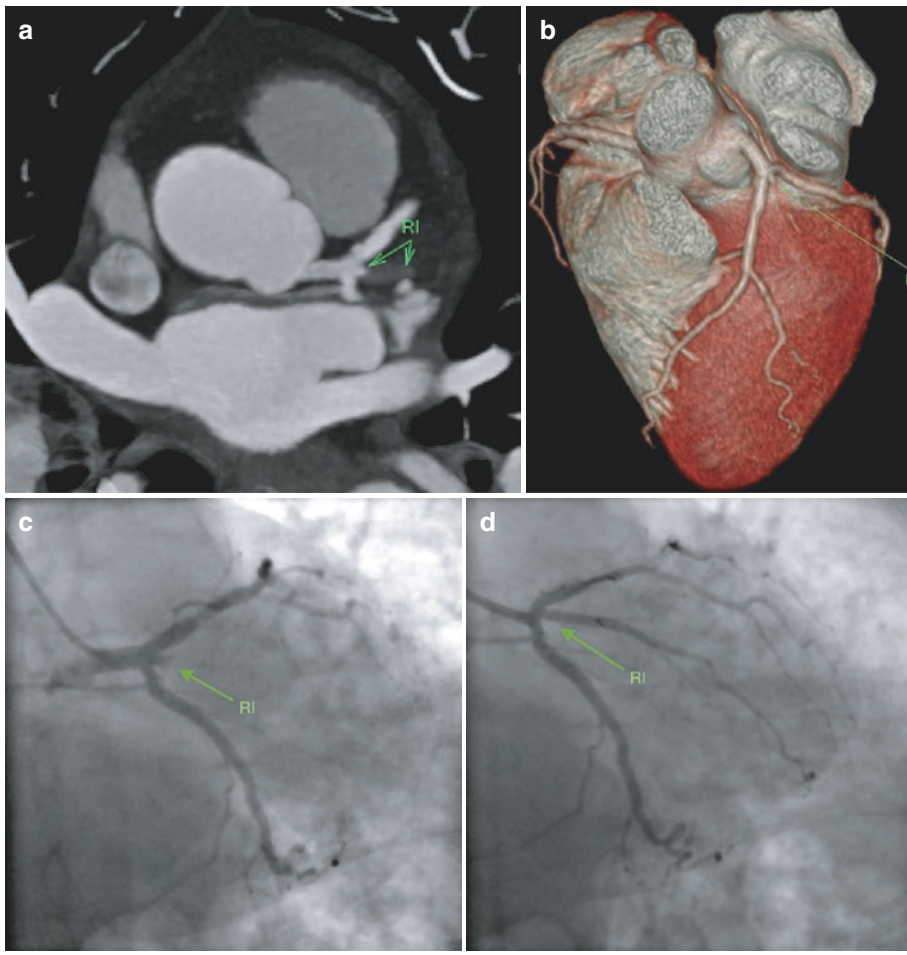

Fig. 6.31 (**a**) Axial MIP (**b**) Volume rendered (**c**) Left coronary angiogram (**d**) Post PCI left coronary angiogram

6.32 Case 6.32

6.32.1 History

A 50-year-old male presented with left-sided chest discomfort.

6.32.2 Findings

Right dominant coronary circulation. The anteroseptal and apical regions have ischemic changes (Fig. 6.32a, b). There is a total occlusion of the LAD (Fig. 6.32c, d) with a collateral (Fig. 6.32e, f). There is a subtotal occlusion of the ramus intermedius artery at the ostium.

6.32.3 Diagnosis

Critical obstruction of the LAD.

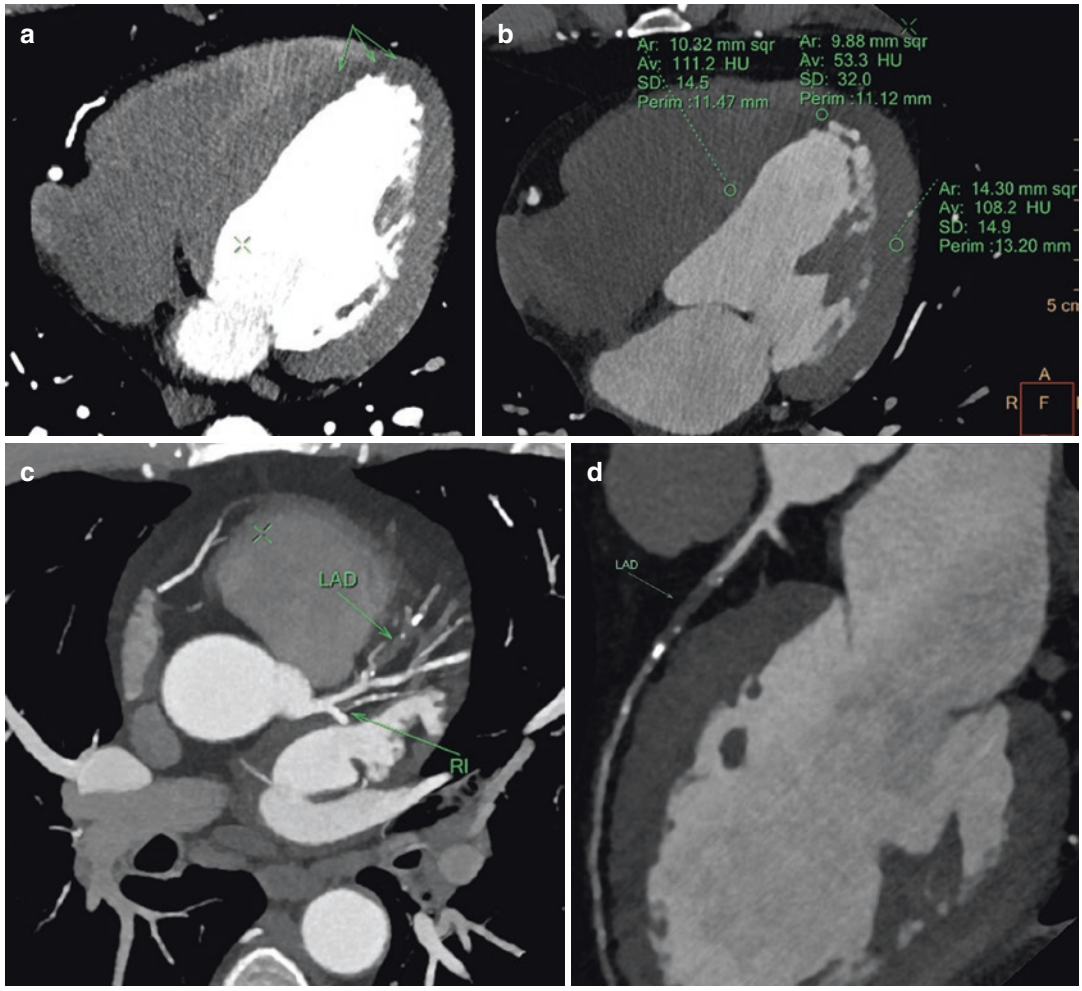

Fig. 6.32 (**a**) Axial MIP: *Arrows* demonstrating areas of ischemia (**b**) Axial MIP: Note different Hounsfield Unit (HU). Previously denoted ischemia areas have less HU compared to non-ischemic areas (**c**) Axial MIP showing a total occlusion of the LAD. (**d**) cMPR (**e**) Axial MIP delineating collateral from the RCA (**f**) Right coronary angiogram showing collateral from the RCA (**g**) Left coronary angiogram showing a subtotal occlusion in the ostium of the ramus

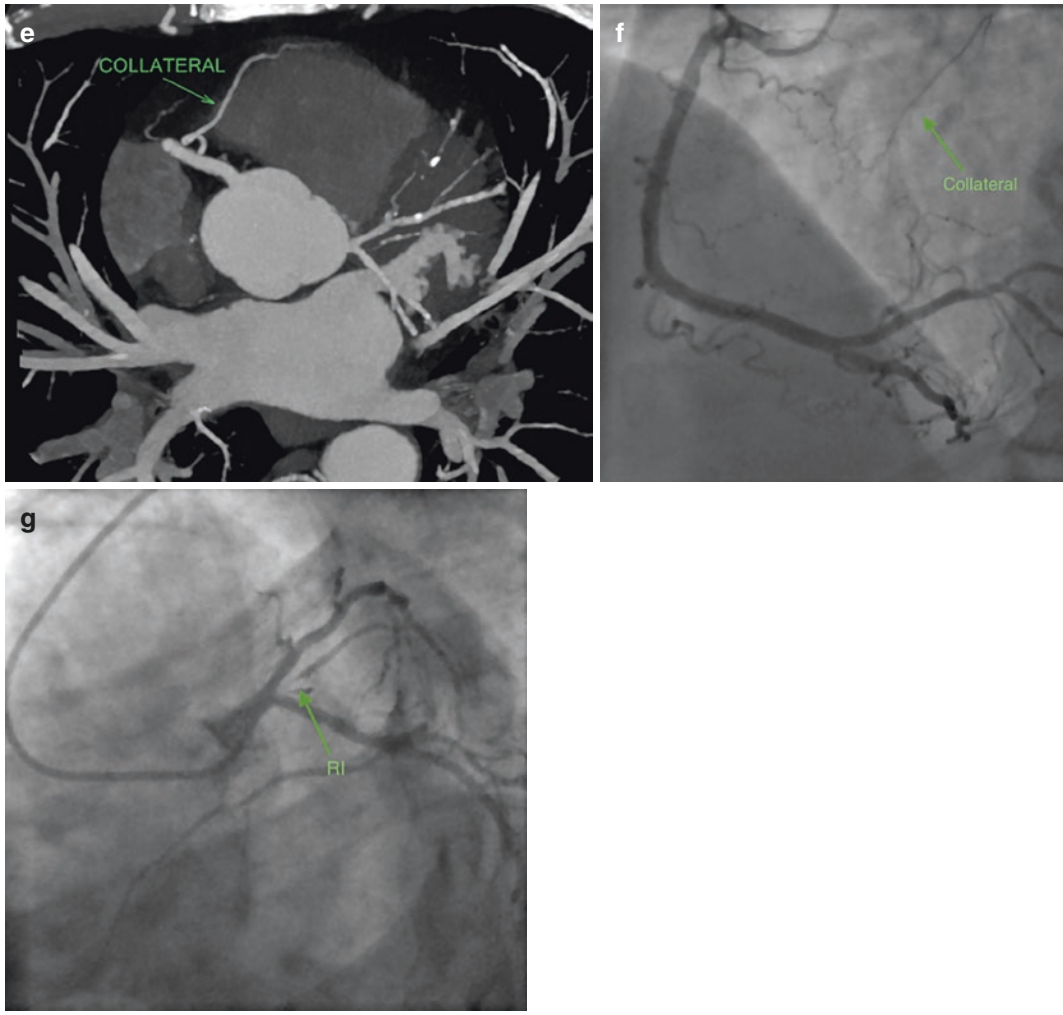

Fig. 6.32 (continued)

6.32.4 Discussion

Areas of myocardial ischemia demonstrate decreased Hounsfield density, which can be measured. When compared to a normal perfused segment, a drop of 20 or greater of Hounsfield density should be considered to be ischemic.

6.32.5 Pearls and Pitfalls

Always look at the myocardium, wall thickness, and density for areas of ischemia, scar or infiltrating process.

6.33 Case 6.33

6.33.1 History

A 63-year-old female with a history of breast cancer, status post-radiation therapy, presented with palpitations.

6.33.2 Findings

There is a heavily calcified circumferential plaque in the proximal LAD that appears to be flow limiting (Fig. 6.33a–d). A coronary angiogram was recommended.

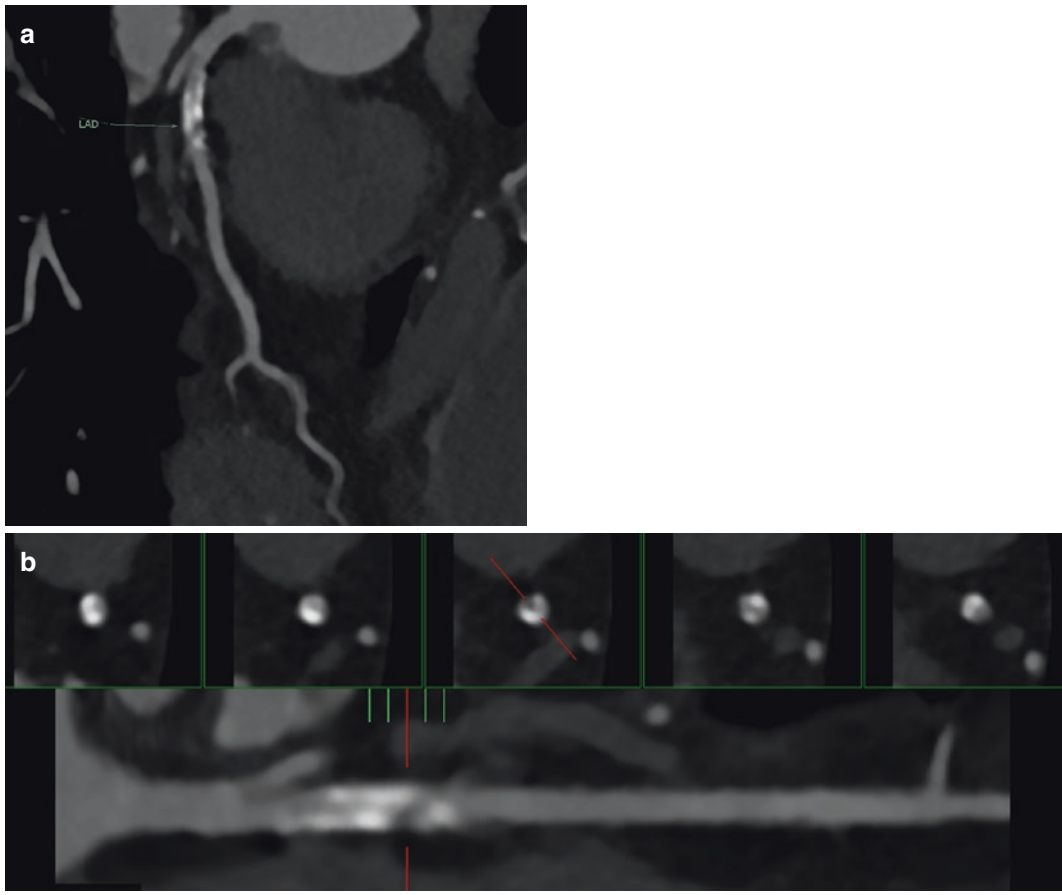

Fig. 6.33 (**a**) cMPR (**b**) cMPR stretch view (**c**) Coronary tree (**d**) Left coronary angiogram: Note the calcification at the *arrow* tip

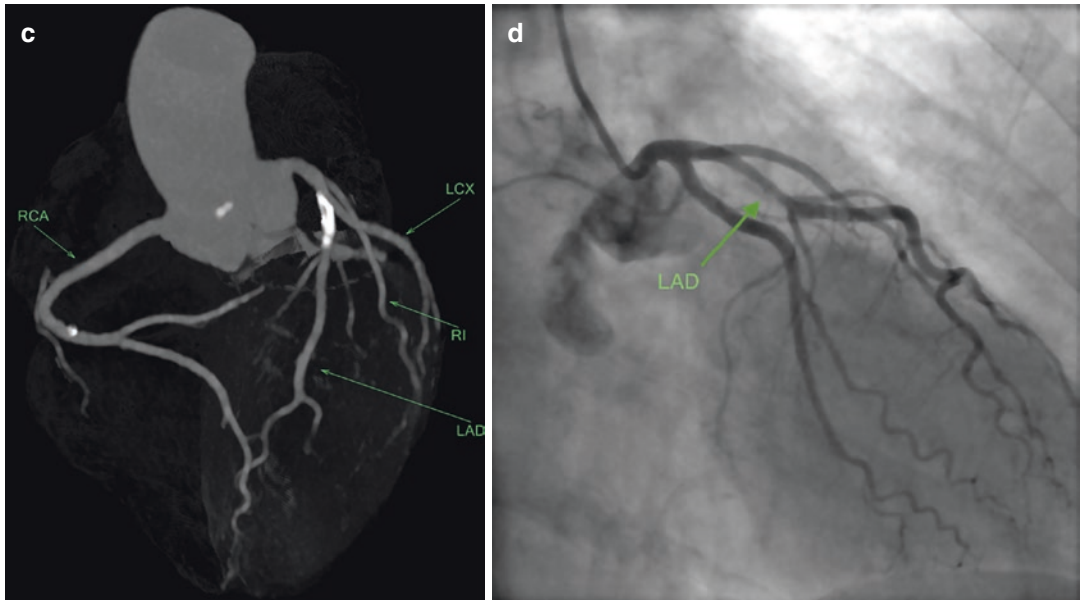

Fig. 6.33 (continued)

6.33.3 Diagnosis

Circumferential calcified plaque in the proximal LAD that appears obstructive.

6.33.4 Discussion

Most calcified plaques are eccentric and rarely flow limiting. Concentric calcified plaques that narrow the lumen maybe flow limiting and should be reported as either suspicious or indeterminate.

The coronary angiogram (Fig. 6.33d) was reported as a 30% stenosis in the proximal LAD. It was not determined whether the disease was induced by the radiation therapy.

6.33.5 Pearls and Pitfalls

Because of blooming artifact, CCTA has decreased specificity and positive predictive value in estimating stenosis in heavily calcified plaques. FFRct holds great promise in improving specificity in these types of cases.

6.34 Case 6.34

6.34.1 History

A 45-year-old presented to the hospital with 3-day history of left-sided atypical chest pain.

6.34.2 Findings

There is significant dilatation of the LAD (Fig. 6.34a) and LCX (Fig. 6.34c, d). There is no coronary obstruction.

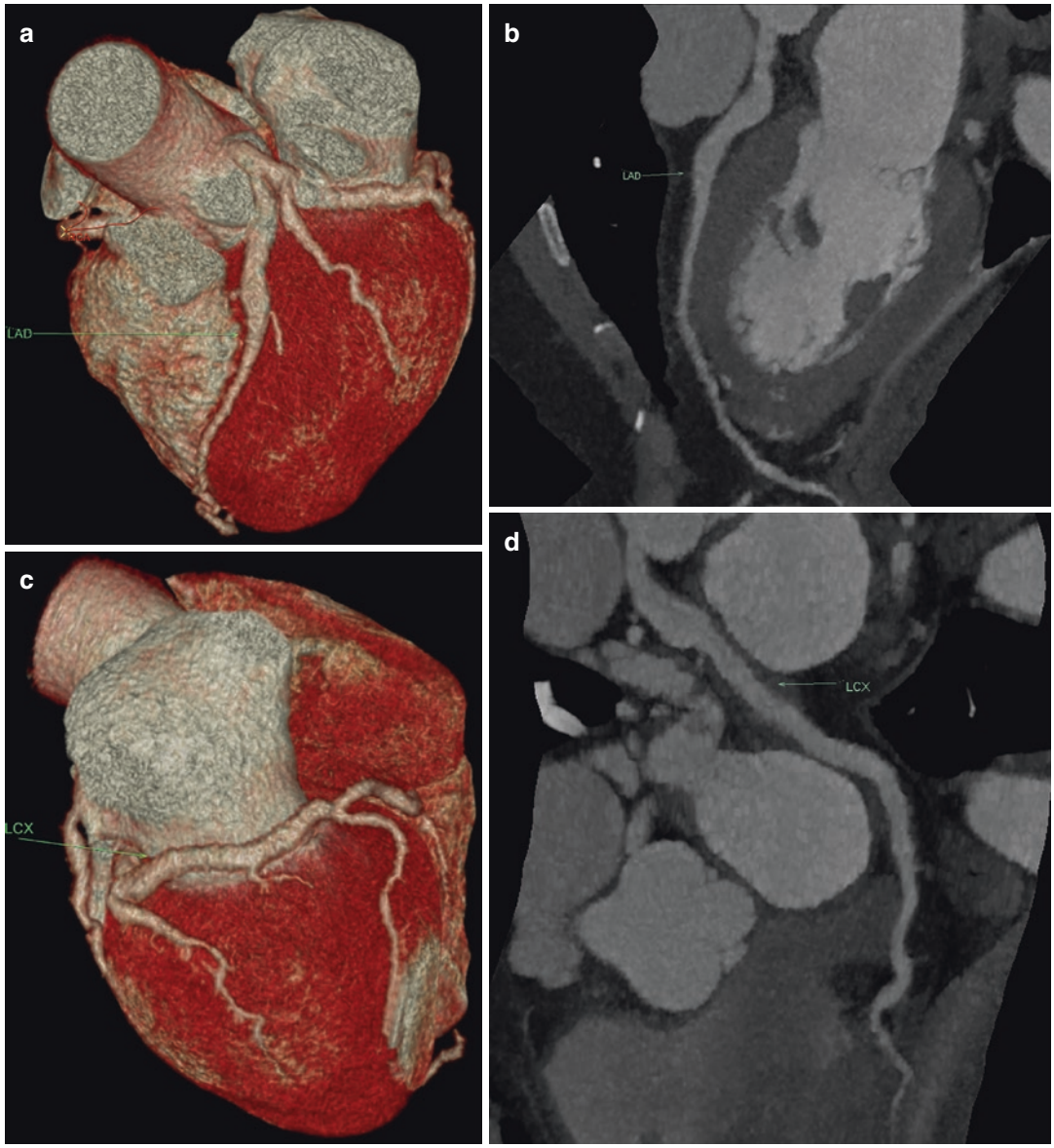

Fig. 6.34 (**a**) Volume rendered-LAD (**b**) cMPR-LAD (**c**) Volume rendered-LCX (**d**) cMPR-LCX

6.34.3 Diagnosis

Coronary ectasia.

6.34.4 Discussion

Coronary artery ectasia is abnormal dilatation of an arterial segment to a diameter at least 1.5 times that of the adjacent normal coronary artery [3]. The etiology of ectasia may be secondary to atherosclerosis, congenital or inflammatory connective tissue disorder (vasculitis). Such condition disrupts laminar blood flow and decreases blood flow in the coronary arteries, due to enlarged diameter of arteries and subsequent vasospasm. This decreased flow can lead to tissue damage. Also, disruption of normal laminar flow can lead to spontaneous thrombosis with acute coronary syndrome. Patients should be treated for underlying or comorbid conditions such as atherosclerosis or hypertension and should be started on anticoagulant therapy [3].

6.34.5 Pearls and Pitfalls

Although the patient had no coronary obstruction, coronary ectasia should always be reported since this condition requires secondary preventive therapy.

6.35 Case 6.35

6.35.1 History

A 67-year-old male underwent cardiac evaluation because of the sudden death of his identical twin.

6.35.2 Findings

There is a long tubular segment of critical obstruction in the proximal LAD and also a critical obstruction in the mid-LAD (Fig. 6.35a). Additionally, there is a critical obstruction in the

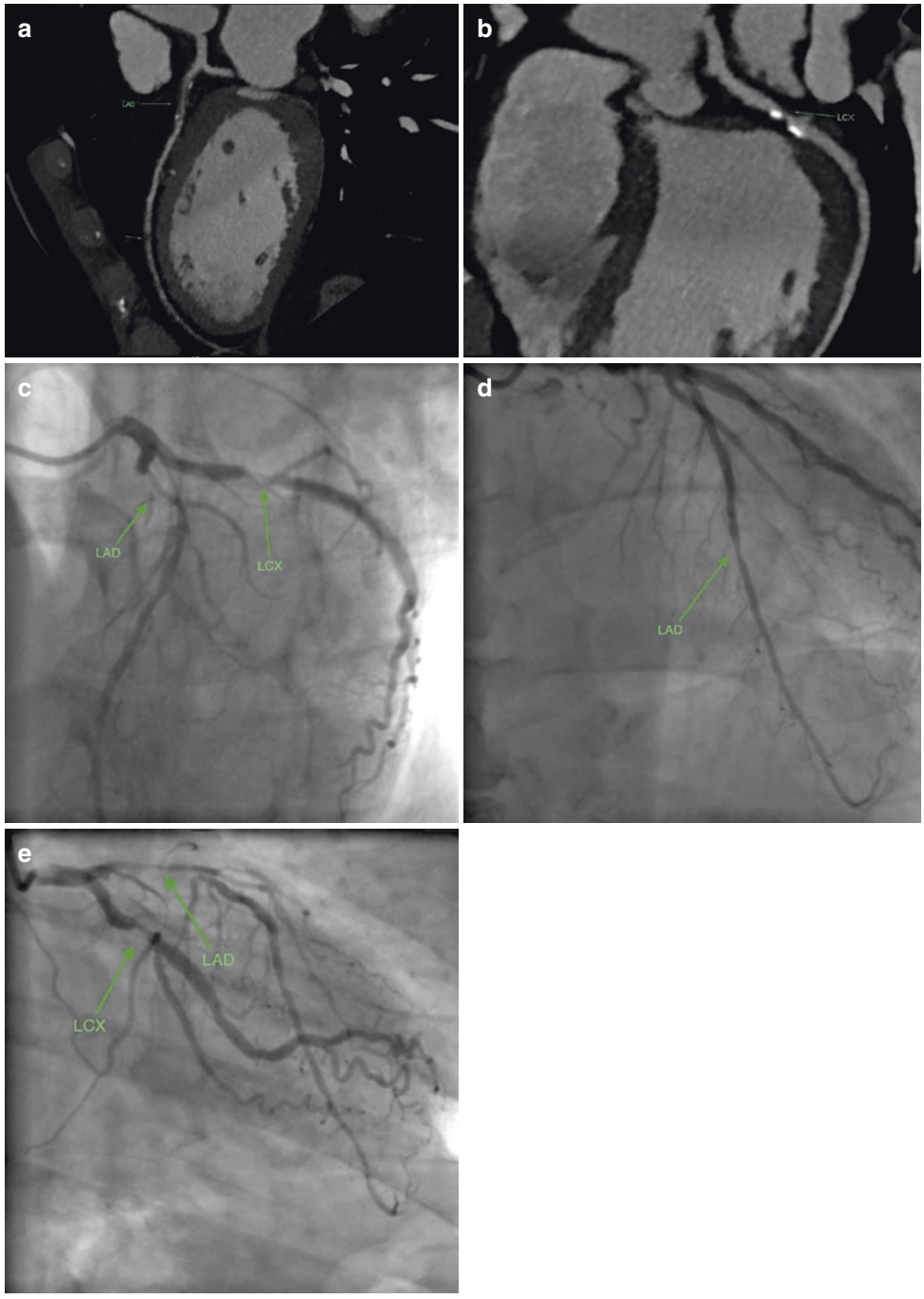

Fig. 6.35 (**a**) cMPR-LAD (**b**) cMPR-LCX (**c**-**e**) Coronary angiograms

proximal to the mid circumflex coronary artery which is a large caliber branch (Fig. 6.35b).

6.35.3 Diagnosis

Multiple critical obstructions in the LAD and the LCX.

6.35.4 Discussion

This patient underwent coronary angiography (Fig. 6.35c–e) which confirmed the findings on the CCTA. Stenting of the LAD was attempted with acute closure of the LAD. After placement of an aortic balloon, the patient underwent an emergent coronary artery bypass-graft surgery.

6.35.5 Pearls and Pitfalls

Concentric stenosis is also referred to as a tubular stenosis.

References

1. Budoff MJ, Dowe D, Jollis JG, et al. Diagnostic performance of 64-multidetector row coronary computed tomographic angiography for evaluation of coronary artery stenosis in individuals without known coronary artery disease results from the prospective multicenter ACCURACY (Assessment by Coronary Computed Tomographic Angiography of Individuals Undergoing Invasive Coronary Angiography) Trial. J Am Coll Cardiol. 2008;52(21):1724–32.
2. Arbab-Zadeh A, Fuster V. The myth of the "vulnerable plaque": transitioning from a focus on individual lesions to atherosclerotic disease burden for coronary artery disease risk assessment. J Am Coll Cardiol. 2015;65(8):846–55. https://doi.org/10.1016/j.jacc.2014.11.041.
3. Hartnell GG, Parnell BM, Pridie RB. Coronary artery ectasia, its prevalence and clinical significance in 4993 patients. Br Heart J. 1985;54:392–5.

Suggested Reading

Bax JJ, Young LH, Frye RL, et al. Screening for coronary artery disease in patients with diabetes. Computed tomography to classify and quantify plaque volumes in the proximal coronary system: a comparative study using intravascular ultrasound. J Am Coll Cardiol. 2006;47(3):672–7.

Cademartiri F, Maffei E, Palumbo A, et al. Diagnostic accuracy of 64-slice computed tomography coronary angiography in patients with low-to-intermediate risk. Radiol Med. 2007;112(7):969–81.

Cademartiri F, Romano M, Seitun S, et al. Prevalence and characteristics of coronary artery disease in a population with suspected ischemic heart disease using CT coronary angiography: correlations with cardiovascular risk factors and clinical presentation. Radiol Med. 2008;113(3):363–72.

Courtney BK, Munce NR, Anderson KJ, et al. Innovations in imaging for chronic total occlusions: a glimpse into the future of angiography's blind-spot. Eur Heart J. 2008;29(5):583–93.

de Feyter PJ. Multislice CT coronary angiography: a new gold-standard for the diagnosis of coronary artery disease? Nat Clin Pract Cardiovasc Med. 2008;5(3):132–3.

Dodd JD, Kalva S, Pena A, et al. Emergency cardiac CT for suspected acute coronary syndrome: qualitative and quantitative assessment of coronary, pulmonary, and aortic image quality. AJR Am J Roentgenol. 2008;191(3):870–7.

Feuchtner G, Postel T, Weidinger F, et al. Is there a relation between non-calcifying coronary plaques and acute coronary syndromes? A retrospective study using multislice computed tomography. Cardiology. 2008;110(4):241–8.

Gaemperli O, Schepis T, Valenta I, et al. Functionally relevant coronary artery disease: comparison of 64-section CT angiography with myocardial perfusion SPECT. Radiology. 2008;248(2):414–23.

Gaemperli O, Valenta I, Schepis T, et al. Coronary 64-slice CT angiography predicts outcome in patients with known or suspected coronary artery disease. Eur Radiol. 2008;18(6):1162–73.

Hachamovitch R, et al. Patient management after noninvasive cardiac imaging results from SPARC (Study of myocardial perfusion and coronary anatomy imaging roles in coronary artery disease). J Am Coll Cardiol. 2012;59(5):462–74.

Haramati LB, Levsky JM, Jain VR, et al. CT angiography for evaluation of coronary artery disease in inner-city outpatients: an initial prospective comparison with stress myocardial perfusion imaging. Int J Cardiovasc Imaging. 2009;25(3):303–13.

Herzog BA, Husmann L, Burkhard N, et al. Accuracy of low-dose computed tomography coronary angiography using prospective electrocardiogram-triggering: first clinical experience. Eur Heart J. 2008;29(24):3037–42.

Hildebrandt HA, Gossl M, Mannheim D, et al. Differential distribution of vasa vasorum in different vascular beds in humans. Atherosclerosis. 2008;199(1):47–54.

Ho JS, Fitzgerald SJ, Stolfus LL, et al. Relation of a coronary artery calcium score higher than 400 to coronary stenoses detected using multidetector computed

tomography and to traditional cardiovascular risk factors. Am J Cardiol. 2008;101(10):1444–7.

Husmann L, Gaemperli O, Schepis T, et al. Accuracy of quantitative coronary angiography with computed tomography and its dependency on plaque composition: plaque composition and accuracy of cardiac CT. Int J Cardiovasc Imaging. 2008;24(8):895–904.

Johnson TR, Nikolaou K, Busch S, et al. Diagnostic accuracy of dual-source computed tomography in the diagnosis of coronary artery disease. Investig Radiol. 2007;42(10):684–91.

Kelly JL, Thickman D, Abramson SD, et al. Coronary CT angiography findings in patients without coronary calcification. AJR Am J Roentgenol. 2008;191(1):50–5.

Kitagawa T, Yamamoto H, Ohhashi N, et al. Comprehensive evaluation of noncalcified coronary plaque characteristics detected using 64-slice computed tomography in patients with proven or suspected coronary artery disease. Am Heart J. 2007;154(6):1191–8. [Epub 6 Sept 2007]. Erratum in: Am Heart J 2008 Feb;155(2):253.

Klepzig H. Diagnostic accuracy of dual-source multi-slice CT-coronary angiography in patients with an intermediate pretest likelihood for coronary artery disease. Eur Heart J. 2008;29(5):680.

Koç O, Kivrak AS, Ozdemir K. Evaluation of small coronary artery aneurysm by 64-slice multi-detector CT coronary angiography and virtual angioscopy. Anadolu Kardiyol Derg. 2008;8(5):E32.

Leber AW, von Ziegler F, Becker A, et al. Characteristics of coronary plaques before angiographic progression determined by Multi-Slice CT. Int J Cardiovasc Imaging. 2008;24(4):423–8.

Lee HY, Yoo SM, White CS. Coronary CT angiography in emergency department patients with acute chest pain: triple rule-out protocol versus dedicated coronary CT angiography. Int J Cardiovasc Imaging. 2009;25(3):319–26.

Matsumoto N, Sato Y, Yoda S, et al. Prognostic value of non-obstructive CT low-dense coronary artery plaques detected by multislice computed tomography. Circ J. 2007;71(12):1898–903.

Meijboom WB, van Mieghem CA, Mollet NR, et al. 64-slice computed tomography coronary angiography in patients with high, intermediate, or low pretest probability of significant coronary artery disease. J Am Coll Cardiol. 2007;50(15):1469–75.

Meijboom WB, Weustink AC, Pugliese F, et al. Comparison of diagnostic accuracy of 64-slice computed tomography coronary angiography in women versus men with angina pectoris. Am J Cardiol. 2007;100(10):1532–7.

Miller JM, Dewey M, Vavere AL, et al. Coronary CT angiography using 64 detector rows: methods and design of the multi-centre trial CORE-64. Eur Radiol. 2009;19(4):816–28.

Mintz GS, Popma JJ, Pichard AD, et al. Limitations of angiography in the assessment of plaque distribution in coronary artery disease: a systematic study of target lesion eccentricity in 1446 lesions. Circulation. 1996;93:924–31.

Mowatt G, Cook JA, Hillis GS, et al. 64-Slice computed tomography angiography in the diagnosis and assessment of coronary artery disease: systematic review and meta-analysis. Heart. 2008;94(11):1386–93.

Panmethis M, Wangsuphachart S, Rerkpattanapipat P, et al. Detection of coronary stenoses in chronic stable angina by multi-detector CT coronary angiography. J Med Assoc Thail. 2007;90(8):1573–80.

Rana JS, et al. Differences in prevalence, extent, severity, and prognosis of coronary artery disease among patients with and without diabetes undergoing coronary computed tomography angiography: results from 10,110 individuals from the CONFIRM (COronary CT Angiography EvaluatioN For Clinical Outcomes): an InteRnational Multicenter Registry. Diabetes Care. 2012;35(8):1787–94.

Rudd JH, Fayad ZA. Imaging atherosclerotic plaque inflammation. Nat Clin Pract Cardiovasc Med. 2008;5(Suppl 2):S11–7.

Sato A, Hiroe M, Tamura M, et al. Quantitative measures of coronary stenosis severity by 64-Slice CT angiography and relation to physiologic significance of perfusion in nonobese patients: comparison with stress myocardial perfusion imaging. J Nucl Med. 2008;49(4):564–72.

Satoda M, Takagi K, Uesugi M, et al. Acute myocardial infarction caused by spontaneous postpartum coronary artery dissection. Nat Clin Pract Cardiovasc Med. 2007;4(12):688–92.

Schoenhagen P, Barreto M, Halliburton SS. Quantitative plaque characterization with coronary CT angiography (CTA): current challenges and future application in atherosclerosis trials and clinical risk assessment. Int J Cardiovasc Imaging. 2008;24(3):313–6.

Scholte AJ, Schuijf JD, Kharagjitsingh AV, et al. Different manifestations of coronary artery disease by stress SPECT myocardial perfusion imaging, coronary calcium scoring, and multislice CT coronary angiography in asymptomatic patients with type 2 diabetes mellitus. J Nucl Cardiol. 2008;15(4):503–9.

Schuijf JD, Jukema JW, van der Wall EE, et al. Multislice computed tomography in the evaluation of patients with acute chest pain. Acute Card Care. 2007;9(4):214–21.

Seneviratne SK, Bamberg F, Hoffmann U. CT angiography: front line for acute coronary syndromes now? Heart. 2007;93(11):1325–6.

Sheth T, Amlani S, Ellins ML, et al. Computed tomographic coronary angiographic assessment of high-risk coronary anatomy in patients with suspected coronary artery disease and intermediate pretest probability. Am Heart J. 2008;155(5):918–23.

Stein PD, Yaekoub AY, Matta F, et al. 64-slice CT for diagnosis of coronary artery disease: a systematic review. Am J Med. 2008;121(8):715–25.

Wann S, Krystowiak M. Case presentations of potential applications of computed tomographic angiography in the geriatric population. Am J Geriatr Cardiol. 2007;16(6):376–80.

White CS, Kuo D. Chest pain in the emergency department: role of multidetector CT. Radiology. 2007;245(3):672–81.

Wilner WT, Mazraeshahi RM, Aboshady I, et al. Quantification of roughness of calcific deposits in computed tomography scans of human coronary arteries. Investig Radiol. 2007;42(11):771–6.

Ulimoen GR, Gjønnæss E, Atar D, et al. Noninvasive coronary angiography with 64-channel multidetector computed tomography in patients with acute coronary syndrome. Acta Radiol. 2008;49(10):1140–4.

Uehara M, et al. Diagnostic accuracy of 320-slice computed-tomography for detection of significant coronary artery stenosis in patients with various heart rates and heart rhythms compared with conventional coronary-angiography. Int J Cardiol. 2013;167(3):809–15.

Utsunomiya D, Tomiguchi S, Yamashita Y. Role of cardiac computed tomography in patients with suspected coronary artery disease: interaction with nuclear cardiology. Radiat Med. 2007;25(10):493–501.

Versteylen MO, et al. Additive value of semiautomated quantification of coronary artery disease using cardiac computed tomographic angiography to predict future acute coronary syndrome. J Am Coll Cardiol. 2013;61(22):2296–305.

Vural M, Aksit Z, Kovanlikaya I, et al. Can multidetector CT angiography detect coronary artery dissection? Tex Heart Inst J. 2007;34(3):388–9.

Zeina AR, Rosenschein U, Barmeir E. Giant coronary-pulmonary artery fistula with multiple saccular aneurysms: multidetector CT evaluation. Heart. 2008;94(3):277.

Zeina AR, Shefer A, Sharif D, et al. Acute myocardial infarction in a young woman with normal coronary arteries and myocardial bridging. Br J Radiol. 2008;81(965):e141–4.

Cardiac CTA Fractional Flow Reserve

7

Lohendran Baskaran, Christopher K. Zarins, and James K. Min

7.1 Overview

Fractional flow reserve (FFR) is measured invasively and is the gold standard for determining lesion-specific ischemia and guiding treatment strategies for patients with stable coronary artery disease. This can now be determined noninvasively using standard coronary CT angiography imaging data. This novel technology provides FFR values using the anatomic data provided by coronary CTA. This provides lesion-specific functional information over and above the anatomic information provided by coronary CTA. FFR_{CT} technology has been validated in prospective clinical trials, demonstrating high diagnostic accuracy and discrimination for the diagnosis of hemodynamically significant CAD when compared to invasive FFR as the reference standard. Hence, FFR_{CT} is a noninvasive tool that can provide physicians with information on both the anatomic degree of coronary stenosis and the functional significance of the lesion to help guide decisions for revascularization in stable CAD.

L. Baskaran, MBBS, BSc
Department of Radiology, Dalio Institute of Cardiovascular Imaging, New York-Presbyterian Hospital and Weill Cornell Medicine, 413 E. 69th St, Suite 108, New York, NY 10021, USA

National Heart Centre, Singapore, 5 Hospital Drive, Singapore 169609, Singapore
e-mail: Lohendran.baskaran@gmail.com

C.K. Zarins, MD
HeartFlow, Inc., 1400 B Seaport Blvd, Redwood City, CA 94063, USA
e-mail: zarins@heartflow.com

J.K. Min, MD (✉)
Department of Radiology, Dalio Institute of Cardiovascular Imaging, New York-Presbyterian Hospital and Weill Cornell Medicine, 413 E. 69th St, Suite 108, New York, NY 10021, USA
e-mail: jkm2001@med.cornell.edu

C. Smuclovisky (ed.), *Coronary Artery CTA*, https://doi.org/10.1007/978-3-319-66988-5_7

7.2 Introduction

Coronary computed tomography angiography (CTA) is an excellent noninvasive method to identify and quantify coronary artery lesions. This is done with high sensitivity and good negative predictive value (NPV) [1–3]. CTA is an effective rule-out tool although it can overestimate the degree of stenosis when compared to invasive coronary angiography (ICA).

Applied conventionally, CTA does not provide information on the functional significance of coronary stenosis, and the clinician usually relies on other noninvasive modalities, such as single photon emission computed tomography (SPECT), stress echocardiogram or stress cardiac magnetic resonance (CMR), to aid decision-making.

The importance of establishing the physiological significance of an "obstructive" coronary lesion to aid decision-making for revascularization has long been established in trials using noninvasive methods [4, 5]. Determining this is the single most important factor in influencing clinical outcomes in patients with CAD [4, 6]. Patients with hemodynamically significant stenosis benefit from revascularization, whereas those without do well on medical therapy alone. Unnecessary revascularization of nonsignificant lesions provides no clinical benefits while exposing patients to the procedural risks [7, 8]. The introduction of the concept of fractional flow reserve (FFR), which is measured invasively, has further consolidated the importance of this point.

FFR is an index that is measured during ICA. It is defined as the ratio of hyperemic maximal coronary flow in a stenotic artery to the maximum coronary flow in the same artery if it were hypothetically completely normal. It is expressed as a ratio of the pressures proximal and distal to the stenosis (Fig. 7.1).

FFR-guided revascularization improves clinical outcomes and its recommended use in guidelines is established [7–9]. However, FFR is still not used routinely in practice, and decisions for coronary revascularization are typically based on visual estimates of the severity of the coronary artery stenosis [10]. This is even though it is well known that coronary angiography has limited value in determining the hemodynamic significance of coronary lesions, particularly for moderate coronary stenosis [7]. This may be because FFR wire usage increases case complexity, is invasive, and has risks related to the guidewire use. As such, there arises a need for a noninvasive method for assessing ischemia on a lesion-specific basis.

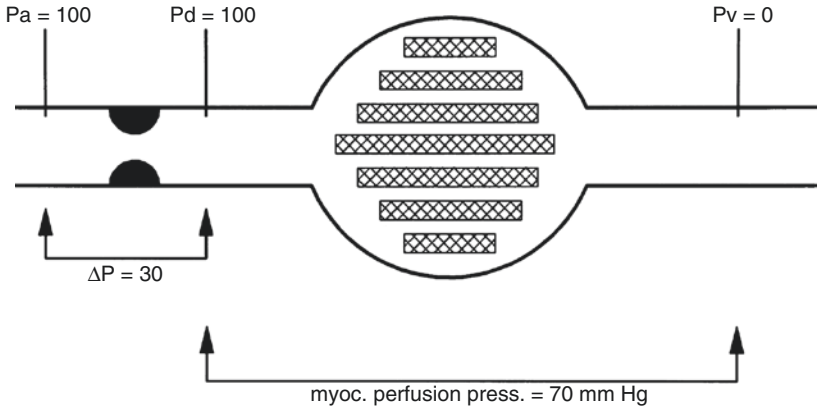

Fig. 7.1 Illustration of the concept of FFR. *FFR* fractional flow reserve, *Pd* Pressure distal to the stenosis, *Pa* Pressure proximal to the stenosis, FFR = Pd/Pa. In this illustration, FFR = 0.7. Reproduced with permission from Circulation, Dec 1995. Pijls, N. H. et al. Fractional flow reserve. A useful index to evaluate the influence of an epicardial coronary stenosis on myocardial blood flow. Circulation 92, 3183–3193 (1995). Copyright (1995), Wolters Kluwer Health, Inc.

7.3 FFR_{CT}

FFR_{CT} applies computational fluid dynamics to the anatomic information provided by coronary CT angiography to compute FFR noninvasively. It uses the same standard CTA images and acquisition protocols, with no need for additional imaging, radiation exposure or pharmacological agents. It relies on post-processing computation to derive a "virtual" FFR. Computation of FFR_{CT} requires the following:

1. Construction of an accurate patient-specific anatomical model of the coronary arteries
2. Mathematical modeling of coronary physiology to derive inflow and outflow patient-specific boundary conditions during hyperemia
3. Solving for the laws of physics governing fluid dynamics based on the boundary conditions

7.3.1 Deriving Physiological Models from Anatomical Information

Conventional CTA images readily provide a source of patient-specific anatomical information. In circulatory systems, form–function relationships are universal, and the circulatory system provides sufficient blood at appropriate perfusion pressures under varying physiological states and chronic changes. Furthermore, at a resting state, total coronary flow is proportional to myocardial mass. Myocardial mass can be easily calculated from volumetric CTA images.

In addition, form–function relationships also apply to the size of the blood vessels and the flow they carry. Blood vessels modulate their size based on the flow they carry and wall shear stress experienced. These are adaptive processes that occur in chronic situations, both in healthy and diseased blood vessels. In other words, blood vessels will adapt. The more flow they carry, the larger they will become and vice versa.

Additional physiological information can be derived from anatomical images. Under resting conditions, the microcirculatory vascular bed has a resistance that is inversely related to the size of the feeding vessel. Smaller blood vessels have a higher resistance than larger blood vessels, and the resistance to flow downstream to a stenosis will be directly related to the number and size of the vessels there [11–17].

7.3.2 Using Computational Fluid Dynamics (CFD)

Fluid dynamics can be used to describe a wide array of phenomena, from air to liquid flow in numerous situations. Solving fluid dynamics problems requires the solution of millions of nonlinear partial differential equations and repeating this process numerous times. The solving of these problems requires approximation at a finite number of points. Coronary blood flow and pressure can be calculated by solving the equations for fluid dynamics. These relate to the conservation of mass and momentum balance. The equations are solved for coronary flow and pressure as a function of coordinates in space and time. Blood is assumed to be a Newtonian (incompressible) fluid with a constant and known viscosity and density [17, 18].

7.3.3 Imposing Boundaries

The assumptions previously mentioned by them are insufficient to solve for blood flow. A specific domain and its boundary conditions must be specified. For the purposes of FFR_{CT}, the domain of interest is the lumen, and the boundaries are the inlet boundary (here the aortic root), the outlet boundary (ascending aorta and coronary arteries), and the lateral surface of the blood vessel. The luminal surface of the major vessels (boundaries) and branches can be obtained from CTA images and are limited only by the CTA resolution. During model construction, the topology of the coronary tree, including the surfaces of plaques and stenosis, are extracted.

To combine it all together, lumped parameter models of the systemic circulation, heart and coronary microcirculation need to be coupled together with the patient-specific model of the aortic root and coronary arteries obtained from CTA images. The mean aortic pressure used is the patient's measured mean brachial pressure. Total coronary flow is calculated from volumetric myocardial wall information obtained from CTA as mentioned above. Total coronary resistance is calculated from total coronary flow. Finally, boundary conditions simulating maximum hyperemia are assigned. This simulates the effect of adenosine on reducing peripheral resistance (as done in invasive FFR). A summary of all the steps above is shown below, along with a pictorial representation (Fig. 7.2).

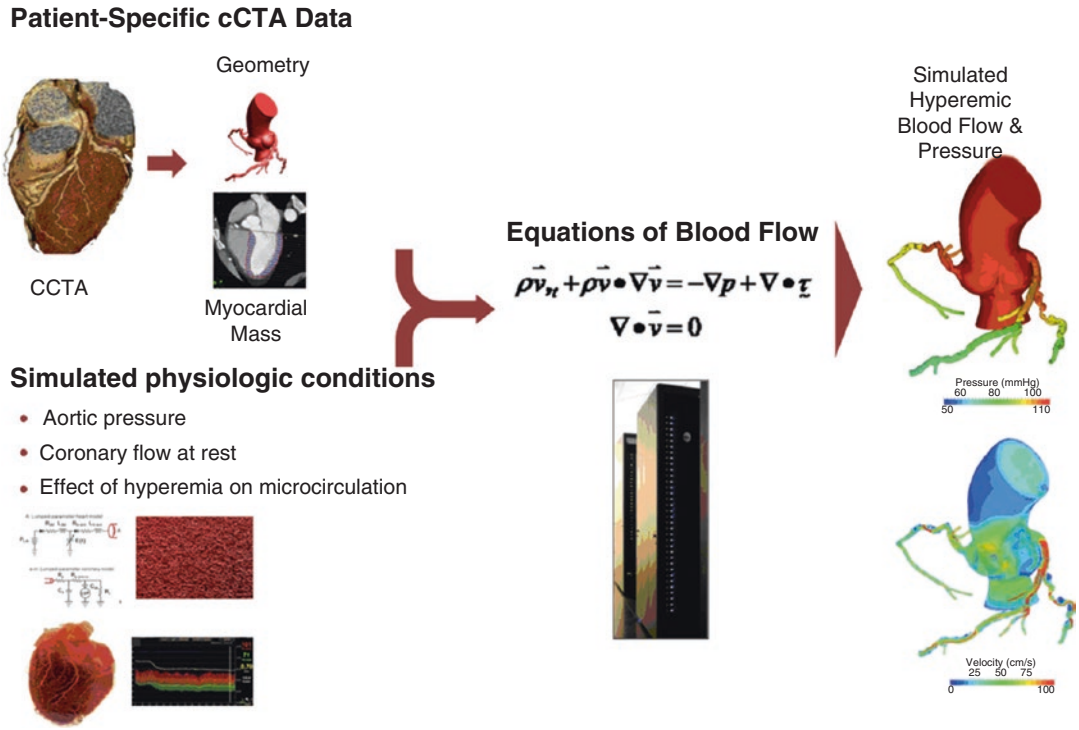

Fig. 7.2 Simplified schematic of computation fluid dynamic techniques applied to CTA data for simulation of hyperemic coronary artery flow and pressure. Reproduced with permission from Journal of Cardiovascular Computed Tomography 2011. Min, J. K. et al. Rationale and design of the DeFACTO (Determination of Fractional Flow Reserve by Anatomic Computed Tomographic Angiography) study. J. Cardiovasc. Comput. Tomogr. 5, 301–309. Copyright (2011) Elsevier, Inc.

7.3.4 To Calculate FFR_{CT}

- Standard CTA dataset used to build a quantitative model
- Combining LV, coronary anatomy, and form–function principles to develop a physiological model
- Calculate flow and pressure under simulated hyperemia using computational fluid dynamics and boundary conditions

7.4 Clinical Evidence

Clinical validation of FFR_{CT} is based on direct comparison to invasive FFR as well as conventional CTA.

Clinical studies have shown that FFR_{CT} adds better discrimination to conventional CTA and ICA with improved diagnostic performance. There is also a good correlation with invasive FFR, even with intermediate stenoses. Three prospective multicenter trials involving 609 patients and 1050 vessels have been carried out, namely the DISCOVER-FLOW, DeFACTO, and NXT trials.

DISCOVER-FLOW was a multicenter prospective trial. It involved 103 patients (159 vessels) with known or suspected CAD who underwent CTA, ICA, and invasive FFR.

A substudy showed that for stenoses of 40–69%, the accuracy, sensitivity, specificity, PPV, and NPV of FFR_{CT} were 86%, 90%, 83%, 82%, and 91%, respectively [19].

The DeFACTO study was a multicenter trial involving 252 patients (407 vessels).

It showed an improvement of FFR_{CT} over CTA in discriminating ischemia both on a per-patient (0.81 vs. 0.68) and per-vessel (0.81 vs. 0.75) basis for the AUC under the ROC [19].

The NXT study included 254 patients from ten centers in eight countries scheduled to undergo clinically indicated coronary angiography [20]. Per-patient diagnostic accuracy to identify hemodynamically significant CAD using measured FFR as the reference standard was significantly higher for FFR_{CT} (81%) than for CTA (53%, $p < 0.001$). This was primarily due to a much higher specificity for FFR_{CT} (79%) compared to CTA (34%, $p < 0.001$). Sensitivity was high for both FFR_{CT} (86%) and CTA (94%, ns). Similarly, per-vessel diagnostic accuracy was significantly higher for FFR_{CT} (86%) than for CTA (65%, $p < 0.001$). Per-vessel specificity was also higher for FFR_{CT} (86%) than for CTA (60%, $p < 0.001$) with no difference in sensitivity (FFR_{CT} 84% and CTA 83%, ns). The ability to discriminate ischemia was significantly improved with FFR_{CT} with the area under the ROC curve for FFR_{CT} 0.90 compared to 0.81 for CTA, $p = 0.0008$. In patients with intermediate stenosis (30–70%), the diagnostic accuracy was high, in keeping with previous studies. This study confirmed that FFR_{CT} provided high diagnostic accuracy and discrimination for the diagnosis of hemodynamically significant CAD compared to anatomic testing using coronary CTA. Furthermore, the NXT study also showed similar improvement in diagnostic accuracy and specificity when was compared to stenosis assessment by invasive coronary angiography.

7.5 Summary

FFR_{CT} then presents a noninvasive, lesion-specific method of identifying physiologically significant coronary artery stenosis, requiring no additional scan time, radiation, or contrast to conventional CTA. The following cases illustrate the utility of FFR_{CT} with comparisons to corresponding ICA, CTA, and invasive FFR.

7.6 Cases

7.6.1 Case 7.1

7.6.1.1 History

A 75-year-old female with typical angina (CCSC I) for 1 month, brought on by her routine 3-mile early morning brisk walk. She is on antihypertensive medication but has no family history or other cardiovascular risk factors.

7.6.1.2 CTA Findings

There is two vessel and left main coronary disease. First, the proximal RCA has non-obstructive mixed plaque. There is mixed plaque in the left main coronary artery with mild disease. The mid LAD (just after D1) has severe disease caused by soft plaque. The distal LCX has moderate disease caused by soft plaque (Fig. 7.3a–c).

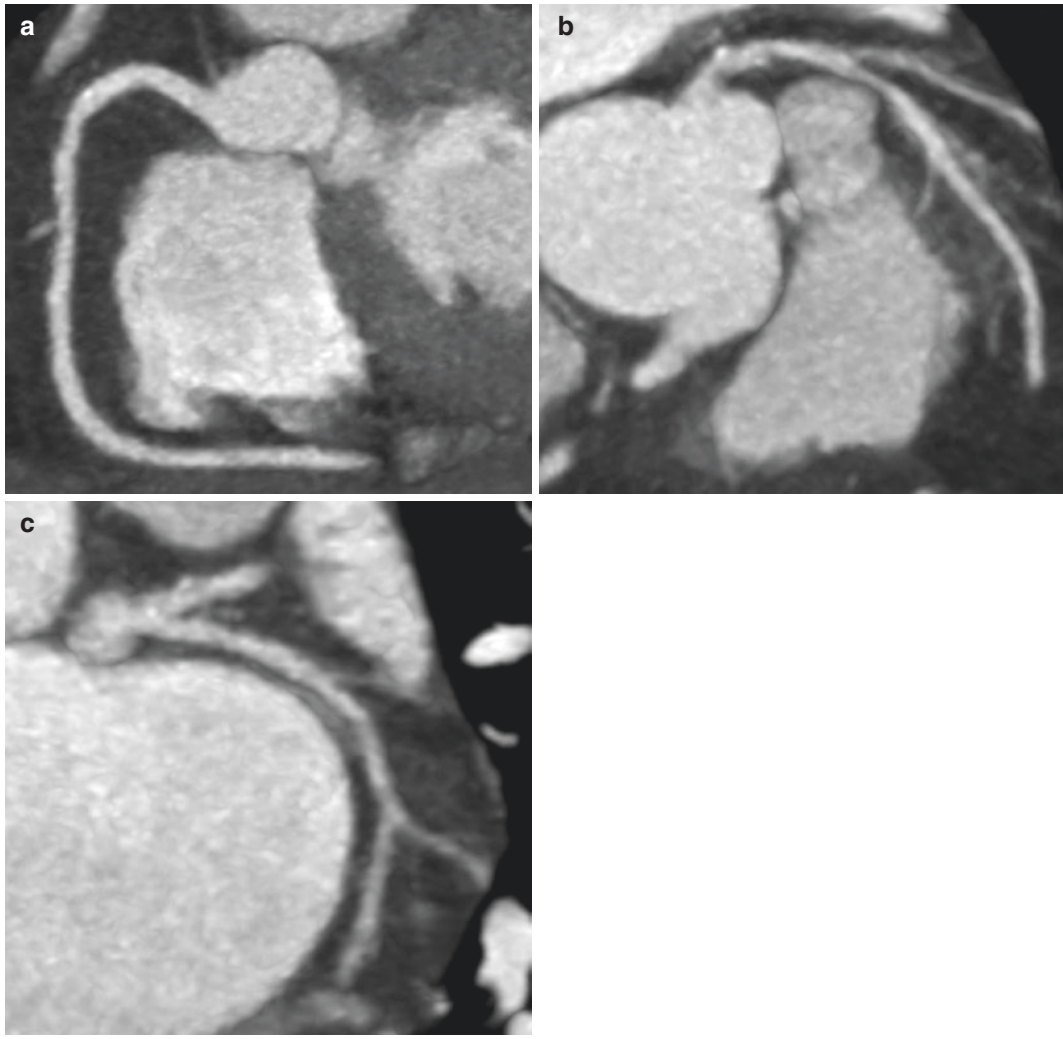

Fig. 7.3 (**a**) Non-obstructive proximal RCA stenosis (**b**) left main and mid-LAD stenosis (**c**) distal LCX. *RCA* right coronary artery, *LAD* left anterior descending coronary artery, *LCx* left circumflex coronary artery stenosis

7.6.1.3 FFR_{CT} Results

FFR_{CT} showed nonsignificance of the RCA stenosis as expected. The left main lesion did not obstruct flow, but the mid LAD lesion was hemodynamically significant with an FFR_{CT} of 0.76 in the distal LAD. The distal LCX stenosis FFR_{CT} value was 0.89 (Fig. 7.4).

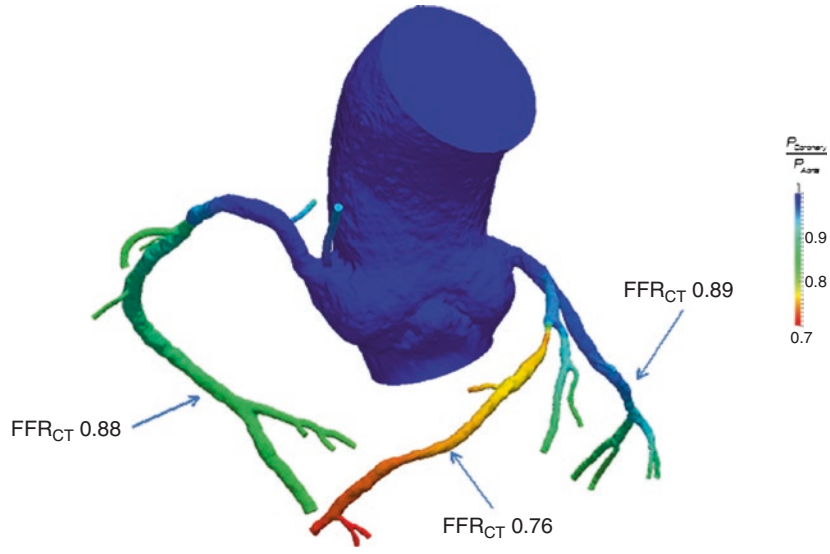

Fig. 7.4 FFR_{CT} showing an FFR_{CT} value of 0.76 in the LAD and 0.89 in the LCX. *LAD* left anterior descending coronary artery, *LCx* left circumflex coronary artery

7.6.1.4 Diagnosis

The diagnosis is single vessel disease in the mid LAD.

7.6.1.5 Discussion

FFR_{CT} has the most utility with intermediate stenoses. In this case, the significance of the LCX lesion on CTA was not known. The FFR_{CT} value of 0.89 (i.e., >0.80) established nonsignificance of the lesion. This was reconfirmed when invasive coronary angiography with FFR was done during the revascularization of the LAD lesion. This showed close correlation between FFR_{CT} and invasive FFR in keeping with the results of clinical trials (Fig. 7.5).

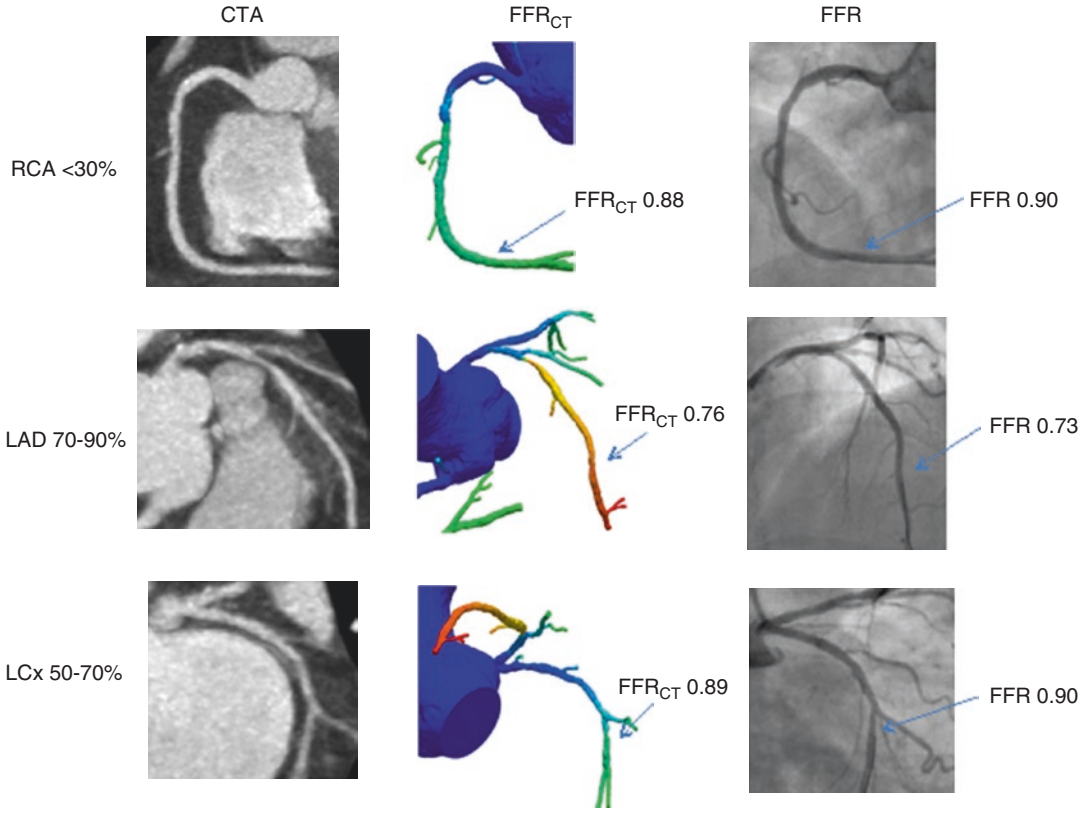

Fig. 7.5 Correlation between FFR_{CT} and invasive FFR. *RCA* right coronary artery, *LAD* left anterior descending coronary artery, *LCx* left circumflex coronary artery, *FFR* fractional flow reserve, *CTA* computed tomography angiography

7.6.1.6 Pearls and Pitfalls

The visual assessment of stenosis severity does not always correlate with hemodynamic significance. While another noninvasive functional test (e.g., SPECT) would establish the presence or absence of patient-specific ischemia, FFR_{CT} is the only single noninvasive test that provides vessel-specific hemodynamic information. Establishing hemodynamic significance of a stenosis is essential to revascularization decisions.

7.6.2 Case 7.2

7.6.2.1 History

A 72-year-old female with new onset atypical angina on waking up in the morning and during episodes of emotional stress. She has a past medical history of hyperlipidemia, hypertension, and is a smoker.

7.6.2.2 CTA Findings

There was a moderate mixed lesion in the proximal LAD and another moderate lesion in the mid LAD (Fig. 7.6).

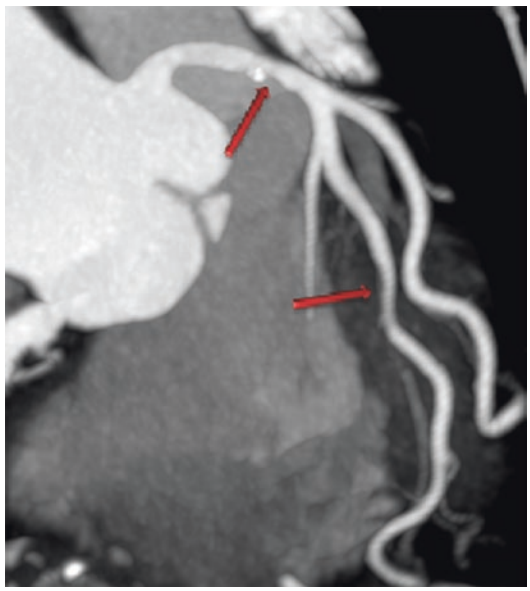

Fig. 7.6 Intermediate stenoses in the proximal and mid LAD (*red arrows*). *LAD* left anterior descending coronary artery

7.6.2.3 FFR_{CT} Results

FFR_{CT} showed that all vessels had FFR_{CT} values of >0.80 (Fig. 7.7).

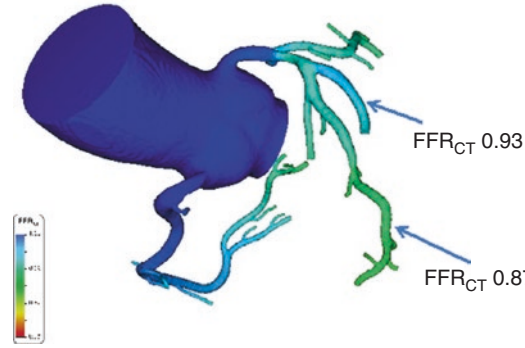

Fig. 7.7 Negative FFR_{CT} of intermediate lesions in the LAD. *LAD* left anterior descending coronary artery

7.6.2.4 Diagnosis

No hemodynamically significant coronary artery disease.

7.6.2.5 Discussion

This patient underwent invasive coronary angiography to ensure the nonsignificance of the lesions. There was good correlation between the FFR_{CT} and invasive FFR values. Although visual assessment of the invasive coronary angiogram showed a 70% stenosis, no revascularization was done and the patient was medically treated (Fig. 7.8).

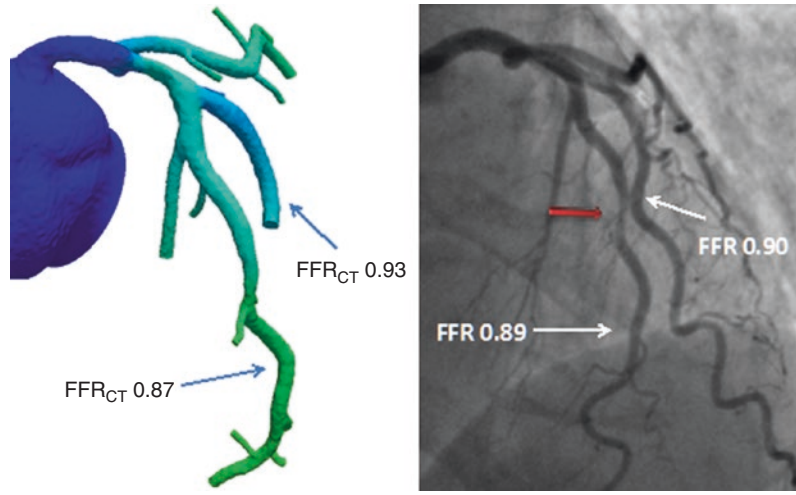

Fig. 7.8 Correlation between FFR_{CT} and invasive FFR. *Red arrow* = non-physiologically significant stenosis. *FFR* fractional flow reserve

7.6.2.6 Pearls and Pitfalls

If there are multiple lesions within the same vessel, an FFR_{CT} of >0.8 in the most distal lesion, ipso facto, means that the more proximal lesions are not significant.

7.6.3 Case 7.3

7.6.3.1 History

A 65-year-old male presented with 2 months of atypical chest pain with dyspnea while playing tennis. He was newly diagnosed with hypertension and hyperlipidemia and was started on a statin and a beta blocker. Despite starting a beta blocker, his symptoms continued. A treadmill EKG was positive.

7.6.3.2 CTA Findings

There were multiple calcified plaques in all three vessels and the left main coronary artery. The LAD had diffuse calcified plaque proximally and focal mixed plaque in the mid LAD. There was focal calcification in the proximal LCX. The RCA had diffuse calcification extending from the proximal to mid RCA (Fig. 7.9a–c).

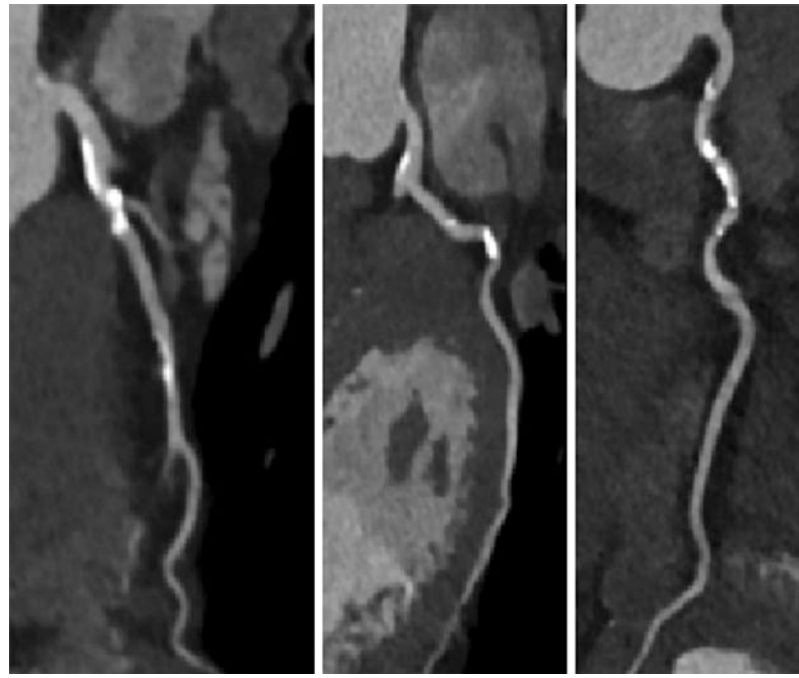

Fig. 7.9 (**a**) diffuse calcification from the left main coronary artery extending into the proximal LAD and focal calcification in the mid LAD (**b**) focal calcification in the proximal LCX and diffuse calcification in the left main coronary artery (**c**) diffuse calcification in the proximal to mid RCA. *RCA* right coronary artery, *LAD* left anterior descending coronary artery, *LCx* left circumflex coronary artery

7.6.3.3 FFR_{CT} Results

FFR_{CT} in the RCA was 0.73. The FFR_{CT} in the LAD was 0.86 and it was 0.82 in the LCX (Fig. 7.10).

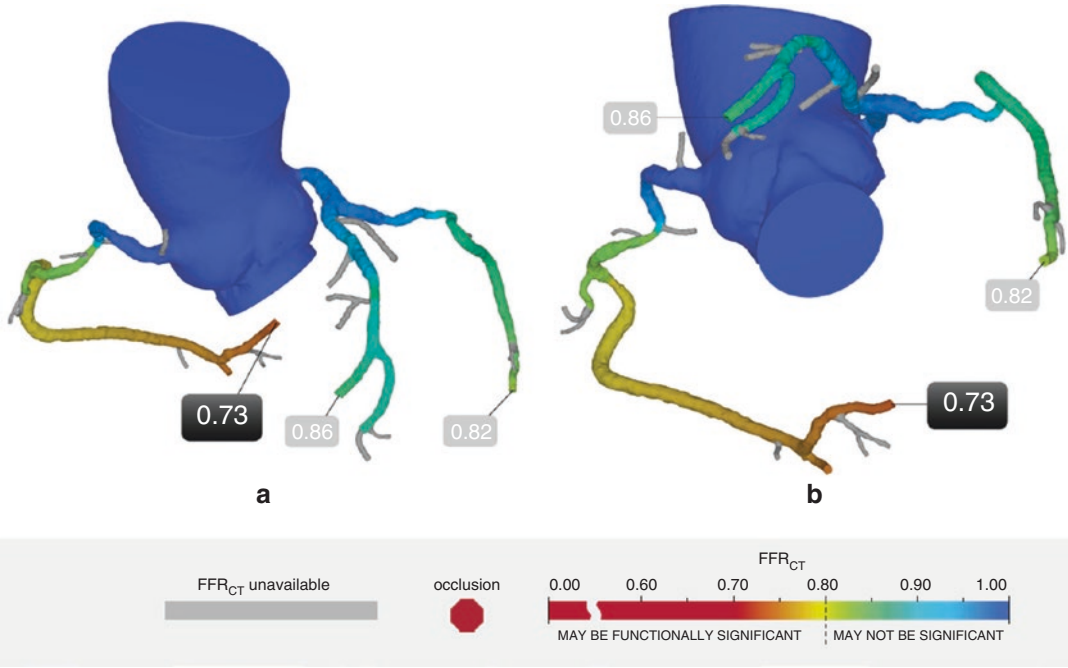

Fig. 7.10 FFR_{CT} values of 0.73 in the RCA, 0.86 in the LAD and 0.82 in the LCX. *RCA* right coronary artery, *LAD* left anterior descending coronary artery, *LCx* left circumflex coronary artery

7.6.3.4 Diagnosis

Single vessel disease of the RCA.

7.6.3.5 Discussion

Here, there are multiple lesions with calcification. The presence of calcified lesions leads to blooming and beam hardening artifacts. This may obscure the lumen and cause a false-positive CTA. The increased presence of calcium increases the risk of misdiagnosis [21, 22]. In addition to that, there are multiple and diffuse lesions in all three vessels. To avoid unnecessary revascularization, it is important to establish hemodynamic significance as well as vessel specificity.

A substudy of the NXT trial examined the diagnostic accuracy of FFR_{CT} versus CTA in the presence of increased calcification, using invasive FFR as the gold standard [23]. FFR_{CT} was significantly more accurate with higher specificity than CTA across all quartiles of calcium severity, while maintaining sensitivity. This improvement was more than twofold to threefold, and was both on a per-patient and per-vessel basis (Table 7.1).

Table 7.1 Diagnostic performance characteristics of FFR_{CT} and coronary CTA in patients and vessels according to quartile of Agatston scores

	Q1			Q2			Q3			Q4		
	FFR_{CT}	CTA	*p* value	FFR_{CT}	CTA	*p* value	FFR_{CT}	CTA	*p* value	FFR_{CT}	CTA	*p* value
Per patient												
Accuracy	85 (73–93)	52 (38–66)	0.0004	83 (71–92)	50 (36–64)	0.0002	83 (70–92)	55 (40–68)	0.0006	74 (60–85)	42 (28–56)	0.0007
Sensitivity	92 (64–100)	100 (75–100)	0.32	77 (46–95)	100 (75–100)	0.66	83 (59–96)	78 (52–94)	0.32	88 (62–98)	94 (70–100)	0.32
Specificity	83 (68–93)	37 (22–53)	0.0001	85 (71–94)	34 (20–51)	<0.0001	83 (66–93)	43 (26–61)	0.0002	68 (50–82)	19 (8–35)	0.0002
PPV	63 (38–84)	33 (19–50)	0.01	63 (35–85)	33 (19–49)	0.02	71 (48–89)	41 (25–59)	0.01	54 (33–73)	33 (20–49)	0.04
NPV	97 (85–100)	100 (78–100)	0.64	92 (79–98)	100 (77–100)	0.95	91 (75–98)	79 (54–94)	0.14	93 (76–99)	88 (47–100)	0.37
Per vessel												
Accuracy	90 (83–95)	74 (65–82)	0.001	85 (74–93)	71 (59–82)	0.03	88 (79–94)	60 (49–71)	<0.0001	83 (73–91)	55 (44–66)	<0.0001
Sensitivity	73 (39–94)	91 (59–100)	0.16	67 (35–90)	92 (62–100)	0.16	93 (68–100)	80 (52–96)	0.16	82 (60–95)	82 (60–95)	1
Specificity	92 (85–97)	72 (62–81)	0.0001	89 (77–96)	67 (53–79)	0.001	87 (76–94)	56 (43–68)	<0.0001	84 (72–92)	46 (33–59)	<0.0001
PPV	53 (27–79)	29 (15–46)	0.06	57 (29–82)	38 (21–58)	0.13	61 (39–80)	29 (16–45)	0.005	64 (44–81)	35 (22–50)	0.0008

Values are proportions (%) with 95% confidence intervals shown in parentheses. The per-patient analysis was performed in 214 patients and the per-vessel analysis in 163 patients (333 vessels). The per-patient and per-vessel AS ranges for Q1 were 0 to 26 and 0 to 0, respectively; for Q2, 27 to 147 and 0 to 22, respectively; for Q3, 148 to 415 and 23 to 120, respectively; and for Q4, 416 to 3599 and 121 to 1703, respectively. *NPV* negative predictive value, *PPV* positive predictive value, *AS* Agatston Score. From Nørgaard, B. L. et al. Influence of Coronary Calcification on the Diagnostic Performance of CT Angiography Derived FFR in Coronary Artery Disease: A Substudy of the NXT Trial. *JACC Cardiovasc Imaging* 2015 Sep;8(9):1045–55. doi: https://doi.org/10.1016/j.jcmg.2015.06.003. Epub 2015 Aug 19. Used with permission

7.6.3.6 Pearls and Pitfalls

The presence of heavy calcification can result in blooming and beam hardening artifacts, resulting in a false-positive CTA. Because the segmentation methods used in FFR_{CT} use models that take both global and local flow, and correct for calcium blooming, the presence of segmental artifacts (e.g., calcium) may not significantly affect the FFR_{CT} value.

7.6.4 Case 7.4

7.6.4.1 History

A 53-year-male ex-smoker with diabetes mellitus, hypertension, and hyperlipidemia. He also has a family history of CAD. He is asymptomatic but leads a sedentary lifestyle.

7.6.4.2 CTA Findings

There is multivessel disease. There is soft plaque causing severe stenosis in the proximal RCA. There is soft plaque causing <50% stenosis in the left main coronary artery. There is diffused mixed plaque causing moderate stenosis in the proximal LAD, with a bifurcation lesion extending into the LAD and D1 (Fig. 7.11a, b).

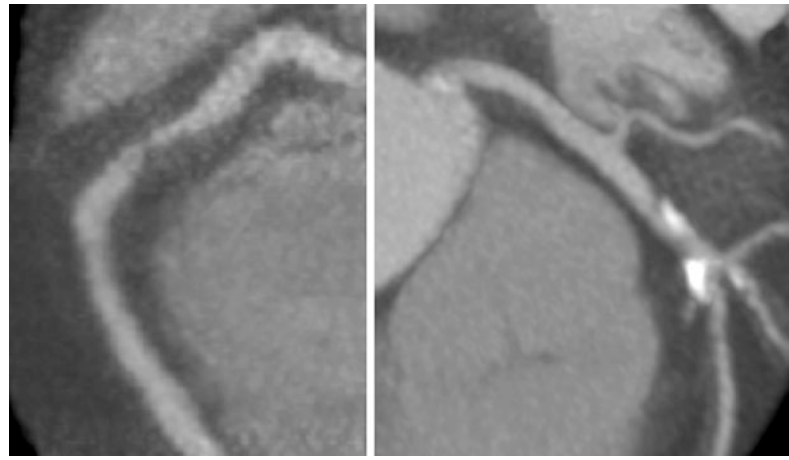

Fig. 7.11 (**a**) Severe stenosis in the proximal RCA. (**b**) <50% stenosis in the left main coronary artery. There is a mixed lesion at the bifurcation of the LAD and D1. *RCA* right coronary artery, *LAD* left anterior descending coronary artery, *D1* first diagonal coronary artery

7.6.4.3 FFR_{CT} Results

FFR_{CT} was 0.62 in the RCA, 0.73 in the LAD, and <0.70 in D1 (Fig. 7.12).

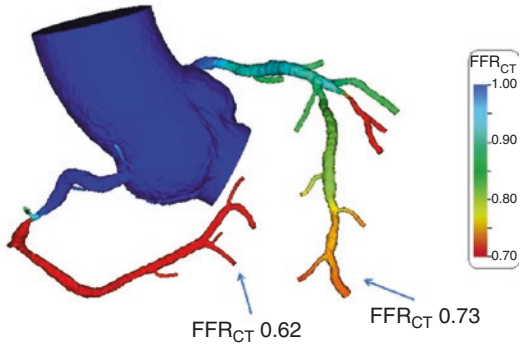

Fig. 7.12 FFR_{CT} showing multivessel disease

7.6.4.4 Diagnosis

Multivessel disease.

7.6.4.5 Discussion

The presence of numerous lesions in multivessel disease does not seem to affect the accuracy of FFR_{CT} values, which correlated well with invasive FFR (Fig. 7.13).

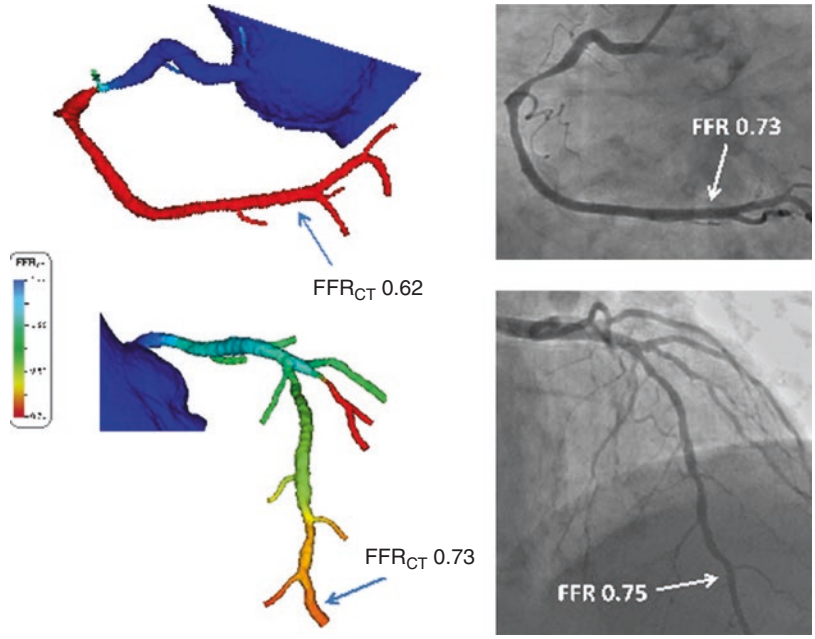

Fig. 7.13 Correlation between FFR_{CT} and invasive FFR showing significant disease in the RCA and LAD. *RCA* right coronary artery, *LAD* left anterior descending coronary artery

7.6.4.6 Pearls and Pitfalls

Despite the presence of significant multivessel disease, patients may be fairly asymptomatic if they lead sedentary lifestyles or modulate their activities to mask their symptoms. The presence of multiple risk factors should alert the clinician to have a high index of suspicion. High risk patients will likely have multivessel disease; it is still important to establish the hemodynamic significance of each lesion on a per-vessel basis.

7.6.5 Case 7.5

7.6.5.1 History

A 61-year-old diabetic male with stable angina. He also has hypertension, hyperlipidemia, and is a current smoker. His angina symptoms continue despite being started on nitrates. He has a normal LVEF.

7.6.5.2 CTA Findings

There is diffuse mixed plaque from the proximal to distal LAD, with mild to moderate disease (Fig. 7.14a, b).

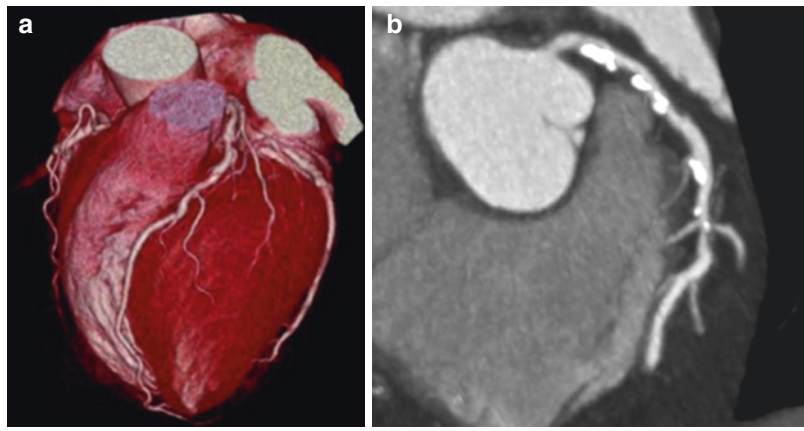

Fig. 7.14 (**a**) volume rendered and (**b**) 2d views showing diffuse mixed plaque from proximal to distal LAD. *LAD* left anterior descending coronary artery

7.6.5.3 FFR_{CT} Results

The FFR_{CT} value was 0.78 in the LAD (Fig. 7.15).

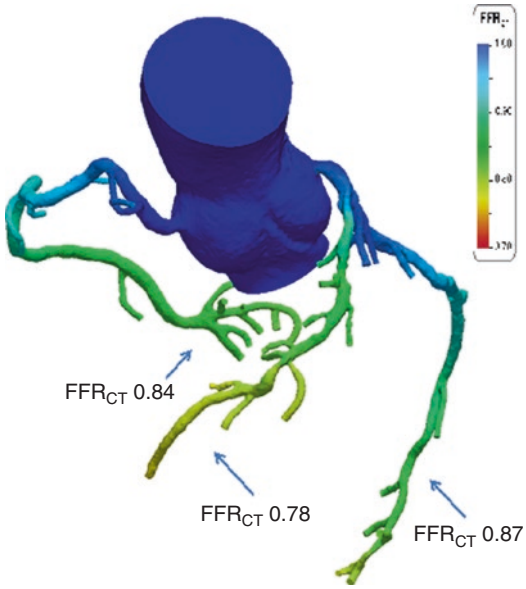

Fig. 7.15 FFR_{CT} of 0.78 in the LAD. *LAD* left anterior descending coronary artery

7.6.5.4 Diagnosis

Diffuse disease in the LAD.

7.6.5.5 Discussion

In this case, CTA shows a 60% stenosis along the LAD. It is important to establish the hemodynamic significance of the lesion. Furthermore, it would be ideal if we were able to predict the FFR post-stenting prior to any intervention. This would help in planning the revascularization.

One of the novel uses of FFR_{CT} is "virtual stenting" [24]. Using the same modeling techniques, it is possible to modify the luminal diameter back to "normal" (as compared to proximal and distal to the stenosis). This virtually stents the lesion and predicts, noninvasively, the FFR_{CT} if stenting were to be actually done. In this case, there was good correlation between the predicted and actual FFR pre- and post-stenting (Fig. 7.16a–d).

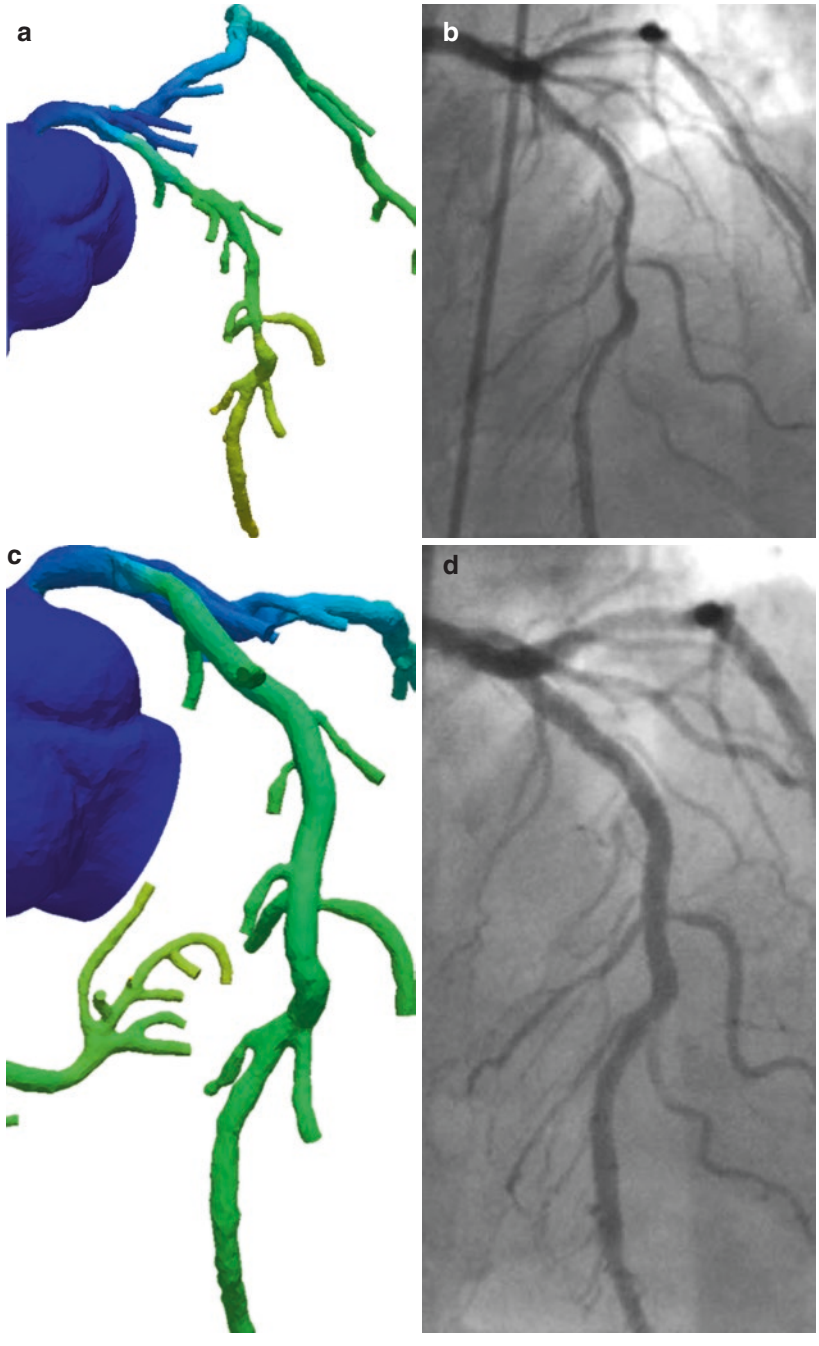

Fig. 7.16 Correlation of FFR_{CT} and invasive FFR pre- and post-stenting. (**a**) FFR_{CT} pre-stenting of 0.78 (**b**) invasive FFR pre-stenting of 0.74 (**c**) virtual stenting FFR_{CT} of 0.86 done pre-intervention (**d**) invasive FFR post-stenting of 0.83. *FFR* fractional flow reserve

7.6.5.6 Pearls and Pitfalls

This illustrates a novel new use of FFR_{CT}. In future, virtual stenting using FFR_{CT} can help predict improvement after stenting a particular segment or lesion. This can be used to help plan the amount or extent of stenting required in cases involving multiple lesions.

References

1. Budoff MJ, et al. Diagnostic performance of 64-multidetector row coronary computed tomographic angiography for evaluation of coronary artery stenosis in individuals without known coronary artery disease: results from the prospective multicenter ACCURACY (Assessment by Coronary Computed Tomographic Angiography of Individuals Undergoing Invasive Coronary Angiography) trial. J Am Coll Cardiol. 2008;52:1724–32.
2. Miller JM, et al. Diagnostic performance of coronary angiography by 64-row CT. N Engl J Med. 2008;359:2324–36.
3. Meijboom WB, et al. Diagnostic accuracy of 64-slice computed tomography coronary angiography: a prospective, multicenter, multivendor study. J Am Coll Cardiol. 2008;52:2135–44.
4. Shaw LJ, et al. Gated myocardial perfusion single photon emission computed tomography in the clinical outcomes utilizing revascularization and aggressive drug evaluation (COURAGE) trial, Veterans Administration Cooperative study no. 424. J Nucl Cardiol. 2006;13:685–98.
5. Hachamovitch R, Hayes SW, Friedman JD, Cohen I, Berman DS. Comparison of the short-term survival benefit associated with revascularization compared with medical therapy in patients with no prior coronary artery disease undergoing stress myocardial perfusion single photon emission computed tomography. Circulation. 2003;107:2900–7.
6. Metz LD, et al. The prognostic value of normal exercise myocardial perfusion imaging and exercise echocardiography: a meta-analysis. J Am Coll Cardiol. 2007;49:227–37.
7. Tonino PAL, et al. Angiographic versus functional severity of coronary artery stenoses in the FAME study fractional flow reserve versus angiography in multivessel evaluation. J Am Coll Cardiol. 2010;55:2816–21.
8. Pijls NHJ, et al. Percutaneous coronary intervention of functionally nonsignificant stenosis: 5-year follow-up of the DEFER Study. J Am Coll Cardiol. 2007;49:2105–11.
9. De Bruyne B, et al. Fractional flow reserve-guided PCI versus medical therapy in stable coronary disease. N Engl J Med. 2012;367:991–1001.
10. Lucas FL, Siewers AE, Malenka DJ, Wennberg DE. Diagnostic-therapeutic cascade revisited: coronary angiography, coronary artery bypass graft surgery, and percutaneous coronary intervention in the modern era. Circulation. 2008;118:2797–802.
11. LaBarbera M. Principles of design of fluid transport systems in zoology. Science. 1990;249:992–1000.
12. West GB, Brown JH, Enquist BJ. A general model for the origin of allometric scaling laws in biology. Science. 1997;276:122–6.
13. Choy JS, Kassab GS. Scaling of myocardial mass to flow and morphometry of coronary arteries. J Appl Physiol (1985). 2008;104:1281–6.
14. Kamiya A, Togawa T. Adaptive regulation of wall shear stress to flow change in the canine carotid artery. Am J Physiol. 1980;239:H14–21.
15. Glagov S, Weisenberg E, Zarins CK, Stankunavicius R, Kolettis GJ. Compensatory enlargement of human atherosclerotic coronary arteries. N Engl J Med. 1987;316:1371–5.
16. Zarins CK, Zatina MA, Giddens DP, Ku DN, Glagov S. Shear stress regulation of artery lumen diameter in experimental atherogenesis. J Vasc Surg. 1987;5:413–20.
17. Taylor CA, Figueroa CA. Patient-specific modeling of cardiovascular mechanics. Annu Rev Biomed Eng. 2009;11:109–34.
18. Zarins CK, Taylor CA, Min JK. Computed fractional flow reserve (FFTCT) derived from coronary CT angiography. J Cardiovasc Transl Res. 2013;6:708–14.
19. Min JK, et al. Effect of image quality on diagnostic accuracy of noninvasive fractional flow reserve: results from the prospective multicenter international DISCOVER-FLOW study. J Cardiovasc Comput Tomogr. 2012;6:191–9.
20. Nørgaard BL, et al. Diagnostic performance of noninvasive fractional flow reserve derived from coronary computed tomography angiography in suspected coronary artery disease: the NXT trial (Analysis of Coronary Blood Flow Using CT Angiography: Next Steps). J Am Coll Cardiol. 2014;63:1145–55.
21. Dewey M, et al. Patient characteristics as predictors of image quality and diagnostic accuracy of MDCT compared with conventional coronary angiography for detecting coronary artery stenoses: CORE-64 Multicenter International Trial. AJR Am J Roentgenol. 2010;194:93–102.
22. Abdulla J, Pedersen KS, Budoff M, Kofoed KF. Influence of coronary calcification on the diagnostic accuracy of 64-slice computed tomography coronary angiography: a systematic review and meta-analysis. Int J Cardiovasc Imaging. 2012;28:943–53.
23. Nørgaard BL, et al. Influence of coronary calcification on the diagnostic performance of CT angiography derived FFR in coronary artery disease. A substudy of the NXT trial. JACC Cardiovasc Imaging. 2015;8(9):1045–55. https://doi.org/10.1016/j.jcmg.2015.06.003.
24. Kim K-H, et al. A novel noninvasive technology for treatment planning using virtual coronary stenting and computed tomography-derived computed fractional flow reserve. JACC Cardiovasc Interv. 2014;7:72–8.

Cardiac CTA in the Emergency Department

8

David Lehmkuhl, Constantino S. Pena, and Ricardo C. Cury

The timely diagnosis of chest pain to this day remains a difficult task in the emergency department (ED). Currently, chest pain is one of the leading causes of presentation to the ED in the United States. However, only a fraction of the patients with chest pain present with sufficient electrocardiogram (ECG) changes that require immediate intervention via catheterization. Therefore, the vast majority of patients require both costly and timely diagnostic workups prior to being safely discharged.

The current standard-of-care for chest pain workup requires serial ECGs and cardiac biomarkers as well as multiple imaging tests. The serial tests increase length of stay and accumulate costs. In response to these problems, cardiac computed tomography angiography (CCTA) has become helpful in the ED setting. In recent studies, CCTA has been shown in low-risk populations to increase the rate of discharge from the ED (49.6% vs. 22.7%, 95% CI, 21.4–32.2) [1], decrease the length of stay (range 27.5–51% less than standard length) [1–4], increase the rate of detection of coronary artery disease (CAD) (9.0% vs. 3.5%, 95% CI, 0–11.2) [1], and reduce costs (range 20–38% reduction) [3, 5] when compared to the current standard-of-care [4, 6].

A recent systematic review and meta-analysis determined the safety of CCTA in the ED using 18 studies containing 9592 patients with a median follow-up time of 20 months [7]. The results of the study demonstrated the effectiveness of CCTA by comparing the combined annual rate of major adverse cardiovascular events (MACE) in patients with minimal or no stenosis (0.17%, $p < 0.05$), nonobstructive CAD defined by <50% coronary lumen diameter stenosis (1.41%, $p < 0.05$), and obstructive CAD defined by >50% coronary lumen diameter stenosis (8.84%, $p < 0.05$). In addition, the pooled negative likelihood ratio for MACE in patients with minimal or no stenosis was 0.008 (95% CI: 0.003–0.21, p 0.001, $I^2 = 0\%$) with a positive likelihood ratio of 1.70 (95% CI: 1.24–2.02, $p < 0.001$, $I^2 = 0\%$), sensitivity of 0.99 (95% CI: 0.93–1.00, $p < 0.001$, $I^2 = 0\%$), and specificity 0.41 (95% CI: 0.31–0.52, $p < 0.001$, $I^2 = 72\%$).

Prior to utilizing CCTA and implementing the technology into clinical workflow in the ED, logistical planning and a methodical stepwise

D. Lehmkuhl, BS
Herbert Wertheim College of Medicine, Florida International University, 11200 SW 8th Street, AHC2, Miami, FL 33199, USA
e-mail: dlehm007@fiu.edu

C.S. Pena, MD (✉)
Miami Cardiac and Vascular Institute, Baptist Hospital, 8900 North Kendall Drive, Miami, FL 33176, USA
e-mail: tinopena@msn.com

R.C. Cury, MD
Department of Radiology, Miami Cardiac and Vascular Institute, Baptist Health of South Florida, 8900 North Kendall Drive, Miami, FL 33176, USA
e-mail: rcury@baptisthealth.net

C. Smuclovisky (ed.), *Coronary Artery CTA*, https://doi.org/10.1007/978-3-319-66988-5_8

approach are required [8]. In order to begin the process, a collaborative multidisciplinary team consisting of cardiologists, emergency physicians, hospitalists, nursing staff, and radiologists trained in cardiovascular CT must be available. The next step involves careful selection of ideal candidates for the study. Candidates best suited for CCTA are those presenting with negative initial cardiac enzymes, a normal or nondiagnostic ECG, and are without contraindications or relative contraindications for a coronary CTA. In addition, candidates should be screened using a standardized risk stratification tool in order to prevent exposure to additional radiation in patients with very low risk or delay patients that require a more invasive test. Lastly, a standardized report should be generated for the providing physician and specific treatment plan should be advised based on the study to create a uniform communication.

Through a joint effort from multiple disciplines at Baptist Hospital of Miami and Miami Cardiac and Vascular Institute (MCVI), a protocol to utilize CCTA was developed and implemented into practice [2, 9]. Upon presentation to the ED, cardiac enzymes are measured, an ECG is performed and a thrombolysis in myocardial infarction (TIMI) score is calculated on all patients who present with chest pain with a possible cardiac etiology. The patient is deemed moderate to high risk of ACS if they possess any of the following criteria: TIMI score > 2, a diagnostic ECG, or positive cardiac enzymes. In this situation, the patient is referred to catheterization lab or single-photon emission computed tomography myocardial perfusion imaging (SPECT MPI) based on the clinical scenario and the ACC/AHA guidelines [10]. If the patient does not meet the moderate- to high-risk category, the patient is deemed low risk and is eligible to receive a CCTA with the primary goal of detection of coronary stenosis.

Prior to the study, patients at MCVI are prepped according to a protocol in order to streamline the procedure and develop the best possible results in the least amount of time. First, patients are screened for contraindications or relative contraindications for the procedure. If a patient has severe renal insufficiency or iodine allergy, they are excluded from CCTA completely. If there is a relative contraindication (pregnancy, inability to perform a breath hold, inability to lay flat, obese, contraindication to beta-blockers, nitrates, recent use of phosphodiesterase-5 inhibitors, previous coronary calcium score > 1000, mild renal insufficiency or arrhythmia that cannot be controlled with beta-blockade), the risks and benefits from the procedure should be examined. If a patient has a relative contraindication, an initial evaluation with stress MPI is a preferred alternative. IV access for contrast injection is established and the heart rate is measured. If the heart rate is regular and >65 beats/min or >60 beats/min and irregular, the patient is given a single dose of oral metoprolol 100 mg 1 h prior to the scan. Last, the patient is given 400 μg of sublingual nitroglycerin a few minutes prior to being injected for the procedure. Prospective ECG-triggered technique is the preferred method if the patient has a stable rhythm and a heart rate < 65 beats/min. Retrospective EGC-triggered techniques may be used if ECG-based tube current modulation is available to reduce radiation dose.

In addition to developing a well-defined algorithm for selecting patients who would benefit from a CCTA, it is also important to stratify patients who have received a CCTA and determine a treatment algorithm based on the results. At MCVI, patients who have less than 40% coronary stenosis are deemed to have mild stenosis. These patients can be safely discharged from the ED and are instructed to have follow-up outpatient management with a cardiologist. Patients

who are found to have between 40 and 70% coronary stenosis are considered to have moderate stenosis and additional tests with stress MPI or catheterization with fractional flow reserve are recommended prior to discharge. If patients are found to have >70% coronary stenosis, they are believed to have severe stenosis and catheterization should be performed for further diagnosis and possible intervention prior to discharging the patients.

In order to ensure proper treatment following CCTA, structured reporting between providers is critical for the implementation of CCTA. Standardized site-dependent templates are recommended in order to reduce the likelihood of neglecting important elements in the report. In addition, a standard template allows the reporter to convey information clearly to the interpreter regardless of training background and improves reliability of the report between different institutions. Furthermore, reports should be completed within 1 h and directly communicated to the ordering physician if there are any positive findings [11].

If a clinician has a high suspicion for a pulmonary embolism (PE) or aortic dissection in addition to ACS and the patient is classified low risk as previously established, the patient can be considered for a "triple-rule-out" (TRO) protocol with extended thoracic coverage. A recent study showed that a TRO protocol had a NPV of 99.4% in 201 patients with low-to-moderate risk ACS patients for adverse outcomes at 30 days [12]. The efficacy of this demonstrates the usefulness for this protocol in situations where the differential diagnosis is broad.

The TRO protocol requires simultaneous attenuation of both the pulmonary arterial vasculature and systemic circulation in order to properly visualize the necessary structures. Since peak enhancement of contrast in the pulmonary arteries occur 10–12 s prior to systemic arterial circulation (bolus transit time), the contrast must be introduced at a high contrast bolus volume of a minimum 130 cm^3 of non-ionic iodine contrast at a slow flow rate of 4 cm^3/s. Both of these modifications allow for an increase in the bolus transit time in order to extend the timeframe for the CT image acquisition. With this altered protocol, the TRO protocol has an advantage to view extracardiac structures but has the drawback of additional radiation dosage and less sensitivity when compared to CCTA [13].

In conclusion, CCTA has been shown to be a highly effective tool in multiple single-center and multicenter trials. CCTA has been shown to lower costs, reduce hospital length of stay, and decrease time to diagnosis. For proper implementation of CCTA to rule out ACS, a hospital system must be equipped with the proper personnel and an algorithm detailing the patients who would benefit. Patients should be streamlined with proper management prior to imitation of the study. In addition, patients undergoing CCTA should also have a comprehensive algorithm for management after results are obtained. Moreover, the physicians involved with the patient's care should have a standardized report within a timely fashion. If the ordering clinician is uncertain of the etiology of chest pain and the possibility of aortic dissection or pulmonary embolism is entertained, a TRO study can be performed due to its high NPV.

8.1 Case 1

A 61-year-old male presented with increasing frequency of chest pain over the last 2 weeks. Upon presentation to the ED, he was found to have one set of negative troponins and ECGs. The patient had hypertension and a family history of heart disease. TIMI risk score: 0.

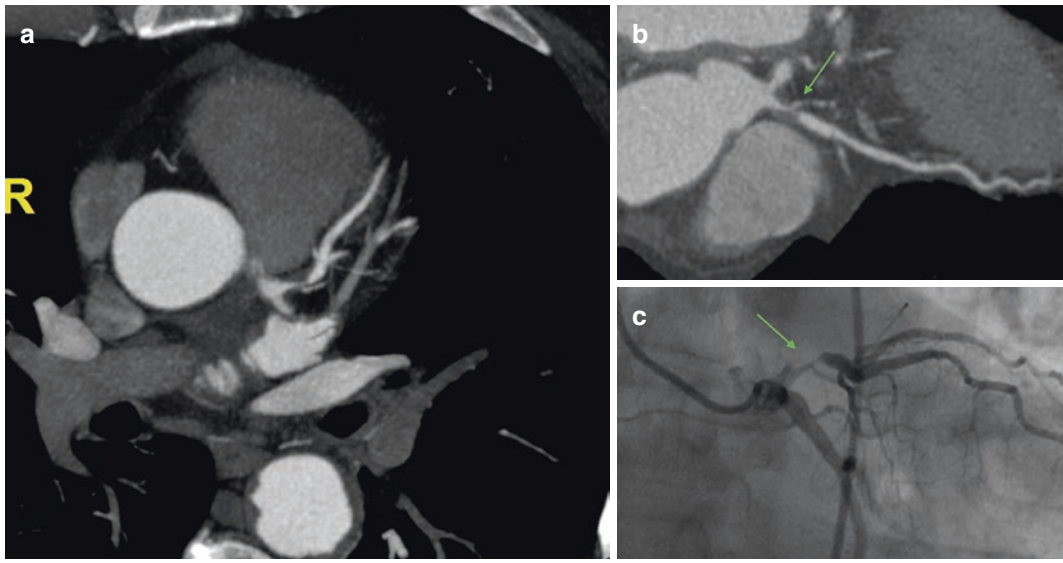

Fig. 8.1 (**a**) Axial and (**b**) curved multiplanar reformation (MPR) views show focal high-grade stenotic lesion in the proximal left anterior descending artery estimated to narrow the lumen by greater than 70% by a noncalcified "soft" plaque. Patient had an Agatston-Janowitz Calcium Score of 4 units all within left circumflex artery. (**c**) Angiography showed mild hypokinesis in the anterior wall of the left ventricle and 95% stenosis in the left anterior descending artery. The stenosis was treated with a drug-eluting stent that resulted in TIMI 3 flow with 0% stenosis

8.2 Case 2

A 53-year-old male presented with intermittent central chest pressure over the past month. The chest pain was unrelated to activity and would last up to 2 h. He had previous noninvasive testing performed a year prior to presentation that was negative for any cardiac abnormalities. The patient's risk factors were hypertension, former smoker, and family history of heart disease. TIMI risk score: 1.

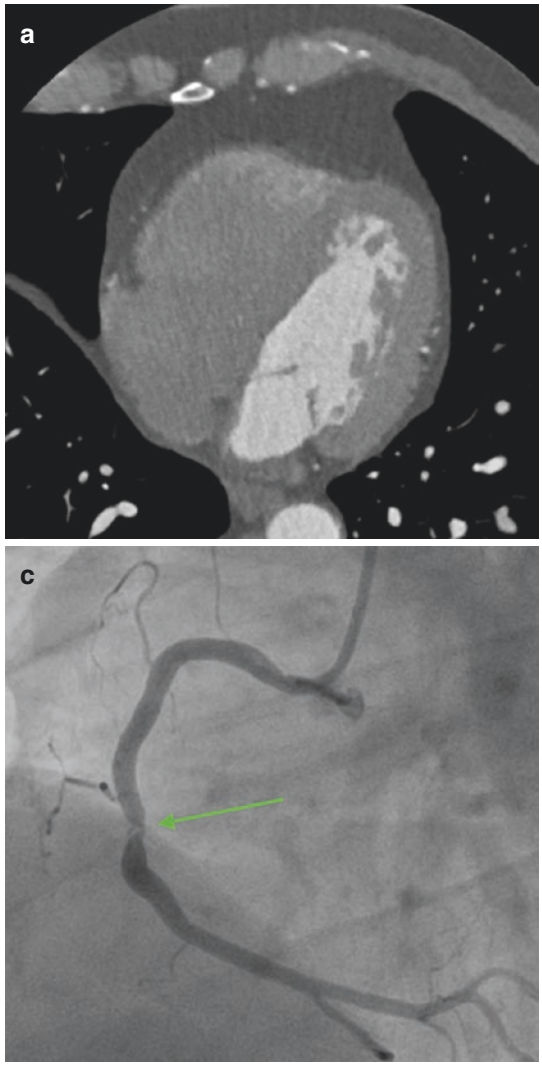

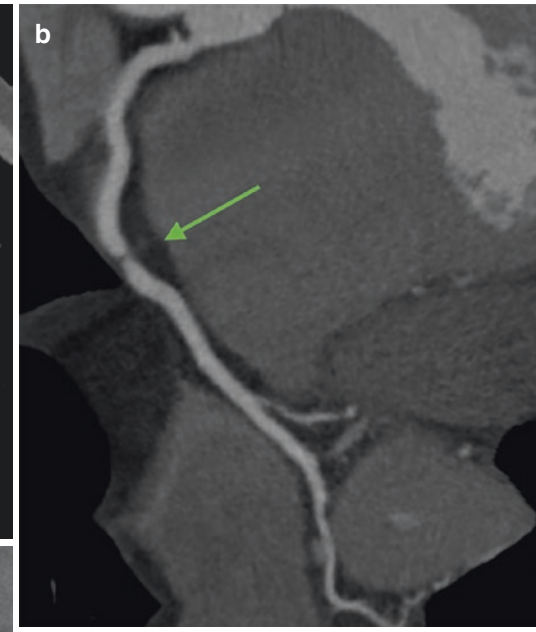

Fig. 8.2 (**a**) Axial and (**b**) curved MPR views show a focal noncalcified plaque in the middle of the right coronary artery creating a greater than 70% stenosis was confirmed on all phases of the cardiac cycle. Patient had an Agatston-Janowitz Calcium Score of 0. (**c**) Angiography showed single vessel coronary disease with a 95% stenotic lesion in the middle of the right coronary artery. The remainder of the coronary tree was normal. A drug-eluting stent provided TIMI 3 flow with 0% stenosis

8.3 Case 3

A 50-year-old male presented with progressive angina over the past month with severe chest pain on arrival to the ED. The patient had hypertension, diabetes mellitus, hyperlipidemia, a family history of heart disease. He had taken aspirin in the past week. TIMI risk score: 2.

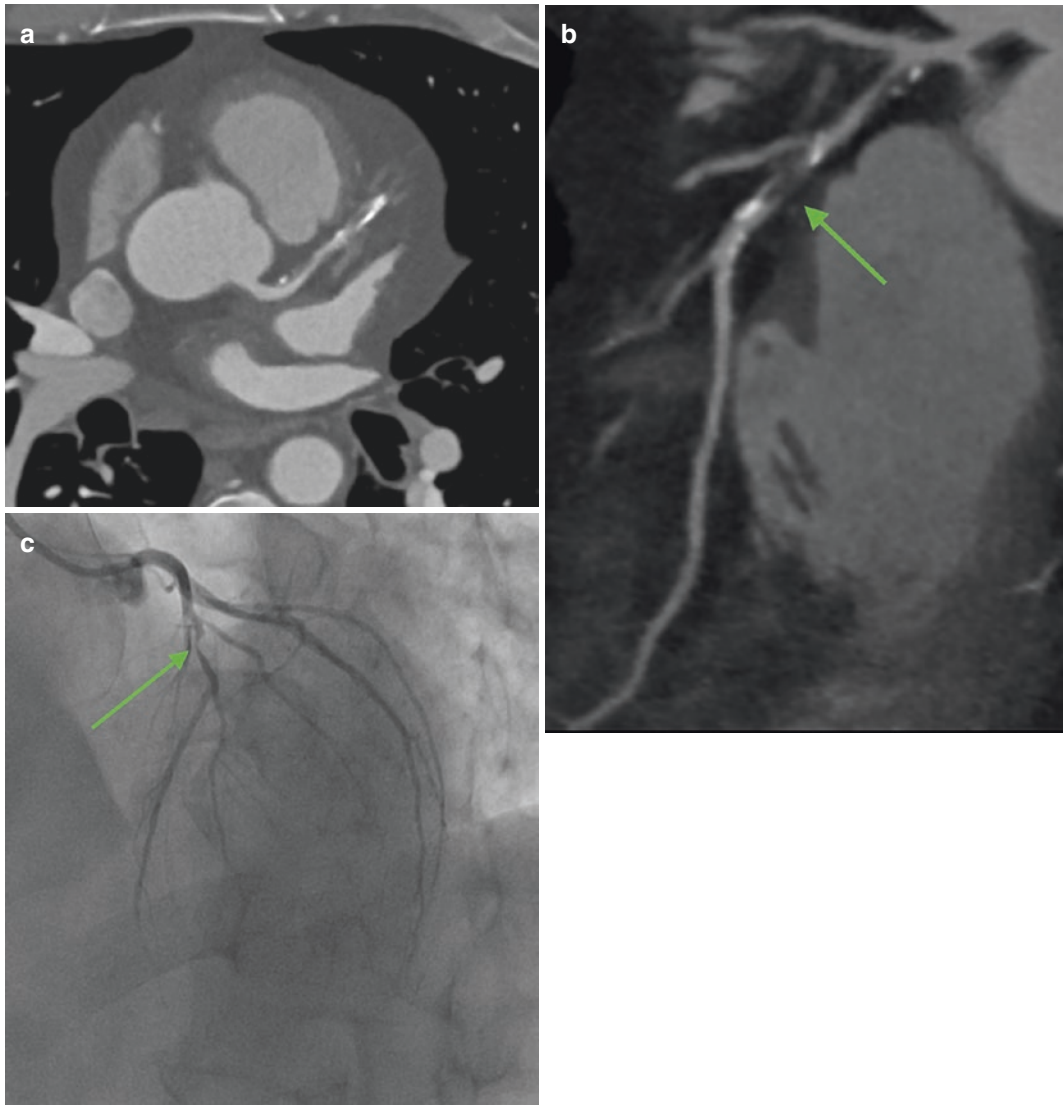

Fig. 8.3 (**a**) Axial and (**b**) curved MPR views show a mixed plaque which was predominantly noncalcified in the mid left anterior descending artery causing a greater than 90% stenosis. Patient had an Agatston-Janowitz Calcium Score of 472; (Percentile: 98). (**c**) Angiography demonstrated single vessel disease with a 99% stenosis of the mid left anterior descending artery with TIMI 2 flow

8.4 Case 4

A 56-year-old male developed chest pain on postoperative day #1 after a laparoscopic cholecystectomy. The patient had a previous myocardial infarction 4 years prior to the event that resulted in placement of two stents placed in the right coronary artery. He had a history of diabetes mellitus, hypertension, and hyperlipidemia. TIMI score: 2.

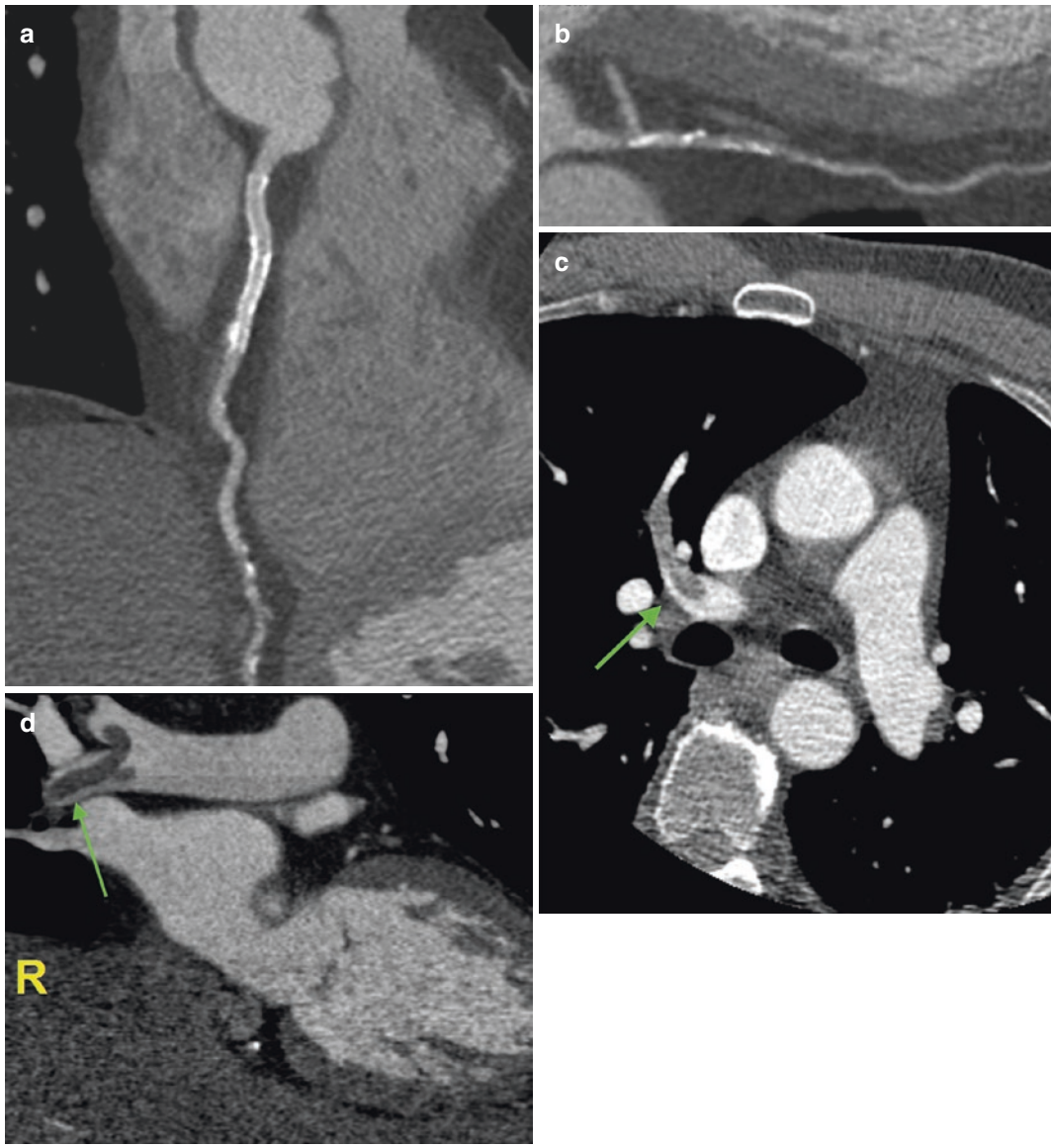

Fig. 8.4 (**a**) A curved MPR view of the right coronary artery demonstrated patent stents with nonobstructive (less than 30% stenosis) disease. (**b**) A curved MPR view of the left anterior descending artery and left main demonstrated nonobstructive disease. (**c**) Axial and (**d**) coronal show pulmonary emboli in the distal right main pulmonary artery that extended into the subsegmental arteries of the right upper lobe and right middle lobe

8.5 Case 5

A 55-year-old male presented with intermittent chest pain unrelated to physical activity. The patient had a history of hypertension, hyperlipidemia, and diabetes mellitus. TIMI risk score: 1.

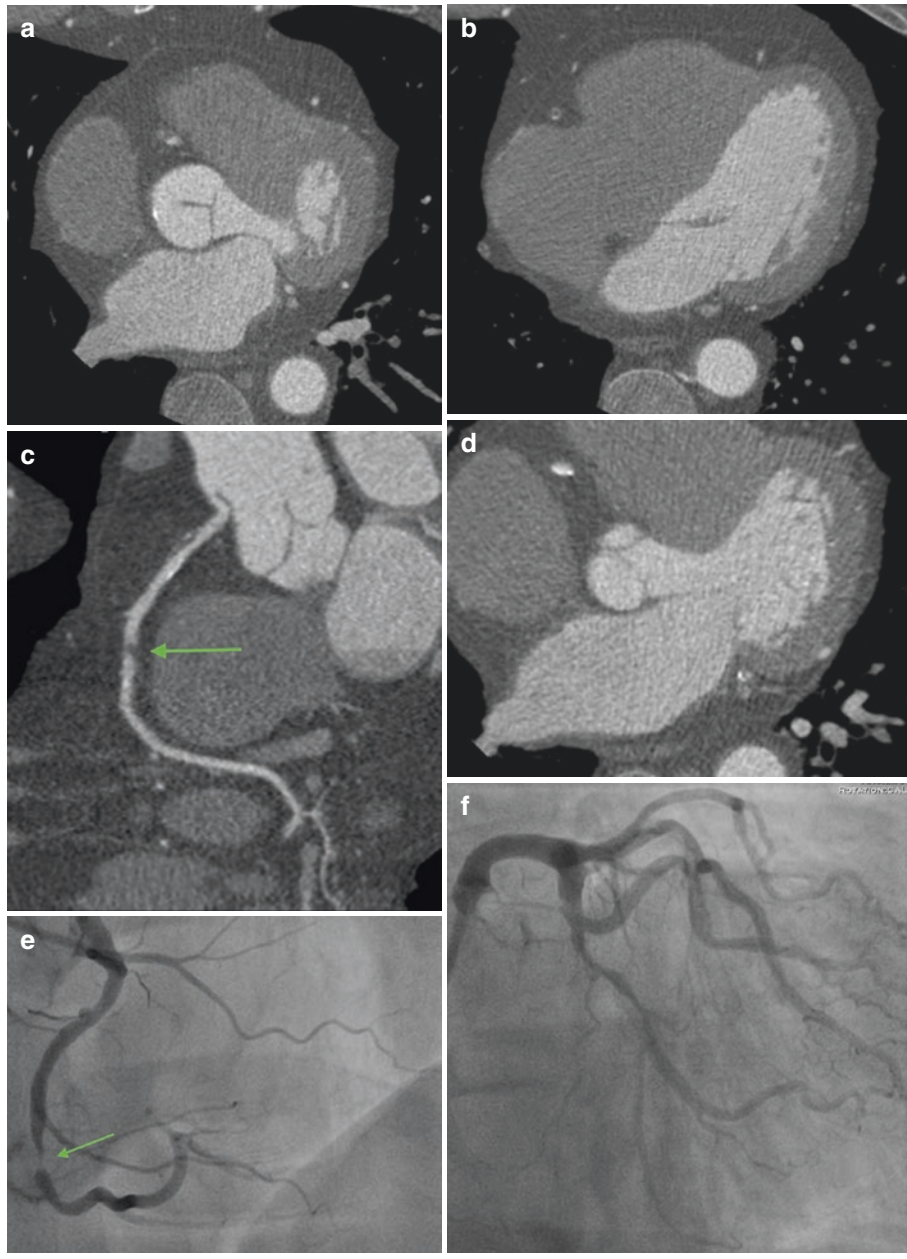

Fig. 8.5 (**a**) Axial view showing a focal greater than 50% obstructing noncalcified plaque within the proximal right coronary artery and (**b**) an axial view of a tandem greater than 70% obstructing noncalcified plaque seen in the mid right coronary artery. (**c**) A curved MPR view shows both lesions in the right coronary artery. (**d**) Axial view showing a nonobstructive (less than 30%) lesion in the left circumflex and a greater than 50% mixed plaque within the first obtuse marginal artery. Patient had an Agatston-Janowitz Calcium Score of 489; Percentile: 96%. (**e**) Angiography demonstrated a greater than 90% eccentric stenosis of the mid right coronary artery and (**f**) a 50–60% narrowing in the left circumflex and 80% narrowing of a mid-obtuse marginal branch. A drug-eluting stent was utilized to treat the right coronary artery. A fractional flow reserve was measured and the left circumflex was not treated

8.6 Case 6

A 53-year-old male presented with chest pain radiating to the upper back for 2 days. Upon arrival to the ED, he had a TIMI risk score of 2. His risk factors were diabetes mellitus, hypertension, hyperlipidemia, smoking history, and family history of heart disease. TIMI score at time of CCTA: 2. After CCTA was performed, he developed positive troponins with a peak of 3.2 and new T wave inversions in leads II, III, aVF, and V5-V6. A 2D-echocardiogram showed no segmental abnormalities.

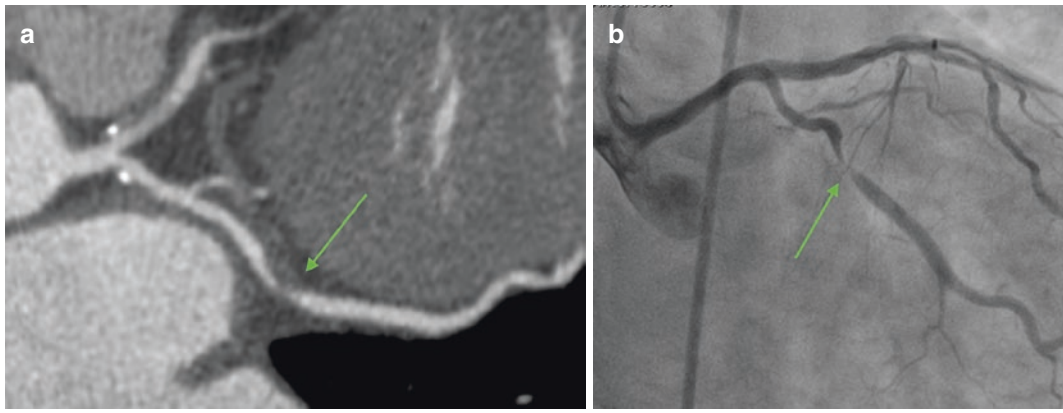

Fig. 8.6 (**a**) A curved MPR showed greater than 70% stenosis secondary to a noncalcified plaque was seen in the mid left circumflex artery. Additionally, nonobstructive disease (less than 30% stenosis) was seen in the left anterior descending artery and right coronary artery (not shown). Patient had an Agatston-Janowitz Calcium Score of 197; Percentile: 93. (**b**) Between 90% stenosis of the mid segment of the circumflex artery was seen on angiography. A drug-eluting stent was deployed

8.7 Case 7

A 48-year-old female presented with acute chest pain. She had a history of peripheral vascular disease, atrial fibrillation, hypertension, systemic lupus erythematosus, hyperlipidemia, and a family history of heart disease. She had used aspirin in the preceding week. TIMI risk score: 2.

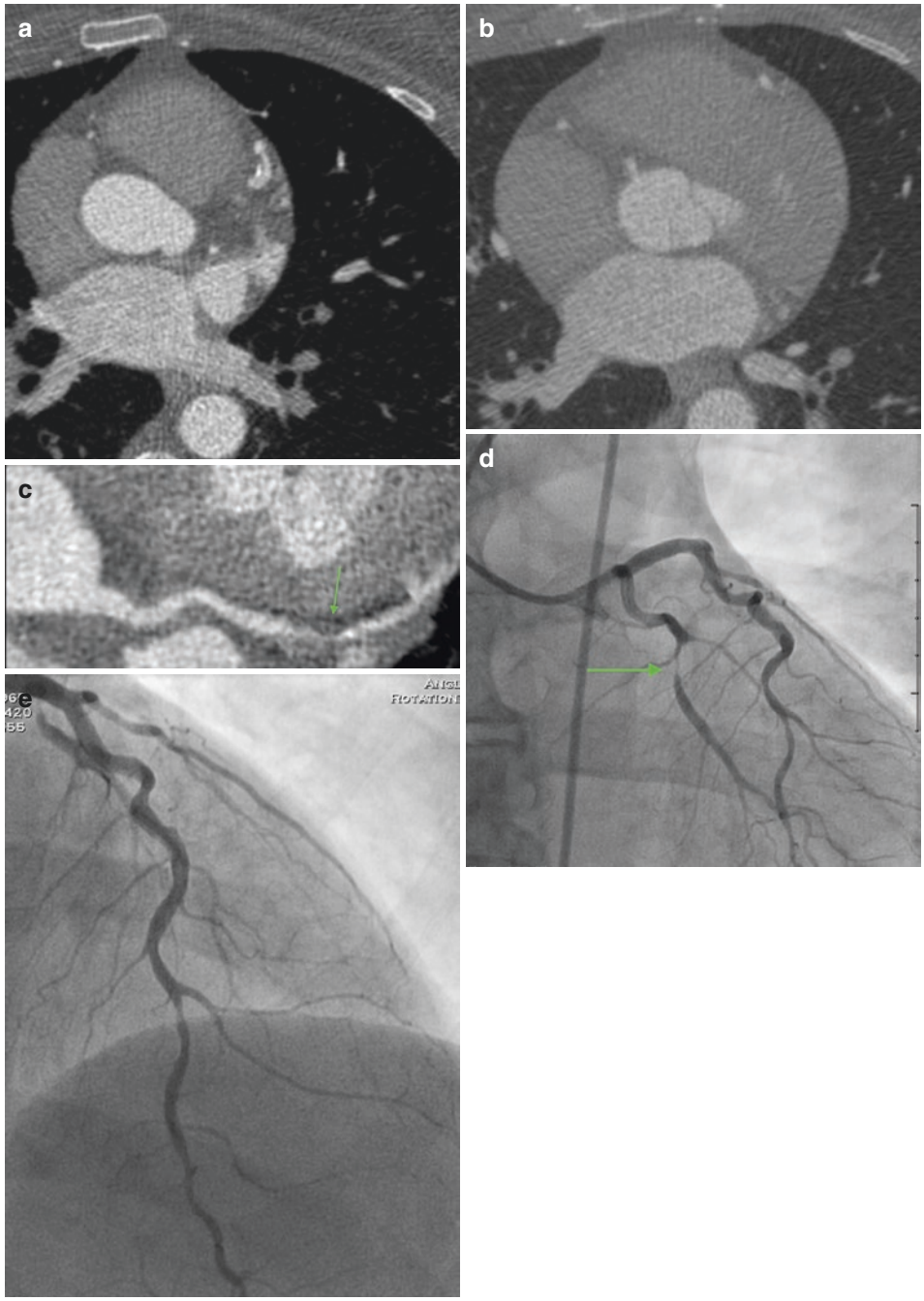

Fig. 8.7 (**a**) Axial view shows a mixed plaque within the left anterior descending artery that was nonobstructive (less than 30%). (**b**) An additional axial view shows a greater than 70% stenosis in the mid left circumflex artery due to a noncalcified plaque. (**c**) Curved MPR of the left circumflex is shown. The patient had an Agatston-Janowitz Calcium Score of 239; Percentile: 99%. (**d**) The left circumflex demonstrated a 90% stenosis that was treated with angioplasty and stent placement. (**e**) There was nonobstructive plaque in the left anterior descending artery

8.8 Case 8

A 66-year-old male presented with worsening chest pain that was consistent with unstable angina. He had a history of peripheral artery disease, diabetes mellitus, hypertension, hyperlipidemia, and kidney disease. He had used aspirin in the preceding week. TIMI risk score: 3.

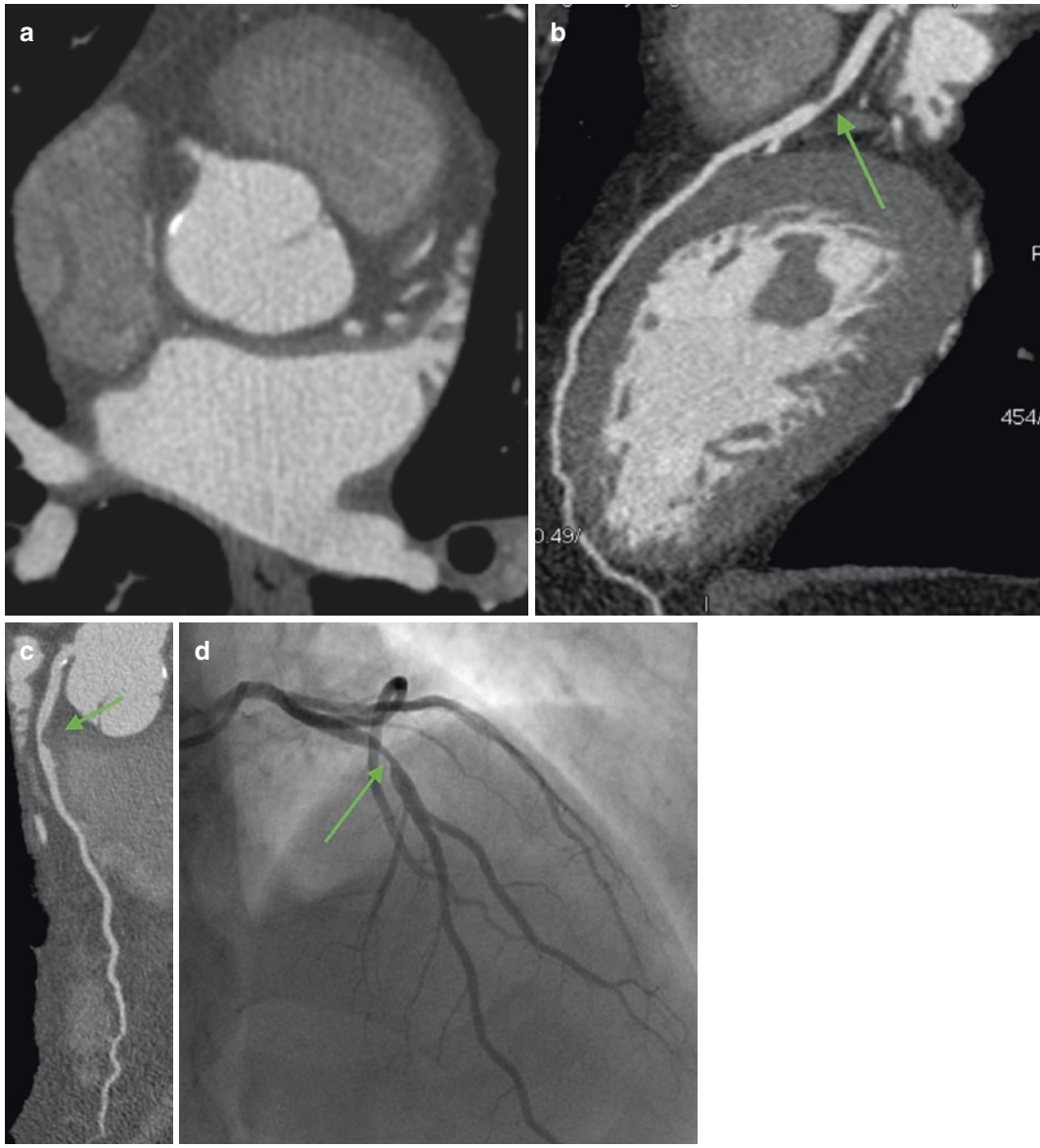

Fig. 8.8 (**a**) Axial view shows focal significant stenosis of 70% was found in the proximal left anterior descending artery due to a noncalcified soft plaque. (**b**, **c**) Two curved MPR views further illustrate the soft plaque. The patient had an Agatston-Janowitz Calcium Score of 54; Percentile: 58. (**d**) The left anterior descending artery showed 80% proximal stenosis that was reduced to 0% via a drug-eluting stent with post-dilatation balloon. TIMI 3 flow was seen after deployment

8.9 Case 9

A 53-year-old male presented with a 1-week history of chest pain that radiated to the left arm. His risk factors were hypertension, hyperlipidemia, and current smoker. TIMI risk score: 1.

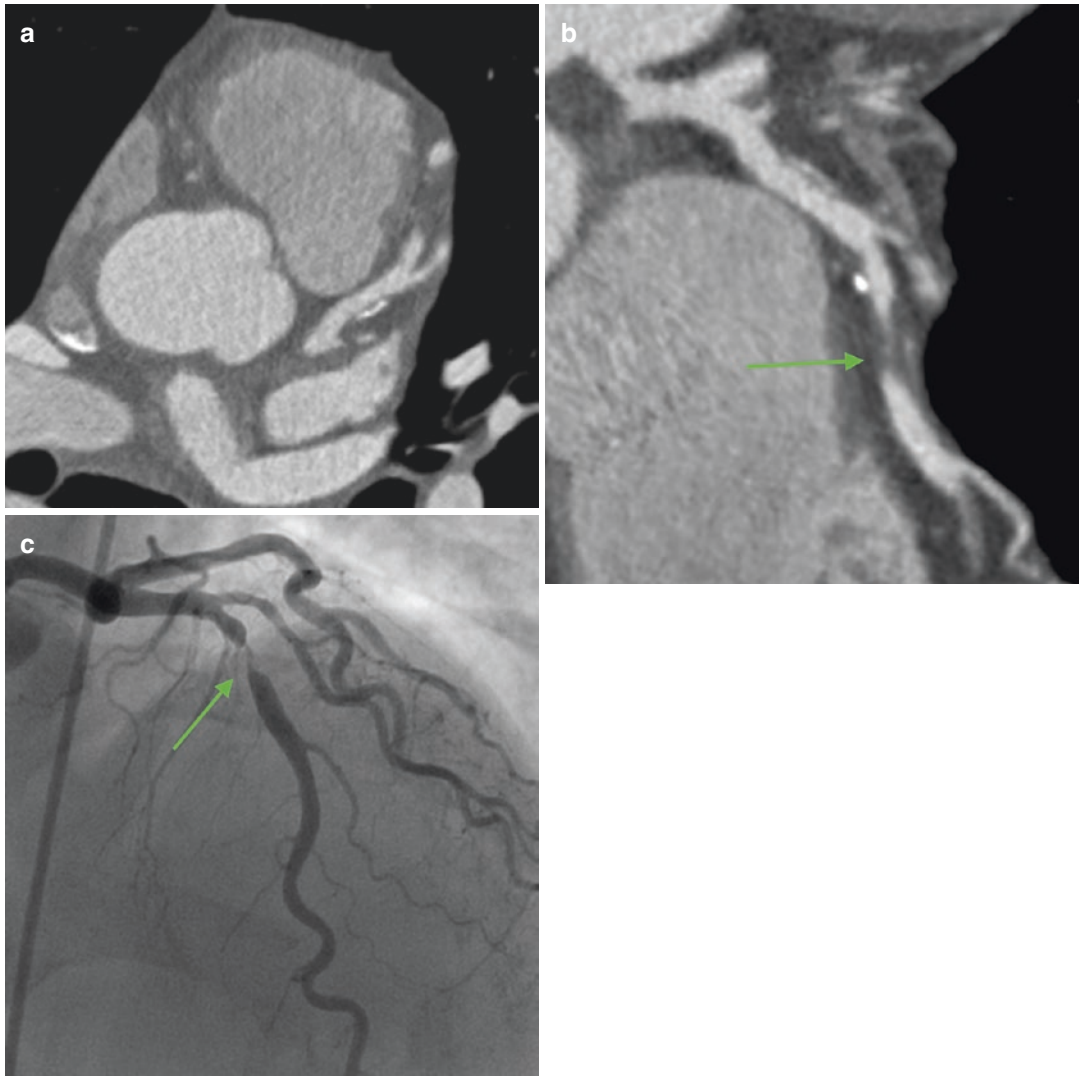

Fig. 8.9 (**a**) Axial and (**b**) curved MPR view depicting a mixed plaque within the proximal left anterior descending artery, which did not cause obstruction of the vessel (less than 30%); however, in the mid left anterior descending artery there was critical obstruction secondary to a non-calcified plaque. The patient had an Agatston-Janowitz Calcium Score of 67; Percentile: 84. (**c**) Angiography showed a single vessel coronary artery disease with a critical lesion in the middle portion of the left anterior descending artery. The patient had drug-eluting stent in middle of the left anterior descending artery

8.10 Case 10

A 51-year-old male presented to the emergency department with acute chest pain. His major risk factors were hypertension and hyperlipidemia. TIMI score: 0.

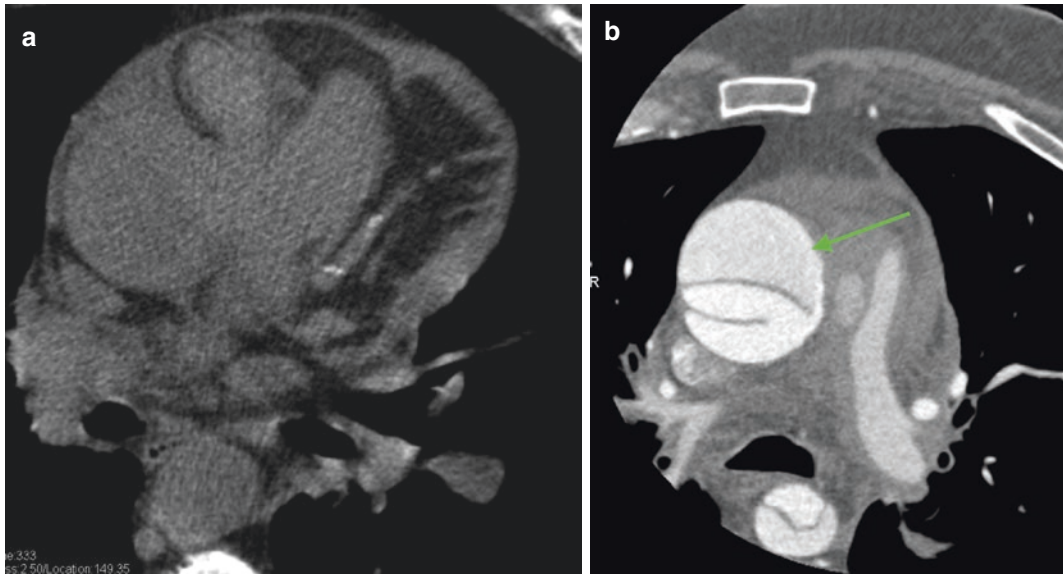

Fig. 8.10 (**a**) Axial view of the noncontrast calcium score image demonstrates loss of tissue distinction between the aortic root and main pulmonary artery with higher density material. In addition, there is a small pericardial effusion seen. (**b**) Coronary CTA examination confirms A Type-A aortic dissection with an intimal flap seen in the proximal ascending aorta just above the root as well as within the descending thoracic aorta. There is a small tear in the medial aspect of the ascending aorta with extravasation of contrast to the mediastinum between the aortic root and main pulmonary artery

8.11 Case 11

A 41-year-old male presented to the emergency department for chest pain. The patient had dyslipidemia and a family history of heart disease. TIMI score at the time of CCTA: 0.

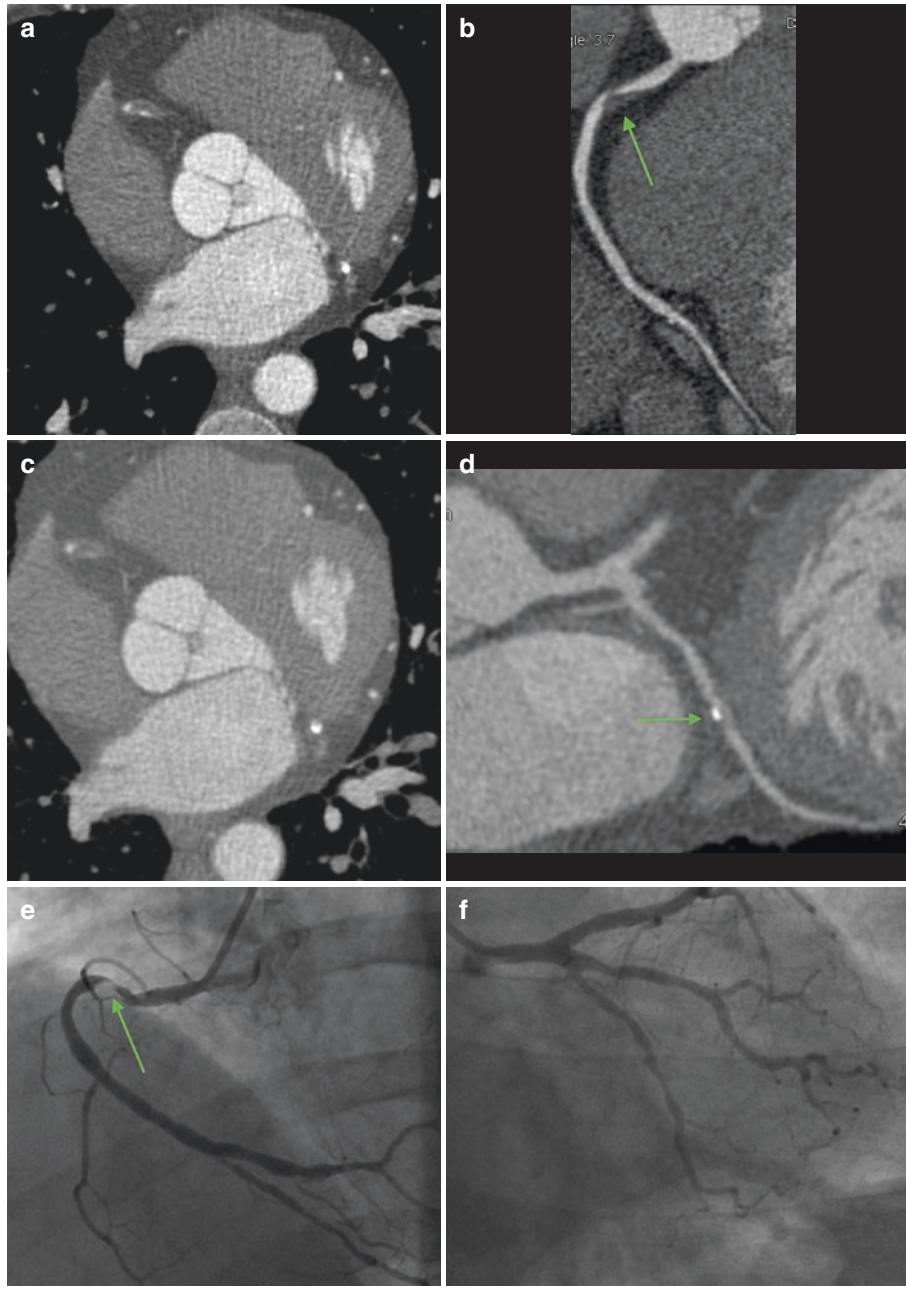

Fig. 8.11 (**a**) Axial and (**b**) curved MPR views illustrate critical obstruction involving the proximal right coronary artery secondary to a large noncalcified plaque. (**c**) Axial (**d**) curved MPR show an additional moderately obstructive 40–70% stenosis in the mid portion of the left circumflex due to a mixed plaque. The patient had an Agatston-Janowitz Calcium Score of 57. (**e**) The right coronary artery demonstrated a 95% obstructive lesion proximally on angiography. (**f**) Additionally, there was a 60% left circumflex lesion viewed on angiography. Successful percutaneous coronary intervention to the right coronary artery was achieved using a drug-eluting stent

8.12 Case 12

A 65-year-old male presented with epigastric pain and was found to have borderline elevated cardiac enzymes upon arrival to the emergency department. The patient has a history of diabetes mellitus, hyperlipidemia, and has a family history of heart disease. TIMI score: 3.

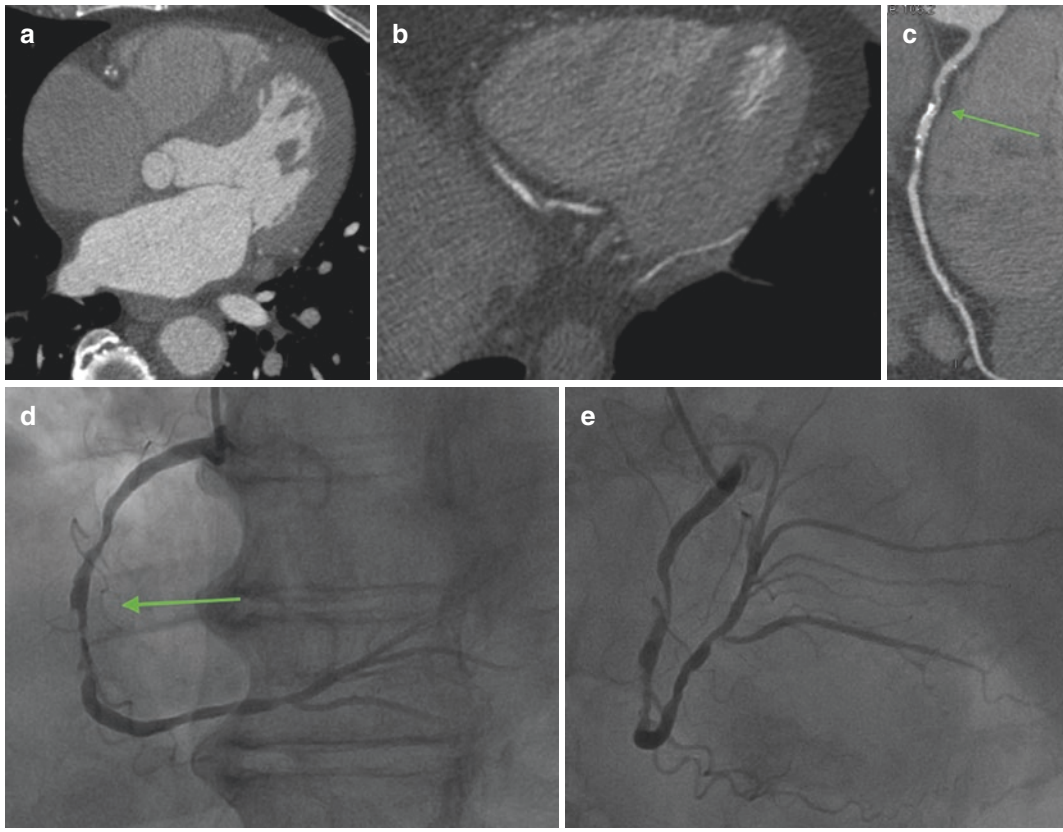

Fig. 8.12 (**a**) Axial view showing a long segment of sequential obstructive disease within the proximal to mid right coronary artery causing a stenosis of greater than 70% due to mixed plaque. (**b**) An axial view shows another mixed plaque which was mostly noncalcified within the proximal posterior descending artery. (**c**) Curved MPR illustrates the lesion in the right coronary artery. Additionally, there were nonobstructive moderate calcified plaque within the left anterior descending and circumflex arteries (not depicted). The patient had an Agatston-Janowitz Calcium Score of 490; Percentile: 91. (**d**) Sequential stenosis of 80 and 90% stenosis was observed in the right coronary artery angiography. There was successful revascularization of the right coronary artery using drug-eluting stents. (**e**) The PDA lesion was less than 60% on angiography

8.13 Case 13

A 70-year-old male presented to the emergency department with a chief complaint of retrosternal chest pressure with generalized weakness occurring at rest. The patient was asymptomatic upon arrival in the ED but had the symptoms for 3 h constantly just prior to arrival. The patient had a known history of coronary artery disease and had previous MI treated with four stents. The patient had serial negative cardiac enzymes and ECGs. TIMI risk score: 2.

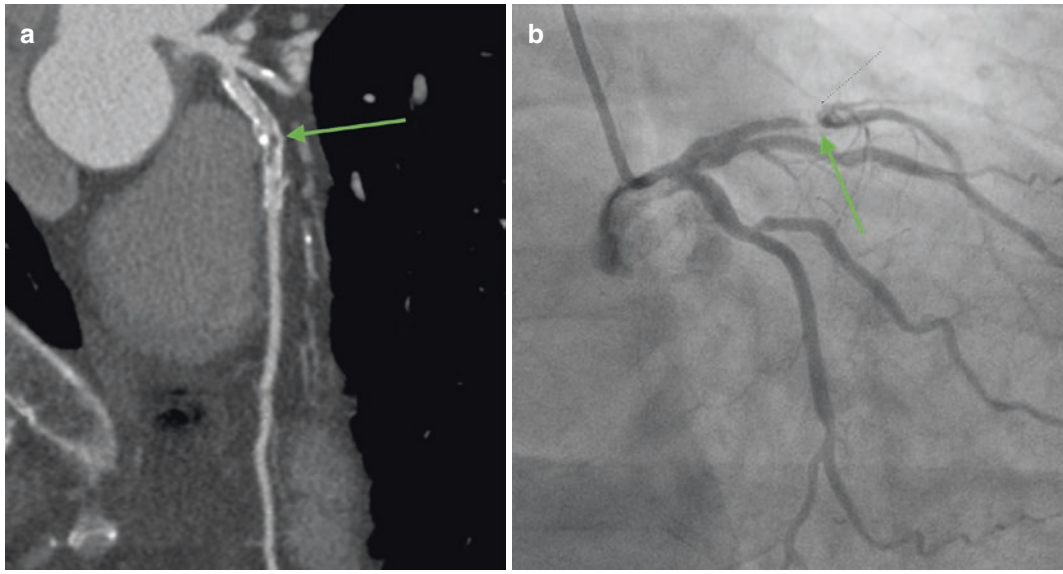

Fig. 8.13 (**a**) A curved MPR view illustrates a long stent in the proximal left anterior descending artery with multifocal areas of intrastent hypodensities that were consistent with restenosis of the stent. There were patent stents in the first obtuse marginal artery and distal right coronary artery (not shown). The patient had an Agatston-Janowitz Calcium Score of 80; Percentile: 55. (**b**) Angiography showed the left anterior descending artery had an in-stent 90% restenosis at the bifurcation with the second diagonal branch. The right coronary artery stent was patent and did not need intervention. Successful treatment with a drug-eluting stent was performed

8.14 Case 14

A 52-year-old male presented with a 1-month history of dyspnea on exertion and acute chest pressure associated with numbness in the right arm after exertion. The patient had a silent in myocardial infarction years prior to presentation and treated with coronary transluminal angioplasty and stenting. Serial troponins and ECGs were negative. His risk factors were: active smoker, hyperlipidemia, family history of heart disease, and hypertension. TIMI risk score: 2.

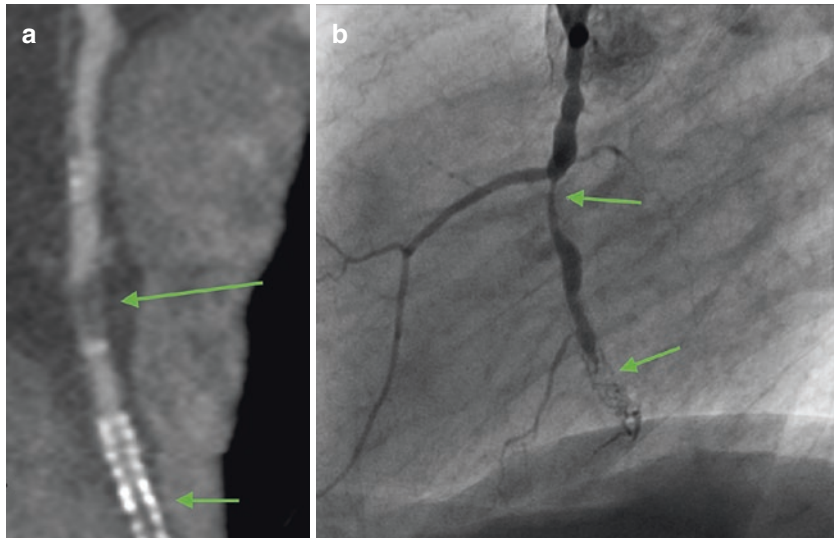

Fig. 8.14 CTA demonstrated multivessel plaques and nonobstructive (less than 40% stenosis) disease. (**a**) A curved MRP demonstrated greater than 70% stenosis in the right coronary artery 1–2 cm proximal to a right coronary artery stent and greater than 70% obstruction within the stent from restenosis. The patient had an Agatston-Janowitz Calcium Score of 142. (**b**) A 90% stenosis of mid segment of the right coronary artery and a total occlusion of the distal stent in the right coronary artery was seen on angiography

8.15 Case 15

A 40-year-old male presented with recurrent angina chest pain. The patient had a history of heart disease and was status post-coronary angioplasty of the right coronary artery that was treated with a stent. The patient had additional risk factors of hypertension, positive family history of heart disease and hyperlipidemia. TIMI risk score: 2.

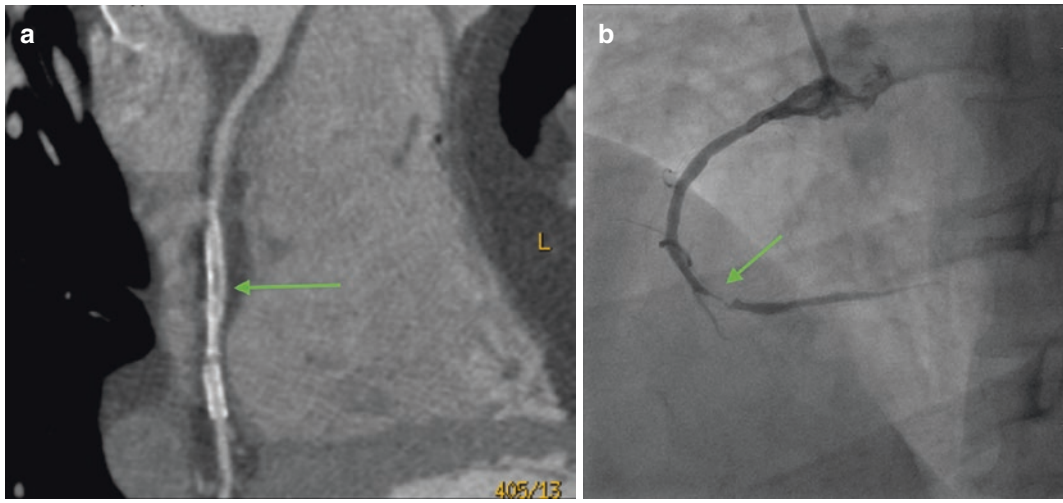

Fig. 8.15 (**a**) A curved MPR shows a focal hypodensity in the lumen of the stent in the middle of the right coronary artery suggesting high-grade in-stent restenosis. The distal right coronary artery was patent. (**a**) Stable moderate stenosis in the proximal and middle portion of the left anterior descending artery was unchanged from previous studies. The patient had an Agatston-Janowitz Calcium Score of 0. (**b**) Severe in-stent restenosis of the proximal right coronary artery stent was seen. Successful percutaneous coronary intervention with stent deployment with drug-eluting stents in the right coronary artery occurred with no complications

References

1. Litt HI, Gatsonis C, Snyder B, et al. CT angiography for safe discharge of patients with possible acute coronary syndromes. N Engl J Med. 2012;366(15):1393–403. https://doi.org/10.1056/NEJMoa1201163.
2. Cury RC, Feuchtner GM, Batlle JC, et al. Triage of patients presenting with chest pain to the emergency department: implementation of coronary CT angiography in a large urban health care system. AJR Am J Roentgenol. 2013;200(1):57–65. https://doi.org/10.2214/AJR.12.8808.
3. Hamilton-Craig C, Fifoot A, Hansen M, et al. Diagnostic performance and cost of CT angiography versus stress ECG—a randomized prospective study of suspected acute coronary syndrome chest pain in the emergency department (CT-COMPARE). Int J Cardiol. 2014;177(3):867–73. https://doi.org/10.1016/j.ijcard.2014.10.090.
4. Poon M, Cortegiano M, Abramowicz AJ, et al. Associations between routine coronary computed tomographic angiography and reduced unnecessary hospital admissions, length of stay, recidivism rates, and invasive coronary angiography in the emergency department triage of chest pain. J Am Coll Cardiol. 2013;62(6):543–52. https://doi.org/10.1016/j.jacc.2013.04.040.
5. Goldstein JA, Chinnaiyan KM, Abidov A, et al. The CT-STAT (Coronary Computed Tomographic Angiography for Systematic Triage of Acute Chest Pain Patients to Treatment) trial. J Am Coll Cardiol. 2011;58(14):1414–22. https://doi.org/10.1016/j.jacc.2011.03.068.
6. Hoffmann U, Bamberg F, Chae CU, et al. Coronary computed tomography angiography for early triage of patients with acute chest pain. J Am Coll Cardiol. 2009;53(18):1642–50. https://doi.org/10.1016/j.jacc.2009.01.052.
7. Hulten EA, Carbonaro S, Petrillo SP, Mitchell JD, Villines TC. Prognostic value of cardiac computed tomography angiography: a systematic review and meta-analysis. J Am Coll Cardiol. 2011;57(10):1237–47. https://doi.org/10.1016/j.jacc.2010.10.011.
8. Maroules CD, Blaha MJ, El-Haddad MA, Ferencik M, Cury RC. Establishing a successful coronary CT angiography program in the emergency department: official writing of the Fellow and Resident Leaders of the Society of Cardiovascular Computed Tomography (FiRST). J Cardiovasc Comput Tomogr. 2013;7(3):150–6. https://doi.org/10.1016/j.jcct.2013.05.001.
9. Cury RC, Feuchtner G, Mascioli C, et al. Cardiac CT in the emergency department: convincing evidence, but cautious implementation. J Nucl Cardiol. 2011;18(2):331–41. https://doi.org/10.1007/s12350-011-9356-1.
10. Amsterdam EA, Wenger NK, Brindis RG, et al. 2014 AHA/ACC guideline for the management of patients with non-ST-elevation acute coronary syndromes: executive summary: a report of the American College of Cardiology/American Heart Association Task Force on Practice Guidelines. Circulation. 2014;130(25):2354–94. https://doi.org/10.1161/CIR.0000000000000133.
11. Raff GL, Abidov A, Achenbach S, et al. SCCT guidelines for the interpretation and reporting of coronary computed tomographic angiography. J Cardiovasc Comput Tomogr. 2009;3(2):122–36. https://doi.org/10.1016/j.jcct.2009.01.001.
12. Takakuwa KM, Halpern EJ. Evaluation of a "triple rule-out" coronary CT angiography protocol: use of 64-Section CT in low-to-moderate risk emergency department patients suspected of having acute coronary syndrome. Radiology. 2008;248(2):438–46. https://doi.org/10.1148/radiol.2482072169.
13. Gruettner J, Fink C, Walter T, et al. Coronary computed tomography and triple rule out CT in patients with acute chest pain and an intermediate cardiac risk profile. Part 1: impact on patient management. Eur J Radiol. 2013;82(1):100–5. https://doi.org/10.1016/j.ejrad.2012.06.001.

Cardiac CTA in the Evaluation of Stents

9

Claudio Smuclovisky

9.1 Case 9.1

9.1.1 History

A 77-year-old female presented with a history of chest pain, subsequent to percutaneous coronary intervention (PCI).

9.1.2 Findings

There is a widely patent stent in the mid-RCA (Fig. 9.1a–c). There is also a minimal calcified nonobstructing plaque in the proximal RCA.

9.1.3 Diagnosis

The diagnosis is patent drug-eluting stent (DES) in the mid-RCA.

9.1.4 Discussion

Although the accuracy of stent evaluation with CT is currently being debated, there is general agreement that the CTA has high sensitivity and specificity for greater than 50% stenosis in stents with a diameter of 3 mm or larger. Essentially, deployment of a stent consists of a collapsed wire mesh that is expanded following ballooning of a lesion. The various techniques for stent placement are beyond the scope of this book.

CTA and evaluation of the stent consists of determining whether the stent was completely deployed across a plaque or there is a stenosis in the lumen of the stent. The lumen and density in the stent should be similar to that of adjacent artery. Areas of low density in the stent indicate either subintimal hyperplasia or thrombus. This should not be confused with parallel metal artifact from the struts of the stent. The areas of low density in the stent are evaluated similar to how we approach atheromas, with curved reformatted reconstruction and cross-sectional imaging to determine whether they are flow limiting. Additional attention is directed to whether the stent is over- or underexpanded, fractured, angulated, or if it obstructs (cages) a branch. It is also not uncommon to develop a tight stenosis at the edge of the stent (napkin ring stenosis). When a stent is occluded, there is diffuse low density in the lumen of the stent, with a distal low-density transition zone.

C. Smuclovisky, MD, FACC, FSCCT
Department of Radiology, Holy Cross Hospital,
South Florida Medical Imaging Cardiovascular Institute,
Fort Lauderdale, FL, USA
e-mail: smuclovisky@gmail.com

C. Smuclovisky (ed.), *Coronary Artery CTA*, https://doi.org/10.1007/978-3-319-66988-5_9

9.1.5 Pearls and Pitfalls

Even minimal motion artifact may cause streaking that mimics in-stent restenosis. Reconstruction of the arteries should be made between 0.5 and 0.8 mm with a sharp kernel. Window width should be set greater than 1000 (average, 1500) and center adjusted between 400 and 800 (average, 650).

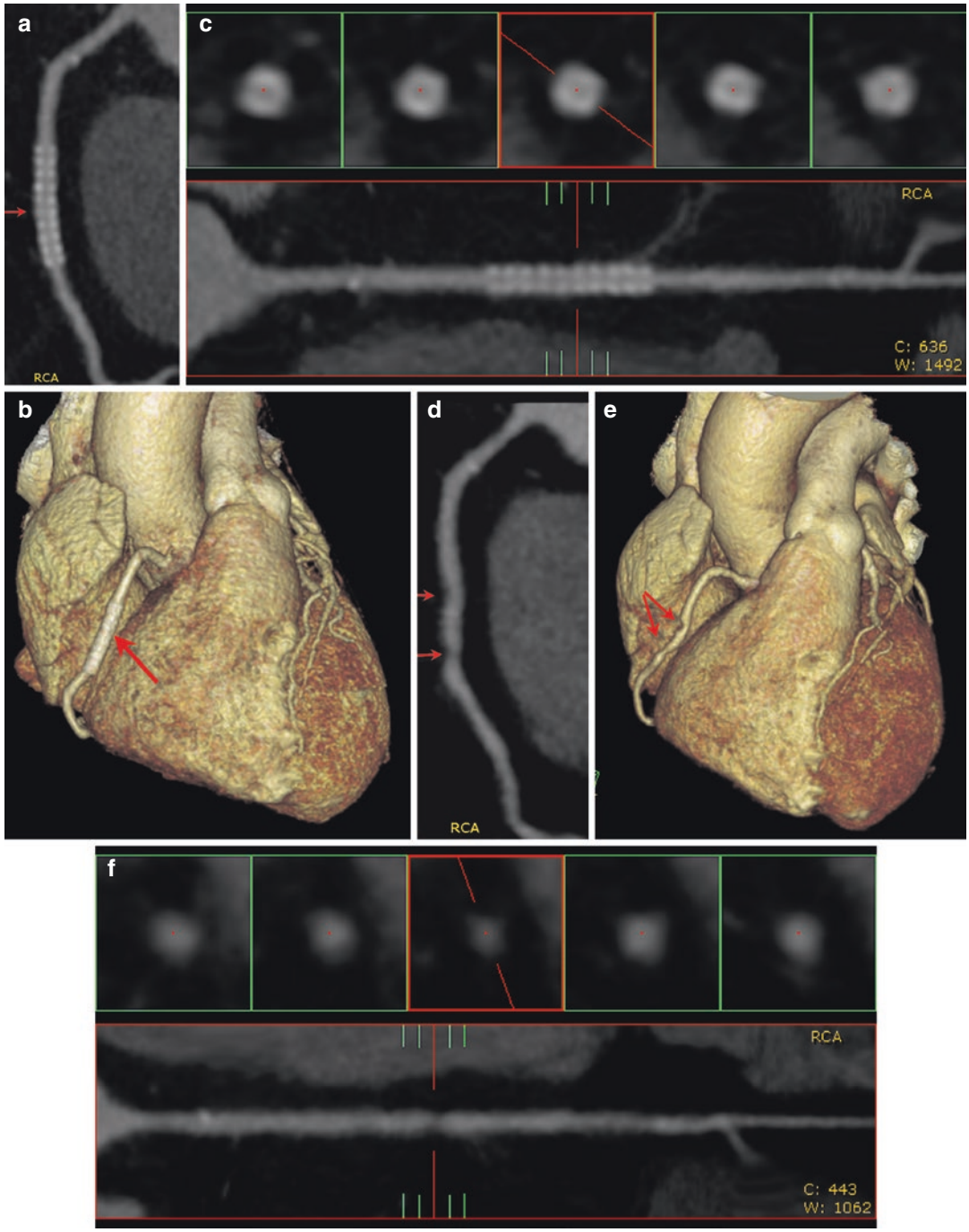

Fig. 9.1 (**a**–**c**) cMPR, 3D volume rendering, and stretched: Patent RCA stent (*arrow*). (**d**–**f**) Pre-intervention CTA: RCA high-grade stenosis (*arrow*)

9.2 Case 9.2

9.2.1 History

A 77-year-old female with a history of prior PCIs with placement of multiple stents in the LAD, presented with subsequent CABG. The CTA was performed for questionable ischemia in the LV apex on a nuclear perfusion scintigram.

9.2.2 Findings

There are multiple sequential occluded stents in the proximal to mid-LAD and a patent left internal mammary artery graft (LIMA) to the distal LAD (Fig. 9.2a–d).

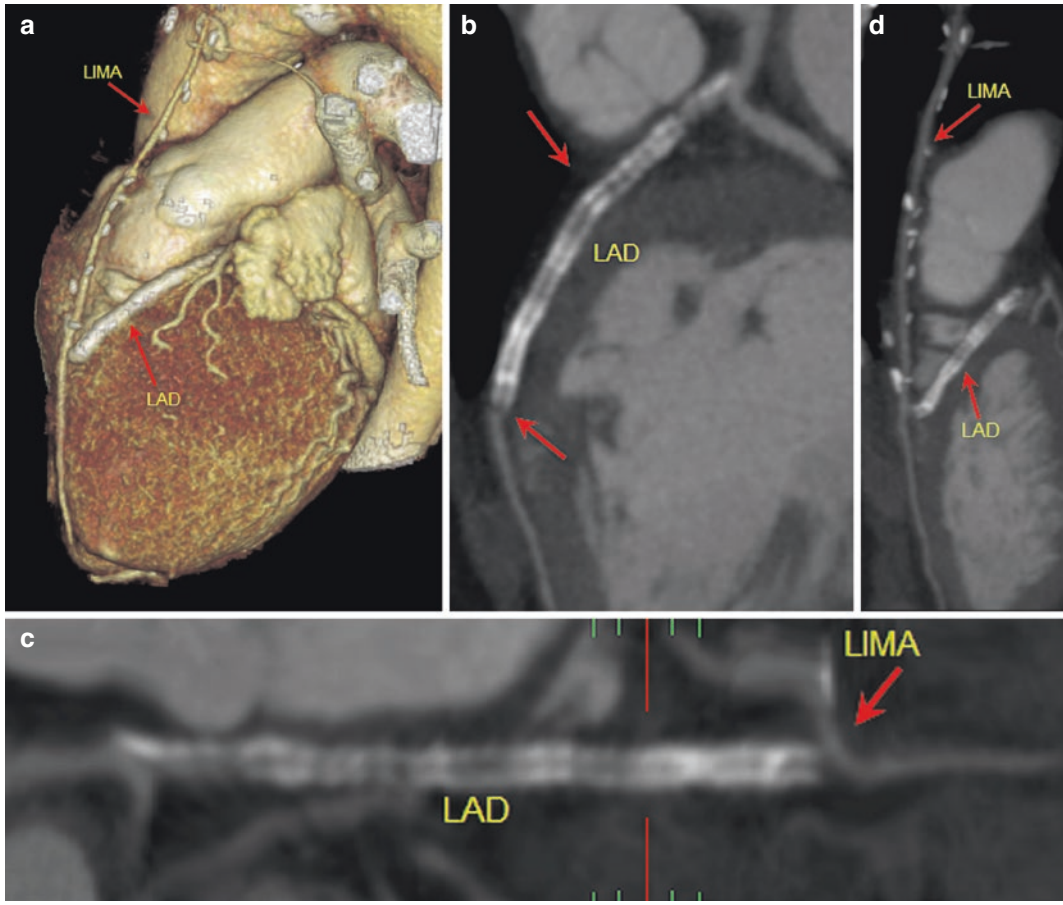

Fig. 9.2 (**a**–**c**) Volume rendering, cMPR, and stretched LAD–LIMA: Occluded sequential stents in the proximal to mid-LAD. The *lower arrow* in (**a**) and (**b**) shows a transition zone between the distal stent and the LAD, indicating an occlusion. There is a patent LIMA graft to the distal LAD. (**d**) cMPR: Patent LIMA graft to the distal LAD

9.2.3 Diagnosis

The diagnosis is chronic total occlusion of the proximal to mid-LAD. The distal LAD has no disease and has been bypassed with a LIMA graft that is patent.

9.2.4 Discussion

There are multiple sequential stents in the proximal to mid-LAD. Note that there is no evidence of contrast density in the lumen of the stents, and there is a transition zone in the distal stent, indicating chronic total occlusion. As in this case, it is not infrequent that following one or multiple coronary interventions, with subsequent failure of the stents by subintimal hyperplasia, or thrombosis, that the patient is referred for surgical revascularization.

9.2.5 Pearls and Pitfalls

Low density alone in the lumen of a stent is not diagnostic of an occluded stent. Extensive subintimal hyperplasia may mimic an occlusion. Additional findings such as a distal short low-density transition zone or lack of contrast opacification of the distal artery are needed to conclude that the stent is occluded.

9.3 Case 9.3

9.3.1 History

A 72-year-old female presented with a history of intermittent chest pain and PCI 2 years prior, with DESs.

9.3.2 Findings

There is a Y stent in the second diagonal, with low density in the lumen of the stent indicating restenosis (Fig. 9.3a, b). There is a stent in the LAD, which has localized focal low density in the lumen of the distal stent (Fig. 9.3c). Incidentally noted is a membranous septal aneurysm bulging into the right ventricle (Fig. 9.3d, e).

9.3.3 Diagnosis

The diagnosis is in-stent restenosis in the second diagonal artery. Nonobstructive neointimal hyperplasia in the distal segment of the stent in the LAD. Incidentally found is a membranous septal aneurysm.

9.3.4 Discussion

Neointimal hyperplasia in a stent that causes decreased contrast opacification in the lumen,

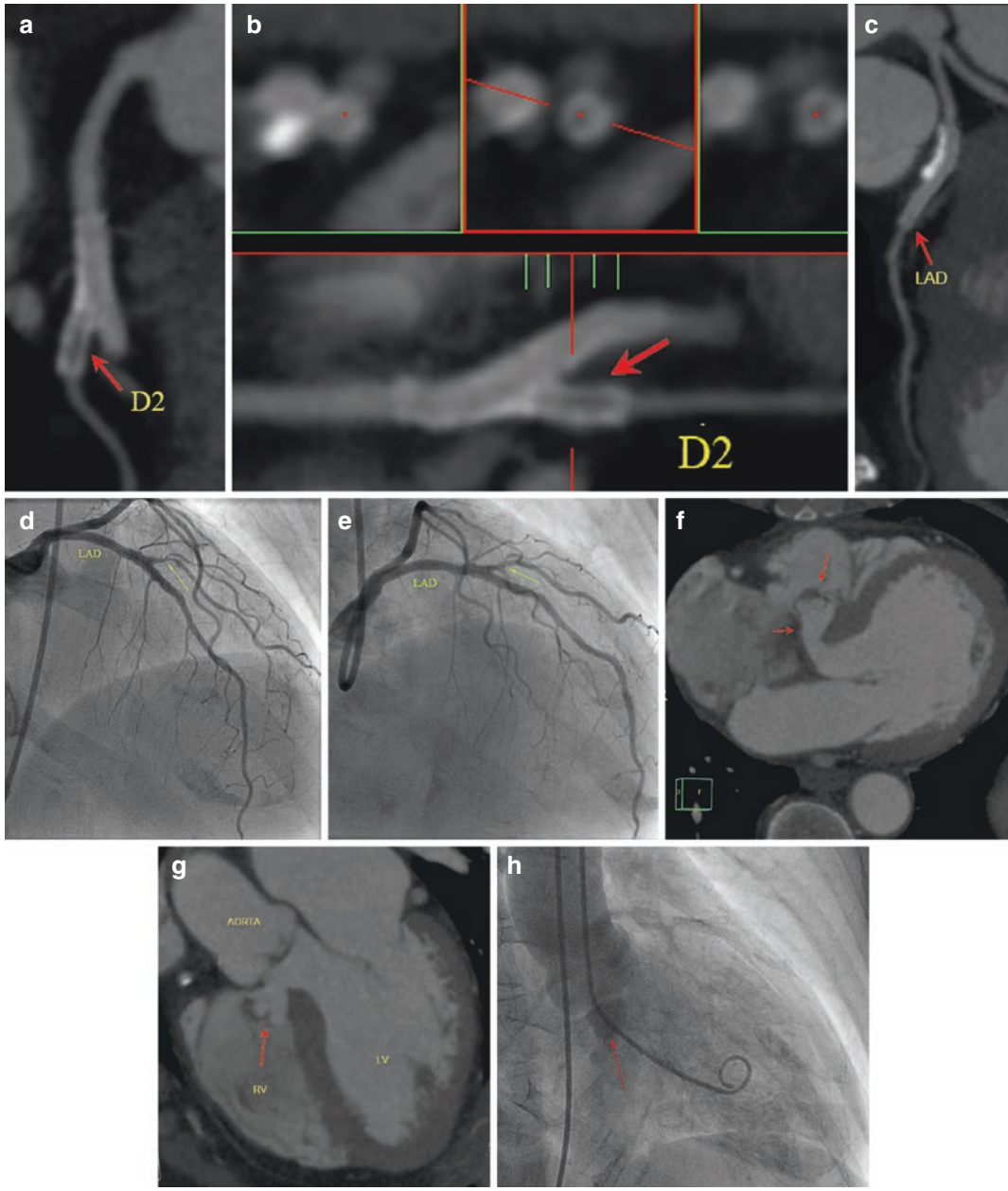

Fig. 9.3 (**a**, **b**) cMPR and stretched D2: In-stent restenosis (*arrow*). (**c**) cMPR LAD: Mild nonobstructing neointimal hyperplasia in the distal stent (*arrow*). (**d**, **e**) Coronary angiogram pre- and postangioplasty of D2 (*arrow*). Patent LAD stent. (**f**, **g**) CTA axial and coronal slices: Membranous septal aneurysm (MSA) (*arrow*). (**h**) Angiogram, LV injection: Membranous septal aneurysm (*arrow*)

which appears as low density. Significant restenosis is defined as vessel lumen narrowing of more than 50% after angioplasty. Restenosis is an iatrogenic process caused by an excessive arterial healing response to vessel injury associated with dilation. It results from the combined effects of elastic recoil, vascular remodeling, and neointimal hyperplasia. Coronary stents represent a mechanical approach to the prevention of restenosis by virtually eliminating elastic recoil and negative remodeling of the vessel after balloon dilation. The occurrence of neointimal hyperplasia is mainly responsible for the observed rates of restenosis, which range from less than 10% with a DES to 40% with an uncoated or bare metal stent. For both stent types, excess stent length is associated with an increased risk of in-stent restenosis. The restenosis in the diagonal artery was confirmed on angiography and was subsequently ballooned. The focal area of neointimal hyperplasia in the distal stent in the LAD was not significant on the angiogram.

There are various techniques for stenting bifurcating lesions. Among these are T stent technique, V stent technique, Y stent technique, crush technique, and the culottes or trousers technique, which is a variant of the Y technique.

The membranous septal aneurysm was an incidental finding. These may be associated with many congenital cardiac anomalies and be a cause of arrhythmia and/or tricuspid valve dysfunction.

9.3.5 Pearls and Pitfalls

The identification of neointimal hyperplasia is common in CT angiography. The greater challenge is determining whether it is flow limiting and/or clinically significant, particularly in smaller caliber vessels, and also overlapping stents. Correlation with the patient's symptoms and a myocardial perfusion scintigram is helpful to determine whether further evaluation with coronary angiography is warranted.

9.4 Case 9.4

9.4.1 History

A 73-year-old male presented with a history of new onset of exertional chest pain and mid-LAD PCI 10 years prior, with a bare metal stent (BMS).

9.4.2 Findings

There is high-grade stenosis in the range of 90% in the mid-LAD (Fig. 9.4a–e).

9.4.3 Diagnosis

The diagnosis is high-grade stent restenosis in the mid-LAD.

9.4.4 Discussion

The neointimal hyperplasia obscures the stent, which is poorly identified. In fact, without the history of the prior PCI, it would not have been possible to determine, with certainty on the CTA, the presence and location of the stent in the mid-LAD.

9.4.5 Pearls and Pitfalls

BMS in place over a number of years may be obscured by the neointimal hyperplasia and therefore may not easily be identified on CTA. It is uncertain at this time whether DES may also develop a similar appearance after many years.

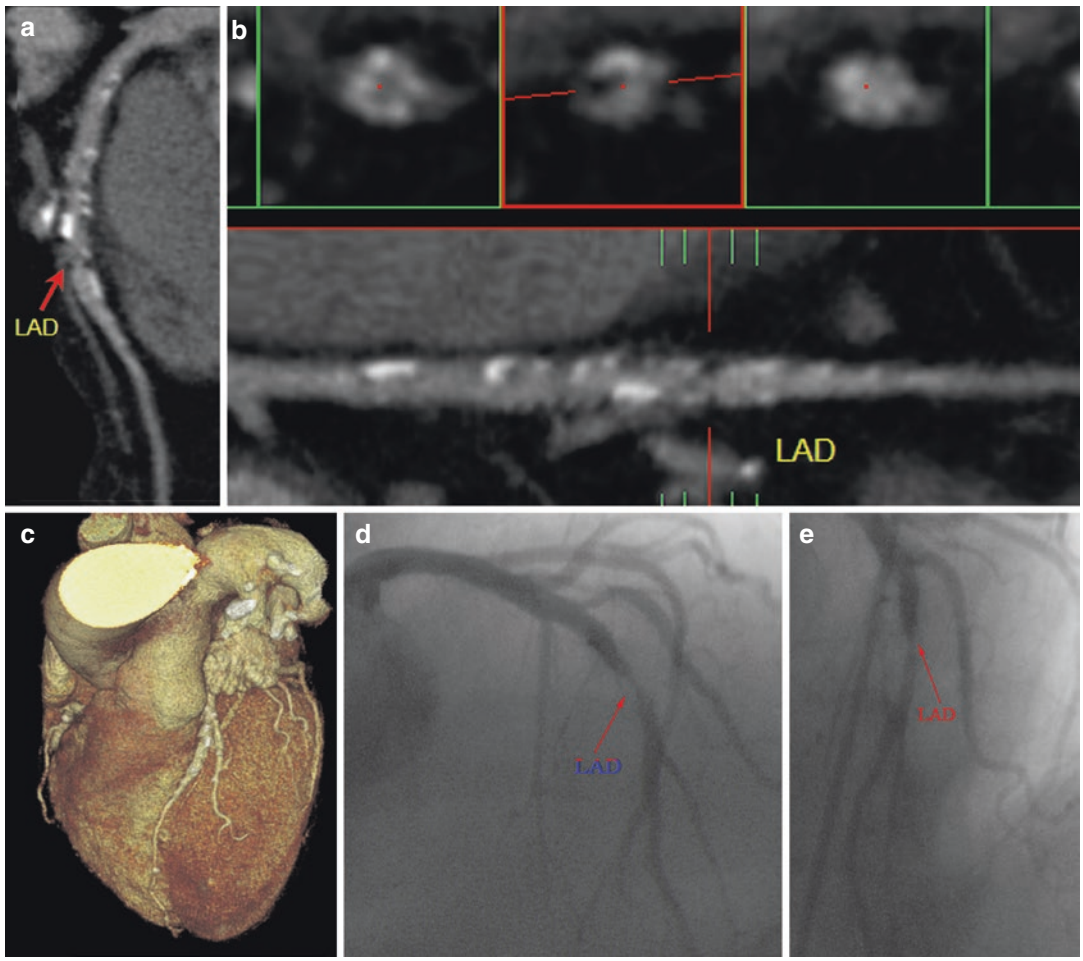

Fig. 9.4 (**a**–**c**) cMPR and stretched, volume rendered LAD: stent high-grade restenosis in the mid-LAD (*arrow*). (**d**, **e**) Correlative coronary angiogram demonstrating 90% stenosis in the mid-LAD (*arrow*)

9.5 Case 9.5

9.5.1 History

A 75-year-old female presented with a history of increasing shortness of breath. The status was post mid-LAD and LCX PCI in the previous 3 years, with BMS.

9.5.2 Findings

There are two areas of high-grade stenosis in the mid-LAD. There is a widely patent stent in the proximal left circumflex (Fig. 9.5a–e).

9.5.3 Diagnosis

High-grade stent restenosis in the mid-LAD and a second distal segment of high-grade stenosis.

9.5.4 Discussion

The extensive neointimal hyperplasia obscures the stent, which is poorly identified. The minimal contrast density (string sign) through the stent and lack of significant transition zone distally would indicate that the lumen is not totally occluded. There is a more distal short segment high-grade stenosis in the LAD (arrow).

9.5.5 Pearls and Pitfalls

The neointimal hyperplasia should not be confused with a thrombus or plaque rupture in the arterial lumen. Notice that the distal segment of the stent is sharp and appears to extend beyond the lumen of the native artery. It is a good clue that a stent is present.

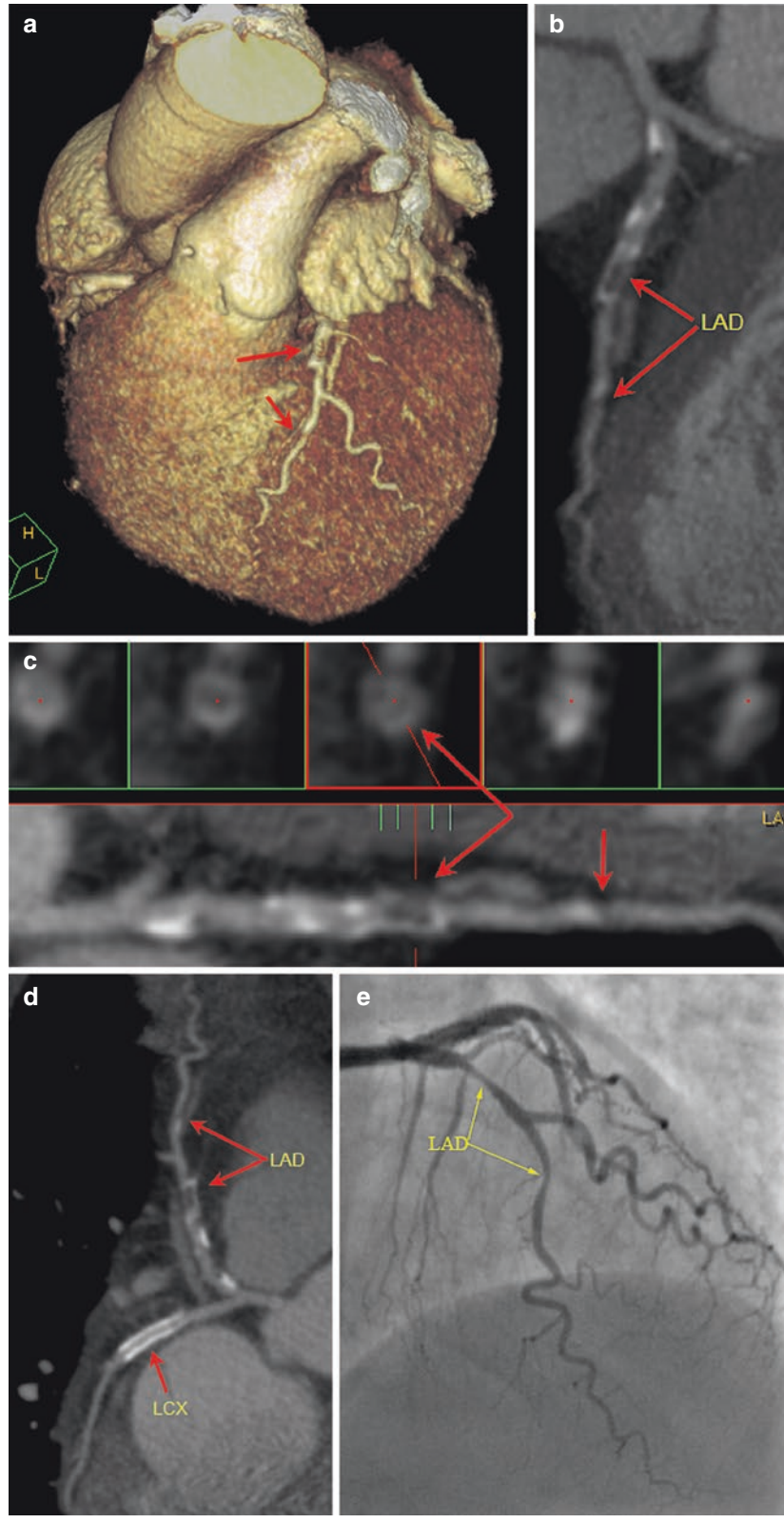

Fig. 9.5 (**a**–**c**) Volume rendering, cMPR and stretched, LAD: Stent high-grade restenosis in the mid-LAD and more distal in the LAD (*arrows*). (**d**) Composite cMPR. Patent stent in the proximal LCX, LAD disease (*arrows*). (**e**) Correlative coronary angiogram demonstrates the two areas of high-grade stenosis in the mid-LAD (*arrows*)

9.6 Case 9.6

9.6.1 History

A 53-year-old male presented with a history of atypical chest pain, CAD, and prior multivessel coronary interventions.

9.6.2 Findings

There is narrowing of the distal lumen of a DES in the left circumflex coronary artery (Fig. 9.6a, b).

9.6.3 Diagnosis

The diagnosis is underexpanded distal segment of a DES in the left circumflex coronary artery.

9.6.4 Discussion

Coronary stents, including DESs, must be optimally deployed with full lesion coverage and complete expansion of the stent and complete apposition to the vessel wall to optimize results. Less than full expansion and apposition significantly increases the risk of complications such as subacute thrombosis, target lesion revascularization, and restenosis, thus compromising the benefits of the intervention. With DES, incomplete expansion and apposition can also impede drug delivery to the vessel wall.

9.6.5 Pearls and Pitfalls

Overlapping stents may have a similar appearance to an underexpanded stent. Significantly increasing the window width on the workstation in the range of 1500–3000 may prove helpful.

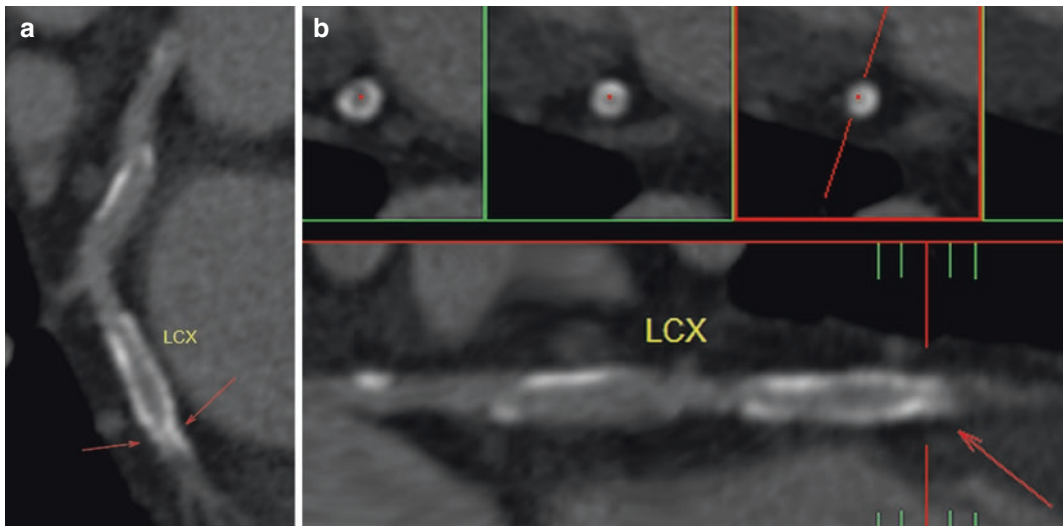

Fig. 9.6 (**a**, **b**) cMPR and stretched, LCX: Underexpanded distal segment of the coronary stent (*arrows*)

9.7 Case 9.7

9.7.1 History

A 72-year-old male presented with RCA-PCI 2 months prior, with increasing atypical chest pain.

9.7.2 Findings

There are widely patent overlapping DESs in the proximal to mid-RCA. The RCA has diffuse disease. There is soft tissue (plaque, hemorrhage?) density in the distal RCA causing high-grade critical stenosis (Fig. 9.7a–c).

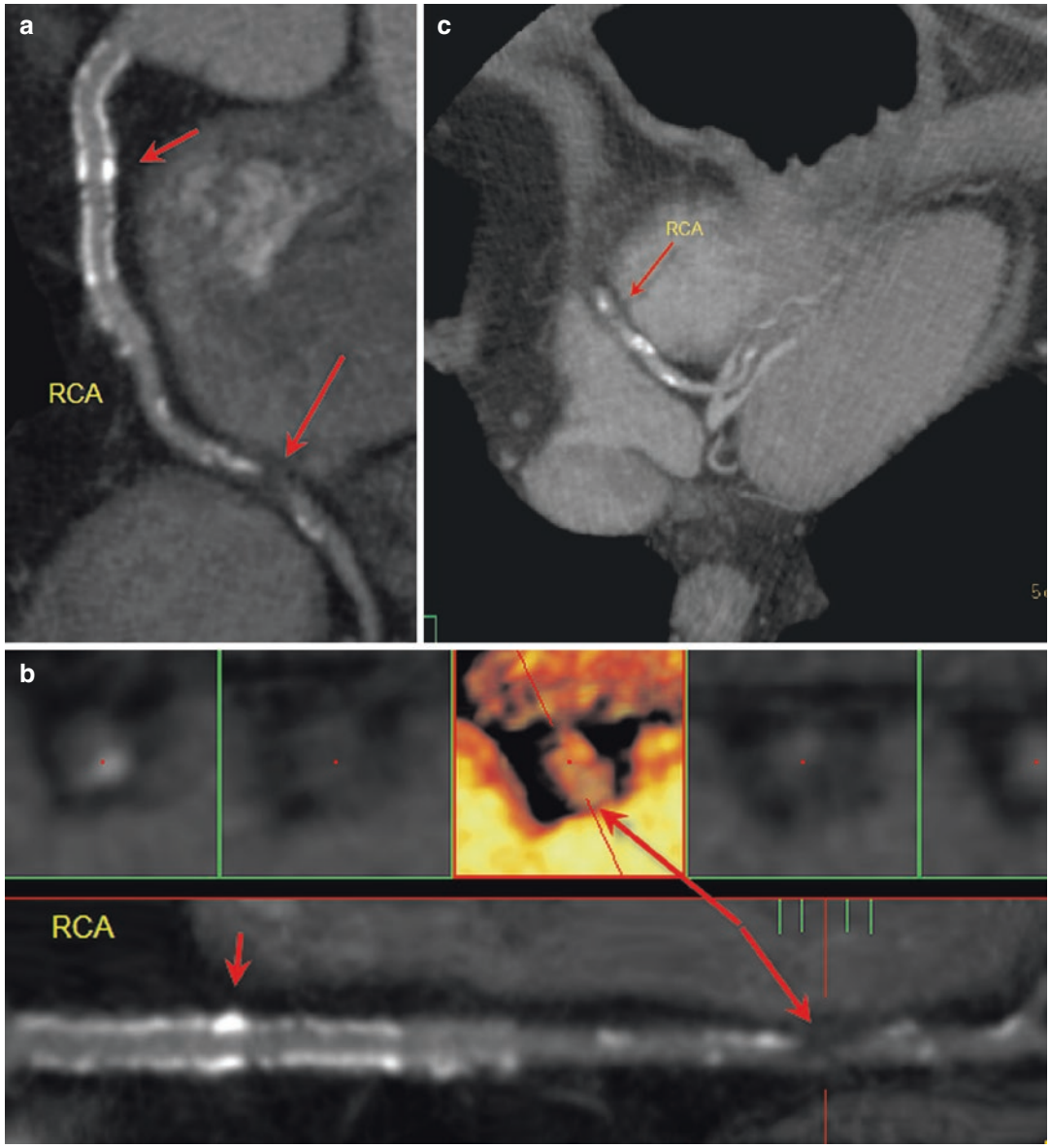

Fig. 9.7 (**a**, **b**) cMPR and stretched, RCA: Widely patent overlapping stents in the proximal to mid-RCA (*short arrow*). High-grade critical obstruction in the distal RCA (*long arrow*). (**c**) Axial slice demonstrating high-grade critical obstruction in the distal RCA (*arrow*)

9.7.3 Diagnosis

Patent overlapping DES in the right coronary artery. New onset of high-grade critical stenosis in the distal RCA, presumably from a guidewire injury during coronary intervention.

9.7.4 Discussion

Sequential coronary stents may overlap causing summation metal density on the CTA. During coronary artery intervention, guidewires are placed distal to the deployment of the stent. Common complications related to the wire tip include perforation of the coronary artery, with development of a hemopericardium, subintimal hemorrhage, and dissection of the coronary artery. Most of these complications are detected at the time of the procedure or suspected clinically within a matter of hours. If not diagnosed and treated, these may lead to chronic unstable angina, acute coronary syndrome, and sudden death. The patient underwent a repeat coronary angiogram, with successful stenting of the distal RCA. Although it was felt that the most likely diagnosis was a wire-related injury, a postprocedure rupture of a plaque, with subintimal hemorrhage in the wall could not be completely excluded.

9.7.5 Pearls and Pitfalls

Increasing the window width on the workstation is helpful in evaluating the segment of overlapping stents.

9.8 Case 9.8

9.8.1 History

A 69-year-old male presented with a history of COPD, presurgical workup for lung CA and prior PCI in the RCA and left circumflex performed 12 years previously. The study was performed for preoperative clearance.

9.8.2 Findings

There is a bare metal stent in the proximal RCA with high-grade proximal edge stenosis. There is a second bare metal stent in the mid-circumflex, which has high-grade stenosis in the proximal and distal edge of the stent and in-stent restenosis (Fig. 9.8a–c).

9.8.3 Diagnosis

High-grade edge stenosis adjacent to coronary stents and high-grade restenosis in the stent in the left circumflex coronary artery.

9.8.4 Discussion

It has been reported that a frequent occurrence (48%) of significant stenosis outside of bare metal stents in patients presenting with symptoms following coronary stent deployment. The majority of these stenosis also involve stenosis inside of the stent (diffuse proliferative

and edge). DES markedly reduce the incidence of in-stent restenosis but are unlikely to affect stenosis outside of the stent. The etiology of restenosis occurring at the edge of a stent is likely multifactorial. Diffuse proliferative restenosis is an aggressive restenotic response primarily within the stent, with extension to the stent edge and beyond. Other causes would include brachytherapy and barotrauma from catheter balloon injury. Additionally, Attila et al. hypothesized that edge restenosis may be related to low-oscillating shear stress, causing expression of several growth factors, which leads to intimal proliferation and restenosis [1, 2].

9.8.5 Pearls and Pitfalls

On CTA, it may be difficult to differentiate an edge stenosis, also referred to as a "napkin ring stenosis," from common CTA artifact that causes decreased, drop out, density in the edge of a stent. The artifact usually does not extend beyond 1–2 mm beyond the edge of the stent.

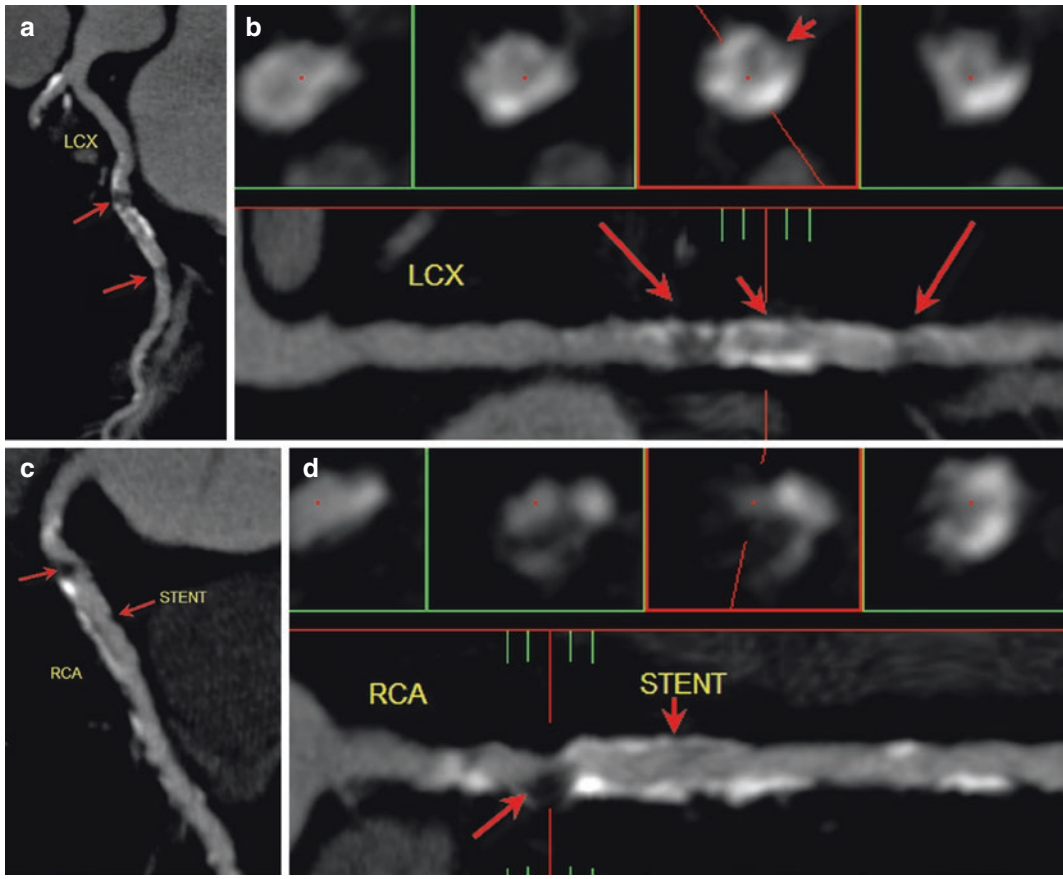

Fig. 9.8 (**a**, **b**) cMPR and stretched, LCX: Proximal and distal stent edge stenosis (*arrow*). Low density in the stent from restenosis (*short arrows*). (**c**, **d**) cMPR and stretched, RCA: Proximal stent edge stenosis (*arrow*)

9.9 Case 9.9

9.9.1 History

A 67-year-old female presented with a history of shortness of breath. The status was post mid-LAD PCI.

9.9.2 Findings

The mid-LAD has an intramyocardial course (appearance of a myocardial bridge) with a stent. The proximal segment of the stent is fractured with a gap in the coronary artery (Fig. 9.9a, b).

9.9.3 Diagnosis

The diagnosis is fractured stent.

9.9.4 Discussion

Stent fracture is an uncommon complication, leading to unstented gaps between two completely opposed segments of a stent. Subsequent restenosis may occur. A more disastrous consequence of a stent fracture would include late distal embolization or migration of the fractured portion of the stent. Multiple mechanisms of stent fracture have been proposed including overexpansion of the stent with a high-pressure inflation, shear stress from vessel tortuosity, or overlapping of stents.

9.9.5 Pearls and Pitfalls

Without detailed knowledge of the procedure, the clue that the stent is fractured instead of there being a second stent is that the stent fragment (<5 mm) is shorter than the manufactured stents (>6 mm).

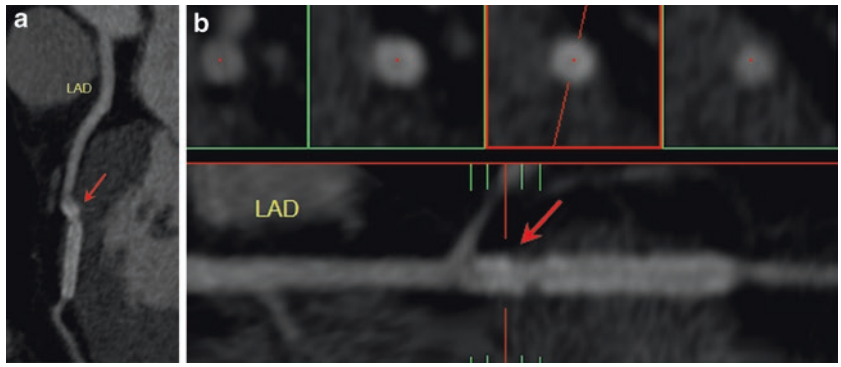

Fig. 9.9 (**a**, **b**) cMPR and stretched, LAD: The proximal segment of the stent is fractured (*arrows*)

9.10 Case 9.10

9.10.1 History

A 74-year-old male, asymptomatic with a history of abnormal stress test, presented with status post left circumflex coronary artery PCI in 1996.

9.10.2 Findings

There is a long bare metal stent in the proximal to mid-left circumflex coronary artery with metallic markers in the proximal and distal ends of the stent, which obscure partially the lumen of the artery; otherwise, the stent appears patent (Fig. 9.10a–c).

9.10.3 Diagnosis

There is a bare metal stent with proximal and distal metallic markers (unknown brand).

9.10.4 Discussion

Since the introduction of percutaneous transluminal coronary angioplasty by Gruntzig in 1977, major advancements have been made in the clinical practice of PCI. Puel and Sigwart, in 1986, deployed the first coronary stent to act as a scaffold, thus preventing vessel closure during percutaneous transluminal coronary angioplasty and reducing the incidence of angiographic restenosis, which had an occurrence rate of 30–40% [3, 4]. By 1999, stenting composed 84.2% of all PCIs. Despite the widespread use of these devices, bare metal stents have been associated with a 20–30% restenosis rate requiring reintervention. Restenosis occurs as a result of neointimal hyperplasia—growth of scar tissue within the stent—due to the proliferation and migration of vascular smooth muscle cells. This phenomenon is clinically evident within the first 6–9 months after stent placement and occurs in response to strut-associated injury and inflammation. Various stent designs were initially created, including the one seen in this case, with metallic markers that were commonly made with gold. The markers allowed the angiographer to identify under fluoroscopy the position of the stent.

9.10.5 Pearls and Pitfalls

The markers at the ends of the stent cause blooming artifact, which obscures the adjacent arterial lumen and consequently the inability to assess stenosis. Fortunately, these are no longer implanted in the United States.

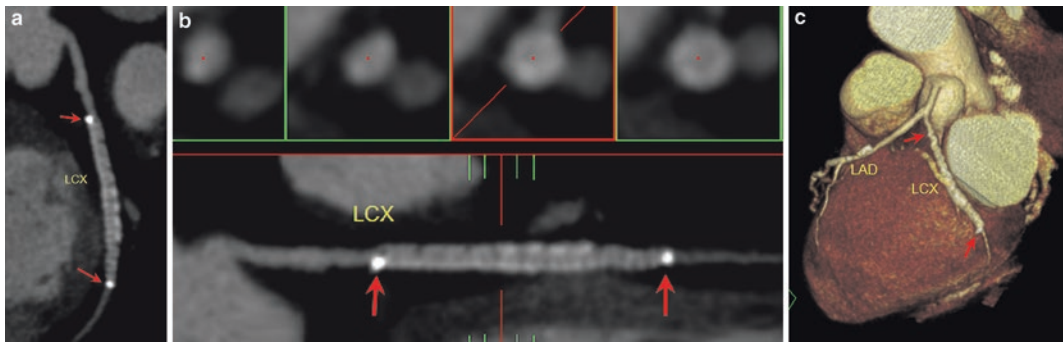

Fig. 9.10 (**a**–**c**) cMPR, stretched, volume rendering. LCX: Long bare metal stent with metal markers in the proximal and distal ends (*arrows*)

9.11 Case 9.11

9.11.1 History

A 76-year-old male presented with atypical chest pain and a history of an abnormal stress test. He is status post first obtuse marginal (OM1) coronary artery PCI approximately 5 years prior, with a bare metal stent.

9.11.2 Findings

There is an advanced diffuse disease in the proximal LAD. There is diffuse low density in a stent in OM1, with no evidence of distal flow (Fig. 9.11a–c).

9.11.3 Diagnosis

The diagnosis is occluded bare metal stent in OM1.

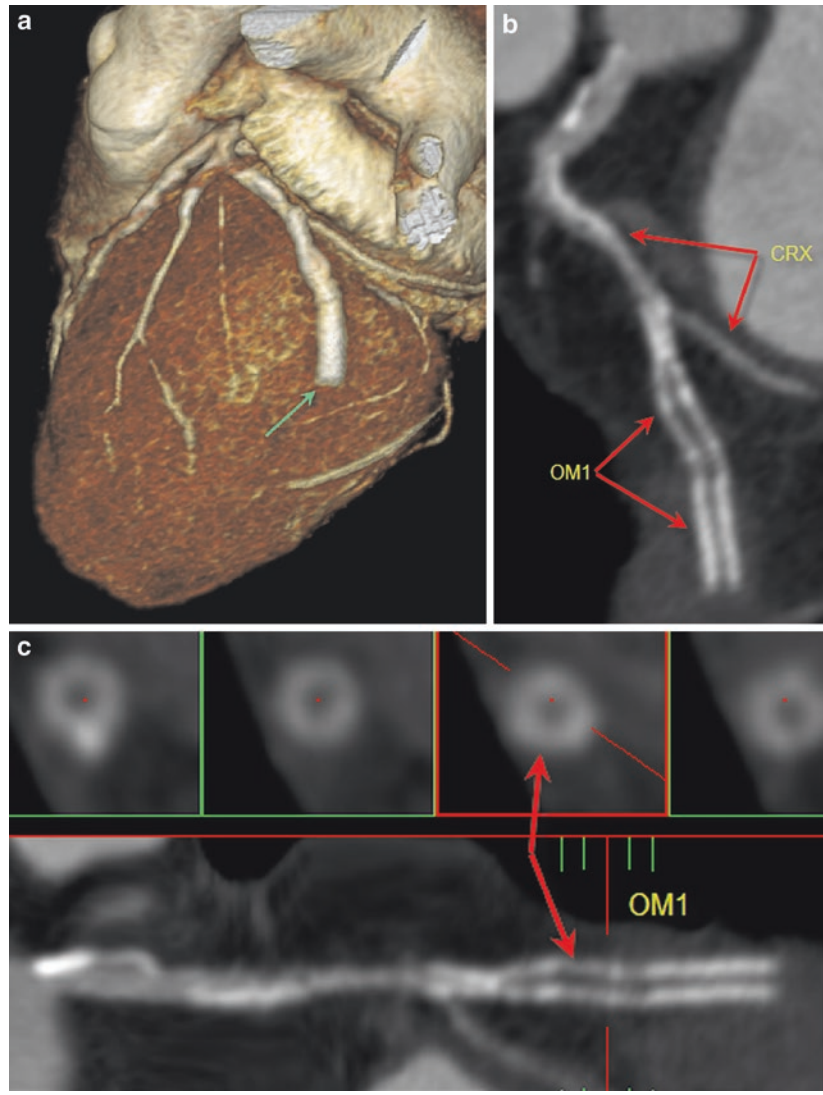

Fig. 9.11 (**a**–**c**) Volume rendering, cMPR, stretched, OM1: Occluded (thrombosed) stent (*arrows*)

9.11.4 Discussion

The images demonstrate diffuse low density in the lumen of the stent, with no distal flow, diagnostic of an occluded stent. Stents are the most widely used devices for coronary intervention despite two problems: subacute stent thrombosis (1–2%) and high restenosis rate (5–40%). Subacute stent thrombosis occurs within the first month after stent placement and can be prevented using the double antiplatelet regimen with aspirin and clopidogrel. Some risk of subacute thrombosis remains beyond the first month when DESs are used. DESs require prolonged antiplatelet therapy. DESs are the most significant innovation in interventional cardiology. They can reduce the incidence of restenosis in native stable coronary arteries to 3–5%. However, the long-term studies comparing bare metal stents and DESs do not show significant differences in the rate of major adverse cardiac events (death, myocardial infarction), especially in patients with diabetes after the treatment of bifurcating lesions.

9.11.5 Pearls and Pitfalls

Severe in-stent restenosis may mimic an occluded stent. The lack of opacification of the artery beyond the stent indicates stent thrombosis and total occlusion.

9.12 Case 9.12

9.12.1 History

A 78-year-old female presented with new onset of atypical chest pain. She had had CABG approximately 10 years prior, with interval occlusion of the vein graft to the distal RCA, with subsequent multiple PCIs with bare metal stents and also DESs in the previous 5 years.

9.12.2 Findings

There is high-grade stenosis in the ostium of the RCA, in the proximal edge of the first stent, and suspected in the mid-RCA (Fig. 9.12a, b). There are multiple sequential and overlapping stents throughout the RCA (full metal jacket), with additional patchy areas of low density in the lumen of the distal stents that were considered indeterminate for a high-grade restenosis. There is adjacent metal artifact from median sternotomy wire sutures.

9.12.3 Diagnosis

The diagnosis is high-grade stent restenosis.

9.12.4 Discussion

The CTA demonstrates definite high-grade stenosis in the proximal edge of the first stent and questionable in the mid- and distal RCA.

The patient underwent coronary angiography that confirmed high-grade ostial and mid-RCA stenosis (Fig. 9.12c). Angioplasty and an additional two stents were deployed in the proximal and mid-RCA, with satisfactory results (Fig. 9.12d).

9.12.5 Pearls and Pitfalls

When clinically indicated, CTA is an excellent noninvasive study in the evaluation of coronary stents.

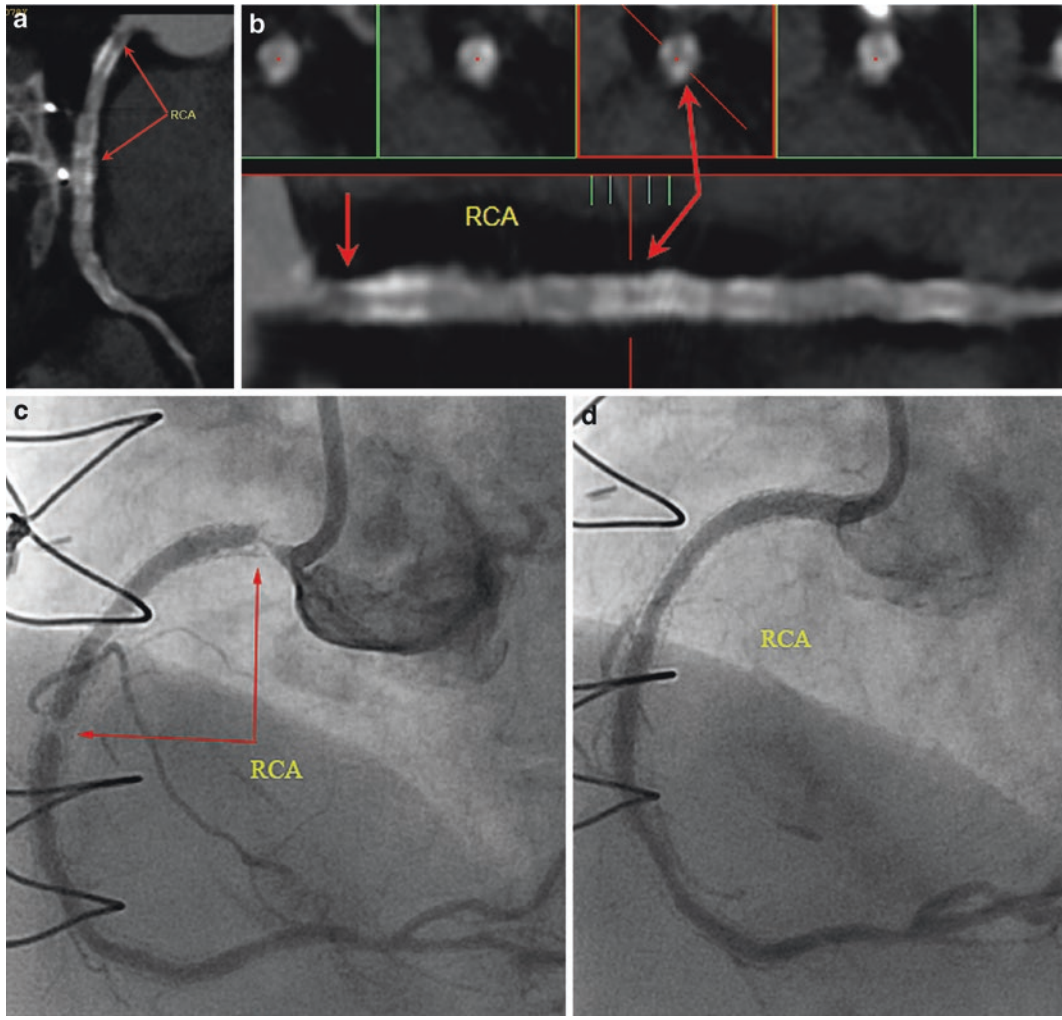

Fig. 9.12 (**a**, **b**) RCA cMPR, stretched: High-grade ostial stenosis in the proximal edge of the first stent and suspected mid-segment high-grade stent restenosis (*arrows*). (**c**) Coronary angiogram confirming high-grade stenosis at the ostium of the RCA and mid-segment (*arrows*). (**d**) Coronary angiogram following angioplasty and deployment of an additional two stents in the RCA, with satisfactory results

9.13 Case 9.13

9.13.1 History

A 47-year-old male presented with a history of PCI in the previous 2 months, with placement of DESs in the mid-LAD and RCA. The patient presented with new onset of chest pain. (Case courtesy of Dr. William Bugni, Tampa, FL.)

9.13.2 Findings

There is a short segment of endoluminal low density in the distal segment of the stent in the LAD (Fig. 9.13a, b). There is also localized endoluminal low density in the distal segment of the stent in the RCA extending just beyond the stent (napkin ring stenosis). There is discontinuity of the struts in the mid-segment of the same stent suggesting the strut fracture (Fig. 9.13c, d).

9.13.3 Diagnosis

The diagnosis is early onset of high-grade in-stent restenosis in the LAD and RCA.

9.13.4 Discussion

In-stent restenosis may involve any part of the stent and frequently involves the proximal or distal ends of stents. The patient underwent coronary angiography (Fig. 9.13e, f) with intravascular ultrasound that confirmed the high-grade stenosis in the distal segments of the stents and in the mid-segment of the RCA stent, where disruption of the struts was previously noted on the CCTA. Due to the early failure (within 2 months) of the stent placement and involving two major coronary vessels, surgical revascularization was recommended.

9.13.5 Pearls and Pitfalls

Localized in-stent restenosis may be difficult to visualize without proper windowing of the images. Widened window width well above 1000 with adjusted window level is commonly required to identify the abnormality.

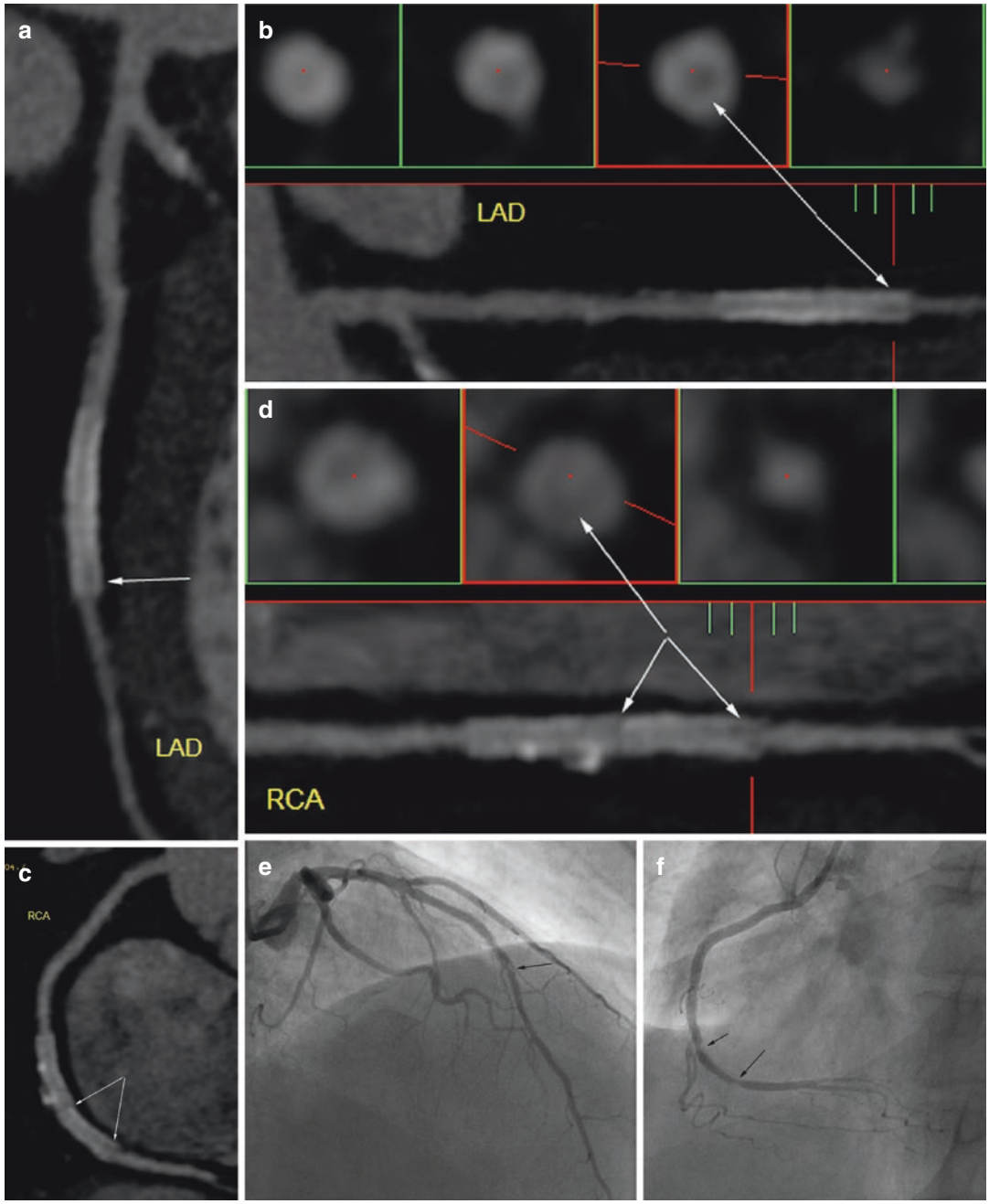

Fig. 9.13 (**a**, **b**) LAD cMPR, stretched: Localized distal stent endoluminal low density indicating high-grade in-stent restenosis (*arrows*). (**c**, **d**) RCA cMPR, stretched. Localized distal stent endoluminal low-density *napkin ring* appearing high-grade in-stent restenosis. Discontinuity of the struts in the mid-segment of the stent suggesting a strut fracture (*arrows*). (**e**) Left coronary angiogram confirming the stenosis in the distal segment of the stent in the LAD (*arrow*). (**f**) Right coronary angiogram confirming the stenosis in the stent in the RCA (*arrows*)

9.14 Case 9.14

9.14.1 History

A 62-year-old female with atypical chest pain status post PCI to the RCA.

9.14.2 Findings

There is a dissection in the RCA distal to the edge of the patent stent.

9.14.3 Diagnosis

Dissection of the RCA distal to the stent (Fig. 9.14a, b).

9.14.4 Discussion

The case demonstrates one of the complications following a PCI, which is a dissection of the non-stented segment of the artery. This may result from a wire injury perforating the intimal layer of the vessel or barotrauma to the intima during the stent deployment and/or ballooning.

9.14.5 Pearls and Pitfalls

Complications from PCI can occur within the stented segment, at the edge of the stent, and beyond the area of intended intervention.

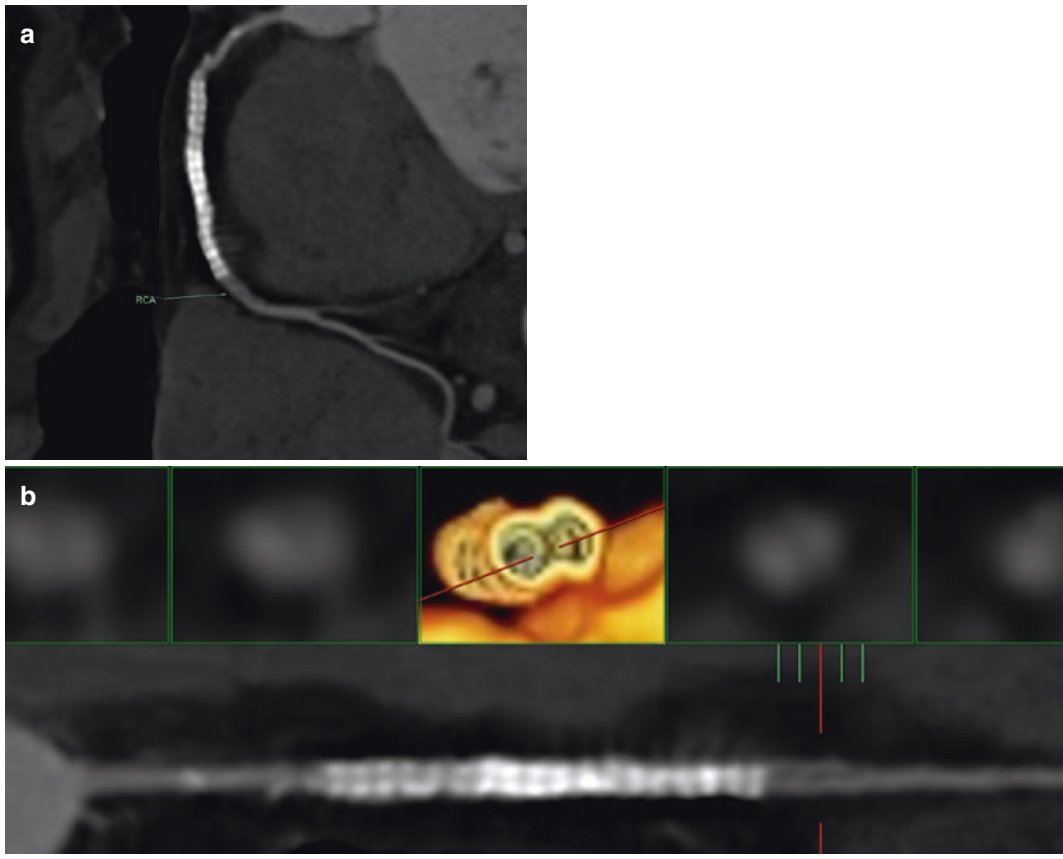

Fig. 9.14 (**a**) cMPR of RCA (**b**) Stretched cMPR of RCA

9.15 Case 9.15

9.15.1 History

A 71-year-old female with acute onset of chest pain. Status post RCA-PCI.

9.15.2 Findings

The patient had a CCTA in the previous 8 months that demonstrated a mid-strut stent fracture located in the proximal RCA, but is otherwise patent (Fig. 9.15a). The new CCTA study demonstrates an acute thrombosis of the stent at the site of the fracture with subtotal occlusion (Fig. 9.15b: arrow indicating the fracture site). A coronary angiogram was performed the following day showing complete thrombosis of the stent (Fig. 9.15c).

9.15.3 Diagnosis

Fractured stent developing an acute thrombosis.

9.15.4 Discussion

Stent fracture is a known complication from a PCI. Fracture of the stent struts cause altered laminar flow through the segment, which results in decreased patency rates and complications such as thrombosis as demonstrated in this case.

9.15.5 Pearls and Pitfalls

In the evaluation of stents, it is important to look carefully to identify the discontinuity of the struts (Fig. 9.15a) in order to diagnose a non-displaced strut fracture.

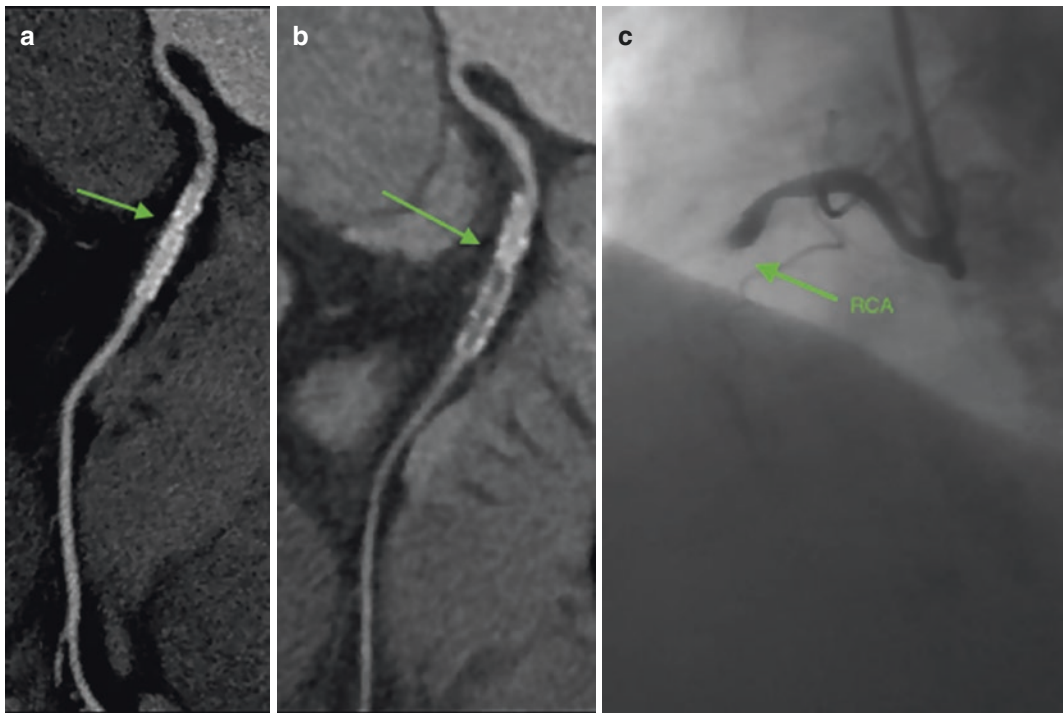

Fig. 9.15 (**a**) cMPR of RCA (**b**) cMPR of RCA with the *arrow* indicating the fractured strut site. (**c**) Right coronary angiogram

9.16 Case 9.16

9.16.1 History

A 50-year-old male with past medical history of IV drug abuse, thymoma status post resection and radiation therapy, presenting to the hospital with atypical chest pain.

9.16.2 Findings

Initial CT angiogram showing a left dominant coronary system with a critical stenosis in the proximal LAD (Fig. 9.16a–c). The plaque also extends proximally into the left main but the narrowing of the left main is less than 50%.

CCTA taken status post stenting of the proximal LAD showing a patent stent (Fig. 9.16d), but it extends proximally into the distal left main and jails the ostium of the dominant left circumflex coronary artery (Fig. 9.16e–g).

9.16.3 Diagnosis

Stent placed in the proximal LAD extending proximally into the left main coronary artery and also jailing the dominant LCX artery.

9.16.4 Discussion

Although the stent is patent, it was unfortunately deployed incorrectly extending into the proximal left main artery and jailing the dominant left circumflex artery. This complication of intervention places the patient at risk of acute coronary syndrome and death. Therapeutic options include double antiplatelet therapy with close clinical follow-up, reintervention with placement of stents in the left main and the LCX, and/or surgical revascularization. The patient was referred for the performance of a nuclear stress test and clinical follow-up.

9.16.5 Pearls and Pitfalls

High quality CCTA can be used for the evaluation of the PCI patency and other complications as demonstrated in this case.

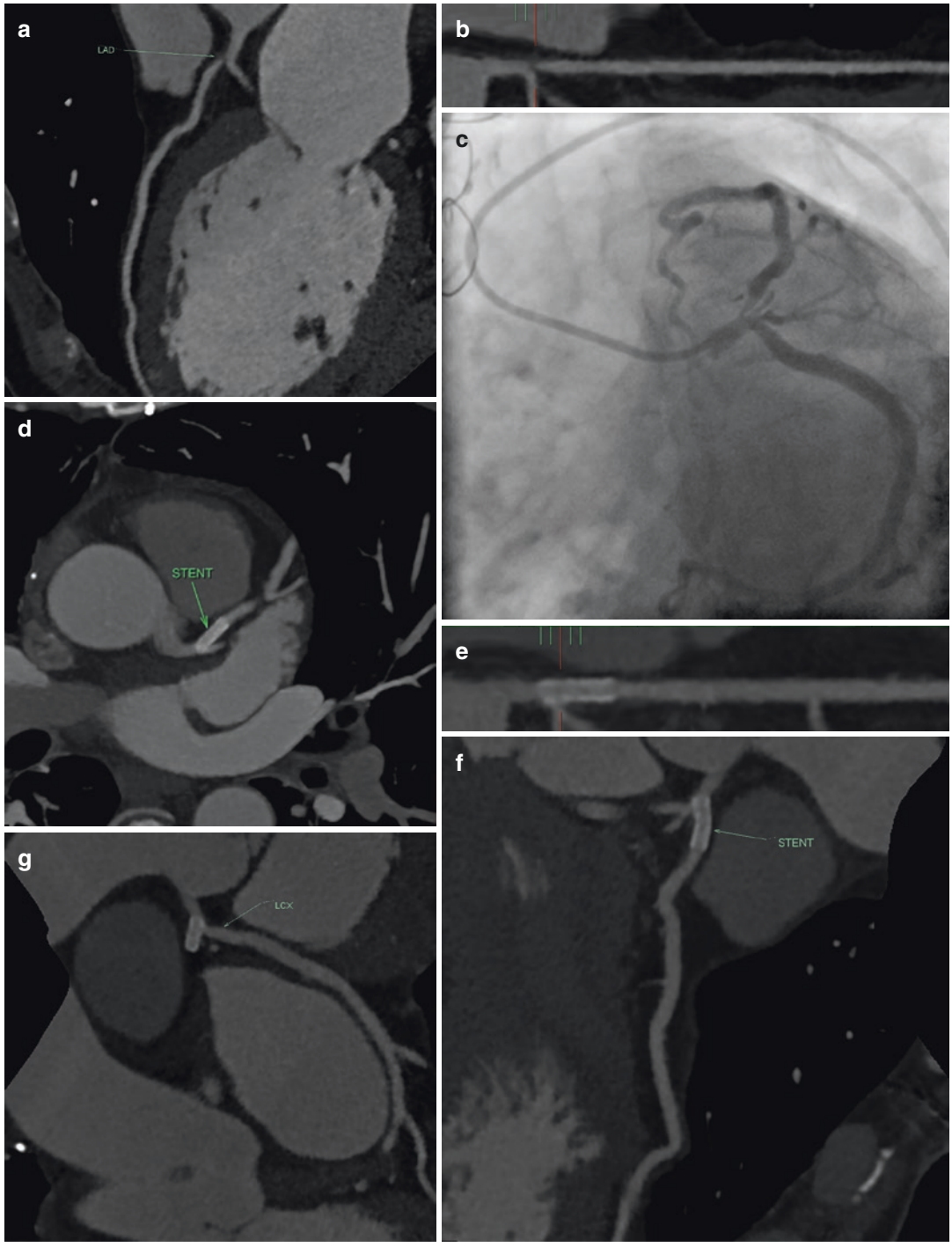

Fig. 9.16 (**a**) cMPR of LAD (**b**) stretched cMPR of LAD (**c**) Left coronary angiogram (**d**) Axial (**e**) stretched MPR of LAD with stent in place (**f**, **g**) cMPRs of LAD and LCX

9.17 Case 9.17

9.17.1 History

A 70-year-old male with a history of stenting in the previous 12 months presents with new onset of chest pain similar to the one described prior to the PCI.

9.17.2 Findings

There is a DES stent in the first diagonal branch with restenosis. The proximal edge of the stent protrudes into the LAD (Fig. 9.17a, c). There is a stent in the RCA, which has mild restenosis and high-grade critical obstruction just distal to the stent (Fig. 9.17d, e). There is a patent stent in the mid-circumflex (Fig. 9.17b).

9.17.3 Diagnosis

High-grade restenosis in the D1 stent that extends into the LAD. High-grade obstruction just distal to the RCA stent.

9.17.4 Discussion

The case demonstrates restenosis in a stent within a branch of the LAD. Unfortunately, the stent is placed incorrectly and is also affecting the flow in the LAD.

The patient was recommended to have surgical revascularization, but opted for additional intervention and subsequently sustained a massive myocardial infarction and became a cardiac cripple awaiting a heart transplant.

9.17.5 Pearls and Pitfalls

This case shows how a misplaced stent can adversely affect two vascular territories.

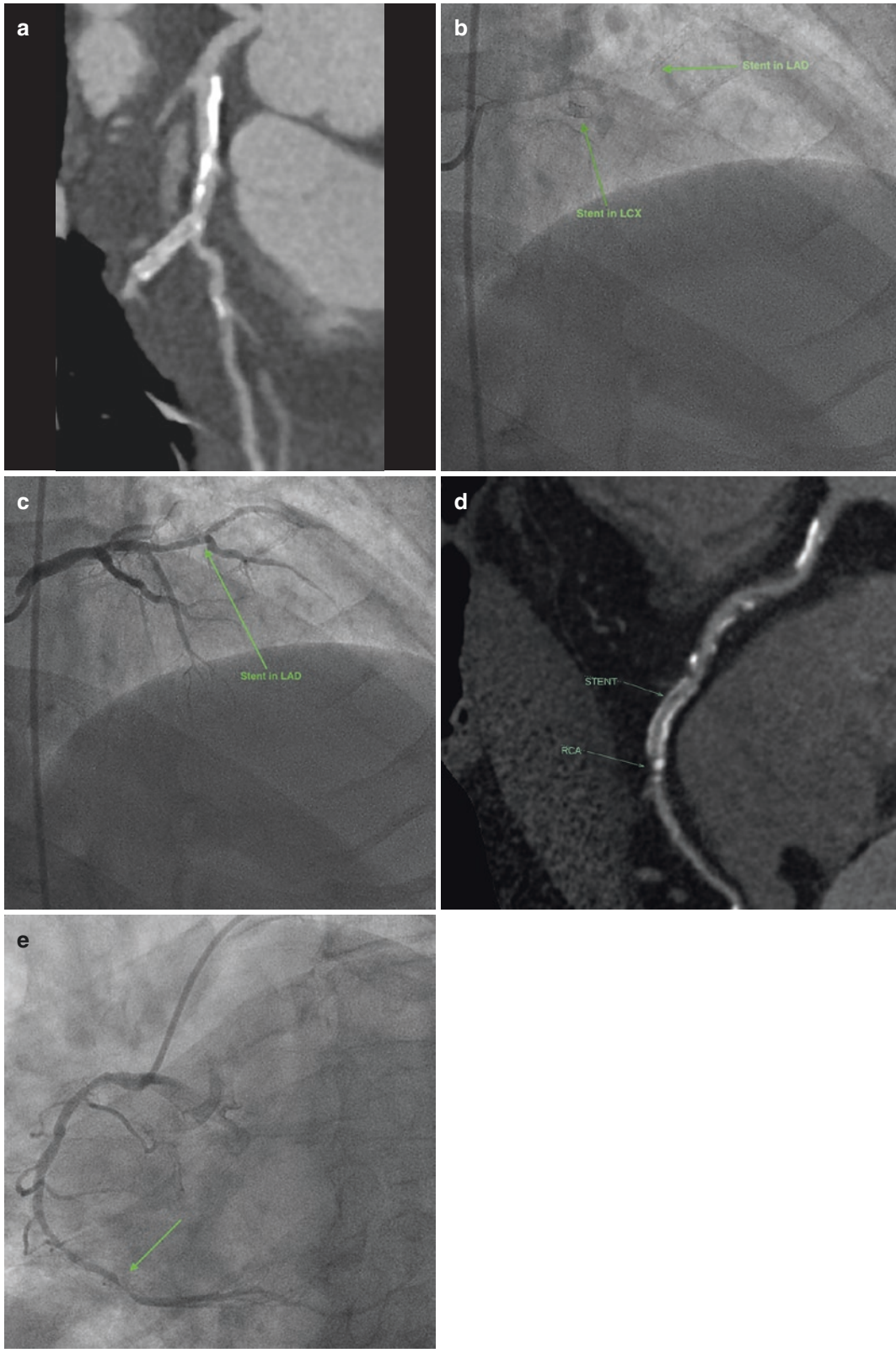

Fig. 9.17 (**a**) cMPR of LAD (**b**) Left coronary angiogram without contrast (**c**) Left coronary angiogram with early filling (**d**) cMPR of RCA (**e**) Right coronary angiogram

References

1. Schweiger MJ, Ansari E, Giugliano GR, et al. Morphology and location of restenosis following bare metal coronary stenting. J Invasive Cardiol. 2006;18(4):165–8. http://www.invasivecardiology.com/article/5455
2. Thury A, Wentzel JJ, Vinke RV, et al. Images in cardiovascular medicine. Focal in-stent restenosis near step-up: roles of low and oscillating shear stress? Circulation. 2002;105:e185–7.
3. Newsome LT, Kutcher MA, Gandhi SK. A protocol for the perioperative management of patients with intracoronary drug-eluting stents. http://www.apsf.org/resource_center/newsletter/2007/winter/12_protocol.htm
4. Sigwart U, Puel J, Mirkovitch V, Joffre F, Kappenberger L. Intravascular stents to prevent occlusion and restenosis after transluminal angioplasty. N Engl J Med. 1987;316:701–6.

Suggested Reading

Boulmier D, Heautot JH, Garreau M, et al. Clinical and angiographic parameters affecting the quality of 16 slice spiral CT in the diagnosis of restenosis after stenting the left main coronary artery. Arch Mal Coeur Vaiss. 2007;100(4):257–63.

Cademartiri F, Palumbo A, Maffei E, et al. Diagnostic accuracy of 64-slice CT in the assessment of coronary stents. Radiol Med. 2007a;112(4):526–37.

Cademartiri F, Palumbo A, Maffei E, et al. Follow-up of internal mammary artery stent with 64-slice CT. Int J Cardiovasc Imaging. 2007b;23(4):537–9.

Chabbert V, Carrie D, Bennaceur M, et al. Evaluation of in-stent restenosis in proximal coronary arteries with multidetector computed tomography (MDCT). Eur Radiol. 2007;17(6):1452–63.

Das KM, El-Menyar AA, Salam AM, et al. Contrast-enhanced 64-section coronary multidetector CT angiography versus conventional coronary angiography for stent assessment. Radiology. 2007;245(2):424–32.

Ebersberger U, et al. CT evaluation of coronary artery stents with iterative image reconstruction: improvements in image quality and potential for radiation dose reduction. Eur Radiol. 2013;23(1):125–32.

Foussas SG, Zairis MN, Patsourakos NG, et al. The impact of oral antiplatelet responsiveness on the long-term prognosis after coronary stenting. Am Heart J. 2007;154(4):676–81.

Gil RJ, Pawłowski T, Dudek D, et al. Investigators of Direct Stenting vs Optimal Angioplasty Trial (DIPOL). Comparison of angiographically guided direct stenting technique with direct stenting and optimal balloon angioplasty guided with intravascular ultrasound. The multicenter, randomized trial results. Am Heart J. 2007;154(4):669–75.

Goldstein JA. CT imaging of coronary stent patency. Catheter Cardiovasc Interv. 2007;69(7):939.

Groen JM, Greuter MJ, van Ooijen PM, et al. Initial results on visualization of coronary artery stents at multiple heart rates on a moving heart phantom using 64-MDCT. J Comput Assist Tomogr. 2006;30(5):812–7.

Kefer JM, Coche E, Vanoverschelde JL, et al. Diagnostic accuracy of 16-slice multidetector-row CT for detection of in-stent restenosis vs detection of stenosis in nonstented coronary arteries. Eur Radiol. 2007;17(1):87–96.

Kinohira Y, Akutsu Y, Li HL, et al. Coronary arterial plaque characterized by multislice computed tomography predicts complications following coronary intervention. Int Heart J. 2007;48(1):25–33.

Kulick D. Coronary balloon angioplasty and stents (Percutaneous coronary intervention, PCI). http://www.medicinenet.com/coronary_angioplasty/article.htm

Larchez C, Daoud B, Ghostine S, et al. Visualization of the intra-stent lumen in the coronary arteries and detection of restenoses with 64-slices tomography scanners with cardiac synchronization: first experience. Arch Mal Coeur Vaiss. 2006;99(12):1184–90.

Leipsic J, Heilbron BG, Hague C. Iterative reconstruction for coronary CT angiography: finding its way. Int J Cardiovasc Imaging. 2012;28(3):613–20.

Lell MM, Panknin C, Saleh R, et al. Evaluation of coronary stents and stenoses at different heart rates with dual source spiral CT (DSCT). Invest Radiol. 2007;42(7):536–41.

Mahnken AH, Mühlenbruch G, Seyfarth T, et al. 64-slice computed tomography assessment of coronary artery stents: a phantom study. Acta Radiol. 2006;47(1):36–42.

Maintz D, Burg MC, Seifarth H, et al. Update on multidetector coronary CT angiography of coronary stents: in vitro evaluation of 29 different stent types with dual-source CT. Eur Radiol. 2009;19(1):42–9.

Nakamura K, Funabashi N, Uehara M, et al. Impairment factors for evaluating the patency of drug-eluting stents and bare metal stents in coronary arteries by 64-slice computed tomography versus conventional coronary angiography. Int J Cardiol. 2008;130(3):349–56.

Nieman K, et al. Multislice computed tomography angiography for noninvasive assessment of the 18-month performance of a novel radiolucent bioresorbable vascular scaffolding device: the ABSORB trial (a clinical evaluation of the bioabsorbable everolimus eluting coronary stent system in the treatment of patients with de novo native coronary artery lesions). J Am Coll Cardiol. 2013;62(19):1813–4.

Oncel D, Oncel G, Karaca M. Coronary stent patency and in-stent restenosis: determination with 64-section multidetector CT coronary angiography—initial experience. Radiology. 2007;242(2):403–9.

Oncel D, Oncel G, Tastan A, et al. Evaluation of coronary stent patency and in-stent restenosis with dual-source CT coronary angiography without heart rate control. AJR Am J Roentgenol. 2008;191(1):56–63.

Otsuka M, Sugahara S, Umeda K, et al. Utility of multislice computed tomography as a strategic tool for

complex percutaneous coronary intervention. Int J Cardiovasc Imaging. 2008;24(2):201–10.
Pan J, et al. Angiographic patterns of in-stent restenosis classified by computed tomography in patients with drug-eluting stents: correlation with invasive coronary angiography. Eur Radiol. 2013;23(1):101–7.
Piers LH, Dikkers R, Willems TP, et al. Computed tomographic angiography or conventional coronary angiography in therapeutic decision-making. Eur Heart J. 2008;29(23):2902–7.
Pinto IM, Sousa AG, Ishikama W, et al. Late outcome of sirolimus-eluting stents: comparison of multidetector computed tomography with quantitative coronary angiography and intravascular ultrasound. Arq Bras Cardiol. 2006;87(5):575–82.
Pugliese F, Cademartiri F, van Mieghem C, et al. Multidetector CT for visualization of coronary stents. Radiographics. 2006;26(3):887–904.
Pugliese F, Weustink AC, Van Mieghem C, et al. Dual source coronary computed tomography angiography for detecting in-stent restenosis. Heart. 2008;94(7):848–54.
Schepis T, Koepfli P, Leschka S, et al. Coronary artery stent geometry and in-stent contrast attenuation with 64-slice computed tomography. Eur Radiol. 2007;17(6):1464–73.
Schlosser T, Scheuermann T, Ulzheimer S, et al. In-vitro evaluation of coronary stents and 64-detector-row computed tomography using a newly developed model of coronary artery stenosis. Acta Radiol. 2008;49(1):56–64.
Schuijf JD, Pundziute G, Jukema JW, et al. Evaluation of patients with previous coronary stent implantation with 64-section CT. Radiology. 2007;245(2):416–23.
Schweiger MJ, Ansari E, Giugliano GR, et al. Morphology and location of restenosis following bare metal coronary stenting. J Invasive Cardiol. 2006;18(4):165–8.
Sheiban I, Meliga E, Moretti C, et al. Long-term clinical and angiographic outcomes of treatment of unprotected left main coronary artery stenosis with sirolimus-eluting stents. Am J Cardiol. 2007; 100(3):431–5.
Sheth T, Dodd JD, Hoffmann U, et al. Coronary stent assessability by 64 slice multi-detector computed tomography. Catheter Cardiovasc Interv. 2007;69(7):933–8.
Soon KH, Cox N, Chaitowitz I, et al. Non-invasive computed tomography angiography in the assessment of coronary stent patency: an Australian experience. Intern Med J. 2007;37(6):360–4.
Soon KH, Cox N, Wong A, et al. CT coronary angiography predicts the outcome of percutaneous coronary intervention of chronic total occlusion. J Interv Cardiol. 2007;20(5):359–66.
Soon KH, Farouque HM, Chaitowitz I, et al. Discrepancy between computed tomography coronary angiography and selective coronary angiography in the pre-stenting assessment of coronary lesion length. Australas Radiol. 2007;51(5):440–5.
Sun Z, Davidson R, Lin CH. Multi-detector row CT angiography in the assessment of coronary in-stent restenosis: a systematic review. Eur J Radiol. 2009;69(3):489–95.
Suzuki S, Furui S, Kuwahara S, et al. Assessment of coronary stent in vitro on multislice computed tomography angiography: improved in-stent visibility by the use of 140-kV tube voltage. J Comput Assist Tomogr. 2007;31(3):414–21.
Togni M, Eber S, Widmer J, et al. Impact of vessel size on outcome after implantation of sirolimus-eluting and paclitaxel eluting stents: a subgroup analysis of the SIRTAX trial. J Am Coll Cardiol. 2007;50(12):1123–31.
Trabattoni D, De Martini S, Galli S, et al. CT-scan heralded left main catheter-induced dissection, successfully treated with PCI. Int J Cardiol. 2008;124(3):e56–7.
Yamamura J, van Stevendaal U, Köster R, et al. Experimental 16-row CT evaluation of in-stent restenosis using new stationary and moving cardiac stent phantoms: experimental examination. Rofo. 2006;178(11):1079–85.

Cardiac CTA in the Evaluation of CABG

10

Claudio Smuclovisky

10.1 Introduction

The purpose of surgical revascularization of the coronary arteries is to bypass an obstruction in an artery using a native artery or vein conduit as a graft. CTA has been demonstrated to be of significant value in the evaluation of coronary revascularization. Grafts are generally easier to evaluate than the native coronary arteries since they are less sensitive to temporal resolution-related motion artifacts. The exceptions are the distal anastomosis that is in the epicardium and areas where there are surgical clip artifacts present.

The most common surgical technique used is a median sternotomy. In recent years, techniques using a mini-thoracotomy (keyhole surgery) and robotic-assisted surgery are currently performed in a limited number of centers. There is also debate whether the use of coronary artery bypass grafting (CABG) without the use of cardiopulmonary bypass and cardioplegia (off-pump CABG) is superior to that performed with the heart–lung machine and the heart chemically arrested (standard CABG). If the surgery is performed on pump, there will be one or two cannulation sites in the ascending aorta that may have been closed with small and usually rectangular-shaped appearing patches (pledgets). These are not to be confused with an occluded graft (stump). The differentiation on CTA is by the visualization of a square patch on the ascending aorta that has a discrete wall separation (Fig. 10.1a, b) that does not communicate with the lumen of the ascending aorta.

C. Smuclovisky, MD, FACC, FSCCT
Department of Radiology, Holy Cross Hospital,
South Florida Medical Imaging Cardiovascular Institute,
Fort Lauderdale, FL, USA
e-mail: smuclovisky@gmail.com

C. Smuclovisky (ed.), *Coronary Artery CTA*, https://doi.org/10.1007/978-3-319-66988-5_10

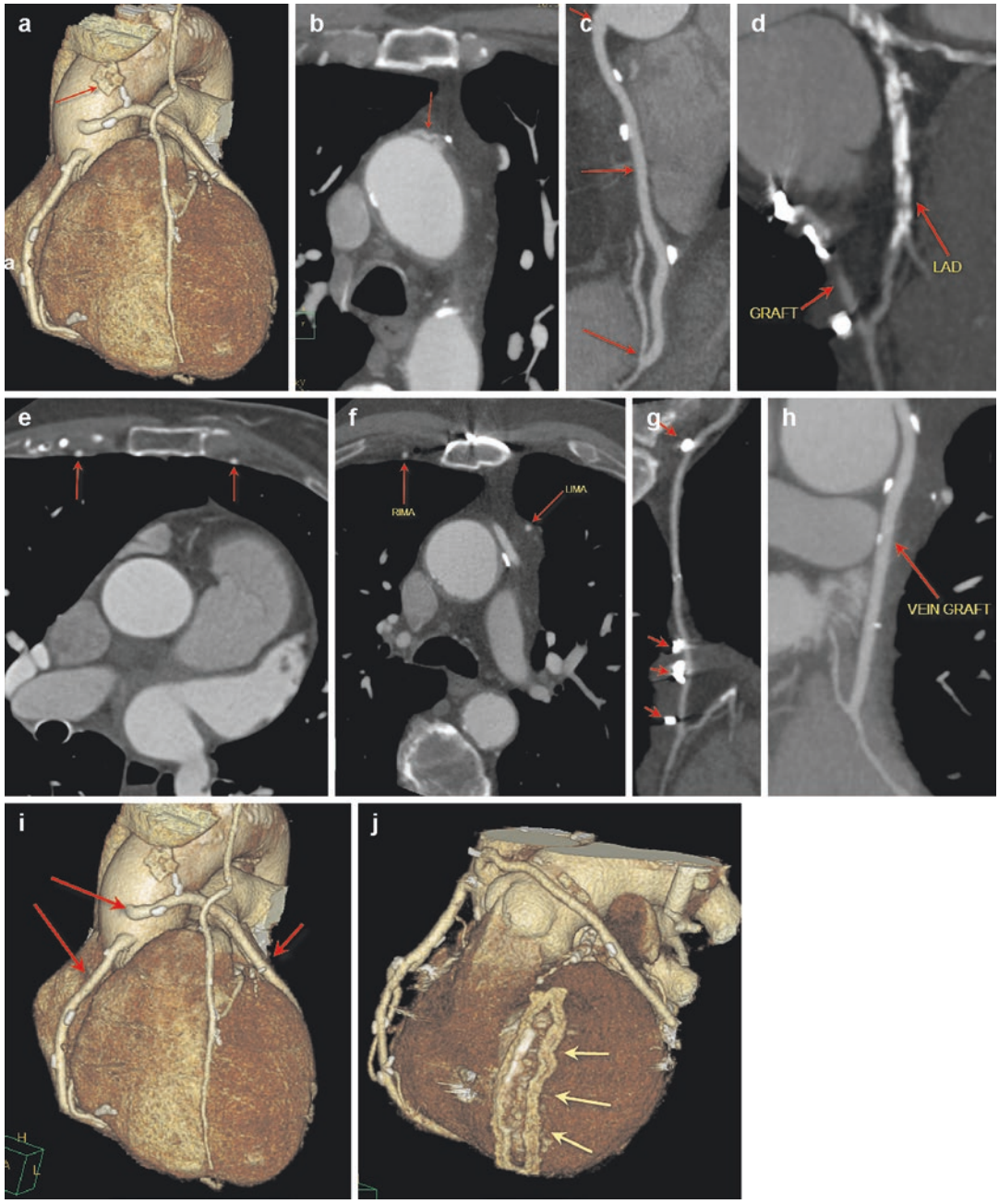

Fig. 10.1 (**a**, **b**) Surgical cannulation repair pledget (*arrows*). Not to be confused with an occluded graft stump. (**c**) Graft proximal, body, and distal anastomosis (*arrows*). (**d**) Advanced disease in the LAD proximal to the graft anastomosis (*arrow*). (**e**) Normal anatomic location of the internal mammary arteries (*arrows*). (**f**) Normal caliber of the RIMA and LIMA grafts (*arrows*). (**g**) Metal surgical clip artifact on the LIMA graft (*arrows*). (**h**, **i**) Vein grafts (*arrows*). (**j**) LAD distribution not grafted due to lack of viable myocardium. Post-LV aneurismectomy (*arrows*)

The choice of surgical technique depends on the patient's coronary anatomy and the experience and training of the surgeon. It is important to note that the only main coronary arteries that are not directly grafted are the left main (LM) and the proximal circumflex (LCX) because they are surgically inaccessible.

The graft consists of either an arterial or venous conduit. It is described by its three important segments that are the proximal anastomosis, the body of the graft, and the distal anastomosis (Fig. 10.1c).

In the CTA evaluation of the graft, it is important to carefully evaluate and comment on these three segments and also whether or not there is disease in the distal native coronary artery runoff. A graft that is without a flow-limiting stenosis is referred to as a *patent graft*. The native coronary artery proximal to the distal anastomosis usually has severe disease with high-grade obstruction or occlusion (Fig. 10.1d).

10.1.1 Arterial Grafts

The most common arterial grafts used are the internal mammary arteries (IMA). These originate from the subclavian arteries, are located bilaterally, and run parallel to the lateral aspect of the sternum in the chest wall (Fig. 10.1e). The most common technique is to dissect the artery from the chest wall and suture the distal end to a coronary artery. The IMA branches are occluded with surgical clips to avoid bleeding and competitive arterial flow to the chest wall. These clips also serve as a visual landmark as to the location and course of the graft. The left internal mammary artery is commonly referred to as a LIMA, and the right as a RIMA. Typically, an arterial graft has a single distal anastomosis; however, it may be used to bypass more than one artery and is then referred to as a *sequential graft*. An example of this would be having a sequential LIMA bypassed to a diagonal (DX) and then to the distal left anterior descending (LAD).

A LIMA graft to the LAD is the preferred bypass as it has superior patency rates. The patency rate at 10+ years is 95% versus 50–60% for a vein graft. Because of this, the LIMA is usually grafted to the mid- or distal LAD, or less frequently, to a diagonal. The RIMA is usually grafted to the right coronary (RCA) distribution, as a free or in situ conduit, or to an obtuse marginal artery (OM). When an arterial graft is diseased, it becomes diffusely smaller in caliber and is referred to as *atretic*. In the evaluation of an IMA, it should have a similar caliber to the contralateral nongrafted artery that is considered normal (Fig. 10.1f). It may also be larger in caliber and then is referred to as a *hypertrophied arterial graft*.

If the graft is occluded, the only clues on the CTA are the visualization of vascular clips in the course of the artery and the lack of visualization of the IMA in the chest wall.

The most important segment for evaluation is the distal anastomosis, which is the most common location of stenosis. Surgical clips along the body of an arterial graft may cause metal artifacts on a CTA (Fig. 10.1g). It is, however, rare to find a stenotic segment from a surgical clip, and I have not personally encountered it, despite evaluating

thousands of grafts. Consequently, I will report the graft as being patent if the proximal and distal anastomoses appear normal despite surgical clip artifacts in the body of an arterial graft.

A free graft is an arterial graft that is completely removed from the chest wall and then surgically grafted proximally and distally. Other commonly used arterial grafts are the radial arteries. A surgical arterial Y graft configuration occurs when a free graft has its proximal anastomosis off another bypass graft. A less commonly used arterial conduit is the gastroepiploic artery, which is freed from the stomach and brought through the diaphragm to be grafted in situ to an inferior coronary artery.

10.1.2 Vein Grafts

Saphenous veins are commonly used as grafts (Fig. 10.1h, i). These are usually grafted from the ascending aorta distally to the coronary arteries. A sequential, or jump, graft is a single conduit used to bypass more than one coronary artery. Vein grafts are placed reversed because of the venous valves.

When there are multiple proximal anastomoses from the ascending aorta, they are distributed in a cranial–caudal sequence as follows: the superior grafts to the territory of the left circumflex, followed by the LAD-diagonal distribution and the inferior graft, from the right of midline, to the territory of the right coronary artery. Rarely, a vein is grafted from the descending aorta via a left lateral thoracotomy. Vein grafts may also be placed in a Y configuration from the surgical anastomosis of two veins, or rarely, using a natural Y (vein branch). These appear as a single proximal to one or more distal limbs. A clinical review of the grafts consists of the evaluation of the proximal anastomosis, the body of the graft, the distal anastomosis, and native coronary artery runoff.

Over time, the veins develop *arterialized* disease with calcifications and soft tissue plaques in the walls that could lead to flow-limiting stenosis and occlusion. These are commonly treated with percutaneous coronary interventions (stenting). Grafts may also have stenoses secondary to surgical complications during harvest, suture disruption with development of a pseudoaneurysm, technical errors during placement, dissection of the aorta, and so forth.

10.1.3 Technical Considerations

In order to completely evaluate the grafts, the cranial field-of-view needs to be extended to the top of the arch for grafts originating from the aorta and to the subclavian arteries for evaluation of the ostium of the internal mammary arteries, if they were used. IV contrast is injected in the right antecubital fossa at a volume of 100 mL of high-density contrast between 320 and 400 mg/mL. Scan triggering in our laboratory is set with the placement of a region of interest (ROI) in the descending aorta at 130 HU with a scan delay of 4–6 s.

10.1.4 Clinical CTA Review of Postsurgical Coronary Revascularization

The CTA review of the surgical revascularized heart consists of evaluation of the native coronary anatomy, the grafts, and the extracoronary structures. The CTA is reviewed on a workstation multiplanar (MPR), curved MPR (MPRc), and 3D volume rendered. A typical approach is commencing with a review of the extracoronary structures followed by the native coronary anatomy. The purpose of reviewing the native coronary arteries first is to understand which arteries are diseased and deserve a bypass. It helps to mentally calculate how many grafts are expected and then proceed to look for them. This systematic approach allows formulation of conclusions that make anatomic sense and are clinically relevant. As an example, in a patient with an intact left ventricle, right dominant anatomy where the left main coronary artery and RCA have high-grade obstruction, one would expect to encounter a minimum of three grafts. In a similar case but with an old large myocardial infarct in the territory of the LAD, there may be only two grafts present, since the infarcted myocardium may not have required revascularization. Thus, a minimum of two grafts would be expected (Fig. 10.1j).

Unfortunately, many times it is not this simple since the surgical technique may have variables such as adequate native distal coronary artery targets, coronary anatomic variants, diseased aorta, combined percutaneous coronary intervention, and previous surgery. Regardless, it is important to attempt to understand anatomically how the myocardium is receiving blood flow, whether it is compromised, correlates with the other noninvasive testing, and the patient symptoms.

The native coronary artery proximal to a patent graft is commonly irrelevant since the graft has taken its place in supplying the distal flow. Also, the proximal native segments typically develop accelerated disease and commonly have a heavily calcified and atretic appearance. The grafts are reported individually as to their origin, targeted coronary artery, and whether they are patent or diseased. The description of graft stenosis may be quantified by a percentage or degree of obstruction.

Disease in the wall of the graft that does not cause obstruction may be termed nonobstructive. High-grade obstruction refers to greater than 70% stenosis. Moderate obstruction refers to 50–70% stenosis and mild obstruction less than 50% stenosis. It is also important to report whether disease is present in the distal anastomosis and distal coronary artery runoff.

Grafts are counted by the number of distal anastomosis. As an example, a LIMA to the distal LAD is considered a CABG ×1. A sequential LIMA to the second diagonal and distal LAD is considered a CABG ×2. Adding a sequential vein graft to three obtuse marginal branches would add to CABG ×5 although there are only two surgical vascular conduits.

Both the terms, SVG and VG, are used to refer to the saphenous vein graft.

10.2 Case 1

10.2.1 History

A 78-year-old, asymptomatic male with a history of questionable ischemia in the anterior wall on a nuclear perfusion scintigram presented, with status post prior coronary artery bypass graft (CABG) ×3, 5 years previously.

10.2.2 Findings

There is a patent left internal mammary artery (LIMA) graft to the distal LAD. There are also two patent vein grafts to the second obtuse marginal (SVG–OM2) and to the posterior descending arteries (SVG–PDA) (Fig. 10.2a–e).

10.2.3 Diagnosis

The diagnosis is multiple patent grafts.

10.2.4 Discussion

CT is an excellent noninvasive study for the evaluation of coronary postsurgical revascularization. Analysis of the grafts consists of the evaluation of the proximal anastomosis, the body of the graft, the distal anastomosis, and runoff. The grafts generally have an equal luminal diameter throughout. It is common for the grafts to have adjacent surgical clips that may cause significant metal artifact and render a segment of the graft nonevaluable. Grafts are evaluated in the axial plane (source images), curved reformatted reconstruction (cMPR), and volume rendered (VR).

10.2.5 Pearls and Pitfalls

A graft cannot be considered patent unless the full extent of the graft has been evaluated. An exception, in our experience, is surgical clip artifacts in the body of an internal mammary graft since a diseased internal mammary artery graft is different from that of a vein graft. For further information, refer to the introduction of this chapter.

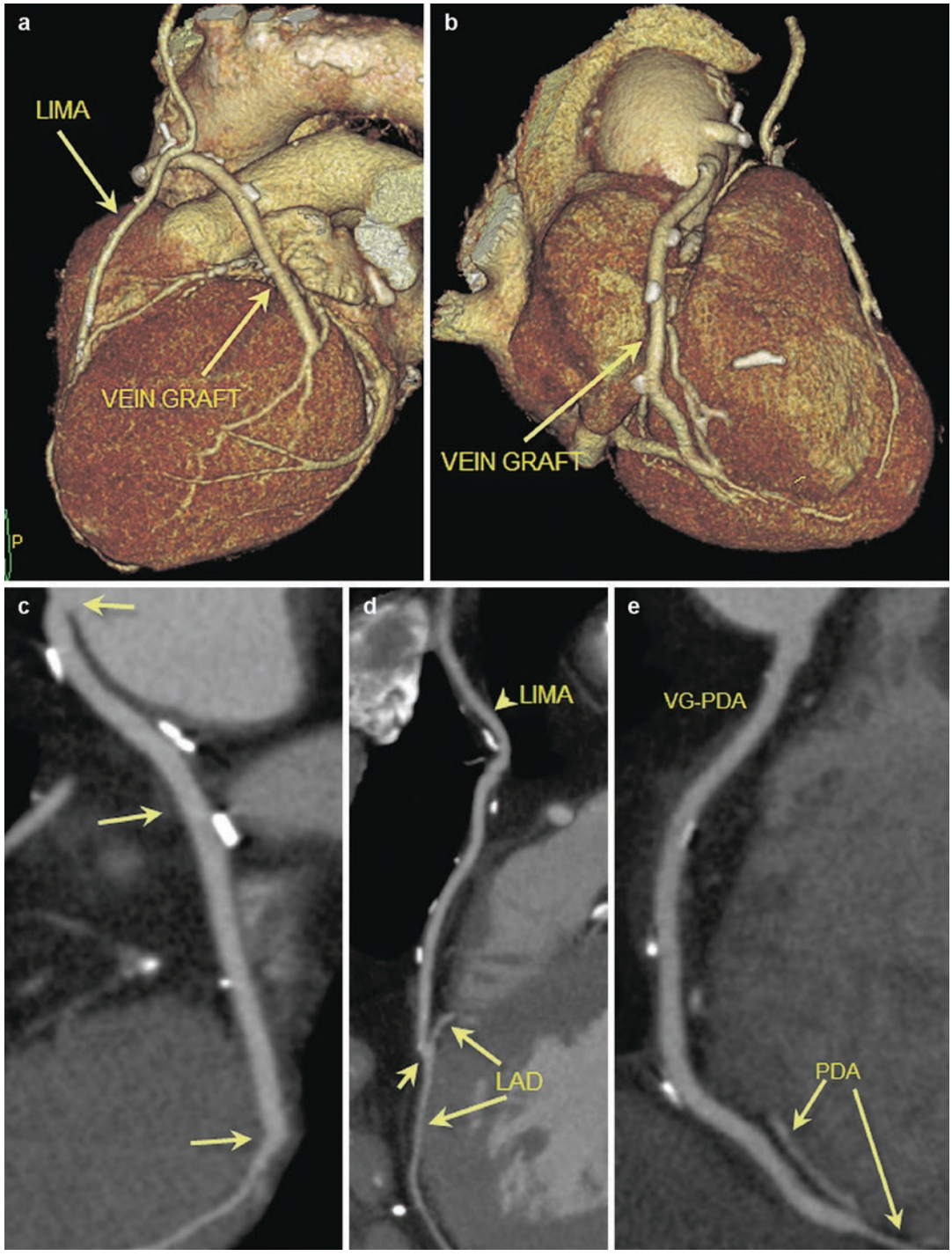

Fig. 10.2 (**a**, **b**) Volume rendering: Patent left internal mammary artery (LIMA) to the distal LAD, vein graft (SVG) to OM2, vein graft to the PDA (*arrows*). (**c**) cMPR, SVG–OM2, proximal, body, and distal anastomosis (*arrows*). Adjacent metal surgical clips do not cause significant artifact. (**d**) cMPR, patent LIMA to the distal LAD. Adjacent metal surgical clips do not cause significant artifact. (**e**) cMPR, patent SVG–PDA. Adjacent metal surgical clips do not cause significant artifact

10.3 Case 2

10.3.1 History

A 77-year-old male presented with a history of mitral regurgitation, a chronic inferior wall MI, and status post CABG ×4 in the previous 10 years. The patient complained of increasing shortness of breath. No reversible ischemia was identified on the nuclear stress test.

10.3.2 Findings

There is a sequential vein graft (VG) to OM1 and OM2. The mid-body of the graft is diseased and is subtotally occluded. More distally in the body of the graft, there is also high-grade obstruction (Fig. 10.3a–c). There is a mildly diseased SVG to the posterior descending artery, without flow-limiting stenosis (Fig. 10.3d). There is a patent LIMA graft to the first diagonal artery (Fig. 10.3e). The LAD is short and occluded. There is a large chronic transmural myocardial infarction involving the inferolateral and posterior walls of the left ventricle. There is also chronic ischemic changes of the posterior papillary muscle (Fig. 10.3e).

10.3.3 Diagnosis

The diagnosis is critically diseased sequential SVG to obtuse marginal arteries.

10.3.4 Discussion

The CTA clearly demonstrates a subtotally occluded SVG to obtuse marginal arteries. The patient underwent coronary angiography (Fig. 10.3g), with subsequent successful PCI and stenting of the subtotally occluded segment and also the more distal area of high-grade obstruction in the graft (Fig. 10.3h). The initial angiogram images demonstrated extremely poor flow beyond the subtotally occluded graft segment and nonvisualization of the first anastomosis. Following stenting, there was brisk flow through the graft with good visualization of OM1 and the distal graft anastomosis (Fig. 10.3i, j).

10.3.5 Pearls and Pitfalls

Although contrast density was not well identified on the CTA in the area of critical stenosis in the SVG, it was concluded that it was subtotally occluded since the rest of the graft opacified. When vein grafts thrombose, the most common finding on CTA and coronary angiography is a proximal short stump in the ascending aorta with no distal flow.

10.4 Case 3

10.4.1 History

A 50-year-old male presented with a history of atypical chest pain and CABG in the previous

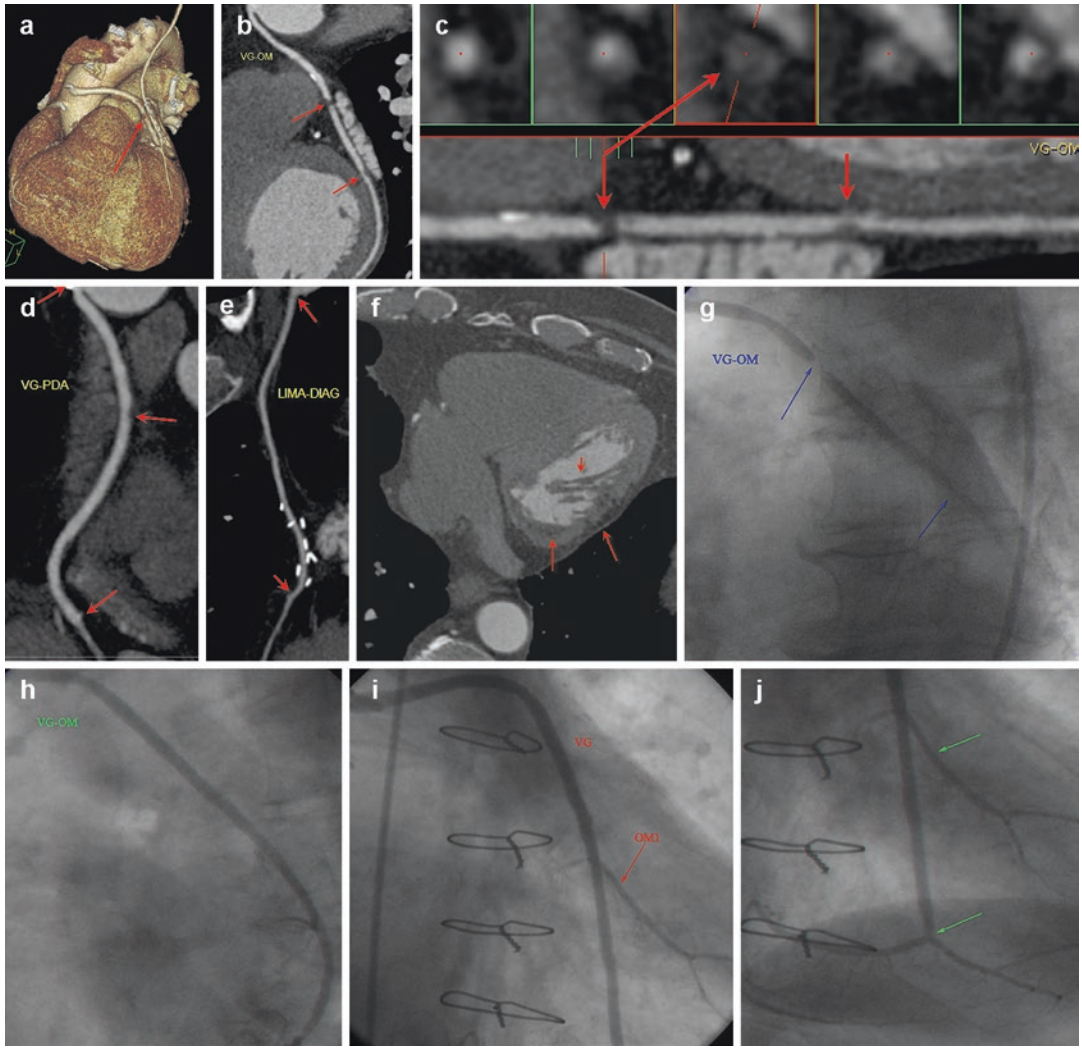

Fig. 10.3 (**a**) Volume rendering: Subtotal occlusion in the mid-body of the VG–OM (*arrow*). (**b**, **c**) cMPR, stretch cMPR: SVG–OM, mid-body graft subtotal occlusion (*proximal arrow*). High-grade obstruction in the graft more distally (*lower arrow*). Proximal to the first stenosis, there is calcification in the wall of the graft. (**d**) cMPR, VG–PDA. Minimally diseased SVG to the posterior descending artery. The proximal anastomosis has an adjacent surgical clip artifact (*upper arrow*). The mid-body of the graft has mild nonobstructive disease (*mid-arrow*). The distal anastomosis is well identified and free of disease (*lower arrow*). (**e**) cMPR, LIMA-D1. Patent internal mammary artery graft to the first diagonal artery. Ostium of the graft (*upper arrow*) and distal anastomosis (*lower arrow*). (**f**) Axial: Chronic transmural inferolateral and posterior wall MI, with involvement of the posterior papillary muscle (*arrows*), causing dysfunction of the mitral valve apparatus and mitral regurgitation. (**g**) Coronary angiogram (CA) of the SVG stenosis (*arrows*). There was sluggish flow with very diminished opacification of the graft beyond the subtotally occluded segment. (**h**) CA, shortly after stenting demonstrates marked improvement of flow in the graft. (**i**, **j**) CA, subsequent good opacification of OM1 and the distal anastomosis (*arrows*)

5 years. The nuclear medicine stress test was equivocal.

10.4.2 Findings

There is a surgical Y graft consisting of a patent LIMA graft to the distal LAD and a patent radial artery graft arising from the LIMA. The radial graft is sequential to obtuse marginal arteries (Fig. 10.4a–d). The RCA is a dominant artery with localized high-grade obstructing calcified plaque in the proximal segment (Fig. 10.4e).

10.4.3 Diagnosis

The diagnosis is patent arterial grafts, with high-grade obstruction in the proximal RCA.

10.4.4 Discussion

The case demonstrates the sole use of arterial grafts and surgically creating a Y anastomosis of a radial artery from the left internal mammary. The selection of the LIMA to the LAD is preferred since the 10-year patency rate is greater than 95%. The radial arteries are occasionally used as grafts and can be surgically grafted from the ascending aorta, a vein graft, or, as in this case, from the internal mammary artery. Some surgeons elect not to perform this type of Y procedure since it is technically challenging and may compromise the mammary artery at the time of surgery.

10.4.5 Pearls and Pitfalls

It may be difficult to identify the arterial graft anastomosis on the axial view, for which the volume rendered images can prove helpful. The LIMA should not be confused as a single sequential graft to the LAD and obtuse marginal arteries since it does not have the required length.

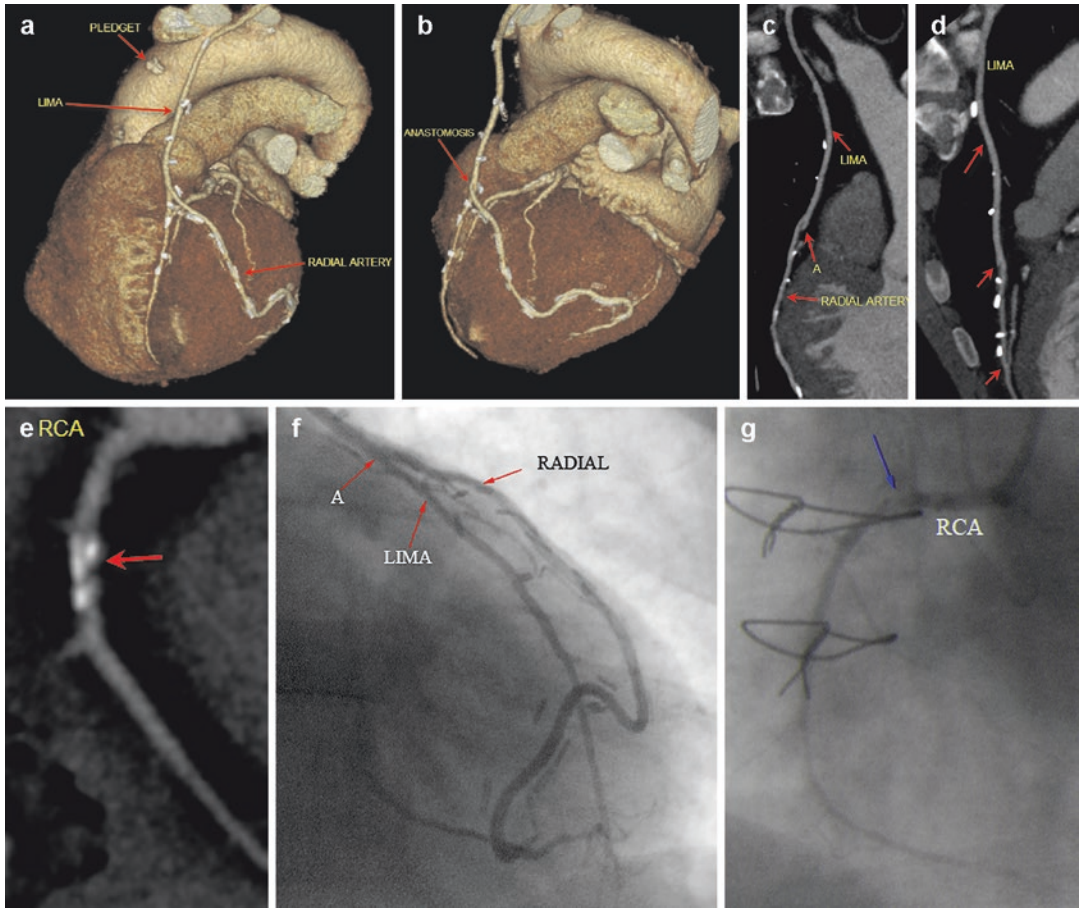

Fig. 10.4 (**a**, **b**) Volume rendering: Surgical Y graft of the left internal mammary artery (LIMA) and a radial artery. (**c**) cMPR: LIMA-radial artery anastomosis (A). (**d**) cMPR: *upper arrow*: LIMA; *middle arrow*: radial artery anastomosis; *lower arrow*: distal LIMA–LAD anastomosis. (**e**) cMPR, RCA: High-grade obstruction in the proximal RCA by calcified plaque (*arrow*). (**f**) Angiogram: Surgical arterial Y graft and anastomosis (A). (**g**) Angiogram, RCA: High-grade obstruction in the proximal RCA (*arrow*)

10.5 Case 4

10.5.1 History

A 72-year-old male presented with a history of atypical chest pain and CABG ×2 in the previous 15 years. The nuclear medicine stress test result was negative.

10.5.2 Findings

There is a patent LIMA graft to the distal LAD. There is a diffusely diseased SVG (VG–OM) to the first obtuse marginal artery. The graft has three distinct focal areas of high-grade and critical obstruction (Fig. 10.5a–d).

10.5.3 Diagnosis

The diagnosis is diffusely diseased vein graft (SVG), with high-grade obstruction.

10.5.4 Discussion

The SVG to the obtuse marginal artery has diffuse disease in the walls consisting of mixed mostly calcified plaque. In the body of the graft, there are three distinct areas of high-grade and critical obstruction. There was no obstruction in the proximal and distal anastomoses (Fig. 10.5a–c). The patient underwent coronary angiography with stenting of the stenotic segments of the graft (Fig. 10.5e, f) and with good results.

The 10-year patency rate of a vein graft is estimated at 50–60%. These develop disease in the wall similar in appearance to that in a native artery and eventually may thrombose and occlude. CTA may easily demonstrate areas of flow-limiting stenosis which are amenable to stenting.

10.5.5 Pearls and Pitfalls

The vein grafts usually (not always) have similar caliber from the proximal to distal anastomosis.

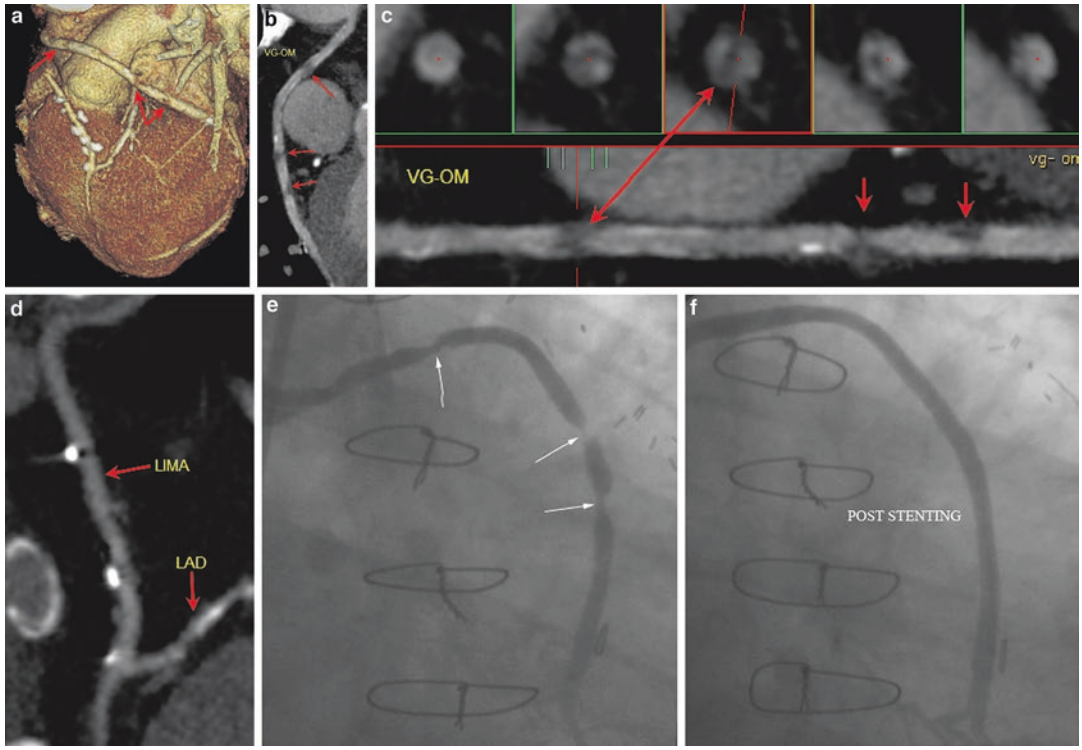

Fig. 10.5 (**a**–**c**) Volume rendering, cMPR and stretched SVG–OM: Diffusely diseased vein graft with three focal areas of high-grade obstruction (*arrows*). (**d**) cMPR: Patent LIMA–LAD. (**e**, **f**) Angiogram: Pre- and post-stenting with good results

10.6 Case 5

10.6.1 History

A 70-year-old male presented with a history of atrial fibrillation, prostate CA, shortness of breath, previous myocardial infarction (MI), and status post CABG ×3.

10.6.2 Findings

There is a patent sequential LIMA graft to D1 and the distal LAD. There is a patent but mildly atretic RIMA graft to OM1 (Fig. 10.6a–d). There is mild enlargement of the left atrium and left ventricle. There is a large chronic left ventricular transmural anteroseptal and apical myocardial

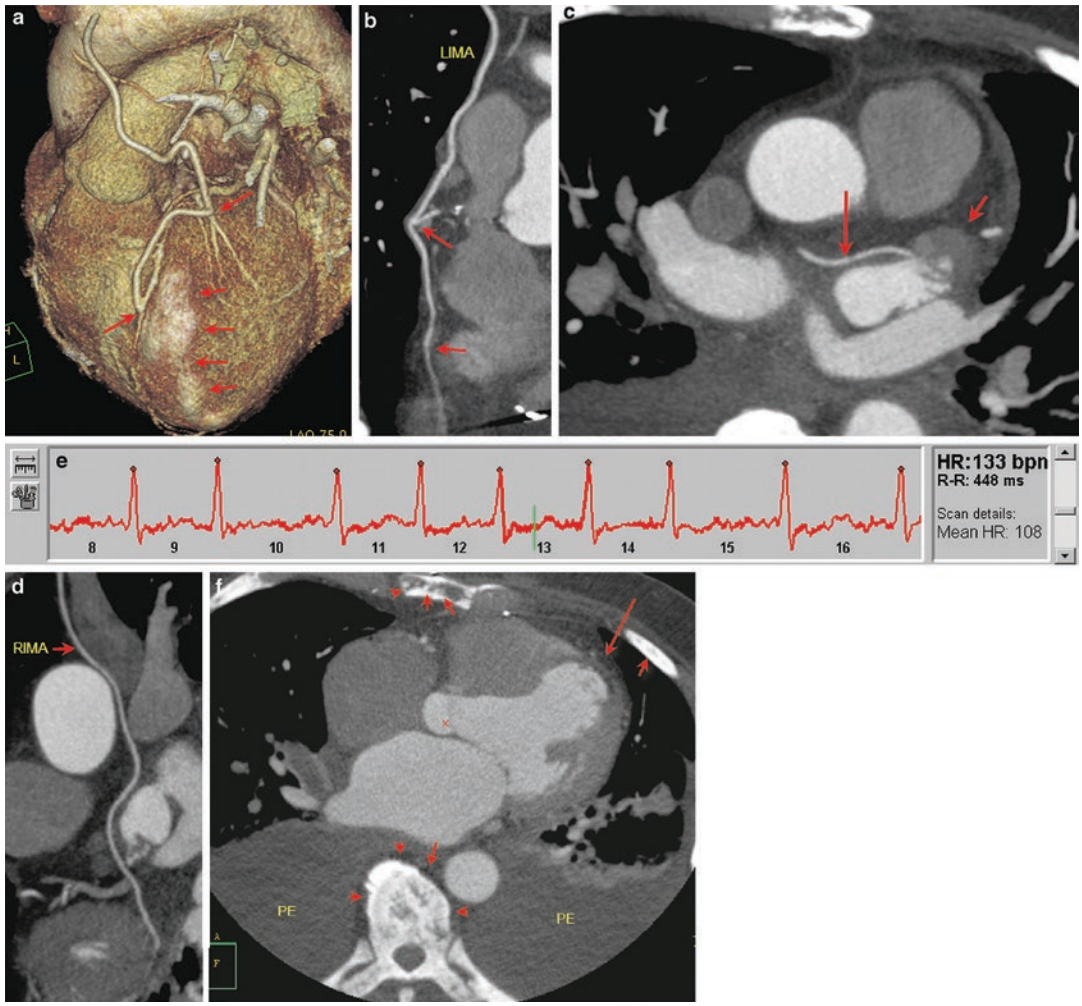

Fig. 10.6 (**a**, **b**) Volume rendering, cMPR: Patent sequential LIMA to D1 and to the distal LAD. Left ventricular anteroseptal and apical MI (*arrows*). (**c**, **d**) Axial and cMPR: Patent mildly atretic RIMA graft to OM1. The RIMA courses posterior to the aortic annulus. There is a filling defect in the left atrial appendage suggesting a thrombus (*arrows*). (**e**) Atrial fibrillation. (**f**) Anteroseptal and apical LV myocardial infarct (*long arrow*). Bilateral pleural effusions (PE). Widespread bony blastic metastatic disease from known prostate carcinoma (*short arrows*)

infarct. There is a filling defect in the left atrial appendage that is consistent with a thrombus. Additionally, there are large bilateral pleural effusions and widespread blastic metastatic disease to the thoracic spine, rib cage, and sternum (Fig. 10.6f).

10.6.3 Diagnosis

The diagnosis is patent internal mammary arterial grafts. Left ventricular failure and widespread bony metastatic disease from prostate carcinoma.

10.6.4 Discussion

LIMA jump grafts are usually placed in the territory of the LAD. The right internal mammary artery (RIMA) can be grafted to the territory of the left circumflex by passing it posterior to the aorta (i.e., through the transverse sinus), as in this case. The RIMA is placed posterior to the aorta since it is the shortest distance to the territory of the circumflex and to avoid injury to the artery during a reoperation. Since the patient had atrial fibrillation (Fig. 10.6e), the study was reconstructed in the 40% phase (end-systole) and obtaining diagnostic images and segmentation of the grafts.

10.6.5 Pearls and Pitfalls

The native position of the internal mammary arteries in the chest wall should be inspected. The absence of an IMA in the expected location is a clue that the artery may have been surgically grafted. Atrial fibrillation is not a contraindication for CTA in our laboratory since we use an adaptive multicycle reconstruction algorithm that corrects for beat-to-beat variability.

10.7 Case 6

10.7.1 History

An 84-year-old male presented with a history of atypical chest pain, LV apical ischemia on a nuclear stress perfusion scintigram, and status post CABG ×4 in the prior 2 years.

10.7.2 Findings

There is a patent LIMA graft to the distal LAD and a vein graft (SVG) to the posterior descending artery. There is a sequential SVG to D1 and OM2 that has high-grade obstruction in the proximal segment (Fig. 10.7a–e).

10.7.3 Diagnosis

The diagnosis is high-grade obstruction in the proximal segment of an SVG.

10.7.4 Discussion

Over time, vein grafts become diseased and can develop obstruction. The unusual finding in this case is that the obstruction was present within the first 2 years of the surgery. Note that the CTA demonstrates no disease in the wall of the rest of the graft, and the area of stenosis has no calcification or other disease other than the focal luminal narrowing, which may suggest an operative complication. When a vein is harvested for grafting, it is important to appropriately handle the graft so as not to cause injury that could later develop stenosis. Pressure injuries, poorly ligated side branches, and kinking or twisting of the vein may cause stenosis. The patient underwent coronary angiography, which confirmed the findings on CTA and was subsequently stented with excellent results (Fig. 10.7f–h).

10.7.5 Pearls and Pitfalls

A perioperative complication should be considered when a vein graft has focal stenosis without disease in the wall, particularly in the first 5 years of revascularization.

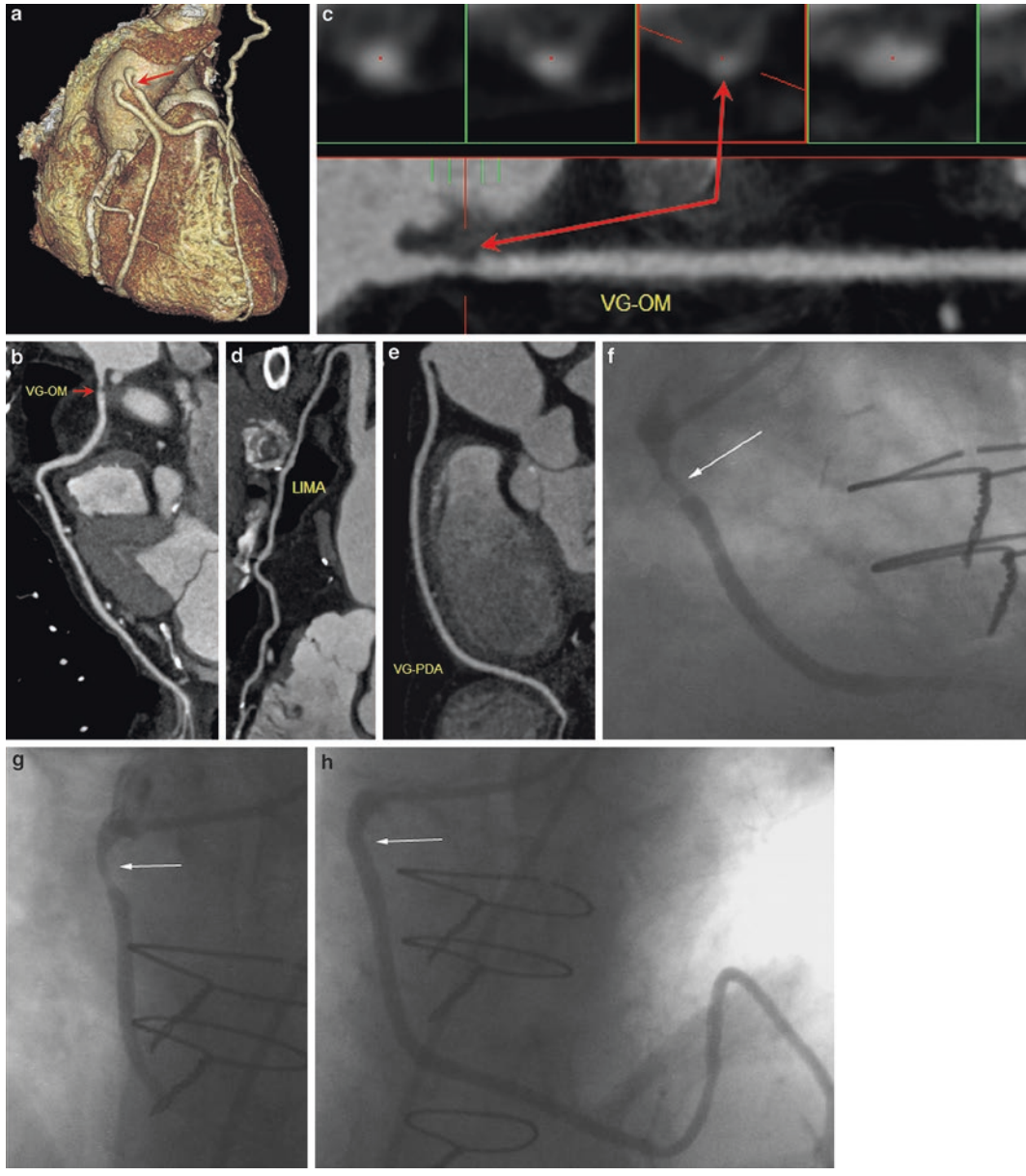

Fig. 10.7 (**a**–**c**) Volume rendering, cMPR, stretched view: High-grade stenosis in the proximal segment of an SVG (*arrows*). Note that the rest of the graft has no disease. (**d**, **e**) cMPR: Patent LIMA graft to distal LAD and vein graft to the PDA. There is mild artifact in the body and distal anastomosis of the mammary artery. (**f**, **g**) Coronary angiogram: Confirms the high-grade stenosis in the proximal segment of the SVG (*arrows*). (**h**) Coronary angiogram: Excellent results following stenting of the graft (*arrow*)

10.8 Case 7

10.8.1 History

A 59-year-old male presented with a history of chest pain and status post CABG ×2 in the prior 10 years and subsequent percutaneous coronary intervention (PCI) of a saphenous vein graft (SVG).

10.8.2 Findings

There is a patent LIMA graft to the distal LAD (not shown) and a proximally occluded SVG to the second diagonal artery, which was previously stented (Fig. 10.8a, b).

10.8.3 Diagnosis

The diagnosis is occluded SVG to a diagonal artery.

10.8.4 Discussion

The CTA demonstrates a proximally occluded vein graft from the ascending aorta. There is contrast opacification of only the proximal anastomosis, which is referred to as a *stump* or *hood*. The rest of the graft is thrombosed, which has low density throughout and has the appearance of a *phantom graft* (Fig. 10.8b). Other times, the occluded segments of the graft become atretic and are not visualized.

Diseased vein grafts are commonly intervened with balloon angioplasty and placement of stents. The initial intervention success is similar among native coronary arteries, internal mammary arteries, and SVGs. However, it has been reported that the late patency rate after interventions on SVGs is significantly lower than that for native coronary arteries.

10.8.5 Pearls and Pitfalls

It is commonly difficult to ascertain the targeted native coronary artery of an occluded graft. Careful evaluation of the coronary anatomy and other grafts present as well as location of surgical clips may provide sufficient clues to determine where the graft was previously anastomosed.

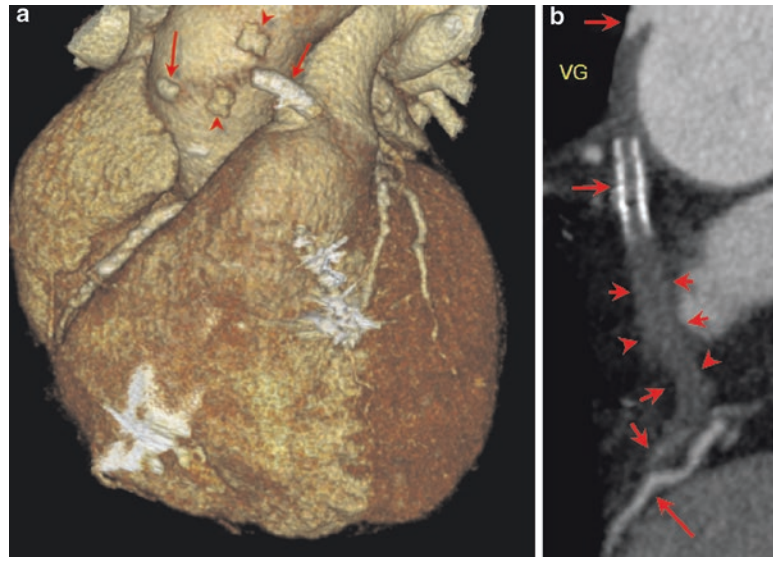

Fig. 10.8 (**a**) Volume rendering: Proximal SVG stump and occluded stent in the graft (*long arrows*). Surgical cannulation sites repair (*short arrows*). (**b**) cMPR: SVG–D2: Proximally occluded SVG stump (*proximal arrow*). Occluded stent in the SVG (*mid-arrow*). Phantom graft (*short arrows*). Native diagonal coronary artery (*lower arrow*)

10.9 Case 8

10.9.1 History

A 70-year-old female presented with a history of atypical chest pain and status post CABG ×5 in the previous 8 years and status post PCI of a graft in the previous 2 years.

10.9.2 Findings

There is a patent sequential vein graft (SVG) to the PDA and PLV. There is a patent stent in the mid-body of the graft with a surrounding mostly thrombosed hematoma. There is also a small pseudoaneurysm (Fig. 10.9a–d).

10.9.3 Diagnosis

The diagnosis is patent sequential SVG to the PDA and PLV, which contains a patent stent that has an adjacent small pseudoaneurysm.

10.9.4 Discussion

The study demonstrates a mostly thrombosed hematoma surrounding the mid-body of the SVG. There is a small and subtle pseudoaneurysm that was previously undiagnosed. This finding was not considered to be clinically significant, and it was decided to perform a follow-up study. Pseudoaneurysms can occur as a complication of coronary intervention secondary to balloon angioplasty or wire perforation.

10.9.5 Pearls and Pitfalls

It is important to evaluate not only the lumen and wall of the graft but also the adjacent soft tissues.

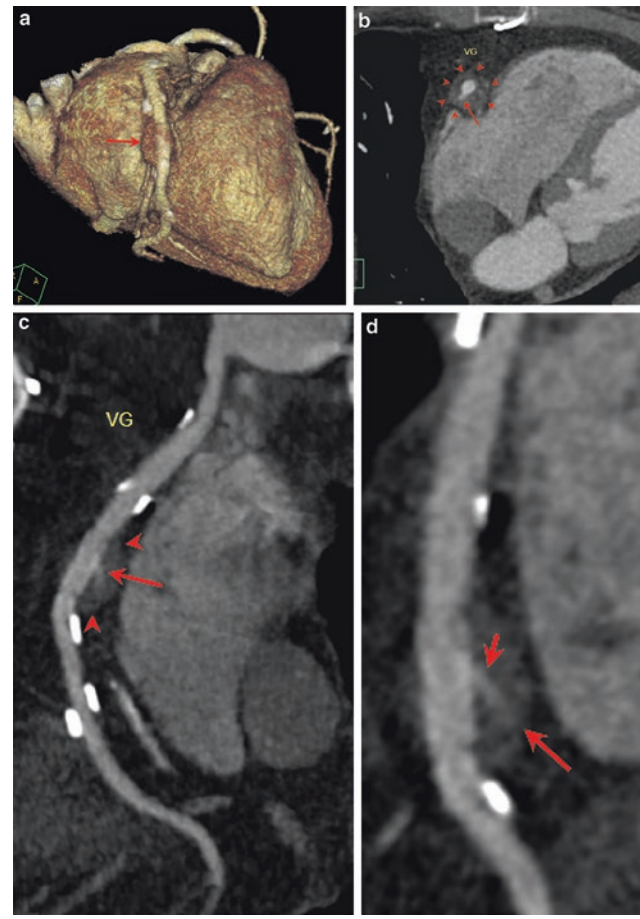

Fig. 10.9 (**a**) Volume rendering: SVG 3D volume rendered image demonstrates a hematoma surrounding the mid-body of the graft (*arrow*). (**b**–**d**) Axial and cMPR: SVG: Extra-luminal chronic hematoma surrounding a stent in the mid-body of the graft (*short arrows*) with a small pseudoaneurysm (*long arrows*)

10.10 Case 9

10.10.1 History

A 71-year-old male presented with a history of recurrent right pleural effusion and status post CABG ×4 in the previous 12 months, with a stormy postoperative course.

10.10.2 Findings

There is a retrosternal collection that has contrast density. There is a right pleural effusion with compressive atelectasis of the right lower lobe (Fig. 10.10a). There is contrast leaking into the anterior mediastinal collection (Fig. 10.10b, c) from a patent sequential surgical Y saphenous vein graft (SVG) to a diagonal and an obtuse marginal artery. The other SVG limb to the RCA is occluded. There is a patent LIMA graft to the distal LAD (not shown).

10.10.3 Diagnosis

The diagnosis is pseudoaneurysm from a leak at a surgical Y vein graft anastomosis.

10.10.4 Discussion

The anterior mediastinal collection has contrast density thus indicating a pseudoaneurysm. Figure 10.10b, c demonstrates a tiny leak from the patent SVG limb that has a distal anastomosis to an obtuse marginal artery. It is uncertain whether the pseudoaneurysm is causing the recurrent right pleural effusion. Without a detailed surgical history, it would not have been possible to determine that there was a leak at a surgical Y anastomosis and with an occluded SVG limb to the RCA. It may only have been suspected since there was a chronic total occlusion of the RCA without visualization of a graft or occluded stump in the aorta.

10.10.5 Pearls and Pitfalls

The most common cause of a pseudoaneurysm originating from a graft is technical or breakdown of the suture anastomosis.

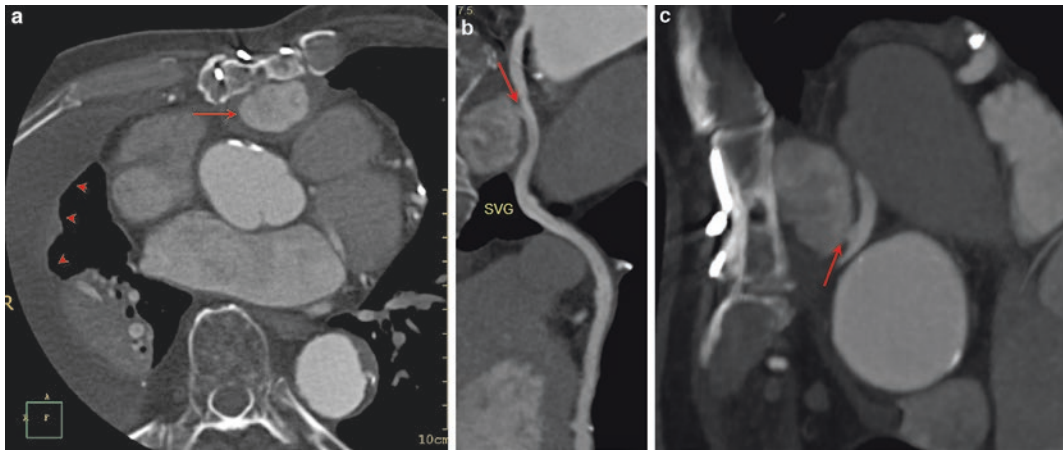

Fig. 10.10 (**a**) Axial. Hyperdense collection containing contrast in the anterior mediastinum representing a pseudoaneurysm (*long arrow*). Right pleural effusion with right lower lobe compressive atelectasis (*short arrows*). (**b**, **c**) cMPR and oblique sagittal MPR: SVG: Contrast leaking from the graft into the pseudoaneurysm is demonstrated (*arrows*)

10.11 Case 10

10.11.1 History

A 71-year-old male presented with a history of new onset of exertional chest pain and stenting of a saphenous vein graft (SVG) in the previous 3 months. His status was post CABG ×4 in the previous 15 years.

10.11.2 Findings

There is a stent with high-grade restenosis in the proximal segment of an SVG to the second obtuse marginal artery. The graft has diffuse disease and also high-grade obstruction just beyond the stent and in the distal anastomosis (Fig. 10.11a–c). There was a patent sequential LIMA graft to the distal LAD and an occluded SVG to the RCA (not shown).

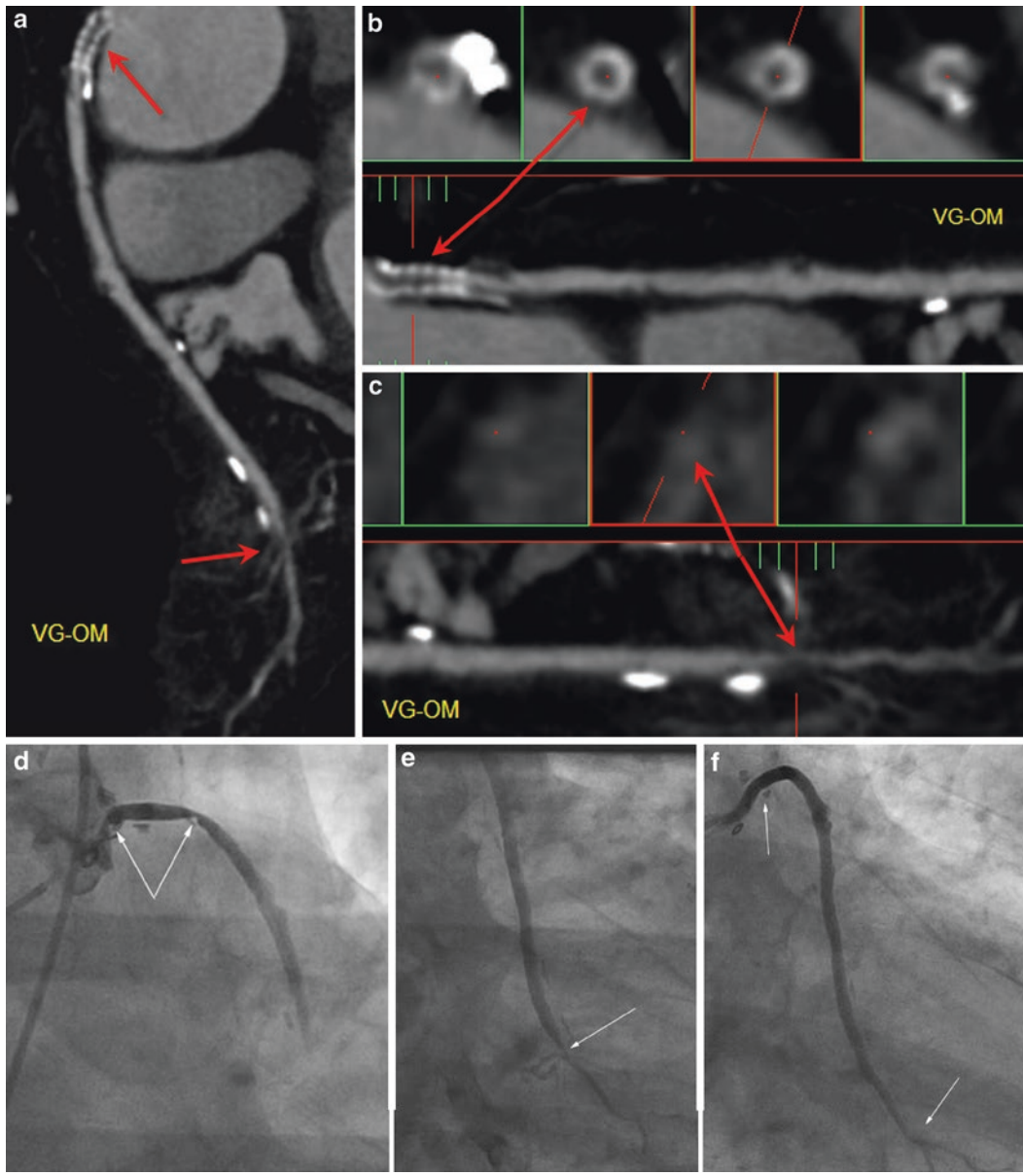

Fig. 10.11 (**a**–**c**) cMPR and stretched, SVG. High-grade restenosis in a stent in the proximal SVG (*upper arrow*) and also high-grade obstruction just distal to the stent. There is a high-grade obstruction in the distal anastomosis (*lower arrow*). (**d**, **e**) Coronary angiogram. Proximal and distal SVG high-grade obstruction (*arrows*). (**f**) Coronary angiogram. Successful intervention

10.11.3 Diagnosis

The diagnosis is diffusely diseased SVG containing a proximal stent with restenosis and also distal anastomosis high-grade obstruction.

10.11.4 Discussion

The patient underwent coronary angiography with successful re-stenting of the proximal segment of the graft and balloon angioplasty of the distal anastomosis (Fig. 10.11d–f). The chest pain resolved.

10.11.5 Pearls and Pitfalls

Although there was no visible contrast density in the lumen of the stent on the CTA, the visualization of the rest of the graft indicates that the SVG was not occluded.

10.12 Case 11

10.12.1 History

An 81-year-old female presented with a history of atypical chest pain and status post CABG ×2 and LV aneurysmectomy in the previous 12 months.

10.12.2 Findings

There are surgical SVG Y grafts from the ascending aorta to the LAD and to the territory of the left circumflex. The proximal segment of the graft is occluded. The rest of the grafts have no disease and retrograde flow (Fig. 10.12a–c).

10.12.3 Diagnosis

The diagnosis is proximal occlusion of an SVG Y grafts and status post LV aneurysmectomy.

10.12.4 Discussion

The CTA clearly demonstrates an occlusion in the proximal segment of the Y graft from the ascending aorta, which has a stump in the proximal anastomosis (Fig. 10.12a). Note that otherwise the grafts have no disease and would suggest that the proximal occlusion is likely related to a surgical complication (Fig. 10.12d–e). Coronary angiography was not performed since the patient was stable. Although the direction of flow cannot be determined with CTA, since there was nonobstructing calcified plaque in the left circumflex (Fig. 10.12d) and severe obstruction of the proximal LAD (Fig. 10.12e), it was presumed that the retrograde flow was likely from the left circumflex limb to the LAD. Note the postsurgical aneurysmectomy changes in the left ventricle. When a ventricular aneurysm is resected, felt strips (large pledgets) are commonly used to suture the myocardium.

10.12.5 Pearls and Pitfalls

Grafts that are anastomosed to the aorta cannot be presumed to be patent unless they are visualized in their entirety.

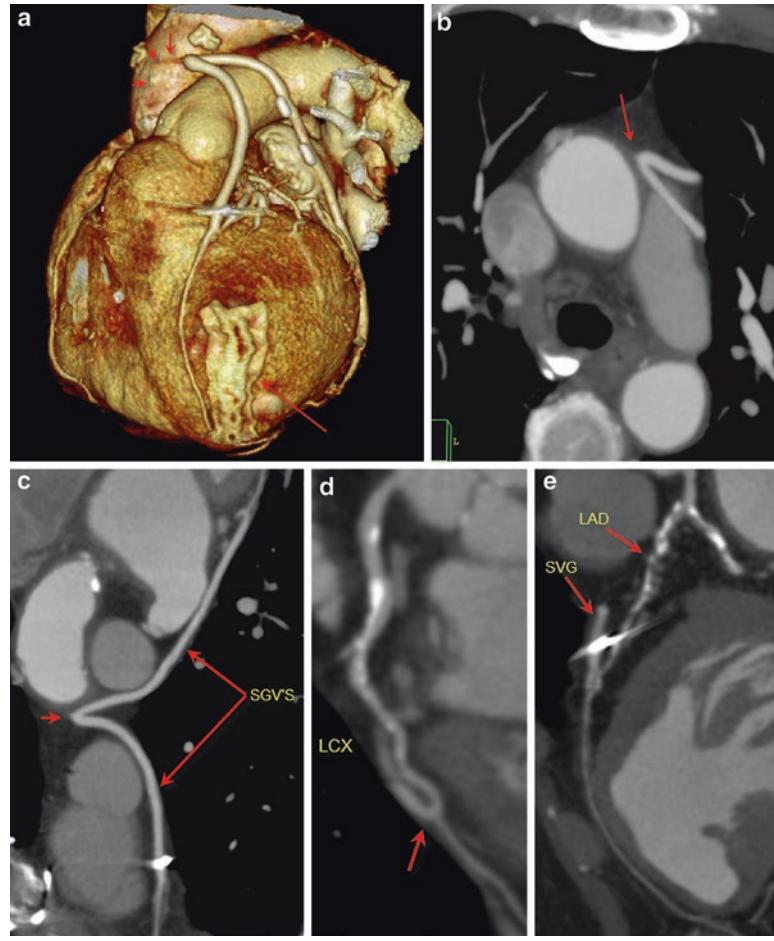

Fig. 10.12 (**a**) Volume rendering. *Upper arrows* demonstrating proximal occlusion of a surgical SVG Y graft and a stump in the ascending aorta. Postsurgical changes from an aneurysmectomy (*lower arrow*). (**b**) Axial. Proximal graft occlusion (*arrow*). (**c**) cMPR. Proximal occlusion (*short arrow*). Otherwise, the limbs of the grafts are open (*double arrows*). The limb in the upper picture is to the territory of the left circumflex. The limb in the lower picture is to the LAD. (**d**) cMPR LCX. Scattered nonobstructive calcified plaque in the left circumflex. Graft anastomosis (*arrow*). (**e**) cMPR LAD. Severe obstruction in the proximal LAD and SVG anastomosis (*arrows*)

10.13 Case 12

10.13.1 History

A 65-year-old male presented with a history of multiple prior myocardial infarctions over many years. His status post CABG in the previous 30 years and repeat CABG ×1 in the previous 3 years.

10.13.2 Findings

There is a diffusely diseased but otherwise patent saphenous vein graft (SVG) to the LAD. There is a patent SVG to the territory of the left circumflex that was proximally grafted to the descending aorta. There are multiple chronic left ventricular myocardial infarcts and a thrombus in the left ventricle apex (Fig. 10.13a–e).

10.13.3 Diagnosis

The diagnosis is patent SVG proximally grafted to the descending aorta.

10.13.4 Discussion

Saphenous veins are most commonly grafted to the ascending aorta. Rarely, as in this case, are these proximally grafted to the descending aorta (Fig. 10.13b–d). The most common surgical approach to anastomosing a graft to the descending aorta is via a left thoracotomy approach. This surgical technique is occasionally used in repeat cardiac surgical revascularization to the left circumflex territory without having to perform another median sternotomy. The patient had extensive previous myocardial infarcts involving the territory of the LAD and left circumflex, which was dominant. There was also a small thrombus in the LV apex (Fig. 10.13e).

10.13.5 Pearls and Pitfalls

Since a full surgical history at the time of interpretation of a CTA might not always be available, it is therefore important to examine carefully the native coronary anatomy and the entire thoracic aorta in order not to exclude reporting additional grafts.

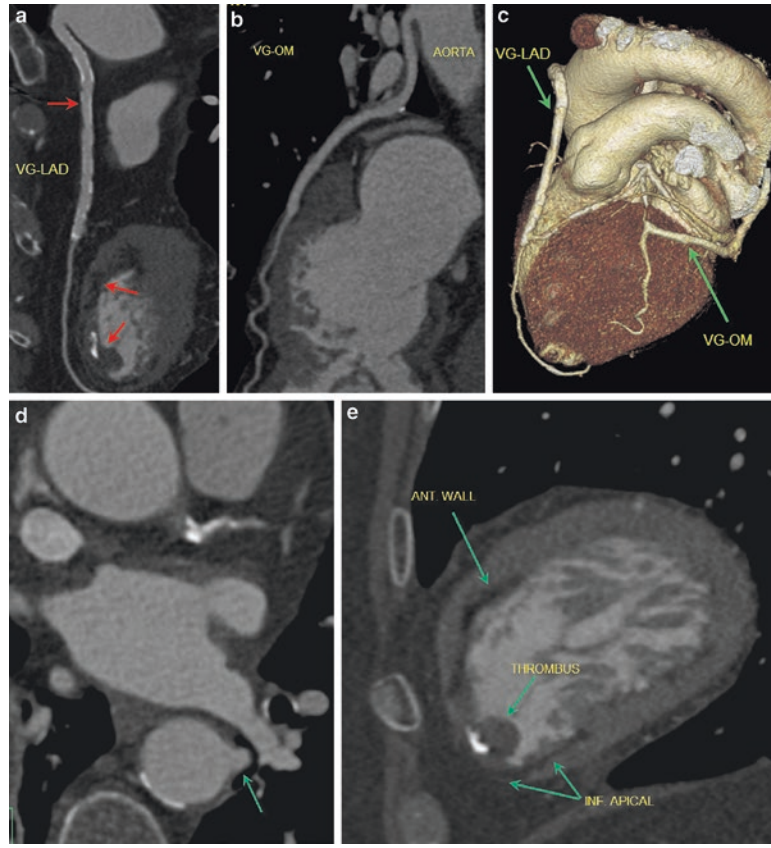

Fig. 10.13 (**a**) cMPR SVG. SVG to the LAD has diffuse disease but is patent (*upper arrow*). Extensive anterior and apical chronic myocardial infarct (*middle arrow*). Thrombus in the LV apex (*lower arrow*). (**b**, **c**) cMPR and volume rendering. SVG proximally grafted to the descending aorta and distally to an obtuse marginal artery. (**d**) Axial. Proximal anastomosis of the SVG from the descending aorta (*arrow*). (**e**) Sagittal MPR LV. Extensive chronic myocardial infarcts and thrombus in the left ventricle apex. (Case courtesy of Dr. William Bugni, Tampa, FL)

10.14 Case 13

10.14.1 History

A 74-year-old male presented with a history of shortness of breath and chronic ischemic cardiomyopathy and status post CABG ×4 in the previous 10 years.

10.14.2 Findings

Coronary circulation is right dominant. There is a patent LIMA to the distal LAD and a saphenous vein graft (SVG) to D2. There is also a patent SVG to the PDA and with distal runoff chronic total occlusion. There is a stump in the ascending aorta from an occluded SVG to the territory of the left circumflex (Fig. 10.14a–d).

10.14.3 Diagnosis

There are three patent grafts and one occluded graft. The SVG to the PDA has chronic total occlusion of the distal runoff.

10.14.4 Discussion

In the evaluation of grafts, it is important to evaluate and comment on the proximal anastomosis, body of the graft, distal anastomosis, and runoff. Although the SVG to the PDA is patent, the targeted artery is occluded just beyond the anastomosis, with retrograde flow into the proximal PDA (Fig. 10.14b–d).

10.14.5 Pearls and Pitfalls

The grafting of coronary targets that are diseased beyond the anastomosis has a significant worse patency rate than nondiseased arteries.

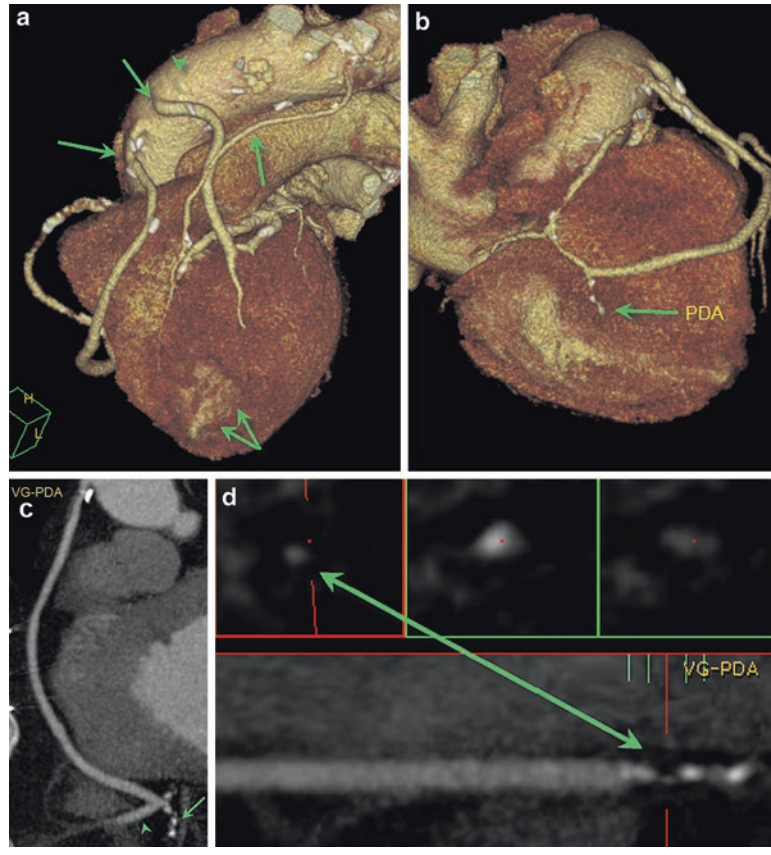

Fig. 10.14 (**a**) Volume rendering. Multiple patent grafts (*long arrows*). Stump in the ascending aorta from an occluded SVG in the left circumflex (*short arrow*). Chronic left ventricular infarct (*double arrow*). (**b**–**d**) Volume rendering, cMPR, stretched. Occluded PDA beyond the distal anastomosis (*arrows*). There is retrograde flow into the proximal PDA (**c**, *short arrow*)

10.15 Case 14

10.15.1 History

An 86-year-old male presented with a history of an inferior wall fixed defect on a nuclear perfusion scintigram and status post two times CABG in the previous 30 and 12 years.

10.15.2 Findings

There is a patent LIMA to the distal LAD and a patent RIMA to the distal RCA. There is a patent sequential right gastroepiploic artery conduit (GEA) to circumflex branches. There were chronic occluded SVGs in the ascending aorta from the first CABG (Fig. 10.15a–e).

10.15.3 Diagnosis

Repeat CABG demonstrates patent internal mammary arteries and a GEA.

10.15.4 Discussion

The internal mammary arteries are commonly used for direct coronary revascularization; it may not be possible to reach the posterior surface of the heart with the internal mammary as either a pedicle or a free graft. The right GEA, which was first implanted as a direct bypass graft in 1974 by Edwards, is occasionally used as a graft to the distal right coronary artery, the posterior descending artery and as in this case, to the distal circumflex branches [1, 2]. This is a technically difficult operation to perform that has not become a popular bypass graft but has a high likelihood of good long-term patency when used in the proper situation, and in some patients represents a significant advantage over vein grafts. Harvesting of the GEA necessitates an abdominal extension of the sternal incision, which may cause additional postoperative pain and may be a potential site for herniation and/or adhesion formation. Additional possible complications include postoperative ileus, pancreatitis, and intra-abdominal hemorrhage. In addition, there was an old inferior wall MI (not shown) that accounted for the abnormality reported on the nuclear study.

10.15.5 Pearls and Pitfalls

It is important to look below the diaphragm in order to confirm that a GEA was harvested.

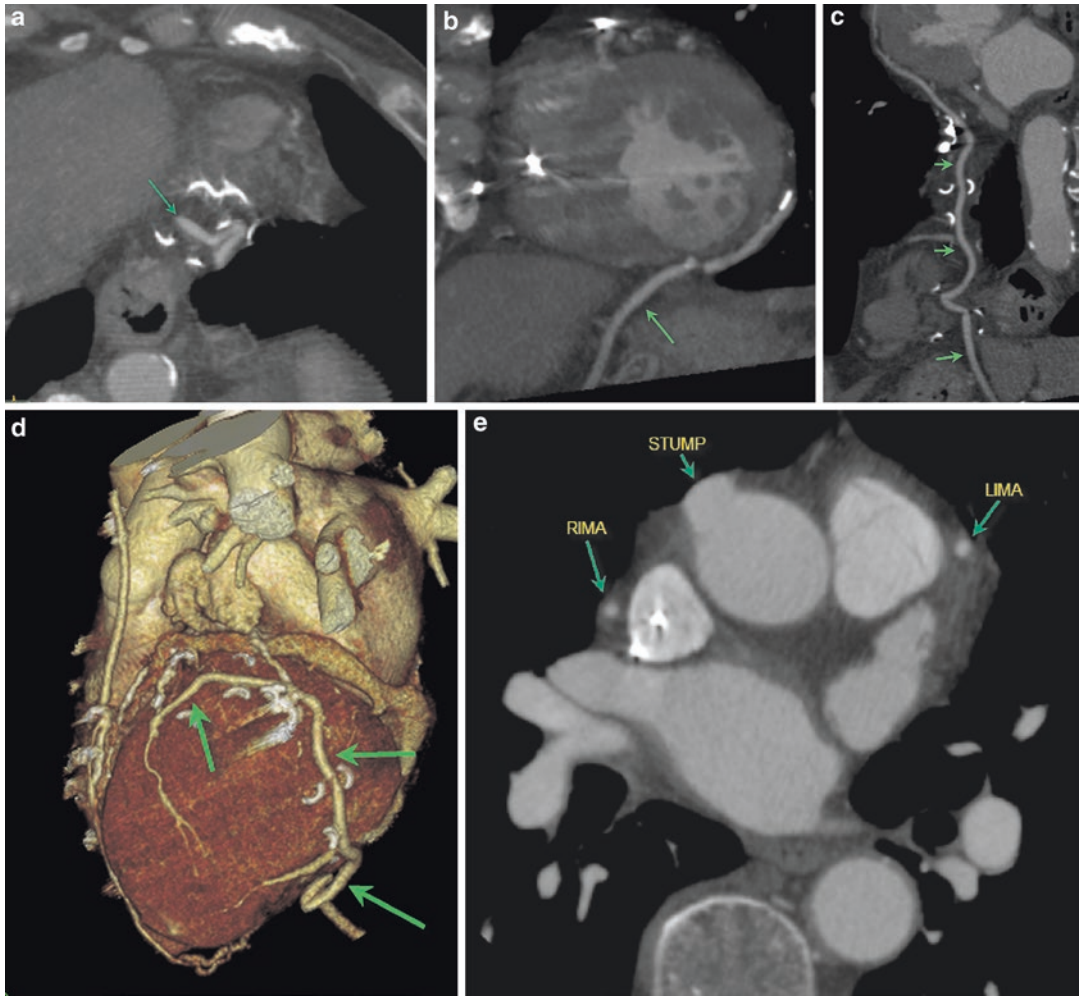

Fig. 10.15 (**a**–**d**) Axial, oblique maximum intensity projection, cMPR, and volume rendering. Sequential GEA to circumflex branches (*arrows*). (**e**) Axial. IMAs and one of the stumps in the ascending aorta from an occluded SVG from previous revascularization (*arrows*)

10.16 Case 15

10.16.1 History

An 84-year-old asymptomatic male presented with a history of an ascending aortic aneurysm and CABG in the previous 15 years.

10.16.2 Findings

There is an ascending aortic aneurysm measuring maximally 6.8 cm, containing a localized dissection in the right lateral wall. There is a patent saphenous vein graft (SVG) with a limb to the distal and sequential to circumflex branches. There is occluded LIMA to the first diagonal and also an occluded SVG to the distal RCA. In addition, there was mild mediastinal adenopathy and a new 4.5-cm peripheral spiculated soft tissue mass in the right upper lobe (Fig. 10.16a–d).

10.16.3 Diagnosis

The diagnosis was large aneurysm of the ascending aorta with a localized dissection; occluded SVG to the distal RCA and LIMA to the first diagonal; patent vein grafts to the LAD and circumflex branches; and new onset of mild mediastinal adenopathy and a peripheral mass in the right upper lobe, which was biopsy-proven sarcoidosis.

10.16.4 Discussion

Aortic dissection can be caused by cardiac surgery, including aortic and mitral valve replacements, CABG surgery, or percutaneous catheter placement (e.g., during cardiac catheterization and percutaneous coronary intervention). Aortic dissection occurs when the layers are split in the process of cannulation or aortotomy.

Since the proximal anastomosis of the SVG to the RCA could not be identified, it is reasonable to assume that the dissection in this case may be secondary to the previous aortotomy site. A CT scan of the chest in the previous 12 months did not demonstrate any abnormality in the area of the current mass or adenopathy. Although the mass had a CT appearance consistent with a primary carcinoma, it would be most unusual for a neoplasm to have grown from undetectable to 4.5 cm in 1 year. The CT-guided or biopsy confirmed the diagnosis of sarcoidosis.

10.16.5 Pearls and Pitfalls

It is important to inspect an ascending aortic aneurysm for the presence of dissection and also the entire field-of-view for additional extracardiac abnormalities.

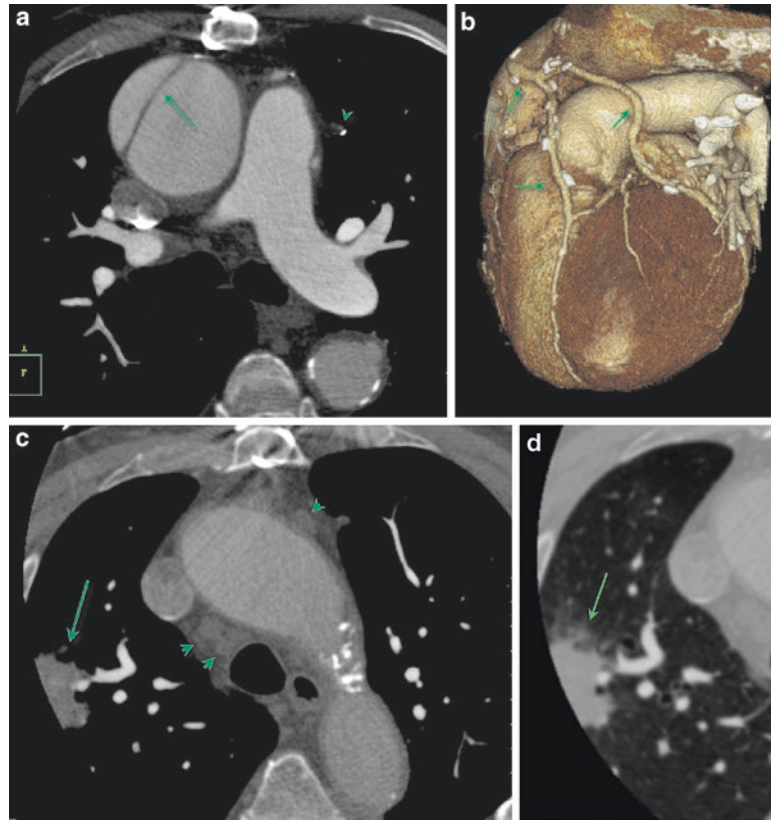

Fig. 10.16 (**a**) Axial. Localized dissection in the right lateral wall of an ascending aortic aneurysm (*long arrow*). Occluded LIMA graft (*short arrow*). (**b**) Volume rendering. Patent SVG with two surgical limbs to the LAD and circumflex branches (*arrows*). (**c**, **d**) Sarcoidosis. Axial mediastinal and lung windows. Peripheral soft tissue mass in the right upper lobe (*long arrow*). Mild mediastinal adenopathy (*short arrows*)

10.17 Case 16

10.17.1 History

A 75-year-old male presented with a history of chronic ischemic heart disease and three prior coronary revascularizations, first in the 1960s and the last in the previous 18 years.

10.17.2 Findings

A large low-density ovoid mass is seen anterolaterally in the mediastinum with adjacent metal artifact that extends into a stump in the ascending aorta (Fig. 10.17a). There is a dissection in the pulmonary artery trunk (Fig. 10.17b, c). There are three stumps in the ascending aorta from old occluded grafts (Fig. 10.17d). There are chronic total occlusions of the LAD, left circumflex, and RCA (not shown). There is a sequential LIMA graft to the distal LAD, which has extensive surgical clip artifact. The distal anastomosis contains a stent that could not be adequately evaluated (Fig. 10.17e). There is a saphenous vein graft with a proximal anastomosis to the descending aorta and distally to circumflex branches (Fig. 10.17f, g). The graft appears to be patent but could not be adequately assessed due to surgical clip artifacts. The RIMA is atretic and distally has been surgically tunneled into the free wall of the right ventricle (Fig. 10.17h–k). There are extensive chronic infarcts in the left ventricle (Fig. 10.17l) and COPD (Fig. 10.17m).

10.17.3 Diagnosis

1. Status post embolization with coils of an SVG pseudoaneurysm
2. Chronic dissection of the main pulmonary artery trunk, with COPD and chronic pulmonary arterial hypertension
3. Multiple occluded grafts in the ascending aorta
4. Sequential LIMA graft to the distal LAD and SVG from the ascending aorta to circumflex branches
5. Previous Vineberg's procedure
6. Multiple chronic infarcts in the left ventricle

10.17.4 Discussion

This complicated case demonstrates findings related to multiple prior cardiac surgical revascularizations and intervention over a period of four decades. Due to the length of time, the surgical history was incomplete but the findings on the CTA are compelling and worthwhile to review.

The patient had unstable angina and underwent a Vineberg's procedure in the 1960s. Arthur M. Vineberg (Canadian thoracic surgeon) developed the procedure of direct implantation of the internal mammary artery into the ventricles for relief of myocardial ischemia. Although the procedure had merit, it never received broad acceptance from the medical and surgical communities. The procedure consisted of dissecting the IMA free from the chest wall and tunneled into the superficial myocardium. He founded this procedure on the belief that the myocardium contains relatively large venous sinusoids that could absorb the flow from the bleeding mammary vessels and consequently improve myocardial perfusion. Thousands of patients underwent this procedure and although it had mixed results, it was considered at that time to be the best available alternative and benefited many patients. In this procedure, primarily the left internal mammary was tunneled into the left ventricular wall. RIMAs to the right free ventricular wall were also performed. It was unknown whether in this case the LIMA was previously implanted and then removed from the left ventricle and reused as a sequential graft.

The patient continued to have unstable angina and was subsequently reoperated with grafting of multiple saphenous vein conduits. One of the grafts developed a pseudoaneurysm that was subsequently embolized successfully with percutaneous intervention and placement of coils. Remarkably, the pulmonary artery dissection was known to the patient for more than 20 years. Pulmonary arterial dissection is usually a lethal complication of congenital (e.g., Eisenmenger's syndrome) or acquired chronic pulmonary hypertension. The condition usually manifests as cardiogenic shock, sudden death, and is typically diagnosed postmortem. There are isolated reported cases of patient's surviving pulmonary artery dissection, as in this case.

Pseudoaneurysms occurring as a complication from surgical revascularization are well documented in the literature and most commonly occur as a result of suture breakdown in the area of anastomosis. Prior to the availability of covered stents, percutaneous embolization with coils or a reoperation was usually necessary.

10.17.5 Pearls and Pitfalls

Complex anatomy requires a patient well-organized step-by-step approach to completely and accurately assess the study. And brace yourself for having to spend a long time in front of the workstation.

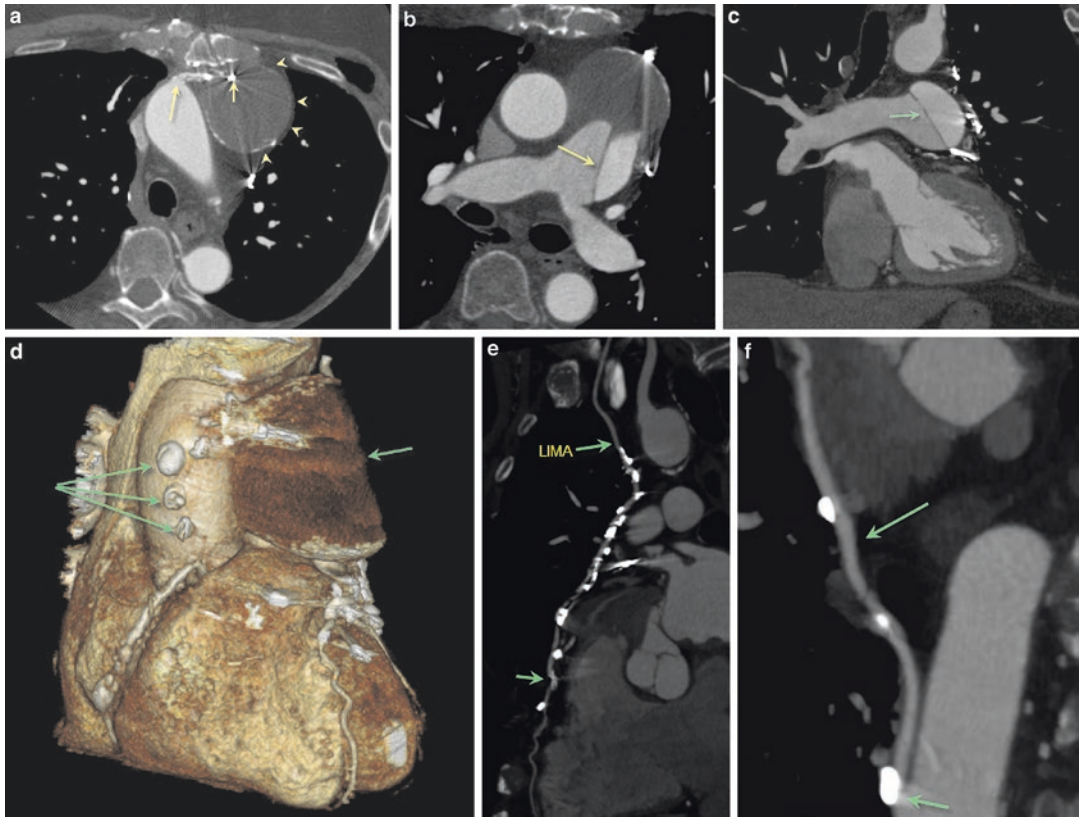

Fig. 10.17 (**a**) Axial and coronal: Proximal occlusion of an SVG (*long arrow*). Embolization coil (*short arrow*). Thrombosed pseudoaneurysm (*arrow heads*). (**b**, **c**) Axial and coronal. Chronic main pulmonary artery dissection (*arrows*). (**d**) Volume rendering. Stumps from occluded grafts in the ascending aorta (*triple arrow*). Thrombosed pseudoaneurysm (*single arrow*). (**e**) cMPR. LIMA–LAD. Extensive surgical clip artifact and distal stent not adequately visualized (*lower arrow*). (**f**, **g**) SFVG from the ascending aorta to circumflex branches (*arrows*). (**h**–**k**) Axial and cMPR. Atretic RIMA tunneled into the free wall of the right ventricle: Vineberg's procedure in the 1960s (*arrows*). (**l**) Sagittal oblique. Multiple chronic LV infarcts (*arrows*). (**m**) Axial lung window. Advanced COPD

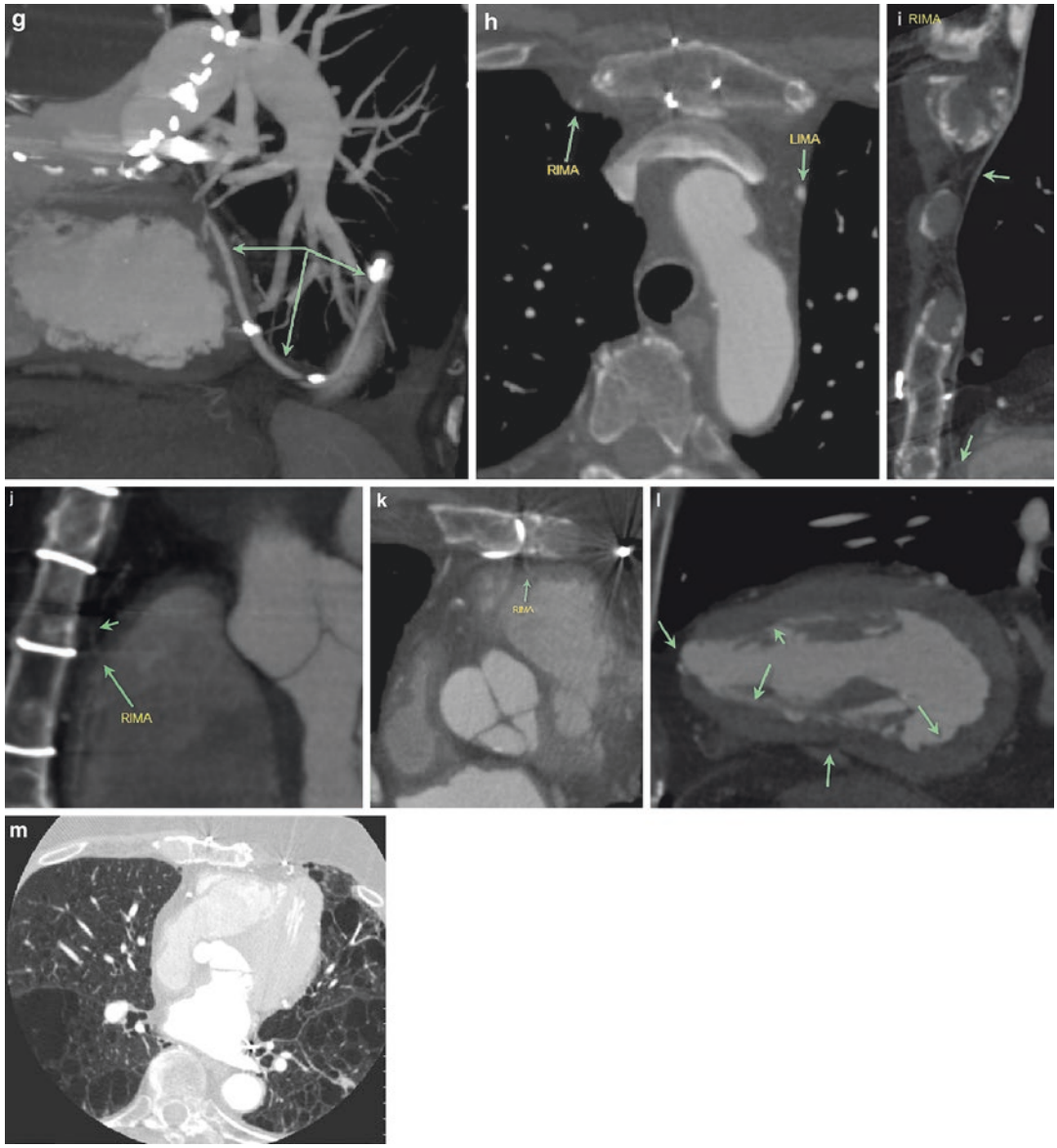

Fig. 10.17 (continued)

10.18 Case 17

10.18.1 History

A 78-year-old female presented with a history of an inconclusive nuclear perfusion scintigram and CABG in the previous 15 years.

10.18.2 Findings

There is dextrocardia with situs inversus (Fig. 10.18a). There is a patent RIMA graft to the LAD and a saphenous vein graft (SVG) to the ramus intermedius. The circumflex is small caliber and was not grafted. There is an occluded SVG to the distal RCA (Fig. 10.18b–d). The native RCA is dominant and has scattered calcified nonobstructing plaques (Fig. 10.18e).

10.18.3 Diagnosis

The diagnosis is situs inversus with dextrocardia. The status was post CABG, with a patent RIMA to the LAD and SVG to the ramus intermedius artery. There is an occluded SVG to the RCA likely from competitive flow from a patent native RCA.

10.18.4 Discussion

Situs describes the position of the cardiac atria and viscera. The prevalence of situs inversus is estimated at 0.01% of the population. Situs solitus is the normal position, and situs inversus is the mirror image of situs solitus. Cardiac situs is determined by the atrial location. In situs inversus, the morphologic right atrium is on the left, and the morphologic left atrium is on the right. The normal pulmonary anatomy is also reversed so that the left lung has three lobes and the right lung has two lobes. In addition, the liver and gallbladder are located on the left, whereas the spleen and stomach are located on the right. The remaining internal structures are also a mirror image of the normal. Situs inversus totalis is associated 20% of the time with primary ciliary dyskinesia and known as Kartagener's syndrome (not in this case). Kartagener's syndrome consists of the triad: bronchiectasis, sinusitis, and situs inversus.

Because of the dextrocardia, the RIMA was used, instead of the LIMA, to bypass the left anterior descending coronary artery. Typically, after a coronary artery is grafted, there is accelerated development of disease proximal to the anastomosis in the native coronary. If the grafted native artery remains patent, competitive flow may cause the graft to fail and occlude early.

10.18.5 Pearls and Pitfalls

The recognition of situs inversus is important for preventing surgical mishaps that result from the failure to recognize reversed anatomy. Competitive flow between a native coronary artery and a graft may cause an early occlusion of the graft.

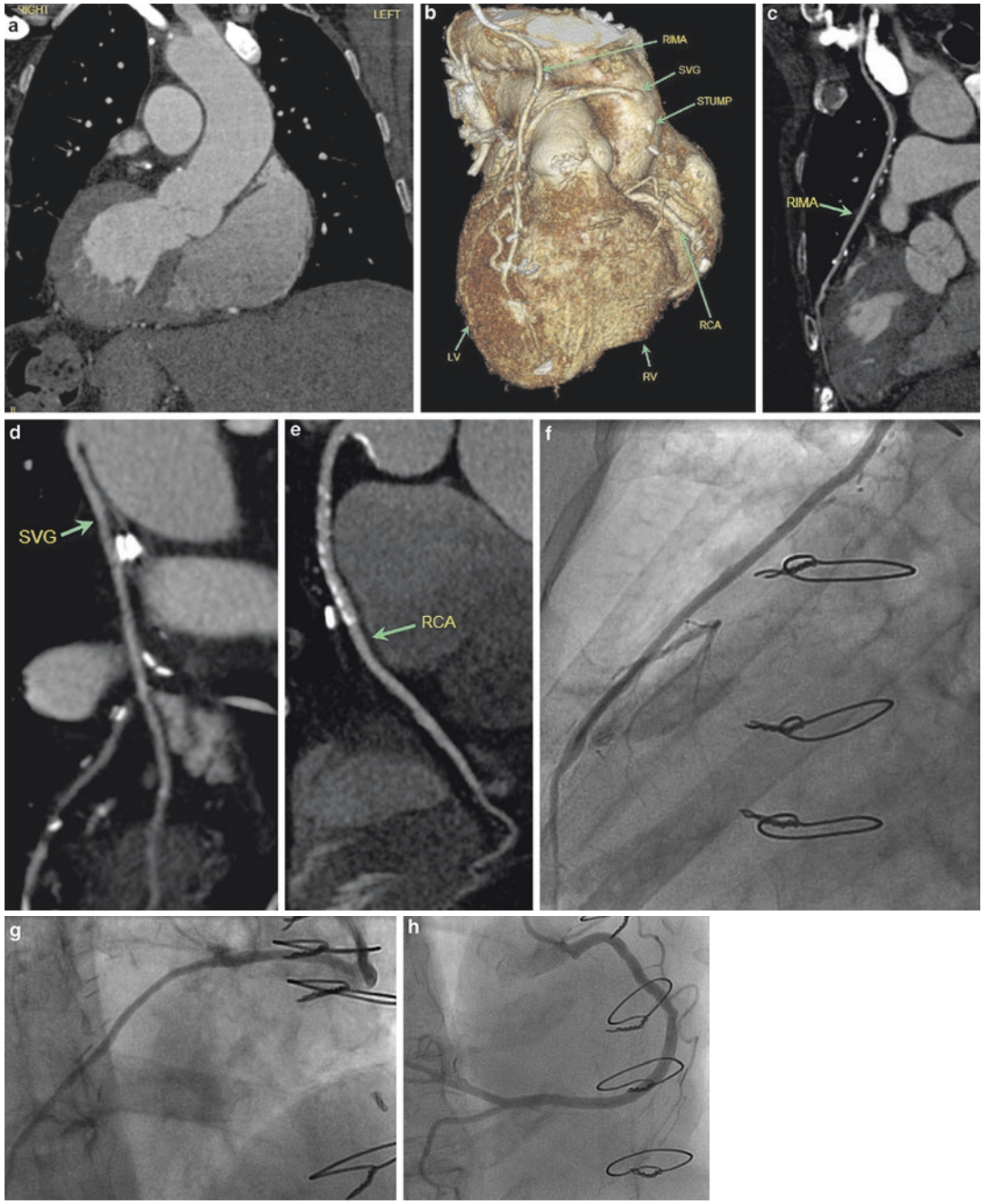

Fig. 10.18 (**a**) Dextrocardia with situs inversus. (**b**) Volume rendering. Dextrocardia and post CABG. (**c**, **d**) cMPR. Patent RIMA to the LAD and SVG to the ramus intermedius. (**e**) cMPR. Calcified nonobstructing calcified plaques in the proximal to mid-large dominant RCA. (**f**–**h**) Coronary angiogram of the patent RIMA to the LAD, SVG to the ramus intermedius, and widely open native RCA

10.19 Case 18

10.19.1 History

A 75-year-old male presented with atypical chest pain.

10.19.2 Findings

There is a severe obstructing proximal mid LAD disease. There is a patent LIMA graft to the mid LAD performed with minimally invasive direct coronary artery bypass surgery (MIDCAB) (Fig. 10.19a–c).

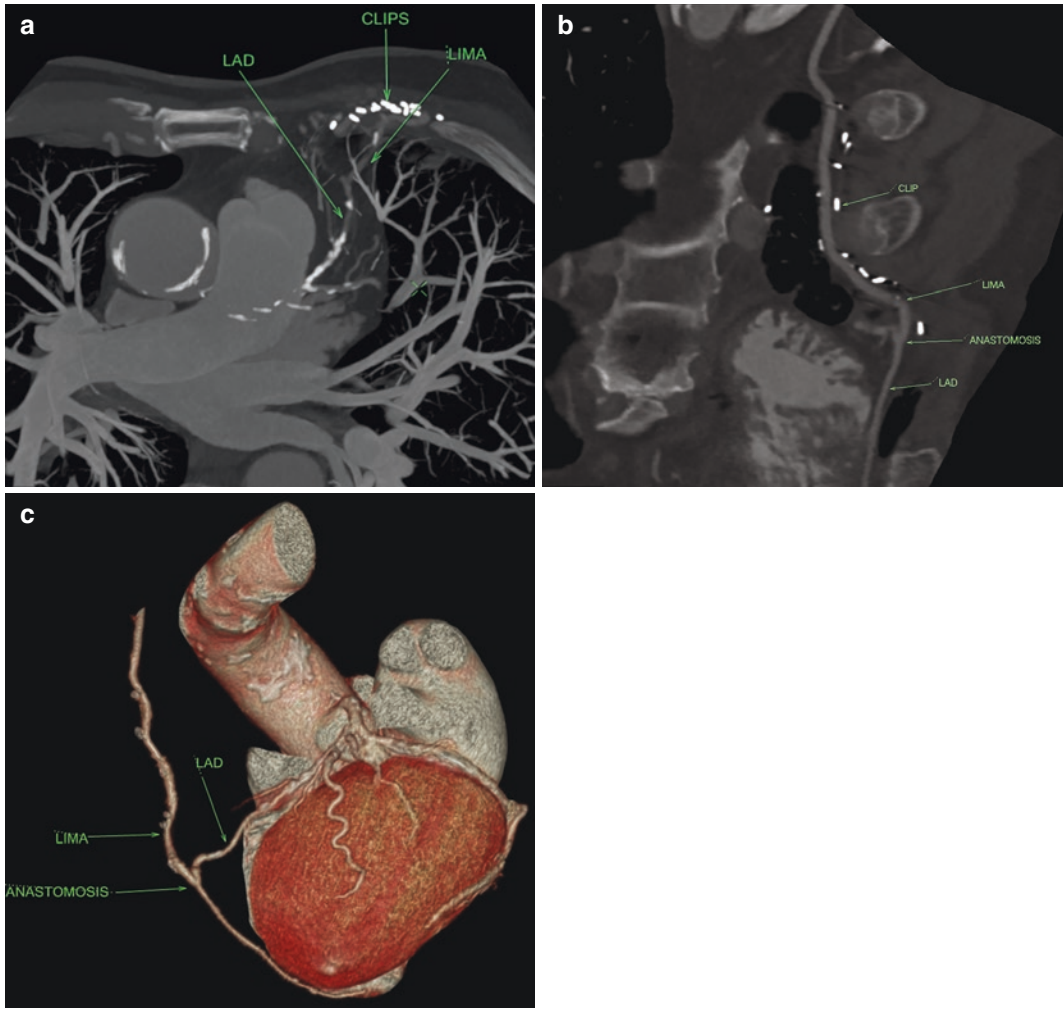

Fig. 10.19 (**a**) Maximum Intensity Projection (MIP) (**b**) curved reformatted reconstruction (cMPR), (**c**) volume rendered (VR)

10.19.3 Diagnosis

Patent MIDCAB to the LAD.

10.19.4 Discussion

MIDCAB is a surgical option that is a less invasive method than a traditional open medial sternotomy CABG and also known as "keyhole surgery." The sternum is spared and the surgery can be performed through a 4–6 cm fifth intercostal thoracotomy. The surgery is performed "off-pump." Although, all myocardial territories can be accessed, MIDCAB surgery is often reserved for single or double obstructing left coronary tree disease. In general, a single pedicle LIMA graft is used to anastomose one or more branches of the LAD.

10.19.5 Pearls and Pitfalls

Clues that a MIDCAB has been performed is lack of sternotomy wire sutures and a small left parasternal surgical defect in the chest wall. Follow the course of the LIMA to assess the surgical anastomosis.

References

1. Mills NL, Everson CT. Right gastroepiploic artery: a third arterial conduit for coronary bypass. Ann Thorac Surg. 1989;47:706–11.
2. Suma H, Isomura T. The right gastroepiploic artery graft. Multimedia manual of cardiovascular surgery. http://mmcts.ctsnetjournals.org/cgi/reprint/2005/0425/mmcts.2004.000802.pdf

Suggested Reading

Alter P, Herzum M, Maisch B. Development of a saphenous vein coronary artery bypass graft pseudoaneurysm. Interact Cardiovasc Thorac Surg. 2004;3:171–3.
Anders K, Baum U, Schmid M, et al. Coronary artery bypass graft (CABG) patency: assessment with high-resolution submillimeter 16-slice multidetector-row computed tomography (MDCT) versus coronary angiography. Eur J Radiol. 2006;57(3):336–44.
Atalay MK. Evaluation of the cardiac surgery patient by MRI and CT imaging: the state of the art. Med Health R I. 2006;89(1):14–9.
Bates ER, Holmes DR, Holmes DR Jr. Saphenous vein bypass graft disease. London: Informa Health Care; 1998.
Celebi M. Cardiomyopathy, dilated. http://www.emedicine.com/med/TOPIC289.HTM
Chaosuwannakit N, et al. Diagnostic accuracy of coronary CT angiography in patients after coronary bypass surgery: evaluation of grafts and native coronary arteries. J Med Assoc Thai. 2014;97(2):211–9.
Chiappini B, Poncelet A, Noirhomme P, et al. Giant aneurysm of aortocoronary saphenous vein graft compressing the left pulmonary artery. J Card Surg. 2006;21(4):425–7.
Cohn LA. Minimally invasive mitral valve repair surgery through a lower mini-sternotomy. http://www.ctsnet.org/sections/clinicalresources/adultcardiac/expert_tech-13.html
Cooley DA. Bypass grafting with bilateral internal thoracic arteries and the right gastroepiploic artery. Circulation. 1998;97:2384–5.
Cosgrove-Edwards A. Annuloplasty system. http://www.edwards.com/products/rings/cosgrove.htm
Crusco F, Antoniella A, Papa V, et al. Evidence based medicine: role of multidetector CT in the follow-up of patients receiving coronary artery bypass graft. Radiol Med. 2007a;112(4):509–25.
Crusco F, Antoniella A, Papa V, et al. Midterm follow-up of patients receiving radial artery as coronary artery bypass grafts using 16-detector-row CT coronary angiography. Radiol Med. 2007b;112(4):538–49.
Desbiolles L, Leschka S, Plass A, et al. Evaluation of temporal windows for coronary artery bypass graft imaging with 64-slice CT. Eur Radiol. 2007;17(11):2819–28.
Dhadwal AK, Abrol S, Zisbrod Z, et al. Pseudoaneurysms of the ascending aorta following coronary artery bypass surgery. J Card Surg. 2006;21(3):221–4.
Feied CF. Pulmonary embolism. http://www.emedicine.com/emerg/topic490.htm
Feuchtner GM, Schachner T, Bonatti J, et al. Diagnostic performance of 64-slice computed tomography in evaluation of coronary artery bypass grafts. AJR Am J Roentgenol. 2007;189(3):574–80.
Frauenfelder T, Boutsianis E, Schertler T, et al. Flow and wall shear stress in end-to-side and side-to-side anastomosis of venous coronary artery bypass grafts. Biomed Eng Online. 2007;6:35.
Gilkeson RC, Markowitz AH. Multislice CT evaluation of coronary artery bypass graft patients. J Thorac Imaging. 2007;22(1):56–62.
Hermann F, Martinoff S, Meyer T, et al. Reduction of radiation dose estimates in cardiac 64-slice CT angiography in patients after coronary artery bypass graft surgery. Invest Radiol. 2008;43(4):253–60.
Houslay ES, Lawton T, Sengupta A, et al. Non-invasive assessment of coronary artery bypass graft patency using 16-slice computed tomography angiography. J Cardiothorac Surg. 2007;2:27.

Huang MP, Yu DQ, Liang CH, et al. Diagnostic value of 64-slice spiral CT coronary angiography for restenosis after bypass surgery. Nan Fang Yi Ke Da Xue Xue Bao. 2007;27(12):1863–5.

Kamada T, Imanaka K, Ohuchi H. Mid-term results of aortoplasty for dilated ascending aorta associated with aortic valve disease. Ann Thorac Cardiovasc Surg. 2003;9(4):253–6.

Khattar RS, Fox DJ, Alty JE, et al. Pulmonary artery dissection: an emerging cardiovascular complication in surviving patients with chronic pulmonary hypertension. Heart. 2005;91:142–5.

Kobayashi T, Ikeda Y, Murakami M, et al. Computed tomographic angiography to evaluate the right gastroepiploic artery for coronary artery bypass grafting. Ann Thorac Cardiovasc Surg. 2008;14(3):166–71.

Kon ZN, White C, Kwon MH, et al. The role of preexisting pathology in the development of neointimal hyperplasia in coronary artery bypass grafts. J Surg Res. 2007;142(2):351–6.

Lau GT, Ridley LJ, Bannon PG, et al. Lumen loss in the first year in saphenous vein grafts is predominantly a result of negative remodeling of the whole vessel rather than a result of changes in wall thickness. Circulation. 2006;114(1 Suppl):I435–40.

Liu ZY, Gao CQ, Li BJ, et al. Diagnostic study on the coronary artery bypass grafts lesions using 64 multislice computed tomography angiography. Zhonghua Wai Ke Za Zhi. 2008;46(4):245–7.

Malagutti P, Nieman K, Meijboom WB, et al. Use of 64-slice CT in symptomatic patients after coronary bypass surgery: evaluation of grafts and coronary arteries. Eur Heart J. 2007;28(15):1879–85.

Mandegar MH, Roshanali F. Surgery of saphenous vein graft aneurysm based on 64-slice computed tomography (CT) diagnostic assessment. Eur J Cardiothorac Surg. 2007;31(6):1137.

Moro J, Almenar L, Igual B, et al. Multislice CT in graft vascular disease. A pilot study. Transplant Proc. 2006;38(8):2563–5.

Mueller J, Jeudy J, Poston R, et al. Cardiac CT angiography after coronary bypass surgery: prevalence of incidental findings. AJR Am J Roentgenol. 2007;189(2):414–9.

Murai S, Hamada S, Yamamoto S, et al. Evaluation of coronary artery bypass grafts using multidetector-row CT with Japanese patients. Radiat Med. 2006;24(1):72–6.

Nikolaou K, Saam T, Rist C, et al. Pre- and postsurgical diagnostics with dual-source computed tomography in cardiac surgery. Radiologe. 2007;47(4):310–8.

Nölke L, McGovern E, Wood AE. Saphenous vein graft aneurysms; the true, false and ugly! Interact Cardiovasc Thorac Surg. 2004;3(4):631–3.

Pache G, Saueressig U, Frydrychowicz A, et al. Initial experience with 64-slice cardiac CT: non-invasive visualization of coronary artery bypass grafts. Eur Heart J. 2006;27(8):976–80.

Peterman MA, Hamman BL, Schussler JM. 64-Slice CT angiography of saphenous vein graft anastomoses fashioned with interrupted nitinol clips. Ann Thorac Surg. 2007;83(3):1204.

Plass A, Grünenfelder J, Leschka S, et al. Coronary artery imaging with 64-slice computed tomography from cardiac surgical perspective. Eur J Cardiothorac Surg. 2006;30(1):109–16.

Pym J, Brown PM, Charrette EJ, et al. Gastroepiploic-coronary anastomosis: a viable alternative bypass graft. J Thorac Cardiovasc Surg. 1987;94(2):256–9.

Robicsek F, Cook JW, Reames MK. Size reduction ascending aortoplasty: is it dead or alive? J Thorac Cardiovasc Surg. 2004;128(4):562–70.

Sadigh G, et al. Impact of coronary CT angiography on surgical decision-making for coronary artery bypass graft surgery. Acad Radiol. 2013;20(9):1083–90.

Senbaklavaci O, Kaneko Y, Bartunek A. Rupture and dissection in pulmonary artery aneurysms: incidence, cause, and treatment—review and case report. J Thorac Cardiovasc Surg. 2001;121:1006–8.

Shrestha M, Khaladj N, Bara C, et al. Quality control after total arterial revascularisation: multislice computer tomography cannot replace coronary angiography. Clin Res Cardiol. 2008;97(6):371–5.

Simon AR, Baraki H, Weidemann J, et al. High-resolution 64-slice helical-computer-assisted-tomographical-angiography as a diagnostic tool before CABG surgery: the dawn of a new era? Eur J Cardiothorac Surg. 2007;32(6):896–901.

Thomas JL. The Vineberg legacy: internal mammary artery implantation from inception to obsolescence. Tex Heart Inst J. 1999;26(2):107–13.

van de Wal RM, van Werkum JW, le Cocq d'Armandville MC, et al. Giant aneurysm of an aortocoronary venous bypass graft compressing the right ventricle. Neth Heart J. 2007;15(7–8):252–4.

Vermeersch P, Agostoni P, Verheye S, et al. Randomized double-blind comparison of sirolimus-eluting stent versus bare-metal stent implantation in diseased saphenous vein grafts: six-month angiographic, intravascular ultrasound, and clinical follow-up of the RRISC Trial. J Am Coll Cardiol. 2006;48(12):2423–31.

Vermeersch P, Agostoni P, Verheye S, et al. DELAYED RRISC (Death and Events at Long-term follow-up AnalYsis: extended duration of the reduction of restenosis in saphenous vein grafts with cypher stent) Investigators. Increased late mortality after sirolimus-eluting stents versus bare-metal stents in diseased saphenous vein grafts: results from the randomized DELAYED RRISC Trial. J Am Coll Cardiol. 2007;50(3):261–7.

Wiesenfarth JM. Dissection, aortic. http://www.emedicine.com/emerg/topic28.htm

Wilhelm A. SITUS INVERSUS. HTTP://WWW.EMEDICINE.COM/RADIO/TOPIC639.HTM

Extracardiac Findings on Cardiac CTA

11

Christopher Brown and Charles S. White

11.1 Introduction

Coronary computed tomographic angiography (CCTA) is a powerful, noninvasive tool to evaluate coronary anatomy, plaque, and areas of stenosis in the coronary arteries. Technological advancements have now given CCTA diagnostic capabilities that approach those of invasive coronary angiography, which remains the gold standard for coronary artery imaging. CCTA is often used in an outpatient setting to evaluate for coronary artery disease as well as graft patency following coronary artery bypass. Recent studies have shown that CCTA can effectively rule out acute coronary syndrome in low to intermediate-risk patients, who present with suspicious chest pain. The use of CCTA is on the rise, and it is important to recognize its diagnostic capabilities not only related to the coronary arteries and heart, but also with respect to extracardiac structures.

C. Brown, MD
Department of Radiology, Hahnemann University Hospital, Drexel University School of Medicine, Philadelphia, PA, USA

C.S. White, MD (✉)
Department of Diagnostic Radiology, University of Maryland Medical Center, 22 S Greene St, Baltimore, MD 21201, USA
e-mail: cwhite@umm.edu

To visualize each of the coronary vessels on CCTA, z-axis coverage must extend from the upper mediastinum to the upper abdomen. Depending on use of a wide or narrow field of view, this will include variable portions of the lungs, mediastinum, chest wall, thoracic spine, and abdomen. Not surprisingly, incidental findings will often be identified that may or may not be clinically significant. An incidental finding is classified as significant if it requires subsequent radiographic evaluation or therapeutic intervention.

Patients undergoing cardiac imaging are not necessarily representative of the general population because of the presence of cardiac disease, additional associated risk factors, and ongoing symptoms, all of which may affect the prevalence and types of clinically significant incidental findings.

In one of the earliest large studies to analyze incidental findings on cardiac electron beam CT in the context of calcium scoring, investigators found that 53% of all patients had one or more incidental findings [1]. Most incidental findings were limited to the heart or pericardium (38%). Extracardiac incidental findings included pneumonia (1.7%), pulmonary malignancy (0.1%), pleural disease (8.9%), esophageal carcinoma (0.06%), lymphadenopathy (4%), hiatal hernia (1%), hepatic tumors (2%), and spinal degenerative disease (5.4%). Regarding clinical significance, 9% of these

C. Smuclovisky (ed.), *Coronary Artery CTA*, https://doi.org/10.1007/978-3-319-66988-5_11

findings required further evaluation, and only 1% resulted in therapeutic intervention.

More recent investigations with modern multi-detector CT scanners have found similar results, with a prevalence of significant findings as high as 23%. One important difference is that CCTA requires contrast administration, which enhances the ability to detect additional pathology such as pulmonary embolism and aortic dissection. For example, in a study looking at patients who underwent CCTA after coronary artery bypass grafts, incidental pulmonary embolism was found in 1.9% of patients in the immediate postoperative period.

There has been considerable debate about the necessity to look for and report incidental findings. Many studies have confirmed that incidental findings are common and have the potential to influence treatment; identifying such findings should be a component of the image interpretation.

11.2 Case 11.1

11.2.1 History

A 56-year-old male screened for coronary artery disease. History is significant for hypertension, hyperlipidemia, and family history of coronary artery disease.

11.2.2 Findings

There is a solitary pulmonary nodule in the left upper lobe of the lung measuring approximately 1 cm in diameter. There is no associated lymphadenopathy or calcification (Fig. 11.1).

11.2.3 Diagnosis

Incidental solitary pulmonary nodule.

11.2.4 Discussion

Solitary pulmonary nodules (SPN) are relatively common findings that must not be overlooked because they may represent malignancy. Most often, patients are asymptomatic, and these lesions are found incidentally or in screening studies for lung cancer in high-risk populations.

By definition, a pulmonary nodule is a discrete opacity that is less than 3 cm; any lesion that is greater than 3 cm is termed a mass. The differential diagnosis of a SPN is large and can be divided into benign and malignant etiologies. Benign causes include infection or abscess, inflammatory disease (e.g., sarcoidosis), vascular abnormalities (e.g., AVM, aneurysm), and benign neoplasms (e.g., hamartoma, lipoma, fibroma). Malignant causes include primary lung cancer or metastasis.

Certain radiographic features help to distinguish a benign versus malignant etiology of SPN. Several patterns of calcification are associated with a benign SPN including complete calcification, laminated calcification, popcorn calcification, and central calcification. Margins that are smooth and well defined are more likely benign. The growth rate of a SPN can be highly predictive of a benign or malignant cause. SPNs that double in less than 1 month usually have an infectious etiology. SPNs that are stable over 2 years are usually benign although ground glass nodules may have longer doubling times and those that double in less than 2 years (and greater than 1 month) are usually malignant.

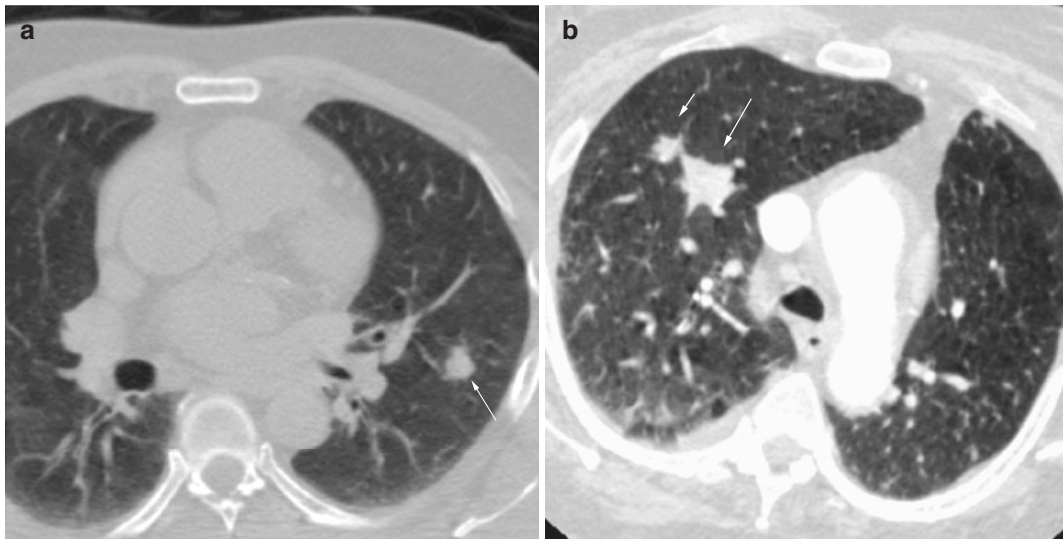

Fig. 11.1 (**a**) Axial. There is solitary pulmonary nodule in the left upper lobe (*arrow*). (**b**) Axial. A different patient with a spiculated nodule suspicious for malignancy (*long arrow*) with an associated satellite nodule (*short arrow*)

Management of SPNs can be difficult because physicians must consider risks of further radiation from follow-up imaging and possible tissue sampling versus the likelihood of diagnosing or missing a lung cancer. The predictable growth rate of malignant and benign SPNs is the basis for the Fleischner Society recommendations for follow-up of lung nodules [2]. These recommendations outline scheduled CT follow-up, PET imaging, and/or biopsy based on the size of the SPN and risk stratification of the patient.

11.2.5 Pearls and Pitfalls

When available, prior imaging studies should be carefully studied to assess for changes in the size or morphology of any nodules. Solid nodules that are stable over 2 years or those that are completely calcified can be considered benign.

11.3 Case 11.2 Contributed by J. Lee and C. Smuclovisky

11.3.1 History

A 75-year-old male presented with new onset of left-sided chest pain.

11.3.2 Findings

There is a mass in the left upper lobe of the lungs infiltrating the adjacent mediastinum and with adenopathy (Fig. 11.2a–c).

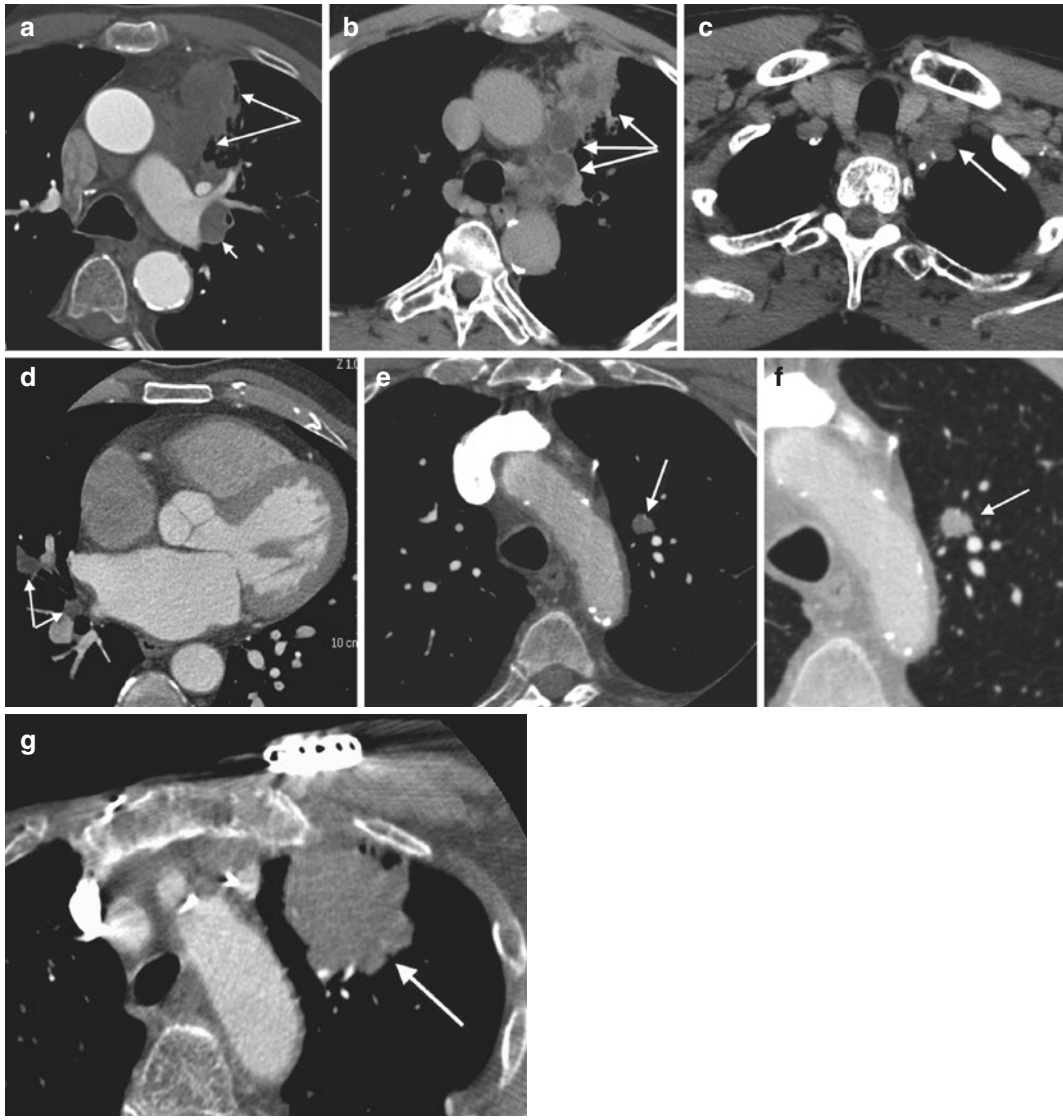

Fig. 11.2 (**a**) Axial. Left upper lobe adenocarcinoma infiltrating the mediastinum (*double arrows*). Left hilar metastatic lymph node (*single arrow*). (**b**) Axial. Delayed images again demonstrating the infiltrating tumor (*arrows*). (**c**) Axial. Metastatic adenopathy adjacent to the left subclavian artery and vein (*arrow*). (**d**) Axial. Incidental small lung cancer (different patient) adjacent to the right hilum with a metastatic lymph node (*arrows*). (**e** and **f**) Axial. Incidental 13-mm lung cancer (different patient) in the left upper lobe adjacent to the aortic arch. Lung window (**f**) demonstrating spiculated borders of the tumor (*arrows*). (**g**) Axial. Incidental 5.5-cm left upper lobe lung cancer (different patient) incidentally found on the cardiac CTA and previously missed on plain radiographs over a period of 3 years. Note that the tumor is posterior to a cardiac pacemaker and would be difficult to suspect on a plain radiograph (Murphy's law)

11.3.3 Diagnosis

The diagnosis is adenocarcinoma of the lung.

11.3.4 Discussion

Lung cancer is the leading cause of cancer-related mortality in both men and women. The prevalence of lung cancer is second only to that of prostate cancer in men and breast cancer in women. Non-small cell lung cancer (NSCLC) accounts for approximately 75% of all lung cancers. NSCLC is divided further into adenocarcinoma, squamous cell carcinoma, and large cell carcinoma.

Extracardiac findings are frequently encountered on cardiac CTA. Primary lung cancer typically appears as a noncalcified soft tissue mass with irregular or spiculated borders. The tumors have variable size and may be located anywhere in the thorax.

11.3.5 Pearls and Pitfalls

Careful attention to the extracardiac structures is of paramount importance in order not to miss reporting a neoplasm in the field of view.

11.4 Case 11.3

11.4.1 History

A 40-year-old male, who presented with chest pain after using cocaine.

11.4.2 Findings

There is a focal consolidation in the right middle lobe (Fig. 11.3).

11.4.3 Diagnosis

Pneumonia, possibly secondary to aspiration given patient's history of drug abuse.

11.4.4 Discussion

Pneumonia develops when pathologic organisms invade lung parenchyma and initiate a host immune response. This manifests as inflammatory exudate in the airspaces, which causes the radiographic appearance of consolidation. Spread of organisms can occur through the airways via inhalation or aspiration, through vasculature (hematogenous spread) or by direct contact with infected adjacent structures such as the mediastinum or abdomen. Pneumonia can be caused by bacteria, viruses, fungi, and parasites. The integrity of the immune system plays an important role in the susceptibility of infections from various organisms.

There are three radiographic patterns of pneumonia: lobar, lobular or bronchopneumonia, and interstitial. Lobar pneumonia usually involves inflammation in the distal airways first, which then spreads proximally along the airways to involve the whole lobe. *S. pneumoniae* and *Klebsiella pneumoniae* often produce lobar pneumonia.

Lobular or bronchopneumonia is caused by inflammation in the bronchi, which then spreads distally to involve the pulmonary lobule. *S. aureus* and *H. influenza* often produce bronchopneumonia.

Interstitial pneumonia is caused by inflammation in the bronchioles and pulmonary interstitium, which causes radiographic thickening of airways and reticulonodular opacities. Viral infections and mycoplasma often produce interstitial pneumonia.

Although each organism has predilection for a specific radiographic appearance, there is considerable overlap. Other complications of infection that can occur with pneumonia are abscess and empyema.

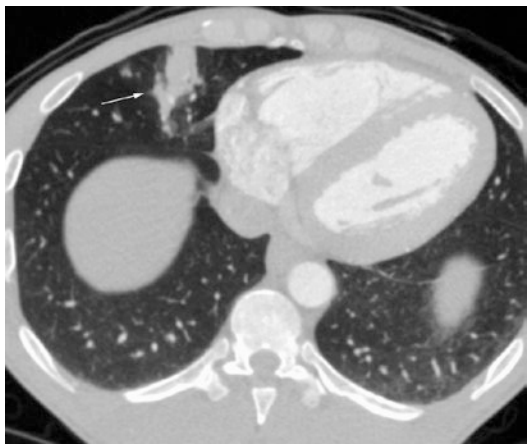

Fig. 11.3 Axial. Right middle lobe consolidation indicative of airspace disease (*arrow*)

11.4.5 Pearls and Pitfalls

In an erect patient, aspiration pneumonia is most common in the right middle lobe or bilateral lower lobes because the bronchi are oriented more vertically.

A chest radiograph may require 4–6 weeks to normalize after pneumonia.

11.5 Case 11.4

11.5.1 History

A 59-year-old female presented to the emergency department with chest pain and shortness of breath.

11.5.2 Findings

There are pulmonary emboli and bilateral main pulmonary arteries and segmental arteries. There is right ventricular strain (Figs. 11.4 and 11.5).

11.5.3 Diagnosis

The diagnosis is extensive pulmonary emboli with right ventricular strain.

11.5.4 Discussion

Pulmonary embolism (PE) is a common yet deadly disease that is responsible for 100,000 deaths in the USA annually. Risk factors for PE are similar to those for DVT and include malignancy, surgery, joint replacements, prolonged immobilization, pregnancy, and hypercoagulable disorders.

Common symptoms of PE are dyspnea, chest pain, and cough. The most common sign on physical exam is tachycardia. Because many patients may be asymptomatic, a high level of suspicion must be maintained among those who are at high risk. PE is often a lethal disease because it may cause right heart failure and subsequent death due to arrhythmias or cardiac shock in up to 30% of patients if not treated. Typical treatment is immediate anticoagulation and supportive therapy although more invasive therapy may be necessary in patients with hemodynamic compromise.

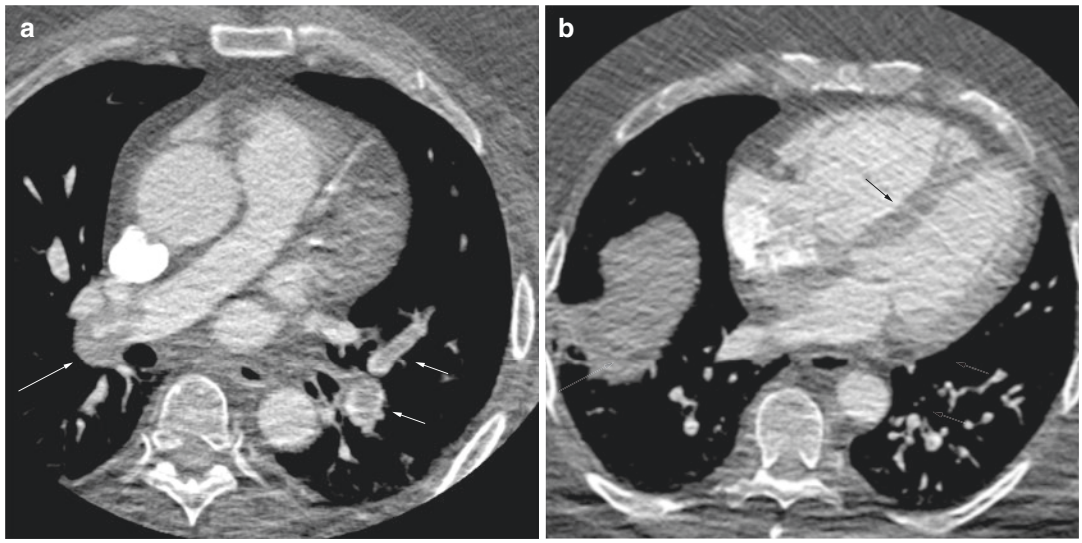

Fig. 11.4 (**a**) Axial. Thrombus in the right main pulmonary artery (*long arrow*) and left lung segmental pulmonary arteries (*short arrows*). (**b**) Axial. Flattening of the interventricular septum (*arrow*) indicates right ventricular strain. Normally, the interventricular septum bows outward from the left ventricle

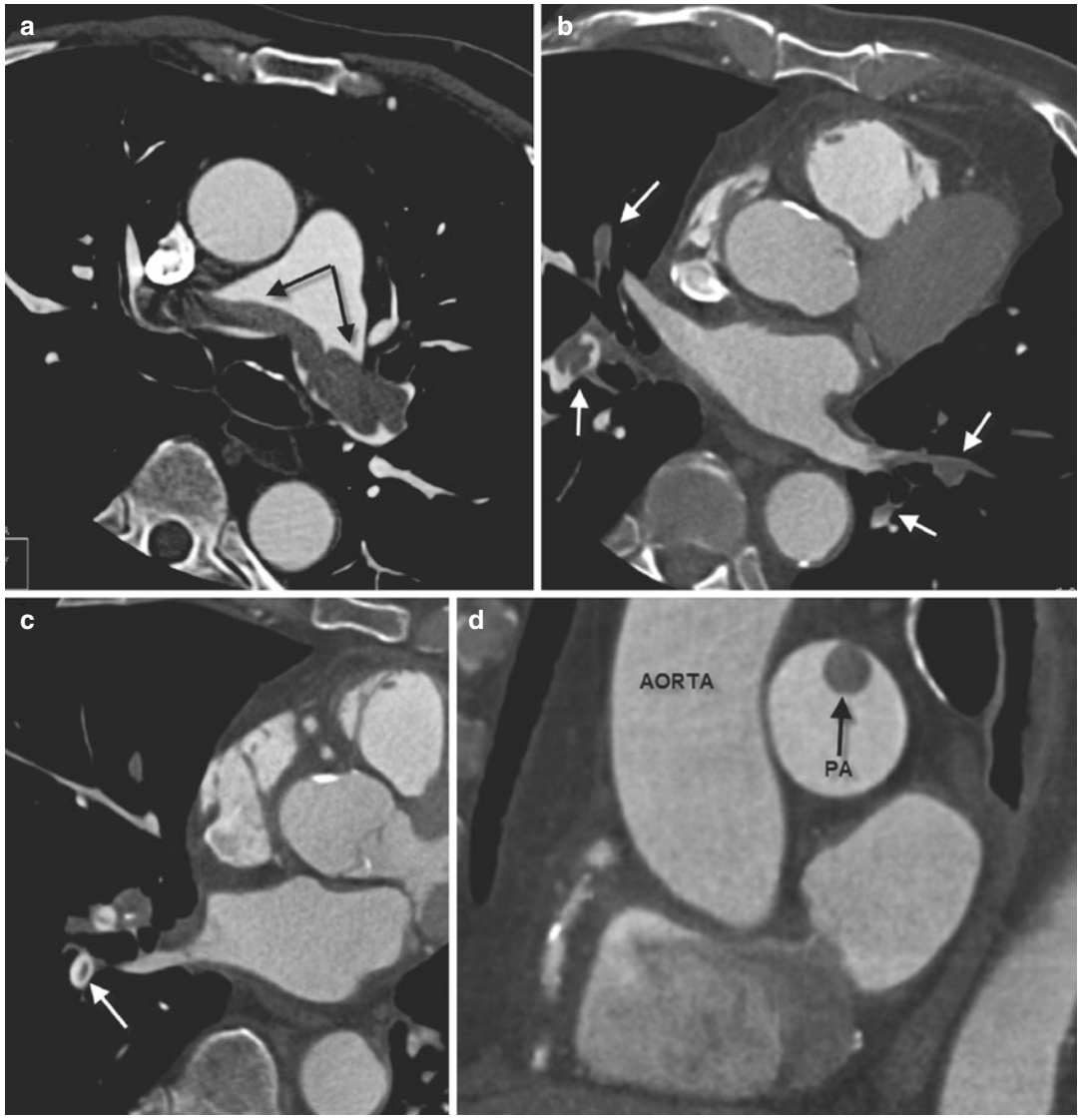

Fig. 11.5 (**a**) Axial. Massive pulmonary embolism with a large saddle embolus in the main pulmonary artery (arrows). (**b**) Axial. Extensive bilateral thrombus in the proximal pulmonary arteries (*arrows*). (**c** and **d**) Axial and sagittal. Arrows pointing to a partial filling defect in an arterial branch to the right lower lobe (**c**) and proximal right pulmonary artery (**d**), which sometimes can have the appearance of an eyeball defect—Contributed by J. Lee & C. Smuclovisky

The presence of right ventricular strain, which can be assessed by right ventricular dilation and flattening of the intraventricular septum, is a negative prognostic indicator in patients with PE.

Historically, the gold standard for diagnosis was pulmonary angiography. However, today similar diagnostic results are achieved with CT angiography.

11.5.5 Pearls and Pitfalls

Timing of the contrast injection is crucial. Opacification extending from the main pulmonary arteries to the subsegmental arteries must be achieved to confidently rule out PE.

11.6 Case 11.5

11.6.1 History

A 65-year-old male underwent a preoperative study for aortic valve replacement. He has history of coronary artery disease and prior coronary artery bypass graft.

11.6.2 Findings

There is right-sided pleural effusion with septal thickening and ground glass opacities in both lung bases (Fig. 11.6).

11.6.3 Diagnosis

Pleural effusion due to volume overload.

11.6.4 Discussion

Pleural effusions can be classified as either transudative or exudative. Transudative effusions are caused by increased plasma hydrostatic pressure, decreased plasma oncotic pressure, or a combination of the two. The most common cause of transudative effusions is left heart failure, which causes increased plasma hydrostatic pressure from vascular congestion. Other causes include volume overload and diseases characterized by hypoalbunemia, such as hepatic disease or nephrotic syndrome. Exudative effusions are caused by infection, inflammation, and malignancy.

Pulmonary edema can develop in setting of volume overload or congestive heart failure. Radiographically, this is demonstrated by the presence of septal lines due to increased interstitial fluid as well as ground glass opacities due to increased fluid in the alveoli.

Thoracentesis can be performed to sample the pleural fluid, which can then be analyzed to help distinguish transudative effusions from exudative effusions. Typically, a transudative effusion has a pleural/serum protein ratio less than 0.5, pleural/serum LDH ratio less than 0.6, and pleural LDH less than 200 IU/L.

11.6.5 Pearls and Pitfalls

Transudative effusions usually have density on CT of 0–20 HU. Exudative effusions tend to have density greater than 20 HU.

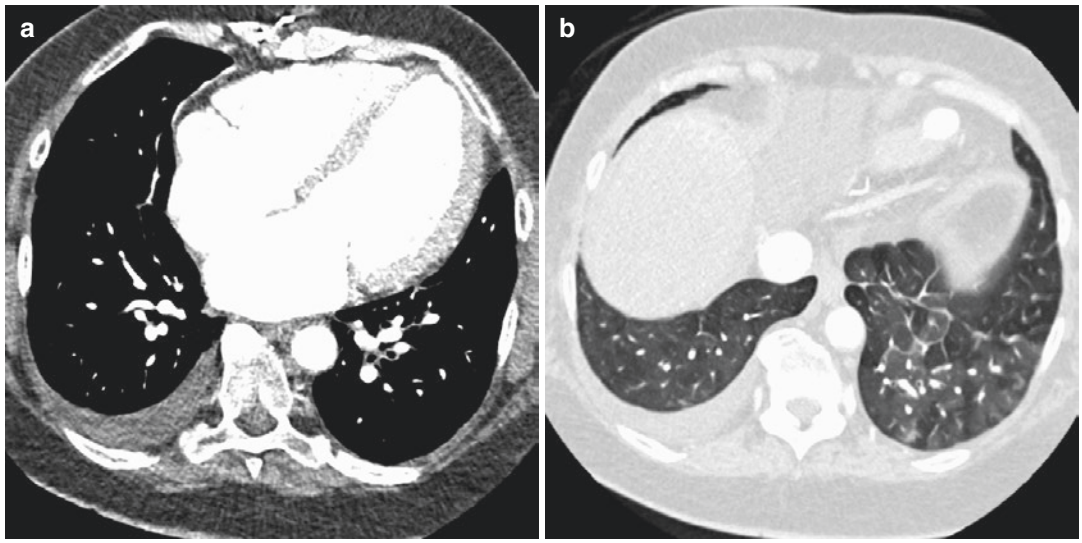

Fig. 11.6 (**a**) Axial. Soft tissue window shows right-sided pleural effusion with density of simple fluid. (**b**) Axial. Lung windows show septal thickening and ground glass opacities in both lung bases

11.7 Case 11.6 Contributed by J. Lee and C. Smuclovisky

11.7.1 History

An 89-year-old male presented with a history of increasing shortness of breath and atypical chest pain.

11.7.2 Findings

There is a pericardial effusion (Fig. 11.7a, b). There was multivessel non-obstructive calcified plaques in the coronary arteries (not shown).

11.7.3 Diagnosis

The diagnosis is pericardial effusion.

11.7.4 Discussion

The pericardial space normally contains up to 50 mL of fluid, which serves as lubrication for the visceral and parietal layers of the pericardium. Pericardial effusion is defined as an abnormal amount fluid or density in the pericardium. Etiologies include infectious, noninfectious, and autoimmune. The cause in this case was idiopathic.

The cause of increased fluid production depends on the underlying etiology. Transudate fluid accumulation results from obstruction of fluid drainage, which occurs through lymphatic channels. Exudate fluids occur secondary to inflammatory, infectious, malignant, or autoimmune processes affecting the pericardium.

Clinical manifestations of pericardial effusion are mostly dependent on the rate of accumulation of fluid in the pericardial sac. Rapid accumulation may cause elevated intrapericardial pressures

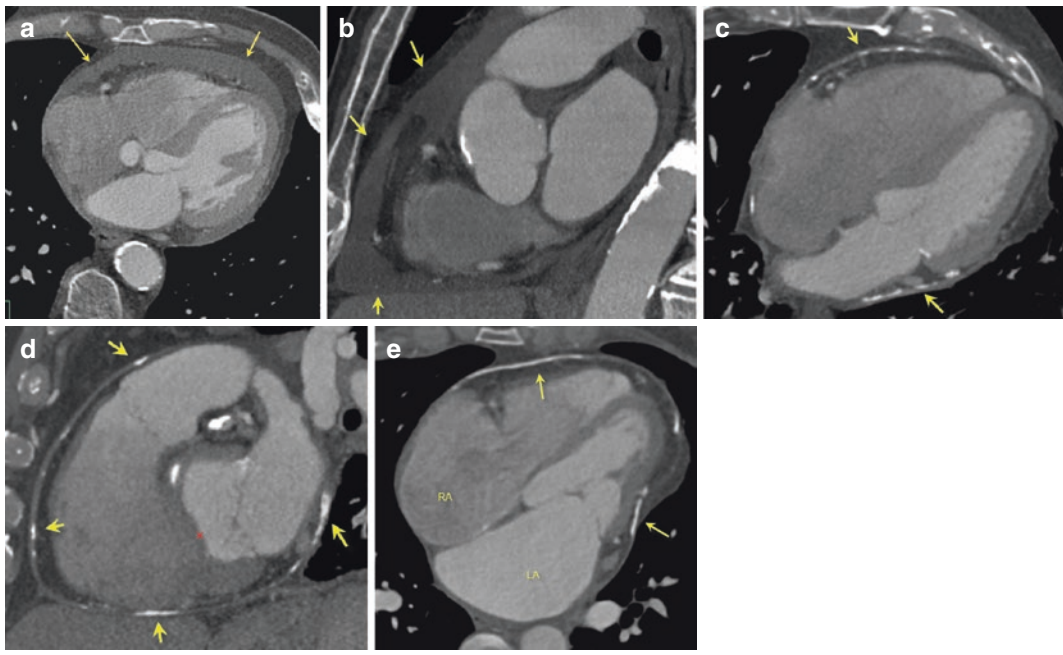

Fig. 11.7 (**a** and **b**) Axial and sagittal. Pericardial effusion (*arrows*). (**c** and **d**) Axial and sagittal. Thickened pericardium with scattered calcifications (*arrows*). (**e**) Axial: Constrictive pericarditis (*arrows*). Thickened and partially calcified pericardium causing compression of the ventricles with secondary dilatation of the atria (*LA* left atrium; *RA* right atrium)

with as little as 80 mL, while slowly progressing effusions can contain up to 2 L with minimal or no symptoms. CT can detect small amounts of fluid in the pericardium and reported as little as 50 mL. Pericarditis can lead to fibrosis and calcifications (Fig. 11.7c, d) in the pericardium that can lead to constrictive pericarditis (Fig. 11.7e), which impedes normal diastolic filling.

11.7.5 Pearls and Pitfalls

It is not uncommon to normally visualize a small amount of fluid in the inferior pericardial recess in asymptomatic patients. With a pericardial effusion, fluid extends superiorly surrounding the heart anterior and posteriorly.

11.8 Case 11.7 Contributed by J. Lee and C. Smuclovisky

11.8.1 History

An 81-year-old asymptomatic male presented with an abnormal nuclear stress test and silent MI.

11.8.2 Findings

There is a 3.9-cm water density mass inseparable from the free wall of the right atrium located in the cardiophrenic angle (Fig. 11.8a, b).

11.8.3 Diagnosis

The diagnosis is pericardial cyst.

11.8.4 Discussion

Most pericardial cysts are congenital and are discovered, as in this case, as an incidental finding. Less common are inflammatory pericardial cysts. These include pseudocysts as well as encapsulated and loculated pericardial effusions. Pericardial scarring may trap portions of an intrapericardial exudate or hemorrhage producing a pocket or cyst-like structure (Fig. 11.8c).

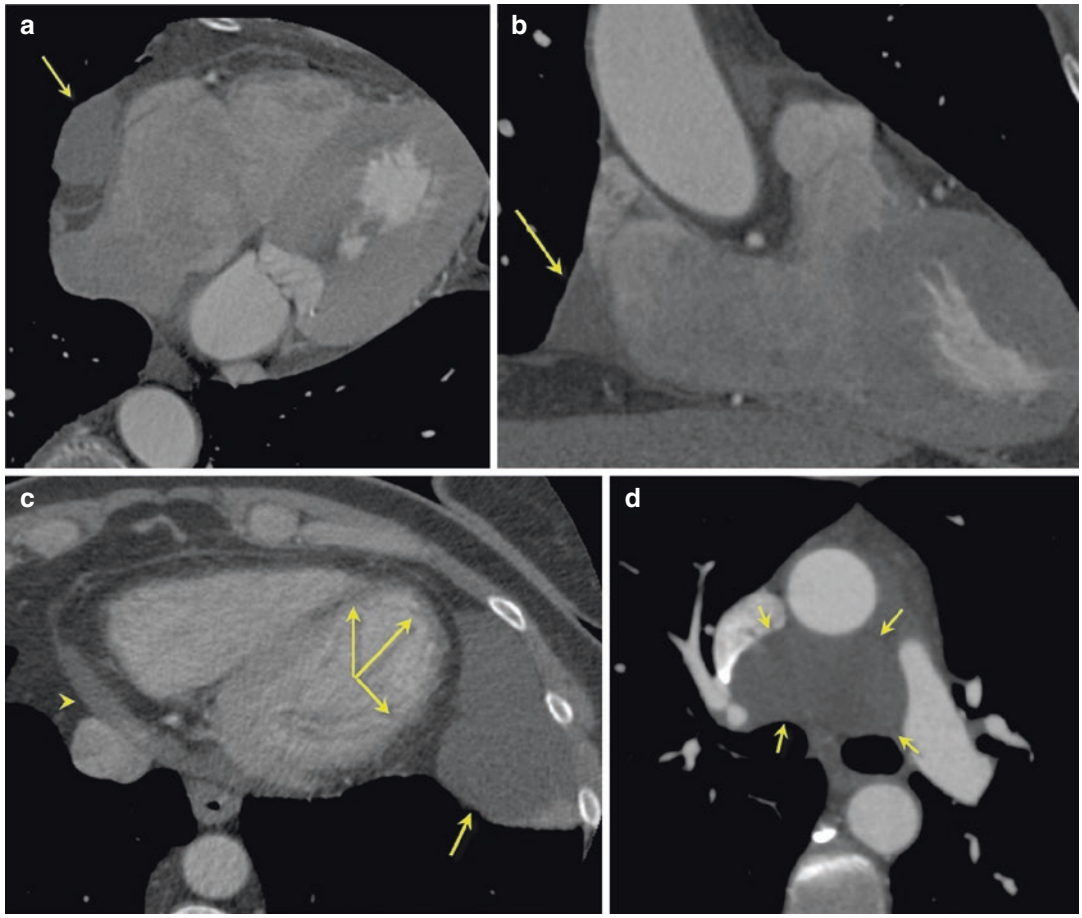

Fig. 11.8 (**a** and **b**) Axial and coronal. Pericardial cyst in the right cardiophrenic angle (*arrows*). (**c**) Axial. Different patient with a large chronic myocardial infarct in the territory of the LAD (*triple arrows*), with a trapped fluid collection (*single arrow*) in the left cardiophrenic angle. There is a small amount of fluid (*arrow head*) in the pericardium. (**d**) Axial. Bronchogenic cyst, on a different patient (*arrows*)

Cysts occur anywhere in the pericardium and are mostly commonly located in the right cardiophrenic angle. Pericardial cysts are usually less than 3 cm in diameter and most are unilocular, have smooth borders, and contain clear fluid. The cyst arises from the parietal pericardium and consists of a single layer of mesothelial cells. Rarely, cysts can be associated with chest pain, dyspnea, cough, and significant arrhythmias, likely secondary to compression and erosion of the adjacent tissues.

The diagnosis on CT is established by the location, ovoid/triangular shape, thin walls, and homogeneous water density. These cysts have similar appearance and histology as bronchogenic cysts (Fig. 11.8d). Pericardial cysts may be hyperdense on CT, likely from containing mucoid or proteinaceous material or both that may mimic a solid mass.

11.8.5 Pearls and Pitfalls

Differential diagnosis of a pericardial cyst would include a bronchogenic cyst that is trapped in or on the pericardium, lymphangiomas, and necrotic tumors. Pericardial diverticula are less common and resemble cysts except that a comparable developmental abnormality has left a communication with the pericardial cavity.

11.9 Case 11.8 Contributed by J. Lee and C. Smuclovisky

11.9.1 History

A 79-year-old male presented with chronic shortness of breath and atrial fibrillation.

11.9.2 Findings

There is a filling defect in the left atrial appendage (Fig. 11.9a).

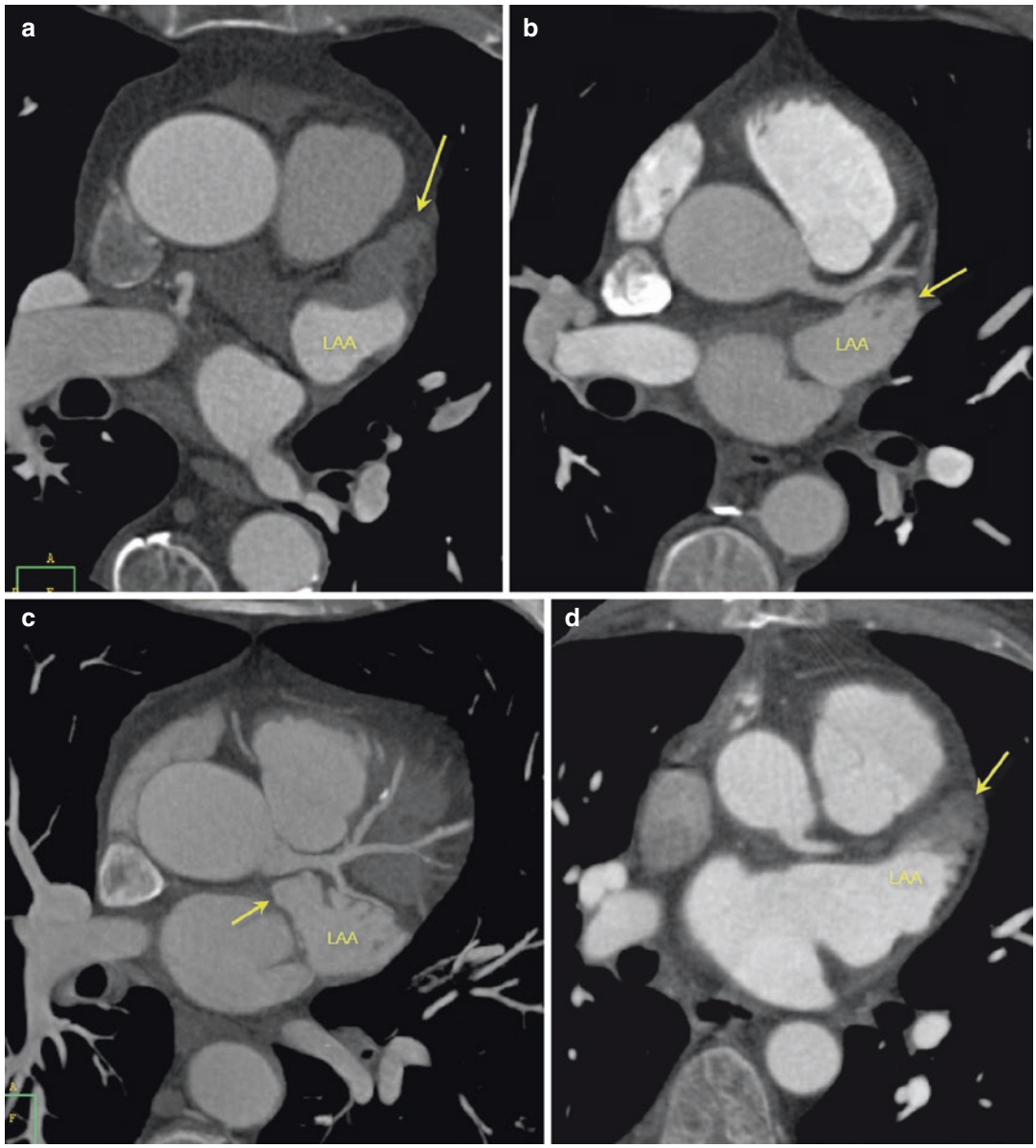

Fig. 11.9 (**a**) Axial. Discrete low density in the left atrial appendage (LAA) confirmed by transesophageal echocardiography (TEE) to represent a thrombus (*arrow*). (**b**) Axial. Normal typical triangular appearance of the LAA (*arrow*) in a different patient. (**c**) Axial: Anatomic variant of the LAA with the apex toward the left sinus of Valsalva (*arrow*) in a different patient. (**d**) Axial. False-positive CTA result. Filling defect (*arrow*) in the LAA in a different patient with a chronic dilated cardiomyopathy and no thrombus and sluggish LAA on a TEE performed the following day

11.9.3 Diagnosis

The diagnosis is chronic nonvalvular atrial fibrillation with a thrombus in the left atrial appendage (LAA).

11.9.4 Discussion

The LAA is well identified on cardiac CT and is contiguous anterior and superiorly with the left atrium and located to the left of the main pulmonary artery. The LAA typically has a triangular shape and enhances homogeneously with IV contrast (Fig. 11.9b). Internal striations in the apex of the appendage are also commonly visualized. Anatomic variants of the LAA are not infrequent and may appear redundant or with the apex adjacent to the left sinus of Valsalva (Fig. 11.9c).

The most common cause of thrombus in the LAA is atrial fibrillation. Other causes include mitral valvular disease, cardiomyopathy, and platelet dysfunction. Atrial fibrillation is a common arrhythmia that is found in 1% of persons older than 60 years to more than 5% of patients older than 69 years. Nonvalvular atrial fibrillation is the most common cardiac disease associated with cerebral embolism. Close to half of the cardiogenic emboli in the USA occur in patients with nonvalvular atrial fibrillation. Overall, 20–25% of ischemic strokes are due to cardiogenic emboli.

LAA thrombus is commonly difficult to identify on transthoracic echocardiography. The most widely used diagnostic test to establish the presence of thrombus is transesophageal echocardiography (TEE). However, TEE is semi-invasive, and cardiac CTA has shown the potential to diagnose noninvasively thrombus in the LAA. Currently, there are no definitive studies establishing that CTA replaces TEE.

11.9.5 Pearls and Pitfalls

The LAA opacifies with contrast maximally in end-systole. This is usually the 30–40% phase on the cardiac CTA. LAA thrombus may be subtle and should be suspected in patients with left atrial (LA) enlargement (LA size 4.0 cm and greater). A sluggish LAA may under fill initially with contrast on CTA, giving the false appearance of a thrombus (Fig. 11.9d). Preliminary studies suggest that delayed imaging of the heart may avoid this pitfall.

11.10 Case 11.9 Contributed by J. Lee and C. Smuclovisky

11.10.1 History

A 51-year-old male presented for workup of coronary artery disease.

11.10.2 Findings

There is an incidental 3.5-cm lobulated noncalcified mass in the left atrium attached to the posterior wall (Fig. 11.10a, b).

11.10.3 Diagnosis

The diagnosis is left atrial myxoma.

11.10.4 Discussion

The tumor was surgically resected and the pathology confirmed. Myxomas are benign and represent the most common type of primary cardiac tumor. Approximately 90% are solitary and pedunculated. About 75–85% occur in the left atrial cavity. The mean age of patients with sporadic myxoma is 56 years. In the left atrium, the usual site of attachment is in the area of the fossa ovalis. Less often, myxomas also may arise from the right atrium and either ventricle. Occasionally myxomas, as in this case, arise from the posterior left atrial wall or the appendage. The mobility of the tumor depends on the extent of the attachment and length of the stalk. Clinical signs include embolization and mechanical interference with the cardiac function. Myxomas may also prolapse through the valve and cause destruction of the annulus or valve leaflets.

Familial cardiac myxomas represent approximately 10% of all myxomas. These may be associated with a syndrome called syndrome myxoma or Carney's syndrome that consists of myxomas in other locations (breast or skin), spotty pigmentation, and endocrine dysfunction.

11.10.5 Pearls and Pitfalls

Not infrequently, mixing of IV contrast from the superior vena cava with nonopacified blood from the inferior vena cava causes a swirling artifact in the right atrium that may mimic a thrombus or tumor.

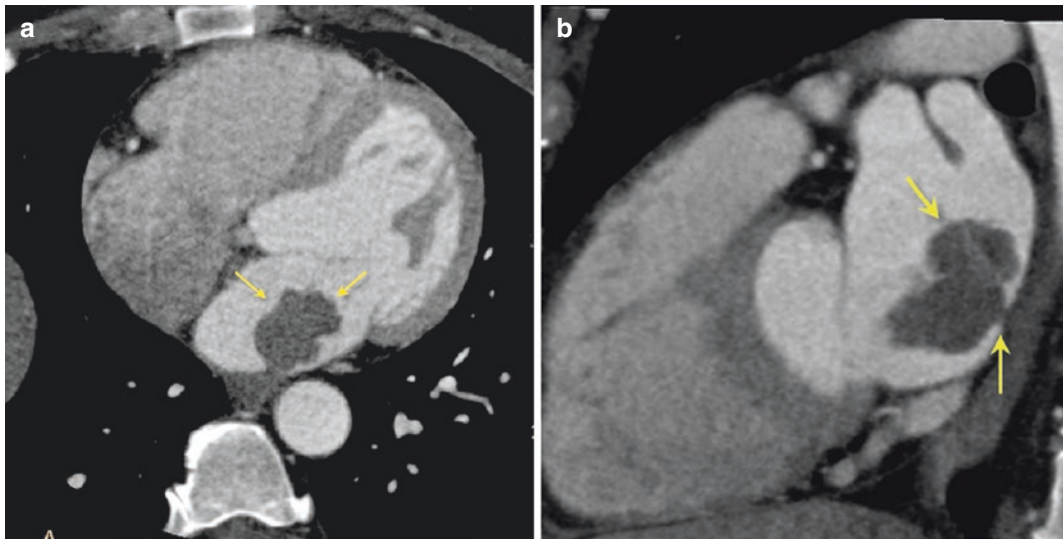

Fig. 11.10 (**a** and **b**) Axial and oblique sagittal. Lobulated 3.5-cm mass in the left atrium attached to the posterior wall corresponding to a left atrial myxoma (*arrow*). (Courtesy of Dr. Constantino Pena, Miami, FL.)

11.11 Case 11.10

11.11.1 History

A 71-year-old male presented with aortic stenosis (AS) and for prevalve replacement workup.

11.11.2 Findings

There is advanced aortic valve calcific deposits (Fig. 11.11a, b).

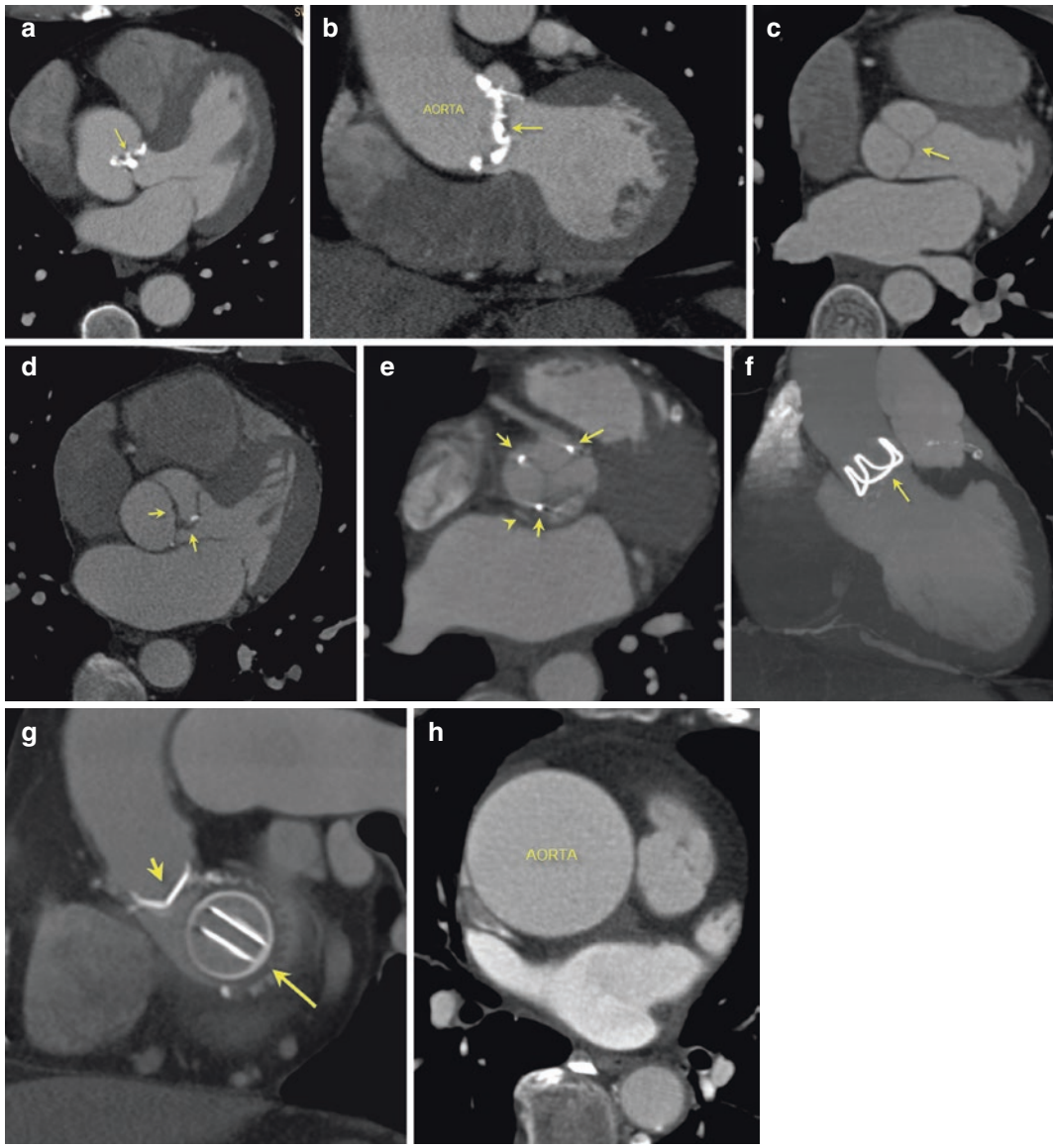

Fig. 11.11 (**a** and **b**) Axial and coronal. There is extensive calcification in the aortic leaflets with severe aortic stenoisis (AS) (*arrows*). (**c**) Axial. Normal leaflets of the aortic valve (*arrow*) in another patient. (**d**) Axial: The aortic leaflets are deformed, thickened, and with mild calcific deposits (*arrows*) in a patient with bicuspid aortic valve and mild AS. (**e** and **f**) Axial and coronal (thick maximum intensity projection). Bioprosthetic aortic valve replacement (*arrows*). The *arrow head* in Fig. 6.5e indicates a pledget used to suture the valve in place. (**g**) Oblique sagittal: Valvular replacement with mechanical valves in the aortic (*short arrow*) and mitral (*long arrow*) position. (**h**) Axial: Dilatation of the ascending aorta in a patient with severe AS

11.11.3 Diagnosis

The diagnosis is aortic valvular stenosis.

11.11.4 Discussion

That aortic valve is well identified on CTA. In the normal aortic valve, the leaflets are thin and without thickening or calcific deposits (Fig. 11.11c). The normal aortic orifice is estimated at 3.0–4.0 cm^2. A valve orifice of 1.0–1.5 cm^2 is considered moderate stenosis, and 1.5–2.0 cm^2 is considered mild stenosis. Less than 1.0 cm^2 is considered critical stenosis. In the presence of a normal cardiac output, critical obstruction to the left ventricular outflow is usually characterized by a peak systolic pressure gradient exceeding 50 mmHg.

Clinical symptoms of AS include shortness of breath, syncope, chest pain, and ultimately signs of heart failure. AS refers to the obstruction of blood flow across the aortic valve. Isolated AS is usually either congenital or degenerative in origin. Congenital malformations of the aortic valve may be unicuspid, bicuspid (Fig. 11.11d), or tricuspid. The abnormal valvular architecture causes turbulent flow that damages the leaflets and leads to fibrosis, rigidity, calcification of the leaflets, and narrowing of the aortic orifice with subsequent AS.

Age-related degenerative calcific AS is currently the most common cause of AS in adults and the most frequent reason for aortic valve replacement (Fig. 11.11e–g). Other causes of acquired calcific AS, or aortic valvular sclerosis, include postinfectious, rheumatoid, and ochronosis.

AS can lead to left ventricular hypertrophy and subsequent LV dilatation. Post-stenotic dilatation of the ascending aorta may also be associated with AS (Fig. 11.11h). The noninvasive test of choice for evaluation of AS is transthoracic echocardiography. Additionally, invasive testing such as TEE and angiography is also commonly used.

11.11.5 Pearls and Pitfalls

Preliminary studies suggest that cardiac CTA appears to be accurate in the estimation of the severity of aortic valvular stenosis.

11.12 Case 11.11 Contributed by J. Lee and C. Smuclovisky

11.12.1 History

A 44-year-old male presented with a history of Marfan syndrome.

11.12.2 Findings

There is severe dilatation of the aortic root measuring 7.0 cm and without dissection. There is LV dilatation related to aortic regurgitation (Fig. 11.12a, b). There is dilatation of the suprahepatic veins and IVC from tricuspid regurgitation.

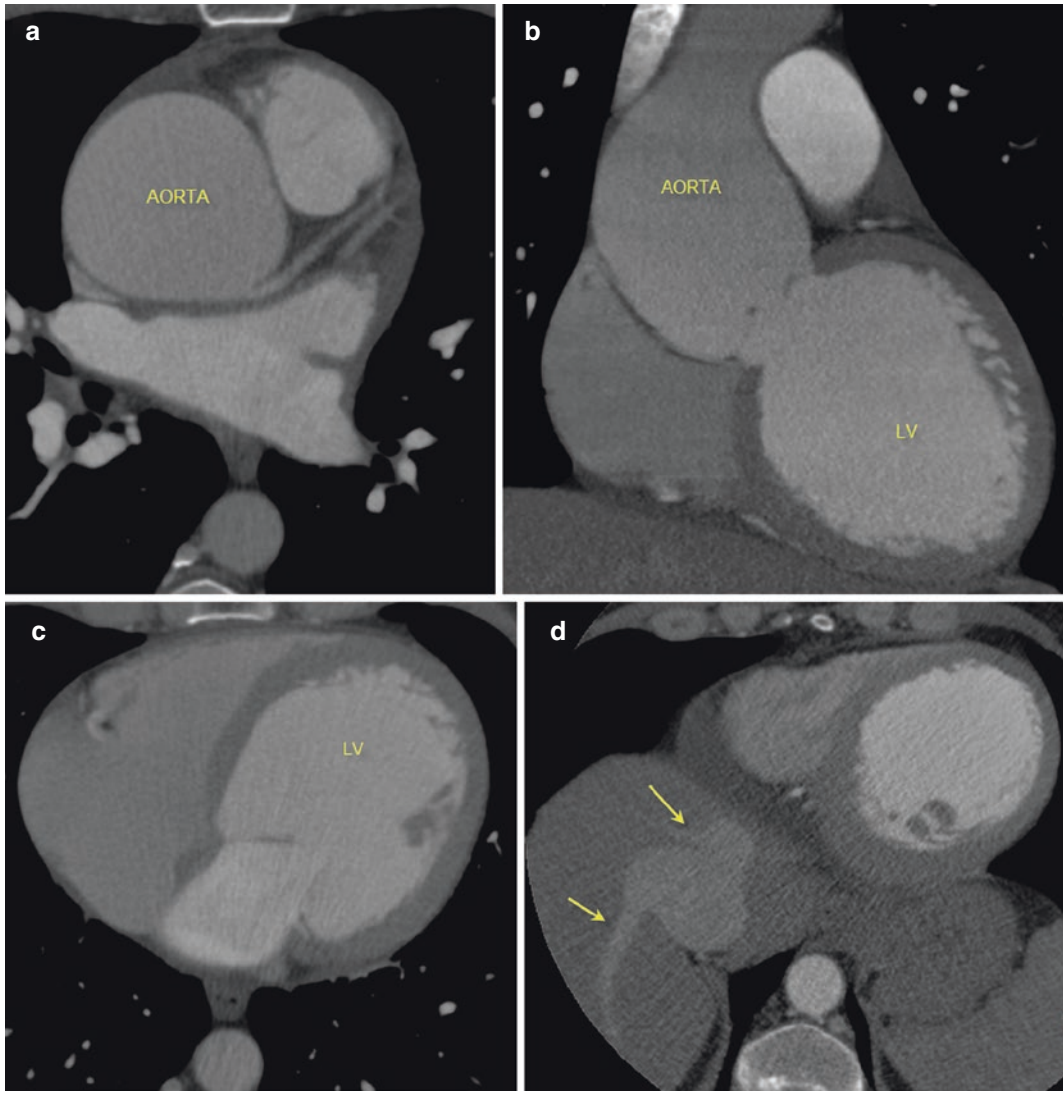

Fig. 11.12 (**a**–**c**) Axial and coronal. Aortic root aneurysm with aortic regurgitation and left ventricular (LV) dilatation. (**d**) Axial. Dilatation of the suprahepatic veins secondary to tricuspid insufficiency (*arrows*)

11.12.3 Diagnosis

The diagnosis is aortic root aneurysm secondary to Marfan syndrome.

11.12.4 Discussion

Marfan syndrome is an autosomal dominant disorder causing a genetic defect of connective tissue. The genetic defect is isolated to the FBN1 chain on chromosome 15, which codes for the connective tissue protein fibrillin. Abnormalities in this protein cause a constellation of clinical disorders, which commonly include the musculoskeletal, cardiac, and ocular system.

The cardiovascular involvement is the most serious problem associated with Marfan syndrome. The incidence of aortic dilatation occurs in 70–80% of cases and involves the sinuses of Valsalva. Aortic dissection is a common and often lethal complication. Mitral valve prolapse occurs in 55–69% cases. Additional findings include tricuspid valve prolapse, dilatation of the main pulmonary and dilatation, or dissection of the descending thoracic and/or abdominal aorta. Dilatation of the aortic root can cause stretching of the aortic valve leaflets resulting in lack of regurgitation.

11.12.5 Pearls and Pitfalls

The aortic root in adults normally measures <3.7 cm above the sinotubular junction.

11.13 Case 11.12

11.13.1 History

A 59-year-old male underwent coronary imaging for preoperative assessment for kidney donation. His history is significant for hypertension and hyperlipidemia.

11.13.2 Findings

There is mediastinal, hilar, and peribronchovascular lymphadenopathy (Fig. 11.13).

11.13.3 Diagnosis

Lymphadenopathy due to sarcoidosis.

11.13.4 Discussion

Lymphadenopathy is a term referring to abnormal lymph nodes, which includes lymph node enlargement, increased number of lymph nodes, and/or abnormal lymph node architecture. Lymphadenopathy is nonspecific finding that can be associated with localized or systemic pathology. Common causes include infection such as tuberculosis, autoimmune diseases, and malignancy such as lymphoma or metastatic disease. Reactive lymphadenopathy is a benign entity that represents a healthy immune response to an antigen stimulus. In some cases, reactive lymphadenopathy can mimic malignancy and a biopsy is required for diagnosis.

Sarcoidosis is a granulomatous disease characterized by noncaseating granulomas involving multiple organs including lungs, skin, joint, eyes, liver, and heart. In the USA, the disease is most common among young adult African Americans, who have an estimated lifetime risk of 2.4%. Half of cases are found incidentally on chest radiography. Definitive diagnosis is obtained by transbronchial biopsy of pulmonary lesions or percutaneous biopsy of other involved organs.

The overwhelming majority of patients with sarcoidosis have lung involvement. Patients who are symptomatic often present with cough, dyspnea, and chest pain. Imaging classically reveals bilateral hilar lymphadenopathy. Later stages of the disease involve the lung parenchyma and can be characterized on imaging by peribronchovascular nodules, ground glass opacities, cysts, and fibrosis with traction bronchiectasis.

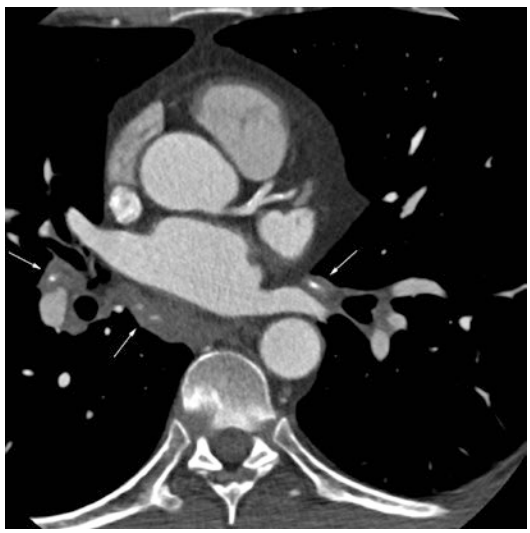

Fig. 11.13 Axial. Soft tissue windows show calcified lymphadenopathy (*arrows*)

11.13.5 Pearls and Pitfalls

Other causes of lymphadenopathy should be ruled out if biopsy is not performed. Sarcoidosis and granulomatous disease due to tuberculosis often causes calcified lymph nodes. In patients with untreated lymphoma and metastatic disease, the enlarged lymph nodes rarely calcify.

11.14 Case 11.13 Contributed by J. Lee and C. Smuclovisky

11.14.1 History

A 54-year-old male presented with a history of arrhythmias. The study was acquired for coronary venous mapping prior to defibrillator (ICD) insertion.

11.14.2 Findings

There is extensive mediastinal and bilateral hilar adenopathy containing scattered calcifications (Fig. 11.14a). There are perihilar infiltrates (Fig. 11.14b). There is marked dilatation of the left ventricle with diffuse thinning of the left ventricular walls. Abnormal density is seen in the lateral and inferolateral walls, with calcification

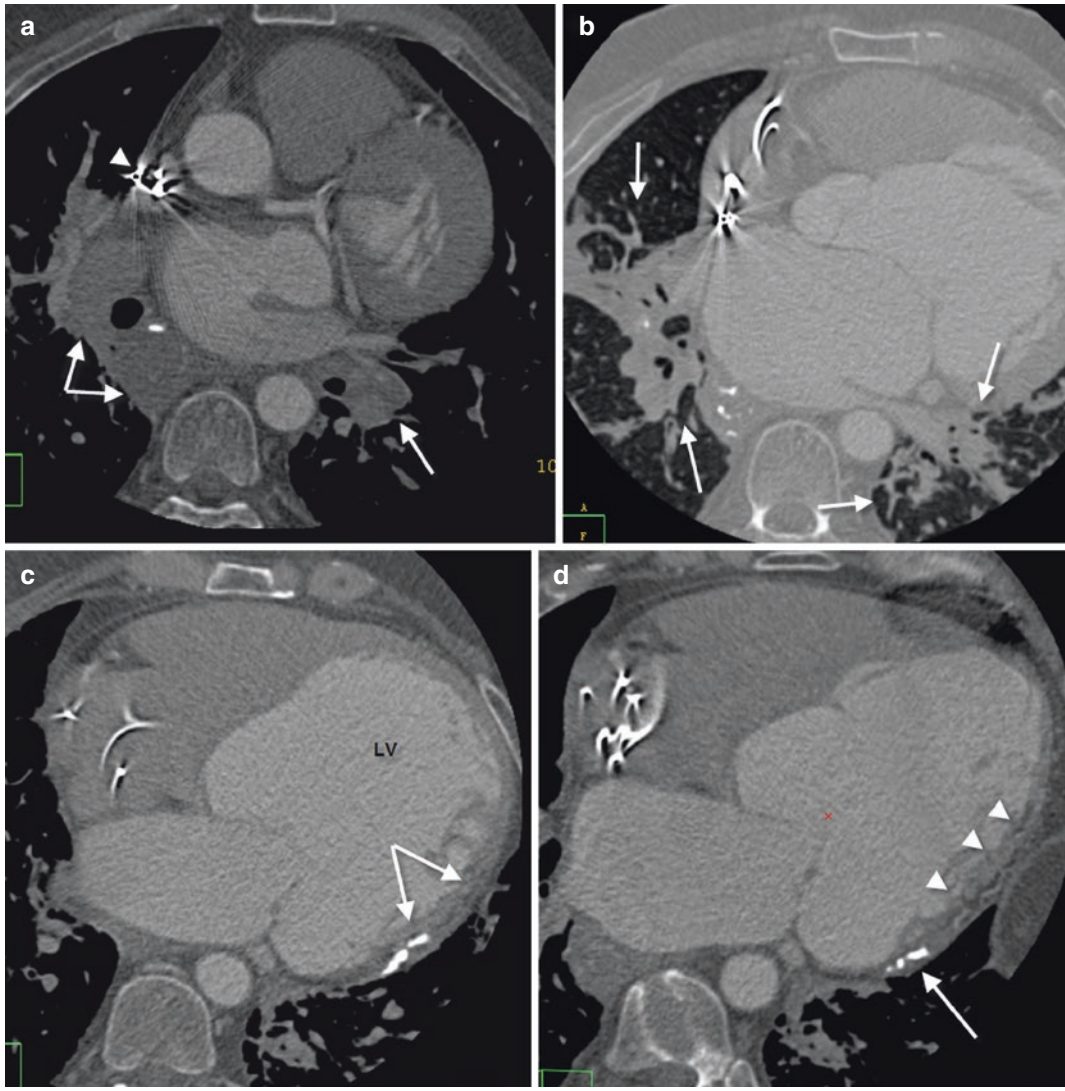

Fig. 11.14 (**a**) Axial. Hilar and mediastinal adenopathy from sarcoidosis (*arrows*). Metal artifact from electrode wire leads in the SVC (*arrowhead*). (**b**) Axial. Sarcoid perihilar infiltrates (*arrows*). (**c**) Axial. Diffuse thinning of the left ventricular walls, LV dilatation, and abnormal density in the lateral wall, which has epicardial calcification from myocardial sarcoidosis (*arrows*). (**d**) Axial. Pericardial thickening with calcification (*arrow*). Sarcoid infiltration of the myocardium (*arrowheads*)

(Fig. 11.14c). There is also focal posterolateral pericardial thickening with calcification (Fig. 11.14d). There is metal artifact in the right atrium from electrode wire leads.

11.14.3 Diagnosis

The diagnosis is granulomatous cardiomyopathy: sarcoidosis.

11.14.4 Discussion

Cardiomyopathies are commonly divided into a dilated or nondilated category. Within both of these groups, the myocardium may be hypertrophic or nonhypertrophic, and it may be accompanied by a restrictive (diastolic ventricular dysfunction) and/or congestive (systolic ventricular dysfunction) physiology. This form of classification may assist in specifying a cause for a cardiomyopathy based on the predominant clinical picture.

Sarcoidosis involving the heart is subclassified as a granulomatous cardiomyopathy. Clinically significant sarcoidosis involving the heart is uncommon and present in approximately 2–7% of patients with sarcoidosis. Clinically silent involvement of the heart has been described as greater than 20%.

Cardiac involvement may occur at any point during the course of the disease and may be present in the absence of pulmonary or systemic involvement. Sarcoidosis can involve any part of the heart, including the myocardium, endocardium, and pericardium. Cardiac sarcoidosis is a leading cause of the death among patients with sarcoidosis and with a mortality of up to 50–85% in autopsy series.

Arrhythmias or conduction defects are the most common cause of death; however, progressive heart failure due to massive granulomatous infiltration of the myocardium accounts for at least 25% of the deaths. Rapidly progressive and fatal congestive heart failure may be the presenting feature of sarcoidosis. Recurrent massive pericardial effusions or constrictive pericarditis accounts for less than 3% of cardiac deaths.

Conduction disturbances and arrhythmias are the most common cardiac manifestation secondary to granulomatous infiltration in the conduction system or ventricular walls. Variable degrees of AV block, bundle branch block, nonspecific intraventricular conduction delay, premature ventricular contractions, ventricular tachycardia, and other arrhythmias may be observed.

Extensive myocardial disease can result in a dilated cardiomyopathy and heart failure. The diagnosis of myocardial sarcoidosis can be difficult to make and may require a biopsy. Diagnostic studies commonly used are echocardiography, Holter monitoring, radionuclide scans with thallium, technetium pyrophosphate, and gallium. MRI and PET are also performed. Coronary angiography may be indicated to rule out obstructive coronary disease.

11.14.5 Pearls and Pitfalls

The accuracy of cardiac CTA in the evaluation of myocardial sarcoidosis has not been established. However, in the absence of significant or obstructive coronary artery disease, a granulomatous cardiomyopathy should be suspected in the presence of arrhythmias with abnormal density and calcifications in the myocardial walls and/or pericardium on the CTA.

11.15 Case 11.14

11.15.1 History

A 44-year-old male with history of hypertension presented to the emergency department with chest pain.

11.15.2 Findings

There was anterior mediastinal soft tissue lesion. Initial interpretation was thymoma versus thymic hyperplasia (Fig. 11.15).

11.15.3 Diagnosis

Thymic hyperplasia.

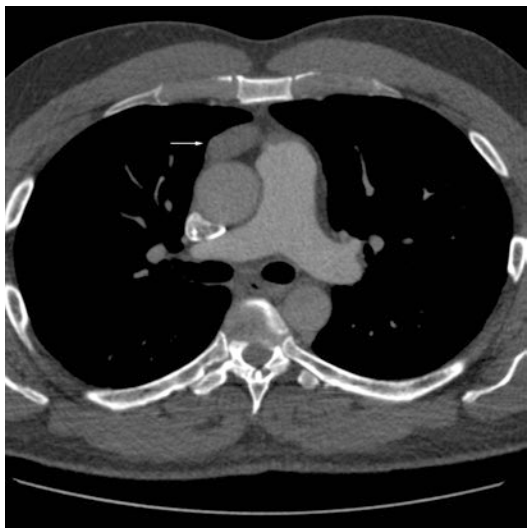

Fig. 11.15 Axial. Soft tissue windows show anterior mediastinal mass (*arrow*)

11.15.4 Discussion

The anterior mediastinum includes all structures behind the sternum, anterior to the pericardium, and below the level of the clavicles. Anterior mediastinal masses have a differential diagnosis often remembered with the mneumonic "4T's," which refers to masses arising from the thyroid, thymus, teratoma, and "terrible" lymphoma. Sometimes, the differential diagnosis is referred to as the "5T's," with the fifth "T" representing thoracic aorta aneurysm.

Thymoma comprises about 20% of mediastinal neoplasms and is the second most common mediastinal neoplasm in adults after lymphoma. Most patients are between 40 and 60 years of age with a slight male predominance. Most thymic tumors are either found incidentally or on workup of symptoms from a paraneoplastic syndrome (e.g., mysasthenia gravis) or mass effect (e.g., superior vena cava syndrome).

Up to half of patients with thymoma have myasthenia gravis, which is uncommon in thymic carcinoma. Other paraneoplastic syndromes can occur which affect the nervous system or muscle. Thymemectomy is usually curative for patients with a paraneoplastic syndrome associated with a thymoma and is often helpful in patients with thymic hyperplasia.

11.15.5 Pearls and Pitfalls

Anterior mediastinal lesions found in patients older than 40 years are likely to be lymphomatous or of thymic origin.

11.16 Case 11.15

11.16.1 History

A 75-year-old female presented to the emergency department with chest pain.

11.16.2 Findings

There is a soft tissue mass posterior to the heart containing multiple air foci (Fig. 11.16).

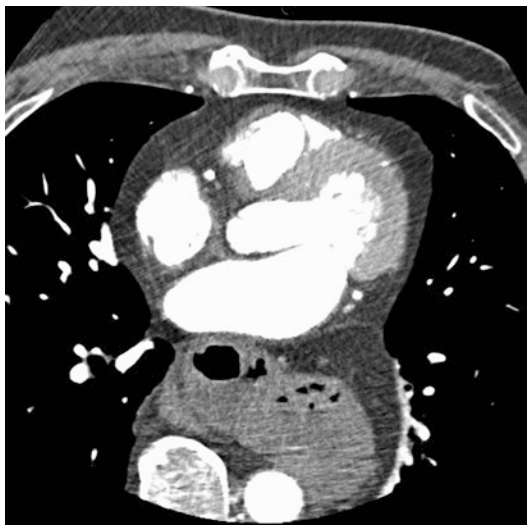

Fig. 11.16 Axial. Soft tissue windows show posterior mediastinal mass with multiple foci of air

11.16.3 Diagnosis

Hiatal hernia.

11.16.4 Discussion

A hiatal hernia occurs when a portion of the stomach protrudes upward into the thoracic cavity.

There are two major types of hiatal hernias: sliding and paraesophageal. Sliding hiatal hernias occur when the gastric-esophageal junction slides upward more than 1 cm past the esophageal hiatus. Sliding hernias are a well-known cause of gastric reflux disease although many patients are asymptomatic. Paraesophageal hernias are much less common (approximately 1% of hiatal hernias) and occur when the fundus of the stomach herniates above the diaphragm, while the gastric-esophageal junction remains in place at the level of the diaphragm. Paraesophageal hernias can cause serious complications such as obstruction or volvulus.

11.16.5 Pearls and Pitfalls

Hiatal hernias are quite common and manifest as an air-filled soft tissue density behind the heart, which can be connected to the stomach.

11.17 Case 11.16

11.17.1 History

A 74-year-old male presented for evaluation of coronary arteries. History is significant for prior four-vessel coronary artery bypass graft.

11.17.2 Findings

There is an intimal flap in the aorta that was visible from just distal to the subclavian artery to above the diaphragmatic hiatus. The false lumen is partially thrombosed (Figs. 11.17 and 11.18).

11.17.3 Diagnosis

Thoracic aorta dissection, Stanford type B.

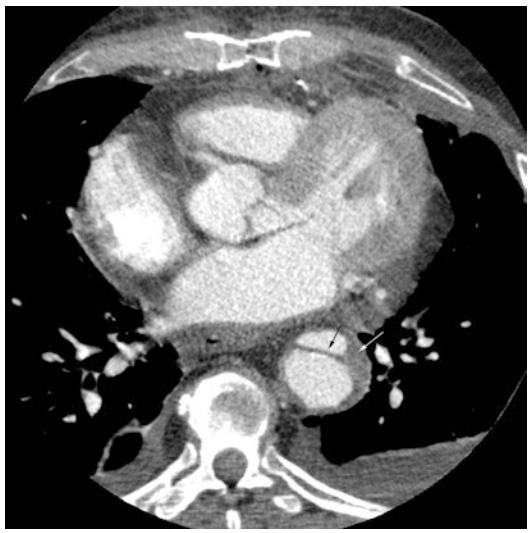

Fig. 11.17 Axial. Intimal flap (*short arrow*) is demonstrated in descending aorta. Partial thrombosis (*long arrow*) is seen in the false lumen

11.17.4 Discussion

Aortic dissection is a potentially life-threatening condition that requires prompt recognition to initiate appropriate management and reduce risk of death. Patients with an acute aortic dissection usually present with sudden onset of chest or back pain. Clinicians must have a high suspicion for aortic dissection because it is relatively rare, and most chest pain among patients who present to emergency departments is non-cardiovascular in origin.

Risk factors for aortic dissection include hypertension, collagen vascular disease, bicuspid aortic valve, a history of cardiac surgery, and trauma. Aortic dissection is most common in the older male population.

The most common classification system used today is the Stanford classification. Stanford type A involves the ascending aorta, and all other dissections are classified as type B. Dissections involving the ascending aorta (type A) carry a substantially worse prognosis because retrograde dissection can cause coronary artery occlusion, severe aortic regurgitation, and cardiac tamponade. Other complications of aortic dissection include hemothorax, limb ischemia, neurologic deficits caused by ischemic stroke or spinal cord ischemia, and abdominal viscera ischemia.

11.17.5 Pearls and Pitfalls

If an intimal flap is observed in the descending thoracic aorta on CCTA, assess the visible ascending aorta. A flap in the ascending aorta would be diagnostic of a more serious type A dissection.

The aortic root in adults is normally <3.7 cm, measured above the sinotubular junction. ECG-gated acquisition CTA is recommended in the evaluation of the thoracic aorta to avoid a pulsation artifact that may mimic a dissection in the proximal segment.

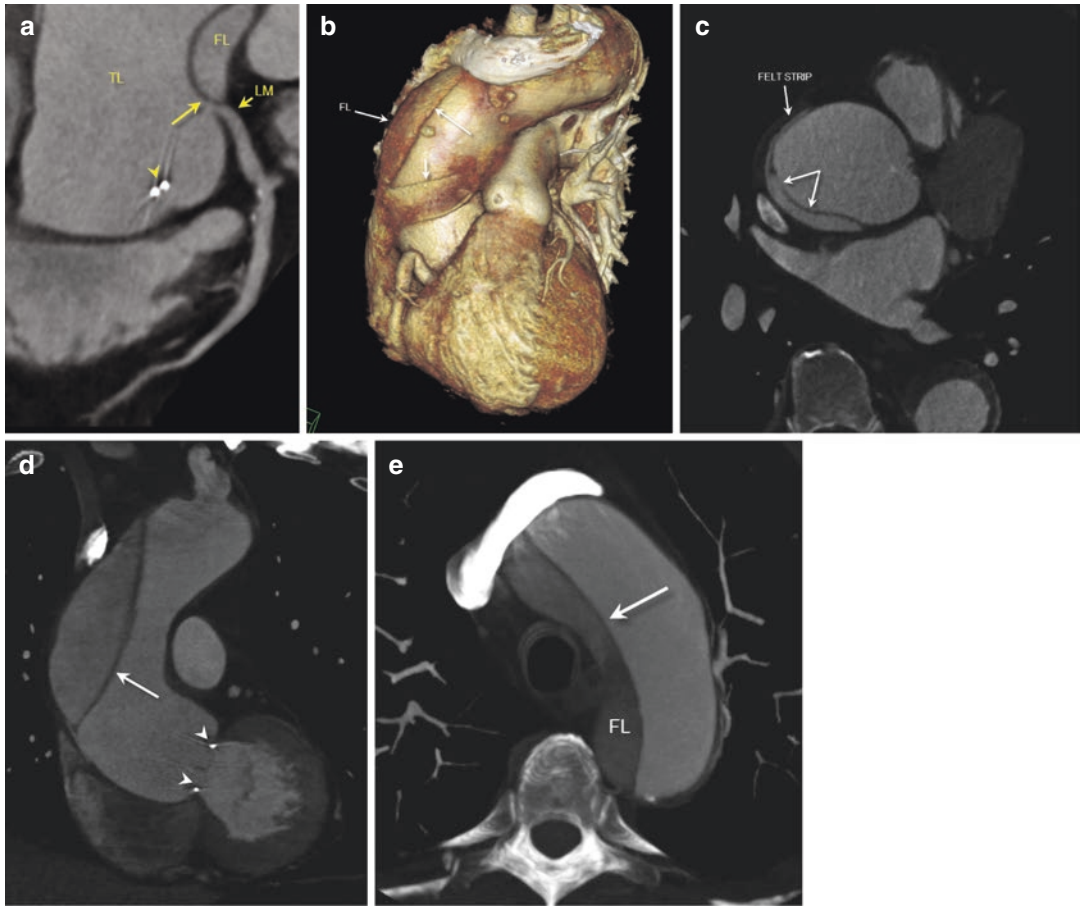

Fig. 11.18 (**a**) cMPR. Type A aortic dissection (*long arrow*) extending proximally to the aortic root and adjacent to the ostium of the left main coronary artery (LM). Metal artifact from bioprosthetic aortic valve (*arrowhead*). *TL* true lumen, *FL* false lumen. (**b**) Volume rendering. The false lumen (FL) has lower intensity on volume rendered 3D reconstruction. A felt strip (*short arrow*) has been placed in the proximal aorta to reinforce the suture lines related to the previous aortic valve replacement. (**c**–**e**) Axials and coronal: Type A aortic dissection—Contributed by J. Lee and C. Smuclovisky

11.18 Case 11.17 Contributed by J. Lee and C. Smuclovisky

11.18.1 History

An 82-year-old male presented with a history of chronic myocardial infarct (MI), CABG, and aortic aneurysm repair.

11.18.2 Findings

There is a large chronic transmural MI involving the anteroseptal and apical segments of the left ventricle. The status was post CABG and ascending aortic aneurysm repair (Fig. 11.19a–c).

11.18.3 Diagnosis

The diagnosis is chronic transmural left ventricular MI.

11.18.4 Discussion

Chronic myocardial infarcts of the left ventricle are well identified with CTA. Both transmural and subendocardial scarrings are visualized. The typical appearance of a transmural MI is thinning of the wall with low density from the scar. The scar may also contain calcification. Functional CTA demonstrates hypokinesis or akinesis in area of the MI. Subendocardial scars are identified as areas of low density in the subendocardial wall.

Transmural MI may develop aneurysmal dilatation, which may lead to a thrombus formation in the left ventricle (Fig. 11.19d, e). Rupture of the LV wall is most commonly fatal, and if the patient survives, can occasionally lead to formation of a pseudoaneurysm.

11.18.5 Pearls and Pitfalls

Normal left ventricular apical thinning may mimic an infarct. Normal LV systolic function with thickening in the apical segment and lack of significant disease in the LAD is helpful in substantiating the conclusion of a normal variant.

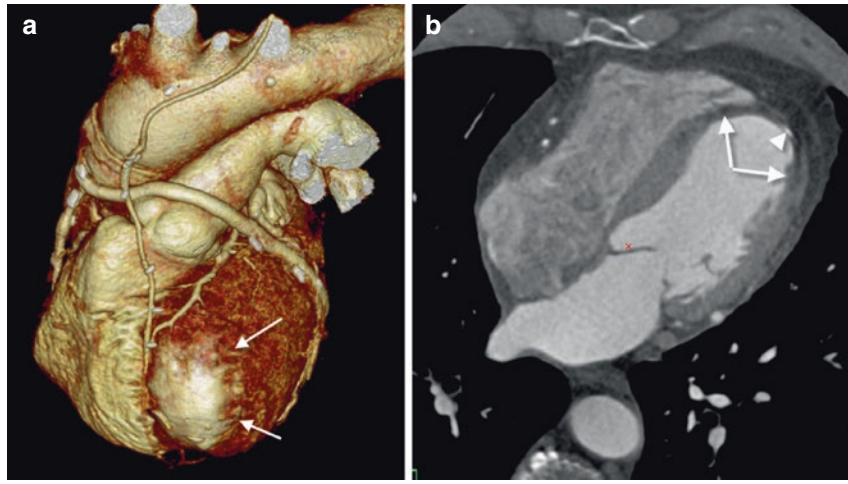

Fig. 11.19 (**a**) Volume rendering. Large anteroseptal and apical MI (*arrows*). Status post CABG and ascending aortic aneurysm repair. (**b** and **c**) Axial, sagittal. Transmural MI. Thinning and low density throughout the scar (*arrows*). Focal calcification in the infarcted wall (*arrowhead*). (**d** and **e**) Oblique sagittal and axial. LV aneurysm containing thrombus in another patient (*arrow*)

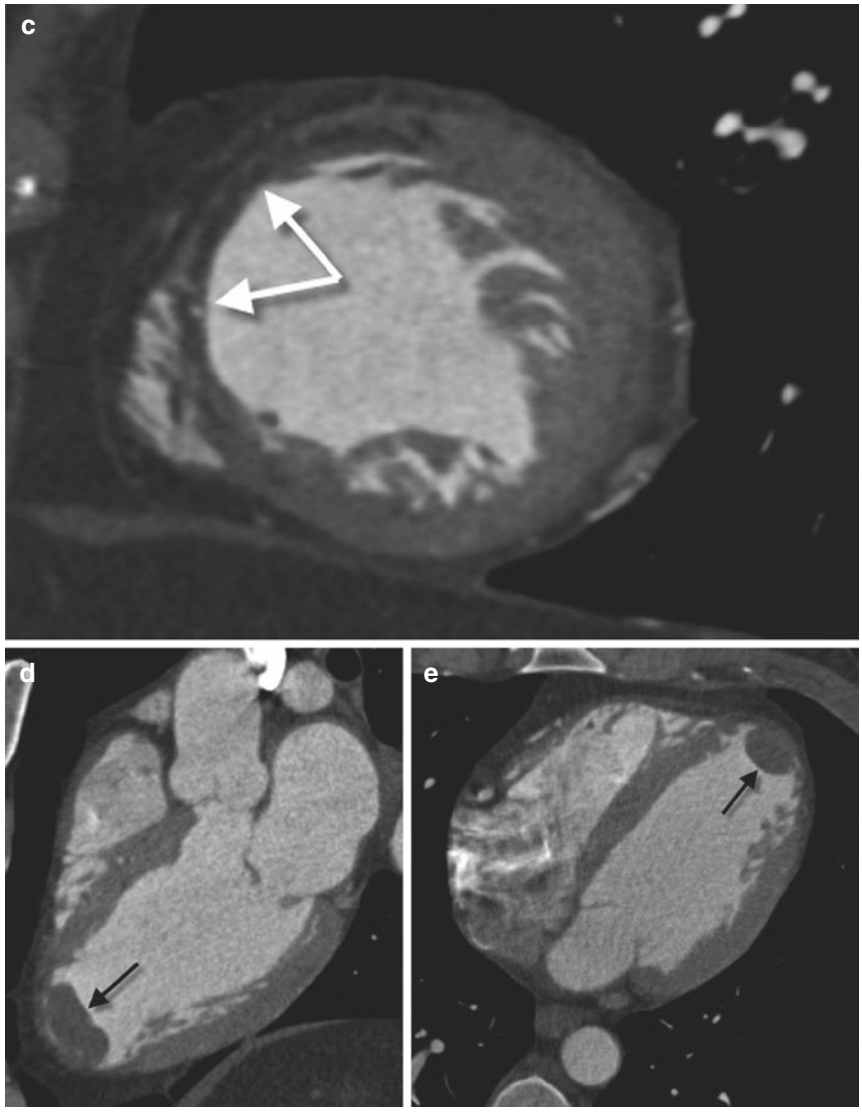

Fig. 11.19 (continued)

11.19 Case 11.18 Contributed by J. Lee and C. Smuclovisky

11.19.1 History

A 51-year-old female presented with a history of a dilated cardiomyopathy and previous surgery for mitral and tricuspid insufficiency.

11.19.2 Findings

There are hyperdense C-shaped rings in the mitral and tricuspid annuli (Fig. 11.20a–c).

11.19.3 Diagnosis

The diagnosis is surgical mitral and tricuspid repair with Cosgrove-Edwards (CE) annuloplasty rings.

11.19.4 Discussion

The patient had viral myocarditis in the previous 2 years with subsequent development of a dilated cardiomyopathy that was complicated by severe mitral and tricuspid regurgitation. Since she was not a candidate for heart transplant, surgical repair of the valves was performed. Diseased cardiac valves may be replaced or repaired. The CE annuloplasty rings are commonly used to repair the mitral and also tricuspid valves.

11.19.5 Pearls and Pitfalls

On CTA, the CE appears as a thin hyperdense C-shaped band in the annulus.

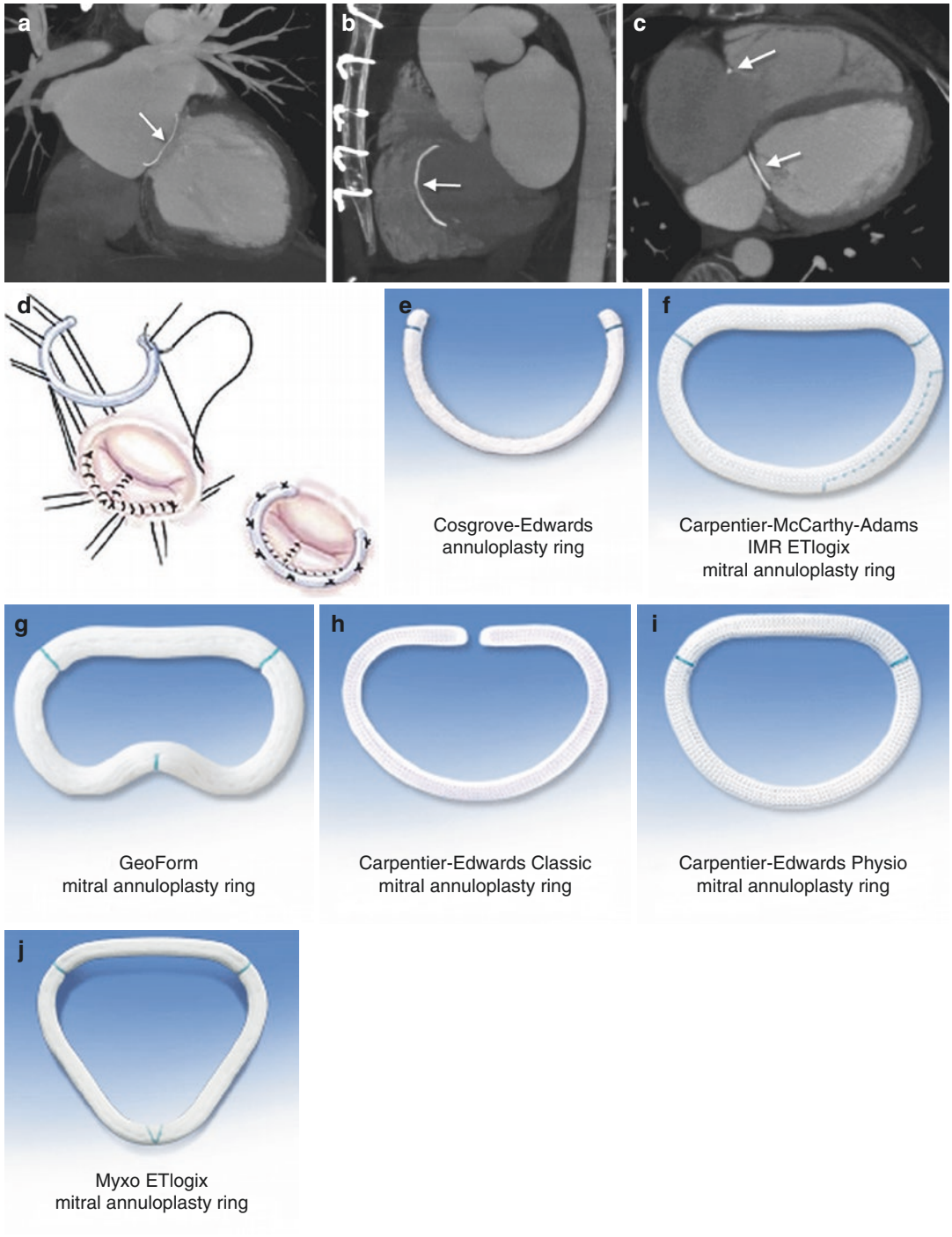

Fig. 11.20 (**a**) Coronal. Cosgrove-Edwards (CE) annuloplasty ring in the mitral annulus (*arrow*). (**b**) Sagittal. CE annuloplasty ring in the tricuspid annulus (*arrow*). (**c**) Axial. Partial visualization of the CE rings in the mitral and tricuspid annuli (*arrows*). (**d–j**) Surgical diagram and six different surgical devices used for valve repair (**d–j**, courtesy of Edwards Life sciences, Irvine, CA)

11.20 Case 11.19

11.20.1 History

A 62-year-old female presented to the emergency department with substernal chest pain and shortness of breath.

11.20.2 Findings

There is a well-circumscribed hypodense hepatic lesion that measures 7 cm. The lesion demonstrates peripheral nodular enhancement (Fig. 11.21).

11.20.3 Diagnosis

Hepatic hemangioma.

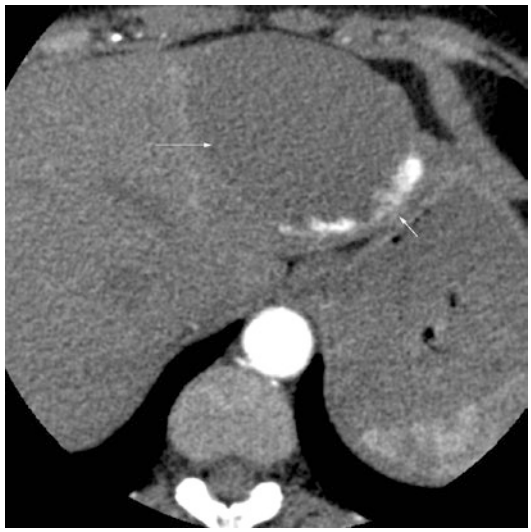

Fig. 11.21 Axial. Soft tissue windows show a large hypodense mass (*large arrow*) with peripheral nodular enhancement (*short arrow*)

11.20.4 Discussion

Hepatic masses in adults have a broad differential diagnosis of both benign and malignant diseases. Common benign etiologies include hepatic hemangioma (also called cavernous hemangiomas), focal nodular hyperplasia (FNH), hepatic adenoma, and idiopathic noncirrhotic portal hypertension. Malignant etiologies include hepatocellular carcinoma, cholangiocarcinoma, and metastatic disease. Parasitic infections and abscesses are less common etiologies. These lesions can often be diagnosed noninvasively by the presence of characteristic imaging features in conjunction with the patient's history and risk factors.

Hepatic hemangiomas are the most common benign hepatic tumor and have been estimated to occur in up to 20% of the population. They are more common in females by a 3:1 ratio. These lesions can be solitary or present in multiple lobes of the liver. Most patients are asymptomatic, but lesions larger than 4 cm may cause abdominal pain, nausea, or early satiety due to mass effect. Rarely, hemorrhage or thrombosis within the tumor can cause acute right upper quadrant pain.

On contrast-enhanced CT imaging, hepatic hemangiomas have early peripheral nodular enhancement and delayed filling in a centripetal pattern. Imaging is usually sufficient for diagnosis. Biopsy of this lesion carries risk of hemorrhage and is not usually necessary for confirmation of the diagnosis.

11.20.5 Pearls and Pitfalls

MRI and ultrasound can be used to assist in distinguishing hepatic hemangiomas from more serious conditions such as metastatic disease.

11.21 Case 11.20

11.21.1 History

An 84-year-old male underwent imaging to assess his coronary arteries. His history is significant prior coronary artery bypass graft for left anterior artery (LAD) disease.

11.21.2 Findings

There is a well-circumscribed 2 cm lesion in the right adrenal gland. The density is somewhat lower than that of soft tissue (Fig. 11.22).

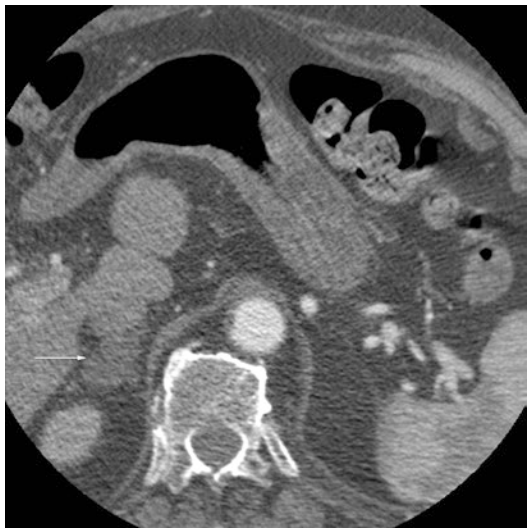

Fig. 11.22 Axial. Soft tissue window shows a hypodense mass within the right adrenal gland (*arrow*)

11.21.3 Diagnosis

Adrenal adenoma.

11.21.4 Discussion

Adrenal adenomas are common findings with use of advanced imaging such as multi-detector CT. Multiple studies have estimated that they are present in 5% or more of the general population. Adrenal adenomas are most often unilateral and nonfunctional. In one study, only 1% of adrenal lesions found incidentally proved to be adrenal carcinoma. Other important differential diagnoses include metastasis, pheochromocytoma, cyst, and hemorrhage.

Certain imaging characteristics can be used to distinguish benign from malignant adrenal lesions. Lesions that are smaller than 3 cm are most likely benign, while lesions greater than 5 cm are more likely malignant. Lesions with density less than 10 HU on a non-contrast CT are lipid-rich and most likely benign. On contrasted CT imaging, benign lesions typically have rapid contrast washout, while malignant lesions have delayed contrast washout. Moreover, lesions that show no growth on follow-up imaging are usually benign.

11.21.5 Pearls and Pitfalls

A density slightly lower than that of soft tissue is often typical of adrenal adenomas. However, dedicated abdominal CT or MRI is often necessary to further characterize incidentally found adrenal lesions.

11.22 Case 11.21

11.22.1 History

An 81-year-old female underwent coronary artery imaging after a positive stress test.

11.22.2 Findings

The abdominal aorta is abnormally enlarged (4.3 cm) and contains mural thrombus (Fig. 11.23).

11.22.3 Diagnosis

Abdominal aortic aneurysm (AAA).

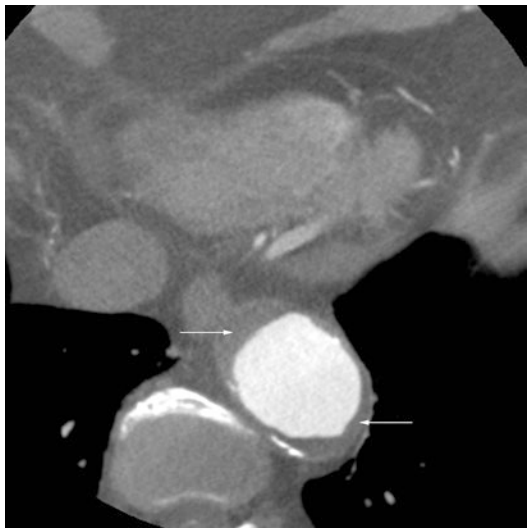

Fig. 11.23 Axial. The abdominal aorta is enlarged with mural thrombus (*arrows*)

11.22.4 Discussion

Early recognition and treatment of this disease is important because a ruptured AAA is a life-threatening emergency. It is estimated that about 15,000 deaths are attributed to AAA in the USA each year.

Abdominal aortic aneurysms are defined as a focal dilation of the aorta to more than 50% of its normal size. Most men and women have an aortic diameter less than 2 cm; therefore, the upper limit of normal is considered to be 3 cm.

Risk factors for AAA include smoking, increasing age, male gender, atherosclerosis, and family history of AAA. Up to 8% of men over 65 are found to have AAA. One study found that prevalence in men peaked at age 80, while prevalence in women kept increasing with age. Patients under age 50 are extremely unlikely to have a clinically significant AAA.

Management of asymptomatic, unruptured AAA is based on size. Elective treatment is recommended for aneurysms greater than 5.5 cm or those with growth rate greater than 1 cm per year. In patients who do not meet these criteria, the risk of surgery is greater than the risk of rupture, and it is recommended that they undergo serial surveillance.

11.22.5 Pearls and Pitfalls

The U.S. Preventative Services Task force recommends a one-time screening with ultrasound to detect AAA in men between ages 65 and 75 with history of smoking.

11.23 Case 11.22

11.23.1 History

A 35-year-old male presented to the emergency department with shortness of breath and chest pain.

11.23.2 Findings

The liver is enlarged and demonstrated low density due to fatty infiltration (Fig. 11.24).

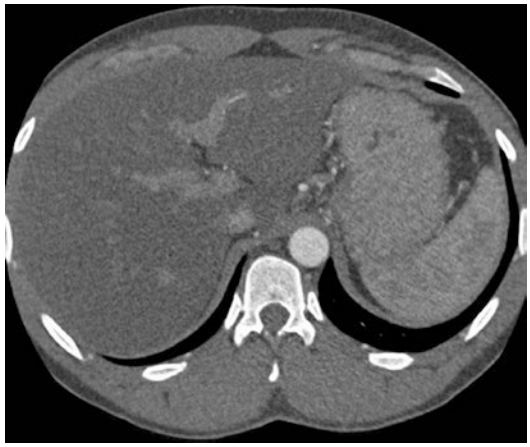

Fig. 11.24 Axial. Soft tissue windows show fatty infiltration of the liver

11.23.3 Diagnosis

Hepatic steatosis (fatty infiltration).

11.23.4 Discussion

Fatty infiltration of the liver is a nonspecific finding that can occur in response to insult from injury, toxins, or other diseases. When hepatic steatosis is present without any known cause, the condition is termed nonalcoholic fatty liver disease (NAFLD). The risk of NAFLD is that it may progress to cirrhosis and ultimately liver failure.

NAFLD is subdivided into two entities: nonalcoholic fatty liver (NAFL) and nonalcoholic steatohepatitis (NASH). Histologically, NASH shows evidence of hepatocellular injury and fibrosis, which is absent in NAFL.

NAFLD is estimated to have a 20% worldwide prevalence. Risk factors include obesity, diabetes mellitus, dyslipidemia, and metabolic syndrome. Most patients are asymptomatic from NAFLD, and a variable number present with hepatomegaly. Biopsy is not always necessary for diagnosis, but is the only way to distinguish NAFL from NASH.

11.23.5 Pearls and Pitfalls

Fatty infiltration of the liver reduces its attenuation to lower than that of the spleen. A normal liver has attenuation higher than that of the spleen.

11.24 Case 11.23

11.24.1 History

A 51-year-old male presented to the emergency department with chest pain.

11.24.2 Findings

There are compression fractures of T6, T7, and T10. There is no retropulsion of bony fragments into the spinal canal (Figs. 11.25 and 11.26).

11.24.3 Diagnosis

Multi-level thoracic compression fractures.

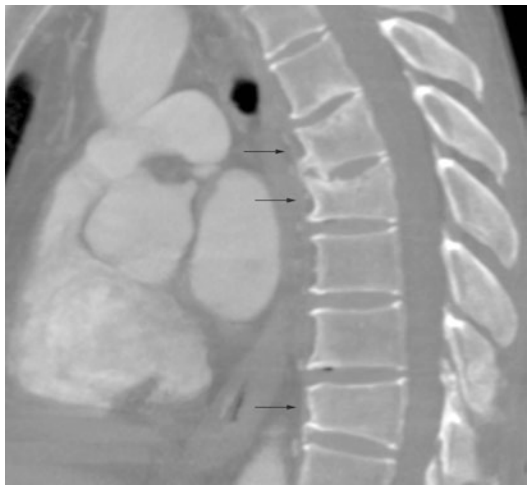

Fig. 11.25 Sagittal. Bone show multiple compression fractures (*arrows*) with loss of anterior vertebral body height

11.24.4 Discussion

Vertebral body compression fractures most commonly occur in the setting of osteoporosis, malignancy, infection, and trauma. Compression fractures are frequently located in the mid-thoracic spine or at the thoracolumbar junction.

Acute compression fractures can be caused by minor trauma such as bending, lifting, or coughing, and most of patients present with severe back pain. Chronic compression fractures may progress slowly over time, and patients may present with asymptomatic loss of height and kyphosis. Neurologic impairment can occur if there is associated compression of the spinal cord or nerve roots. In cases of severe kyphosis of the thoracic spine, patients can develop impaired respiratory function.

Pain caused by compression fractures can be managed conservatively with a back brace to provide support for the spine. Vertebroplasty and kyphoplasty are also effective techniques to reduce pain. To perform a vertebroplasty, cement is injected percutaneously through the pedicles into the vertebral body to stabilize and prevent further collapse of the vertebral body. The technique for kyphoplasty is similar, except that it also uses balloon inflation within the vertebral body to help restore vertebral body height. Surgery may be appropriate if there is spinal cord compression with neurologic deficit or frank instability of the spine.

11.24.5 Pearls and Pitfalls

Pathologic fractures should be followed up with MRI to assess for malignancy or infection. MRI will also evaluate for spinal cord compression.

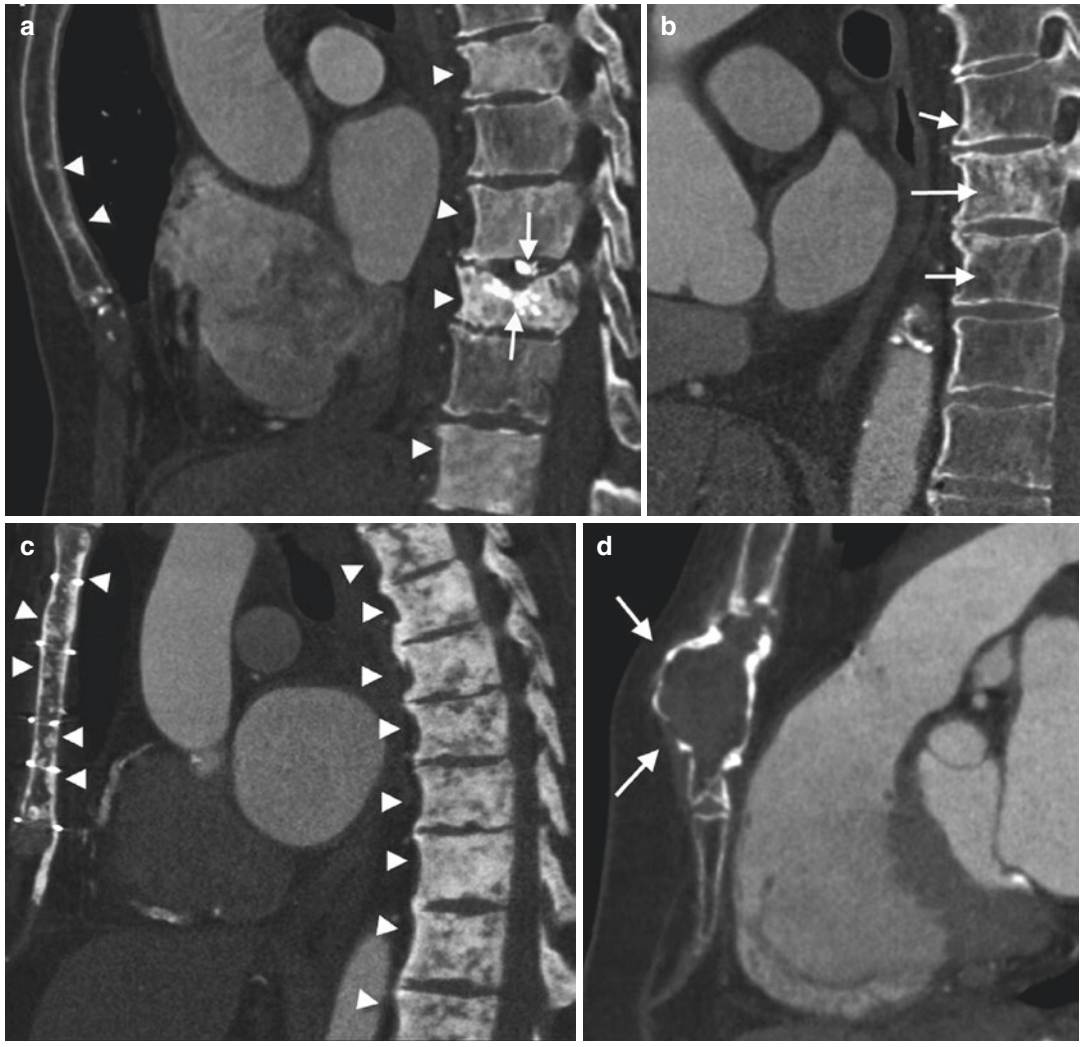

Fig. 11.26 (**a**) Sagittal. Widespread metastatic bone disease from breast carcinoma (*arrowheads*). Status post vertebroplasty with injection of methylmethacrylate into a vertebral body with a small amount of leakage of the cement into the disc space (*long arrows*). (**b**) Sagittal. B-cell lymphoma involving the thoracic spine (*arrows*). (**c**) Sagittal. Widespread bony blastic metastases from prostate carcinoma (*arrowheads*). Status post CABG. (**d**) Sagittal. Expansile lytic lesion in the lower sternum (*arrows*) incidentally found in a 91-year-old female with intractable chest pain. Diagnosis: myeloma—Contributed J. Lee and C. Smuclovisky

11.25 Case 11.24 Contributed by J. Lee and C. Smuclovisky

11.25.1 Extracoronary Disease

During the interpretation of cardiac CT, extracoronary findings are frequently identified. It is important to evaluate the entire anatomy in the field of view in order not to miss a clinically relevant finding (Fig. 11.27a–h).

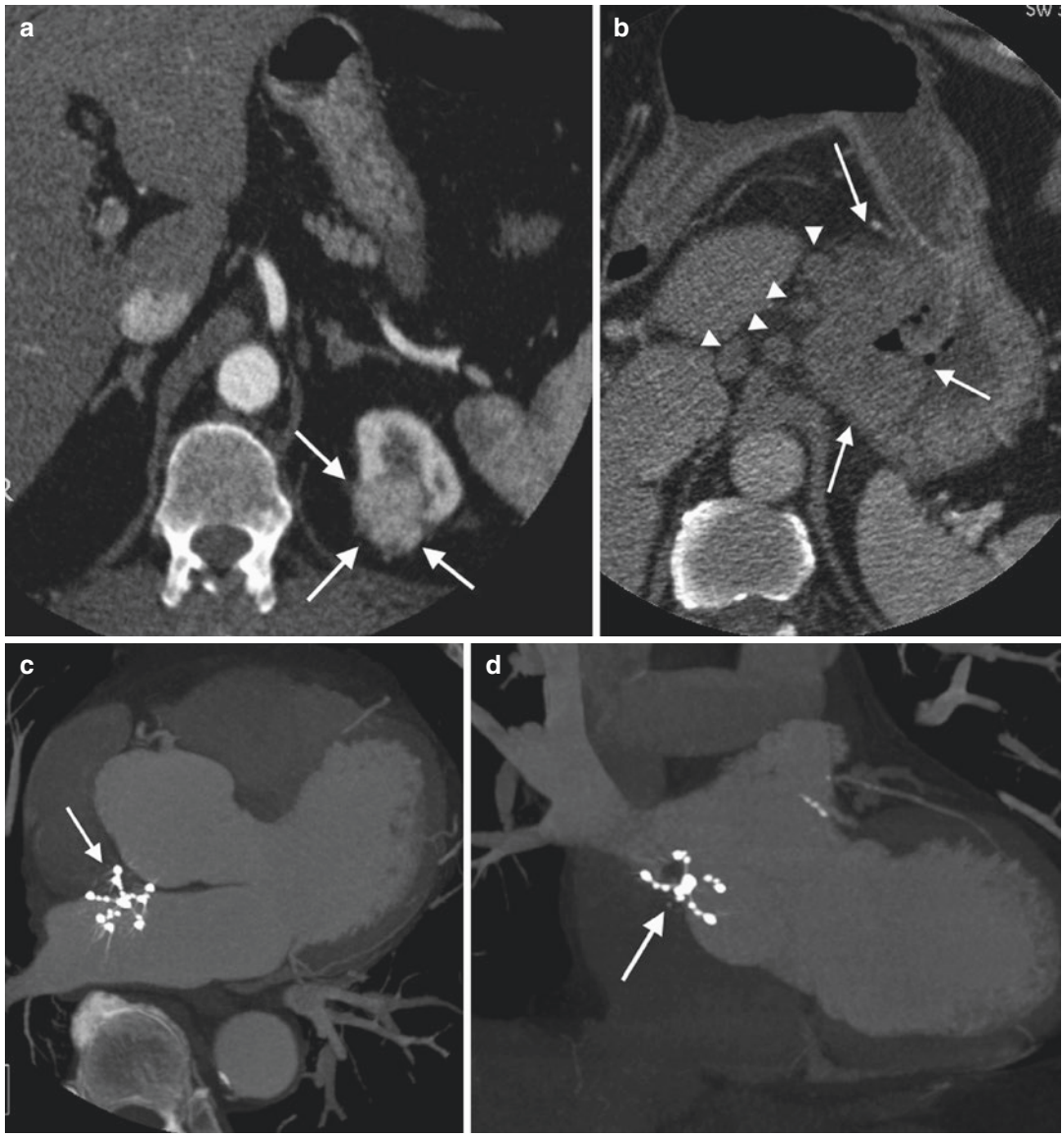

Fig. 11.27 (**a**) Axial. Left renal upper pole carcinoma (*arrows*). (**b**) Axial. Gastric carcinoma with ulceration of the tumor (*long arrow*) and adjacent adenopathy (*arrowheads*). (**c** and **d**) Axial and coronal maximum intensity projection. PFO closure device (*arrow*). (**e** and **f**) Coronal and axial. Foreign body in the right pulmonary artery from a wire lost during placement of an ICD device (*arrows*). ICD wires in the SVC (**f**, *long arrow*). Status post CABG. (**g**) Sluggish filling in the LA appendage; questionable for clot (*arrow*). (**h**) Immediate delay acquisition demonstrates complete filling with no evidence of thrombus (*arrow*)

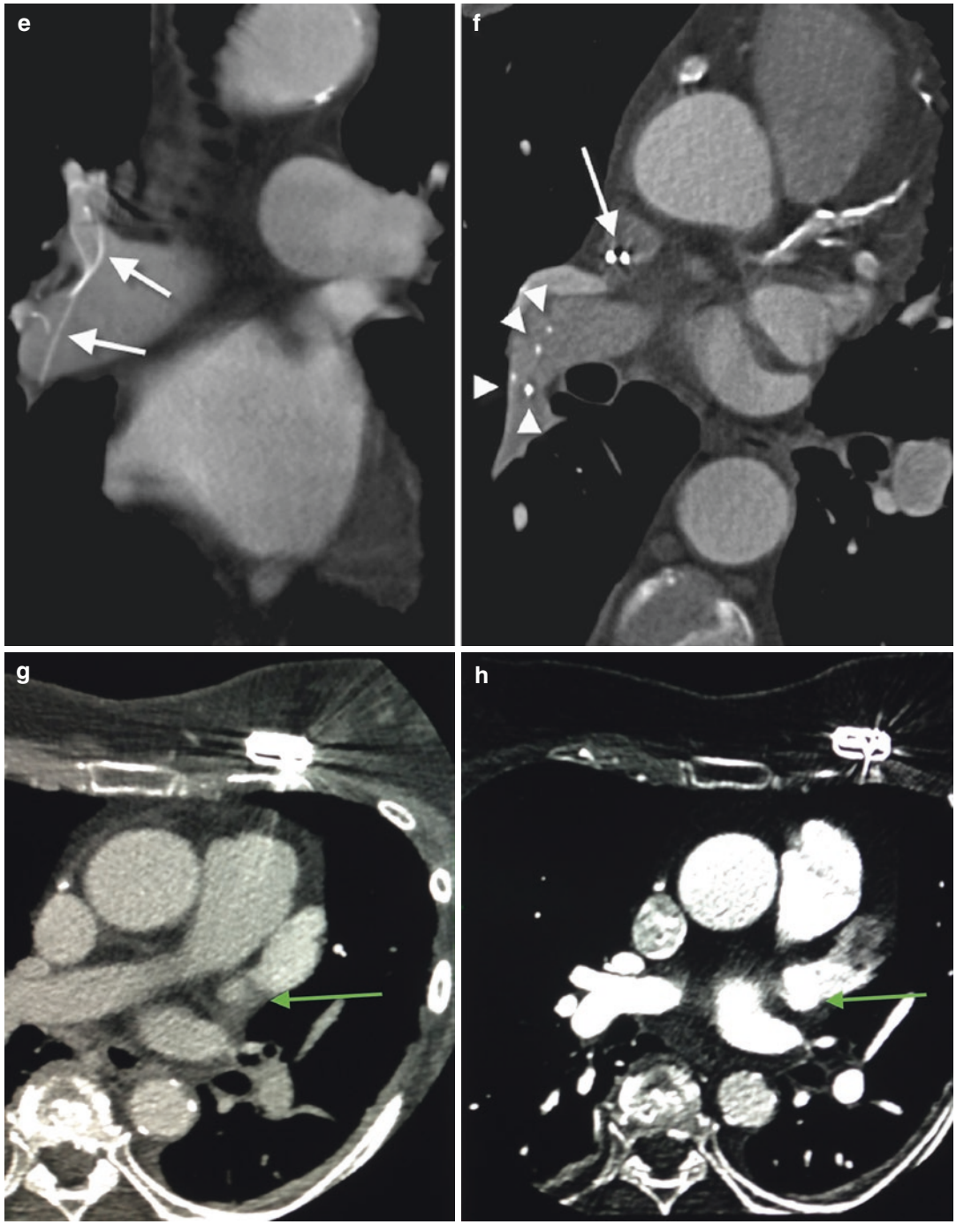

Fig. 11.27 (continued)

References

1. Hunold P, Schmermund A, Seibel RM, Gronemeyer DH, Erbel R. Prevalence and clinical significance of accidental findings in electron beam tomographic scans for coronary artery calcification. Eur Heart J. 2001;22:1748–58.
2. Macmahon H, Austin JH, Gamsu G, et al. Guidelines for management of small pulmonary nodules detected on CT scans: a statement from the Fleischner society. Radiology. 2005;237:395–400.

Suggested Reading

Abbara S, Kalan MM, Lewicki AM. Intrathoracic stomach revisited. AJR Am J Roentgenol. 2003;181:403–14.

Baughman RP, Teirstein AS, Judson MA, et al. Clinical characteristics of patients in a case control study of sarcoidosis. Am J Respir Crit Care Med. 2001;164:1885–9.

Bonder A, Afdhal N. Evaluation of liver lesions. Clin Liver Dis. 2012;16:271–83.

Bosanko CM, Korobkin M, Fantone JC, et al. Lobar primary pulmonary lymphoma: CT findings. J Comput Assist Tomogr. 1991;15(4):679–82.

Chakko S. Pleural effusion in congestive heart failure. Chest. 1990;98:521–2.

Delmas PD, van de Langerijt L, Watts NB, Eastell R, Genant H, Grauer A, Cahall DL. Underdiagnosis of vertebral fractures is a worldwide problem: the IMPACT study. J Bone Miner Res. 2005;20:557–63.

Descombes E, Gardiol D, Leuenberger P. Transbronchial lung biopsy: an analysis of 530 cases with reference to the number of samples. Monaldi Arch Chest Dis. 1997;52:324–9.

Franquet T. Imaging of pneumonia: trends and algorithms. Eur Respir J. 2001;18:196–208.

Gharib AM, Stern EJ. Radiology of pneumonia. Med Clin North Am. 2001;85:1461–91. x

Haniuda M, Kondo R, Numanami H, et al. Recurrence of thymoma: clinicopathological features, re-operation, and outcome. J Surg Oncol. 2001;78:183–8.

Jang HJ, Kim TK, Lim HK, et al. Hepatic hemangioma: atypical appearances on CT, MR imaging, and sonography. AJR Am J Roentgenol. 2003;180:135–41.

Kahrilas PJ, Kim HC, Pandolfino JE. Approaches to the diagnosis and grading of hiatal hernia. Best Pract Res Clin Gastroenterol. 2008;22:601–16.

Konstantinides SV, Torbicki A, Agnelli G, et al. 2014 ESC guidelines on the diagnosis and management of acute pulmonary embolism. Eur Heart J. 2014;35:3033–69.

Lee SS, Park SH. Radiologic evaluation of nonalcoholic fatty liver disease. World J Gastroenterol. 2014;20:7392–402.

Light RW, MacGregor MI, Luchsinger PC, Ball WC. Pleural effusions: the diagnostic separation of transudates and exudates. Ann Intern Med. 1972;77:507–13.

Lillington GA, Caskey CI. Evaluation and management of solitary and multiple pulmonary nodules. Clin Chest Med. 1993;14:111–9.

Lombardi G, Zustovich F, Nicoletto MO, et al. Diagnosis and treatment of malignant pleural effusion: a systematic literature review and new approaches. Am J Clin Oncol. 2010;33:420–3.

Midthun DE, Swensen SJ, Jett JR. Approach to the solitary pulmonary nodule. Mayo Clin Proc. 1993;68:378–85.

Mueller J, Jeudy J, White CS. Cardiac CT angiography after coronary artery bypass surgery: prevalence of incidental findings. AJR Am J Roentgenol. 2007;189:414–9.

Onuma Y, Tanube K, Hatori M, et al. Non-cardiac findings in coronary imaging with multi-detector computed tomography. J Am Coll Cardiol. 2006;48:402–6.

Patel U, Skingle S, Campbell GA, Crisp AJ, Boyle IT. Clinical profile of acute vertebral compression fractures in osteoporosis. Br J Rheumatol. 1991;30:418–21.

Pickhardt PJ, Park SH, Hahn L, et al. Specificity of unenhanced CT for non-invasive diagnosis of hepatic steatosis: implications for the investigation of the natural history of incidental steatosis. Eur Radiol. 2012;22:1075–82.

Rybicki BA, Major M, Popovich J Jr, et al. Racial differences in sarcoidosis incidence: a 5-year study in a health maintenance organization. Am J Epidemiol. 1997;145:234–41.

Savage JW, Schroeder GD, Anderson PA. Vertebroplasty and kyphoplasty for the treatment of osteoporotic vertebral compression fractures. J Am Acad Orthop Surg. 2014;22:653–64.

Smith SB, Geske JB, Maguire JM, et al. Early anticoagulation is associated with reduced mortality for acute pulmonary embolism. Chest. 2010;137:1382–90.

Statement on sarcoidosis. Joint Statement of the American Thoracic Society (ATS), the European Respiratory Society (ERS) and the World Association of Sarcoidosis and Other Granulomatous Disorders (WASOG) adopted by the ATS Board of Directors and by the ERS Executive Committee. Am J Respir Crit Care Med. 1999;160:736–55.

Stein PD, Beemath A, Matta F, et al. Clinical characteristics of patients with acute pulmonary embolism: data from PIOPED II. Am J Med. 2007;120:871–9.

Ströbel P, Bauer A, Puppe B, et al. Tumor recurrence and survival in patients treated for thymomas and thymic

squamous cell carcinomas: a retrospective analysis. J Clin Oncol. 2004;22:1501–9.
Thomas KW, Hunninghake GW. Sarcoidosis. JAMA. 2003;289:3300–3.
Van Belle A, Büller HR, Huisman MV, et al. Effectiveness of managing suspected pulmonary embolism using an algorithm combining clinical probability, D-dimer testing, and computed tomography. JAMA. 2006;295:172–9.
Yun EJ, Choi BI, Han JK, et al. Hepatic hemangioma: contrast-enhancement pattern during the arterial and portal venous phases of spiral CT. Abdom Imaging. 1999;24:262–6.

Structural Intervention: A Cardiologist's Perspective

12

John J. Lee, Igor F. Palacios, and Alexander Llanos

12.1 Case 12.1

12.1.1 History

A 76-year-old male presenting with chest discomfort and shortness of breath.

12.1.2 Findings

Cardiac CT Angiogram (CCTA) demonstrated multi-vessel coronary disease with a critical lesion that was very short in length of the ostial LAD (Fig. 12.1a–c).

Coronary angiography demonstrated a critical stenosis involving the ostial LAD involving the bifurcation of a large first diagonal artery. Mild non-obstructive disease involving the circumflex artery and the right coronary artery (Fig. 12.1d, e).

12.1.3 Diagnosis

Critical ostial LAD disease (short lesion length ~3 mm).

12.1.4 Discussion

The ability for the interventional cardiologist to know the distribution of coronary stenosis prior to arrival to the cath lab facilitates better defining lesion severity with invasive angiography. In particular, ostial coronary lesions of short length can potentially be overlooked at the time of cardiac catheterization due to overlapping of vessel segments. This patient underwent a minimally invasive off-pump coronary bypass surgery consisting of a LIMA to the LAD. Description of the coronary anatomy by CCTA allows for more detailed discussion with our patients regarding options for therapy prior to their arrival to the cath lab for invasive angiography where they may receive sedation agents.

J.J. Lee, MD
Department of Medicine,
University of Miami at Holy Cross Hospital,
Fort Lauderdale, FL, USA

I.F. Palacios, MD
Department of Medicine and Cardiology,
Massachusetts General Hospital,
Boston, MA, USA

A. Llanos, MD (✉)
Department of Cardiology, Holy Cross Hospital,
Jim Morgan Heart and Vascular Research Institute,
Fort Lauderdale, FL, USA
e-mail: alexander.llanos@holy-cross.com

C. Smuclovisky (ed.), *Coronary Artery CTA*, https://doi.org/10.1007/978-3-319-66988-5_12

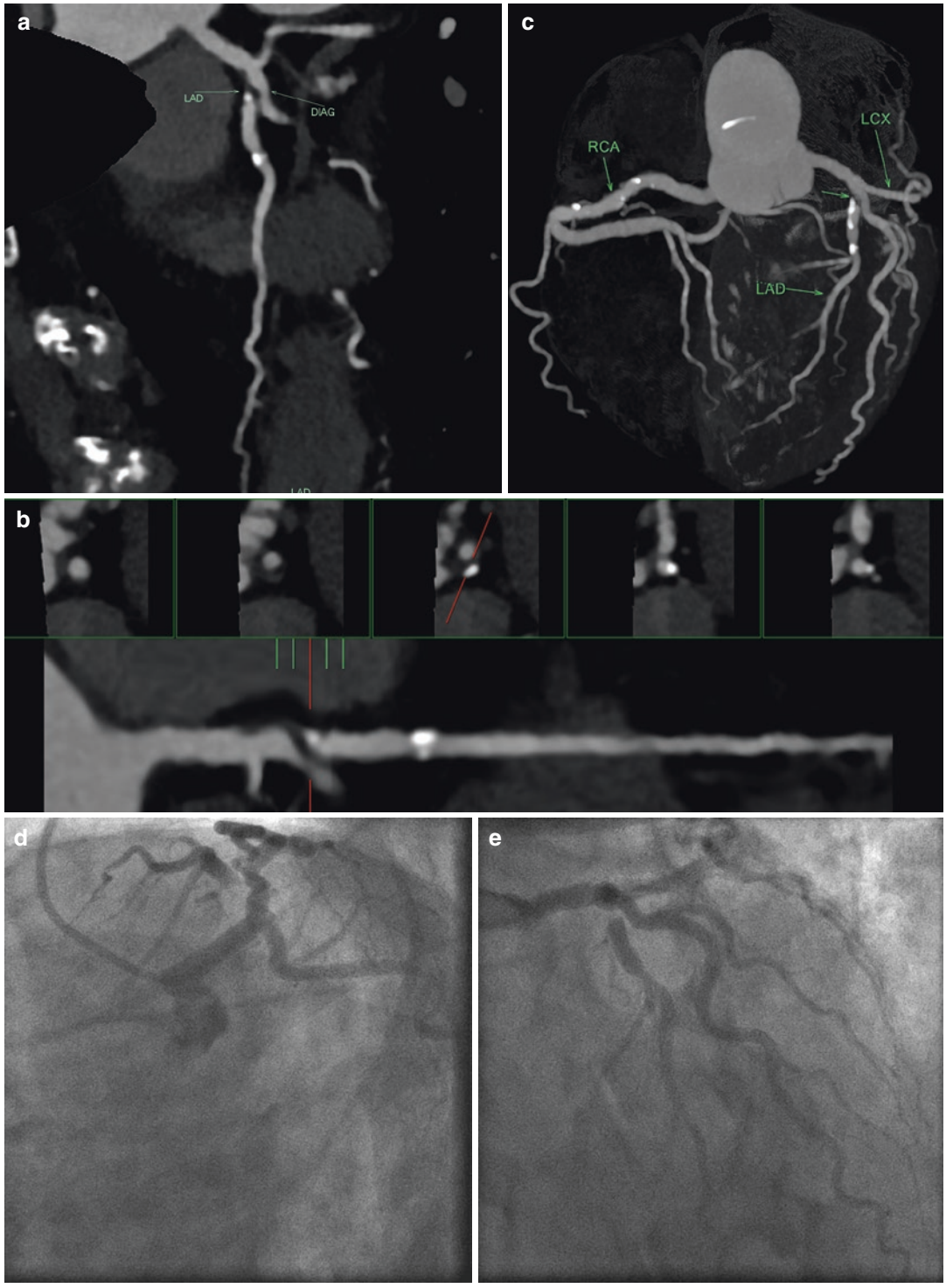

Fig. 12.1 (**a**) cMPR of LAD (**b**) stretched MPR of LAD (**c**) coronary tree view (**d** and **e**) coronary angiograms

12.2 Case 12.2

12.2.1 History

A 67-year-old male with previous history of coronary artery disease status post percutaneous coronary intervention to the right coronary artery and the left anterior descending, now presenting with recurrent chest pain.

12.2.2 Findings

CCTA demonstrated hard and soft plaque in the mid LAD past the first diagonal that appeared to be hemodynamically significant with a stenosis of at least 70% (Fig. 12.2a, b). There was an occluded proximal RCA stent (Fig. 12.2c).

Coronary angiography demonstrated a well-collateralized right coronary system from the left coronary system. Moderate disease in the left anterior descending system at the distal edge of a previously placed stent: non-flow limiting lesion as evaluated by both angiography and FFR (FFR 0.88) (Fig. 12.2d, e).

12.2.3 Diagnosis

Non-flow limiting lesion in the LAD.

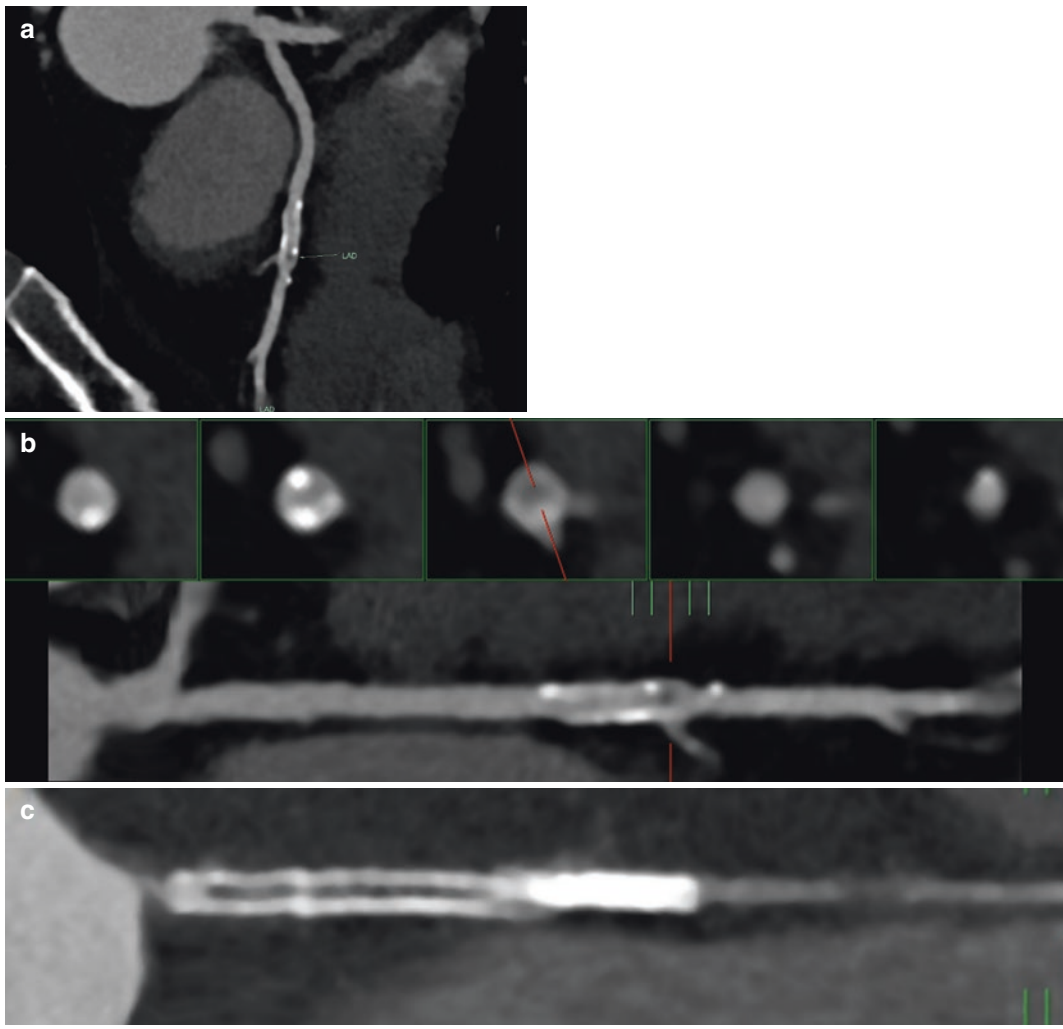

Fig. 12.2 (**a**) cMPR of LAD (**b**) stretched MPR of LAD (**c**) stretched MPR of RCA (**d** and **e**) LAD and LCX coronary angiogram (**f**) RCA Coronary angiogram demonstrating proximal total occlusion (**g**) Coronary angiogram demonstrating left to right collaterals

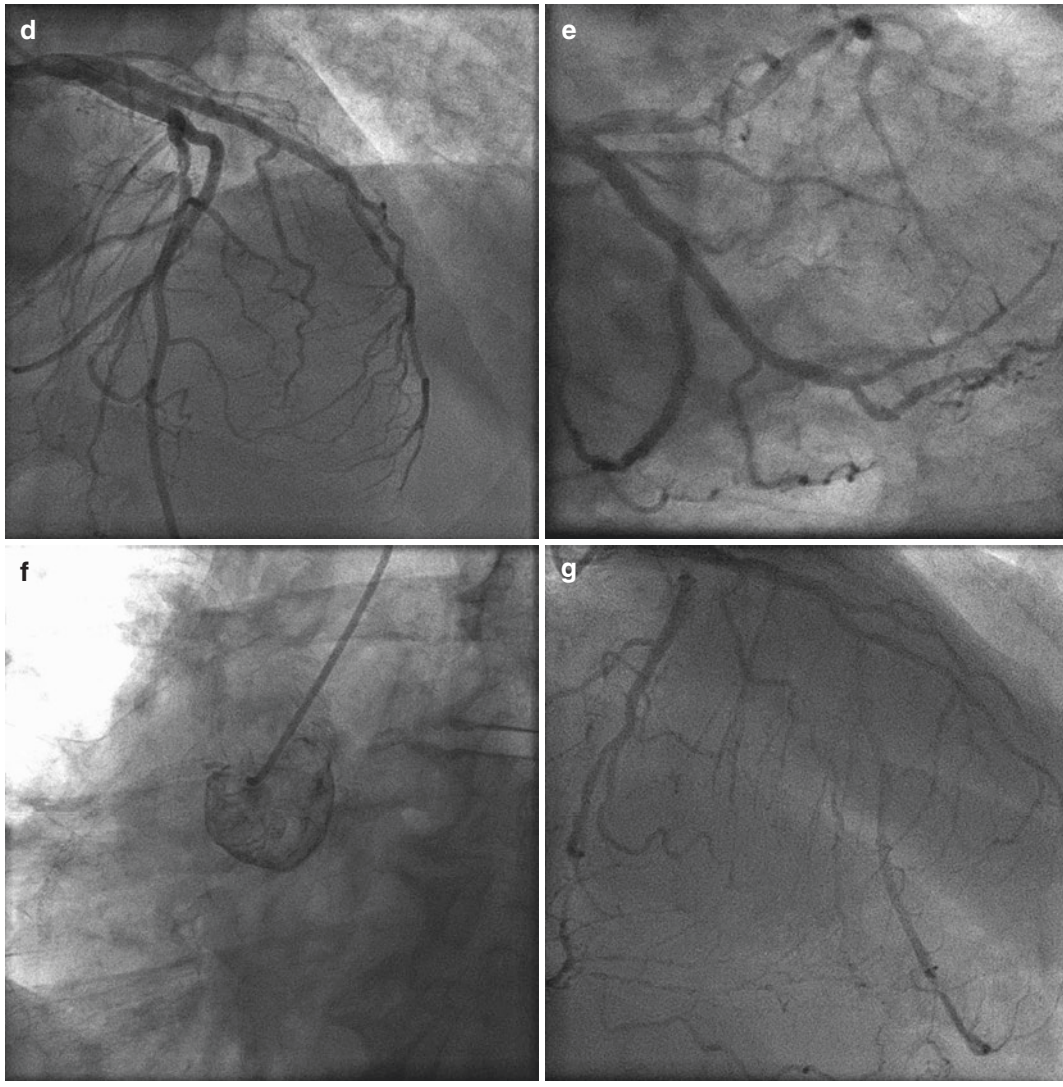

Fig. 12.2 (continued)

12.2.4 Discussion

Being able to understand the coronary anatomy prior to arriving to the cath lab is helpful. The planned addition of physiologic coronary assessment by means of flow evaluation is an exciting future advancement that will help to further enhance the utility of CT angiography to the cardiologist.

This patient was found to have an occluded proximal RCA and a 70% lesion in the LAD by coronary CTA. He was further evaluated with invasive angiography which verified the above findings. FFR evaluation of the LAD determined that the lesion was not significantly flow limiting and the decision was made for medical therapy. As detailed in previous chapter, the addition of fractional flow reserve to CCTA imaging will better allow us to determine care options.

12.3 Case 12.3

12.3.1 History

A 52-year-old male with past medical history of hyperlipidemia and hypertension who presented with exertional chest discomfort.

12.3.2 Findings

CCTA demonstrated critical two vessel disease involving the LAD and LCX. There was a chronic total occlusion of the mid LAD with collateral filling of the distal LAD. There was suspicion of high-grade obstruction in the proximal to mid circumflex (Fig. 12.3a, b).

Invasive coronary angiography was performed and demonstrated a 50% proximal LAD lesion followed by a total occlusion in the distal segment of the LAD with a well-collateralized apical LAD segment (anterograde bridging collateral). The left circumflex had a mid 85% lesion and the right coronary had a mid 70% lesion.

12.3.3 Diagnosis

Severe two vessel coronary artery disease of the LAD and LCX.

12.3.4 Discussion

We performed three vessel fractional flow reserve and found the RCA lesion to be non-flow limiting (FFR = 0.90). Evaluation of the proximal LAD 50% lesion also demonstrated non-flow limiting value (FFR = 0.88). FFR of the mid LCX 85% lesion was found to be flow limiting (FFR = 0.69). It was decided to proceed with percutaneous intervention of the mid left circumflex. A bioabsorbable stent was placed without complication (Fig. 12.3c). The remaining coronary disease was medically managed.

Current advances in coronary CT angiography are likely to involve the ability to evaluate a noninvasive fractional flow reserve which will help us to better evaluate patients and help guide therapy.

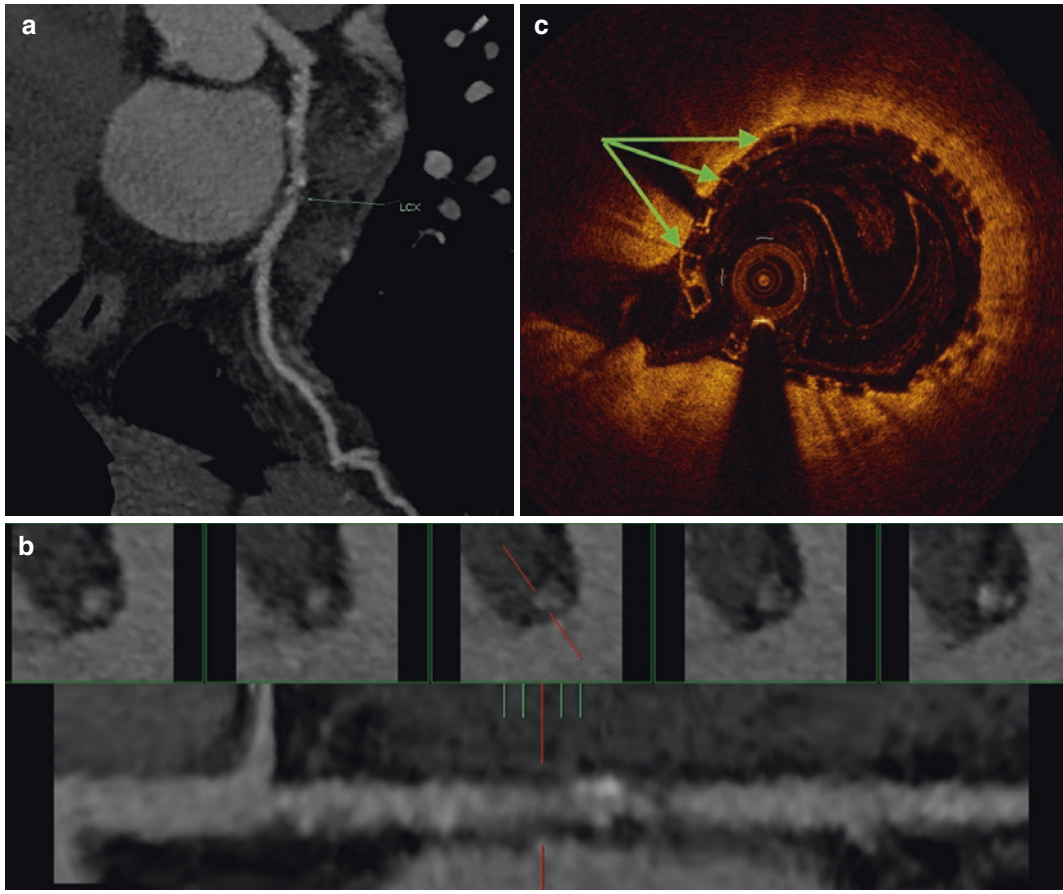

Fig. 12.3 (**a**) cMPR of LCX (**b**) stretched MPR of LCX (**c**) optical coherence tomography (OCT) of LCX showing bioabsorbable stent; *arrows* indicating bioabsorbable stent struts

12.4 Case 12.4

12.4.1 History

A 75-year-old male with coronary artery disease status post CABG and aortic stenosis undergoing evaluation for possible transcatheter aortic valve replacement.

12.4.2 Findings

CCTA demonstrated a calcified aortic valve. The bypass anatomy was defined as a saphenous vein graft to the right coronary artery, saphenous vein graft to an obtuse marginal and a left internal mammary artery (LIMA) graft to LAD (Fig. 12.4a–c).

12.4.3 Diagnosis

Previous history of CABG with new severe symptomatic aortic stenosis.

12.4.4 Discussion

In the evaluation of patients for transcatheter aortic valve therapy, cardiac CT scanning has many roles. In addition to evaluation of aortic valve characteristics, it can also be used for defining coronary artery bypass grafting anatomy in patients with remote history of coronary arterial bypass grafting surgery for whom the surgical report is not available. This is particularly important in setting of renal insufficiency. Significant amounts of contrast volume can be used in trying to define bypass anatomy in individuals in whom the operative report/bypass anatomy is not available at the time of invasive coronary angiography. Also, it is also possible in the same setting with CTA to evaluate the thoracic, abdominal, and pelvic vasculature to determine access routes for a transcatheter procedure with use of minimal contrast.

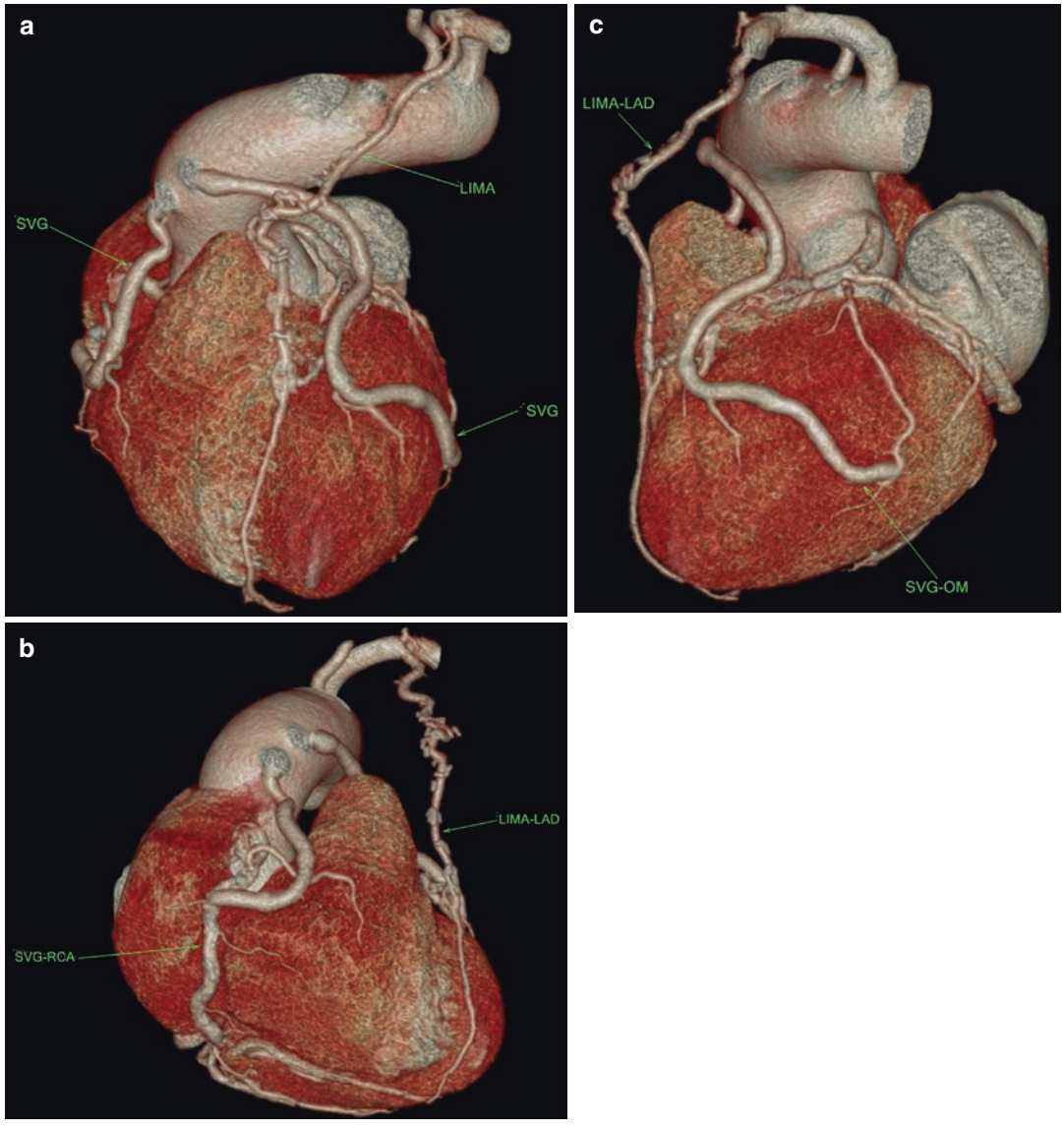

Fig. 12.4 (**a**–**c**) Volume rendered

12.5 Case 12.5

12.5.1 History

A 82-year-old male presents with progressive exertional chest discomfort.

12.5.2 Findings

CCTA demonstrated a critical stenosed and heavily calcified lesion in the mid LAD (Fig. 12.5a, b).

12.5.3 Diagnosis

Critical mid calcified mid LAD lesion.

12.5.4 Discussion

In addition to determining the presence of critically stenotic lesions, CCTA also allows for morphologic characteristics of coronary lesions that can be useful to determining the best treatment modality. In particular, the distribution and extent of calcium in coronary lesions is important in choosing the treatment options. The presence of heavy, and in particular, circumferential calcium in coronary lesions is an important consideration for use of plaque modification techniques (rotablator, orbital atherectomy, etc.) that lead to improved percutaneous intervention results.

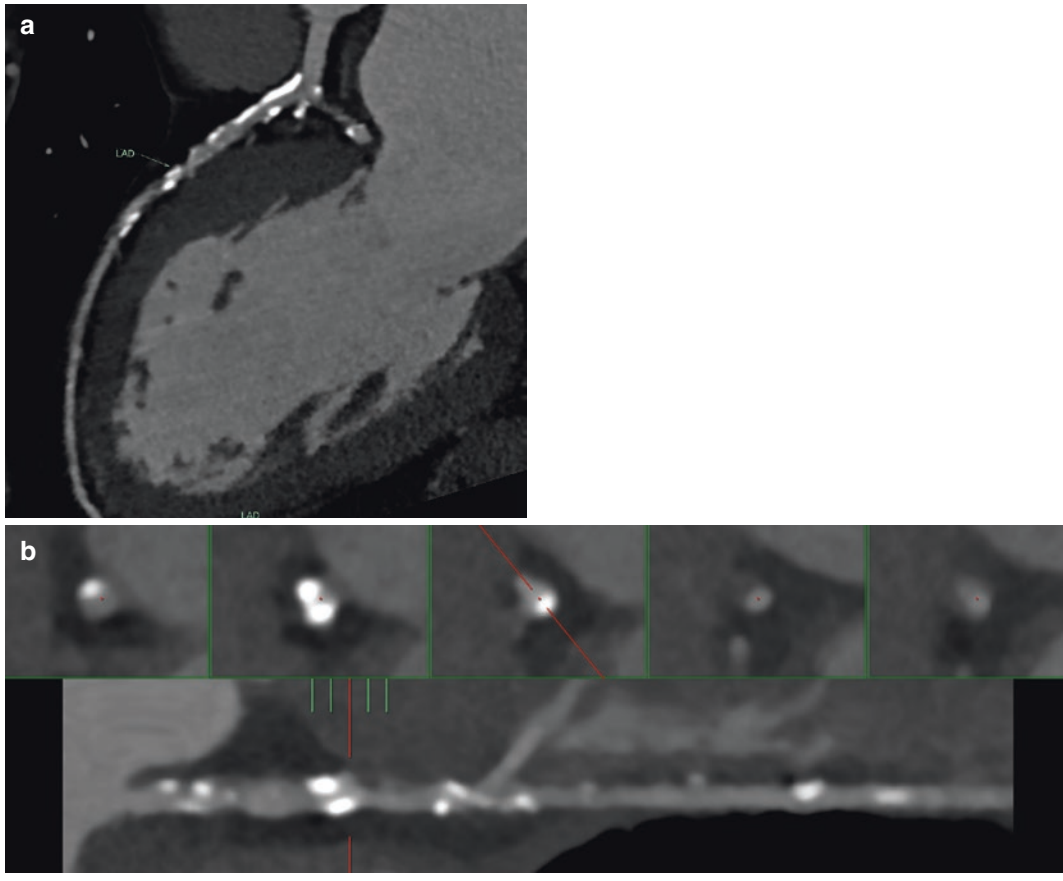

Fig. 12.5 (**a**) cMPR of LAD (**b**) stretched MPR of LAD

12.6 Case 12.6

12.6.1 History

A 46-year-old male presents with progressive shortness of breath on exertion.

12.6.2 Findings

Transthoracic echo demonstrated a patent ductus arteriosus (PDA) with coronary CTA demonstrated a PDA (Type B) (Fig. 12.6a, b).

12.6.3 Diagnosis

Type B PDA.

12.6.4 Discussion

CCTA with inclusion of the aortic arch is useful for planning of percutaneous intervention for closure of PDAs. Defining of the shape, length, and width of the PDA facilitates choosing the appropriate device for closure. In this case, an Amplatzer PDA occlude was chosen. In contrast, a type C PDA (Fig. 12.6c) in a separate patient was occluded with an Amplatzer vascular plug 2.

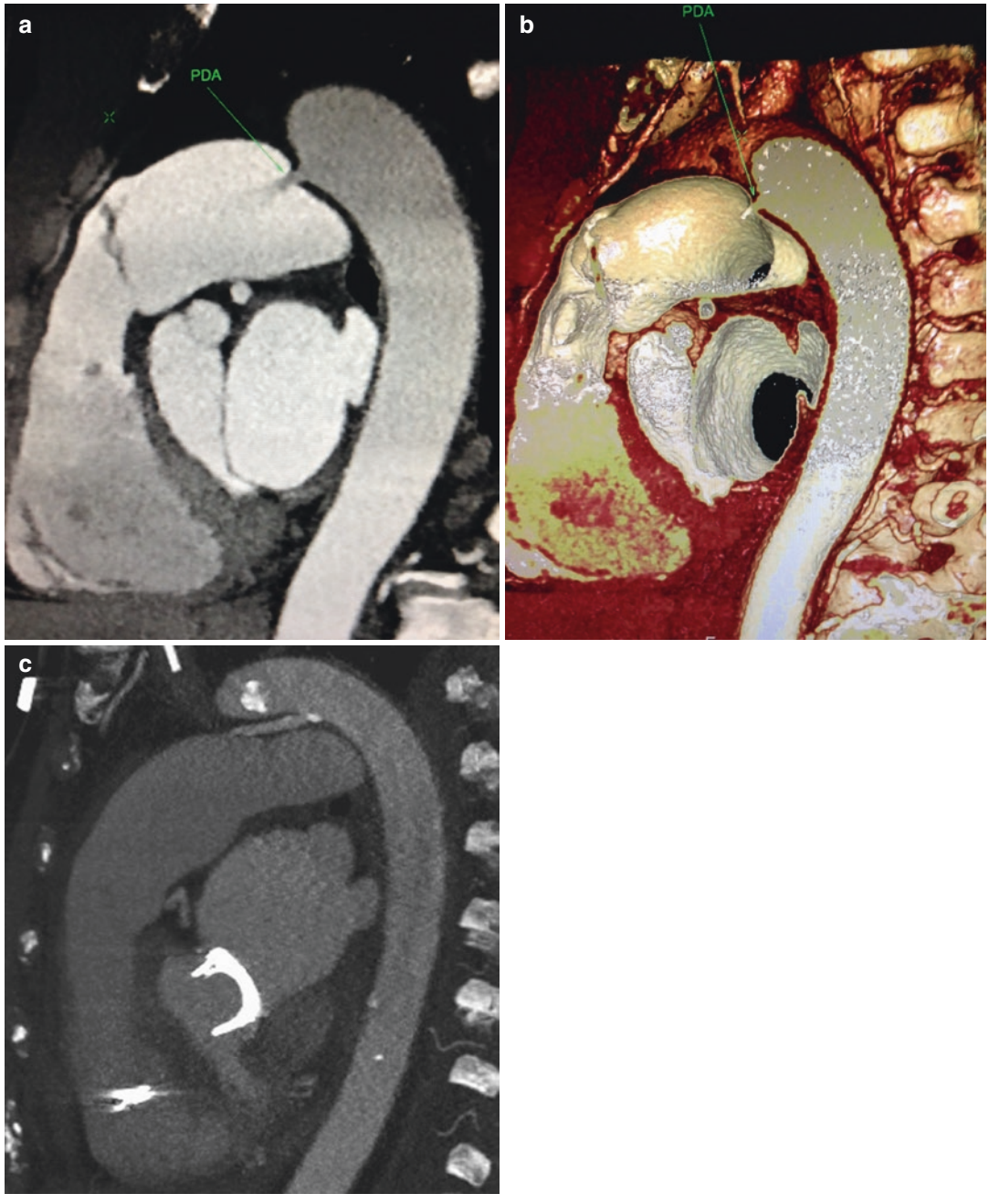

Fig. 12.6 (**a**) Sagittal view of type B PDA (**b**) volume rendered (**c**) sagittal view of type C PDA

12.7 Case 12.7

12.7.1 History

A 66-year-old female presented with atypical chest discomfort. She was evaluated in the emergency room and found to have normal cardiac biomarkers.

12.7.2 Findings

CCTA demonstrated non-obstructive coronary disease. She was found to have a secundum atrial septal defect with enlargement of the right atrium and right ventricle (Fig. 12.7).

12.7.3 Diagnosis

Ostium secundum atrial septal defect.

12.7.4 Discussion

The benefits of CCTA to the cardiologist in this setting are numerous. The CT scan allows for evaluation of the septal defect anatomy and can be used to planning of percutaneous closure. It allows for evaluation of associated congenital defects (Anomalous pulmonary venous return, ventricular septa defects, etc.). It also facilitates decisions as to the feasibility of percutaneous closure versus surgical intervention (as in the case of an ostium primum ASD or sinus venosus defect which are usually corrected with surgical intervention).

The pairing of CT with transesophageal echo helps to plan an effective closure of secundum atrial septal defects.

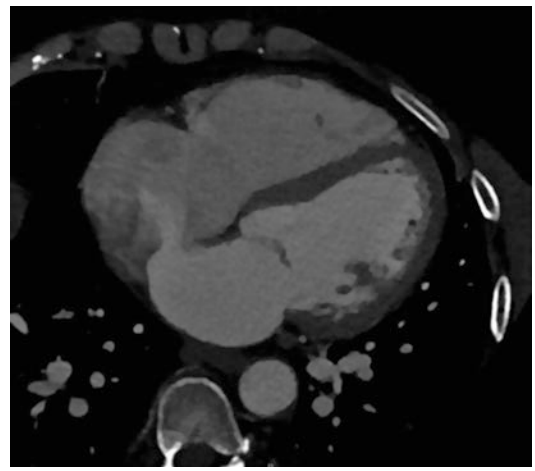

Fig. 12.7 Axial MIP showing ASD

12.8 Case 12.8

12.8.1 History

An 84-year-old female with significant past medical history of aortic stenosis presented with complaints of progressive shortness of breath on exertion.

12.8.2 Findings

Severe aortic stenosis with numerous comorbidities and significant frailty. She was deemed not an ideal candidate for surgical aortic valve replacement and was referred to transcatheter aortic valve replacement (TAVR).

CCTA was performed as part of her evaluation. Significant aortic annular calcification was noted that extended 2.5 cm into the left ventricle (Fig. 12.8).

12.8.3 Diagnosis

Severe aortic stenosis.

12.8.4 Discussion

Anatomic information regarding the distribution and extent of calcification in patients with aortic stenosis aids in choosing an optimal transcatheter aortic valve technology. In this case, it was decided to use a self-expanding transcatheter valve technology instead of using a balloon expandable transcatheter to minimize the risk of disruption of the aortic annulus due to the calcification pattern seen on CT.

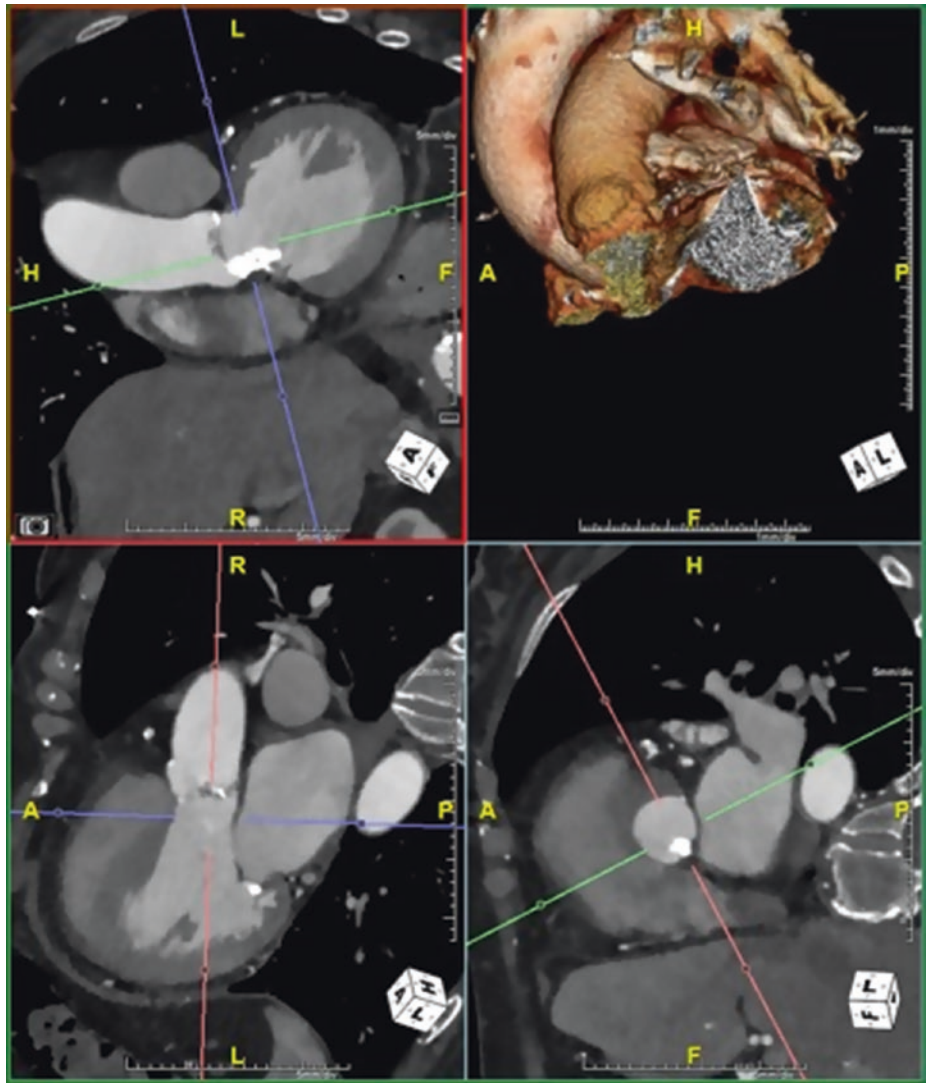

Fig. 12.8 Cardiac CT angiography showing severe nodular aortic annular calcification extending into the left ventricle

12.9 Case 12.9

12.9.1 History

A 67-year-old male presents with new onset chest discomfort.

12.9.2 Findings

Coronary angiography demonstrated a saphenous vein graft pseudoaneurysm.

Coronary CTA defined the dimensions of the pseudoaneurysm that developed from the proximal segment a saphenous vein bypass conduit (Fig. 12.9b).

12.9.3 Diagnosis

Expanding saphenous vein graft pseudoaneurysm (Fig. 12.9c).

12.9.4 Discussion

Invasive angiography demonstrated the existence of a saphenous vein graft pseudoaneurysm, but did not define well the expansion that had occurred over the 2-year interval between the invasive angiograms. Invasive angiography is limited in its nature to define a pseudoaneurysm as it provides a "luminogram" of the lesion. Lesions such as this saphenous vein graft pseudoaneurysm benefit from imaging using CCTA to better determine their true size and interval changes that may cause symptoms and require invasive therapy. Coronary CTA was also performed and clearly demonstrated the expansion of the saphenous vein graft pseudoaneurysm that had occurred in the 2-year interval (Fig. 12.9a, b). This patients pseudoaneurysm was subsequently treated percutaneously (Fig. 12.9d).

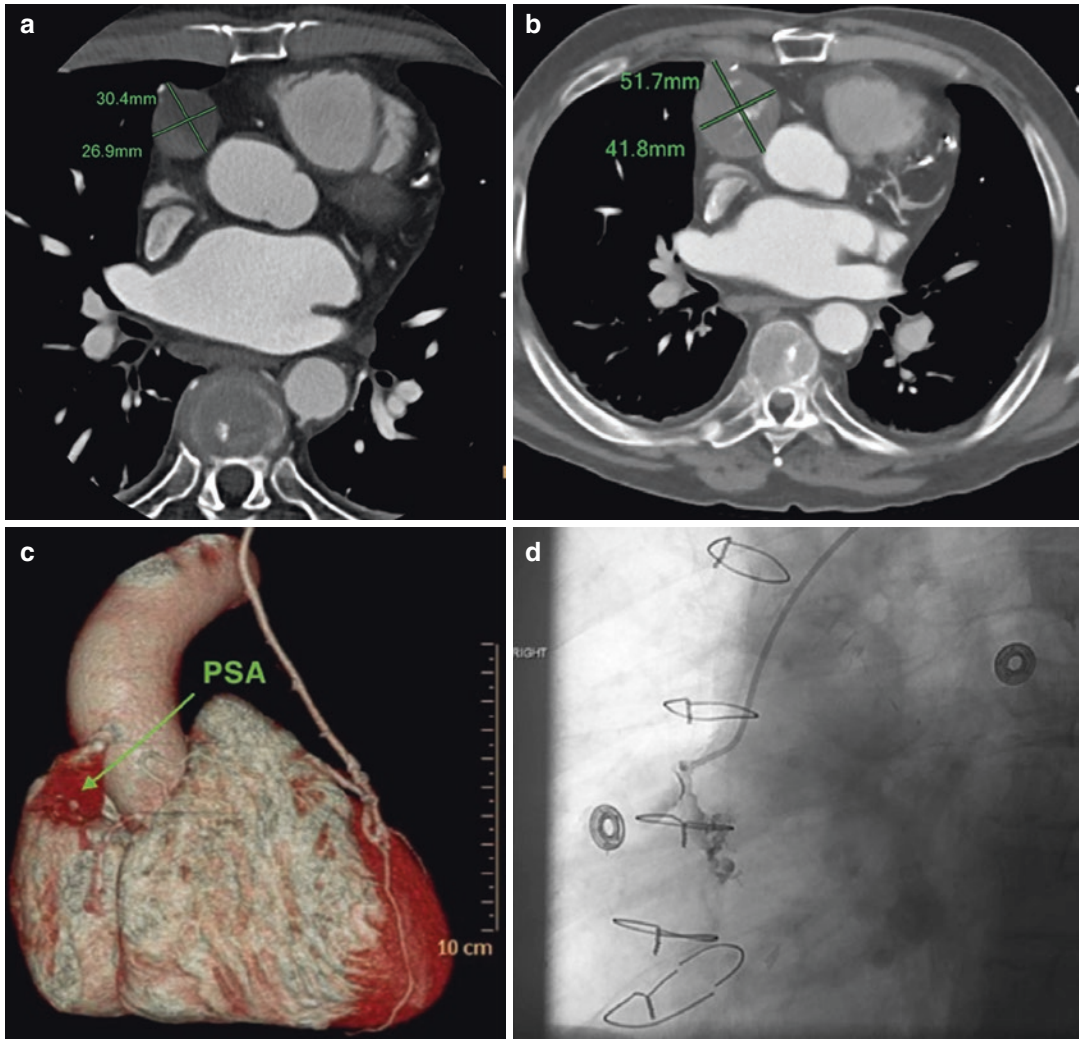

Fig. 12.9 (**a**) Axial view of PSA (**b**) axial view of PSA—2-year follow-up (**c**) volume rendered (**d**) coronary angiogram showing coils

12.10 Case 12.10

12.10.1 History

A 63-year-old female past medical history of severe three vessel coronary artery disease (CAD) and mixed valvular disease presented with progressive shortness of breath on exertion.

12.10.2 Findings

CCTA confirmed diagnosis of severe three vessel CAD with patent bypasses by cardiac catheterization with mixed valvular disease with severe mitral stenosis (Fig. 12.10a, b). Transesophageal echo demonstrated mitral mean gradient of 10 mmHg as well as severe mitral regurgitation. Also, patient had severe ascending aortic calcification shown on CCTA (Fig. 12.10c).

12.10.3 Diagnosis

Severe coronary artery disease, severe ascending aortic calcification with severe symptomatic mitral valvular disease: mitral stenosis, mitral regurgitation.

12.10.4 Discussion

Three years prior to presentation, patient underwent coronary artery bypass to address her coronary artery disease. Due to patient's severe ascending aortic calcification and severe mitral annular calcification, which extended into the posterior left ventricular wall, only off-pump coronary bypass was performed without surgical correction of the mitral disease. In the 3 years since the CABG, an attempt had been made to treat her valvular congestive heart failure with maximal medical therapy, but was unsuccessful. She was evaluated by our Heart Team for additional therapeutic options.

After being evaluated by our Heart Team and various other heart surgical programs, patient was deemed inoperable due to the extent of aortic calcification and the inability to cross clamp the aorta. She was offered the option of a transcatheter aortic valve to be placed in the native mitral position. The CT scan was used to plan the size of the valve to be used as well as to define the pattern of mitral calcification. The left ventricular outflow tract (LVOT) dimensions were also evaluated by the CCTA. LVOT obstruction can occur with transcatheter implantation of an aortic valve in the native mitral position.

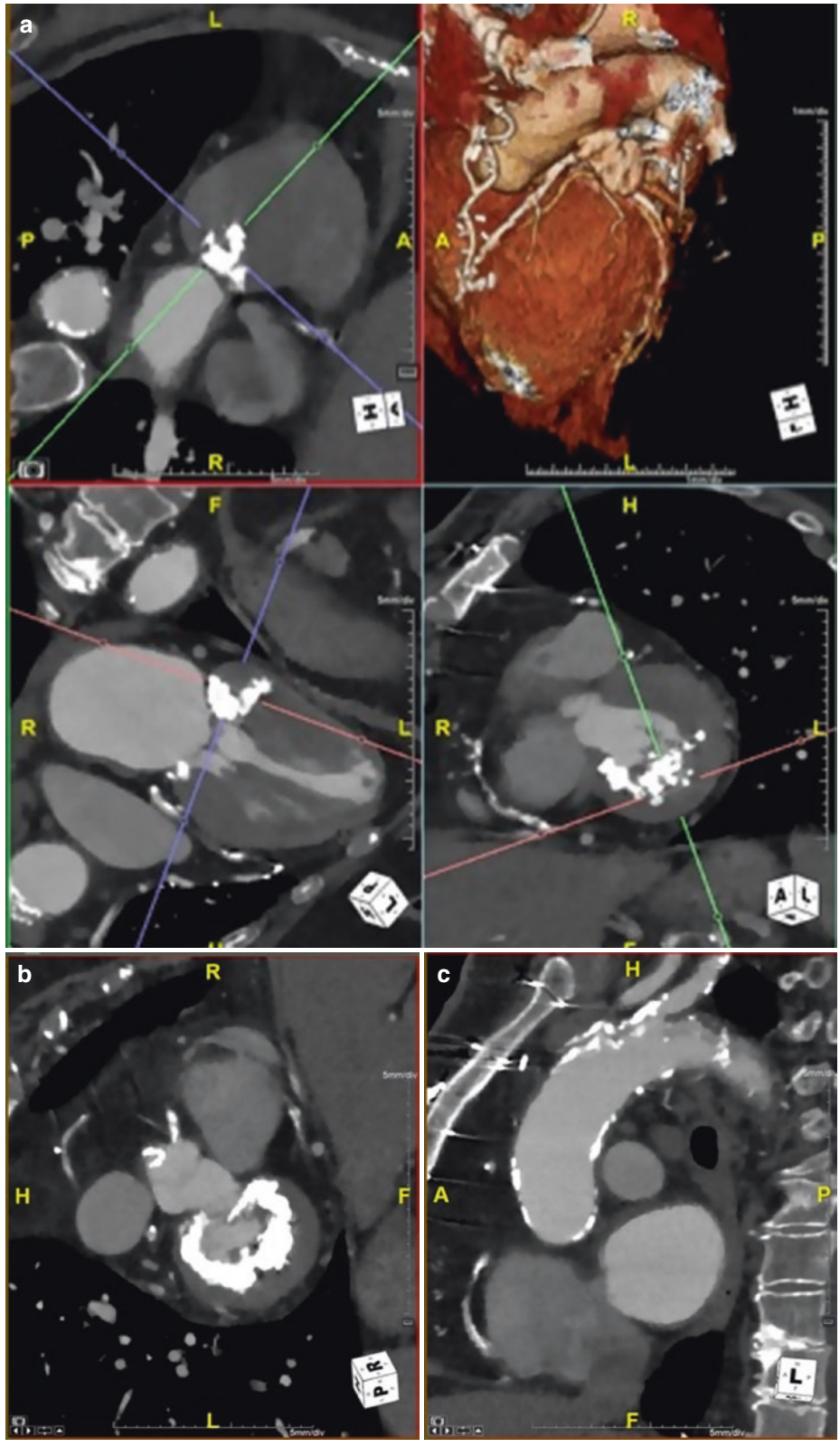

Fig. 12.10 (**a**) CCTA views showing heavy annular calcification of the mitral valve. (**b**) Sagittal MIP of mitral valve (**c**) sagittal MIP of calcified ascending aorta

12.11 Case 12.11

12.11.1 History

A 67-year-old female with progressive shortness of breath on exertion.

12.11.2 Findings

Transesophageal echocardiography demonstrated severe para-valvular regurgitation of a previously implanted surgical bioprosthetic mitral valve.

CCTA was used to define the para-valvular leak dimensions.

12.11.3 Diagnosis

Decompensated heart failure due to severe mitral para-valvular regurgitation.

12.11.4 Discussion

In the planning of a percutaneous closure of a para-valvular leak closure the use of CCTA allows for sizing of the defect. It also allows for determination of the proximity of important surrounding structures. Determination of the size of the device to be used to close the leak can also be facilitated by CCTA as demonstrated in Fig. 12.11a. In this case, a large PDA Amplatzer occlude device was used to close the leak (Fig. 12.11b). Acquisition of a retrospective gated CCTA allows for sizing of the defect's maximum dimensions (the sizes of the defect changes during the cardiac cycle).

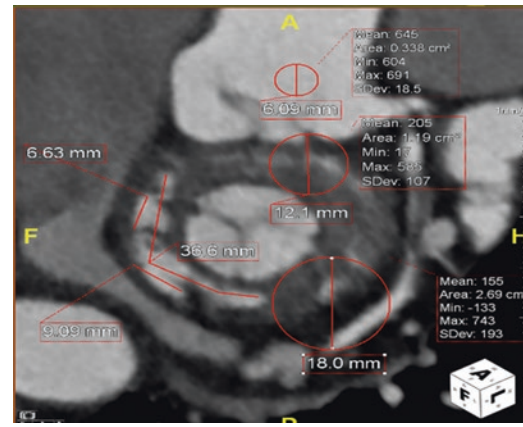

Fig. 12.11 (**a**) Sagittal MIP of mitral valve. (**b**) Volume rendered

Suggested Reading

Apfaltrer P, et al. Computed tomography for planning transcatheter aortic valve replacement. J Thorac Imaging. 2013;284:231–9.

Chambers JW, et al. Pivotal trial to evaluate the safety and efficacy of the orbital atherectomy system in treating de novo, severely calcified coronary lesions (ORBIT II). J Am Coll Cardiol Intv. 2014;75:510–8.

Cole JH, et al. Cost implications of initial computed tomography angiography as opposed to catheterization in patients with mildly abnormal or equivocal myocardial perfusion scans. J Cardiovasc Comput Tomogr. 2007;11:21–6.

Douglas PS, et al. Clinical outcomes of fractional flow reserve by computed tomographic angiography-guided diagnostic strategies vs. usual care in patients with suspected coronary artery disease: the prospective longitudinal trial of FFRCT: outcome and resource impacts study. Eur Heart J. 2015;36(47):3359–67.

Faella HJ, Hijazi ZM. Closure of the patent ductus arteriosus with the Amplatzer PDA device: immediate results of the international clinical trial. Catheter Cardiovasc Interv. 2000;51(1):50–4.

Frances C, Romero A, Grady D. Left ventricular pseudoaneurysm. J Am Coll Cardiol. 1998;32(3):557–61.

Nakazato R, et al. Non-invasive fractional flow reserve derived from CT angiography (FFRCT) for coronary lesions of intermediate stenosis severity: results from the DeFACTO study. Circ Cardiovasc Imaging. 2013;6(6):881–9.

Ruiz CE, et al. Clinical outcomes in patients undergoing percutaneous closure of periprosthetic paravalvular leaks. J Am Coll Cardiol. 2011;5821:2210–7.

Thanopoulos BD, et al. Closure of atrial septal defects with the Amplatzer occlusion device: preliminary results. J Am Coll Cardiol. 1998;31(5):1110–6.

Whitlow PL, et al. Results of the study to determine rotablator and transluminal angioplasty strategy (STRATAS). Am J Cardiol. 2001;876:699–705.

Cardiac CTA: Electrophysiology

13

John J. Lee, Rishi Anand, and Daniel Weitz

Cardiac computed tomography angiogram (CCTA) has evolved from a simple structural assessment tool to a key instrument used for complex ablation procedures in clinical cardiac electrophysiology. CCTA's fast acquisition and better image resolution allow for precise anatomic assessment that increases the efficacy and safety of these procedures.

CCTA has become integral in preparing for left atrial-based electrophysiology (EP) procedures, such as atrial fibrillation (AF) ablation. The cornerstone of AF ablation procedures is application of radiofrequency energy in a wide circumferential manner around the antrum of the pulmonary veins. Prior to insertion of catheters into the left atrium, it is essential to assess the number of pulmonary veins present, the presence of common pulmonary vein antrums, and the presence of potentially impending structures such as left atrial diverticula and the presence of cor triatriatum. In addition, in preparation for AF ablation in patients who had previous left atrial ablation, it is mandatory to assess for iatrogenic pulmonary vein stenosis. Evaluation of these structures is performed with volume rendering into a three-dimensional (3D) reconstruction. 3D CT images are reconstructed and vascular and coronary structural images are segmented away until pulmonary venous and left atrial anatomies are isolated for a more focused evaluation.

The left atrial anatomy includes a venous portion that receives the PVs, which encloses a left atrial dome, a vestibule that conducts to the mitral valve, the left atrial appendage (LAA) and interatrial septum [1]. The left atrium (LA) is also closely examined to assess for its size and for the presence or the absence of thrombus [1, 2]. In addition, the esophagus can be included in the 3D rendering to note its proximity to the posterior aspect of the pulmonary veins [2]; Avoidance of direct energy application to areas abutting the esophagus can prevent atrial-esophageal fistulas.

These images and the dataset are then translated to intra-procedure electro-anatomic mapping

J.J. Lee, MD
Department of Medicine,
University of Miami at Holy Cross Hospital,
Fort Lauderdale, FL, USA

R. Anand, MD • D. Weitz, MD (✉)
Electrophysiology Lab, Department of Cardiology,
Holy Cross Hospital, Fort Lauderdale, FL, USA
e-mail: daniel.weitz@gmail.com

C. Smuclovisky (ed.), *Coronary Artery CTA*, https://doi.org/10.1007/978-3-319-66988-5_13

systems, such as the CARTO mapping system (Biosense Webster, Diamond Bar, CA, USA) and the Endocardial Solutions, Inc. (ESI). By superimposing images from CCTA on the electroanatomical imaging created with the mapping systems, it helps to precisely map PVs and guide ablation catheters to target locations (i.e., the PV angle of insertions, size) [3, 4]. These modalities can in turn facilitate localization of anatomic structures and track intracardiac instruments and the ablation lesion set, effectively decreasing the procedure and fluoroscopy time [2].

In addition to functions described above, CCTA can be used to check for possible complications following EP procedures such as pulmonary vein stenosis. This chapter will use clinical cases with images to demonstrate and further explain CCTA application in EP procedures.

13.1 Case 13.1

13.1.1 History

A 72-year-old male with paroxysmal atrial fibrillation, despite being on propafenone 300 mg three times a day and carvedilol 20 mg. CCTA performed for pre-ablation planning.

13.1.2 Findings

The left atrium (LA) appears dilated measuring in the range of 4.3 cm. There is no visualized thrombus in the left atrial appendage (Fig. 13.1a).

There is a common trunk from the right upper and middle lobes draining anterosuperiorly into the left atrium. There is a draining venous trunk from the right lower lobe into the inferoposterior right side of the left atrium. There is a common draining trunk from the left upper lobe into the anterosuperior aspect of the left atrium and the left lower lobe venous trunk draining into the inferoposterior aspect of the left atrium (Fig. 13.1b, c).

There is no pericardial effusion and no dilation of the aortic root or the pulmonary arterial trunk.

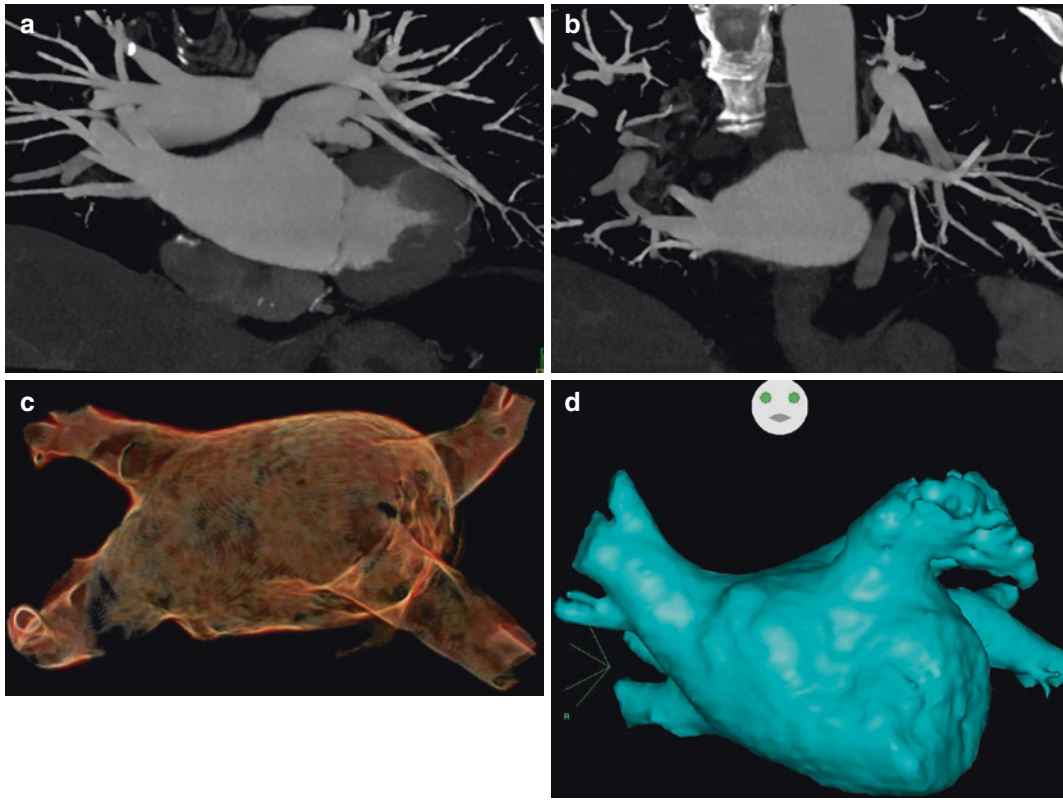

Fig. 13.1 (**a**) Volume rendered-left atrium (**b**) MIP axial-superior vein (**c**) MIP axial-inferior vein (**d**) volume rendered-left atrium (**e**) 3D fast anatomical mapping (FAM) posterior anterior view (**f**) 3D FAM left anterior oblique CT: *Pre-Isolation* (**g**) 3D FAM left anterior oblique CT: *Isolation* (**h**) 3D FAM right CT

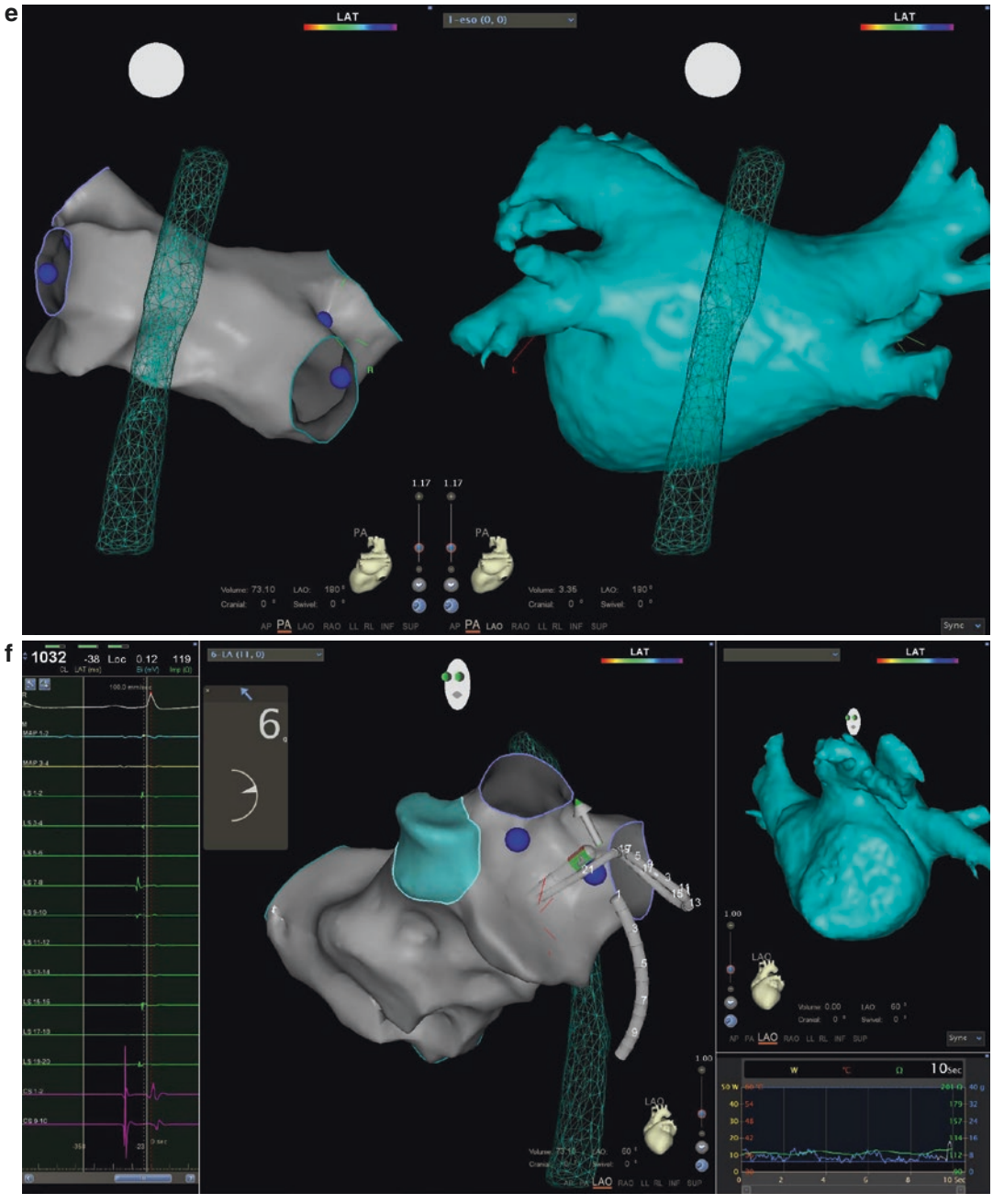

Fig. 13.1 (continued)

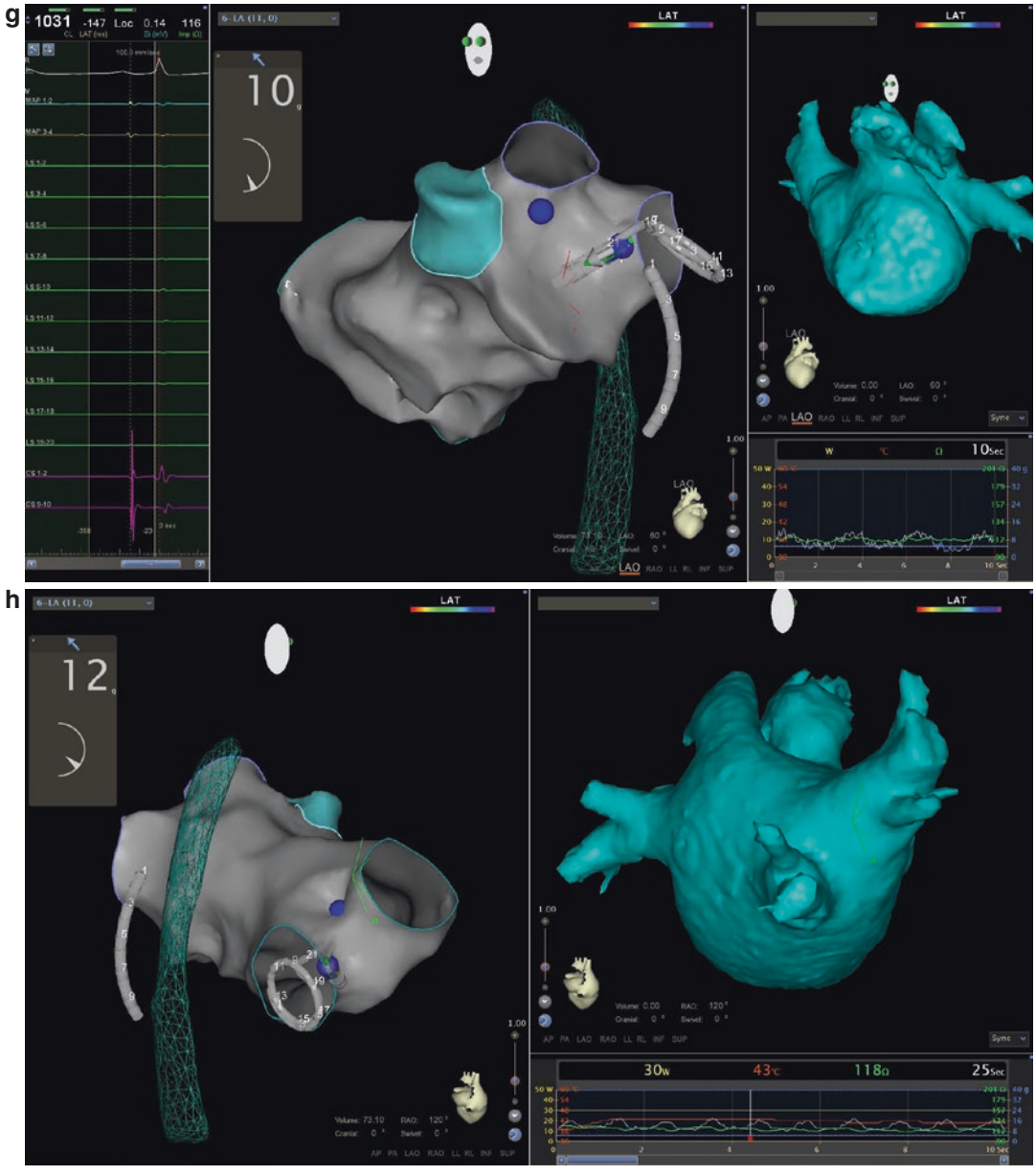

Fig. 13.1 (continued)

13.1.3 Diagnosis

Normal anatomic features of the pulmonary venous trunks draining into the left atrium.

13.1.4 Discussion

Although, there are three lobes in the right lung and two in the left lung, the right middle and the superior lobar veins join together, and, most commonly, two pulmonary veins (PV) from each lung drain into the left atrium [1]. Other anatomical variations include:

1. The three right lobar veins could remain separate. Such information can be useful to ensure that all PVs are electrically isolated [1].
2. The two left PVs may form a single trunk. This single trunk usually has a larger ostium. A larger ostium can allow limited lesion application at the ostium with greater confidence in avoiding pulmonary vein stenosis [1].
3. An accessory lobar vein from each lobe can join and augment the two left PVs. On the contrary, this accessory lobar trunk has a smaller ostium. This accessory vein and its small ostium should be noted before the procedure to ensure that all PVs are electrically isolated and to avoid pulmonary vein stenosis [1].

Left atrial size is also evaluated with CCTA. The enlargement of the LA can estimate the duration and the difficulty of the ablation procedure; it is also a risk factor for stroke and atrial fibrillation before and after the procedure [5, 6]. In the AFFIRM study, large transthoracic echocardiographic LA sizes were associated with recurrent AF (HR = 1.21, 1.16, and 1.32 for mild, moderate, and severe enlargement, respectively) [7]. Moreover, according to the substudy of the ENGAGE AF-TIMI 48 trial, there were strong correlations between increasing abnormalities of LA structure and function with greater burdens of AF and higher $CHADS_2$ score, an estimate of stroke risk [8].

13.1.5 Pearls and Pitfalls

Radiofrequency ablation to modify the atrial myocardial substrate should be considered for patients with atrial fibrillation refractory to conventional pharmacological therapy [9]. CCTA could provide crucial information prior to the EP procedure, by demonstrating patient's coronary anatomy for the pre-procedural guideline.

13.2 Case 13.2

13.2.1 Findings

Intra-operative imaging for EP procedure:

Figure 13.1d is an image of a left atrium volume rendered from a preoperative CT. Four pulmonary veins and a left atrial appendage are visualized in this figure.

Figure 13.1e is a 3D Fast Anatomical Mapping (FAM) reconstruction (*left*) with a synchronized posterior-anterior view of the CT (*right*). Note that an esophagus has been reconstructed with the same technique to delineate its location relative to the posterior wall of the LA.

Figure 13.1f is again a 3D FAM with the corresponding left anterior oblique (LAO) CT. In this figure, an ablation catheter is shown pointing anteriorly and superiorly (note the vector) on a carina between a left inferior pulmonary vein (LIPV) and a left superior pulmonary vein (LSPV). An electrical activity sensing catheter is also visualized inside the LIPV. The local intracardiac electrograms inside the pulmonary veins show electrical activity.

Figure 13.1g shows an electrical isolation of the LIPV. Here, we can see that there is no electrical activity on the local intracardiac electrograms while the catheter is in the LIPV. The blue dot is used as a location marker for the electroanatomical location of an applied lesion where complete electrical isolation was achieved.

Figure 13.1h is a right posterior view of the 3D FAM and a corresponding CT. This real-time

graph view allows us to monitor the force applied as the distal tip of the catheter, impedance, temperature, and power throughout the ablation.

13.2.2 Diagnosis

Successful pulmonary vein isolation without complications.

13.2.3 Discussion

The electrophysiologist can utilize this 3D reconstruction to safely maneuver the catheter inside the heart and precisely locate the ablation points.

There is a thin layer of fat, insulating the posterior wall of the LA from the anterior esophagus [10]. This relationship between the left atrium and the esophagus is carefully evaluated before the procedure and monitored during the procedure to avoid esophageal injury during the procedure.

During a post-op follow-up visit, patient reported feeling well and no longer having any symptoms of atrial fibrillation. Patient is active with no exertional symptoms and no shortness of breath.

13.2.4 Pearls and Pitfalls

A careful, efficient intra-operative maneuvering of the ablation catheter is possible with the CCTA reconstruction superimposed with the CARTO, 3D electro-anatomic and non-fluoroscopic system [11]. This has increased the safety of the procedure while cutting down both the procedure and fluoroscopy times.

13.3 Case 13.3

13.3.1 History

A 56-year-old male with history of AF, status post ablation 8 years ago at an outside hospital, presented with recurrent AF. Three years ago, 5 years after his initial ablation, the patient started to redevelop symptomatic palpitations and he began taking flecainide and metoprolol. Despite being on anti-arrhythmic therapy, the patient continued to complain of palpitations without significant shortness of breath.

Upon review of the outside hospital records, there were no post-procedure images taken. The pre-ablation echocardiogram demonstrated normal ventricular function and pulmonary pressures. The pre-procedural computed tomography (CT) scan along with the three-dimensional (3D) reconstruction was done on the procedural table prior to the transeptal puncture, but did not pick up the pulmonary vein stenosis.

Pulmonary vein potential mapping noted that there was a potential at the ostium of the left superior pulmonary vein. During the left atrial catheter manipulation, the occlusion of the left superior PV was discovered, secondary to the AF ablation 8 years ago. The procedure was aborted for further diagnostic workup.

13.3.2 Findings

The computed tomography scan (Fig. 13.2a) and the left atrium 3D reconstruction (Fig. 13.2b) demonstrated subtotal occlusion of the left upper pulmonary venous trunk. The lung perfusion scan revealed significantly decreased left lung perfusion (Fig. 13.2c). The levophase pulmonary angiogram demonstrated well-developed collateral circulation from the left upper lobe to the mid segment of the left lung and left upper PV occlusion. The levophase angiogram of the right middle lobe pulmonary arterial system demonstrated venous return confined to the area of the lung supplied by the arterial vasculature (Fig. 13.2d and e, respectively).

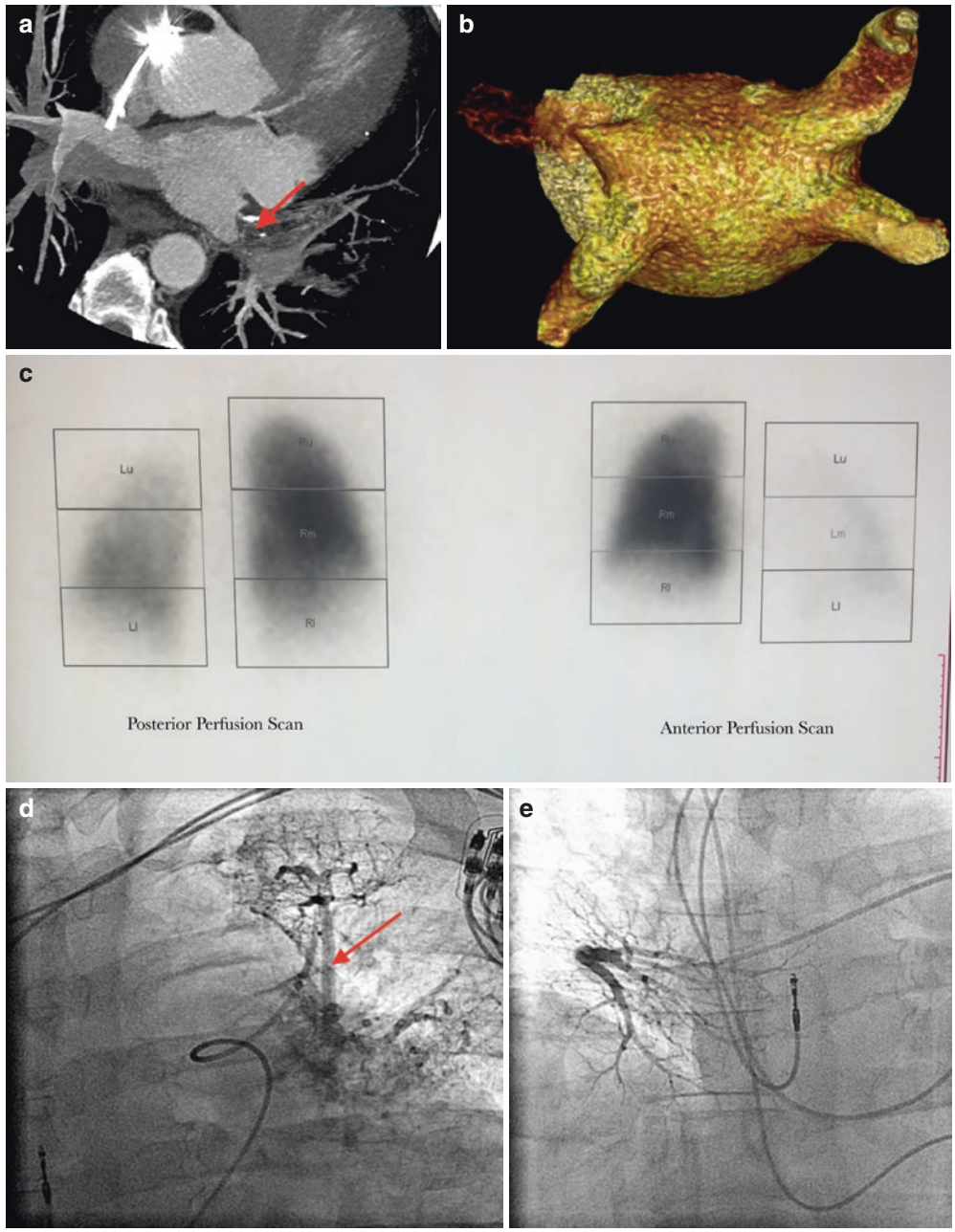

Fig. 13.2 (**a**) Axial MIP (**b**) volume rendered (**c**) lung perfusion scan (**d**) left pulmonary angiogram. *Arrow* indicating collateral (**e**) right pulmonary angiogram

13.3.3 Diagnosis

Pulmonary vein stenosis on the LSPV.

13.3.4 Discussion

The patient's asymptomatic PV stenosis is likely secondary to compensatory hemodynamic adaptations via a well-developed collateral circulation. The patient has remained asymptomatic since the incidental finding of PV stenosis and no further attempts at AF ablation have been undertaken.

13.3.5 Pearls and Pitfalls

The frequency of PV stenosis, a well-established possible complication following an AF ablation of pulmonary veins, has been declining due to the improvement of technique. However, depending on the technique and diagnostic modalities used, PV stenosis occurs as often as 40% of patients who underwent AF ablation [12].

PV stenosis acquired after AF ablation varies in severity from asymptomatic to nonspecific symptoms including persistent cough, hemoptysis, and exertional dyspnea [13]. Given these nonspecific clinical symptoms, physicians should be highly suspicious of the diagnosis of PV stenosis in post-ablation patients, and further evaluate patients with multiple imaging modalities. In most cases of PV stenosis, including severe cases, clinical symptoms improve without intervention secondary to the compensatory hemodynamics [12]; only about 22% of severe PV stenosis, defined as more than 50% luminal occlusion, required intervention [14]. Further supporting the compensatory mechanism, absent perfusion on lung perfusion scan is indicative of pulmonary artery to systemic collaterals, which in our case is further demonstrated by the pulmonary angiogram (Fig. 13.2d) [15, 16]. Patient undergoing repeat AF ablation should undergo a CCTA to further evaluate the possibility of PV stenosis preoperatively.

References

1. Cronin P, Sneider MB, Kazerooni EA, Kelly AM, Scharr C, Oral H, Morady F. MDCT of the left atrium and pulmonary veins in planning radiofrequency ablation in planning radiofrequency ablation for atrial fibrillation: a how-to-guide. AJR Am J Roentgenol. 2004;183(3):767–8.
2. Joshi SB, Blum AR, Mansour M, Abbara S. CT applications in electrophysiology. Cardiol Clin. 2009;27:619–31.
3. Maksimovic R, Dill T, Ristic AD, Seferovic PM. Imaging in percutaneous ablation for atrial fibrillation. Eur Radiol. 2006;16:2491–1504.
4. Martinek M, Nesser HJ, Aichinger J, Boehm G, Purerfellner H. Impact of integration of multislice computed tomography imaging into three dimensional electroanatomic mapping in clinical outcomes, safely and efficacy using radiofrequency ablation for atrial fibrillation. Pacing Clin Electrophysiol. 2007;30:1215–23.
5. Mahabadi AA, Samy B, Seneviratne SK, Toepker MH, Bamberg F, Hoffman U, Truong QA. Quantitative assessment of left atrial volume by echocardiographic-gated contrast-enhanced multidetector computed tomography. J Cardiovasc Comput Tomogr. 2009;3:80–7.
6. Lin FY, Devereux RB, Roman MJ, Meng J, Jow VM, Jacobs A, Weinsaft JW, Shaw LI, Berman DS, Callister TQ, Min JK. Cardiac chamber volumes, function and mass as determined by 64 multidetector row computed tomography; mean values among healthy adults free or hypertension and obesity. JACC Cardiovasc Imaging. 2008;1:782–6.
7. Olshansky B, et al. Are transthoracic echocardiographic parameters associated with atrial fibrillation recurrence or stroke?: results from the atrial fibrillation follow-up investigation of rhythm management (AFFIRM) study. J Am Coll Cardiol. 2005;4512:2026–33.
8. Gupta DK, et al. Left atrial structure and function in atrial fibrillation: ENGAGE AF-TIMI 48. Eur Heart J. 2014;3522:1457–65.
9. Rajiah P, Schoenhagen P. The role of computed tomography in pre-procedural planning of cardiovascular surgery and intervention. Insights Imaging. 2013;4(5):671–89.
10. Daoud EG, Hummel JD, Houmsse M, Hart DT, Weiss R, Liu Z, Augostini R, Kalbfleisch S, Smith MC, Mehta R, Gangasani A, Raman SV. Comparison of computed tomographic imaging with intraprocedural contrast esophagogram. Implications for catheter ablation of atrial fibrillation. Heart Rhythm. 2008;5(7):975–80.
11. Shen M, DS F, Helguera M, Cherla A. 3D CTA mapping for electrophysiological procedures. Volumetric Cardiac Imaging 3:89–98.
12. Saad EB, Marrouche NF, Saad CP, et al. Pulmonary vein stenosis after catheter ablation of atrial fibrillation:

emergence of a new clinical syndrome. Ann Intern Med. 2003;138:634–8.
13. Yun D, Jung JI, YS O, Youn H-J. Hemodynamic change in pulmonary vein stenosis after radiofrequency ablation: assessment with magnetic resonance angiography. Korean J Radiol. 2012;13(6):816–9.
14. Cappato R, Calkins H, Chen SA, et al. Updated worldwide survey on the methods, efficacy, and safety of catheter ablation for human atrial fibrillation. Circ Arrhythm Electrophysiol. 2010;3:32–8.
15. Kluge A, Dill T, Ekinci O, et al. Decreased pulmonary perfusion in pulmonary vein stenosis after radiofrequency ablation: assessment with dynamic magnetic resonance perfusion imaging. Chest. 2004;126:428–37.
16. Nanthakumar K, Mountz JM, Plumb VJ, Epstein AE, Kay G. Functional assessment of pulmonary vein stenosis using radionuclide ventilation/perfusion imaging. Chest. 2004;126(2):645–51.

Transcatheter Aortic Valve Replacement Planning

14

Tariq A. Hameed

14.1 Transcatheter Aortic Valve Replacement

Severe stenosis of aortic valve is associated with high morbidity and there is high mortality in untreated symptomatic patients. Severe aortic stenosis is treated by surgical replacement of aortic valve. However, many patients are poor surgical candidates due to other comorbidities. In these patients, the replacement of aortic valve by transcatheter procedure is also a treatment option with improved outcomes compared to medical treatment.

Transcatheter aortic valve replacement (TAVR), also called transcatheter aortic valve implantation (TAVI), involves placement of a bioprosthetic aortic valve within the native diseased aortic valve (Fig. 14.1a–f). The crimped prosthetic valve contained within a sheath is advanced into the native aortic valve via a catheter over a guide-wire during fluoroscopic guidance. Following appropriate alignment and positioning, the valve is expelled out of the sheath and depending on the type of valve, allowed to expand or expanded over a balloon within the native aortic valve apparatus. The prosthetic valve is anchored in surrounding tissues with the native aortic valve leaflets displaced or sometimes crushed against the walls of the aortic root.

Two commonly used types of bioprosthetic valves are:

- Balloon-expandable Edwards valves (Edwards Lifesciences, Irvine, CA) including Sapien, Sapien XT, and Sapien 3 (Fig. 14.2a, b).
- Self-expandable Medtronic CoreValve system (Fig. 14.2c) including CoreValve and Evolut R (Medtronic, Minneapolis, MN).

The transcatheter heart valve (THV) is usually implanted via transfemoral approach (Fig. 14.3a), which is preferred due to lower risk of potential complications. This requires appropriate caliber of access vessels such as iliac arteries and aorta to accommodate the sheath with the valve. Less tortuous course of access vessels is desirable as severe tortuosity limits catheter maneuverability during valve implantation. In patients whose iliofemoral arterial anatomy is unfavorable, other approaches are utilized, which include transapical approach via left ventricular apex (Fig. 14.3b–d), direct aortic approach via ascending aorta (Fig. 14.3e–g), and trans-axillary or subclavian arterial approach.

Pre-TAVR workup of patients includes evaluation with multiple imaging modalities including echocardiography, catheter angiography, and computed tomography (CT). The prosthetic valves for TAVR come in a specific variety of sizes and accurate determination of aortic valve

T.A. Hameed, MD, FCPS
Indiana University School of Medicine and Indiana University Health, Indianapolis, IN, USA
e-mail: thameed@iupui.edu

C. Smuclovisky (ed.), *Coronary Artery CTA*, https://doi.org/10.1007/978-3-319-66988-5_14

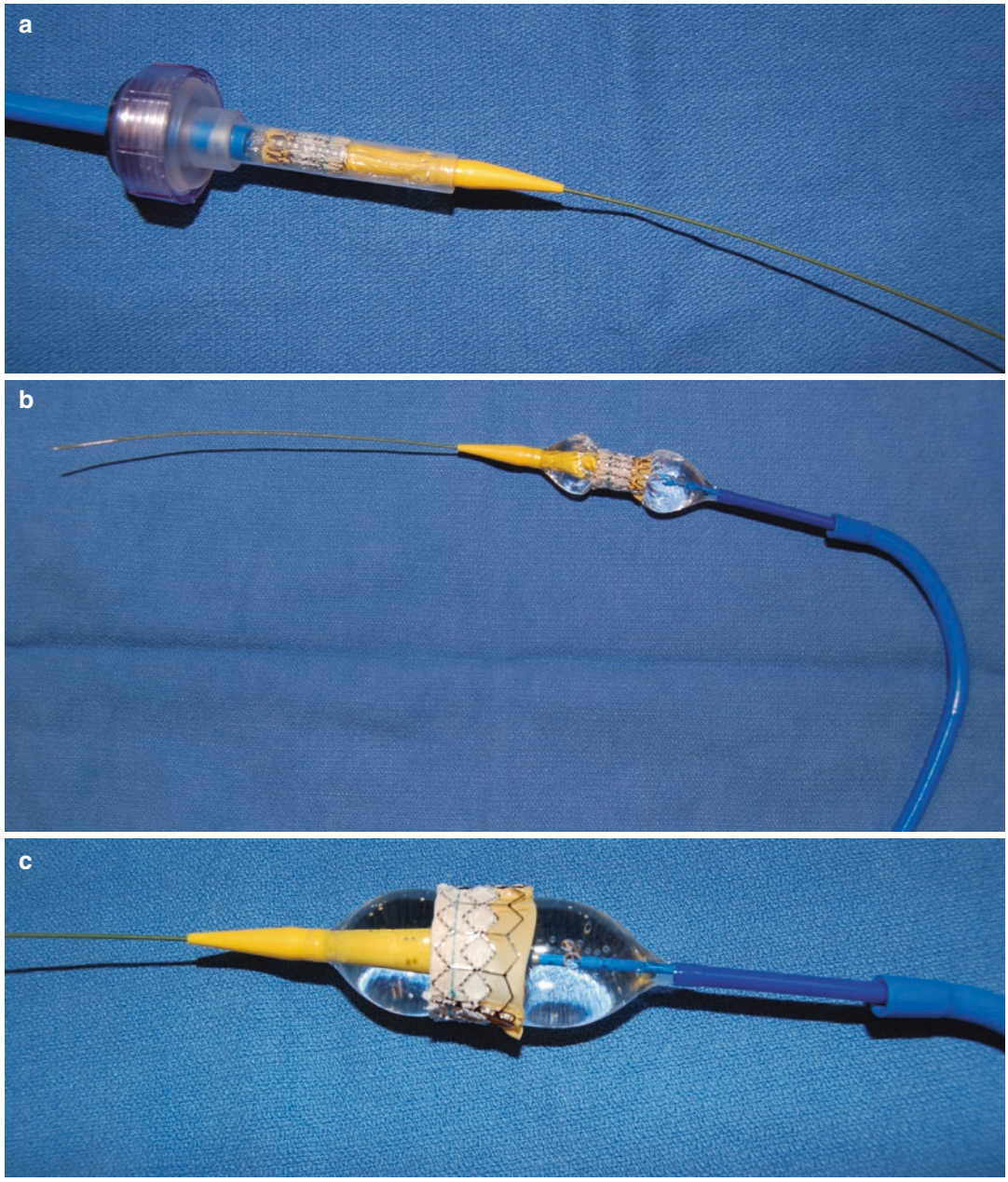

Fig. 14.1 (**a**) Valve in sheath (**b**) Valve on partially expanded balloon (**c**) Valve on expanded balloon (**d–f**) Angiogram of transcatheter valve deployment

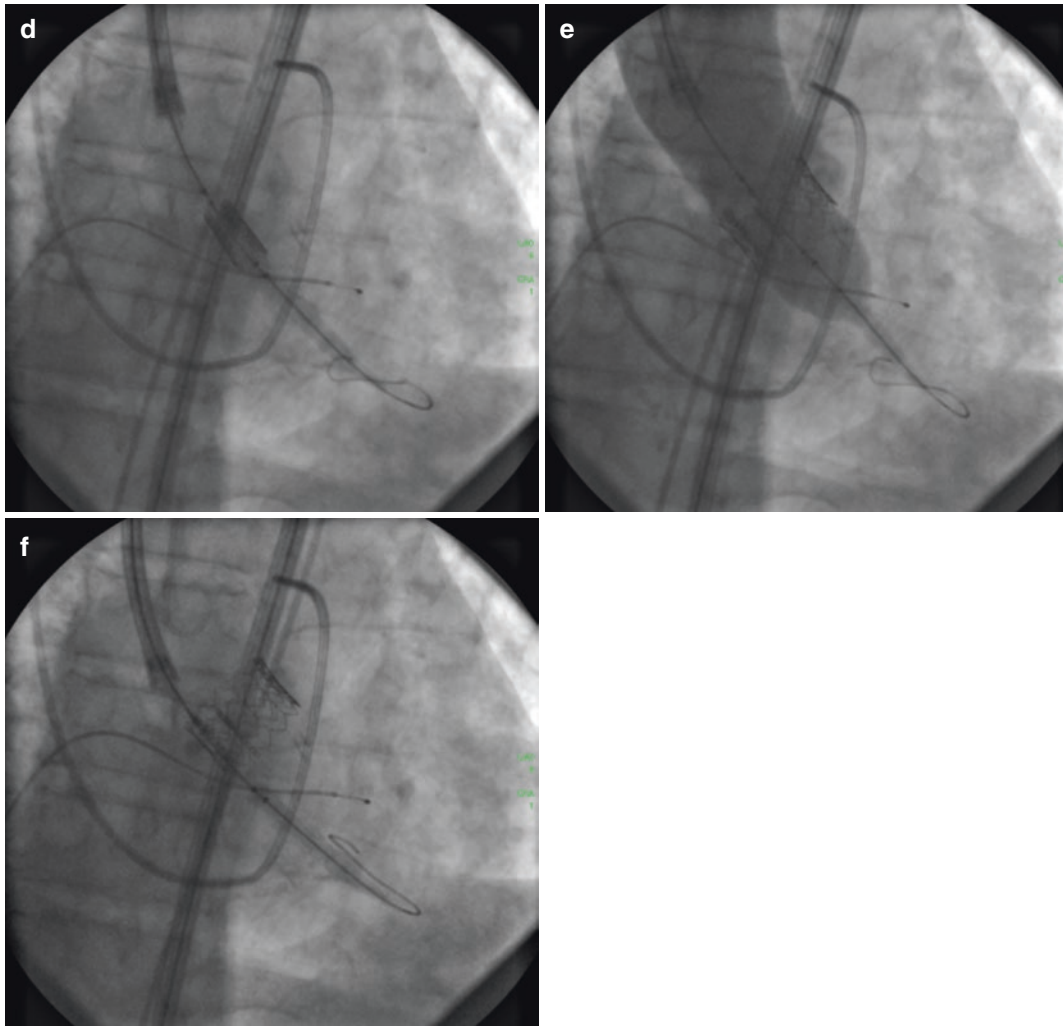

Fig. 14.1 (continued)

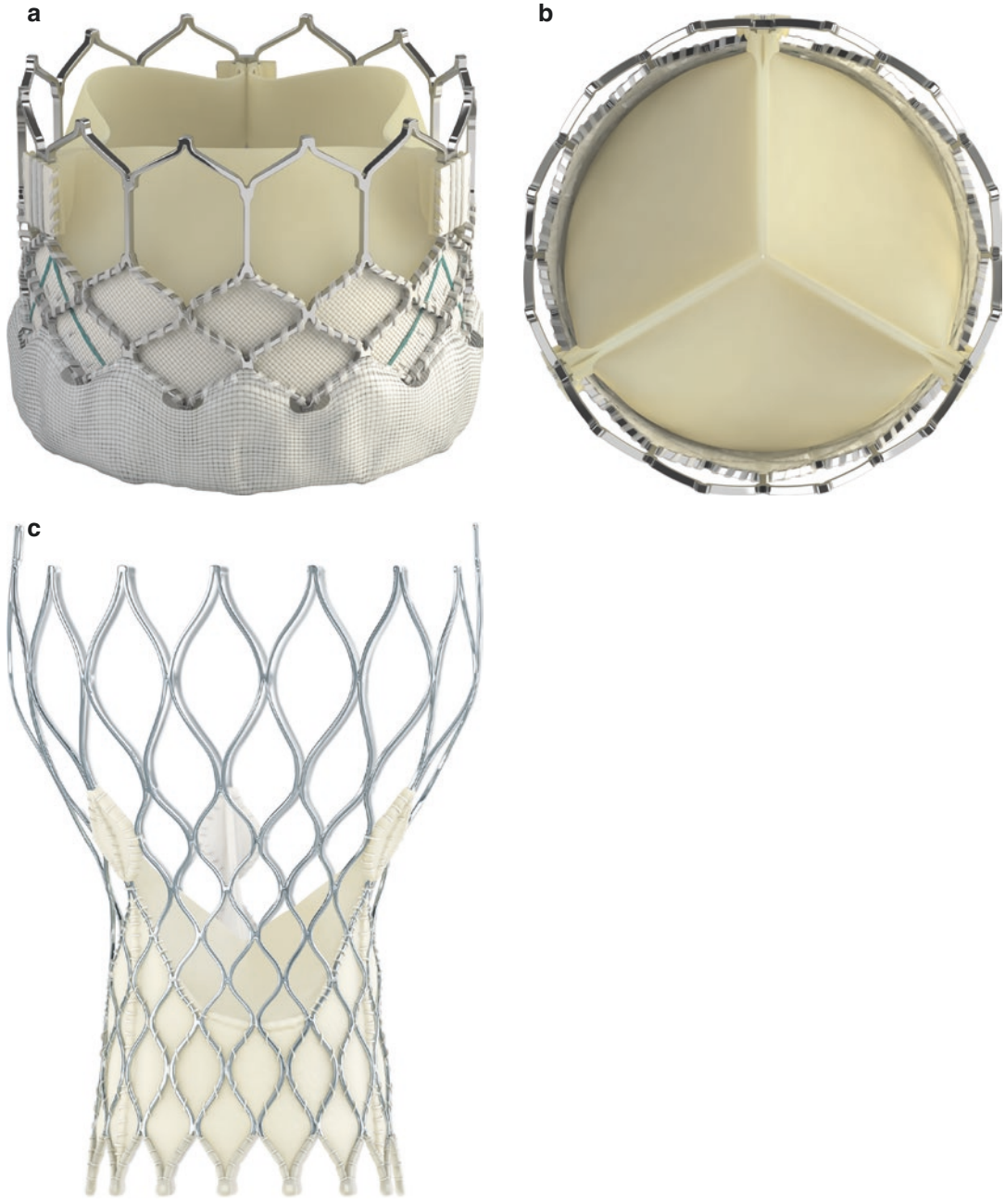

Fig. 14.2 (**a**) Sapien 3 side view (**b**) Sapien 3 leaflet view (**c**) CoreValve 26 mm (**a**, **b** used with permission by Edwards Lifesciences LLC, Irvine, CA. **c** is used with permission by Medtronic © 2016)

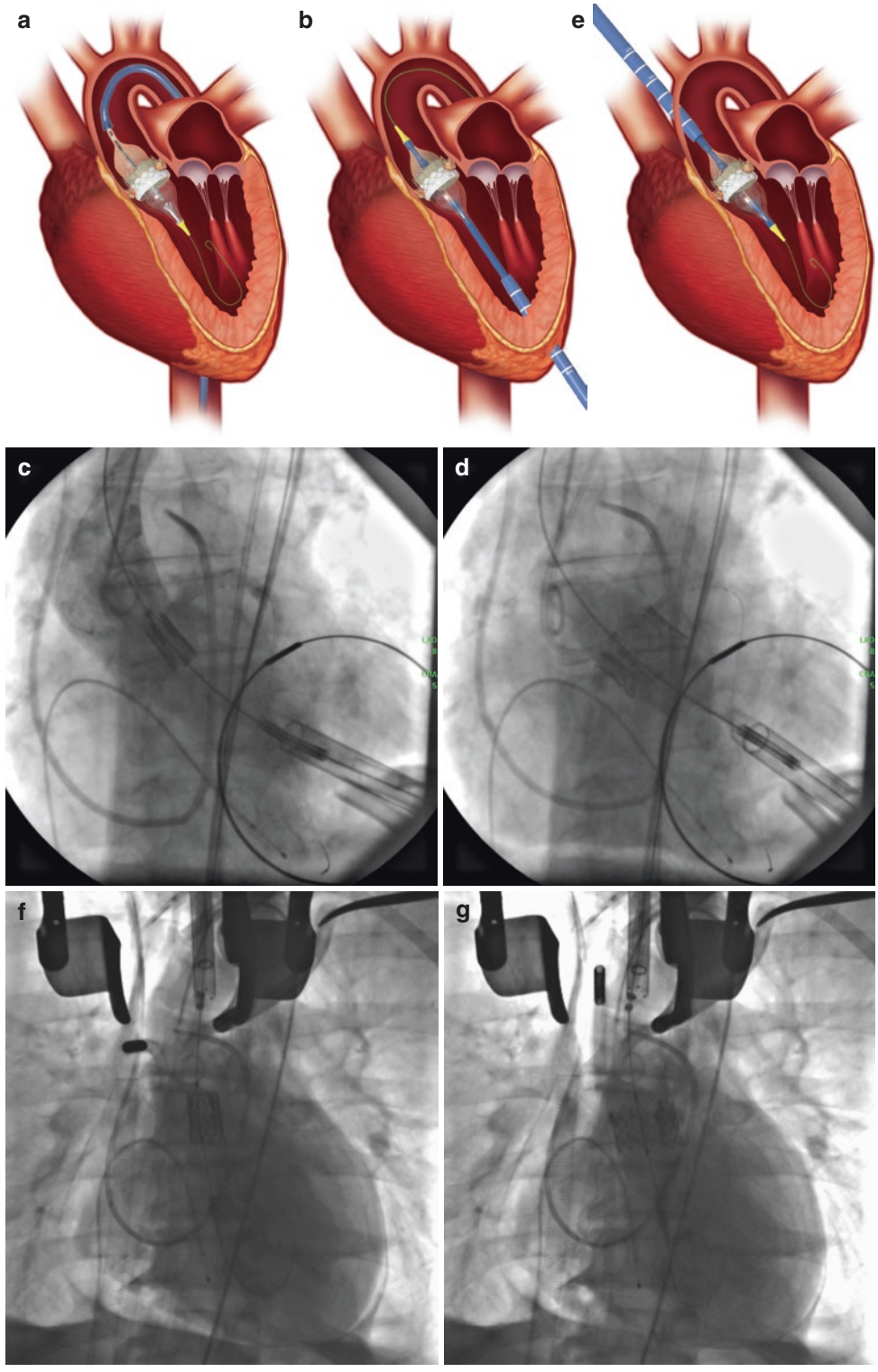

Fig. 14.3 (**a**) Commander Edwards valve via transfemoral approach (**b**) Certitude Edwards valve via transapical approach (**c**, **d**) Angiogram of transapical approach (**e**) Certitude Edwards trans-aortic approach (**f**, **g**) Angiogram of trans-aortic approach. (**a**, **b**, **e** are used with permission by Edwards Lifesciences LLC, Irvine, CA. Edwards, Edwards Lifesciences, CERTITUDE, COMMANDER, Edwards SAPIEN, SAPIEN, SAPIEN XT, and SAPIEN 3 are trademarks of Edwards Lifesciences Corporation)

size for transcatheter replacement is of critical importance as a larger than appropriate size may cause annulus rupture during valve implantation or a small valve-size may lead to valve embolization or post-procedure para-valvular leak. Although echocardiography (including trans-esophageal technique) and catheter angiography are also used for the assessment of aortic valve size, CT is able to provide more accurate estimate of size as the aortic valve annulus is more commonly oval or elliptical than circular, which is better evaluated with 3-D capability of CT imaging compared to 2-D techniques.

CT is also utilized for evaluation of other features of aortic root morphology such as the presence of tri-leaflet versus bicuspid valve, which may make the procedure challenging for appropriate alignment of the prosthetic valve during implantation. Assessment of the amount and distribution of calcifications in aortic valve is important as asymmetric distribution or inferior extent of calcifications into the ventricular outflow tract may lead to higher risk of post-procedure aortic valve regurgitation or para-valvular leak. CT evaluation of the height of coronary artery ostia from the level of annulus plane and the size of native valve leaflets is important to assess the risk of coronary artery occlusion due to displaced leaflets of native valve or potential superimposition of prosthetic valve. As the CoreValve is longer and extends from the left ventricular outflow tract (LVOT) to ascending aorta, minimum diameter and height of aortic sinus to accommodate the valve size is assessed by CT and the size of ascending aorta and sinotubular junction (STJ) is evaluated to exclude an aneurysm. CT images of aortic root are also used to predict appropriate fluoroscopy tube angle for visualization of aortic annulus plane for TAVR procedure.

The caliber, calcifications, and tortuosity of access vessels are assessed by CT for feasibility of transfemoral or, if necessary, subclavian artery approach. The amount and irregularity of atherosclerotic plaque or the presence of thrombi in aortic arch is evaluated for potential risk of cerebral embolization during catheter manipulation. CT is also used to assess the length of ascending aorta and calcifications in its wall for feasibility of direct trans-aortic approach via mini-thoracotomy as short ascending aorta or large amount of calcifications may preclude safe access.

14.1.1 CT Imaging for Pre-TAVR Planning

CT angiography (CTA) examination of the thorax, abdomen, and pelvis is performed. This includes helical ECG-gated CTA data acquisition of the thorax in the arterial phase following intravenous (I.V.) contrast administration (using bolus triggering or timing run in the ascending aorta) for the assessment of aortic root and thoracic aorta. CTA examination of the abdomen and pelvis for abdominal aorta and iliofemoral arteries is usually obtained by a separate helical acquisition without ECG gating. The total intravenous contrast dose is variable for the two examinations depending on the scan duration, usually 100–120 mL.

14.1.2 Image Reconstructions

CT images of chest with ECG synchronization are reconstructed in the cardiac systolic phase (20–35% R-R interval) to obtain maximum size of the aortic valve annulus. The maximum annulus size has been reported to correlate with images at 20% R-R interval. Using the acquired dataset, multiplanar reformats and 3-D images are obtained for pre-procedure assessment of TAVR (Cases 1–5).

14.1.3 CT Angiography with low contrast dose

(<13 G iodine or less than 35 mL I.V. contrast with 370 mg/100 mL iodine concentration): Many patients with severe aortic stenosis being evaluated for TAVR have comorbidities including reduced renal function which places them at high risk of contrast induced nephropathy (CIN). In these patients, CT techniques can be utilized to reduce their exposure to iodinated contrast and CTA may be performed with very small doses of I.V. contrast. The diagnostic image quality with small contrast doses is achieved by optimizing different aspects of CT imaging and higher density of enhancement is primarily achieved with the use of 80 Kilovoltage Peak (KVp) technique as the mean energy of 80 KVp X-ray beam matches closely with the absorption k-edge of iodine, thereby producing higher attenuation for a given concentration and volume of iodinated contrast (Fig. 14.4a, b). Higher image noise associated with 80 KVp imaging may be reduced by corresponding increase in tube current or by the use of newer image reconstruction techniques such as model-based iterative reconstruction (Fig. 14.4c). Timing bolus run to determine the arrival of contrast in the aorta is then used to plan for peak contrast enhancement at the time of imaging. CTA examination of chest is performed with ECG synchronization and the imaging can be continued to include abdomen and pelvis with the same small volume contrast injection or a separate non-gated examination may be obtained with a second injection of small contrast dose (Cases 6–8).

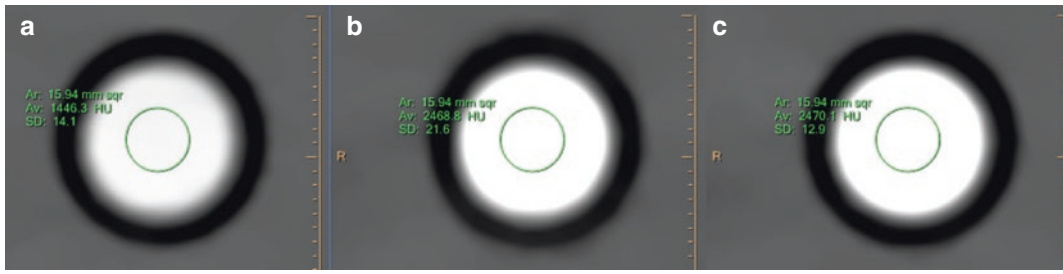

Fig. 14.4 Attenuation of iodinated contrast with different kilovoltage (**a**) 120 KVp image (HU) (**b**) 80 KVp image with higher attenuation and increased noise (SD) using hybrid image reconstruction (**c**) 80 KVp image (same as **b**) with reduced noise using model-based image reconstruction

14.2 Case 1

14.2.1 History

An 88-year-old with severe aortic stenosis for pre-TAVR evaluation.

14.2.2 Findings

Standard helical cardiac/chest CT imaging with intravenous contrast dose of 57 mL was performed on a 256-slice scanner with a bolus triggering at 150 HU with ROI in ascending aorta. Images were reconstructed at 20% and 25% RR interval. Images in true transverse plane at select levels demonstrate the size of aortic valve annulus, sinus of Valsalva, STJ, and LVOT (Figs. 14.5 and 14.6). Image at the level of valve leaflets shows tri-leaflet configuration with moderate calcification. Coronal images with the left and right coronary arteries in profile at origin show the height of ostia from the level of aortic annulus (Fig. 14.7). Figure 14.8 shows reference levels for the transaxial images. The mean diameter of the annulus, and the effective diameter calculated from perimeter as well as area is 28.6 mm.

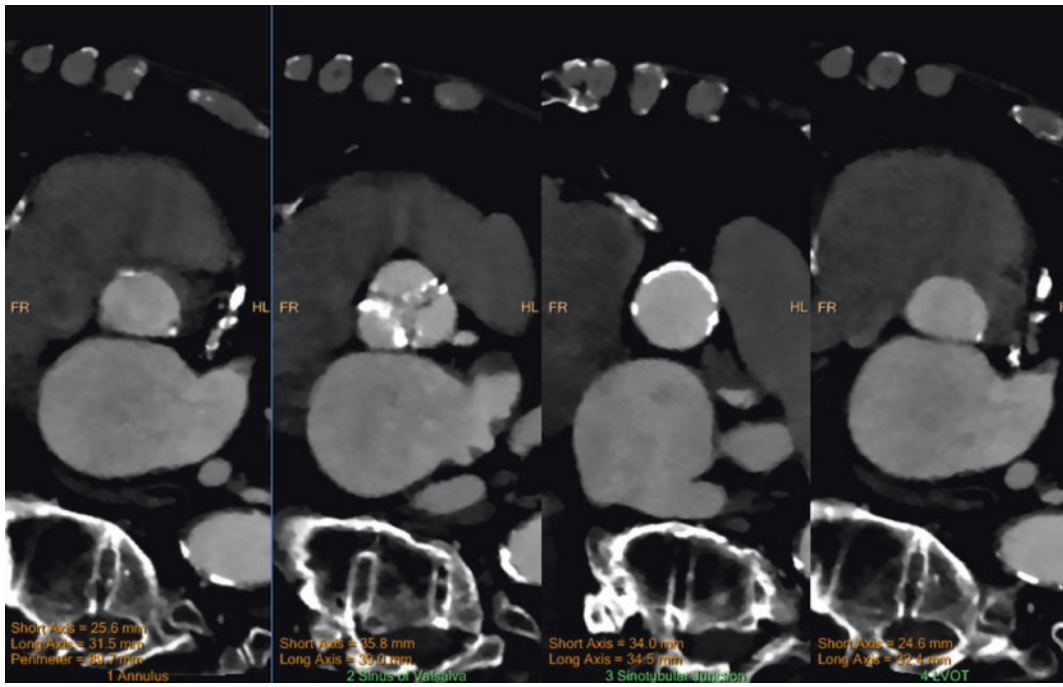

Fig. 14.5 Transverse images (*left-right*) of annulus, sinus of Valsalva, STJ, and LVOT

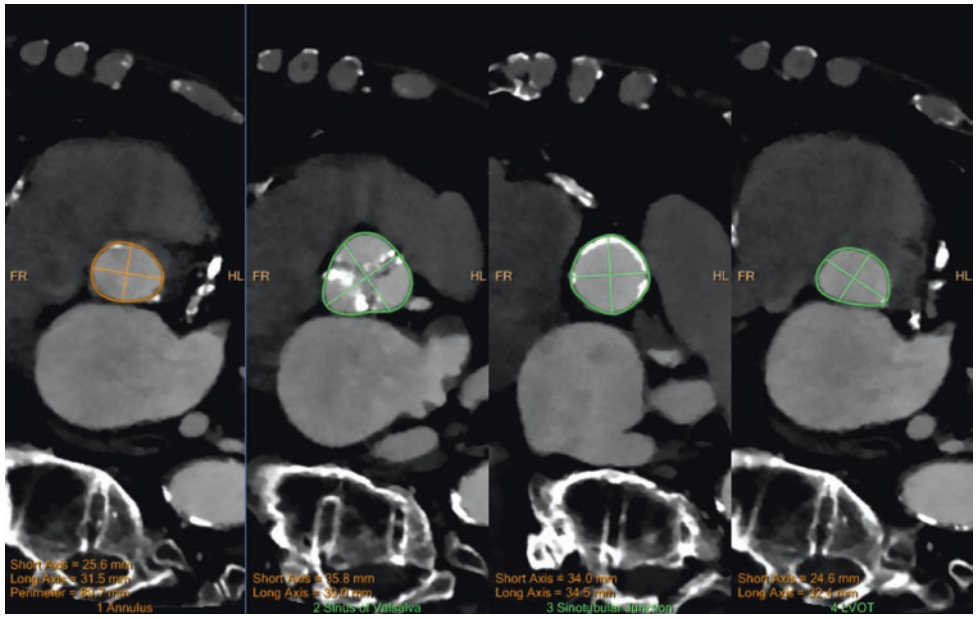

Fig. 14.6 Transverse images (*left-right*) of annulus, sinus of Valsalva, STJ, and LVOT with markings

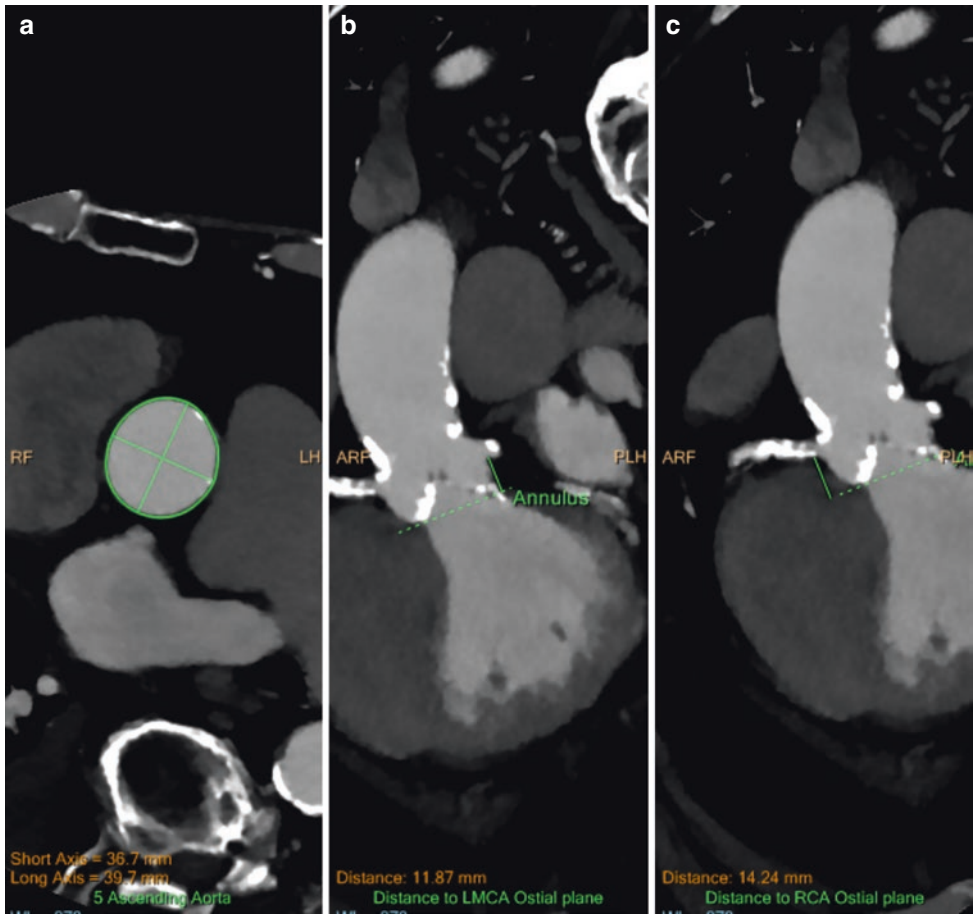

Fig. 14.7 (**a**) Axial image of ascending aorta and coronal images (**b**, **c**) showing coronary arteries

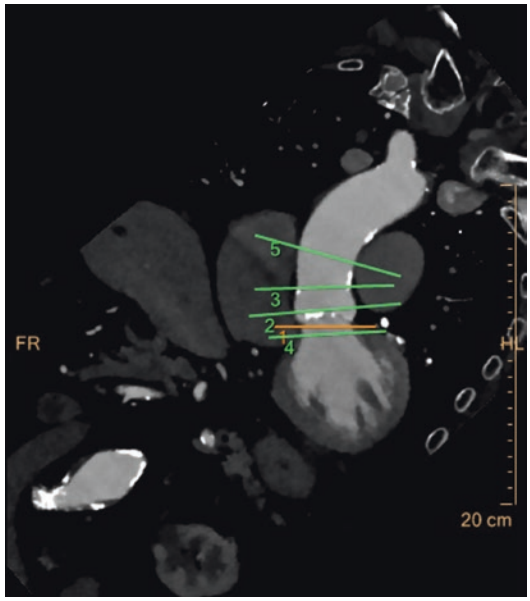

Fig. 14.8 Reference coronal image depicting levels of transaxial images

14.2.3 Discussion

The size of aortic annulus is measured on true transverse image which is acquired orthogonal to the long axis through the aortic annulus by first obtaining oblique coronal (Fig. 14.9) and oblique sagittal (Fig. 14.10) images passing through the center of the annulus. The measurement is made at the level of inferior attachment of the valve leaflets (Fig. 14.11). The long and short axis diameters of the annulus are measured at this level to obtain mean diameter. Effective diameter may be calculated from the perimeter or by obtaining the area of the lumen at the level of annulus by planimetry. Since the annulus is usually oval or elliptical, the diameter derived from area has been shown to match more closely with the appropriate valve size selection for the procedure. Similarly, transaxial images are obtained at other levels orthogonal to the long axis derived from oblique sagittal and coronal images (Figs. 14.12, 14.13, 14.14, and 14.15). For coronary ostium height from the annulus, a coronal image passing through the ostium of coronary artery is obtained using the transverse image at the level of coronary artery and the distance is measured from annulus plane (Fig. 14.16, 14.17, 14.18, and 14.19). During the THV placement, optimal angiographic projections perpendicular to the plane of native aortic valve are needed. CT can be used to predict the optimal angiographic angle. Figures 14.20 and 14.21 show the reference image of aorta and curve generated by computer software using the annulus plane to predict the appropriate fluoroscopic tube angle during angiography for TAVR procedure for projection perpendicular to the valve plane for appropriate valve positioning thereby reducing the contrast use and procedure time. This patient was treated with transfemoral implantation of 29 mm Sapien 3 valve (Fig. 14.22).

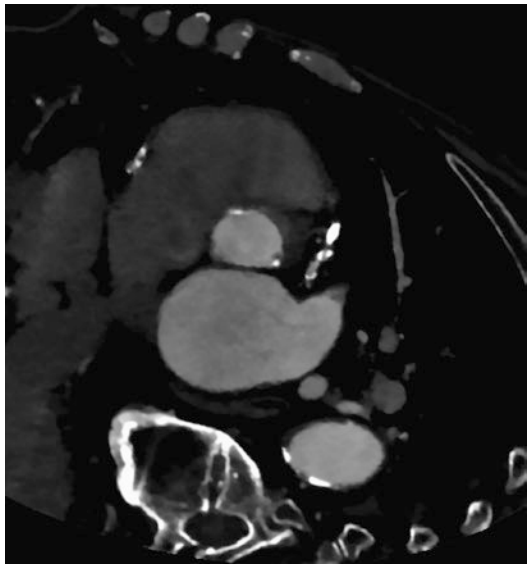

Fig. 14.9 Oblique coronal image to select appropriate plane for transverse image of aortic annulus

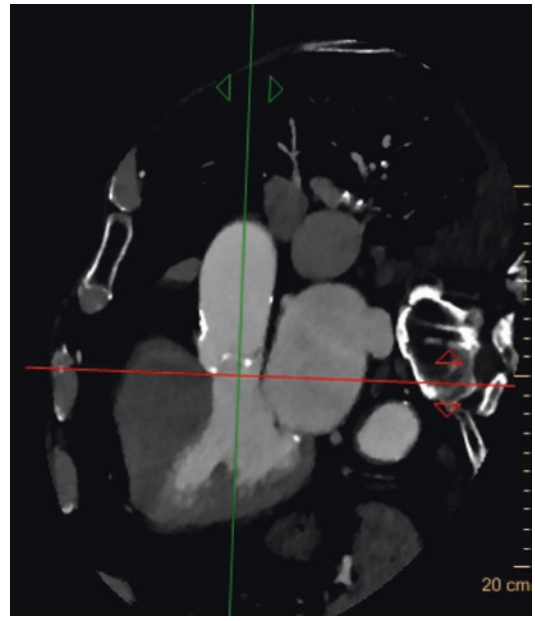

Fig. 14.11 Transverse image of aortic annulus derived from Figs. 14.9 and 14.10

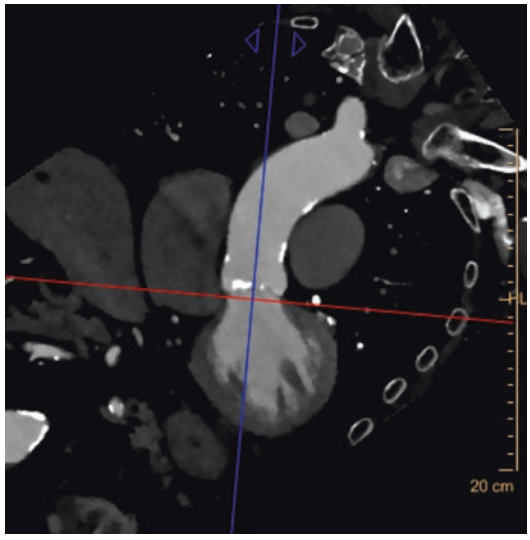

Fig. 14.10 Oblique sagittal image to select appropriate plane for transverse image of aortic annulus

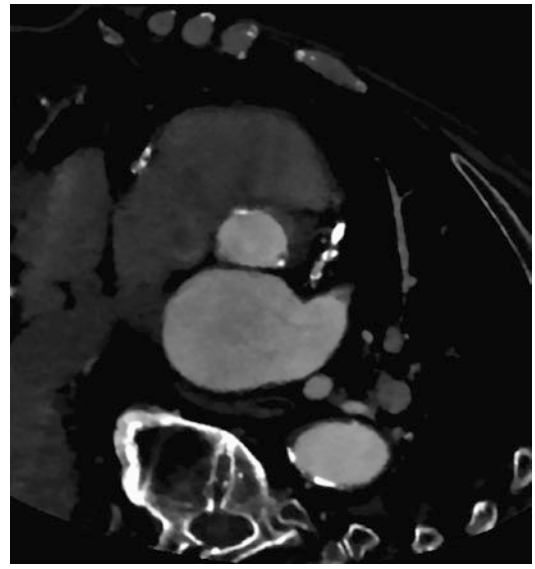

Fig. 14.12 Transaxial image of sinus of Valsalva

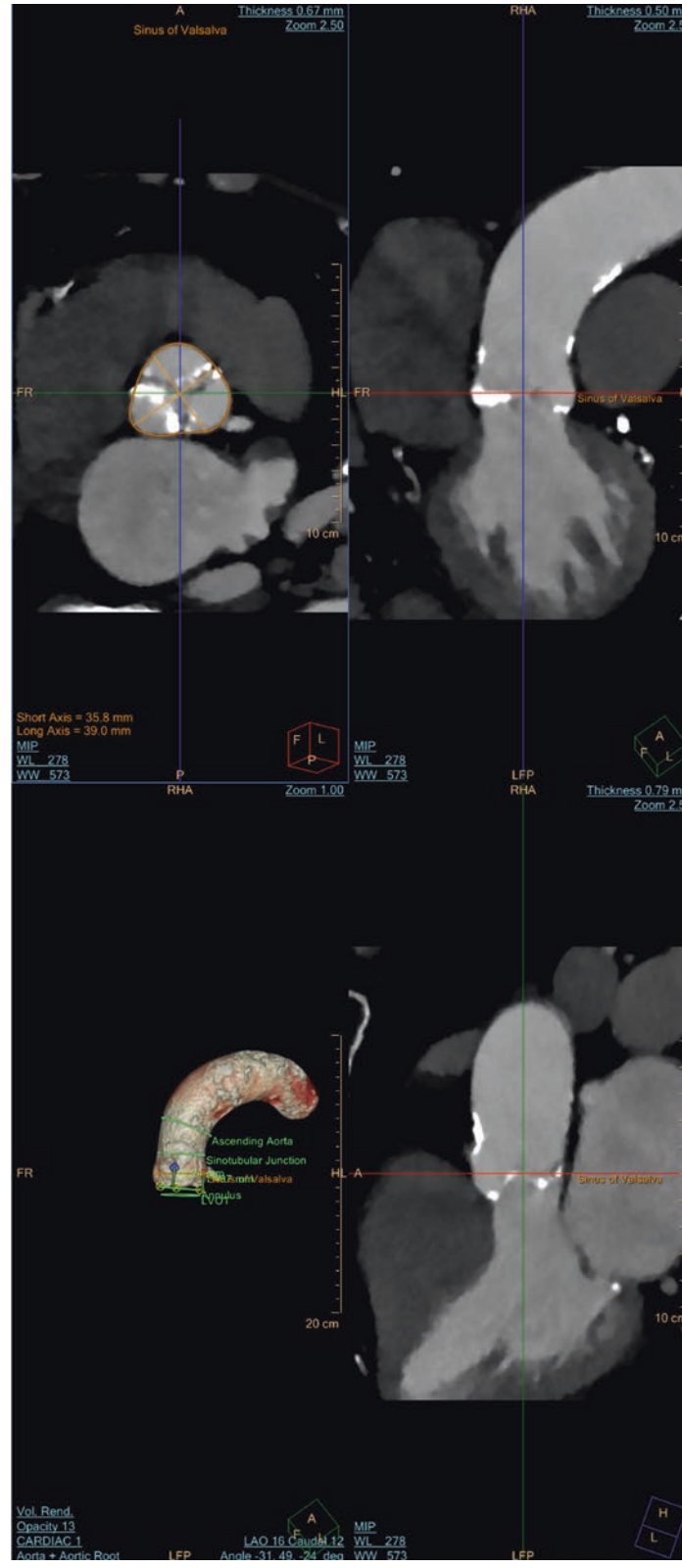

Fig. 14.13 Transaxial image of sinotubular junction

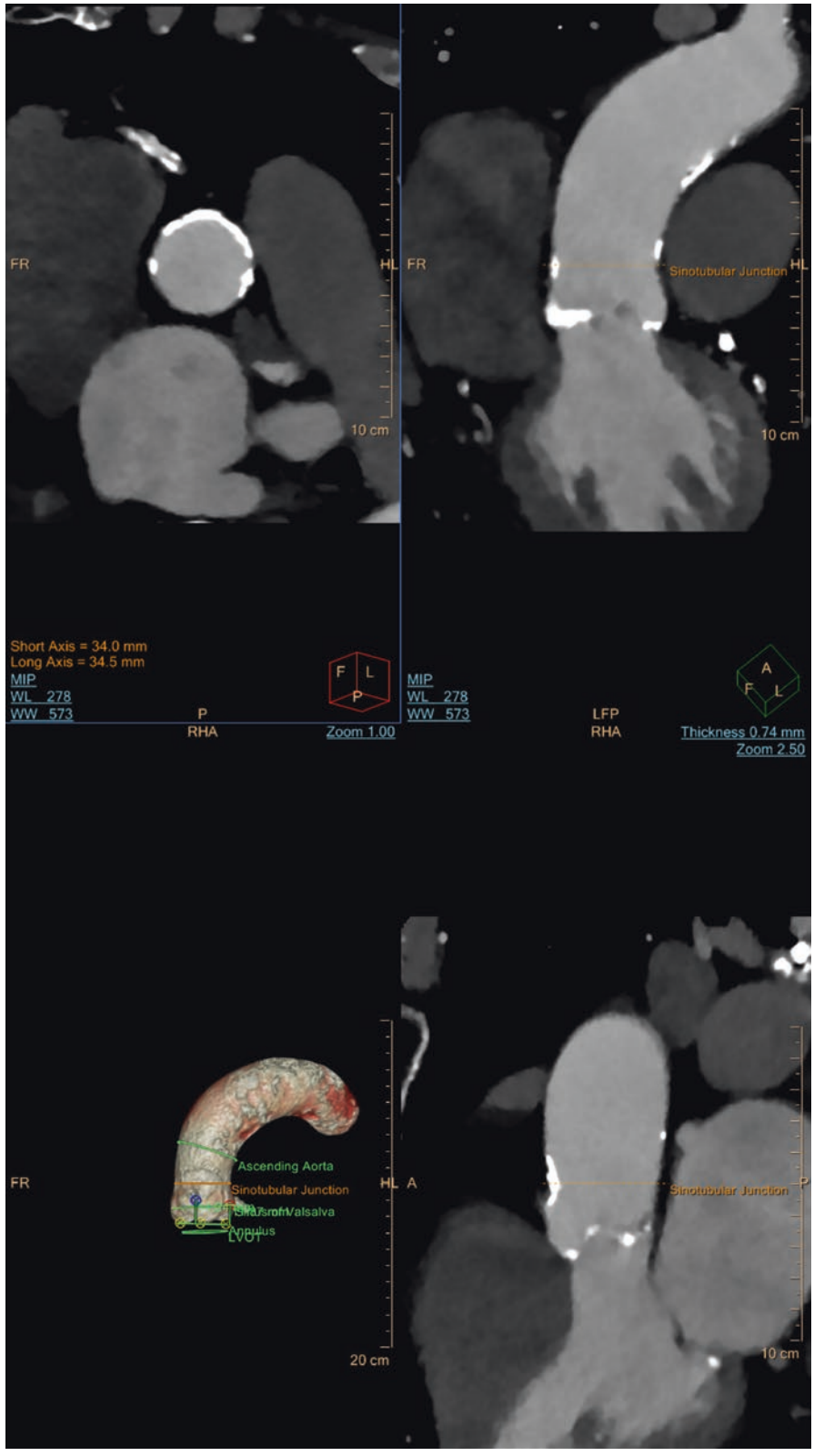

Fig. 14.14 Transaxial image of ascending aorta

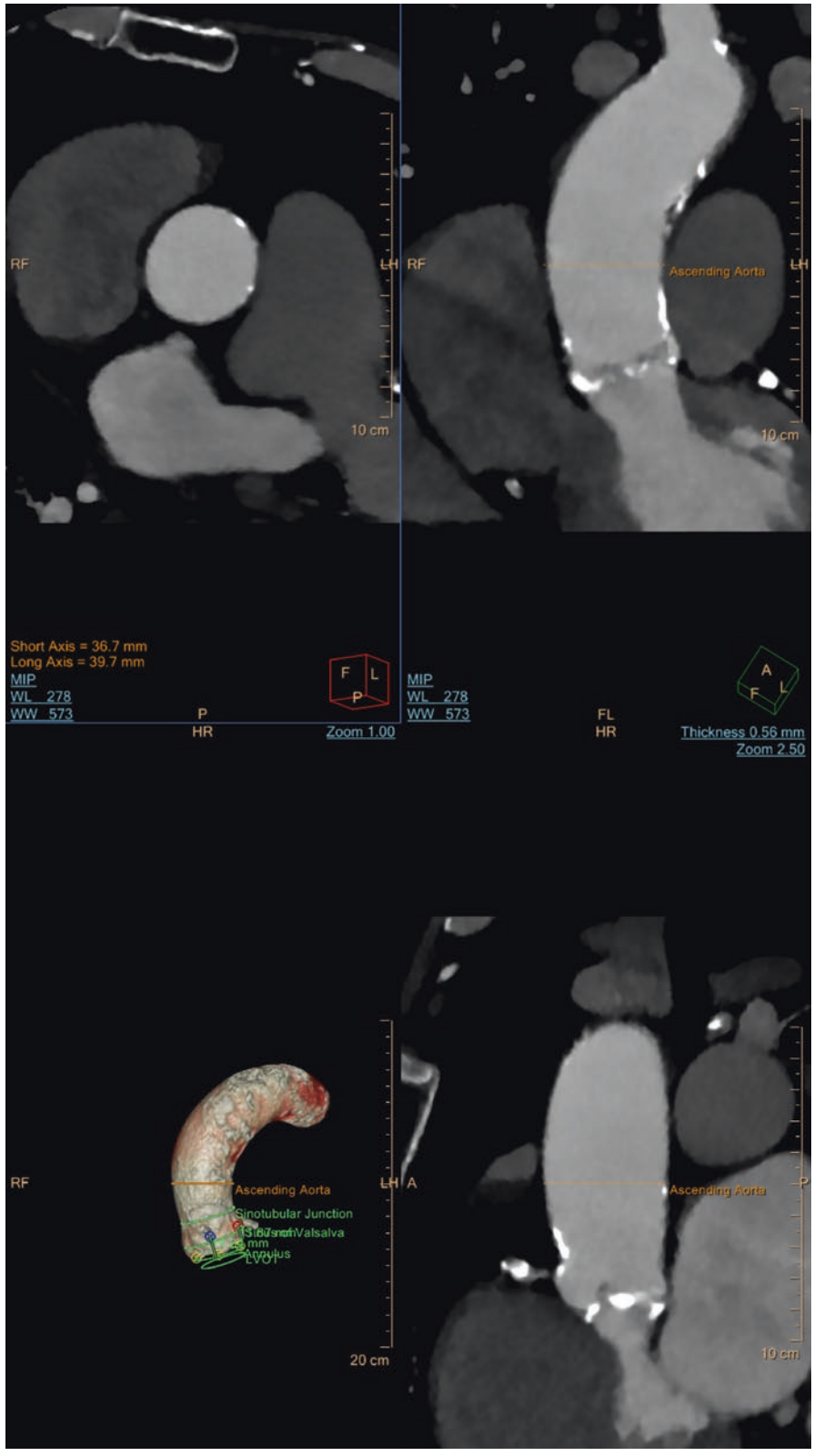

Fig. 14.15 Transaxial image of aorta at the level of LVOT

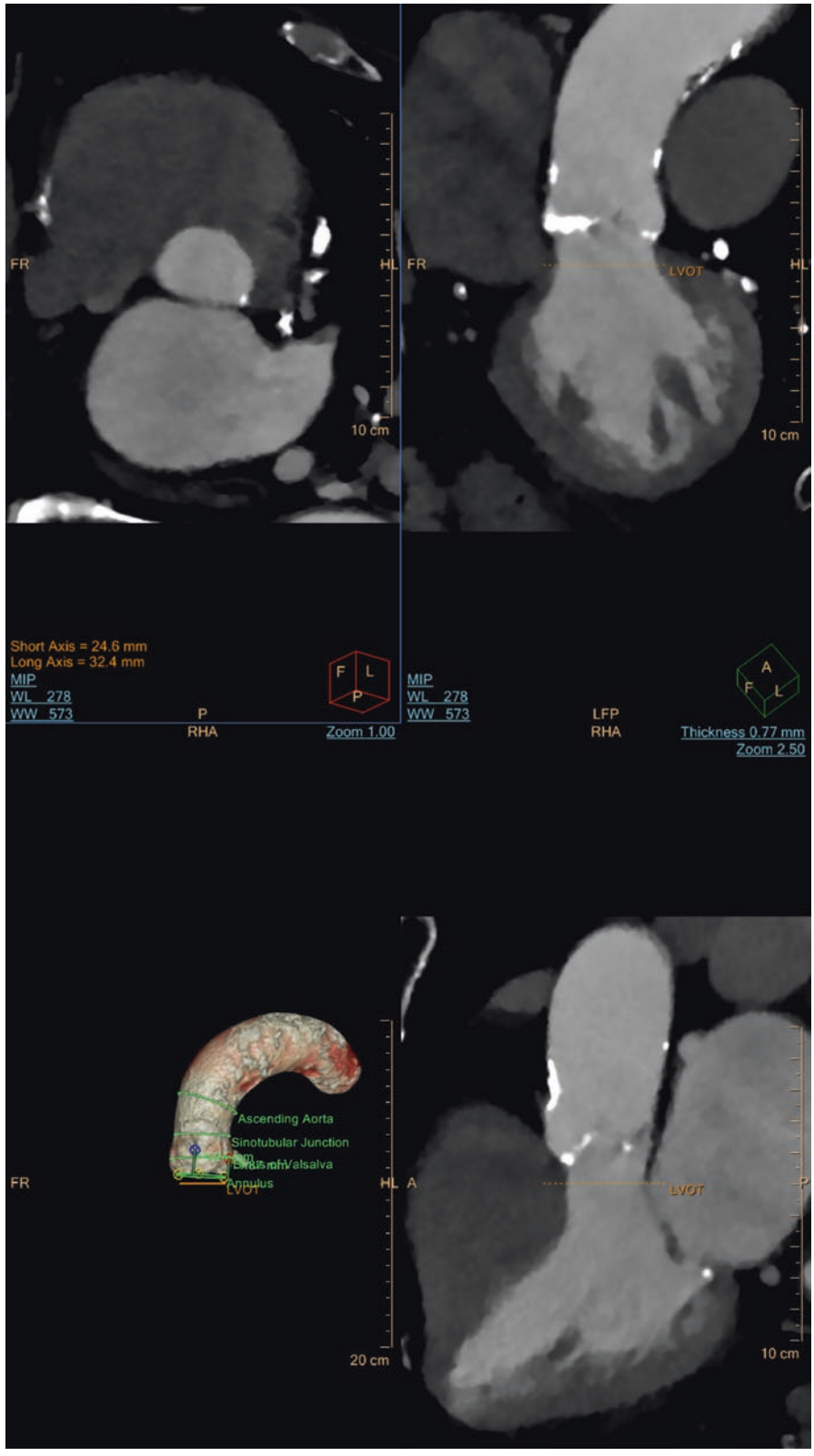

Fig. 14.16 Transaxial image at the level of LMCA

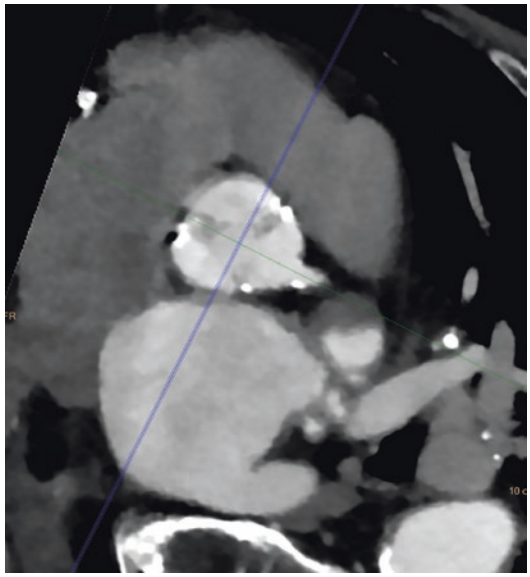

Fig. 14.17 Coronal image of aorta to assess height of ostium of LMCA (derived from Fig. 14.16)

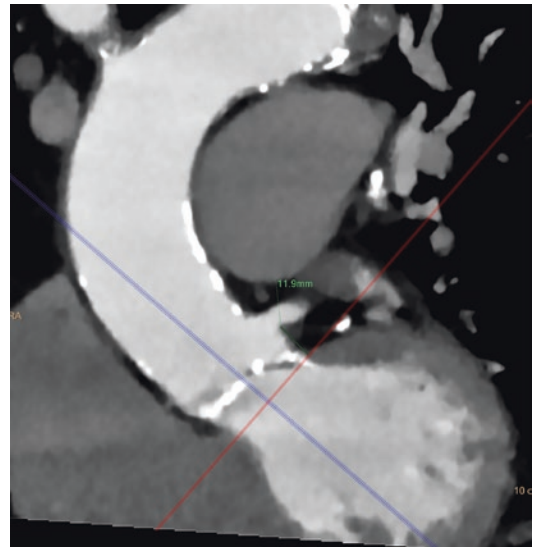

Fig. 14.19 Coronal image showing LMCA ostium height from the level of annulus

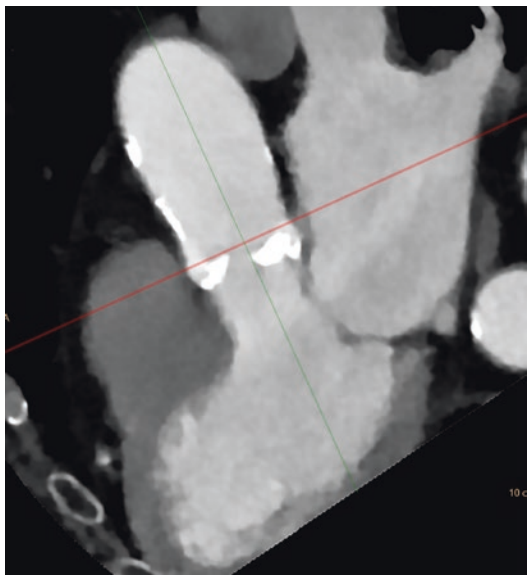

Fig. 14.18 Sagittal image at the level of LMCA

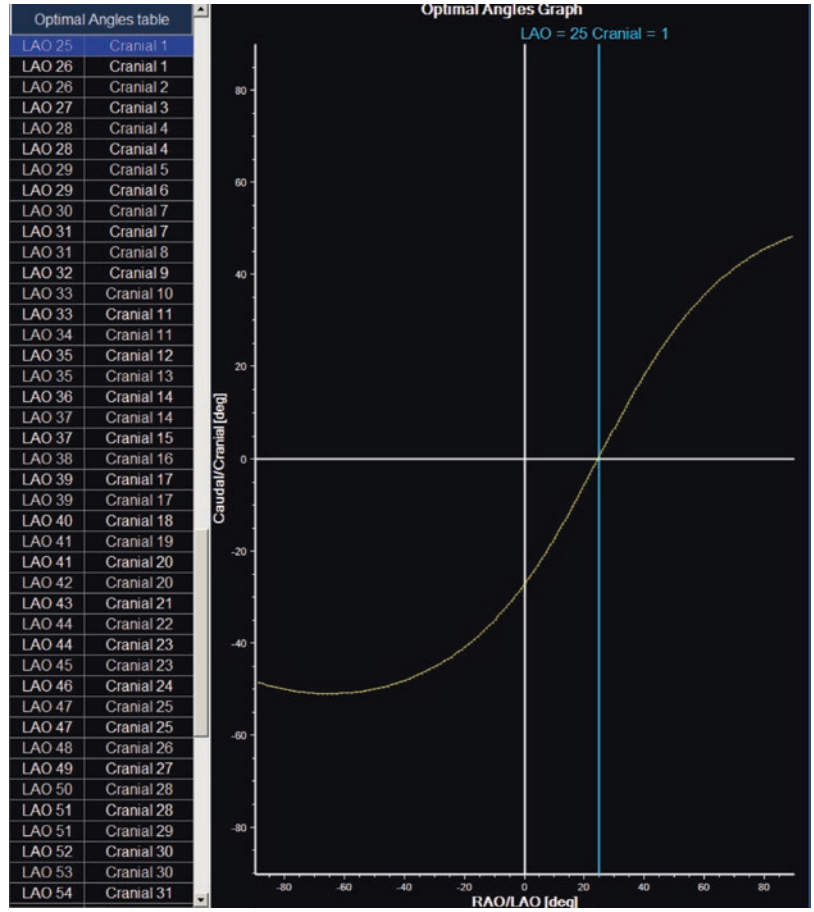

Fig. 14.20 Computer software generated curve predicting the appropriate fluoroscopic tube angle

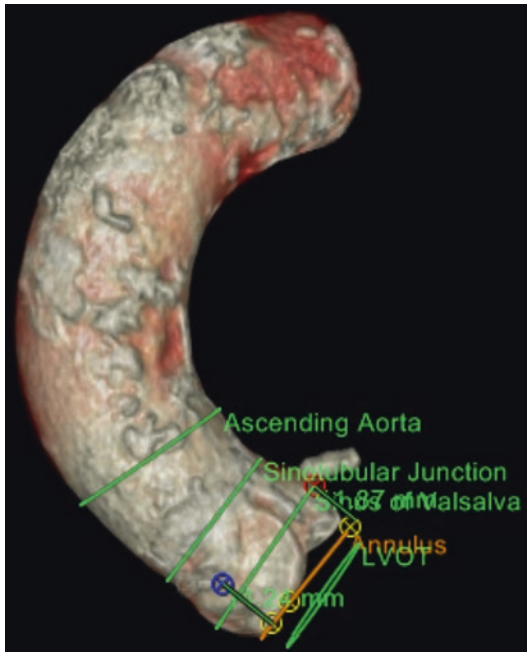

Fig. 14.21 3D Volume rendered image of aortic root and ascending aorta showing the annulus plane corresponding to Fig. 14.20

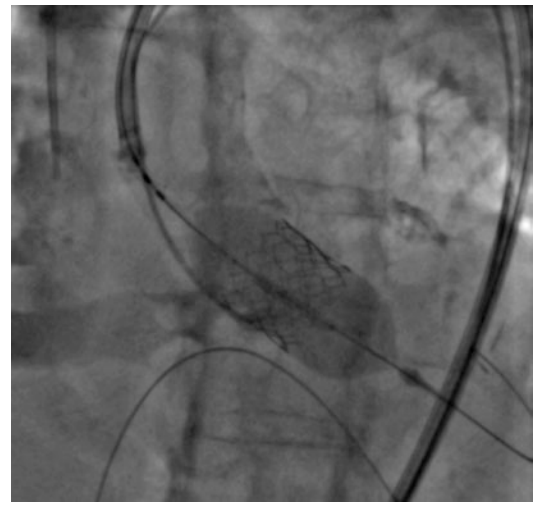

Fig. 14.22 Angiogram during implantation of Sapien 3 29 mm valve via transfemoral approach

14.2.4 Pearls and Pitfalls

Transaxial image of aortic valve annulus is easier to acquire by first obtaining transverse view of aortic valve leaflets at mid sinus level with the three leaflets symmetrical in appearance, and by making adjustments to the sagittal oblique and coronal oblique images to find the appropriate longitudinal axis through the valve. The transverse plane may then be moved inferiorly along the long axis to the level of inferior hinge point of the leaflets for annulus image.

14.3 Case 2

14.3.1 History

CT examinations performed in patients with severe aortic stenosis for pre-TAVR evaluation.

14.3.2 Findings

Contrast enhanced CT angiography examinations for evaluation of iliofemoral access.

Figure 14.23a–d: There is mild to moderate tortuosity of right iliac arteries and mild tortuosity of left iliac arteries. Transaxial image of the iliac artery demonstrates normal caliber and no vascular calcifications.

Figure 14.24a, b: There is relatively small caliber of the iliac artery with circumferential calcification.

Figure 14.25a–d: There is large calcified plaque with severe stenosis of distal aorta and common iliac arteries.

Figure 14.26a, b: There is severe tortuosity of aorta and iliac arteries.

Diagnosis:

CT examinations in different patients demonstrate normal and abnormal appearances for the evaluation of risk of vascular complications for TAVR procedure by iliofemoral route.

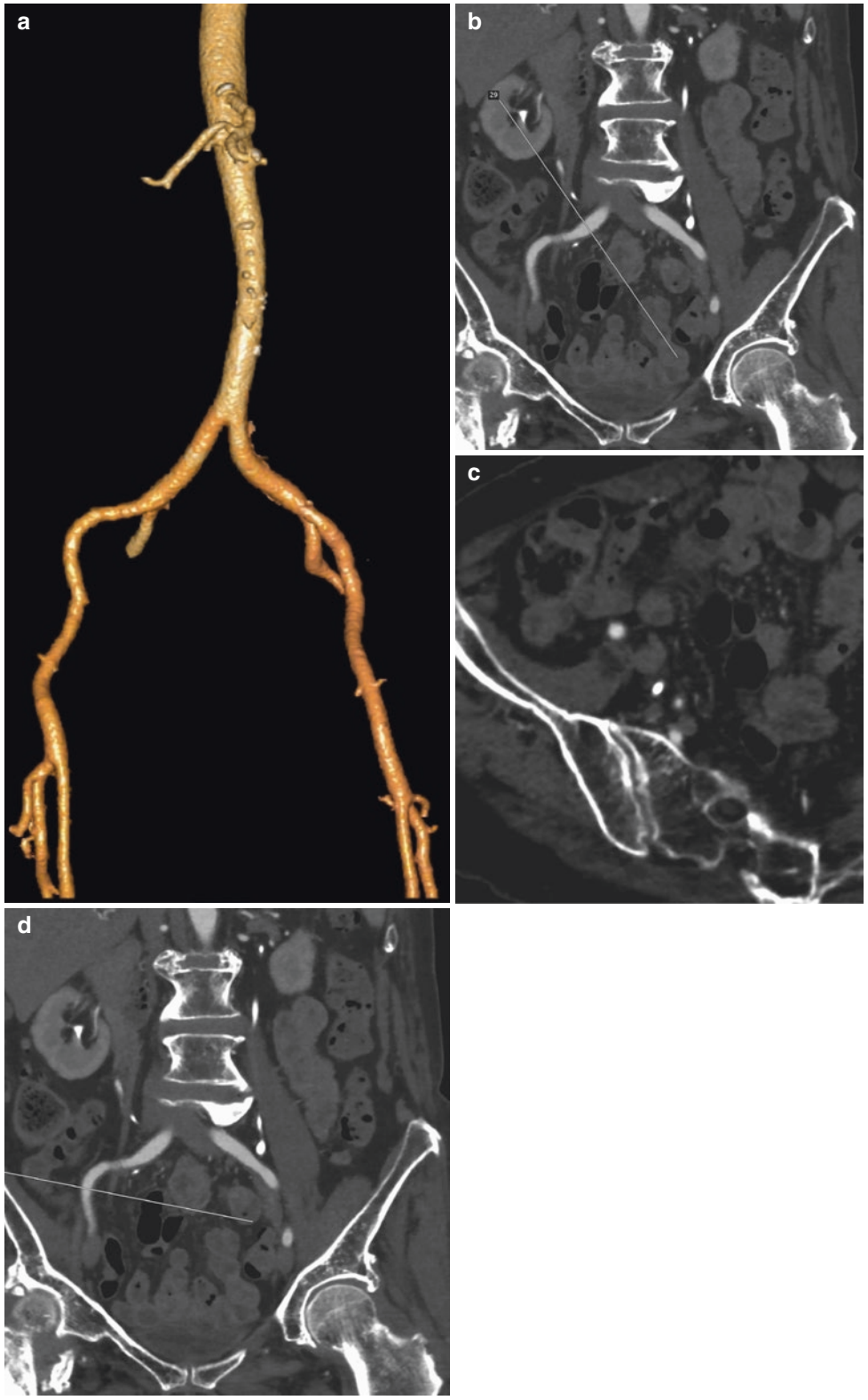

Fig. 14.23 (**a**) Volume rendered image of aorta and iliac arteries (**b**) Right common iliac reference image (**c**) Transaxial image of right external iliac artery (**d**) Right external iliac reference image

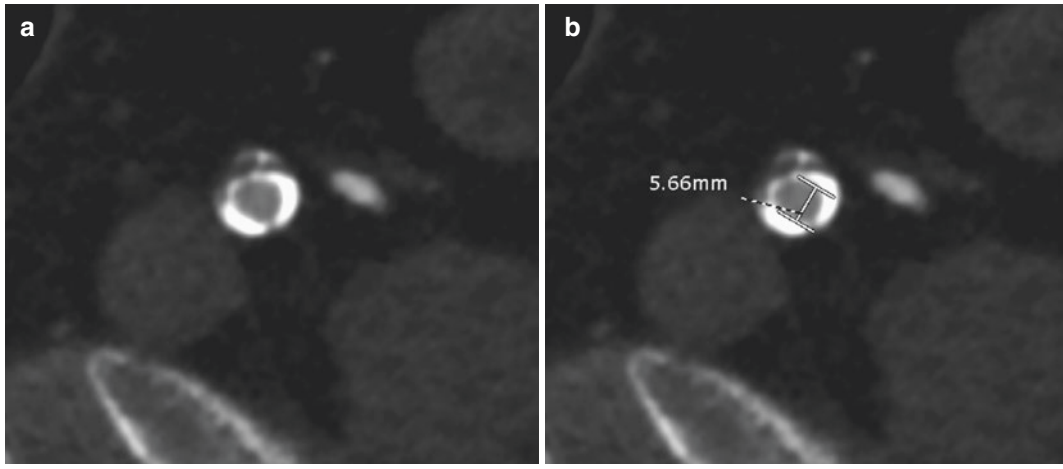

Fig. 14.24 (**a**, **b**) Iliac artery with circumferential calcification luminal diameter of 5.66 mm

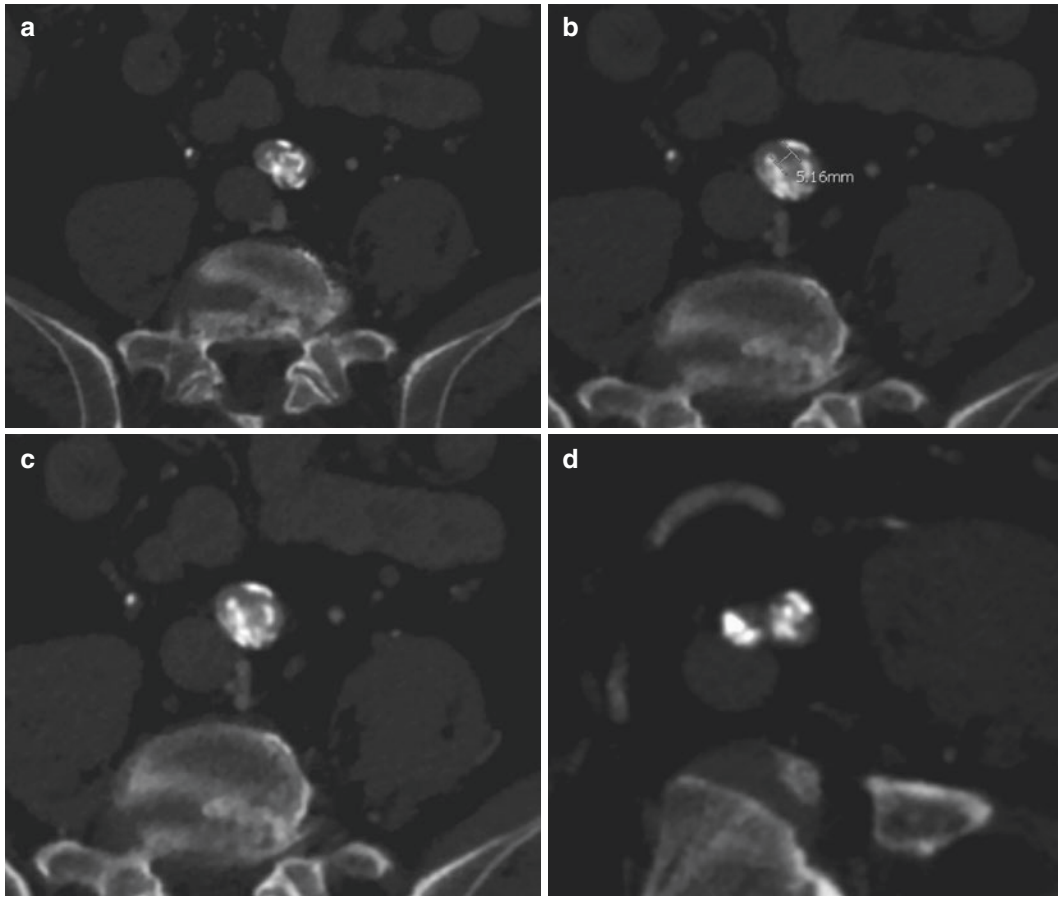

Fig. 14.25 Axial images (**a**–**d**) and Coronal Image (**e**) showing large calcified plaque with severe stenosis of distal aorta and common iliac arteries

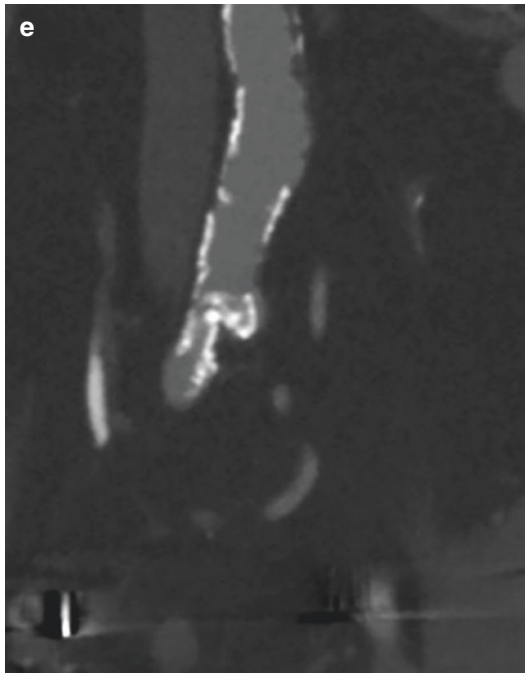

Fig. 14.25 (continued)

14.3.3 Discussion

A variety of image reformats are acquired to optimally assess the aorta and iliac arteries. These include curved multiplanar reformats with transaxial images using centerline reformats, MIP and 3D VR.

The size criteria for arterial caliber for safe access vary with the type and size of the valve and the size of its vascular access device/sheath. With recent developments, the size of vascular access devices has decreased. Although it is preferable to have the diameter of iliac arteries larger than the size of access sheath, the procedure can still be performed safely with slight vessel/sheath size mismatch over a short distance due to distensibility of normal vessels. This distensibility is reduced with diseased vessels with calcifications. Circumferential or horse-shoe calcifications increase the risk of vascular injury and rupture.

Marked tortuosity of aorta or iliac arteries can limit catheter maneuverability for TAVR. This becomes more important in patients with severe atherosclerotic calcifications with decreased vessel compliance or with vessel stenosis. In the case presented (Fig. 14.26), the TAVR was performed via transfemoral route.

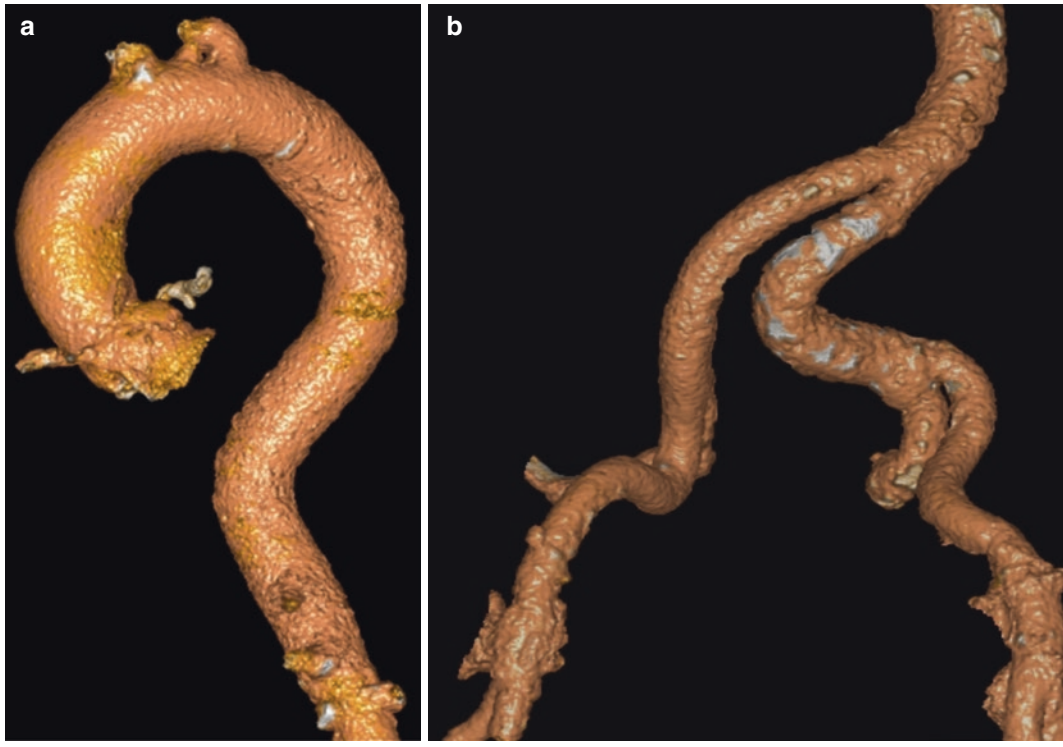

Fig. 14.26 (**a**, **b**) Volume rendered images of aorta and iliac arteries showing severe tortuosity

14.3.4 Pearls and Pitfalls

True transaxial images of the arteries are important in the assessment of arterial caliber, particularly in the region of vessel bifurcation or tortuosity or in cases of arteries with relatively small caliber. The centerline reformats through the vessels at bifurcation or tortuosity should be carefully scrutinized to ascertain true axial images perpendicular to the long axis of the vessels, so as not to over- or underestimate vessel size due to obliquity of plane.

The presence of dense arterial calcifications can cause difficulty in the assessment of luminal size due to similar attenuation of contrast enhanced arteries in some cases. Selecting a wide window width for display is useful to maximize the difference between contrast enhanced lumen and calcification in the wall particularly for vessels with generally small caliber such as external iliac arteries. Dense calcifications may cause low density streaks secondary to beam hardening artifacts.

14.4 Case 3

14.4.1 History

An 84-year-old male patient with severe aortic stenosis diagnosed on echocardiography; being evaluated for TAVR.

14.4.2 Findings

Figure 14.27: Transaxial images at the level of aortic valve cusps reconstructed in the systolic phase at 30% R-R interval: There is a bicuspid aortic valve (BAV) with fused, small right and left coronary cusps with a single raphe corresponding to Type 1 BAV. There is heavy calcification in the cusps. Incomplete opening of the valve during systole is consistent with severe aortic stenosis. Figure 14.28: Transaxial image at the level of the aortic annulus demonstrates a diameter of 31 × 25.3 mm. The area was 607 mm^2 with effective diameter based on area 27.8 mm. Figure 14.29: Intraoperative fluoroscopy/angiography images during TAVR procedure demonstrate placement of a 29 mm Medtronic Core-valve just prior to, during, and after expansion in aortic valve. Figure 14.30: Chest X-ray showing the implanted CoreValve.

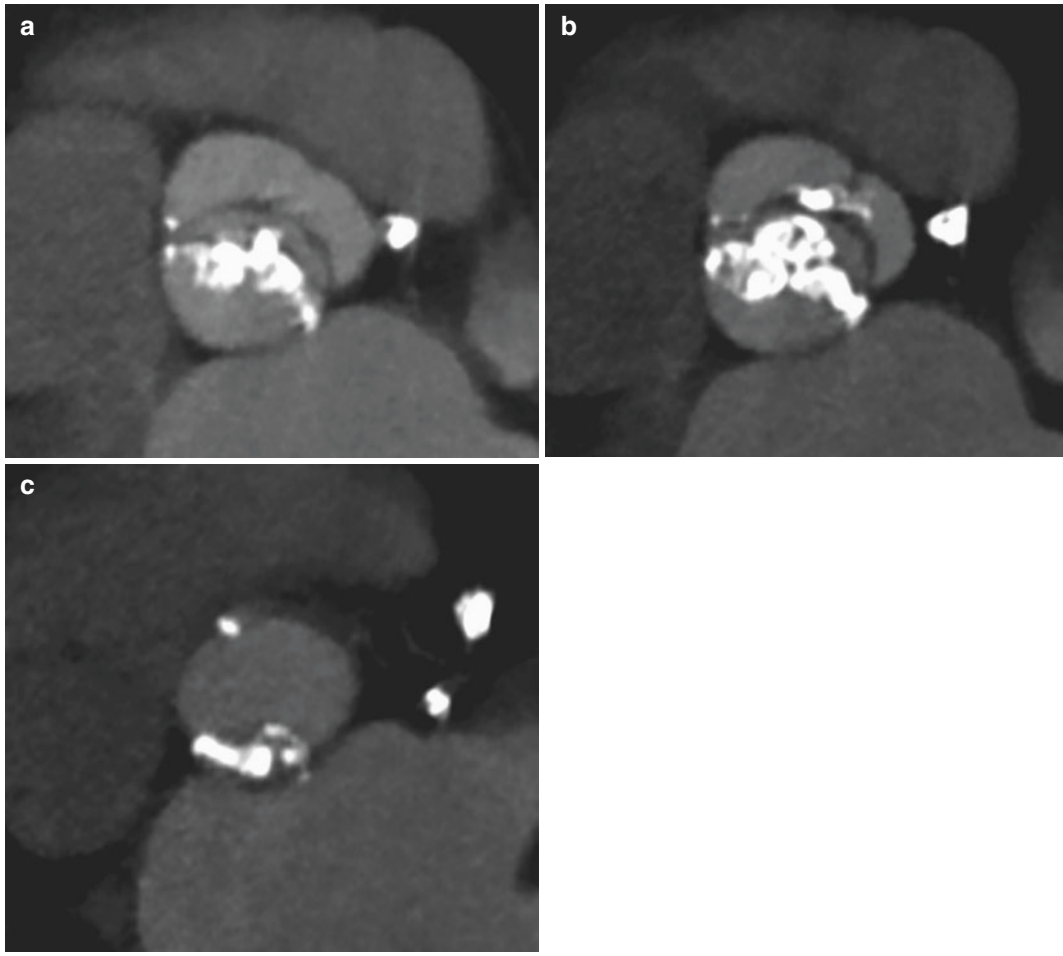

Fig. 14.27 (**a**, **b**, **c**) Transaxial images at the level of aortic valve cusp showing bicuspid aortic valve and large amount of calcifications

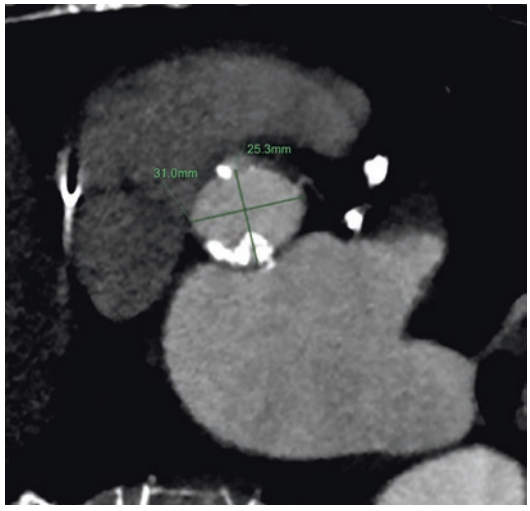

Fig. 14.28 Transaxial image at the level of the aortic annulus

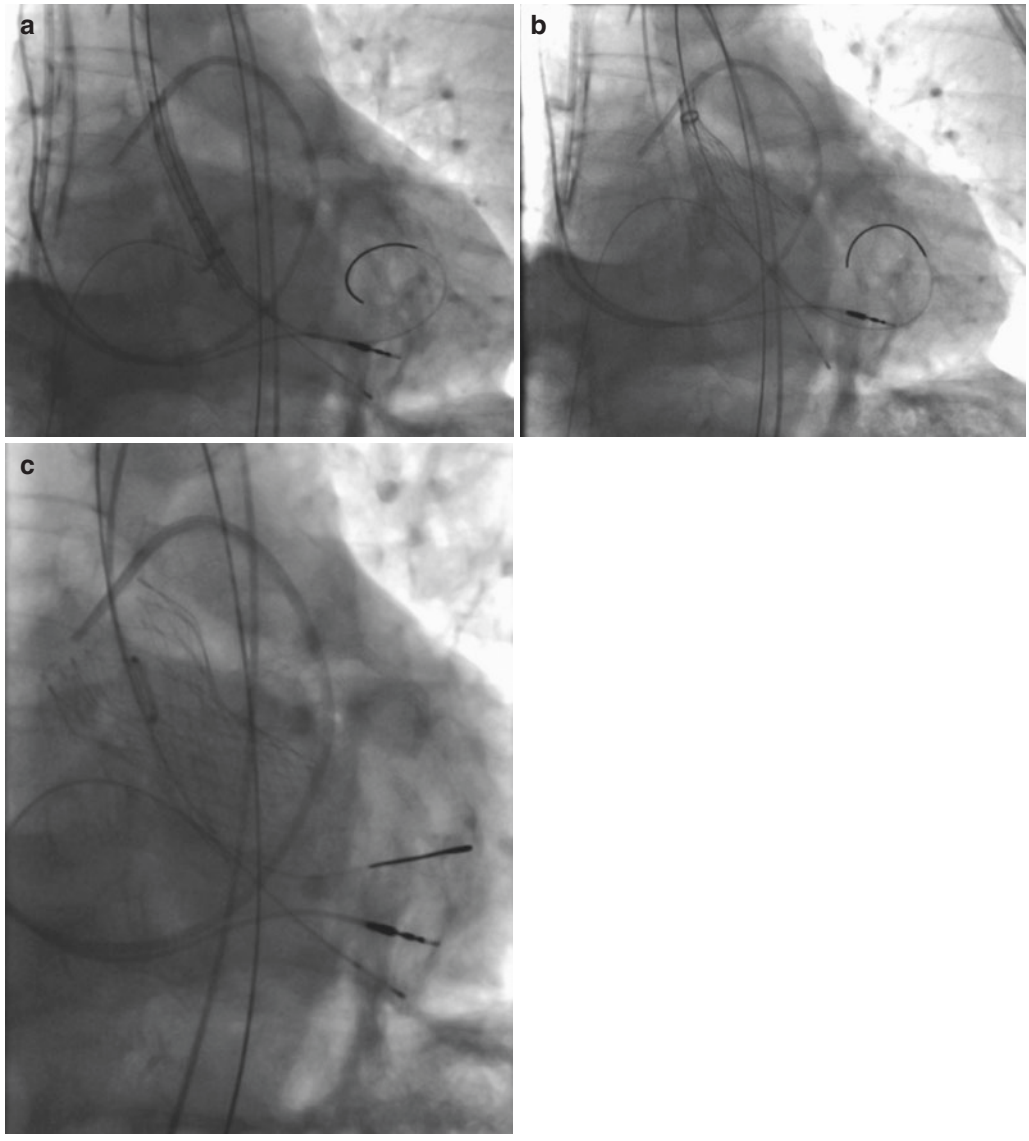

Fig. 14.29 Angiogram images of TAVR: Prior to (**a**), during (**b**), and after expansion (**c**) of Core-valve

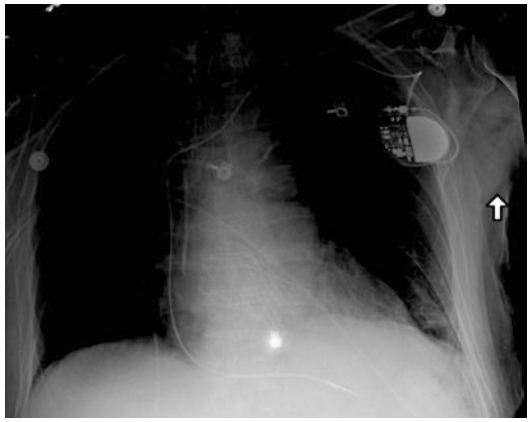

Fig. 14.30 Chest X-ray after the CoreValve implantation

14.4.3 Diagnosis

Bicuspid aortic valve with heavy calcification.

14.4.4 Discussion

The bicuspid aortic valve (BAV) presents special challenges for transcatheter valve implantation. The asymmetric shape and associated fibrotic or heavily calcified cusps can lead to abnormal expansion or suboptimal alignment of the prosthetic valve, which may cause significant aortic regurgitation. The detection of BAV may sometimes be difficult on transthoracic echocardiography due to calcifications or in patients with large body habitus and BAV may initially be diagnosed on CT, performed for pre-TAVR valve sizing. The data regarding long-term outcomes of TAVR in BAV is limited.

14.4.5 Pearls and Pitfalls

The shape of the annulus of BAV is more likely to be elliptical than circular and CT is thus particularly important in BAV for accurate sizing for prosthetic valve implantation, which currently is circular in shape. Pre-TAVR CT can provide initial diagnosis of bicuspid aortic valve or confirmation of findings on echocardiography and also provide information regarding the degree of calcifications, which may affect valve alignment.

14.5 Case 4

14.5.1 History

A 98-year-old female with severe aortic valve stenosis for pre-procedure CT evaluation for TAVR.

14.5.2 Findings

Figure 14.31 demonstrates the height of the ostium of left main coronary artery from the level of aortic valve annulus measuring 5.6 mm and the height of ostium of right coronary measuring 10.9 mm. The ostium of LMCA is at the level of mid portion of sinus of Valsalva on the transaxial view (Fig. 14.32) indicating low position.

Images during TAVR demonstrate catheterization and opacification of left coronary artery (Fig. 14.33) and balloon expansion of the aortic valve with the catheter in left coronary artery (Fig. 14.34). Figure 14.35 shows the implanted aortic valve with patent left coronary artery.

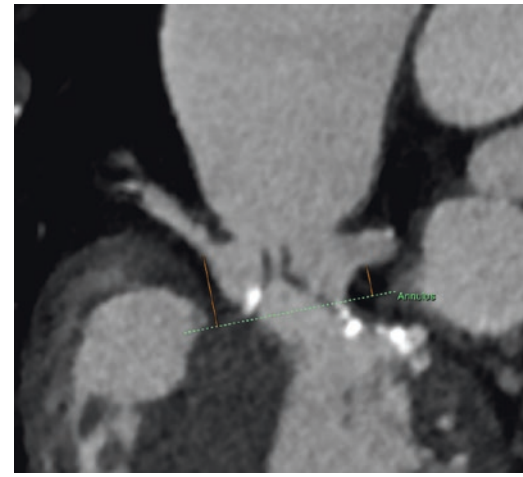

Fig. 14.31 Low ostium of left main coronary artery (LMCA)

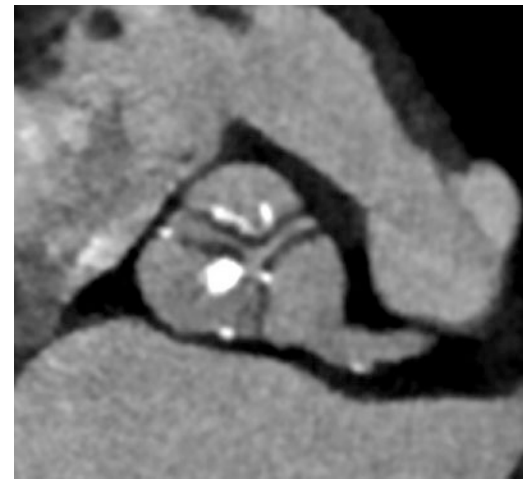

Fig. 14.32 Transaxial view at the level of mid sinus of Valsalva showing the ostium of LMCA

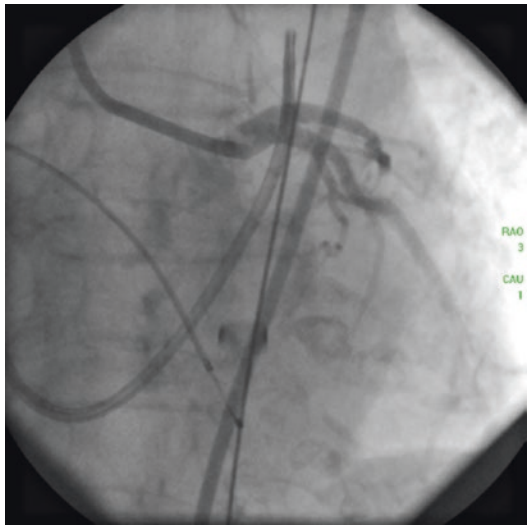

Fig. 14.33 Angiogram with opacification of left coronary artery

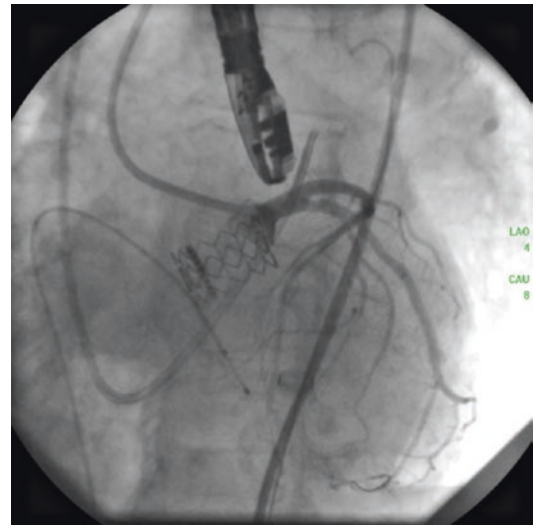

Fig. 14.35 Angiography image showing the implanted aortic valve and patent LMCA

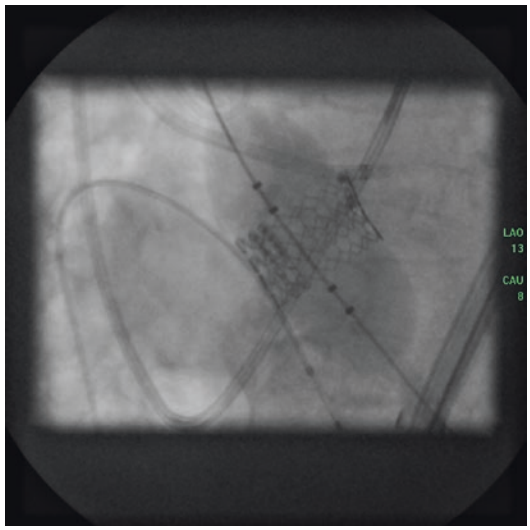

Fig. 14.34 Fluoroscopy image during balloon expansion of prosthetic aortic valve with a catheter in LMCA

14.5.3 Diagnosis

Low height of LMCA ostium from the aortic valve annulus.

14.5.4 Discussion

The low position of the ostium of the coronary artery predisposes it to the risk of occlusion due to displaced cusp of the native calcified aortic valve during prosthetic valve implantation or potentially due to superimposition of the prosthetic aortic valve. Coronary ostia height of less than 10 mm increases the risk of coronary occlusion which depends on specific type and size of prosthetic valve to be implanted. The risk is higher with larger size of aortic valve. It is therefore important to accurately assess the height of coronary artery ostium from the plane of aortic valve annulus as these patients may become unsuitable for TAVR. In the case above, the ostium of left coronary artery was protected during the valve implantation by placing a catheter into it.

14.5.5 Pearls and Pitfalls

Demonstration of the coronary ostia in appropriate planes on CTA for accurate assessment of height helps pre-procedure planning. Depending on overall condition and other risk factors for the patient, TAVR could be performed by modifying the implantation technique.

14.6 Case 5

14.6.1 History

An 80-year-old male with prior history of surgically placed bioprosthetic aortic valve (25 mm SJM Biocor valve); now presenting with valve dysfunction with aortic stenosis and regurgitation on echocardiography. CT is performed for pre-TAVR evaluation.

14.6.2 Findings

Cardiac gated CTA images demonstrate prosthetic aortic valve (Figs. 14.36, 14.37, 14.38, 14.39, 14.40, 14.41, 14.42, 14.43, 14.44, and 14.45).

Figure 14.36 shows images of the valve in transaxial plane, generated from oblique coronal (Fig. 14.37) and oblique sagittal views (Fig. 14.38).

Figure 14.39 shows inner luminal diameter of 18 × 17.7 mm for this valve with nominal diameter of 25 mm.

Figures 14.40 and 14.41: The valve posts are visualized as hypodense structures; but the leaflets are not visible on CT. The three hyperdense structures represent superior margin of the valve posts to which the leaflets are attached.

Figures 14.42, 14.43, 14.44, and 14.45: Virtual ring drawn around the valve posts at the level of superior margin demonstrates a distance of 2.7 mm to the LMCA ostium.

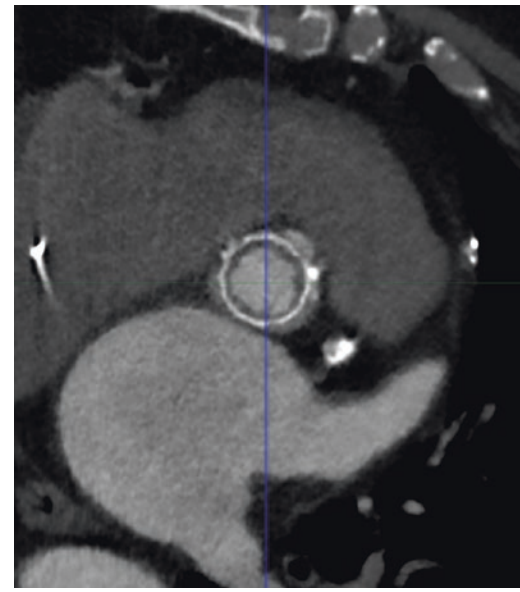

Fig. 14.36 Transaxial view at the level of bioprosthetic valve

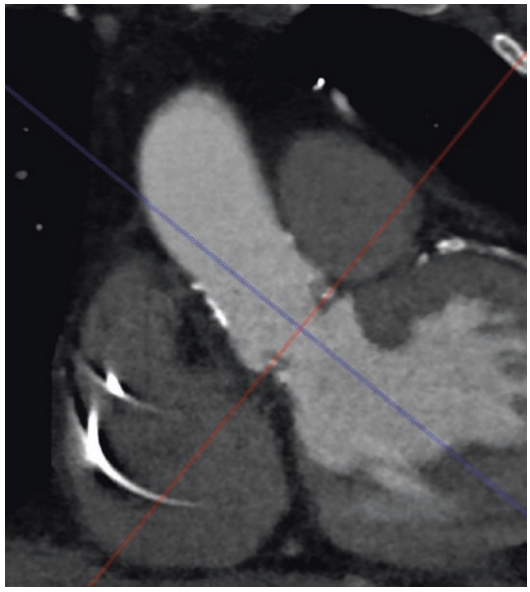

Fig. 14.37 Oblique coronal view with reference axial plane through the level of bioprosthetic valve

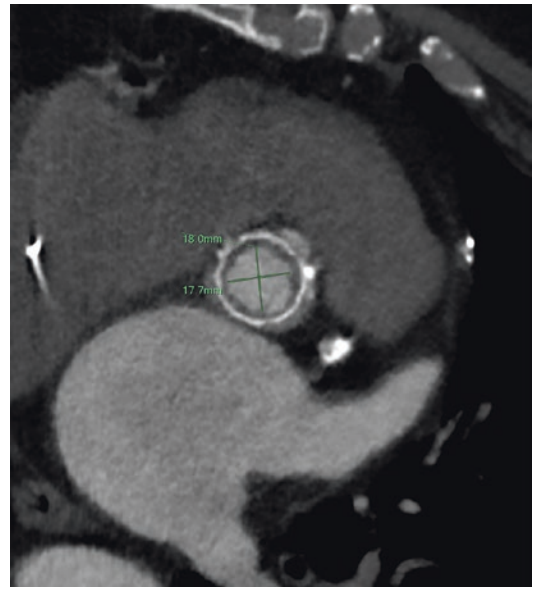

Fig. 14.39 Transaxial view: bioprosthetic valve luminal diameter

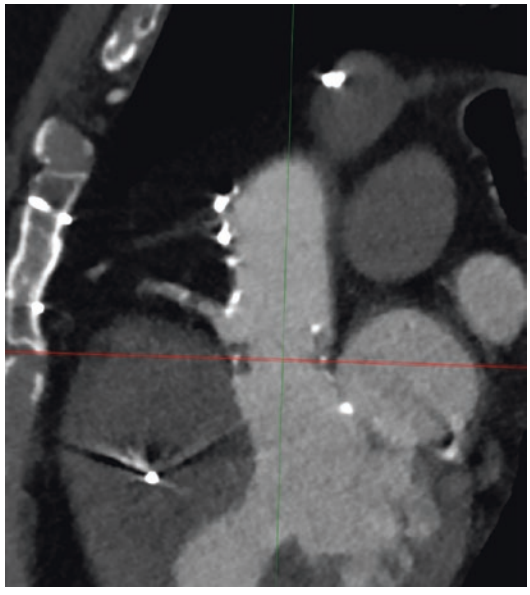

Fig. 14.38 Oblique sagittal view with reference axial plane through the level of bioprosthetic valve

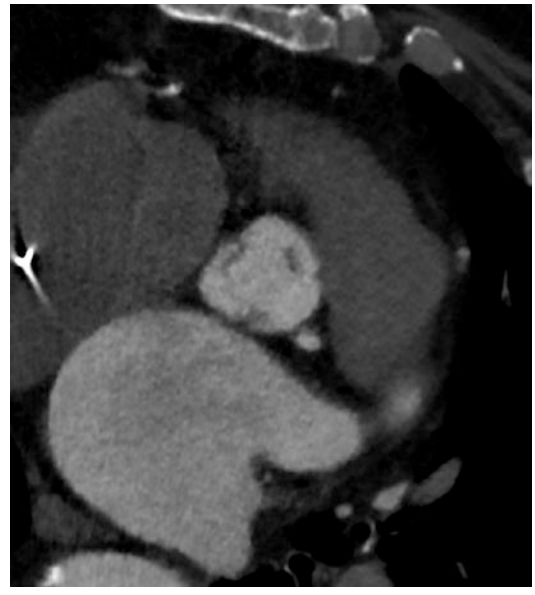

Fig. 14.40 Transaxial view showing hypodense valve posts

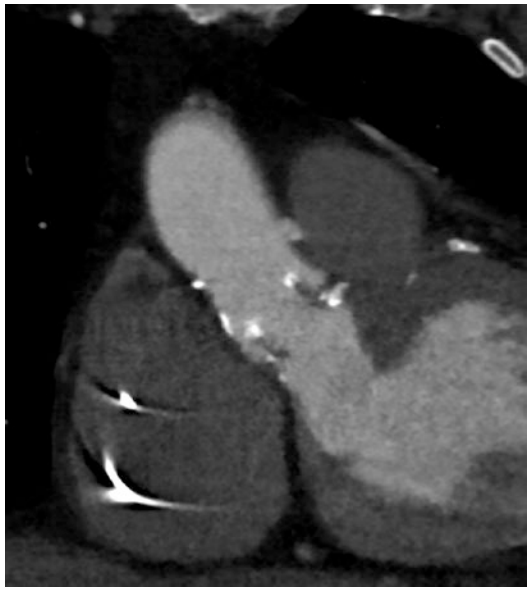

Fig. 14.41 Oblique sagittal showing valve posts

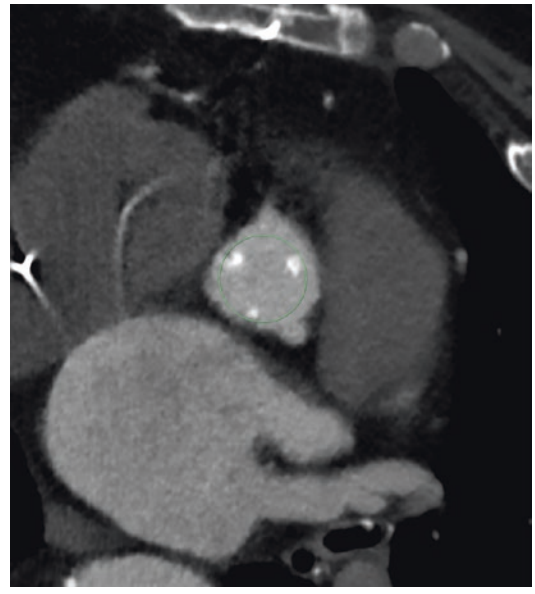

Fig. 14.43 Transaxial view with a virtual ring drawn

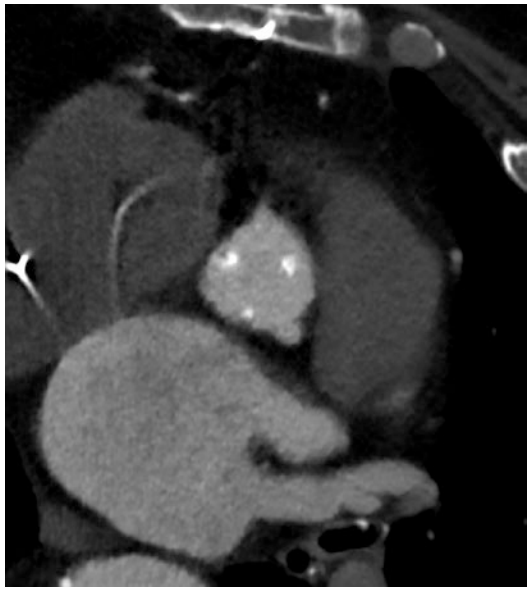

Fig. 14.42 Transaxial view at the level of superior margin of valve posts

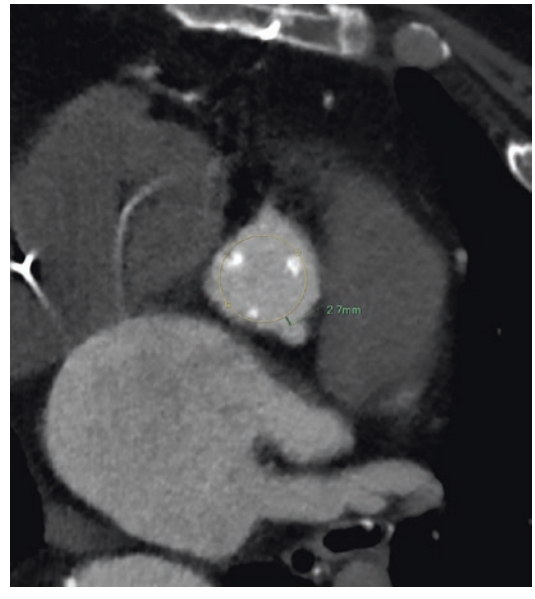

Fig. 14.44 Transaxial view with a virtual ring drawn with superior margin demonstrating a measured distance of 2.7 mm to the LMCA ostium

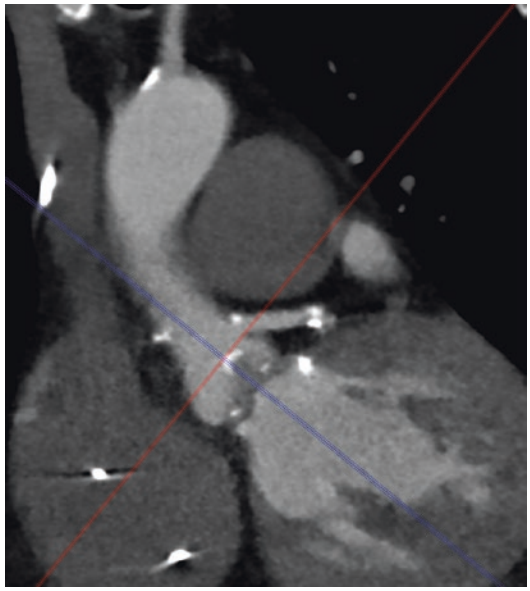

Fig. 14.45 Coronal view with reference axial line at the level of superior margin of valve posts and LMCA ostium

14.6.3 Diagnosis

Prosthetic aortic valve with inner luminal diameter of 18 × 17.7 mm. The distance of virtual ring at the level of superior margin of valve posts from LMCA ostium is 2.7 mm which will be at high risk for coronary obstruction for valve-in-valve TAVR.

14.6.4 Discussion

Bioprosthetic surgical aortic valves include stented and stentless variety. These valves are surgically placed at or above the level of native annulus. Dysfunction of bioprosthetic valves may present with stenosis or regurgitation or both and is treated with surgical replacement. TAVR with valve-in-valve treatment is performed in patients who are at high risk for surgical repair.

The valve-in-valve procedure is associated with higher risk of complications which include post-procedure high trans-aortic gradients, malposition of the valve, and coronary obstruction. However, the risk of annulus rupture or conduction system abnormalities is low, as the annulus may be protected by the firm ring of the surgical valve.

The diagnosis of dysfunction of surgical aortic valve is made by echocardiography. CT is used for pre-TAVR planning including the assessment of luminal diameter which is different from the nominal diameter and orientation of the valve, which may be tilted from the long axis of aortic root.

The assessment for expected position of displaced cusps of surgical valves relative to coronary ostium is also relevant for pre-procedure planning. A large size of aortic root is at low risk for coronary occlusion. Drawing a virtual ring of anticipated THV size at the level of superior margin of the posts of the bioprosthetic valve on pre-TAVR CT images has been proposed to evaluate the relationship with the coronary ostium. A distance of less than 3 mm is considered high risk for coronary occlusion and a distance greater than 6 mm is at low risk with valve-in-valve replacement by transcatheter heart valve (THV). The risk of coronary occlusion can be reduced by low placement of THV or placing a THV with smaller diameter to reduce lateral displacement of valve posts and leaflets.

14.6.5 Pearls and Pitfalls

The nominal size of the surgical valve commonly refers to the outer diameter or sewing ring size, whereas the inner luminal diameter is used for TAVR size selection. The bioprosthetic valve leaflets are not visible by CT. CT can be useful in detecting thrombus or calcifications within the dysfunctional prosthetic valve.

14.7 Case 6

History: An 88-year-old with severe aortic stenosis and decreased renal function; for pre-TAVR evaluation CT with low contrast dose.

14.7.1 Findings

ECG-gated helical CTA examination of the chest, abdomen, and pelvis performed with total contrast volume of 28 mL (Iopamidol 370 mgI/dL) with 80 KV technique (Figs. 14.46, 14.47, 14.48, 14.49, 14.50, 14.51, 14.52, 14.53, 14.54, 14.55, 14.56, 14.57, 14.58, and 14.59).

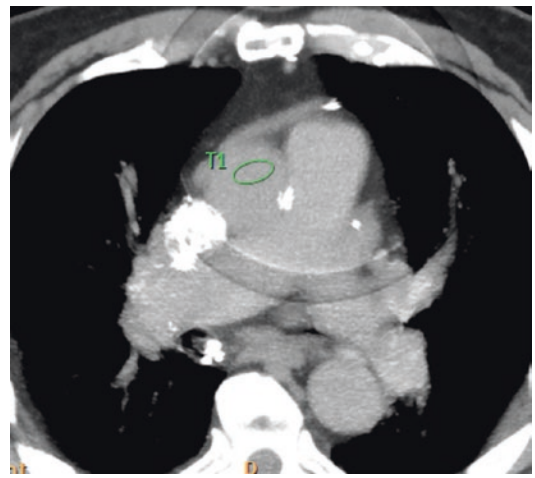

Fig. 14.46 80 KVp technique: Bolus timing run with 1 mL at ascending aorta

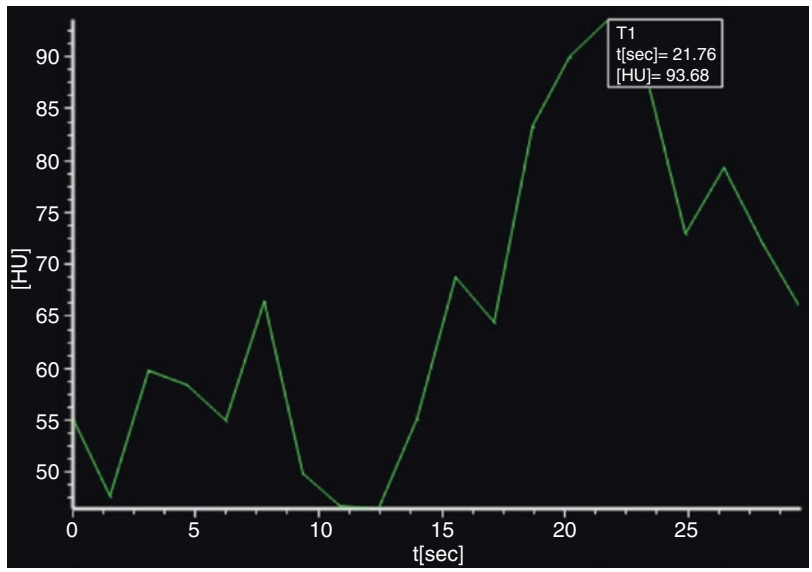

Fig. 14.47 Graph generated from bolus timing run (Fig. 14.46) showing the time of contrast arrival in aorta

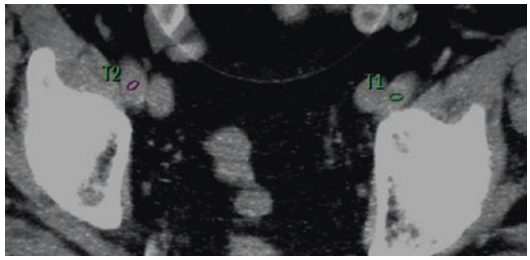

Fig. 14.48 80 KVp technique: Bolus timing run with 2 mL contrast at external iliac arteries

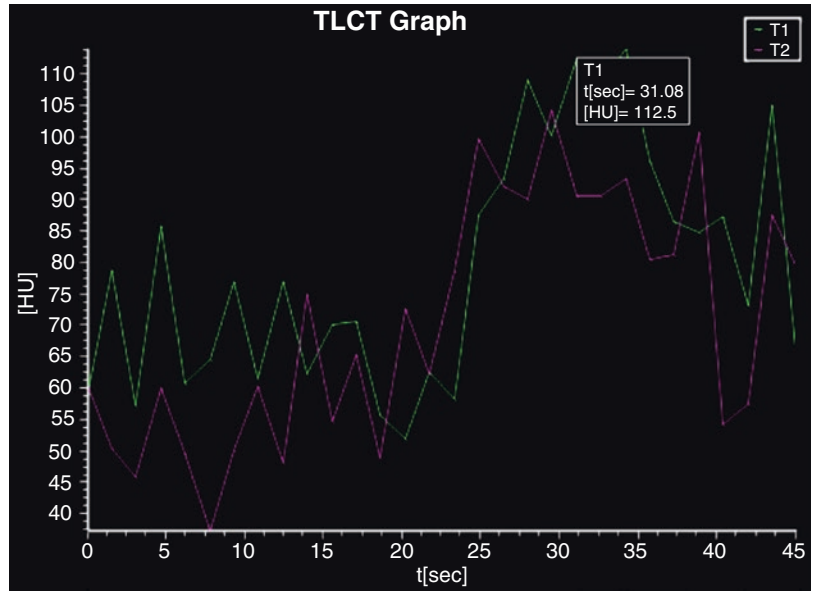

Fig. 14.49 Graph generated from bolus timing run (Fig. 14.48) showing the time of contrast arrival in iliac arteries

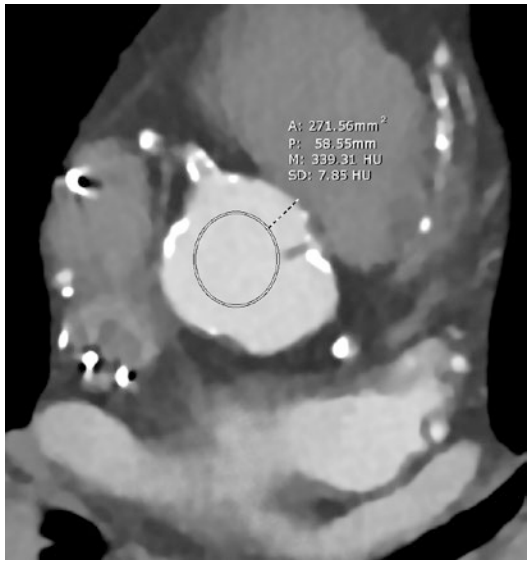

Fig. 14.50 80 KVp technique with 25 mL contrast: Contrast enhanced aortic root at sinus of Valsalva with attenuation of 339 HU

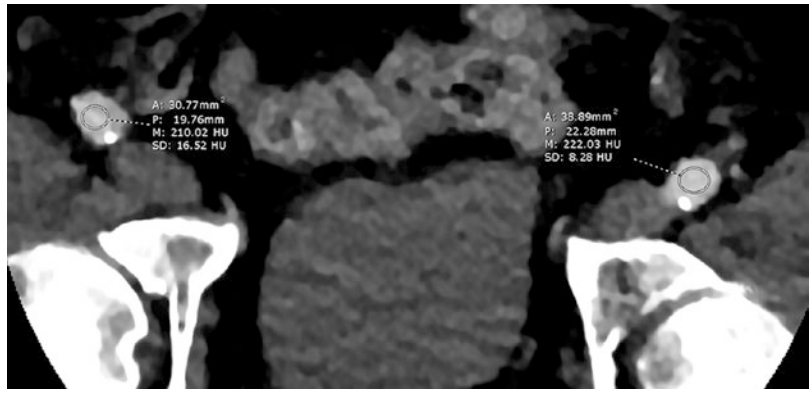

Fig. 14.51 80 KVp technique: Contrast enhanced iliac arteries with attenuation of 210 HU and 222 HU

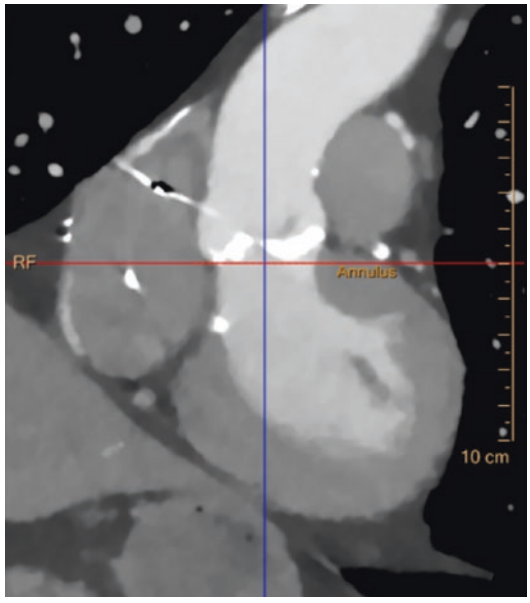

Fig. 14.52 Oblique coronal view to select appropriate axial plane for aortic annulus

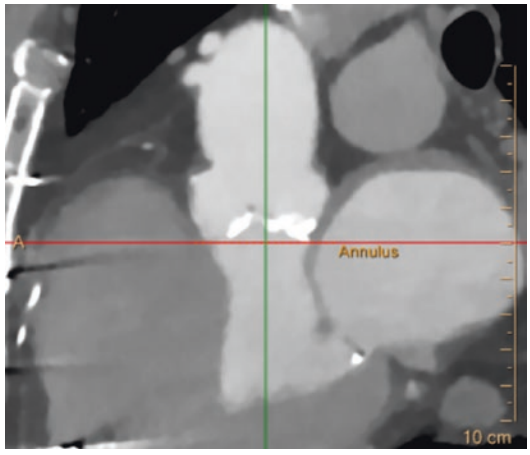

Fig. 14.53 Oblique sagittal view to select appropriate axial plane for aortic annulus

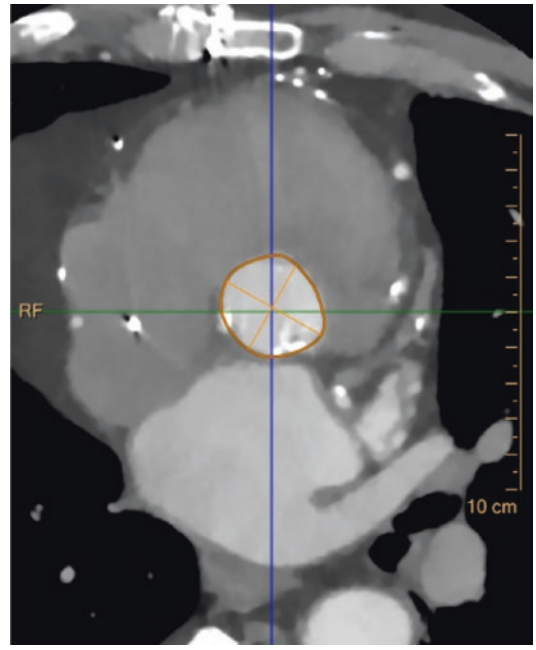

Fig. 14.54 Axial image of annulus with borders

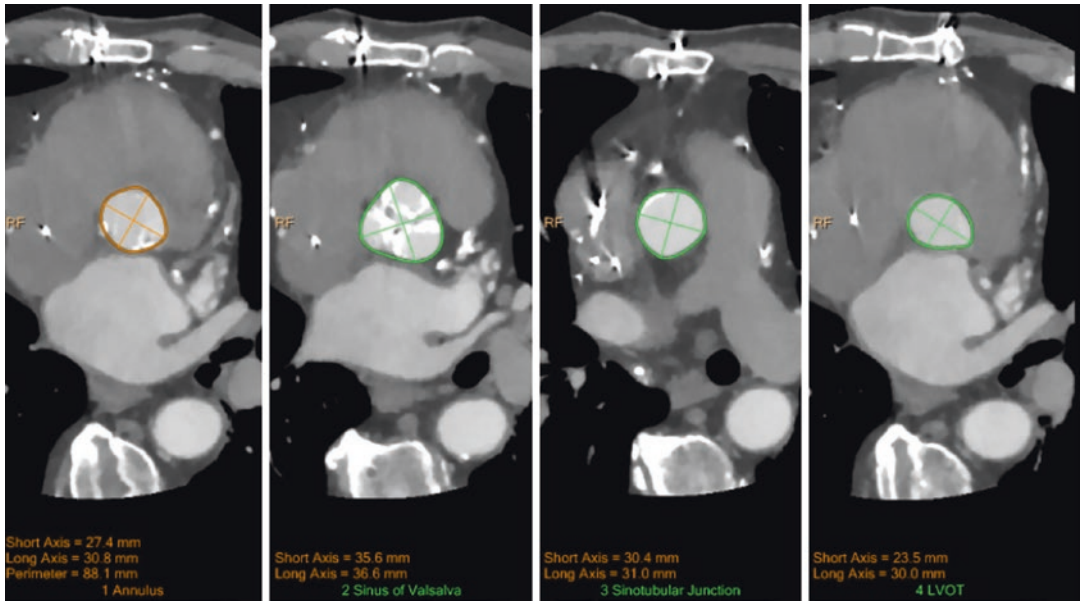

Fig. 14.55 Axial images of: annulus, sinus of Valsalva, sinotubular junction, and LVOT

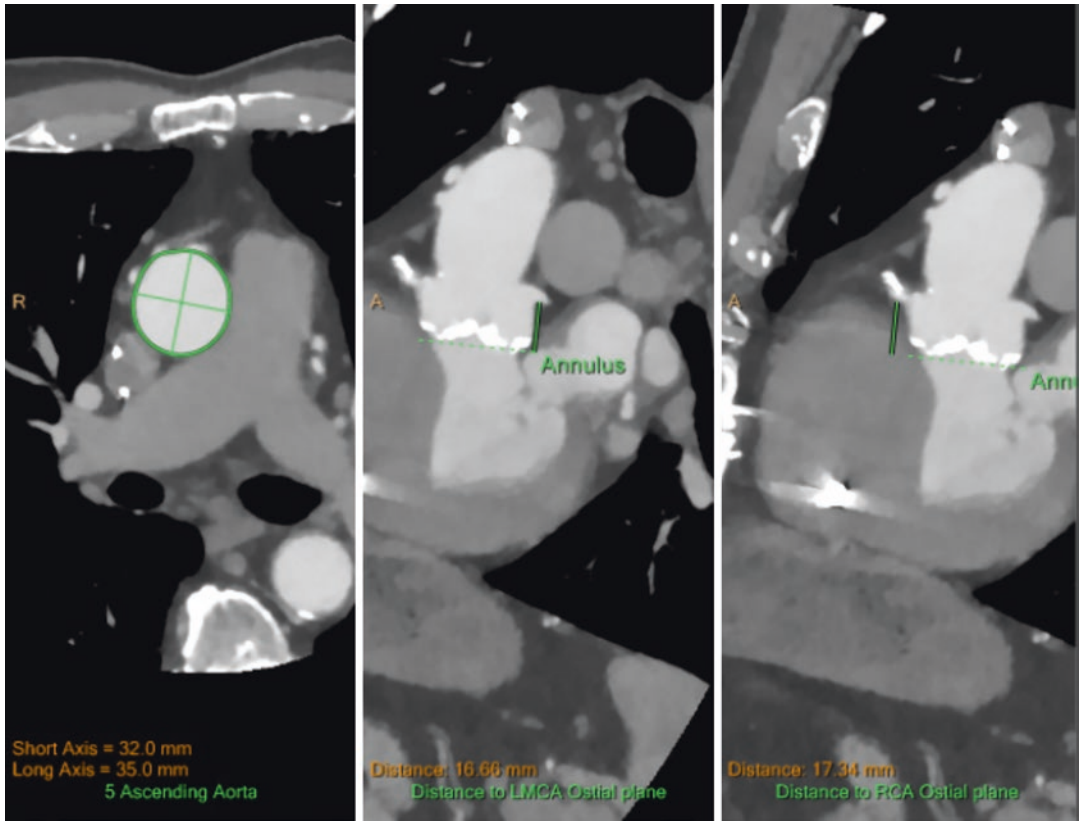

Fig. 14.56 Measurement images of: ascending aorta, and distance of LMCA and RCA from annulus

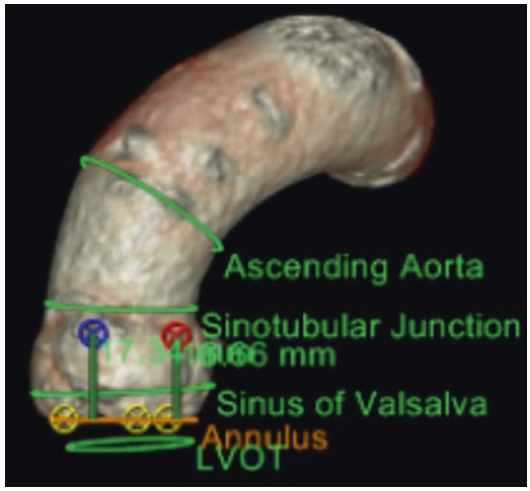

Fig. 14.57 80 KVp technique with 25 mL contrast: 3D Volume rendered image of aorta with reference levels

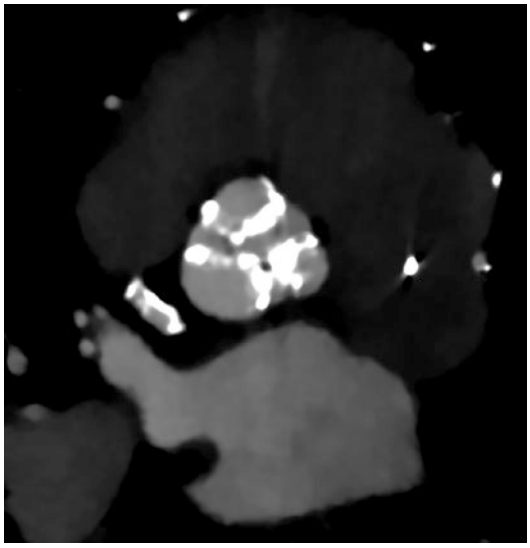

Fig. 14.58 Tricuspid aortic valve with calcification

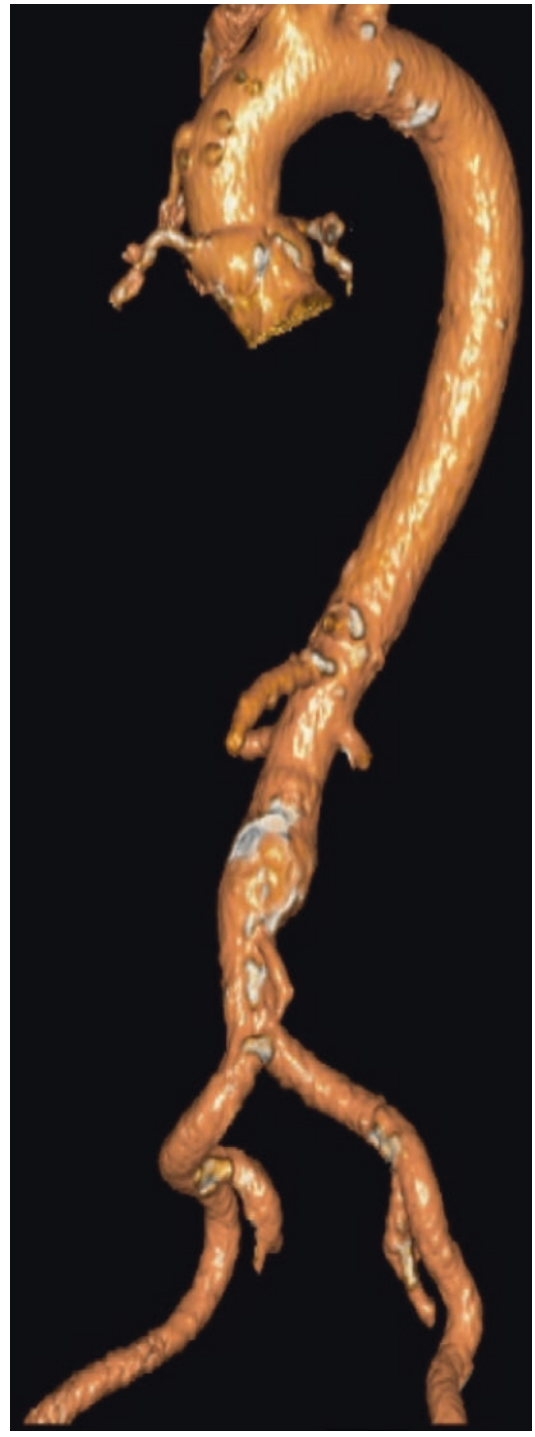

Fig. 14.59 80 KVp technique with 25 mL contrast. 3D Volume rendered image of aorta and iliac arteries

14.7.2 CT Technique

Timing run 1: 1 mL@3.5/s, saline push 20 mL@3.5/s: 22 s
Timing run 2: 2 mL@3.5/s, saline push 25 mL@3.5/s: 31 s

CT scanner: 4 cm long detector array, 128-channel MDCT
Scan coverage: Aortic arch to common femoral arteries (Single scan acquisition)
KVp 80
mAs 1260
Scan time 25 s
Scan delay 28 sec
Contrast Injection: 25 mL (10 mL@3/s + 15 mL@2/s) + saline push 30 mL@2/s

Images demonstrate diagnostic quality examination with enhancement density > 200 HU in the aortic root and iliac arteries (Figs. 14.50 and 14.51). Images acquired in standard locations and planes demonstrate aortic annulus with effective diameter of 28.4 mm. There is a trileaflet valve with moderate calcifications..

The patient was treated by implantation of 29 mm Sapien 3 valve via transfemoral approach (Fig. 14.60). Chest radiograph after TAVR demonstrates the prosthetic valve in place (Fig. 14.61).

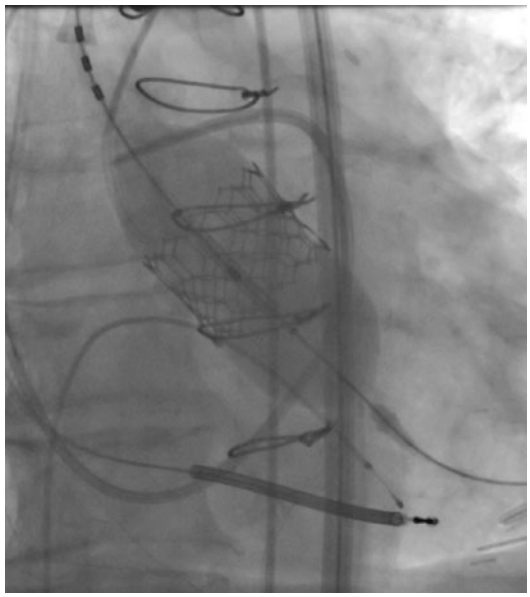

Fig. 14.60 Fluoroscopy image during placement of 29 mm Sapien 3 valve via transfemoral approach

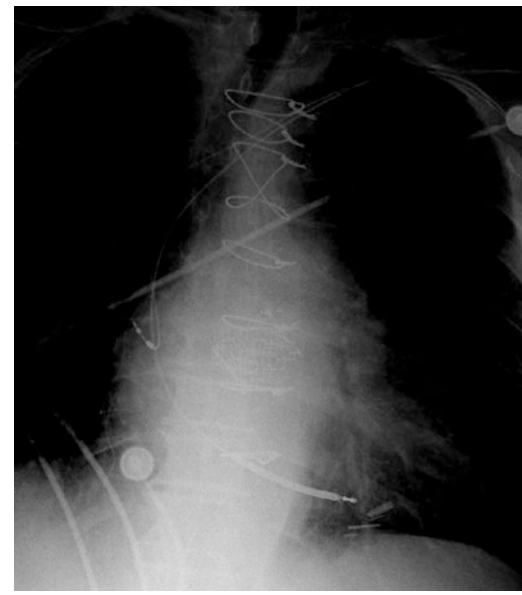

Fig. 14.61 Chest radiograph with transcatheter heart valve in place

14.7.3 Diagnosis

CTA for pre-TAVR planning with low contrast dose with good diagnostic quality.

14.7.4 Discussion

The risk of CIN must be considered relative to the potential benefits of the contrast enhanced examination. The risk of CIN is higher with larger contrast dose and the CTA examination may thus be obtained with as low a contrast dose as possible. The goal is to attain adequate contrast enhancement in the aorta and iliac arteries. For a given volume of contrast, the attenuation is higher with 80 KV compared to 120 KV. The contrast enhancement in blood vessels also depends on the volume and concentration of iodinated contrast. Use of bolus timing run helps in determining contrast arrival time and expected peak enhancement to determine appropriate time to scan (scan delay). With standard bolus triggering technique, there is a variable scan delay for the scanner to get ready to scan, usually around 4–5 s, requiring a larger volume of contrast to be injected. Bolus timing run to determine the time of contrast arrival can be used to plan the start of injection more accurately without the need for scan delay after bolus triggering.

14.7.5 Pearls and Pitfalls

The contrast injection duration is selected to be close to the scan duration. In order to achieve higher attenuation in the aorta, the time to begin CT scanning after contrast injection (scan delay) should be near the end of contrast bolus train, i.e., contrast bolus arrival time + injection duration. Due to overall higher attenuation achieved with 80 KVp, injection rate can be slower (~2 mL/s) compared to 4–5 mL/s otherwise used with 120 KVp imaging. Biphasic injection (3–3.5 mL/s followed by 2 mL/s) can be useful in achieving a higher initial attenuation which is sustained by a slower, longer injection for scan duration.

14.8 Case 7

14.8.1 History

An 85-year-old with severe symptomatic aortic stenosis and decreased renal function; for pre-TAVR evaluation CT with low contrast dose.

14.8.2 Findings

ECG-gated helical CTA examination of the chest, abdomen, and pelvis performed with total contrast volume of 34 mL with 80 KV technique (Figs. 14.62, 14.63, 14.64, 14.65, 14.66, 14.67, 14.68, 14.69, 14.70, 14.71, 14.72, 14.73, 14.74, and 14.75).

Scout image demonstrates a large patient with transverse diameter of greater than 500 cm at the level of pelvis (Fig. 14.62).

The examination was performed with 80 KVp on 8 cm long MDCT detector array (256-slice 128-channel) CT scanner. Two bolus timing runs using 1 and 2 mL in ascending aorta and in femoral arteries demonstrate time of contrast arrival at 17 s and 23 s, respectively (Figs. 14.63 and 14.64).

Two separate sets of CT images through the chest (ECG gated) (Figs. 14.65, 14.66, 14.67, 14.68, 14.69, and 14.70) and abdomen/pelvis (Figs. 14.71, 14.72, 14.73, 14.74, and 14.75) (without ECG gating) were acquired using 15 mL for chest and 16 mL for the abdomen and pelvis, respectively. CTA images through the chest are of adequate quality showing the aortic annulus area of 584 mm^2 (Fig. 14.70). There is moderate calcification in the aortic valve (Fig. 14.69). 3D VR image shows no significant tortuosity of thoracic aorta (Fig. 14.70).

The CTA images through lower abdomen and pelvis (Figs. 14.71, 14.72, 14.73, and 14.74) demonstrate good diagnostic quality with normal size of aorta and iliac arteries without significant plaque or tortuosity (Fig. 14.75).

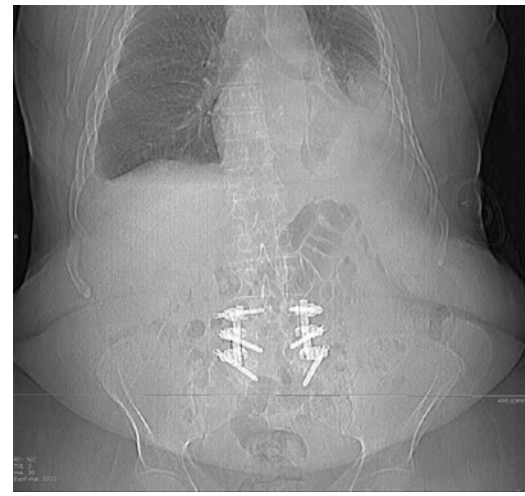

Fig. 14.62 Scout radiograph—transverse diameter of greater than 500 cm at the level of pelvis

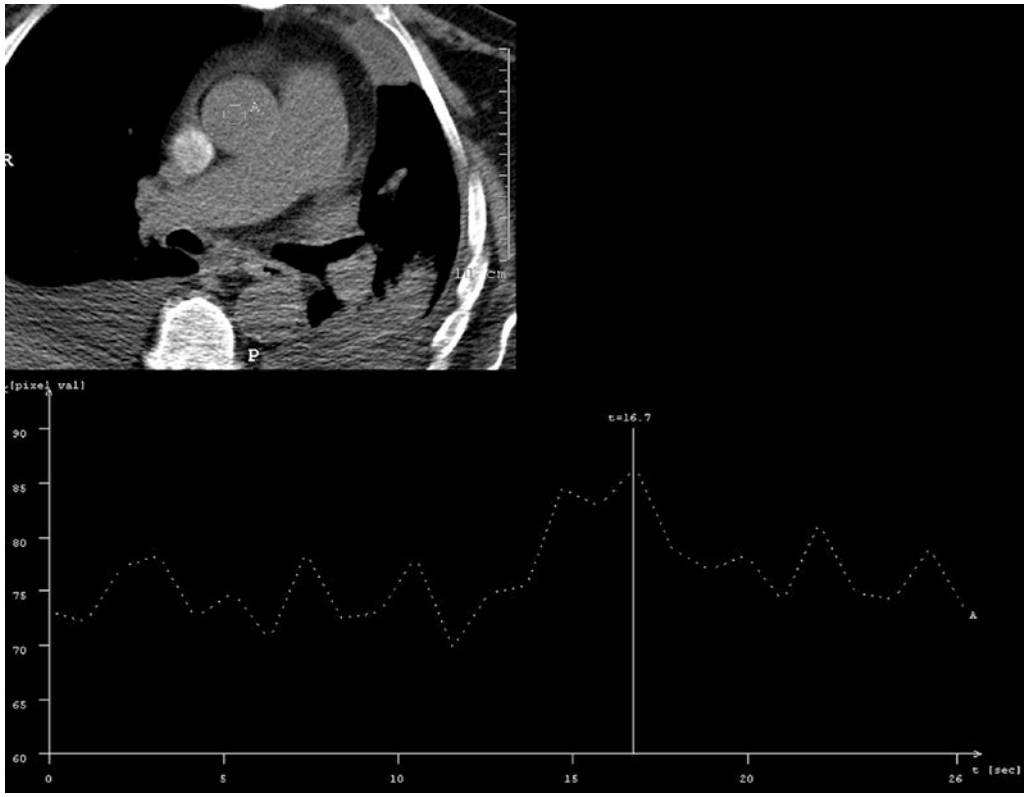

Fig. 14.63 80 KVp, 1 mL contrast. Timing run—in ascending aorta

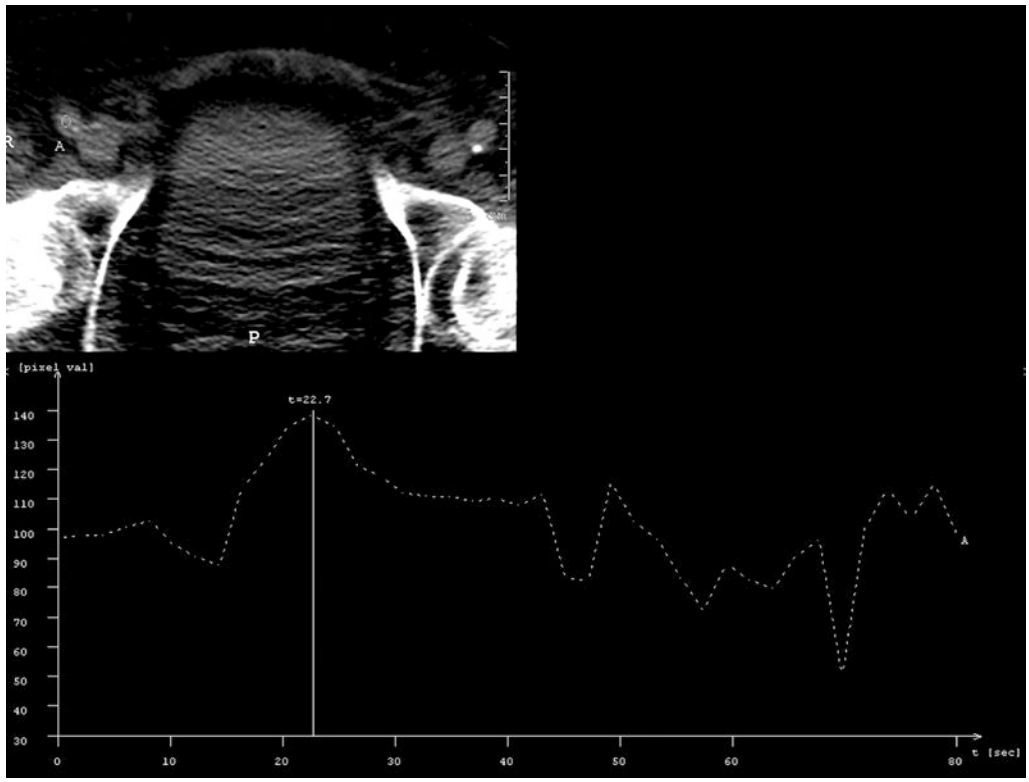

Fig. 14.64 80 KVp, 2 mL contrast. Timing run—in femoral arteries

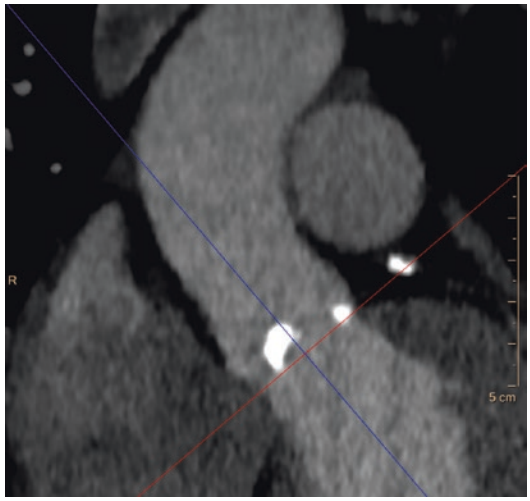

Fig. 14.65 Oblique coronal view for selection of aortic annulus plane

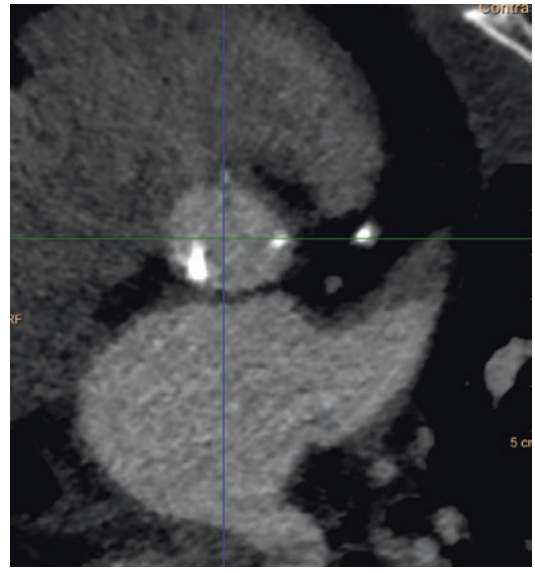

Fig. 14.67 KVp 80, mAs 1650, ECG gated: 15 mL contrast for chest. Aortic valve annulus

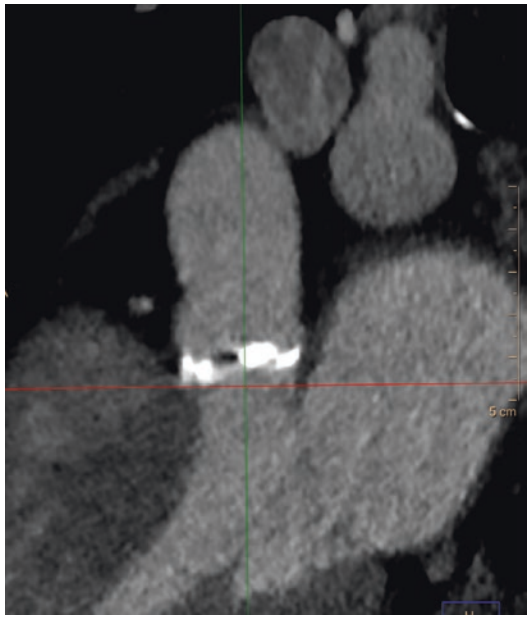

Fig. 14.66 Oblique sagittal view for selection of aortic annulus plane

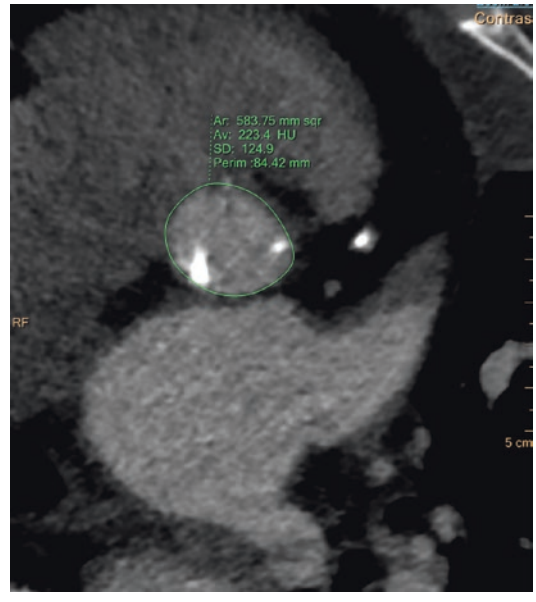

Fig. 14.68 Aortic annulus area measured with annulus area of 583.75 mm sq

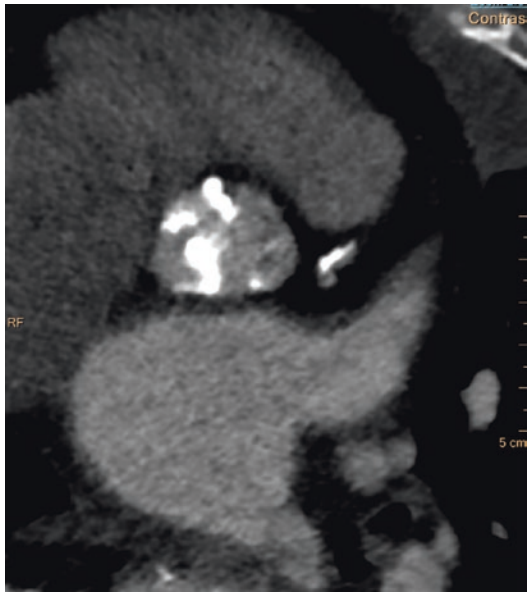

Fig. 14.69 Aortic Valve with moderate calcification

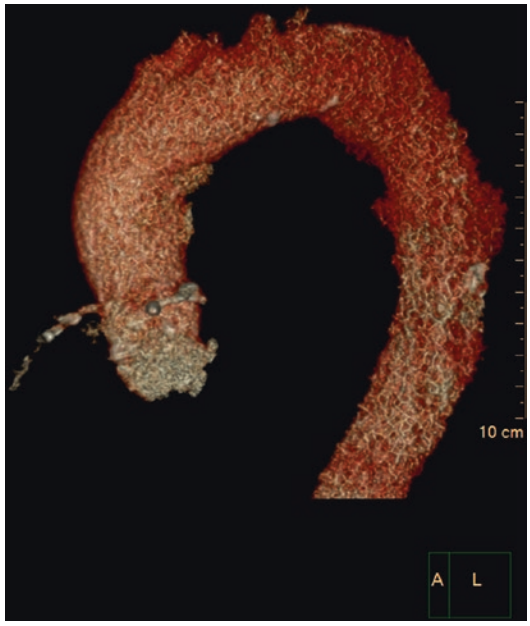

Fig. 14.70 80 KVp, 15 mL contrast. 3D VR: thoracic aorta

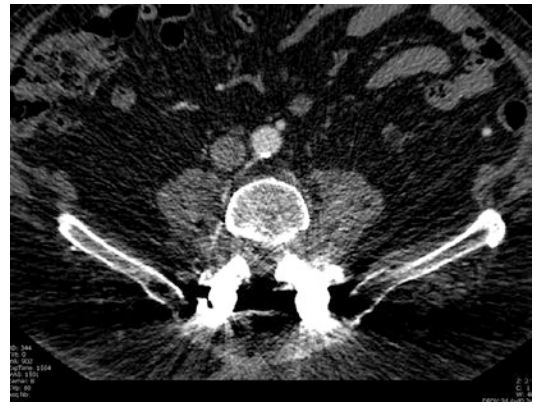

Fig. 14.71 80 KVp, 16 mL contrast for abdomen and pelvis: axial image, infrarenal aorta, metallic hardware in spine

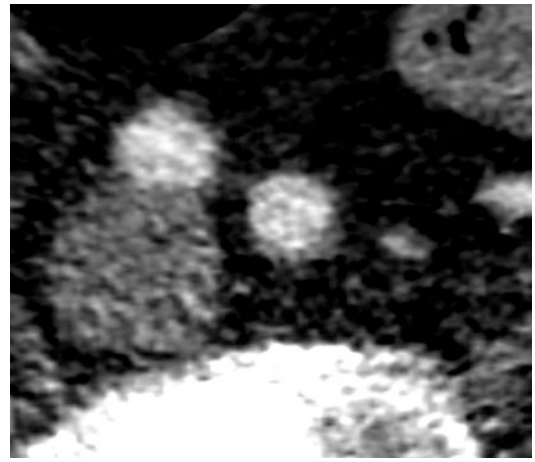

Fig. 14.72 Axial image: Adequately enhanced common iliac arteries

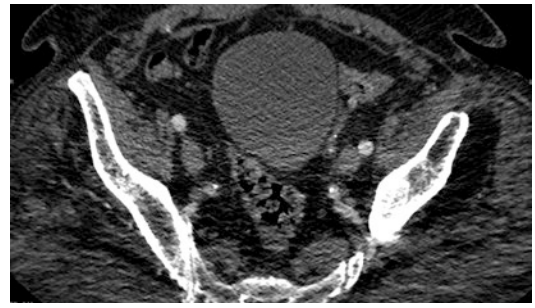

Fig. 14.73 Axial image: Adequately enhanced external iliac arteries

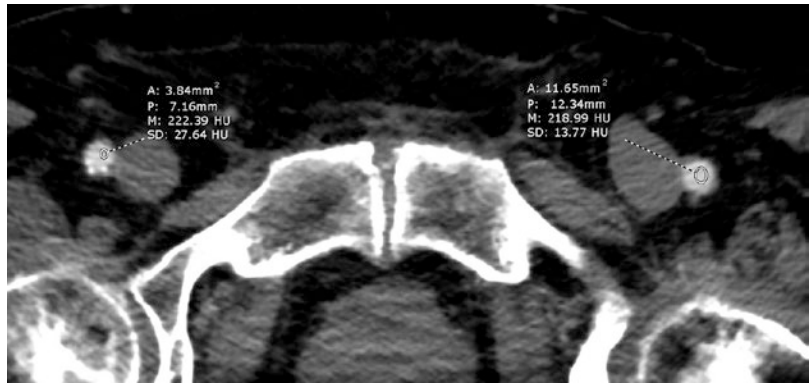

Fig. 14.74 Axial image. Adequately enhanced femoral arteries

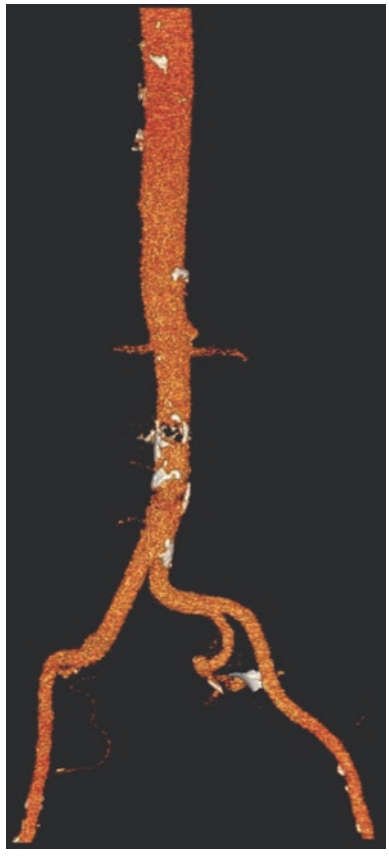

Fig. 14.75 KVp 80, mAs 1500, Non-gated. 16 mL contrast. 3D VR. Abdominal aorta without tortuosity and mild to moderately tortuous iliac arteries

14.8.3 Diagnosis

CTA with adequate quality for pre-procedure evaluation of TAVR with low contrast dose.

14.8.4 Discussion

The patient is of large size and has metallic hardware in the spine. Factors affecting contrast enhancement in aorta include patient size and there is decreased enhancement with higher body mass index (BMI). Use of imaging with 80 KV will increase the contrast enhancement for a given contrast dose. However, low KV is associated with higher noise, which is to be compensated by increasing the tube current by several fold and this can become a limiting factor particularly in large patients. ECG-gated imaging requires even higher tube current for optimal image quality compared to non-gated imaging. In this case with large patient size and imaging with 80 KVp, there is high noise in the ECG-gated images. However, as CTA utilizes high contrast resolution, diagnostic quality can still be obtained with relatively high noise compared to low contrast resolution needed for imaging of viscera or other extravascular soft tissues.

For the second set of images through the abdomen and pelvis, a high tube current (1500 mAs) was possible due to non-gated imaging over a shorter distance (abdomen and pelvis compared to combined chest, abdomen, and pelvis) which is able to provide good image quality with low noise (<25 HU) even with large patient size and metal in spine. Adequate density of contrast enhancement in the arteries was achieved with only 15–16 mL contrast due to 80 KV and optimal timing using bolus timing run.

14.8.5 Pearls and Pitfalls

Image noise is decreased with higher tube current for a given tube voltage. Newer image reconstruction techniques utilizing iterative techniques and iterative model based reconstruction are very helpful in reducing noise. The image noise can also be reduced with the use of a smooth filter (soft tissue) compared to a high resolution filter (cardiac), which may not be necessary in case of imaging of large vessels such as aorta.

14.9 Case 8

14.9.1 History

A 77-year-old with failed prosthetic aortic valve and decreased renal function for pre-TAVR evaluation CT with low contrast dose.

14.9.2 Findings

CTA performed with a total of 28 mL intravenous contrast dose using two separate image acquisitions demonstrates adequate image quality for assessment of aortic root including the bioprosthetic valve and aorta and iliac arteries.

14.9.3 Technique

Two timing bolus runs using 1 mL contrast each were performed. Two separate contrast injections using 17 mL and 9 mL contrast were used for two separate CT imaging through chest (ECG gated) and abdomen/pelvis (non-gated), respectively.

Timing run 1: 1 mL@3.5/s, saline 20 mL@3.5/s: 18 s
Timing run 2: 1 mL@3.5/s, saline 25 mL@3.5/s: 23 s

CTA Chest:
Helical ECG gated
KVp 80
mAs 1525
Scan time 5 s
17 mL (7 mL@3.5/s, 10 mL@2/s) + NS 30 mL@2/s

CTA Abdomen and Pelvis:
Helical non-gated
KVp 80
mAs 615
Scan time 5 s
Contrast: 9 mL (3 mL@3/s, 6 mL@2/s) + NS 20 mL@2/s

The images demonstrate adequate image quality with density of greater than 200 HU in the aortic root (Figs. 14.76, 14.77, 14.78, 14.79, 14.80, 14.81, 14.82, 14.83, 14.84, 14.85, 14.86, and 14.87). The density in iliac arteries is less than 200 HU but adequate for diagnosis. There is bioprosthetic valve in place. The virtual ring drawn at the superior margin of the posts shows a relatively spacious sinus with ring to left coronary artery ostium distance of 7 mm placing this at low risk for coronary occlusion.

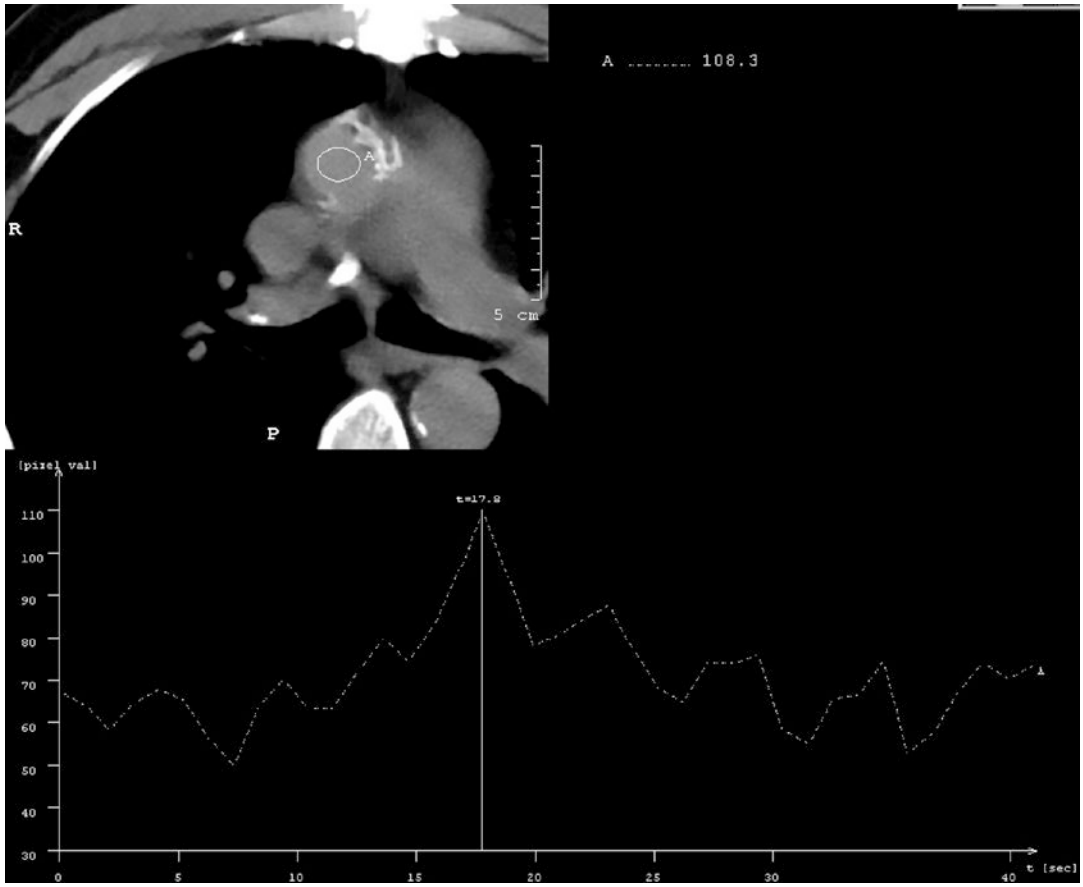

Fig. 14.76 80 KVp technique: Bolus timing run with 1 mL at ascending aorta with attenuation curve showing peak enhancement at 18 s

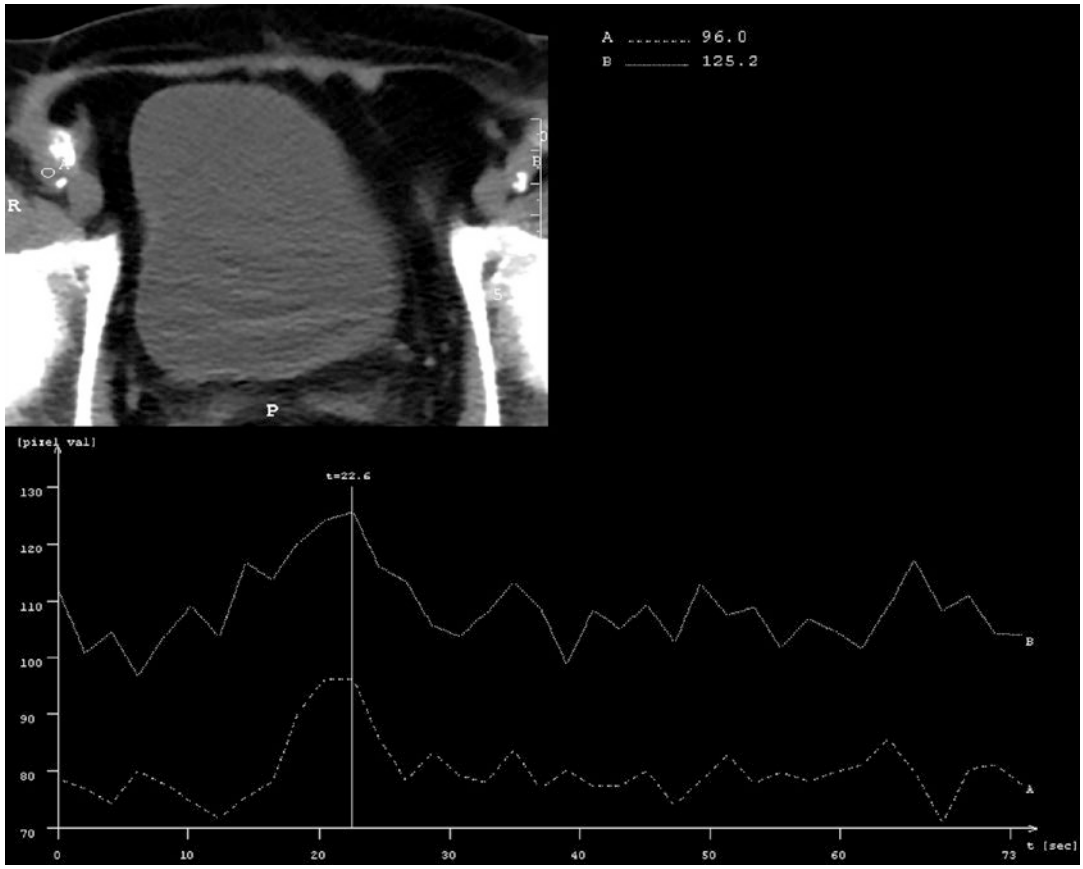

Fig. 14.77 80 KVp technique: Bolus timing run with 1 mL at iliac arteries/graft with attenuation curve showing peak enhancement at 23 s

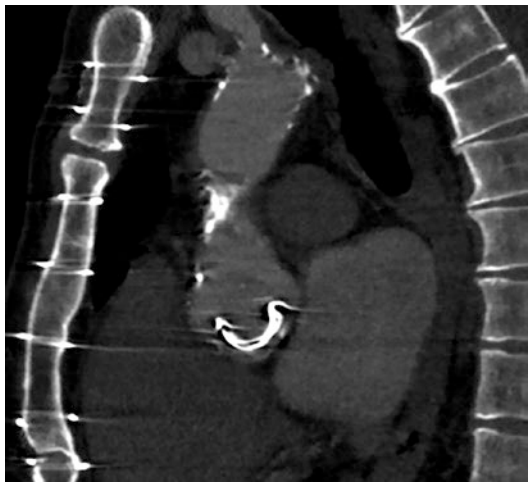

Fig. 14.78 Sagittal view of contrast enhanced aorta showing prosthetic valve

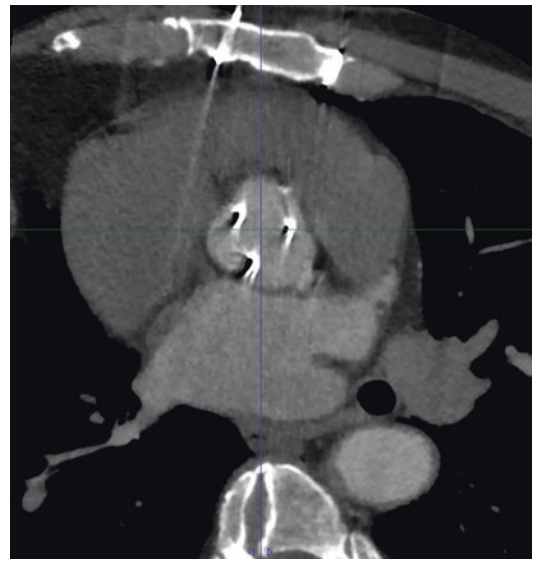

Fig. 14.79 80 KVp technique. 17 mL contrast. Axial view: adequately enhanced aortic root with bioprosthetic valve

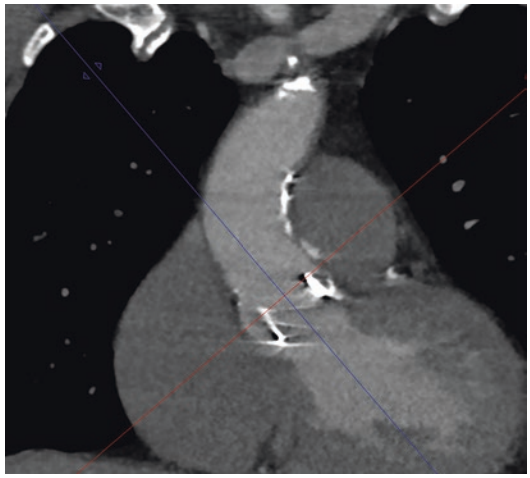

Fig. 14.80 Coronal view for reference level of axial image

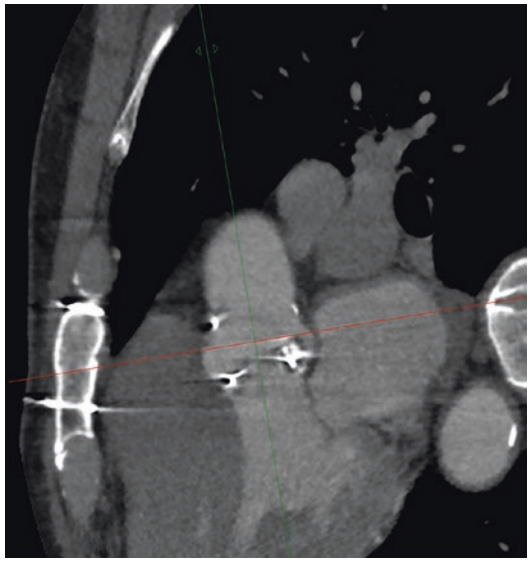

Fig. 14.81 Sagittal view for reference level of axial image

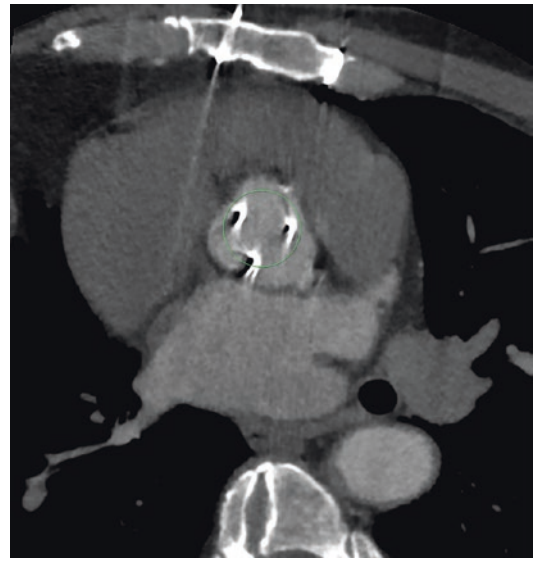

Fig. 14.82 Axial image at superior margin of valve posts with virtual ring

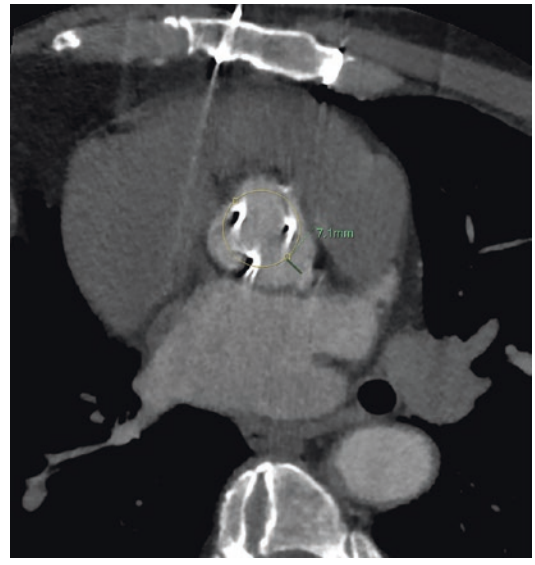

Fig. 14.83 Axial image at superior margin of valve posts with virtual ring, 7 mm from LMCA ostium

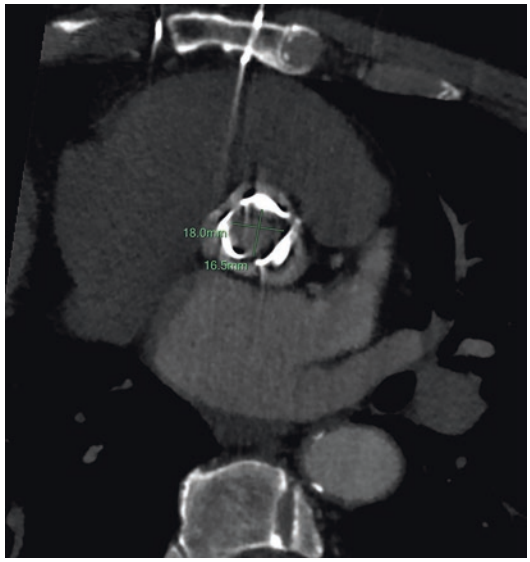

Fig. 14.84 Aortic annulus with bioprosthetic valve in place with luminal measurements

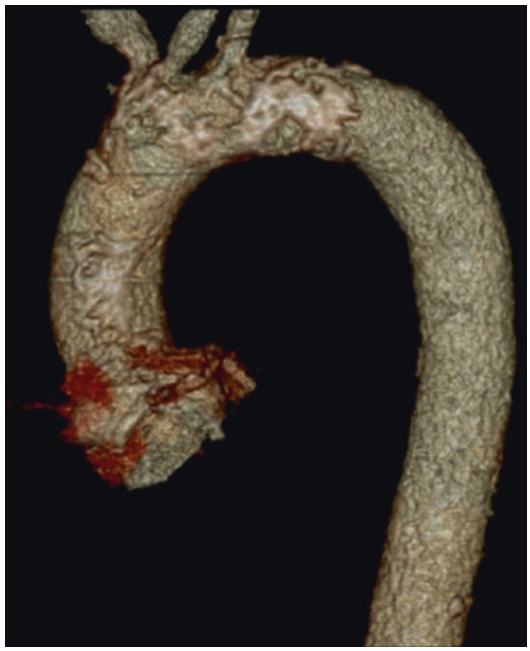

Fig. 14.85 80 KVp technique with 17 mL contrast. 3D VR: thoracic aorta

The CTA images for aortoiliac arteries demonstrate aorto-bifemoral bypass graft (Fig. 14.86). The lumen of the iliac artery graft is small with the diameter measuring less than 5 mm bilaterally (Fig. 14.87).

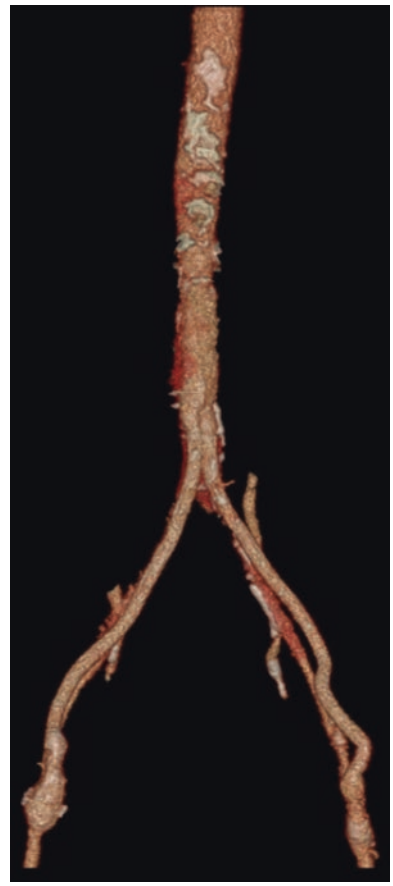

Fig. 14.86 80 KVp technique with 9 mL contrast. 3D VR: Abdominal aorto-biiliac bypass graft

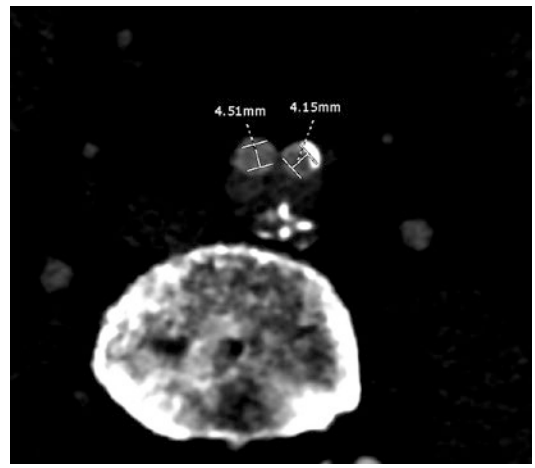

Fig. 14.87 Axial image: Lumen of the bilateral iliac artery graft less than 5 mm

14.9.4 Diagnosis

CTA for pre-TAVR assessment with low contrast dose. Bioprosthetic valve with inner luminal diameter of 17.3 mm.

Small caliber of iliac arteries (aorto-biiliac graft); not suitable for transfemoral access.

14.9.5 Discussion

The use of timing runs allows for small volume of contrast used in determining the volume of contrast to match with scan duration, without the need for additional scan delay after bolus trigger. The use of two timing runs helps in assessing the time during which contrast will be expected to be present in arteries if the injection train is long enough for that time. The time difference of only 4 s between time of contrast arrival in aortic root and femoral arteries allows for a very small contrast dose particularly for non-gated scan through the pelvis. The image quality is adequate even with only 9 mL contrast for imaging of pelvis due to 80 KVp technique with high mAs, rapid blood flow with short scan time, iterative image reconstruction, and overall small patient size.

Due to small caliber of iliac vessels, TAVR was performed via cardiac transapical approach and 23 mm Edwards Sapien valve was implanted within the preexisting bioprosthetic valve (Figs. 14.88 and 14.89).

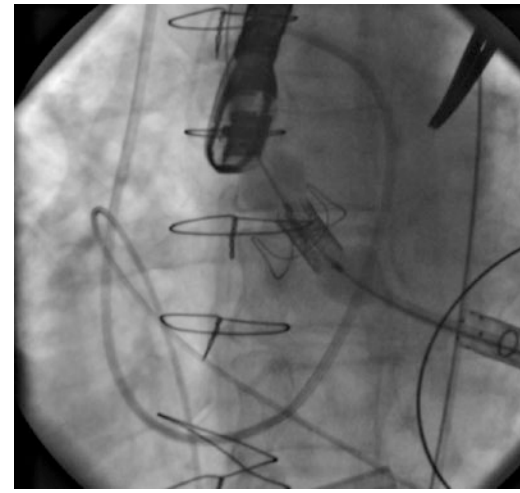

Fig. 14.88 Fluoroscopy image during implantation of 23 mm Edwards Sapien valve via transapical approach

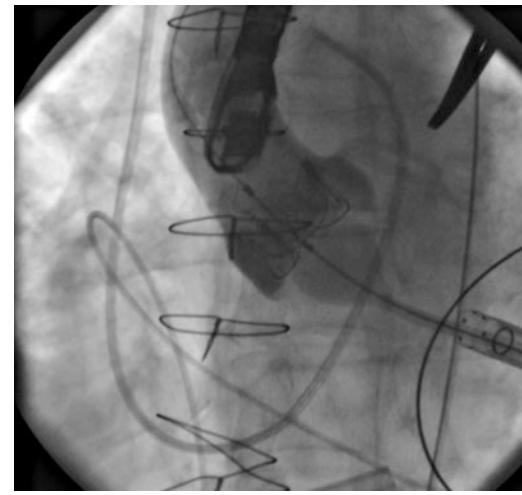

Fig. 14.89 Angiogram showing valve-in-valve implantation of 23 mm Edwards Sapien valve via transapical approach

14.9.6 Pearls and Pitfalls

For a given scan area coverage, the scan time for ECG-gated CTA is longer than the non-gated exam due to low pitch which will require longer contrast injection. To reduce scan time for ECG-gated component, imaging can be tailored to scan only the aortic root with ECG-gated exam and the rest of the area with a separate scan without ECG gating.

Further Reading

Bloomfield GS, Gillam LD, Hahn RT, Kapadia S, Leipsic J, Lerakis S, Tuzcu M, Douglas PS. A practical guide to multimodality imaging of transcatheter aortic valve replacement. JACC Cardiovasc Imaging. 2012;5(4):441–55.

de Heer LM, Habets J, Kluin J, Stella PR, Mali WP, van Herwerden LA, Budde RP. Assessment of a transcatheter heart valve prosthesis with multidetector computed tomography: in vitro and in vivo imaging characteristics. Int J Cardiovasc Imaging. 2013;29(3):659–68.

Delgado V, Kapadia S, Schalij MJ, Schuijf JD, Tuzcu EM, Bax JJ. Transcatheter aortic valve implantation: implications of multimodality imaging in patient selection, procedural guidance, and outcomes. Heart. 2012;98(9):743–54.

Dvir D, Leipsic J, Blanke P, Ribeiro HB, Kornowski R, Pichard A, Rodés-Cabau J, Wood DA, Stub D, Ben-Dor I, Maluenda G, Makkar RR, Webb JG. Coronary obstruction in transcatheter aortic valve-in-valve implantation: preprocedural evaluation, device selection, protection, and treatment. Circ Cardiovasc Interv. 2015;8(1)

Gurvitch R, Wood DA, Leipsic J, Tay E, Johnson M, Ye J, Nietlispach F, Wijesinghe N, Cheung A, Webb JG. Multislice computed tomography for prediction of optimal angiographic deployment projections during transcatheter aortic valve implantation. JACC Cardiovasc Interv. 2010;3(11):1157–65.

Kalva SP, Sahani DV, Hahn PF, Saini S. Using the K-edge to improve contrast conspicuity and to lower radiation dose with a 16-MDCT: a phantom and human study. J Comput Assist Tomogr. 2006;30(3):391–7.

Kurra V, Kapadia SR, Tuzcu EM, Halliburton SS, Svensson L, Roselli EE, Schoenhagen P. Preprocedural imaging of aortic root orientation and dimensions: comparison between X-ray angiographic planar imaging and 3-dimensional multidetector row computed tomography. JACC Cardiovasc Interv. 2010;3(1):105–13.

Leipsic J, Gurvitch R, Labounty TM, Min JK, Wood D, Johnson M, Ajlan AM, Wijesinghe N, Webb JG. Multidetector computed tomography in transcatheter aortic valve implantation. JACC Cardiovasc Imaging. 2011;4(4):416–29.

Leipsic J, Wood D, Manders D, Nietlispach F, Masson JB, Mayo J, Al-Bugami S, Webb JG. The evolving role of MDCT in transcatheter aortic valve replacement: a radiologists' perspective. AJR Am J Roentgenol. 2009;193(3):W214–9.

Mylotte D, Lefevre T, Søndergaard L, et al. Transcatheter aortic valve replacement in bicuspid aortic valve disease. J Am Coll Cardiol. 2014;64(22):2330–9.

Index

C. Smuclovisky (ed.), *Coronary Artery CTA*, https://doi.org/10.1007/978-3-319-66988-5